USING MATHEMATICAL MODELLING TO UNDERSTAND HOW PLANT CELL GROWTH IS CONTROLLED

by

EUAN THOMAS SMITHERS

A thesis submitted to
The University of Birmingham
for the degree of
DOCTOR OF PHILOSOPHY

School of Mathematics
College of Engineering and Physical Sciences
The University of Birmingham
March 13, 2022

UNIVERSITY OF
BIRMINGHAM

University of Birmingham Research Archive

e-theses repository

This unpublished thesis/dissertation is copyright of the author and/or third parties. The intellectual property rights of the author or third parties in respect of this work are as defined by The Copyright Designs and Patents Act 1988 or as modified by any successor legislation.

Any use made of information contained in this thesis/dissertation must be in accordance with that legislation and must be properly acknowledged. Further distribution or reproduction in any format is prohibited without the permission of the copyright holder.

Abstract

Understanding plant growth is essential for a future sustainable world and to ensure food security. With a growing population there will be an increasing need for higher crop yields as well as plants that can cope with the problems that climate change will bring. Plants are also fascinatingly complex, which have many intertwining mechanical and chemical processes, with many pathways yet to be fully unravelled.

To investigate cell growth control, first on the microscale, we derive and analyse a simple mathematical model for the effective mechanical properties of the evolving cell wall network, incorporating cellulose microfibres, which reorient with cell growth and are linked via biological hotspots made up of regions of crosslinking hemicellulose. Assuming a visco-elastic response for the cell wall and using a continuum approach, we calculate the total stress resultant of the cell wall for a given overall growth rate. By changing appropriate parameters effecting the breakage rate and viscous properties, we provide evidence for this biological hotspot hypothesis and develop a mechanistic understanding of how these enzymes work. Next, to investigate pavement cell development, a joint experimental and theoretical approach is taken. Using GFP transgenic and Atomic force microscopy, signs of chemical initiation were observed, with actin cytoskeleton observations contracting some previous studies. We combine a stochastic microtubule model, a reaction-diffusion model for the signalling processes, and a vertex-element mechanical growth model to form a novel hybrid model for pavement cell development incorporating effects at multiple spatial and time scales. Model simulations demonstrate that the currently hypothesised signalling network can reinforce but not initiate lobe formation. Lobe initiation could be generated through spatial variations in mechanical properties, differential growth rates between neighbouring cells or a buckling mechanism when growth is restricted. We conclude by discussing these results in the context of current biological research.

Acknowledgements

Firstly, I would like to greatly thank my PhD supervisors Dr Rosemary Dyson, Dr Galane Luo, and Professor Dave Smith. Your wisdom and support have been invaluable to me.

Secondly, I wish to thank Dr Siobhan Braybrook, who helped me get and supervised me during my UCLA lab placement. Your expertise and my experience in your research group were both very stimulating and good fun.

Thirdly, I need to acknowledge the great help of my fellow PhD student, particularly (in no particular order) Cara Neal, Atticus Hall-McNair, Dr John Ellis, and Alexander Brune.

I wish to also thank both EPSRC for funding my PhD and the Company of Biologists for funding my research placement at UCLA with Dr Siobhan Braybrook.

Lastly, I would like to thank the tremendous support from my family and partner.

Contents

0.1 List of terms 1

1 Introduction **3**

1.1 The world of plants 4

1.1.1 Plant cell basics 4

1.1.2 The mechanics of cell wall growth 8

1.2 Aims, methodology and thesis structure 11

2 Preliminaries **15**

2.1 Biological background 16

2.1.1 Cell wall structure, enzyme action and biological hotspots 16

2.1.2 Microtubule dynamics 18

2.1.3 Experimental background 21

2.1.4 Pavement cells and their development 22

2.2 Previous modelling 34

2.2.1 Wall growth models, understanding the cell wall structure and its components 34

2.2.2 Mathematical models to understand microtubule behaviour 38

2.2.3 Pavement cell development models 41

2.3 Summary 44

3 Enzyme action and cell wall structure **45**

3.1 Introduction and aims 46

3.2 Model formulation 47
3.2.1 Model assumptions and set up 47
3.2.2 Principal equations 50
3.2.3 Nondimensionalisation 56
3.3 Model analysis 58
3.3.1 Semi-analytical solutions 58
3.3.2 Leading-order cell wall behaviour 61
3.4 Results and discussion 65
3.4.1 Cell wall structural implications 65
3.4.2 Enzyme action on the cell wall 69
3.4.3 Closing remarks and future work 72
3.5 Conclusion and summary 75

4 Experimental methods to understand pavement cell development 77
4.1 Introduction and experimental aims 78
4.2 Experimental methods 79
4.2.1 Plant seeding and maintenance 79
4.2.2 Imaging pavement cells 80
4.2.3 Image processing 84
4.2.4 Atomic force microscopy 85
4.3 Experimental results and discussion 87
4.3.1 Pavement cell outlines 88
4.3.2 The microtubule cytoskeleton 89
4.3.3 The actin cytoskeleton 91
4.3.4 Atomic force microscopy results 94
4.4 Summary 97

5 Building and validating a microtubule stochastic model 98
5.1 Introduction 99

5.2 Model set up, assumptions and analysis methods . . . 100
5.2.1 Microtubule model implementation principles . . . 100
5.2.2 Model analysis methods . . . 104
5.3 Model parameters . . . 106
5.4 Microtubule model results, validation and discussion . . . 108
5.4.1 Square domain simulations . . . 109
5.4.2 Rectangular domain simulations . . . 114
5.4.3 Pavement cell simulations . . . 119
5.5 Microtubule model conclusions, further remarks and summary . . . 123

6 Getting to know the ROPS: a partial differentiable reaction diffusion system to understand pavement cell signalling pathways 125

6.1 Introduction . . . 126
6.2 Mathematical preliminaries . . . 127
6.3 Signalling protein and microtubule network model outline and description . 128
6.4 Solving the system and the model implementation . . . 131
6.4.1 Solving the reaction diffusion equations . . . 132
6.4.2 ROP6 boundary conditions . . . 142
6.4.3 Solving the RIC1 equation . . . 144
6.4.4 Combining the reaction diffusion system with the microtubule network 145
6.4.5 Model parameters . . . 149
6.5 Results and discussion . . . 149
6.5.1 Testing the signalling protein and microtubule network localisation establishment . . . 151
6.5.2 The signalling network in mutant pavement cells . . . 153
6.5.3 Can the signalling network initiate lobes? . . . 164
6.6 Concluding remarks . . . 169

7 A visco-elastic vertex element model to simulate pavement cell growth 173

7.1 Introduction . . . 174
7.2 Vertex element modelling of pavement cell growth . . . 175
7.2.1 Setting up the vertex element model . . . 175
7.2.2 Discretisation . . . 178
7.2.3 Nondimensionlisation . . . 185
7.2.4 Fixing the parameters and using the signalling protein and microtubule dynamics results to influence their values . . . 186
7.2.5 Numerical implementation . . . 190
7.3 Results and Discussion . . . 199
7.3.1 Pavement cell lobe development . . . 200
7.3.2 Lobe initiation strategies . . . 206
7.4 Concluding remarks . . . 214

8 Conclusion **218**

A Appendix **222**

A.1 Biological hotspots . . . 223
A.1.1 Proving constant density . . . 223
A.1.2 Solving stress terms . . . 223
A.1.3 Solving the evolving bond densities . . . 226
A.1.4 Solving the cellulose angle equation . . . 227
A.1.5 Asympototic expansion . . . 229
A.2 Experimental methods to understand pavement cell development . . . 242
A.2.1 Pavement cell shape extraction . . . 242
A.2.2 Atomic force microscopy: Hertzian indentation model . . . 245
A.3 Microtubule model . . . 246
A.3.1 Microtubule model implementation details . . . 246
A.3.2 Order parameter calculation . . . 251
A.3.3 Microtubule pavement cell simulations . . . 252

A.3.4 Calculating the lobe and indent indicator function, $\tilde{\kappa}$ 252
A.4 Reaction diffusion 255
A.4.1 Estimating model parameters 255
A.4.2 Testing the signalling protein and microtubule network localisation establishment additional figures 257
A.4.3 The signalling network in mutant pavement cells additional figures . 267
A.4.4 Can the signalling network initiate lobes? additional figures 334
A.5 Vertex element model 361
A.5.1 Mesh testing 361
A.5.2 Relative aspect ratio pavement cell calculation 364

Bibliography **366**

List of Figures

1.1 The features of interest in a plant cell 5

1.2 Depiction of the consequence of cellulose alignment on cell growth where the thick solid line represent the cell boundaries and the dotted lines represent cellulose molecules embedded in the cell wall 10

1.3 Prodendium iodide stained *Arabidopsis thaliana* pavement cells showing how their puzzle like shapes develop as they grow 13

2.1 Diagram depicting current understanding of pavement cell development . . 23

2.2 Inhibition and stimulation relationships in pavement cell devlopment . . . 32

3.1 A segment of the cell wall. The two curved (light blue) surfaces are the two boundaries for the cell wall. The thick (purple) rods represent the cellulose molecules, and the groups of thin (orange) fibres represent the hotspots where both become increasingly stretched as they traverse to the outside of the cell. The equation (3.2.1) imposes this movement and deformation in the model's domain of the x-y plane. 49

3.2 Depiction of a single unit of the continuum model with the cellulose (see A) and hotspot (see B) contributions to the stress joined in parallel. The hotspot stress $\tilde{\sigma}_H^*$ arises from a collection of hemicelluloses represented as maxwell elements, crosslinked with bond density n^* (where the yellow star represents a bond breakage). The cellulose stress σ_C^* is represented by a box that resists the strain elastically proportionally to the cellulose's angle θ. The whole unit's stress is then dependant on the biological hotspot density $\tilde{n}^*$ such that when it is zero, the only contribution is coming from cellulose crosslinked by other molecules. 51

3.3 The effect on the stress resultant of expansin acting on (a) the resting length, L_0; or (b) the viscosity, μ, where the small (large) a_1 value represents reduced (enhanced) cellulose crosslinking by the BHs. Other parameters: $\tilde{\beta} = 0.01$ and $\gamma = 0.05$. 70

3.4 The effect on the BH density of expansin acting on (a) the resting length, L_0; or (b) the viscosity, μ, with $\alpha = 5$, $\tilde{\beta} = 0.01$ and $\gamma = 0.05$. 71

3.5 Enzyme cutting action with $\tilde{\beta}$ and γ representing cel12a and XTH's action respectively on (a) the stress resultant with $\alpha = 50$ and (b) XTH's action on the BH density $\tilde{n}$ with $\beta = 0.1$ and $\alpha = 10$. 72

3.6 The effect of varying (a) Cel12a's action with $\alpha = 10$ and (b) α with $\tilde{\beta} = 0.01$, on the BH bond density $\tilde{n}$, both with $\gamma = 0.05$. 73

3.7 Changes in the stress resultant as we affect the cellulose fibre orientation by changing (a) the time point and (b) θ_0 with $\beta = 0.01$ and $\gamma = 0.05$. . . 73

3.8 Comparison between the axial stress resultant's numerical solution (solid line) to our asymptotic approximations, equation (3.3.19)-(3.3.21) (dashed line) and equation (3.3.22) (dotted line) both plotted for different values of $\tilde{\beta}$ and γ. 74

3.9 Hypothesised enzyme action. The purple rods represent cellulose molecules, and the red rods are the hemicellulose fibres in a hotspot. a) XTH hydrolysis action only cutting a select amount of hemicellulose fibres. b) Cel12A hydrolysis action cutting the whole hotspot. c) Expansin loosening action allowing the hotspot to be intact while allowing extension. 75

4.1 Pavement cells with PI stained cells walls at different stages of development (all pictures are in different cotyledons). a) 2 day old *Arabidopsis thaliana* abaxial pavement cells. b) 4 day old *Arabidopsis thaliana* abaxial pavement cells c) 2 weeks old *Nicotiana benthamiana* adaxial pavement cells. 88

4.2 Confocal microscope images of GFP marked microtubules (shown in green) in *Arabidopsis thaliana* combined with PI stained cell walls (shown in magenta). The meanings of the different coloured arrows are defined in the main text. 90

4.3 Confocal microscope images of GFP marked actin (shown in green) combined with PI stained cell walls (shown in magenta) 93

4.4 Atomic force microscopy on cotyledons using $500nN$ of force where the experimental details are (where Z and then a number shows the z length) a) Z10 64 pixel $100\mu m$ b) Z5 32 pixel $50\mu m$ c)Z5 64 pixel $25\mu m$ d)Z5 64 pixel $25\mu m$ e) Z5 32 pixel $50\mu m$ f)Z5 32 pixel $50\mu m$ g) Z5 64 pixel $25\mu m$ h)Z5 32 pixel $50\mu m$ i) Z5 64 pixel $25\mu m$ j) Z5 128 pixel $50\mu m$ 95

4.5 Example AFM image from Daher et al. [2018] showing consistent stiffness values across the longitudinal and horizontal walls. 96

5.1 Diagram illustrating microtubule interaction principles upon microtubule collision with another. The lines represent microtubules, and the arrows their growth direction. a) When the angle of interaction is small, the microtubule can bundle up and begin to grow in the same direction as the other or simply crossover. b) When the angle of interaction is big, this can cause a collision-induced catastrophe, causing the microtubule to shrink from its plus end, or it can simply crossover. 102

5.2 Snapshots from an example microtubule simulation progressing in time where the thickness of the line represents the number of microtubules in that bundle. 103

5.3 Example angle distributions of varying organisation with a bias in the vertical direction 106

5.4 How the order parameter changes with time for simulations with probability $\mathcal{P}_{CC} = 0.1$ and $\mathcal{P}_B = 0.1$ with the simulation domain's length and height stated in the figure subcaptions 111

5.5 How the order parameter changes with time for simulations with probability $\mathcal{P}_{CC} = 0.2$ and $\mathcal{P}_B = 0.2$ with the simulation domain's length and height stated in the figure subcaptions 111

5.6 How the order parameter changes with time for simulations with probability $\mathcal{P}_{CC} = 0.3$ and $\mathcal{P}_B = 0.3$ with the simulation domain's length and height stated in the figure subcaptions 112

5.7 How the order parameter changes with time for simulations with probability $\mathcal{P}_{CC} = 0.4$ and $\mathcal{P}_B = 0.4$ with the simulation domain's length and height stated in the figure subcaptions 112

5.8 How the order parameter changes with time for simulations with probability $\mathcal{P}_{CC} = 0.5$ and $\mathcal{P}_B = 0.5$ with the simulation domain's length and height stated in the figure subcaptions 112

5.9 Microtubule arrays with different interaction probabilities of size $50\mu m$, where the thickness of the lines represent how many microtubules are in that bundle with the simulation's interactions probabilities stated in the figure subcaptions 113

5.10 How the order parameter changes with time for simulations with probability $\mathcal{P}_{CC} = 0.6$ and $\mathcal{P}_B = 0.6$ with the simulation domain's length and height stated in the figure subcaptions 113

5.11 How the order parameter changes with time for simulations with probability $\mathcal{P}_{CC} = 0.7$ and $\mathcal{P}_B = 0.7$ with the simulation domain's length and height stated in the figure subcaptions 113

5.12 How the order parameter changes with time for simulations with probability $\mathcal{P}_{CC} = 0.8$ and $\mathcal{P}_B = 0.8$ with the simulation domain's length and height stated in the figure subcaptions 114

5.13 How the order parameter changes with time for simulations with varying max microtubule number all with size size $50\mu m$ and probabilities $\mathcal{P}_{CC} = 0.7$ and $\mathcal{P}_B = 0.7$ with the simulation's max microtubule number stated in the figure subcaptions 115

5.14 How the order parameter changes with time for simulations with probabilities $\mathcal{P}_{CC} = 0.5$ and $\mathcal{P}_B = 0.5$ and varying aspect ratios where the subcaptions state the aspect ratios. 116

5.15 The aspect ratio's effect on the cumulative angle distribution for simulations with probability $\mathcal{P}_{CC} = 0.5$ and $\mathcal{P}_B = 0.5$ where the subcaptions state the aspect ratios. 117

5.16 How the order parameter changes with time for the simulations run in a rectangular domain with aspect ratio 5 when testing the effect of different interaction probabilities 119

5.17 The angle distributions for the simulations run in a rectangular domain with aspect ratio 5 when testing the effect of different interaction probabilities. 120

5.18 The results of running the model in pavement cells with (b and d) and without the (a and c) stress stabilisation with the bar charts (a and b) showing the cumulative microtubule lobe and indent localisation instances and the microtubule diagrams (c and d) showing the microtubule arrays in the pavement cell outlines. 122

6.1 Example mesh of one of the pavement cell outlines where the dots represent the nodes and the lines represent elements 132

6.2 Flow diagram illustrating how the system is solved. 148

6.3 Reaction diffusion model results in the 6th mature pavement cell outline where figures a b c and d show the different signalling protein concentrations and e shows the microtubule array where the lines increase in thickness as more microtubules are contained in that bundle. Figures c and d have nonlinear scalebar in order to see concentration variations clearly. 151

6.4 Reaction diffusion model results in the 8th less developed pavement cell outline where each figure shows the different signalling protein concentrations where figures a c and e are the results from the control simulations and b, d and f show the result from the CA ROP2 simulations 156

6.5 Reaction diffusion model results in the 8th less developed pavement cell outline where figures a and b shows the RIC1 concentrations and c and d show the microtubule arrays where the lines increase in thickness as more microtubules are contained in that bundle. Figures a and c show the control simulation results and b and d show the CA ROP2 simulations results. . . 157

6.6 The average number of microtubule indent localisation instances with standard deviation error bars over all pavement cell outlines calculated from the 3000, 2000, 1500, 1000 and 500 time steps 158

6.7 Reaction diffusion model results in the 5th less developed pavement cell outline where each figure shows the different signalling protein concentrations where figures a c and e are the results from the control simulations and b, d and f show the result from the CA ROP6 simulations 159
6.8 Reaction diffusion model results in the 5th less developed pavement cell outline where figures a and b shows the RIC1 concentrations, c and d show the microtubule arrays where the lines increase in thickness as more microtubules are contained in that bundle and e and f showing the microtubule arrays angle distribution with the black line showing the long axis direction. Figures a c, and e show the control simulation results and b, d and f show the CA ROP6 simulations results. 160
6.9 Reaction diffusion model results in the 2nd less developed pavement cell outline where each figure shows the different signalling protein concentrations where figures a c and e are the results from the control simulations and b, d and f show the result from the DN ROP2 simulations. 163
6.10 Reaction diffusion model results in the 2nd less developed pavement cell outline where figures a and b shows the RIC1 concentrations and c and d show the microtubule arrays where the lines increase in thickness as more microtubules are contained in that bundle. Figures a and c show the control simulation results and b and d show the DN ROP2 simulations results. . . 164
6.11 The average number of microtubule co-ordinate points contained in bundles for each cell outline averaged over the 500, 1000, 1500, and 2000, 3000th time steps with standard deviation bars. 165
6.12 Reaction diffusion model results in the 10th less developed pavement cell outline where each figure shows the different signalling protein concentrations where figures a c and e are the results from the control simulations and b, d and f show the result from the DN ROP6 simulations. 166

6.13 Reaction diffusion model results in the 10th less developed pavement cell outline where figures a and b shows the RIC1 concentrations and c and d show the microtubule arrays where the lines increase in thickness as more microtubules are contained in that bundle. Figures a and c show the control simulation results and b and d show the DN ROP6 simulations results. . . 167

6.14 The average number of microtubule coordinate points contained in bundles for each cell averaged over the 500, 1000, 1500, 2000 and 3000th time steps with standard deviation bars 168

6.15 Reaction diffusion model results in our 7th young pavement cell outline where each figure shows the different signalling protein concentrations. . . 169

6.16 Reaction diffusion model results in our 7th young pavement cell outline where figure a shows the RIC1 concentrations and b shows the microtubule array where the lines increase in thickness as more microtubules are contained in that bundle. 170

7.1 An example vertex element setup with 9 cells where the bold black lines represent the cell walls between neighbouring cells, the anticlinal walls, and the grey triangulation represent the cell walls in the plane of the simulation, the periclinal walls. 175

7.2 Model principles behind equation (7.2.3) where a network of nodes and anticlinal wall elements can be seen demonstrating the total force on vertex $\mathbf{x}_i^{*k}$ from the pressure in cell m. 177

7.3 The reference triangle with coordinates $\mathbf{x}_{\tau_{u,1}}^{*k-1}, \mathbf{x}_{\tau_{u,2}}^{*k-1}, \mathbf{x}_{\tau_{u,3}}^{k-1}$ is mapped onto the current configuration with coordinates $\mathbf{x}_{\tau_{u,1}}^{*k}, \mathbf{x}_{\tau_{u,2}}^{*k}, \mathbf{x}_{\tau_{u,3}}^{*k}$ via the deformation gradient F^*. The deformation gradient is calculated by $F^* = F_2^* F_1^{*-1}$ where F_1^* is the gradient map to the reference configuration and F_2^* the gradient map to the current configuration both from the unit triangle. The reference triangle has fibre direction $\mathbf{A}$ where the fibres is embedded within the material and is deformed with the triangle to the fibre direction $\mathbf{a}$. . . . 179

7.4 Evaluation of the viscous stress in a example periclinal wall triangle with the dashed lines representing the periclinal elements 181
7.5 Evaluation of the edge stress in a example anticlinal wall, where the bold lines represent the anticlinal walls and the dash lines the periclinal walls . 183
7.6 Depiction of the boundary elements shown as dotted lines connected to the boundary anticlinal wall node $\mathbf{x}_i^*$ where the black lines represent the anticlinal wall elements, and the dashed lines represent the periclinal wall elements 183
7.7 Parameter values in the pavement cells. a) the stiffness values, b) the viscosity values, c) the anisotropy directions and magnitude where the blues arrow show the normalised directions and the orange arrows represent the anisotropy directions and their scaling with the microtubule concentration. 187
7.8 Parameter values in an example pavement cell in an embedded tissue with complimentary tissue parameters. a) Example mesh of a pavement cell embedded in a tissue, b) viscosity values in a complementary tissue c) the scaled anisotropy directions in a complimentary tissue. 201
7.9 Pavement cell outlines for $G_{tr} = 0.5$ at the 500th time step (apart from a). a) Original pavement cell outline. b) Pavement cell outline from the control simulation. c) Pavement cell outline from the varying viscous and elastic properties simulation. d) Pavement cell outline from the varying viscous, elastic and anisotropic properties simulation. e) Pavement cell outline from the varying viscous, elastic, anisotropic with complimentary tissue parameters simulation. f) Pavement cell outline from the varying viscous, elastic, anisotropic, with complimentary tissue parameters and spring growth simulation with $G_{sr} = 0.3$. 206

7.10 The parameters applied to the different simulations. a) The varying viscosity values in the isotropic initiation tests. b) The varying scaled anisotropy directions in our anisotropy initiation tests. c) The varying plastic spring growth rates for the first differential cell growth rates initiation test. d) The varying viscosity values for the second differential cell growth rates initiation test. 209

7.11 The 4 inner cells of the isotropic initiation simulations with a) the base viscosity values at the 10th time step b) the raised viscosity values at the 500th time step. 211

7.12 The 4 inner cells of the anisotropic initiation simulation at the 1596th time step 211

7.13 The 4 inner cells from the differential cell growth rates simulations where the figures display a) the differential anticlinal wall spring growth rate simulation at the 180th time step and b) the differential periclinal wall viscosity simulation at the 100th time step. 212

7.14 The 4 inner cells from the excess growth buckling simulations at the 10th time step. 214

A.1 CellSeT software output 242

A.2 MorphopLibJ's morphological segmentation tool pavement cell silhouette example 243

A.3 The effect of stress stabilisation on the microtubule array in the different pavement cell outlines. a) Simulation in the 2nd pavement cell outline. b) Simulation in the 3rd pavement cell outline. c) Simulation in the 4th pavement cell outline. d) Simulation in the 5th pavement cell outline. e) Simulation in the 6th pavement cell outline. f) Simulation in the 7th pavement cell outline. g) Simulation in the 8th pavement cell outline. h) Simulation in the 9th pavement cell outline. i) Simulation in the 10th pavement cell outline. 253

A.4 The $\tilde{\kappa}$ values along an example pavement cell outline 254
A.5 Parameter setting test simulations where the figures display (a) the ROP2 concentration when the microtubules are fixed. (b) the fixed microtubule array (c) the fixed ROP2 concentration. (d) the fixed ROP6 concentration. (e) the microtubule array with ROP2 and ROP6 array fixed 257
A.6 The signalling network model results in the 1st mature pavement cell outline, where the figures show the different proteins concentrations. Figures c has a non-linear scalebar in order to see concentration variations clearly. . 258
A.7 The signalling network model results in the 1st mature pavement cell outline, where the figures show the RIC1 concentration and the microtubule array. Figure a has a non-linear scalebar in order to see concentration variations clearly. 258
A.8 The signalling network model results in the 2nd mature pavement cell outline, where the figures show the different proteins concentrations. Figures c has a non-linear scalebar in order to see concentration variations clearly. . 258
A.9 The signalling network model results in the 2nd mature pavement cell outline, where the figures show the RIC1 concentration and the microtubule array. Figure a has a non-linear scalebar in order to see concentration variations clearly. 259
A.10 The signalling network model results in the 3rd mature pavement cell outline, where the figures show the different proteins concentrations. Figures c has a non-linear scalebar in order to see concentration variations clearly. . 259
A.11 The signalling network model results in the 3rd mature pavement cell outline, where the figures show the RIC1 concentration and the microtubule array. Figure a has a non-linear scalebar in order to see concentration variations clearly. 260

A.12 The signalling network model results in the 4th mature pavement cell outline, where the figures show the different proteins concentrations. Figures c has a non-linear scalebar in order to see concentration variations clearly. . 260
A.13 The signalling network model results in the 4th mature pavement cell outline, where the figures show the RIC1 concentration and the microtubule array. Figure a has a non-linear scalebar in order to see concentration variations clearly. 261
A.14 The signalling network model results in the 5th mature pavement cell outline, where the figures show the different proteins concentrations. Figures c has a non-linear scalebar in order to see concentration variations clearly. . 261
A.15 The signalling network model results in the 5th mature pavement cell outline, where the figures show the RIC1 concentration and the microtubule array. Figure a has a non-linear scalebar in order to see concentration variations clearly. 262
A.16 The signalling network model results in the 7th mature pavement cell outline, where the figures show the different proteins concentrations. Figures c has a non-linear scalebar in order to see concentration variations clearly. . 262
A.17 The signalling network model results in the 7th mature pavement cell outline, where the figures show the RIC1 concentration and the microtubule array. Figure a has a non-linear scalebar in order to see concentration variations clearly. 263
A.18 The signalling network model results in the 8th mature pavement cell outline, where the figures show the different proteins concentrations. Figures c has a non-linear scalebar in order to see concentration variations clearly. . 263
A.19 The signalling network model results in the 8th mature pavement cell outline, where the figures show the RIC1 concentration and the microtubule array. Figure a has a non-linear scalebar in order to see concentration variations clearly. 264

A.20 The signalling network model results in the 9th mature pavement cell outline, where the figures show the different proteins concentrations. Figures c has a non-linear scalebar in order to see concentration variations clearly. . 264
A.21 The signalling network model results in the 9th mature pavement cell outline, where the figures show the RIC1 concentration and the microtubule array. Figure a has a non-linear scalebar in order to see concentration variations clearly. 265
A.22 The signalling network model results in the 10th mature pavement cell outline, where the figures show the different proteins concentrations. Figures c has a non-linear scalebar in order to see concentration variations clearly. . 265
A.23 The signalling network model results in the 10th mature pavement cell outline, where the figures show the RIC1 concentration and the microtubule array. Figure a has a non-linear scalebar in order to see concentration variations clearly. 266
A.24 The signalling network model results of the CA ROP2 simulations in the 1st less developed pavement cell outline, where the figures show the ROP2 concentrations in the control and the mutant with non-linear scalebar. . . . 267
A.25 The signalling network model results of the CA ROP2 simulations in the 1st less developed pavement cell outline, where the figures show the RIC4 concentrations in the control and the mutant with non-linear scalebar. . . . 268
A.26 The signalling network model results of the CA ROP2 simulations in the 1st less developed pavement cell outline, where the figures show the ROP6 concentrations in the control and the mutant with non-linear scalebar. . . . 268
A.27 The signalling network model results of the CA ROP2 simulations in the 1st less developed pavement cell outline, where the figures show the RIC1 concentrations in the control and the mutant with non-linear scalebar. . . . 269

A.28 The signalling network model results of the CA ROP2 simulations in the 1st less developed pavement cell outline, where the figures show the microtubule array in the control and the mutant. 269
A.29 The signalling network model results of the CA ROP2 simulations in the 2nd less developed pavement cell outline, where the figures show the ROP2 concentrations in the control and the mutant with non-linear scalebar. . . . 270
A.30 The signalling network model results of the CA ROP2 simulations in the 2nd less developed pavement cell outline, where the figures show the RIC4 concentrations in the control and the mutant with non-linear scalebar. . . . 270
A.31 The signalling network model results of the CA ROP2 simulations in the 2nd less developed pavement cell outline, where the figures show the ROP6 concentrations in the control and the mutant with non-linear scalebar. . . . 271
A.32 The signalling network model results of the CA ROP2 simulations in the 2nd less developed pavement cell outline, where the figures show the RIC1 concentrations in the control and the mutant with non-linear scalebar. . . . 271
A.33 The signalling network model results of the CA ROP2 simulations in the 2nd less developed pavement cell outline, where the figures show the microtubule array in the control and the mutant. 272
A.34 The signalling network model results of the CA ROP2 simulations in the 3rd less developed pavement cell outline, where the figures show the ROP2 concentrations in the control and the mutant with non-linear scalebar. . . . 272
A.35 The signalling network model results of the CA ROP2 simulations in the 3rd less developed pavement cell outline, where the figures show the RIC4 concentrations in the control and the mutant with non-linear scalebar. . . . 273
A.36 The signalling network model results of the CA ROP2 simulations in the 3rd less developed pavement cell outline, where the figures show the ROP6 concentrations in the control and the mutant with non-linear scalebar. . . . 273

A.37 The signalling network model results of the CA ROP2 simulations in the 3rd less developed pavement cell outline, where the figures show the RIC1 concentrations in the control and the mutant with non-linear scalebar. . . . 274
A.38 The signalling network model results of the CA ROP2 simulations in the 3rd less developed pavement cell outline, where the figures show the microtubule array in the control and the mutant. 274
A.39 The signalling network model results of the CA ROP2 simulations in the 4th less developed pavement cell outline, where the figures show the ROP2 concentrations in the control and the mutant with non-linear scalebar. . . . 275
A.40 The signalling network model results of the CA ROP2 simulations in the 4th less developed pavement cell outline, where the figures show the RIC4 concentrations in the control and the mutant with non-linear scalebar. . . . 275
A.41 The signalling network model results of the CA ROP2 simulations in the 4th less developed pavement cell outline, where the figures show the ROP6 concentrations in the control and the mutant with non-linear scalebar. . . . 276
A.42 The signalling network model results of the CA ROP2 simulations in the 4th less developed pavement cell outline, where the figures show the RIC1 concentrations in the control and the mutant with non-linear scalebar. . . . 276
A.43 The signalling network model results of the CA ROP2 simulations in the 4th less developed pavement cell outline, where the figures show the microtubule array in the control and the mutant. 277
A.44 The signalling network model results of the CA ROP2 simulations in the 5th less developed pavement cell outline, where the figures show the ROP2 concentrations in the control and the mutant with non-linear scalebar. . . . 277
A.45 The signalling network model results of the CA ROP2 simulations in the 5th less developed pavement cell outline, where the figures show the RIC4 concentrations in the control and the mutant with non-linear scalebar. . . . 278

A.46 The signalling network model results of the CA ROP2 simulations in the 5th less developed pavement cell outline, where the figures show the ROP6 concentrations in the control and the mutant with non-linear scalebar. . . . 278
A.47 The signalling network model results of the CA ROP2 simulations in the 5th less developed pavement cell outline, where the figures show the RIC1 concentrations in the control and the mutant with non-linear scalebar. . . . 279
A.48 The signalling network model results of the CA ROP2 simulations in the 5th less developed pavement cell outline, where the figures show the microtubule array in the control and the mutant. 279
A.49 The signalling network model results of the CA ROP2 simulations in the 6th less developed pavement cell outline, where the figures show the ROP2 concentrations in the control and the mutant with non-linear scalebar. . . . 280
A.50 The signalling network model results of the CA ROP2 simulations in the 6th less developed pavement cell outline, where the figures show the RIC4 concentrations in the control and the mutant with non-linear scalebar. . . . 280
A.51 The signalling network model results of the CA ROP2 simulations in the 6th less developed pavement cell outline, where the figures show the ROP6 concentrations in the control and the mutant with non-linear scalebar. . . . 281
A.52 The signalling network model results of the CA ROP2 simulations in the 6th less developed pavement cell outline, where the figures show the RIC1 concentrations in the control and the mutant with non-linear scalebar. . . . 281
A.53 The signalling network model results of the CA ROP2 simulations in the 6th less developed pavement cell outline, where the figures show the microtubule array in the control and the mutant. 282
A.54 The signalling network model results of the CA ROP2 simulations in the 8th less developed pavement cell outline, where the figures show the ROP2 concentrations in the control and the mutant with non-linear scalebar. . . . 282

A.55 The signalling network model results of the CA ROP2 simulations in the 8th less developed pavement cell outline, where the figures show the RIC4 concentrations in the control and the mutant with non-linear scalebar. . . . 283
A.56 The signalling network model results of the CA ROP2 simulations in the 8th less developed pavement cell outline, where the figures show the ROP6 concentrations in the control and the mutant with non-linear scalebar. . . . 283
A.57 The signalling network model results of the CA ROP2 simulations in the 8th less developed pavement cell outline, where the figures show the RIC1 concentrations in the control and the mutant with non-linear scalebar. . . . 284
A.58 The signalling network model results of the CA ROP2 simulations in the 8th less developed pavement cell outline, where the figures show the microtubule array in the control and the mutant. 284
A.59 The signalling network model results of the CA ROP2 simulations in the 9th less developed pavement cell outline, where the figures show the ROP2 concentrations in the control and the mutant with non-linear scalebar. . . . 285
A.60 The signalling network model results of the CA ROP2 simulations in the 9th less developed pavement cell outline, where the figures show the RIC4 concentrations in the control and the mutant with non-linear scalebar. . . . 285
A.61 The signalling network model results of the CA ROP2 simulations in the 9th less developed pavement cell outline, where the figures show the ROP6 concentrations in the control and the mutant with non-linear scalebar. . . . 286
A.62 The signalling network model results of the CA ROP2 simulations in the 9th less developed pavement cell outline, where the figures show the RIC1 concentrations in the control and the mutant with non-linear scalebar. . . . 286
A.63 The signalling network model results of the CA ROP2 simulations in the 9th less developed pavement cell outline, where the figures show the microtubule array in the control and the mutant. 287

A.64 The signalling network model results of the CA ROP6 simulations in the 1st less developed pavement cell outline, where the figures show the ROP2 concentrations in the control and the mutant. 288
A.65 The signalling network model results of the CA ROP6 simulations in the 1st less developed pavement cell outline, where the figures show the RIC4 concentrations in the control and the mutant. 289
A.66 The signalling network model results of the CA ROP6 simulations in the 1st less developed pavement cell outline, where the figures show the ROP6 concentrations in the control and the mutant with non-linear scalebars. . . 289
A.67 The signalling network model results of the CA ROP6 simulations in the 1st less developed pavement cell outline, where the figures show the RIC1 concentrations in the control and the mutant with non-linear scalebars. . . 290
A.68 The signalling network model results of the CA ROP6 simulations in the 1st less developed pavement cell outline, where the figures show the microtubule array in the control and the mutant. 290
A.69 The signalling network model results of the CA ROP6 simulations in the 1st less developed pavement cell outline, where the figures show the microtubule array's angle distribution in the control and the mutant. 291
A.70 The signalling network model results of the CA ROP6 simulations in the 2nd less developed pavement cell outline, where the figures show the ROP2 concentrations in the control and the mutant. 291
A.71 The signalling network model results of the CA ROP6 simulations in the 2nd less developed pavement cell outline, where the figures show the RIC4 concentrations in the control and the mutant. 292
A.72 The signalling network model results of the CA ROP6 simulations in the 2nd less developed pavement cell outline, where the figures show the ROP6 concentrations in the control and the mutant with non-linear scalebars. . . 292

A.73 The signalling network model results of the CA ROP6 simulations in the 2nd less developed pavement cell outline, where the figures show the RIC1 concentrations in the control and the mutant with non-linear scalebars. . . 293
A.74 The signalling network model results of the CA ROP6 simulations in the 2nd less developed pavement cell outline, where the figures show the microtubule array in the control and the mutant. 293
A.75 The signalling network model results of the CA ROP6 simulations in the 2nd less developed pavement cell outline, where the figures show the microtubule array's angle distribution in the control and the mutant. 294
A.76 The signalling network model results of the CA ROP6 simulations in the 3rd less developed pavement cell outline, where the figures show the ROP2 concentrations in the control and the mutant. 294
A.77 The signalling network model results of the CA ROP6 simulations in the 3rd less developed pavement cell outline, where the figures show the RIC4 concentrations in the control and the mutant. 295
A.78 The signalling network model results of the CA ROP6 simulations in the 3rd less developed pavement cell outline, where the figures show the ROP6 concentrations in the control and the mutant with non-linear scalebars. . . 295
A.79 The signalling network model results of the CA ROP6 simulations in the 3rd less developed pavement cell outline, where the figures show the RIC1 concentrations in the control and the mutant with non-linear scalebars. . . 296
A.80 The signalling network model results of the CA ROP6 simulations in the 3rd less developed pavement cell outline, where the figures show the microtubule array in the control and the mutant. 296
A.81 The signalling network model results of the CA ROP6 simulations in the 3rd less developed pavement cell outline, where the figures show the microtubule array's angle distribution in the control and the mutant. 297

A.82 The signalling network model results of the CA ROP6 simulations in the 5th less developed pavement cell outline, where the figures show the ROP2 concentrations in the control and the mutant 297
A.83 The signalling network model results of the CA ROP6 simulations in the 5th less developed pavement cell outline, where the figures show the RIC4 concentrations in the control and the mutant. 298
A.84 The signalling network model results of the CA ROP6 simulations in the 5th less developed pavement cell outline, where the figures show the ROP6 concentrations in the control and the mutant with non-linear scalebars. . . 298
A.85 The signalling network model results of the CA ROP6 simulations in the 5th less developed pavement cell outline, where the figures show the RIC1 concentrations in the control and the mutant with non-linear scalebars. . . 299
A.86 The signalling network model results of the CA ROP6 simulations in the 5th less developed pavement cell outline, where the figures show the microtubule array in the control and the mutant. 299
A.87 The signalling network model results of the CA ROP6 simulations in the 5th less developed pavement cell outline, where the figures show the microtubule array's angle distribution in the control and the mutant. 300
A.88 The signalling network model results of the CA ROP6 simulations in the 6th less developed pavement cell outline, where the figures show the ROP2 concentrations in the control and the mutant. 300
A.89 The signalling network model results of the CA ROP6 simulations in the 6th less developed pavement cell outline, where the figures show the RIC4 concentrations in the control and the mutant. 301
A.90 The signalling network model results of the CA ROP6 simulations in the 6th less developed pavement cell outline, where the figures show the ROP6 concentrations in the control and the mutant with non-linear scalebars. . . 301

A.91 The signalling network model results of the CA ROP6 simulations in the 6th less developed pavement cell outline, where the figures show the RIC1 concentrations in the control and the mutant with non-linear scalebars. . . 302
A.92 The signalling network model results of the CA ROP6 simulations in the 6th less developed pavement cell outline, where the figures show the microtubule array in the control and the mutant. 302
A.93 The signalling network model results of the CA ROP6 simulations in the 6th less developed pavement cell outline, where the figures show the microtubule array's angle distribution in the control and the mutant. 303
A.94 The signalling network model results of the CA ROP6 simulations in the 7th less developed pavement cell outline, where the figures show the ROP2 concentrations in the control and the mutant. 303
A.95 The signalling network model results of the CA ROP6 simulations in the 7th less developed pavement cell outline, where the figures show the RIC4 concentrations in the control and the mutant. 304
A.96 The signalling network model results of the CA ROP6 simulations in the 7th less developed pavement cell outline, where the figures show the ROP6 concentrations in the control and the mutant with non-linear scalebars. . . 304
A.97 The signalling network model results of the CA ROP6 simulations in the 7th less developed pavement cell outline, where the figures show the RIC1 concentrations in the control and the mutant with non-linear scalebars. . . 305
A.98 The signalling network model results of the CA ROP6 simulations in the 7th less developed pavement cell outline, where the figures show the microtubule array in the control and the mutant. 305
A.99 The signalling network model results of the CA ROP6 simulations in the 7th less developed pavement cell outline, where the figures show the microtubule array's angle distribution in the control and the mutant. 306

A.100The signalling network model results of the CA ROP6 simulations in the 8th less developed pavement cell outline, where the figures show the ROP2 concentrations in the control and the mutant. 306
A.101The signalling network model results of the CA ROP6 simulations in the 8th less developed pavement cell outline, where the figures show the RIC4 concentrations in the control and the mutant. 307
A.102The signalling network model results of the CA ROP6 simulations in the 8th less developed pavement cell outline, where the figures show the ROP6 concentrations in the control and the mutant with non-linear scalebars. . . 307
A.103The signalling network model results of the CA ROP6 simulations in the 8th less developed pavement cell outline, where the figures show the RIC1 concentrations in the control and the mutant with non-linear scalebars. . . 308
A.104The signalling network model results of the CA ROP6 simulations in the 8th less developed pavement cell outline, where the figures show the microtubule array in the control and the mutant. 308
A.105The signalling network model results of the CA ROP6 simulations in the 8th less developed pavement cell outline, where the figures show the microtubule array's angle distribution in the control and the mutant. 309
A.106The signalling network model results of the CA ROP6 simulations in the 9th less developed pavement cell outline, where the figures show the ROP2 concentrations in the control and the mutant. 309
A.107The signalling network model results of the CA ROP6 simulations in the 9th less developed pavement cell outline, where the figures show the RIC4 concentrations in the control and the mutant. 310
A.108The signalling network model results of the CA ROP6 simulations in the 9th less developed pavement cell outline, where the figures show the ROP6 concentrations in the control and the mutant with non-linear scalebars. . . 310

A.109The signalling network model results of the CA ROP6 simulations in the 9th less developed pavement cell outline, where the figures show the RIC1 concentrations in the control and the mutant with non-linear scalebars. . . 311
A.110The signalling network model results of the CA ROP6 simulations in the 9th less developed pavement cell outline, where the figures show the microtubule array in the control and the mutant. 311
A.111The signalling network model results of the CA ROP6 simulations in the 9th less developed pavement cell outline, where the figures show the microtubule array's angle distribution in the control and the mutant. 312
A.112The signalling network model results of the DN ROP2 simulations in the 1st less developed pavement cell outline, where the figures show the ROP2 concentrations in the control and the mutant with non-linear scalebars. . . 313
A.113The signalling network model results of the DN ROP2 simulations in the 1st less developed pavement cell outline, where the figures show the RIC4 concentrations in the control and the mutant with non-linear scalebars. . . 314
A.114The signalling network model results of the DN ROP2 simulations in the 1st less developed pavement cell outline, where the figures show the ROP6 concentrations in the control and the mutant with non-linear scalebars. . . 314
A.115The signalling network model results of the DN ROP2 simulations in the 1st less developed pavement cell outline, where the figures show the RIC1 concentrations in the control and the mutant with non-linear scalebars. . . 315
A.116The signalling network model results of the DN ROP2 simulations in the 1st less developed pavement cell outline, where the figures show the microtubule array in the control and the mutant. 315
A.117The signalling network model results of the DN ROP2 simulations in the 3rd less developed pavement cell outline, where the figures show the ROP2 concentrations in the control and the mutant with non-linear scalebars. . . 316

A.118 The signalling network model results of the DN ROP2 simulations in the 3rd less developed pavement cell outline, where the figures show the RIC4 concentrations in the control and the mutant with non-linear scalebars. . . 316
A.119 The signalling network model results of the DN ROP2 simulations in the 3rd less developed pavement cell outline, where the figures show the ROP6 concentrations in the control and the mutant with non-linear scalebars. . . 317
A.120 The signalling network model results of the DN ROP2 simulations in the 3rd less developed pavement cell outline, where the figures show the RIC1 concentrations in the control and the mutant with non-linear scalebars. . . 317
A.121 The signalling network model results of the DN ROP2 simulations in the 3rd less developed pavement cell outline, where the figures show the microtubule array in the control and the mutant. 318
A.122 The signalling network model results of the DN ROP2 simulations in the 4th less developed pavement cell outline, where the figures show the ROP2 concentrations in the control and the mutant with non-linear scalebars. . . 318
A.123 The signalling network model results of the DN ROP2 simulations in the 4th less developed pavement cell outline, where the figures show the RIC4 concentrations in the control and the mutant with non-linear scalebars. . . 319
A.124 The signalling network model results of the DN ROP2 simulations in the 4th less developed pavement cell outline, where the figures show the ROP6 concentrations in the control and the mutant with non-linear scalebars. . . 319
A.125 The signalling network model results of the DN ROP2 simulations in the 4th less developed pavement cell outline, where the figures show the RIC1 concentrations in the control and the mutant with non-linear scalebars. . . 320
A.126 The signalling network model results of the DN ROP2 simulations in the 4th less developed pavement cell outline, where the figures show the microtubule array in the control and the mutant. 320

A.127 The signalling network model results of the DN ROP2 simulations in the 5th less developed pavement cell outline, where the figures show the ROP2 concentrations in the control and the mutant with non-linear scalebars. . . 321
A.128 The signalling network model results of the DN ROP2 simulations in the 5th less developed pavement cell outline, where the figures show the RIC4 concentrations in the control and the mutant with non-linear scalebars. . . 321
A.129 The signalling network model results of the DN ROP2 simulations in the 5th less developed pavement cell outline, where the figures show the ROP6 concentrations in the control and the mutant with non-linear scalebars. . . 322
A.130 The signalling network model results of the DN ROP2 simulations in the 5th less developed pavement cell outline, where the figures show the RIC1 concentrations in the control and the mutant with non-linear scalebars. . . 322
A.131 The signalling network model results of the DN ROP2 simulations in the 5th less developed pavement cell outline, where the figures show the microtubule array in the control and the mutant. 323
A.132 The signalling network model results of the DN ROP2 simulations in the 6th less developed pavement cell outline, where the figures show the ROP2 concentrations in the control and the mutant with non-linear scalebars. . . 323
A.133 The signalling network model results of the DN ROP2 simulations in the 6th less developed pavement cell outline, where the figures show the RIC4 concentrations in the control and the mutant with non-linear scalebars. . . 324
A.134 The signalling network model results of the DN ROP2 simulations in the 6th less developed pavement cell outline, where the figures show the ROP6 concentrations in the control and the mutant with non-linear scalebars. . . 324
A.135 The signalling network model results of the DN ROP2 simulations in the 6th less developed pavement cell outline, where the figures show the RIC1 concentrations in the control and the mutant with non-linear scalebars. . . 325

A.136 The signalling network model results of the DN ROP2 simulations in the 6th less developed pavement cell outline, where the figures show the microtubule array in the control and the mutant. 325
A.137 The signalling network model results of the DN ROP2 simulations in the 7th less developed pavement cell outline, where the figures show the ROP2 concentrations in the control and the mutant with non-linear scalebars. . . 326
A.138 The signalling network model results of the DN ROP2 simulations in the 7th less developed pavement cell outline, where the figures show the RIC4 concentrations in the control and the mutant with non-linear scalebars. . . 326
A.139 The signalling network model results of the DN ROP2 simulations in the 7th less developed pavement cell outline, where the figures show the ROP6 concentrations in the control and the mutant with non-linear scalebars. . . 327
A.140 The signalling network model results of the DN ROP2 simulations in the 7th less developed pavement cell outline, where the figures show the RIC1 concentrations in the control and the mutant with non-linear scalebars. . . 327
A.141 The signalling network model results of the DN ROP2 simulations in the 7th less developed pavement cell outline, where the figures show the microtubule array in the control and the mutant. 328
A.142 The signalling network model results of the DN ROP2 simulations in the 8th less developed pavement cell outline, where the figures show the ROP2 concentrations in the control and the mutant with non-linear scalebars. . . 328
A.143 The signalling network model results of the DN ROP2 simulations in the 8th less developed pavement cell outline, where the figures show the RIC4 concentrations in the control and the mutant with non-linear scalebars. . . 329
A.144 The signalling network model results of the DN ROP2 simulations in the 8th less developed pavement cell outline, where the figures show the ROP6 concentrations in the control and the mutant with non-linear scalebars. . . 329

A.145 The signalling network model results of the DN ROP2 simulations in the 8th less developed pavement cell outline, where the figures show the RIC1 concentrations in the control and the mutant with non-linear scalebars. . . 330
A.146 The signalling network model results of the DN ROP2 simulations in the 8th less developed pavement cell outline, where the figures show the microtubule array in the control and the mutant. 330
A.147 The signalling network model results of the DN ROP2 simulations in the 9th less developed pavement cell outline, where the figures show the ROP2 concentrations in the control and the mutant with non-linear scalebars. . . 331
A.148 The signalling network model results of the DN ROP2 simulations in the 9th less developed pavement cell outline, where the figures show the RIC4 concentrations in the control and the mutant with non-linear scalebars. . . 331
A.149 The signalling network model results of the DN ROP2 simulations in the 9th less developed pavement cell outline, where the figures show the ROP6 concentrations in the control and the mutant with non-linear scalebars. . . 332
A.150 The signalling network model results of the DN ROP2 simulations in the 9th less developed pavement cell outline, where the figures show the RIC1 concentrations in the control and the mutant with non-linear scalebars. . . 332
A.151 The signalling network model results of the DN ROP2 simulations in the 9th less developed pavement cell outline, where the figures show the microtubule array in the control and the mutant. 333
A.152 The signalling network model results of the DN ROP6 simulations in the 1st less developed pavement cell outline, where the figures show the ROP2 concentrations in the control and the mutant. 334
A.153 The signalling network model results of the DN ROP6 simulations in the 1st less developed pavement cell outline, where the figures show the RIC4 concentrations in the control and the mutant. 335

A.154 The signalling network model results of the DN ROP6 simulations in the 1st less developed pavement cell outline, where the figures show the ROP6 concentrations in the control and the mutant with non-linear scalebars. . . 335
A.155 The signalling network model results of the DN ROP6 simulations in the 1st less developed pavement cell outline, where the figures show the RIC1 concentrations in the control and the mutant with non-linear scalebars. . . 336
A.156 The signalling network model results of the DN ROP6 simulations in the 1st less developed pavement cell outline, where the figures show the microtubule array in the control and the mutant. 336
A.157 The signalling network model results of the DN ROP6 simulations in the 2nd less developed pavement cell outline, where the figures show the ROP2 concentrations in the control and the mutant. 337
A.158 The signalling network model results of the DN ROP6 simulations in the 2nd less developed pavement cell outline, where the figures show the RIC4 concentrations in the control and the mutant. 337
A.159 The signalling network model results of the DN ROP6 simulations in the 2nd less developed pavement cell outline, where the figures show the ROP6 concentrations in the control and the mutant with non-linear scalebars. . . 338
A.160 The signalling network model results of the DN ROP6 simulations in the 2nd less developed pavement cell outline, where the figures show the RIC1 concentrations in the control and the mutant with non-linear scalebars. . . 338
A.161 The signalling network model results of the DN ROP6 simulations in the 2nd less developed pavement cell outline, where the figures show the microtubule array in the control and the mutant. 339
A.162 The signalling network model results of the DN ROP6 simulations in the 3rd less developed pavement cell outline, where the figures show the ROP2 concentrations in the control and the mutant. 339

A.163 The signalling network model results of the DN ROP6 simulations in the 3rd less developed pavement cell outline, where the figures show the RIC4 concentrations in the control and the mutant. 340
A.164 The signalling network model results of the DN ROP6 simulations in the 3rd less developed pavement cell outline, where the figures show the ROP6 concentrations in the control and the mutant with non-linear scalebars. . . 340
A.165 The signalling network model results of the DN ROP6 simulations in the 3rd less developed pavement cell outline, where the figures show the RIC1 concentrations in the control and the mutant with non-linear scalebars. . . 341
A.166 The signalling network model results of the DN ROP6 simulations in the 3rd less developed pavement cell outline, where the figures show the microtubule array in the control and the mutant. 341
A.167 The signalling network model results of the DN ROP6 simulations in the 4th less developed pavement cell outline, where the figures show the ROP2 concentrations in the control and the mutant. 342
A.168 The signalling network model results of the DN ROP6 simulations in the 4th less developed pavement cell outline, where the figures show the RIC4 concentrations in the control and the mutant. 342
A.169 The signalling network model results of the DN ROP6 simulations in the 4th less developed pavement cell outline, where the figures show the ROP6 concentrations in the control and the mutant with non-linear scalebars. . . 343
A.170 The signalling network model results of the DN ROP6 simulations in the 4th less developed pavement cell outline, where the figures show the RIC1 concentrations in the control and the mutant with non-linear scalebars. . . 343
A.171 The signalling network model results of the DN ROP6 simulations in the 4th less developed pavement cell outline, where the figures show the microtubule array in the control and the mutant. 344

A.172 The signalling network model results of the DN ROP6 simulations in the 5th less developed pavement cell outline, where the figures show the ROP2 concentrations in the control and the mutant. 344
A.173 The signalling network model results of the DN ROP6 simulations in the 5th less developed pavement cell outline, where the figures show the RIC4 concentrations in the control and the mutant. 345
A.174 The signalling network model results of the DN ROP6 simulations in the 5th less developed pavement cell outline, where the figures show the ROP6 concentrations in the control and the mutant with non-linear scalebars. . . 345
A.175 The signalling network model results of the DN ROP6 simulations in the 5th less developed pavement cell outline, where the figures show the RIC1 concentrations in the control and the mutant with non-linear scalebars. . . 346
A.176 The signalling network model results of the DN ROP6 simulations in the 5th less developed pavement cell outline, where the figures show the microtubule array in the control and the mutant. 346
A.177 The signalling network model results of the DN ROP6 simulations in the 6th less developed pavement cell outline, where the figures show the ROP2 concentrations in the control and the mutant. 347
A.178 The signalling network model results of the DN ROP6 simulations in the 6th less developed pavement cell outline, where the figures show the RIC4 concentrations in the control and the mutant. 347
A.179 The signalling network model results of the DN ROP6 simulations in the 6th less developed pavement cell outline, where the figures show the ROP6 concentrations in the control and the mutant with non-linear scalebars. . . 348
A.180 The signalling network model results of the DN ROP6 simulations in the 6th less developed pavement cell outline, where the figures show the RIC1 concentrations in the control and the mutant with non-linear scalebars. . . 348

A.181 The signalling network model results of the DN ROP6 simulations in the 6th less developed pavement cell outline, where the figures show the microtubule array in the control and the mutant. 349
A.182 The signalling network model results of the DN ROP6 simulations in the 7th less developed pavement cell outline, where the figures show the ROP2 concentrations in the control and the mutant. 349
A.183 The signalling network model results of the DN ROP6 simulations in the 7th less developed pavement cell outline, where the figures show the RIC4 concentrations in the control and the mutant. 350
A.184 The signalling network model results of the DN ROP6 simulations in the 7th less developed pavement cell outline, where the figures show the ROP6 concentrations in the control and the mutant with non-linear scalebars. . . 350
A.185 The signalling network model results of the DN ROP6 simulations in the 7th less developed pavement cell outline, where the figures show the RIC1 concentrations in the control and the mutant with non-linear scalebars. . . 351
A.186 The signalling network model results of the DN ROP6 simulations in the 7th less developed pavement cell outline, where the figures show the microtubule array in the control and the mutant. 351
A.187 The signalling network model results of the DN ROP6 simulations in the 8th less developed pavement cell outline, where the figures show the ROP2 concentrations in the control and the mutant. 352
A.188 The signalling network model results of the DN ROP6 simulations in the 8th less developed pavement cell outline, where the figures show the RIC4 concentrations in the control and the mutant. 352
A.189 The signalling network model results of the DN ROP6 simulations in the 8th less developed pavement cell outline, where the figures show the ROP6 concentrations in the control and the mutant with non-linear scalebars. . . 353

A.190 The signalling network model results of the DN ROP6 simulations in the 8th less developed pavement cell outline, where the figures show the RIC1 concentrations in the control and the mutant with non-linear scalebars. . . 353
A.191 The signalling network model results of the DN ROP6 simulations in the 8th less developed pavement cell outline, where the figures show the microtubule array in the control and the mutant. 354
A.192 The signalling network model results in the 1st young pavement cell outline, where the figures show the different proteins concentrations. 354
A.193 The signalling network model results in the 1st young pavement cell outline, where the figures show the RIC1 concentration and the microtubule array. 354
A.194 The signalling network model results in the 2nd young pavement cell outline, where the figures show the different proteins concentrations. 355
A.195 The signalling network model results in the 2nd young pavement cell outline, where the figures show the RIC1 concentration and the microtubule array. 355
A.196 The signalling network model results in the 3rd young pavement cell outline, where the figures show the different proteins concentrations. 355
A.197 The signalling network model results in the 3rd young pavement cell outline, where the figures show the RIC1 concentration and the microtubule array. 356
A.198 The signalling network model results in the 4th young pavement cell outline, where the figures show the different proteins concentrations. 356
A.199 The signalling network model results in the 4th young pavement cell outline, where the figures show the RIC1 concentration and the microtubule array. 356
A.200 The signalling network model results in the 5th young pavement cell outline, where the figures show the different proteins concentrations. 357

A.201 The signalling network model results in the 5th young pavement cell outline, where the figures show the RIC1 concentration and the microtubule array. 357
A.202 The signalling network model results in the 6th young pavement cell outline, where the figures show the different proteins concentrations. 357
A.203 The signalling network model results in the 6th young pavement cell outline, where the figures show the RIC1 concentration and the microtubule array. 358
A.204 The signalling network model results in the 8th young pavement cell outline, where the figures show the different proteins concentrations. 358
A.205 The signalling network model results in the 8th young pavement cell outline, where the figures show the RIC1 concentration and the microtubule array. 358
A.206 The signalling network model results in the 9th young pavement cell outline, where the figures show the different proteins concentrations. 359
A.207 The signalling network model results in the 9th young pavement cell outline, where the figures show the RIC1 concentration and the microtubule array. 359
A.208 The signalling network model results in the 11th young pavement cell outline, where the figures show the different proteins concentrations. 359
A.209 The signalling network model results in the 11th young pavement cell outline, where the figures show the RIC1 concentration and the microtubule array. 360
A.210 The signalling network model results in the 12th young pavement cell outline, where the figures show the different proteins concentrations. 360
A.211 The signalling network model results in the 12th young pavement cell outline, where the figures show the RIC1 concentration and the microtubule array. 360

A.212 The area curves over different meshsizes with a)$h = 1$ b) $h = \frac{2}{3}$ c) $h = 0.5$. 364

List of Tables

3.1 Model 1 parameter values 66

5.1 Microtubule model parameters 107

6.1 All parameters values for the signalling network model 149

7.1 Vertex element base parameter values 187

7.2 Further vertex element parameter values 190

7.3 Relative circularity shape index values at the 500th and 50th (shown in brackets) time step when varying the tissue growth rate G_{tr} and including different wall material properties. 205

7.4 Relative circularity shape index values at the 300th time step when varying the tissue growth rate G_{sr} in our simulations that include varying viscosity, elasticity, anisotropy, complimentary tissue parameters and plastic spring growth. 205

7.5 Relative circularity shape index values at the 300th time step in the different cell outlines simulations that all include varying viscosity, elasticity, anisotropy, complimentary tissue parameters and plastic spring growth. . . 207

A.1 Asymptotic expansion constants for Σ_1^∞ 236

A.2 Asymptotic expansion constants for Σ_2^∞ 239

A.3 Test simulations for mesh size $h^* = 1$, with time stepping $\Delta t = 0.1, 0.01$ where the numbers with no brackets are from the simulations with $\Delta t = 0.1$ and those with the brackets are from the simulation with $\Delta t = 0.01$ 362

A.4 Test simulations for mesh size $h^* = \frac{2}{3}$, with time stepping $\Delta t = 0.1, 0.01$ where the numbers with no brackets are from the simulations with $\Delta t = 0.1$ and those with the brackets are from the simulation with $\Delta t = 0.01$ 362

A.5 Test simulations for mesh size $h^* = 0.5$, with time stepping $\Delta t = 0.1, 0.01$ where the numbers with no brackets are the numbers from the simulations with $\Delta t = 0.1$ and those with the brackets are the values from the simulation with $\Delta t = 0.01$ 363

A.6 Boundary growth rate variable effect on the relative average aspect ratio . 364

A.7 The effect of the changing the spring growth rate on the average relative lobe aspect ratio increase. 365

0.1 List of terms

Stomata: Are air holes mainly found in the epidermis of leaves and cotyledons which can be opened and closed by stomata guard cells and are responsible for controlling gas exchange.

Cellulose: Long and stiff molecules that lie in the cell wall and give it anisotropic properties dependant on their direction of deposition.

Pectin: Load bearing components in the cell wall, where when deposited in their Methyl esterified state are soft and viscous and become stiffer after de-esterification by the enzyme PME.

Hemicellulose: Molecules (also called xyloglucan) that are found in the cell wall where they crosslink the cellulose molecules.

Turgor: The isotropic force created from the water uptake into the cell that inflates the cell membrane, which is then restricted by the cell wall.

Abdaxial: The bottom/lower side of the plant leaf.

Adaxial: The top/higher side of the leaf.

GFP: Means green fluorescent protein, which can be attached to other molecules where they emit light when hit with a laser (alternatively YFP, yellow fluorescent protein).

Microtubules:Dynamic cytoskeleton filaments made up of tubulin that are said to guide the deposition of cellulose.

Actin: Cytoskeletal filaments that play an essential role in vesicle transportation in cells.

ROPS: Signalling proteins that belong to the family of Rho small GTPases conserved in eukaryotic cells and function as central regulators of the polar/local plasma membrane domains and the breakage of symmetry.

PME: Meaning pectin methylesterase, which is an enzyme that performs de-esterification on methylated pectins by removing their methyl groups to increase their viscosity.

XTH: Standing for xyloglucan endotransglucosylase/hydrolase, which is an enzyme that performs hydrolysing action on the cell wall where it can cut and rejoin xyloglucans.

Expansin: A protein that manipulates the cell wall causing cell wall loosening, which

then allows the cell wall to extend.

Cel12A: A wall loosening fungal enzyme that is said to hydrolyse both xyloglucan and cellulose.

Chapter 1

Introduction

Plant growth is a complex and intriguing process, with many unknowns as to how exactly growth takes place. Faced with climate change and population growth, humanity needs plants that can cope with extreme weather events, diseases and rising demands on yield. As a result, understanding plant growth is essential to secure a sustainable future [Ahuja et al., 2010, Flood, 2010]. Modification and adaptations can provide a solution to optimising plant development. Plant growth research spans from studying the individual molecules and proteins that make up and influence the cell wall, to researching whole ecosystems. This thesis aims to examine how plants control their cell wall growth. To tackle this problem, we take a multidisciplinary and multiscale approach. We begin this investigation on the microscale by examining how a small cell wall segment grows to reveal insights into cell wall structure and its manipulation to permit growth. Our project continues on the larger cell scale by examining the chemical and mechanical pathways controlling cell wall growth and shape using the jigsaw like shaped plant pavement cells as an example.

We first outline some basic plant biology and principles of how plants grow in section 1.1. After these preliminaries, we outline the specific questions and objectives we consider in this thesis in section 1.2.

1.1 The world of plants

1.1.1 Plant cell basics

Plants have many key differences to animal cells, one being that plant cells are tightly fixed to one another, meaning that tissue growth and morphology arises due to collaborative expansion, cell division, and communication between cells [Cosgrove, 2005, Mirabet et al., 2011, Hamant and Haswell, 2017]. The main plant cell areas of focus for this thesis are the cell wall, and cytoskeleton, however, other relevant features are the nucleus, cell membrane and vacuole (figure 1.1).

The nucleus contains nearly all of the cells genetic material, and by controlling gene expression, the nucleus regulates cell activity. The cell membrane acts as a barrier between the cell and its surrounding environment and is made up of lipids, proteins and carbohydrates. The cell membrane controls what is transported in and out of the cell, meaning it helps regulate new cell wall material deposition to the outside of the cell, permits communication between neighbouring cells, and links the inner cytoskeleton to the cell wall. Importantly the cell membrane also contains the cytoplasm, which holds all the organelles and is composed of water, sugars and proteins. The vacuole is a fluid filled organelle which, on average, occupies 30% of the cell volume [Buchanan et al., 2015]. The vacuole serves many roles, such as storage of needed proteins, where interestingly, it is where the substances that give fruits and vegetables their flavour are found. The vacuole also plays a vital role in cell growth which shall be discussed later. None of these plant cell features shall be explicitly modelled in this report.

The cell cytoskeleton is a forever changing network of filamentous protein polymers that controls the movement of the cell's content (and in animal cells, controls the movement of the cell itself) [Buchanan et al., 2015]. The two cytoskeleton filaments in plants are actin filaments built from the protein actin and microtubules constructed from the protein tubulin. Each cytoskeleton element is very dynamic where they can spontaneously form, grow and shrink in length, completely break down and interact with the cell membrane and other cytoskeleton filaments. Both of these filaments are polar, where the more dynamic end is called the plus end and the less active end is called the minus end [Allard et al., 2010a]. Both filaments are crucial in

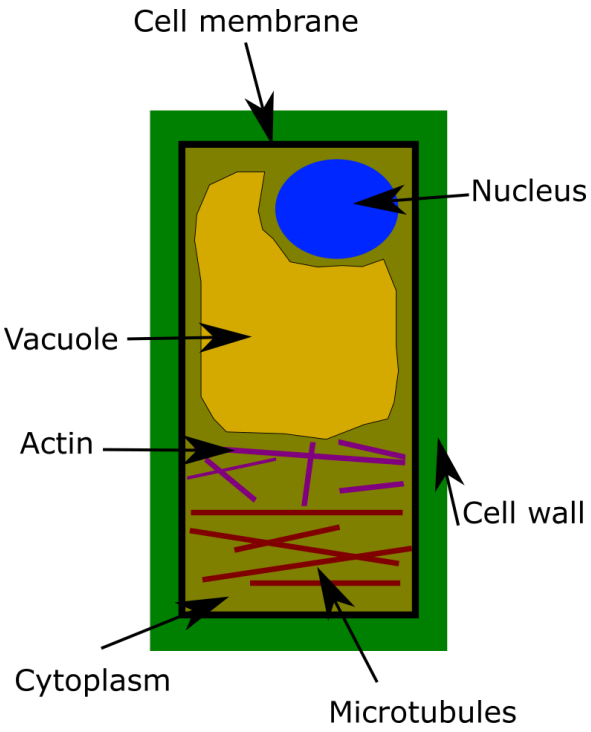


Figure 1.1: The features of interest in a plant cell

plant growth

The plant cell is bounded by the cell wall, where it plays an important role in controlling cell shape by regulating the rate and direction of growth [Buchanan et al., 2015]. Upon removing the cell wall, the cell returns to its state of minimal energy and becomes spherical. It is the cell wall that we shall be primarily modelling in this thesis. The cell wall is highly dynamic, where changes are made to its structure and composition throughout the life of a plant cell. The cell wall consists of three main polysaccharides, cellulose (CMF), hemicellulose and pectin [Scheller and Ulvskov, 2010, Höfte et al., 2012, Park and Cosgrove, 2015, Jarvis, 2009, Cosgrove, 2014]. The cell wall properties, specifically how stiff, anisotropic and viscous the cell wall is, are carefully mediated via active control of the wall's mechanical structure (e.g. via enzymatic action or new material deposition). These properties can be highly localised, where it can be softer or stiffer in different regions in the same cell. Plants form a primary cell wall while growing which later transforms into a secondary cell wall that is stiffer when the cell has stopped growing. Our focus is on growth, and as a result, we shall only consider the primary cell wall, which is made up of two (sometimes three) structurally independent but interacting networks [Buchanan et al., 2015]. The first being the cellulose molecules crosslinked by hemicellulose fibres, and the second being a network of pectin molecules.

Celluloses are long and stiff molecules embedded in a matrix of hemicellulose and pectin. Cellulose molecules are deposited in the cell wall in lamella layers at a variety of angles [Zhang et al., 2016] by cellulose synthase complexes (CSC) in the plasma membrane, which form and orient the cellulose molecules [Kafle et al., 2014]. Due to cellulose's strength, their deposition angle is highly influential on the growth direction creating anisotropic stiffness in the cell wall. Evidence has shown microtubules guide the deposition of cellulose [Szymanski and Cosgrove, 2009, Bidhendi and Geitmann, 2015], by binding to proteins in the cell membrane or possibly to the CSC directly and altering their arrangement in the cell membrane. However, some observations have shown no correlation between microtubules and cellulose orientation [Baskin, 2001]. A few of these

experiments disrupted the microtubules to show cellulose molecules can organise themselves. It is possible that these observations were made after the microtubules arranged the CSC leading to the continuation of cellulose deposition into the cell wall in an ordered manner [Buchanan et al., 2015]. Microtubules influence over cellulose orientation remains a contentious issue. It is likely that microtubules help to align cellulose but are not the only aspect controlling their deposition direction [Baskin, 2001, Kafle et al., 2014]. In this thesis, we shall assume that microtubule direction directly influences cellulose direction.

Hemicelluloses (e.g. arabinoxylan or xyloglucan) strengthen the cell wall by forming hydrogen bonds with cellulose molecules to crosslink cellulose molecules to one another [Scheller and Ulvskov, 2010, Höfte et al., 2012]. These crosslinks are important in the wall properties, where breaking or loosening these bonds could lead to wall softening or relaxation, possibly leading to growth. The exact arrangement and structure of the hemicellulose crosslinks is an open question, where the answer can reveal insights into how plant cells control their growth. This question shall be examined in more detail later.

Pectins serve many responsibilities in the wall, such as controlling wall porosity and providing a charged surface to govern wall pH. We are however interested in their contribution to the cell wall properties where they have been shown to be load-bearing and able to directly control cell wall growth [Bidhendi and Geitmann, 2015]. Pectins are deposited in the cell wall in their methylated state. Methyl esterificated pectins are said to form gels with low viscosity and porosity that helps wall loosening [Sotiriou et al., 2018]. The enzyme pectin methylesterase (PME) performs de-esterification on the methylated pectins by removing the methyl groups where these pectins can then use calcium ions to bind to one another. The number of calcium ion bonds influences the porosity of the cell wall where they can reduce the accessibility of cell wall modifying proteins to the cellulose-hemicellulose network, which can consequently decrease the extensibility of the cell wall [Höfte et al., 2012]. De-esterification of pectins has been linked to both increases and decreases in stiffness [Bidhendi and Geitmann, 2015]. To go into more detail, pectins demethyl esterification can lead to increased elastic compliance [Thompson, 2005, Sotiriou

et al., 2018] while, in hypocotyls, slow-growing walls contained more de-methylated pectin [Daher et al., 2018] where other studies have also shown de-methyl esterification of pectin to be a stiffening agent [Altartouri et al., 2019, Altartouri and Geitmann, 2015]. These contradictions were clarified by Wang et al. [2020] who said that the de-esterification leads to wall softening but a reduction in wall loosening, meaning the wall is more compliant to mechanical perturbation but does not deform plastically

Both hemicellulose and pectins after synthesis are transported in secretory vesicles (phospholipids shells) to the cell wall by the actin cytoskeleton (where the vesicles undergo exocytosis) [Buchanan et al., 2015]. Therefore, actin highly influences where new wall materials (and cell wall loosening enzymes) are deposited. As a result, actin localisation at a specific site can lead to local changes in the cell wall properties.

1.1.2 The mechanics of cell wall growth

Plant growth is the process of irreversible cell expansion. The growth pattern can take many different forms in plant cells. They can expand isotropically, anisotropically or develop into more complex shapes such as plant cell root hairs, where a cuboid like cell forms a long thin protrusion from their main body. The driving force behind cell growth is the isotropic turgor pressure maintained by water uptake into the vacuole. This pressure inflates the cell membrane, whose expansion is then restricted by the cell wall (an inflated balloon in a box) creating a great tension in the cell wall, equivalent to 100-1000 atmospheres ($10^8 Nm^{-2}$) of tensile stress [Cosgrove, 2005, 1993a]. Consequently, as plants grow, their cell walls need to be strong enough to resist bursting but weak enough to allow permanent expansion. Controlled cell wall growth is an amazing feat, where some cells can increase in volume by over $30,000$ times [Cosgrove, 2005].

Plant cell walls extend via a controlled creep [Cosgrove, 2005]. Turgor pressure on the cell wall provides the mechanical energy for cell expansion which causes the wall components to stretch and become stressed. Plastic deformation or growth begins when the mechanical load (turgor pressure) exceeds some critical value (yield threshold). Upon

reaching this critical threshold the wall components yield, allowing the cellulose molecules to move further apart and the cell wall extends.

One of the earliest models of plant cell growth was the Lockhart equation which describes this yielding principle. The Lockhart equation states that the relative elongation rate, α^* (where $*$ denotes dimensional quantities in this thesis), is proportional to the turgor pressure, T^*, if it is above a yield threshold, Y^* [Lockhart, 1965]. This idea is expressed in the form

$$\alpha^* = \frac{1}{L^*}\frac{dL^*}{dt^*} = \begin{cases} 0, & T^* \leq Y^*, \\ \phi^*(T^* - Y^*), & T^* > Y^*, \end{cases} \tag{1.1.1}$$

where L^* is the length of the cell and ϕ^* is the extensibility. If the pressure does not exceed the yield threshold, the cell does not grow as the turgor cannot overcome the wall's strength. This formulation was a useful initial model, but the understanding of plant growth has now improved. Rather than changes in turgor pressure, growth is often controlled via careful control of the yield threshold [Höfte et al., 2012].

Different wall loosening mechanisms control the yield threshold and, consequently, the rate of cell wall creep. Wall loosening refers to the modifications on the cell wall that causes stress relaxation. These modifications can be mediated by the action of proteins and/or enzymes, such as expansins, xyloglucan endotransglucosylase/hydrolase (XTH), and pectin-modifying enzymes, and are regulated by the action of hormones (morphogens), such as auxin, gibberellins, abscisic acid, and so on [Cosgrove, 2005, 2016]. The cell wall alterations can come in the form of scissoring certain mechanically loaded crosslinks, or allowing the viscous flow of these crosslinks [Cosgrove, 2005]. Upon cell wall extension, water is then drawn into the cell to restore high levels of turgor and wall stress. This extension and consequently the thinning of the wall can be balanced by deposition of new wall material to maintain cell wall integrity, where cell wall material deposition is also a method of wall loosening.

Since turgor acts in all directions, cell walls must be highly anisotropic to allow di-

rectional growth. As previously mentioned, anisotropy arises mainly due to cellulose's orientation, where we often see cellulose orientated perpendicular to the primary growth direction [Crowell et al., 2011]. As depicted in figure 1.2, when the cellulose molecules are oriented isotropically, this leads to uniform wall stress resulting in isotropic growth upon wall relaxation. However, when the cellulose molecules are arranged horizontally, it leads to higher stress levels in the cellulose direction, meaning when the cell wall is loosened, it extends in the direction of minimal stress, and the cell grows vertically [Mirabet et al., 2011]. We can also have more localised anisotropy. In figure 1.2 we see cellulose molecules localising at a specific location on the cell wall leading to restricted growth at that point.

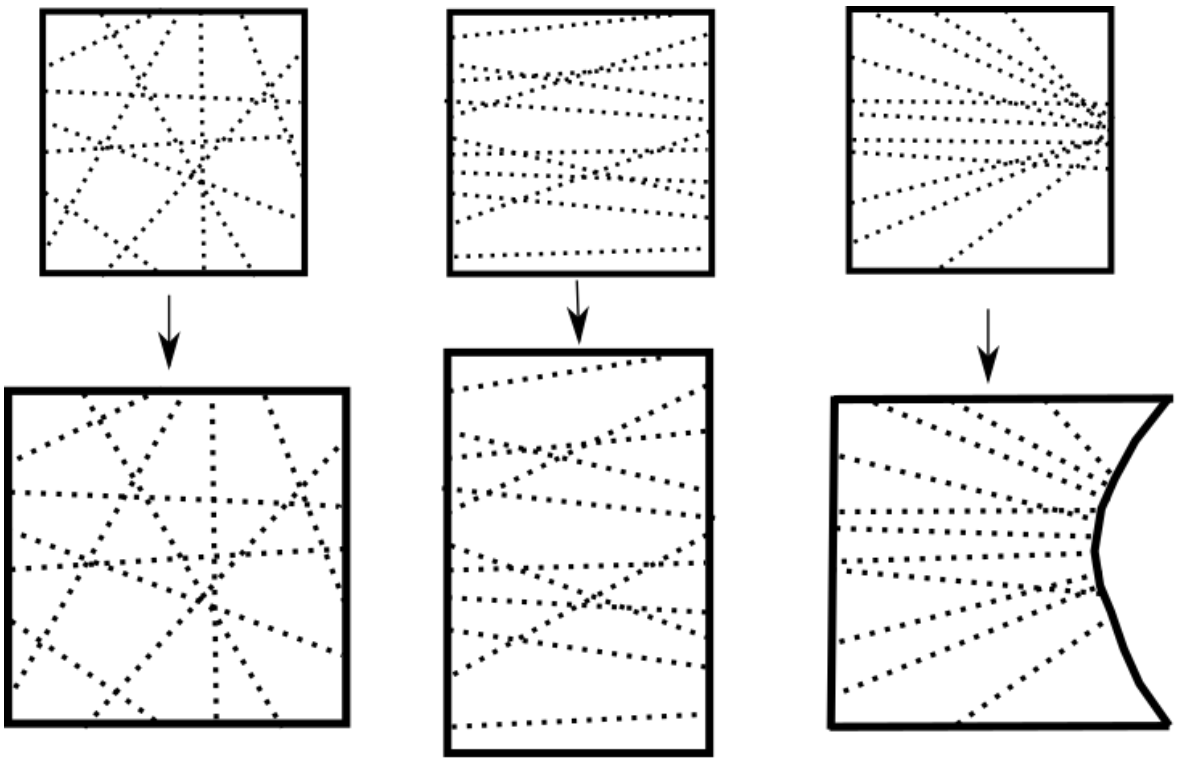


Figure 1.2: Depiction of the consequence of cellulose alignment on cell growth where the thick solid line represent the cell boundaries and the dotted lines represent cellulose molecules embedded in the cell wall

Plant cell growth can therefore be described as a mechanical process in which we have a pressurised vessel restricted by a viscoelastic cell wall [Saito et al., 2006, Cosgrove, 1993b].

The growth rate is then determined by the cell wall's elastic and viscous properties, where these properties will vary depending on the materials and structure of the cell wall and the active wall loosening mechanisms. For example, insertion of methylated pectin into the cell wall can lead to an increase in the viscous flow of the cell wall, cellulose deposition can lead to an increase in stiffness in the cellulose fibre direction, and wall loosening effects such a fibres slippage could reduce crosslink strain.

1.2 Aims, methodology and thesis structure

Growth is a complex multiscale process with many unknowns as to how exactly it is controlled. On the microscale, how the rings of cellulose are crosslinked is not precisely understood [Zhang et al., 2019]. This lack of understanding is directly connected to our lack of knowledge of how enzymes and proteins loosen the cell wall. On the cell level, the grasp of the intricate chemical and mechanical signalling pathways controlling the cytoskeleton and cell wall material deposition is also not complete. We therefore lack the comprehension to understand how plant cells form intricate shapes. It is these open questions on how growth is controlled that we shall attempt to answer in this thesis.

Mathematical models can help to unravel these mysteries. Mechanics is fundamental to plant growth and morphogenesis, as a result, a mathematical framework can therefore describe these mechanistic processes [Smithers et al., 2019]. Such frameworks allow access to details that experiments cannot determine [Chickarmane et al., 2010] by bypassing the practical challenges of experimentation on living tissue [Dupuy et al., 2008], and can provide a means of testing whether proposed mechanisms are sufficient to explain observed behaviour. We shall therefore be adopting several mathematical methodologies using numerical, analytical and stochastic techniques to gain understanding of how plants control their growth.

We begin our investigations of growth control on the microscale by taking a continuum approach and model a small segment of a growing primary cell wall. We incorporate

crosslink dynamics (between cellulose and hemicellulose), and by assuming certain cell wall structure characteristics, we can calculate a stress resultant. By simulating hypothesised wall loosening mechanisms and comparing to experimental observations, we can explore the feasibility behind proposed wall structure and how certain enzymes and proteins could induce growth.

To examine how growth is controlled on the cellular level, we consider a specific type of plant cell called a pavement cell. Pavement cells lie in the epidermis of plant leaves, where they provide strength to the leaf structure and present a protective physical barrier between the inner leaf and the environment preventing moisture loss, outside invasion, as well as containing the inside materials and maintaining temperature. As a result, pavement cells are fundamental to plants as a whole [Qian et al., 2009]. As shown in figure 1.3, as pavement cells develop, they form jigsaw-like shapes, displaying one of the most intricate morphologies of any plant cell type. In this project, we call the concave parts (the protrusions) of the cell, lobes and the convex sections, indents and refer to the wall parallel to the leaf's flat surface as the periclinal wall and the wall perpendicular to the leaf surface as the anticlinal wall. No one truly knows why or how these lobes form [Sapala et al., 2018]. The cells contain a complex network of interacting signalling proteins in the cytoplasm, which affect the cytoskeleton. Through wall material deposition, the cytoskeleton causes large variations in the cell wall properties depending on where in the cell you are. The wall properties then decide the shape of the cell wall, where the morphology of the cells feeds back onto the microtubules and signalling protein network. An understanding of pavement cell growth can help to decode the mechanisms behind growth in other cell types.

Our study of pavement cells takes a multidisciplinary approach by first using experimental methods to examine and confirm hypothesised cytoskeleton dynamics and cell wall mechanical properties. We then derive a novel system of three independent but interacting models:

1. A stochastic model to simulate the important microtubule dynamics, which is vali-

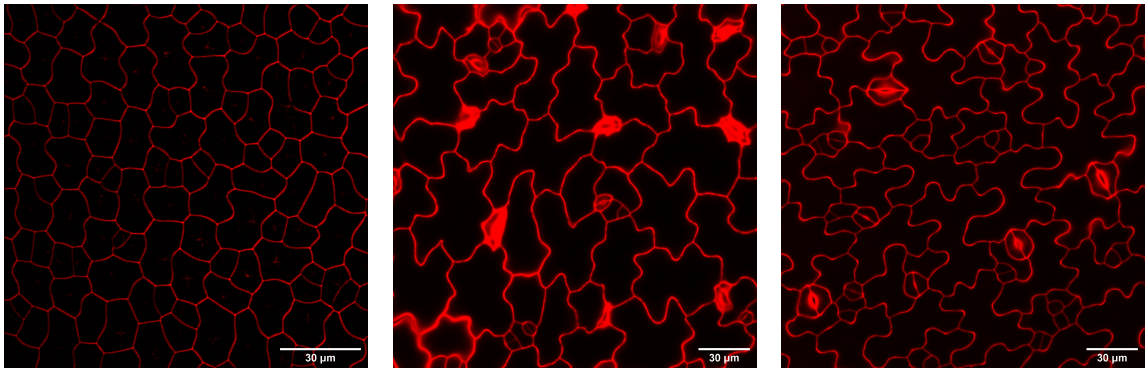


Figure 1.3: Prodendium iodide stained *Arabidopsis thaliana* pavement cells showing how their puzzle like shapes develop as they grow

dated by recreating past results.

2. A system of partial differential reaction-diffusion equations to model the protein signalling pathways that simultaneously interact with the microtubule dynamics in the pavement cell shapes.

3. A vertex element viscoelastic mechanical model to simulate pavement cell growth using the previous two models to inform the parameter choices.

As the reaction diffusion timescale of the signalling proteins we model is much faster (its scale is seconds [Payne and Grierson, 2009]) than the growth rate (which is on the scale of days Zhang et al. [2011]) and as the microtubule array can change formation in a matter of hours [Jacques et al., 2013] we can model the protein signalling network reacting with the microtubules separately from the growth dynamics, in a similar manner to Higaki et al. [2016].

In all models of pavement cell dynamics we restrict our attention to 2D models for computational simplicity with the following justifications. The first being is the vertex element model we are using (which incorporates aspects of a 3D system) is based on previous work [Fozard et al., 2013] which managed to successfully and accurately model root growth. Secondly, pavement cells share their anticlinal walls with neighbouring cells meaning that the rate of expansion must be identical in the lobes and indents [Kotzer and Wasteneys, 2006] and when combined with the fact that it is the periclinal wall which

controls lobe growth [Bidhendi et al., 2019] means that we do not lose significant amounts of information by ignoring the anticlinal wall. Finally, as in the reaction-diffusion model, we are modelling the active forms of the relevant signalling proteins, which lie primarily in the plasma membrane [Yang and Lavagi, 2012] where the proteins diffuse and interact along a 2D surface, we once again do not lose that much information by modelling in 2D.

We begin this thesis with an in-depth background of the requisite biological knowledge and previous relevant mathematical models in chapter 2. Our modelling commences with investigating the cell wall structure and its wall loosening mechanisms in chapter 3. We then start our investigation of pavement cell development by using experimental methods in chapter 4. Following this beginning, we then develop our models of pavement cell dynamics by starting with simulating microtubule dynamics in chapter 5. We then derive our partial differential reaction-diffusion equations in chapter 6. Our vertex element viscoelastic model is then formulated in chapter 7. We finish by summarising and discussing our findings on how plants control their growth in chapter 8. Additional fully detailed equation derivations and some results not suitable for the main text can be found in the appendix in chapter A.

Chapter 2

Preliminaries

Before delving into the modelling process more preliminary information needs to be covered. We detail an in-depth background biological background of the microscale cell wall dynamics and pavement cell development in section 2.1. This section is then followed by a literature review of previous relevant mathematical models in section 2.2.

2.1 Biological background

We shall now further detail the prerequisite knowledge and the specific open questions to be investigated. Hypothesised wall loosening mechanisms and how this relates to problems with existing theories as to how the cell wall is crosslinked is discussed in section 2.1.1, where we also explain a possible alternative called the biological hotspot hypothesis. This is the biology that will be explored in the continuum model in chapter 3. An explanation of microtubule dynamics follows in section 2.1.2, which will be needed to understand the stochastic microtubule model in chapter 5. Experimental and biological terms are then defined in section 2.1.3 to provide the background knowledge for our experimental work in chapter 4. We finish by detailing and examining the evidence for the signalling and mechanical pathways that are hypothesised to influence pavement cell shape in section 2.1.4, pathways that we shall be modelling in chapters 6 and 7.

2.1.1 Cell wall structure, enzyme action and biological hotspots

Experimental observations of the cell wall (in *Arabidopsis thaliana* roots and hypocotyls) found that cellulose molecules are transversely directed to the growth direction after deposition in the inner cell wall and passively reorient to a longitudinal direction as they move to the outside of the cell wall due to cell wall extension [Anderson et al., 2010, Burgert and Fratzl, 2009, Geitmann, 2010, Kafle et al., 2014]. When reorientated the cellulose molecules can then resist strain in all directions.

It was previously thought that cellulose molecules are crosslinked via a tethered network where the cellulose fibres run parallel to each other and are continuously joined

together by hemicellulose fibres, which form hydrogen bonds with the cellulose filaments and peel off when the network is deformed [Cosgrove, 2016]. There are several problems with this theory. Studies on the cell wall found that xyloglucan-cellulose interactions are not as common as what the tethered network predicts and that pectin-cellulose interactions are more prevalent than expected [Cosgrove, 2016]. It was also found that some plants that lack xyloglucan (mutant forms of *Arabidopsis thaliana* and celery) displayed only a small reduction in growth [Park and Cosgrove, 2015] implying the role of xyloglucan in cell wall strength could have been exaggerated.

The protein expansin is a pH-controlled wall-loosening protein [Cosgrove, 2005]. Experiments have shown expansin action to induce growth [Zhang et al., 2019, Sampedro and Cosgrove, 2005] while in contrast, other tests have observed the cell wall to withstand more force without bursting [Cosgrove, 2016]. Expansin action seems to loosen but not soften the wall [Zhang et al., 2019], where there has been no observed hydrolysis action by expansin [Cosgrove, 2000]. Consequently, expansin's wall loosening mechanism remains elusive. It is hypothesised that expansin might target cellulose-cellulose sites [Zhang et al., 2019, Cosgrove, 2015] where they may induce viscous slippage of the fibres [Cosgrove, 2000, Arsuffi and Braybrook, 2017]. Cel12A, an enzyme present in fungi, also causes wall loosening. Evidence has shown Cel12A to perform hydrolysis of both xyloglucan and cellulose; however, unlike expansin, Cel12A leads to a reduction in wall strength [Cosgrove, 2016, Yuan et al., 2001] and thus causes both wall loosening and wall softening [Zhang et al., 2019]. XTH has been observed to have a hydrolysing action on the cell wall where it can cut and rejoin xyloglucans; despite this observed effect, it strangely does not induce significant cell wall extension, contradicting the predictions made by the tethered network model [Cosgrove, 2005, 2016]. In summary, enzymes that individually cut either hemicellulose or cellulose are unable to induce cell wall extension, while ones that cut both do [Cosgrove, 2016].

These studies present evidence that the tethered network model is not a feasible explanation of how the cell wall is structured and emphasises the mechanical role of other

molecules like pectin. It has been suggested that walls are loosened only when relatively inaccessible cellulose-hemicellulose junctions are targeted. Such that when xyloglucan is present, it could be concentrated around a limited number of tight distinct biological hotspots (BH) [Park and Cosgrove, 2015] where cellulose molecules come into close proximity with one another. These close cellulose-cellulose junctions incorporating xyloglucan have been observed in the cell wall using atomic force microscopy [Cosgrove, 2016] and solid-state NMR spectroscopy [Wang et al., 2013]. Pectin is also theorised to have a role to play in these hotspots [Zhang et al., 2016].

These concentrated hotspots could allow the controlled extension of the cell wall where these distinct spots are selected to allow growth [Park and Cosgrove, 2015, Cosgrove, 2014, 2016, 2015]. Expansin could permit wall slippage and cell12A could perform hydrolysis action at these sights to induce wall loosening. The hotspot hypothesis claims that a small amount of degradation of the hotspots could lead to the load being carried by pectin and other cell wall components, which then enables the viscous flow of the cell wall, providing a possible mechanism for growth. In chapter 3 we shall examine the feasibility of the biological hotspot hypothesis and explore its implications on possible enzyme loosening mechanisms in order to explain observed experimental behaviour.

2.1.2 Microtubule dynamics

Microtubules are part of the cytoskeleton in plant cells and are crucial for cell function where they influence and are influenced by the cell shape, stress patterns and signalling pathways within the cell. Microtubules are interesting because they are said to arrange in highly organised arrays where they can align transversely or longitudinally to the elongation axis [Wasteneys and Ambrose, 2009]. It is said the microtubule organisation is a result of their stochastic interactions and behaviour and not as a result of being initiated in an organised way. For example, in a plant cell after drug-induced disassembly, microtubules regained their parallel organisation after time, showing that their organised arrays are an emergent property [Ehrhardt and Shaw, 2006, Ehrhardt, 2008]. Ordered

arrays of microtubules are essential as this allows them to deposit cellulose in specific directions, which creates anisotropy in the cell walls. Therefore to model their important dynamics in chapter 5 we first need to know their biology.

In this thesis, we are only discussing cortical microtubules, i.e. ones that are bound to the membrane, in the interphase stage of a plant cell (when the cell is not undergoing mitosis) [Chi and Ambrose, 2016]. Paradez et al. [2006] say that microtubules lie mainly on the cell membrane where they are anchored to it by CLASP proteins. Consequently, all their dynamics are on a 2D surface. By examining only cortical microtubules, we are therefore characterising the majority of the microtubule's dynamics.

Microtubules spawn randomly at any point in a cell where they can also spawn/branch from other microtubules [Wasteneys and Ambrose, 2009, Murata et al., 2005]. A microtubule's minus end is more stable and tends to be non-growing, while the plus end is more dynamic and gains tubulin to grow or loses tubulin to shrink. Microtubules' plus ends randomly and often switch between growth, pauses and rapid shrinkage, a behaviour known as dynamic instability [Allard et al., 2010b, Goodson and Jonasson, 2018]. This switch between growth and shrinkage is called a catastrophe and, in reverse, is called a rescue. Their minus ends can also have dynamic instability (primarily in plus ends though), which can lead to a treadmilling effect where the plus end is growing, and the minus end is shrinking [Dixit and Cyr, 2004]. On average, the plus end is growing while the minus end is shrinking [Chakrabortty et al., 2018, Mirabet et al., 2018, Eren et al., 2015]. A microtubule is completely broken down when the minus end catches up with the plus end or when the plus end's shrinkage reaches the minus end. Some plant cells possess flat surfaces, which creates intersection points with high curvature where the different faces of the cell join. As a consequence, it has been observed that microtubules can have edge induced catastrophes which increase in likelihood with increased curvature [Chakrabortty et al., 2018].

Due to their 2D surface confinement, microtubules often interact/collide with one another. On these occasions, three things can occur depending on their angle of collision

[Chi and Ambrose, 2016]. When a microtubule collides into another above some critical angle, it can cause the microtubule to undergo a catastrophe or simply pass over the other microtubule. If instead, the collision angle is small, the microtubule colliding into another can change direction, bundle up, form crosslinks with, and run parallel with the other microtubule, or it can crossover [Allard et al., 2010b]. These events are explicitly dependant on the angle of interaction, with the probability of bundling increasing with a decrease in the collision angle and vice versa for collision induced catastrophe events [Dixit and Cyr, 2004]. Other phenomena are possible upon microtubule collision, such as the microtubule buckling on collision, the microtubule's direction is perturbed or a microtubule could be severed on collision. When a microtubule collides into another, it is often followed by a pause before bundling, crossing over or catastrophe. Through tracking of florescent markers, it was observed that this contact time (pause) for microtubules undergoing bundling is sevenfold longer than the contact time for catastrophe events [Dixit and Cyr, 2004]. Chi and Ambrose [2016] also mention that encounter based catastrophe events were followed by a pause more often than random catastrophe events where the latter events also pause for a shorter amount of time.

There is significant evidence that microtubules align with the direction of maximal tensile stress, [Szymanski and Cosgrove, 2009, Hamant et al., 2019, Mirabet et al., 2018, Colin et al., 2020], and that this plays a more significant part in their organisation than the geometry of the domain they are contained in. Microtubules have been repeatably shown to change orientation in response to externally imposed tension, showing that they can detect tissue stress and respond quickly [Jacques et al., 2013]. There is evidence that this reaction is as a result of microtubule's being stabilised by stress [Hamant et al., 2019]. The microtubule severing protein katanin has been shown to mediate microtubule's response to changes in mechanical stress, where katanin severing could be biased to microtubules not aligned with the stress direction [Sampathkumar et al., 2014, Szymanski, 2014].

2.1.3 Experimental background

In this thesis we make use of several experimental terms which we shall now define. Firstly we refer to plants that have had their genome unedited as wildtype plants, those which have had theirs altered, or induced to change, as mutants and plants that have had foreign DNA introduced into their genome as transgenic [Rani and Usha, 2013]. Constitutively active (CA) mutants are plants that have been edited such that a set gene is overexpressed, meaning that more of a specific protein is produced when compared to the wildtype [Parnot et al., 2002]. Oppositely, dominant negative (DN) mutants have had their genome edited such that a gene is now expressed at decreased levels resulting in a set protein being produced at a reduced concentration [Alberts et al., 2002]. Loss of function mutants have once again had their genome changed, resulting in a slightly different protein being produced, meaning it is less effective or does not work at all.

Other plants with their genome edited do not necessarily affect the plant cell's day to day processes but instead allow us to observe them. Genes can be edited such that the proteins are made with Green fluorescence markers, GFP (or yellow fluorescent markers, YFP or other such alternatives) so that the proteins are tagged [DeBlasio et al., 2010]. This is an example of a transgenic plant (as the GFP marker is a foreign protein). This tagging means that when a laser produced by a confocal microscope hits the markers at a specific emission range, the GFP markers emit light and allows us to observe the proteins' locations.

The majority of plant studies are done on the model plant *Arabidopsis thaliana* (where we shall also be performing experiments on this plant) as it has been thoroughly studied with its genome being well categorised and many different mutants being available for research [Koornneef and Meinke, 2010].

It is important to know that embryonic plants in their seeds contain organs called cotyledons which are their first leaves, where cotyledons also have jigsaw like pavement cells. We also define the term, abaxial side to be the bottom/lower side of the plant leaf and the adaxial as the top/higher side of the leaf. To match with the existing literature,

we use the term lobeyness to generally describe the combination of how many lobes and how big are the amplitudes of these lobes in pavement cells.

2.1.4 Pavement cells and their development

Pavement cells seem to form random and varied interlocking shapes. Very similar species exhibit morphological variations in their pavement cells, where some species of plants have evolved undulated pavement cells and then de-evolved them, suggesting that the mechanisms behind pavement cell morphology could be very subtle [Vőfély et al., 2018]. Pavement cells start off polygonal early on in development, where they develop small undulations which grow in amplitude and number, making the pavement cell's shape increasingly complex as they grow while also maintaining the number of cellular neighbours they have [Carter et al., 2017]. We note that the vast majority of experiments discussed below are done on the plant *Arabidopsis thaliana*.

We are exploring how pavement cells form these shapes. Two relatively unconnected theories have been proposed for the generation of undulating pavement cells: the first deals with the patterning of intracellular molecules responsible for organizing the cytoskeleton [Craddock et al., 2012]; the second deals with cell wall mechanics, cell shape/stress and tissue stress [Sapala et al., 2018, Bidhendi et al., 2019]. These ideas can be linked since the cytoskeleton directly influences cell wall deposition and, therefore its mechanical properties where on the other hand cell/tissue stress patterns can also affect the cell cytoskeleton (figure 2.1).

We break down this discussion of pavement cell development into different sections. Firstly, we give a general introduction to pavement cells by detailing why they possibly form these shapes and the observed differing growth rates and cell wall stiffness's that help create their intricate morphology in section 2.1.4.1. Leading on from this we then detail how these differing cell wall stiffnesses arise as a result of the cell cytoskeleton spatially varying in concentration causing differential cell wall material deposition and loosening in section 2.1.4.2. We then cover what chemical signalling pathways could cause these spatial

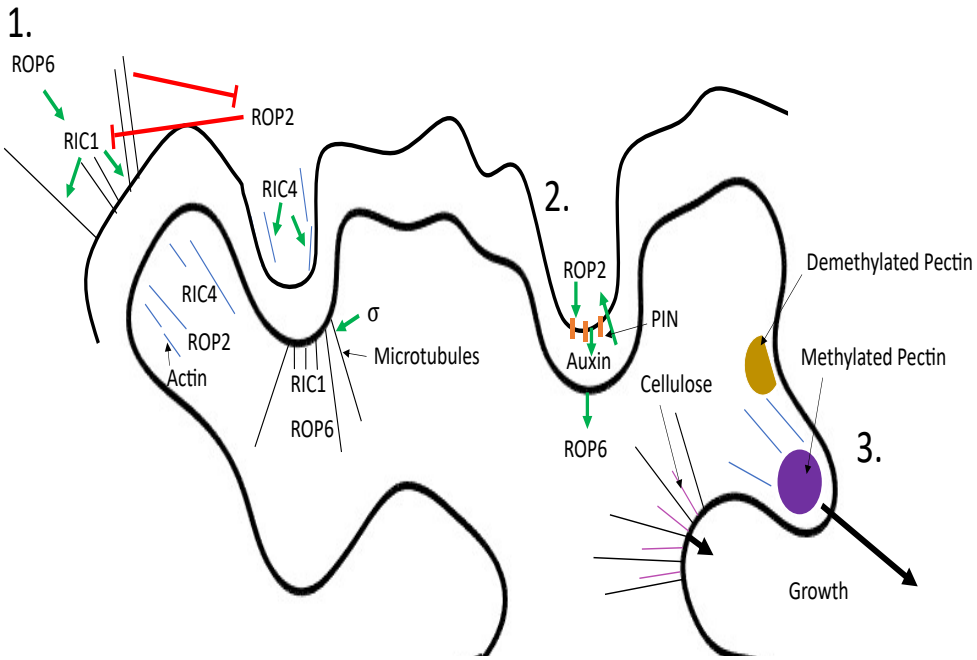


Figure 2.1: Diagram depicting current understanding of pavement cell development

variations in the cell cytoskeleton in section 2.1.4.3. A summary of the chemical signalling pathways, their interactions with and effect of the cell cytoskeleton, the feedback loops in the system and all of their possible roles in lobe initiation is then made in section 2.1.4.4. Finally, we cover the possible mechanical mechanisms for lobe initiation in section 2.1.4.5.

2.1.4.1 Introduction to pavement cells

Pavement cell shape could be advantageous to plants, helping explain why they form. Since the spongy mesophyll layer, which lies underneath the epidermis, contains air holes, it might not be able to provide strength to the tissue. As a result, the epidermis could be under increased tension. On top of this, as a result of the pavement cells large size, they are also under increased levels of turgor imposed stress. It has been shown that pavement cell's jigsaw morphology helps reduce their stress. This stress reduction could be advantageous by helping decrease the resources needed to strengthen the tissue and/or reduce the chance of the tissue rupturing [Sapala et al., 2018]. The outstanding question is therefore how they form.

Tracking pavement cell growth over time has shown that differential growth rates

across the pavement cell periclinal surface help create their jigsaw-like shapes. The indents displayed anisotropic growth where the primary direction of extension was tangential to the indents anticlinal wall, whereas, the lobes were found to be expanding isotropically. On top of this, the growth rates in the lobes were shown to be higher than the indents [Armour et al., 2015]. The differing growth rates and directions that permit further lobe development are caused by local differences in the cell wall viscoelastic and anisotropic properties [Altartouri et al., 2019]. It has been evidenced that the indents are stiffer than the lobes [Sampathkumar et al., 2014] where these local differences in stiffness can occur before initial lobe formation [Altartouri et al., 2019]. These local differences in cell wall properties could result from an alternating pattern of stiffer cell wall components being deposited in the indents (and indent precursor sites) and softer material and wall loosening enzymes being deposited in the lobes (and lobe precursor sites). However, the controls behind lobe initiation or what could cause this alternating pattern of cell wall material deposition are still not completely clear.

2.1.4.2 The influence of the different cell wall materials and the cytoskeleton on pavement cell development

In fully developed pavement cells, much evidence has shown cellulose to be deposited at the indents on the anticlinal and periclinal cell wall where they fan out, causing local anisotropy, which restricts growth at the indents [Altartouri et al., 2019, Bidhendi et al., 2019]. Cellulose's role in lobe formation is also evidenced by the fact that when we interfere with cellulose alignment, it causes a reduction in lobe formation [Bidhendi et al., 2019]. Microtubules have been observed to mirror cellulose alignment in pavement cells where they also form organised arrays perpendicular in direction to the indent anticlinal wall curve [Armour et al., 2015, Qian et al., 2009, Altartouri et al., 2019, Kotzer and Wasteneys, 2006, Bidhendi et al., 2019]. It was also found that they were fewer microtubules in the lobes. The localisation of the periclinal microtubules to the indents was shown to be persistent, where they were consistently enriched throughout lobe development [Armour

et al., 2015, Zhang et al., 2011]. However, it was found that the localisation of the anticlinal microtubules to the indents was not as consistent and stable [Belteton et al., 2018]. This lack of anticlinal microtubule localisation may not matter as it is claimed that is it the periclinal microtubules that primarily control lobe development [Zhang et al., 2011].

It has been claimed that early in pavement cell development when the cell wall is straight, there are localised areas of wall thickening on the periclinal and anticlinal wall where cellulose localises and restricts growth. This has lead to suggestions that it is the cellulose wall reinforcement, controlled by the microtubule array, that causes lobes initiation [Panteris et al., 1994, Panteris and Galatis, 2005]. Other studies seem to back up this idea where it was found that microtubule localisation sites on a straight wall in young pavement cells (1 day old) predicted indent locations [Armour et al., 2015]. However, timelapse images have shown these bundles in early pavement cells to be unstable on the timescale of cell expansion [Lin and Yang, 2020]. Mutants that have a disordered microtubule array develop pavement cells that have wider and fewer lobes [Armour et al., 2015, Szymanski, 2014] where in some cases these mutants developed no indents [Panteris and Galatis, 2005]. Other mutants, which have microtubules observed to be short, sparse and misaligned, have been observed to have severe phenotypes where pavement cells remained polygonal [Qian et al., 2009]. Depolymerising microtubules early in development also led to fewer lobes (per cell perimeter, so it was not due to inhibited growth) in older pavement cells [Armour et al., 2015, Altartouri et al., 2019]. Furthermore, treating pavement cells so that they had no microtubules caused pavement cells to display little or no lobe development in early development [Panteris and Galatis, 2005]. Microtubules, through their deposition of cellulose, obviously have an essential role to play. However, when examining another mutant, which had the same amount of cellulose but was less organised than the wildtype, it was found that lobes, albeit shallower, still formed. Analysis was also performed on the degree of cellulose anisotropy in this mutant and found insignificant differences in the degree between the lobe and indent sites. It was similarly found that in early pavement cells, microtubules did not necessarily have different concentrations on

either side of the cell wall at a lobe-indent precursor site [Altartouri et al., 2019]. As a result, it was suggested that microtubules are important in making lobes more prominent but are not necessarily needed for lobe initiation [Altartouri et al., 2019].

It has been shown that the indents are regions of increased stress [Szymanski, 2014]. As mentioned in section 2.1.2, microtubules align in the direction of maximal stress. Cellulose deposition at the indents inhibits growth allowing for the creation of more prominent lobes. As the lobes increase in length, the stress held in the indents increases further, making the microtubules more likely to align with the indents permitting the deposition of more cellulose. This process is a possible feedback loop where the cell morphology influences the cytoskeleton and vice versa [Szymanski, 2014, Lin and Yang, 2020].

Both Xu et al. [2010] and Fu et al. [2002] observed GFP marked actin (GFP-mTalin) to localise in pavement cell lobes where they could be delivering cell wall material and wall loosening enzymes [Armour et al., 2015] to induce growth. Mutants that affect actin were found to have reduced lobe amplitude but lobe width was not affected [Qian et al., 2009, Smith, 2003]. Depolymerising actin filaments early in development also leads to fewer lobes (per cell perimeter) in older pavement cells [Armour et al., 2015]. Mutants of maise pavement cells that displayed no actin localisation but still formed microtubule bands developed no lobes demonstrating the possible importance of actin in lobe initiation [Frank et al., 2003]. These results have led to suggestions that actin localisation to the lobes leads to tip growth [Armour et al., 2015, Smith, 2003]. Contradictory results have also been observed. Armour et al. [2015] observed no localisation of filamentous actin in either developing indents or lobes. When localisation did occur in older pavement cells, they found actin enriched in the indents instead. However, they comment that the difference could occur as a result of the GFP marker they used. Another experiment also found lobes to still form in mutant maise pavement cells that were lacking in actin [Panteris and Galatis, 2005]. Actin's role and localisation is therefore uncertain, however, it has been suggested that the actin localisation comes in after lobes have been initiated [Panteris and Galatis, 2005].

Pectin has been recently shown to be important in pavement cell development. Demethylated pectin was observed to be higher in concentration in the indenting regions of the periclinal wall (and stiffening the region) [Bidhendi et al., 2019, 2020a] when compared to its adjacent lobe on the other side of the cell wall. It was also found that there was a high amount of methylated pectin turnover and remodelling in the lobe regions (thus softening the region) [Sotiriou et al., 2018]. Importantly demethylated pectin's differential concentration was shown to be high in early pavement cell development where this localisation came before microtubule localisation [Altartouri et al., 2019]. It is hypothesised that pectin causes lobe initiation by first stiffening a region, leading to an indent resulting in an area of increased stress which the microtubules can then align with and deposit cellulose to reinforce, allowing an indent to further develop [Altartouri et al., 2019].

2.1.4.3 The signalling proteins and their effect on pavement cells

There is evidence of influential Rho like GTPase's, specifically ROP2 and ROP6, which are cell membrane bound (when activated) signalling proteins that can control the cell cytoskeleton. ROP2 has been shown to activate RIC4 (another signalling protein), which promotes the assembly of actin filaments needed for localised lobe expansion, [Yang and Lavagi, 2012, Xu et al., 2010] where GFP ROP2 has been observed to localise in the lobes [Smith, 2003, Fu et al., 2009]. Evidence for ROP2's role in pavement cell development was presented by Fu et al. [2005], who used mutant analysis to show that when you knock out ROP2 expression in *Arabidopsis thaliana*, pavement cells developed tiny undulations. By also analysing dominant negative ROP2 mutants with GFP marked actin, they found that pavement cell lobe formation was prevented due to a combination of reduced levels of actin and a lack of actin localisation to the lobes [Fu et al., 2005, Xu et al., 2010]. This observation is complemented by Panteris and Galatis [2005] who also examined dominant negative ROP2 mutants to find that pavement cell lobes developed with smaller amplitudes. Alternatively, by inspecting constitutively active ROP2 mutants, it was observed that the pavement cells had an even distribution of actin across the cell, where the for-

mation of the organised microtubule array was also delayed with a lack of microtubule localisation at the indents. The disorganised cytoskeleton components in these constitutively active ROP2 mutants led to a lack of lobes and raised levels of isotropic cell expansion. Further observations of constitutively active ROP2 mutants showed RIC4 to be prominent in the whole cell [Fu et al., 2005] demonstrating ROP2's activation of this protein. ROP2 is therefore an important signalling protein in pavement cell shape development. Another signalling protein, ROP4, also acts in a very similar way to ROP2, with its knockout mutant expressing a similar but weaker phenotype to the ROP2 knockout mutant [Fu et al., 2005].

When promoted by ROP2, GFP marked RIC4 has been shown to localise to the lobes [Fu et al., 2005, Xu et al., 2010] where it is said to promote actin's accumulation and stabilisation [Craddock et al., 2012, Yang and Lavagi, 2012]. This effect can be observed when overexpressing RIC4 in pavements which results in increased accumulation and distribution of actin [Fu et al., 2005]. Furthermore, a knockout mutation of RIC4 led to pavement cells that had lobes with reduced amplitude [Fu et al., 2005], a result consistent with the idea that without actin localisation, the lobes cannot extend further.

ROP6 is said to promote RIC1, which promotes the organisation of cortical microtubules in the indents, allowing for the deposition of cellulose that restrict growth there [Yang and Lavagi, 2012, Feiguelman et al., 2018, Xu et al., 2010, Lin et al., 2015]. By using GFP markers, ROP6 has been shown to localise at the cell indents [Fu et al., 2009]. ROP6's influence on pavement cell morphology is demonstrated by examining the loss of function mutants which displayed a reduced lobeyness with wider necks from increased growth in the indents. By using GFP-tubulin, this mutant exhibited fewer cortical microtubule's, with them being more disorganised and less bundled with one another [Fu et al., 2009]. Following up on this experiment, over expression of ROP6 caused the microtubules to form transverse arrays perpendicular to the elongation axis resulting in rectangular like pavement cells. ROP6's interactions with RIC1 have been directly shown in experiments where it was observed that ROP6 causes RIC1 to bind to the microtubules [Fu et al.,

2009].

It has been observed using fluorescent markers that RIC1 can strongly associate with the microtubules (where they are otherwise bound to the plasma membrane) [Fu et al., 2005, Craddock et al., 2012]. RIC1's importance in pavement cell shape development has been shown through mutant analysis, where changing its expression displays similar results to the ROP6 mutants. Over expression and loss of function mutants both lead to defective pavement cell shapes where the former inhibits lobe formation to form rectangular like cells with the microtubules forming transverse arrays, and the latter causes lobes to have wider necks but no significant difference in lobe length where the microtubules were found to be in reduced numbers and when present were more disorganised [Fu et al., 2009, Feiguelman et al., 2018]. These experiments led to the conclusion that RIC1 promotes well-ordered microtubule arrays in the indenting regions [Fu et al., 2005]. It has been suggested that RIC1 promotes an ordered array by increasing the microtubule severing activity of microtubules that branch of one another, thus removing nonaligned microtubules, to induce a densely packed and aligned microtubule array [Lin et al., 2013, Feiguelman et al., 2018]. It alternatively has been proposed that RIC1's removal from microtubules increases the microtubule disassembly [Fu et al., 2005].

It is hypothesised that ROP2 inhibits RIC1, a signalling protein that binds to the microtubule's and helps microtubules organise themselves [Yang and Lavagi, 2012, Xu et al., 2010]. This inhibition would explain the delayed formation of organised microtubules in constitutively active ROP2. Evidence of this inhibition was found by using knock out and dominant negative mutants of ROP2 where, by observing GFP marked RIC1, it was discovered that RIC1 associated with the microtubule's sooner on in pavement cell development and in increased levels. The microtubules were also found to form more and thicker bundles than the control. On the other hand, by examining constitutively active ROP2, they found RIC1 to move from the microtubule's to the plasma membrane [Fu et al., 2005]. This inhibition is not in only one direction though. De-polymerising the microtubules using oryzallin treatment was shown to increase the RIC4 ROP2 interactions.

This has led to suggestions that microtubules suppress ROP2 activity [Xu et al., 2010, Yang and Lavagi, 2012, Fu et al., 2005]. This could be a possible feedback loop where, in the lobes, ROP2 could prevent the microtubules from localising and along the indents, the microtubules could prevent ROP2 from localising, leading to increased levels of both of these substances in their respective areas and leading to further inhibition.

Another important compound in pavement cell development is the plant hormone auxin, which has been shown to promote lobeyness in pavement cells [Yang and Lavagi, 2012, Lin et al., 2015, Lin and Yang, 2020]. Mutants that express auxin at reduced levels displayed a reduced lobeyness, where the application of synthetic auxin allowed these mutants to recover a normal (wildtype) phenotype [Xu et al., 2010]. This promotion of lobeyness in pavement cells was found to be dose dependant, where increases in the concentration of applied synthetic auxin in wildtype pavement cells further increased their lobeyness [Xu et al., 2010]. It has been suggested that auxin affects pavement cells because it promotes both ROP2 and ROP6. Applying synthetic auxin to ROP2 loss of function mutants did not allow the recovery to a wildtype phenotype [Xu et al., 2010] suggesting ROP2 acts downstream from auxin. When examining GFP marked ROP2 in wildtype pavement cells, upon auxin application, ROP2's concentration quickly increased, suggesting auxin directly promotes and activates ROP2. Auxin's relationship with ROP6 follows similar trends, where mutants expressing lower amounts of auxin decreased RIC1's association with the microtubules, resulting in a disorganised microtubule array [Xu et al., 2010]. In wildtype pavement cells, ROP6 concentration was also seen to rapidly increase upon auxin treatment [Xu et al., 2010, Pan et al., 2020] showing that auxin also activates ROP6.

It has been theorised that auxin causes lobe initiation by promoting both ordered plasma membrane lipid domains which randomly form and ROP6's association with these domains [Pan et al., 2020]. This effect is combined with auxin's observed influence of decreasing the diffusion speed of these lipid groups, which could increase their size. It has been suggested that these ROP6 ordered plasma membrane lipid domains could be the

precursor sites for indentation formation [Xu et al., 2010].

PIN1, a molecule that lies in the plasma membrane that actively transports auxin from one cell to another [Omelyanchuk et al., 2016] has also been shown to be influential in pavement cell development [Xu et al., 2010, Guo et al., 2015]. Their influence was demonstrated by examining PIN1 loss of function mutants which reduced pavement cell lobeyness where applying auxin could not recover the wildtype phenotype [Xu et al., 2010]. It has been observed through examining GFP marked PIN1 that PIN1 undergoes endocytosis (internalised into the cytoplasm from the cell membrane) mainly along the indents and is inhibited on the lobes. Thus PIN1 is mainly localised in the lobe regions of the plasma membrane [Yang and Lavagi, 2012, Xu et al., 2010, Craddock et al., 2012, Lin et al., 2015]. This localisation has been hypothesised to be as a result of ROP2 stabilising the actin cytoskeleton, which in turn inhibits PIN1 endocytosis [Nagawa et al., 2012, Xu et al., 2010]. Evidence of this phenomenon was provided when examining the dominant negative ROP2 mutant where PIN1 endocytosis increased [Xu et al., 2010]. It is theorised that PIN1 localisation to the lobes allows the exportation of auxin into the cell wall region between a neighbouring indent and lobe where it can diffuse back into the adjacent cells, where it activates ROP6 and ROP2 at the indent and lobe respectively [Craddock et al., 2012, Yang and Lavagi, 2012]. This activation could lead to a feedback loop where the activation of ROP2 in the lobes further promotes actin stabilisation which can increasingly help inhibit the endocytosis of PIN1. PIN1 could be the primary mechanism of how neighbouring cells communicate with one another, as a lobe needs to be matched by an indent on the opposite side of the cell wall and vice versa. However, there is some contradicting evidence where further observations of PIN1 mutants have shown them not to affect pavement cell morphogenesis [Belteton et al., 2018].

It is worth noting that other proteins and hormones have been shown to affect pavement cell morphology. The proteins TOPP4, SPK1, and SCAR, and other plant hormones such as gibberellic acid and brassinosteroid have also been found to promote pavement cell lobeyness [Lin and Yang, 2020, Guo et al., 2015, Feiguelman et al., 2018, Liu et al.,

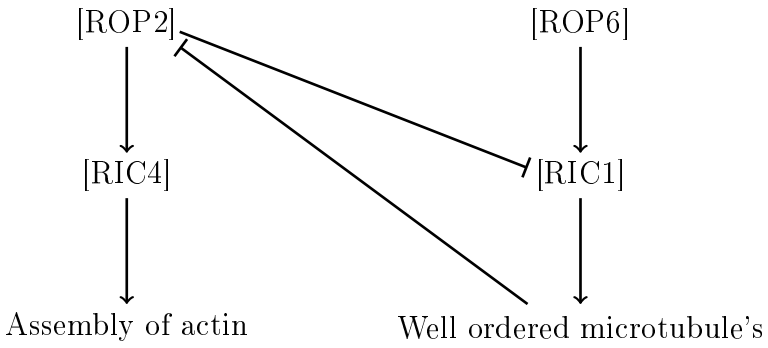


Figure 2.2: Inhibition and stimulation relationships in pavement cell devlopment

2018, Qian et al., 2009].

2.1.4.4 Summarising the chemical signalling pathways

We can now summarise the chemical signalling pathways and interactions hypothesised to further develop and possibly initiate pavement cell lobes. These pathways consist of ROP2 promoting RIC4, which promotes actin accumulation but inhibits RIC1; ROP6 promotes RIC1, stabilising microtubule bundling where the microtubules inhibit ROP2. These interactions lead to a system where the two ROPs mutually inhibit each other and can set up a spatial organisation of alternating patches of actin and microtubules in the lobes and indents respectively, where the microtubules are also stabilised by stress [Craddock et al., 2012, Yang and Lavagi, 2012, Xu et al., 2010]. Actin patches can focus delivery of pectin molecules and modifying enzymes (softening the wall) where they enable the localisation of PIN1, which exports auxin and promotes ROP6 on the opposite side of the lobe. Microtubule bundles then lead to the accumulation of cellulose fibres in an orientated manner (stiffening the wall anisotropically) [Panteris and Galatis, 2005]. These alternating patches result in different wall mechanical properties and thicknesses, leading to different growth rates and directions in these regions. Within these pathways are several feedback loops, including the development of the lobes leading to higher stress at the indents and thus increasing microtubules localisation to the indents, the localisation of PIN1 to the lobes helping promote more ROP2 which stabilises more PIN1 in this region, and ROP2 inhibiting microtubule stabilisation and vice versa. The chemicals interactions

are displayed in figure 2.2, where a detailed map of these signalling pathways in a pavement cell is displayed in figure 2.1. In this thesis, we shall test the feasibility behind the suggestion that these signalling pathways enable further development of pavement cell shape. We shall also test the possibility that these signalling pathways, depicted in figure 2.2 can set up alternating patches of stiffer and softer regions in order to initiate lobes. This is explored in chapter 6 and continued in chapter 7.

2.1.4.5 Mechanical lobe initiation pathways

The chemical signalling pathways are not the only way lobes could be initiated. It has been theorised that differing growth rates and the effect of the tissue mechanics could initiate lobes. One such theory is that lobes could be an emergent feature due to stresses imposed on them by the cell layers below, as a result of differential growth rates between the epidermis and the mesophyll [Kotzer and Wasteneys, 2006]. This effect has lead to suggestions that lobes form as a result of a buckling mechanism [Bidhendi and Geitmann, 2015, Majda et al., 2017]. This theory and a possible problem with it is discussed in section 2.2.3. In other tissues like plant stems, the cells contained within them have to grow at similar rates when positioned at the same height. However, pavement cells have been shown to have varying growth rates with their neighbours [Elsner et al., 2012]. As a result, it was suggested that slow growing cells could form indents with their neighbouring cells to allow their fast growing neighbours in [Szymanski, 2014]. Analysis of leaf growth has led to the observation that the leaf margin's growth rate is slower than the centre in early leaf development [Rolland-Lagan et al., 2014, Remmler and Rolland-Lagan, 2012]. This observation led to the theory that pavement cells form lobes because they are being constrained by the leaf margin [Kotzer and Wasteneys, 2006] and as a result, they buckle. Both of these theories are tested in chapter 7 using a mechanical model to simulate several pavement cells growing with differential growth rates and when their growth is being restricted, respectively.

2.2 Previous modelling

We now review the relevant mathematical models for our project. We begin by examining models looking at the microscale dynamics, which investigate the cell wall structure and the roles of the different cell wall components in section 2.2.1 which will be relevant to our continuum model in chapter 3. This section is followed by looking at previous microtubule simulations in section 2.2.2 which study their stochastic behaviour and response to stress, studies that will be important for our microtubule model in chapter 5. We then finish by surveying prior mathematical efforts to understand why and how pavement cells form jigsaw like shapes in section 2.2.3 (with the vast majority of models taking mechanical approaches). These studies provide the basis for what we investigate in chapters 4-7.

2.2.1 Wall growth models, understanding the cell wall structure and its components

Previous models have explored how the cell wall is crosslinked as well as the impact of these crosslinks. A statistical model of the cell wall describing the plastic and elastic shear strain between cellulose molecules was created by Sridhar et al. [2018] who also incorporated tethering dynamics where attachment and reattachments were considered to be Poisson processes. By assuming the tethers are linear springs, considering the distribution of attached tethers at different stages of strain and calculating the total force held in the system, they derived a version of the Lockhart equation where they achieved good agreement when fitting their model to data. They found that the wall extension is controlled by a parameter describing the ratio of relative elastic and plastic growth, which in the model is explicitly restricted by the detachment rate of the tethers, demonstrating the impact of these crosslinks and the effect that wall loosening enzymes have on wall growth.

Models examining crosslinks and thus the cell wall structure have explored the feasibility behind the tethered network hypothesis. By calculating the total bond energy holding

the cellulose molecules together and assuming a tethered network structure, Thompson [2005] found that this results in a much weaker cell wall than experimentally observed and the energy needed to deform the system is less the work done by the expanding cell wall. It was concluded that the bonds in the tethered network system are unlikely to limit growth [Thompson, 2005]. Similarly, Yi and Puri [2012] also tested the load bearing capacity of the hemicellulose crosslinks. They created a stochastically assembled wireframe network featuring cellulose molecules tethered together by hemicellulose via hydrogen bonds, using beam elements to represent the molecules where they then use finite element approximations to calculate the mechanical response of the network when displaced [Kha et al., 2010]. It was discovered that the bonds between the cellulose and hemicellulose were the major load bearing component and that a deformed network (in the perpendicular direction to cellulose alignment) is not strong enough to withstand the strain caused by turgor.

Other modellers have then gone on to test different crosslinking/cell wall structure hypotheses. For example, Nili et al. [2015] created a model to test the biological hotspot hypothesis. They considered a network of celluloses represented as beam elements and connected by xyloglucan modelled as a truss element (so it can only bear axial load and assumes the xyloglucan are fully extended). The connections between the two molecules were then represented by linear springs where the stiffnesses was changed depending on if it was a single xyloglucan strand or a biological hotspot. By calculating the cumulative Young's modulus of the network, they found that a biological hotspot of entangled short xyloglucan strands is stiffer than a single fully extended long strand. Thus at low crosslink density, by using hotspots and combining with pectin, the cell wall produced the requisite wall stiffness to oppose turgor. Nili et al. [2015] suggest a glass transition to explain plant growth mechanics, where the hotspots carry some of the turgor load and the pectin matrix makes up the rest. Upon hotspot degradation, the extra load now carried by the pectin matrix makes the matrix transition (to a viscous state) to allow the cell wall to slowly flow.

Modellers have also examined the exact contributions of each cell wall component to the wall strength. Dyson et al. [2012] found that the different fibres may play different roles at different states of the cell wall. This was investigated using a continuum model of the cell wall, considering growth as a fluid flow which drives the stretching and straining of a network of hemicellulose fibres, each represented by a spring. These fibres then connect the cellulose molecules with a breakage rate depending on the current strain. The stress resultant (essentially the axial tension) of the cell wall is then found by summing the effect of all the bonds across the wall thickness. From this stress resultant, it was discovered that pre-yield (low strain) dynamics of the cell wall are dominated by hemicellulose fibres stretching and breaking, while pectins dominate post-yield behaviour (high strain). Veytsman and Cosgrove [1998] examined the microscopic properties of the fibres to found how they determine the macroscopic properties of the cell wall. This relationship was found by re-deriving the Lockhart equation from thermodynamic principles by imposing a cell length increase and balancing the work done with the excess heat (caused by the friction produced by the irreversible process of fibres stretching). They found that the flexibility of the fibres influences cell wall stress because hemicellulose could be trapped within the cellulose fibres. They also showed that the cell wall yield is primarily determined by the concentration of xyloglucans and cellulose, and not the bonds between them, demonstrating the effect of wall material deposition. However, increasing the xyloglucan concentration increases the wall yield, which they comment contradicts previous biological findings that wall deposition allows for wall relaxation. Nevertheless, Veytsman and Cosgrove [1998] say that their cell wall with increased xyloglucan concentration could be capable of further extension beyond the prescribed length. They also note that interactions with pectin are not incorporated within this framework.

In examining the contribution of the different cell wall components, specific work has been done on the influence of the cellulose molecules. By modelling a cell surrounded by other cells on all sides, assuming the cell walls to be transversely isotropic linear elastic materials and imposing turgor, Ptashnyk and Seguin [2016] examined the impact

of cellulose orientation. The cellulose orientation in the upper and lower parts of the cell wall was found to affect the radial elastic deformation at the ends of the cell, but the presence of cellulose molecules on the cell end plates made little difference to the cell's axial expansion. The model predicts that shifting the positions of the cells out of alignment in the tissue (i.e. lined up like bricks in a wall) allows for larger strains and increases the effect of varying microfibril configurations on axial expansion. They also discovered that a variety of orientations throughout the wall resulting from cellulose reorientation also strongly reduces axial expansion and slightly increases radial growth. Dyson and Jensen [2010] also found that the cell radius is maintained via the cellulose molecules. Representing the cell wall as a fibre-reinforced thin sheet of viscous fluid, this model includes fibres (representing the cellulose molecules) which are convected by growth and is analysed and solved using asymptotics. The model also finds that various fundamental geometric and mechanical parameters related to the composite cell wall properties govern the cell wall extensibility.

The contribution of pectin to the control of wall growth has also been examined. Using thermodynamic constitutive laws which involve turgor, temperature, volume, free and bound pectate, and the synthesis of pectates, a growth rate that principally depends on pectate cross-link synthesis was derived by Barbacci et al. [2013]. The comparison of this model's predictions with data concerning *Chara corallina* (a freshwater green algae) is 'quite good'. Meanwhile, by balancing the cell wall growth rate and pectin insertion rate, Ali and Traas [2016] argued that turgor-driven deposition leads to cell wall polymerization, which is a primary growth control mechanism. The insertion rate in the model is derived from the thermodynamics principle of balancing the free energy difference between bound and unbound pectin states. Although the results match data qualitatively to *C. corallina*, the authors acknowledge that other mechanisms are at play. These studies emphasize the role of pectin insertion and its essential role in allowing the viscous flow of the cell wall. Both of these pectin studies consider *C. corallina* which contain a high amount of pectin, so these results may not be generalizable.

2.2.2 Mathematical models to understand microtubule behaviour

2D models have been previously derived to simulate microtubules' stochastic behaviour to understand how they form organised arrays. Dixit and Cyr [2004] used Monte Carlo simulations to verify that the microtubule interactions of bundling and collision induced catastrophes are required and sufficient for the parallel organisation of microtubules to permit cell anisotropy. They emphasise that both catastrophe and bundling were needed for organised microtubules configurations as when they simulated only one feature (catastrophes or bundling), they did not get organisation. From their simulations, they also found that the parallel organisation was not dependant on the contact time (pauses) differences before bundling between longitudinally and transversely aligned microtubules, a phenomenon that has been experientially observed. Allard et al. [2010b] produced computer simulations of cortical microtubules to also attempt to understand how an ordered microtubule array arises. They included microtubule plus end dynamic instability and the microtubule interactions of bundling and catastrophe, where both were dependant on the angle of interaction. Through their simulations, they discovered that collision induced catastrophes alone could not cause microtubule alignment but including bundling with or without collision induced catastrophes could. They also recreated plant mutants like mor1-1 which have short microtubules, and found that microtubule's could not organise, in agreement with experimental data. By testing the effect of the microtubule minus end also having dynamic instability, they found that microtubule organisation still occurred with or without this feature, but the onset of organisation was delayed with it. However, this feature affects microtubule organisation in the mutant examples as a static minus end leads to longer microtubules and allows the array to organise. Gomez et al. [2016] created a microtubule model following the rules of angle dependant probabilities of catastrophe, and bundling occurring upon microtubule collision, and constant probabilities of shrinkage and rescue. They used this model to show that microtubule organisation depends on cell geometry (the eccentricity), where they become increasingly aligned with the long axis as the eccentricity increases. Gomez et al. [2016] comment that they were able to fit

their data to experiments using these simple rules and say that the angle dependence is an essential part of the model.

Other models have looked into more detail on the behaviour of a single microtubule. Allard et al. [2010a] considered microtubule interactions in a energetic dimer model of microtubule assembly to calculate the energies needed for catastrophe, cross-over and bundling events when another dimer was added to the microtubule. They use these energies to calculate the angle dependant probabilities of such events occurring on collision, where they achieve good agreement with data. This model also finds that the angle dependence of whether a microtubule bundles or crosses over is due to the competition between the energetic favourability of crosslinks attaching to the collided into microtubule or the bending stiffness if it is to pass over. Allard et al. [2010a] considers microtubule dynamics when connected to the cell membrane by CLASP proteins. By writing an expression for the density of attached anchors, they conclude that due to small detachment rates when microtubules are in their growing states, once an anchor is attached, on average is will stay attached for a week and comment that faster anchoring rates lead to higher rates of edge induced catastrophes. They note that their model does have flaws but creating a more accurate model would rely on non-measurable parameters.

3D models of the stochastic behaviour of microtubules have also been produced. Mirabet et al. [2018] showed that microtubules still spontaneously organise through their interaction with one another in 3D. They additionally include microtubule anchoring to the membrane and find that microtubule's become shorter but form more bundles with one another with strong anchoring when compared to weak anchoring (where microtubules can move away from the membrane more freely). Through their model, they also discover that elongated cells are more likely to have longer and more bundled microtubules where on average, the microtubules align with the long axis. Lagomarsino et al. [2007] modelled microtubules as inextensible filaments that resist bending when running along the 2D surface of the cell membrane. By minimising the energy in the system, they found that microtubules did not naturally align in the transverse direction, meaning that addi-

tional factors/forces must drive the microtubule's perpendicular alignment to the growth axis (such as proteins that hold the microtubules in place). Chakrabortty et al. [2018] simulated microtubules in realistic cell shapes extracted from images taken on a confocal microscope. By including angle dependant microtubule interactions, they used these cell shapes to study the contribution of spatially varying catastrophe probabilities and geometry on microtubule organisation. By altering the probability of cell edge induced catastrophe in a cuboid cell in the transverse direction, they found that microtubules organised transversely when this parameter was high and longitudinally when low. To simulate face induced stability, they reduced the rate of spontaneous catastrophes on specific faces to find that this can also influence microtubule organisation. They then simulated microtubule dynamics in pavement cells where they found that microtubules do not align on the anticlinal wall and discovered several snapshots displaying examples of local order on the periclinal wall to the indents. They also claim that through their inclusion of edge induced catastrophes in pavement cells, they can predict the unique division plane of the cell where including face induced stability could also add further predictive power.

Tissue level mechanical models have also been made to understand microtubule behaviour and their role in responding to mechanical cues. Hamant et al. [2008] examined the *Arabidopsis thaliana* shoot apex where they combined experimental work, including the examination of GFP marked microtubules, with a shell model (only the epidermal cells are modelled where these cells have pressure forces acting upon them from the inside to represent the inner tissue) that included growing elastic walls (by increasing resting lengths), proliferation, and anisotropy in the defined microtubule direction, which also changes due to stress feedback (microtubule directions are updated). This model can replicate observed microtubule orientations in different experimental scenarios, such as primordium growth (initiation of an organ from the shoot apex). They theorise that the shoot apex shape depends on the microtubule cytoskeleton, which in turn is regulated by the mechanical stress in a feedback loop. The microtubule's relationship with stress is also

examined in a model of sepal growth by Hervieux et al. [2016], where microtubules have been shown to align with maximal tension. The model includes a generalised Hooke's law, with Young's moduli that increase from the base to the tip, and is solved by finite element methods. At the sepal tip where growth slows down, paradoxically, microtubules are orientated in a set-up that corresponds to fast anisotropic growth. Comparing this model with experiments led to the hypothesis that microtubule stress feedback operates as a shape sensor at the tip and resists further radial expansion. These studies show that, firstly, microtubules are highly important in stress sensing, and secondly, they have regulatory effects on the geometry of a tissue.

2.2.3 Pavement cell development models

Several previous models have attempted to understand the mechanics of why lobes form and how they develop further. Sapala et al. [2018] built finite element simulations of hyperelastic inflated idealised ellipsoidal cells to find that growing in 3 or 2 directions leads to a higher increase in stress than growing in one, suggesting that the majority of plant cells may favour anisotropic growth for this reason. However, pavement cells have to grow in 2 directions which could lead to excess stress. For this reason, they simulated cells with or without protrusions and found the stress to be transferred from the centres of cells to the indent regions, consequently reducing the overall stress. This stress reduction demonstrates the advantageous nature of lobes which may allow the pavement cells to grow bigger, where other epidermal cells are said to undergo more division to minimise their stress, like in the shoot apical apex. By also building a 2D model of growing cells, where the walls are represented as nodes connected by linear springs, with additional intra-cell springs to represent stiffening components such as cellulose, and experimentally examining cotyledons growth, Sapala et al. [2018] found a positive relationship between isotropic growth of the tissue and lobeyness. Sampathkumar et al. [2014] found the stress to be higher in the indent regions by extracting 3D cell shapes using MorphoGraphX [de Reuille et al., 2015] and meshing the resulting surface that is inflated by turgor pressure

in a hyperelastic finite element model. They also showed that microtubules align with the direction of maximal stress, fanning out from the indents, where they can reinforce the necks through the deposition of cellulose. From this combined result, Sampathkumar et al. [2014] reiterates the theory that microtubules are caught in a feedback loop between the stress in the indents and the further development of the lobes, first mentioned in section 2.1.4.

Several interesting papers have recently presented mechanical theories as to how pavement cell lobes are initiated. Using finite element modelling and assuming linear elasticity Majda et al. [2017], simulated the 2D anticlinal wall segments of a pavement cell. They suggested that lobe formation results from wall heterogeneities of alternating sections that have weak and strong elastic composite layers, which cause buckling when the leaf epidermis is under tension from variations in growth rates across different cell layers. They also performed atomic force microscopy experiments (used to find the stiffness values of a tissue) and claim that they found these wall heterogeneities in actual pavement cells walls. However, Bidhendi and Geitmann [2019] found a problem with these findings. By producing a model using finite element methods assuming the cell wall is neo-Hookean hyperelastic material with alternating stiffness heterogeneities in the anticlinal rule like in Majda et al. [2017]'s paper, they found that the lobe amplitude was not as significant as previously reported. By then including the periclinal wall in their simulations, they found the lobes to disappear completely. This result demonstrates the importance of the periclinal wall in controlling pavement cell shape. They also cast doubt on the epidermis being under tension from the different cell layers. Again using a neo-Hookean hyperelastic finite element model Bidhendi et al. [2019] created a 3D model of pavement cells to investigate the effect of the periclinal wall further. When they examined a single cuboidal cell, due to inflation by turgor pressure and the geometry, they found wrinkles to form on the anticlinal wall. They hypothesise that these wrinkles could be centres of raised stress where microtubules can localise to initiate indents. However, pavement cells are not mechanically independent structures and are strictly connected to their neighbours. As a result, they

also simulated a system of 4 connecting cells, whereupon inflation bulges formed between neighbouring cells. Of concern though, is the varied set of turgor pressure values between these cells (in one case, a 10 to 1 difference in their nondimensionalised system), so these bulges could result from differing pressures like in a Hele Shaw cell. Large variations in turgor pressure in pavement cells have not been reported [Hayot et al., 2012, Li et al., 2021] (and similarly in neighbouring plant cells in other tissues [Beauzamy et al., 2015]), where Zhang et al. [2011] states that turgor forces cancel out along the anticlinal wall in lobe initiation. However, Bidhendi et al. [2019] continued to explore different possibilities. It was discovered that varying the periclinal wall stiffness between neighbouring cells can induce lobe formation, where they also found the indents to be centres of increased stress. Moreover, by including a feedback loop where areas of increased stress increased in stiffness, they demonstrated that this helps sustain lobe formation even when starting at a 1% stiffness difference between neighbouring cells. Haas et al. [2020] combined both experimental and modelling to study pectins roles in lobe initiation. They proposed that the local variations in the demethylation of pectin and its asymmetric structure mean that pectin deposition in the anticlinal wall can lead to local swelling independent of turgor, where it causes wall extension. They backed this up using a non-linear finite element model that incorporates pectins anisotropic organisation and demonstrate that lobes can be produced from a initially straight anticlinal wall. However, these results have been disputed by Cosgrove and Anderson [2020] who find inconsistencies with past literature. Inconsistencies such as, Haas et al. [2020]'s model predicting higher growth rates at the tips of the lobe than expected, their claim that it is the anticlinal wall driving bending and not the periclinal and the fact that cellulose is not included, whose stiffness contribution to the cell wall exceeds that of pectin [Sampathkumar, 2020].

Limited previous work has also been done on the signalling dynamics of the ROPS. By creating a reaction-diffusion system with fast diffusing (in the cytoplasm) inactive ROP6 and ROP2, slow diffusing active ROP6 and ROP2 (bound to the cytosplasm) and RIC1 Champneys et al. [2021] demonstrated that sub critical Turing instabilities in a 1D domain

can form, where they observed alternating periodic patterns of peaks of activated ROP6 and ROP2. These alternating peaks could then cause differential stiffness in pavement cells. Thus by assuming certain interactions, they have found that chemical lobe initiation is possible.

2.3 Summary

In this chapter we have covered all the relevant biological background for the research presented in this thesis alongside prior modelling studies. To investigate how growth is controlled we begin on the microscale by using a continuum approach to investigate the biological hotspot hypothesis and how the proteins XTH, cel12A and expansin effect the cell wall in chapter 3 before considering pavement cells formation in chapters 4-7.

Chapter 3

Enzyme action and cell wall structure

3.1 Introduction and aims

The examination of how plant growth is controlled begins at the microscale. In this chapter, we shall be trying to understand how the cell wall is structured and how it is loosened in order to induce growth (see section 2.1.1 for details).

Specifically, the feasibility behind the biological hotspot hypothesis will be tested by assuming the cellulose molecules are crosslinked via this mechanism and observing if this can explain experimentally observed enzyme behaviour. Meaning it shall also be examined how XTH performs hydrolysis on hemicellulose fibres but does not induce cell wall growth, how Cel12A induces creep through cutting both cellulose and hemicellulose while also weakening the cell wall, and finally, how expansin supposedly induces fibre slippage to induce growth and not weakens the cell wall. The consequences of cellulose reorientation are also examined.

The primary cell wall is modelled as a continuum incorporating crosslink dynamics (between cellulose and hemicellulose) where we then calculate the stress resultant when acted on by a prescribed growth rate. This model is designed to be a simplification of the system in order to test the feasibility behind proposed wall structure and protein mechanisms. By changing model parameters, simulating fibre slippage and performing asymptotic analysis, we can build up a mechanistic understanding of cell wall structure and enzyme action. We focus the modelling on inner tissues cells with predominately transversely orientated CMF with negligible cell division, for example, cells within the root elongation zone [Creff et al., 2015, Derbyshire et al., 2007, Baskin and Jensen, 2013].

This chapter is begun with an explanation of the mathematical model of the cell wall in section 3.2. This is followed by an analysis of the results and the discussion of the implications of the findings in section 3.4. The results are summarised and conclusions drawn in section 3.5.

3.2 Model formulation

The model comprises three distinct aspects of cell wall dynamics: the emergent macroscopic stress and CMF orientation evolution from the microscopic cell wall network (section 3.2.2.1), hotspot bond density evolution (section 3.2.2.2) and enzyme action (section 3.2.2.3). We will first detail the assumptions behind each aspect (section 3.2.1), before deriving the relevant governing equations (section 3.2.2). This model is based on the framework originally developed in Dyson et al. [2012], with significant differences in the treatment of material properties, network composition and fibre orientation evolution. We will simplify the governing equations through nondimensionalisation (section 3.2.3) and solve the resulting system (section 3.3). The solutions are further simplified via asymptotic reduction (section 3.3.2).

3.2.1 Model assumptions and set up

The crucial output of the model is an expression for the axial stress resultant of the cell wall Σ^* (see figure 3.1). This stress resultant captures the strength of the cell wall generated by the underlying polymer network, as well as the relationship between turgor pressure and the growth rate; higher values of turgor increase the load on the cell wall, resulting in raised stress levels and possible further extension of the wall. The stress resultant is calculated by summing up the stress held by each component of the cell wall polymer network at all points in the cell wall. We assume the cell wall is a evolving continuum with embedded cellulose molecules that are initially orientated perpendicularly to the axial direction. As the cell wall elongates, with growth rate, α^*, the molecules are stretched, and the cellulose molecules are additionally re-oriented. These cellulose molecules are connected by a mix of cell wall components including BH crosslinks as described in section 2.1.1 where the hotspot bond and the hemicellulose density functions are, $\tilde{n}^*$ and n^* respectively ($*$ denotes dimensional quantities). All functions that represent the whole hotspot are denoted with a tilde on top ($\tilde{}$) where functions that represent a

single fibre are without tildes. This bond density is dependent on the energy held in the fibres, meaning that as they get increasingly stretched via cell wall extension, the more likely they are to break. Enzyme action will be modelled by changes in the bond density evolution parameters. The wall segment is initially unstressed at time $t^* = 0$, and undergoes uniform stretching in such a way that the cell wall grows with a fixed growth rate α^*.

We introduce the coordinate system (x^*, y^*, z^*) with the origin positioned on the edge of the outer wall (figure 3.1). The cell wall is stretched in the axial x^* direction with the y^*, z^* directions being perpendicular to the growth direction, such that y^* points radially inwards, and z^* is perpendicular and hence tangential to the cell wall. We define θ to be the angle between the cellulose fibres and the z^* axis. New wall material is deposited on the inner surface of the wall at $y^* = h^*$, moves through the wall at rate α^* until it reaches the outer wall surface at $y^* = 0$. We therefore model the growth via the incompressible flow field,

$$\mathbf{u}^* = \alpha^*(x^*, -y^*, 0) \text{ for } 0 < y^* < h^*, \tag{3.2.1}$$

meaning that $dx^*/dt^* = \alpha^* x^*$ and $dy^*/dt^* = -\alpha^* y^*$. This flow describes the material moving through the flat x-y plane in a thin segment of the cell wall (figure 3.1). Due to the modelling domain being thin, we assume the cellulose molecules do not bend radially. Since there is no stretching in the z^* direction, the model simplifies to a 2D system.

We now consider how a generic element of cell wall material changes in length as the cell wall stretches. Let $L^*(y^*, t^*)$ be the length of such a segment lying in the x^* direction. From the Lockhart equation (1.1.1) we have that the material extends with rate

$$\alpha^* = \frac{1}{L^*}\frac{dL^*}{dt^*}. \tag{3.2.2}$$

The strain the segment is under in the x^* direction is therefore $s^* = \frac{L^*}{L_0^*} - 1$ where L_0^* is the natural length of the material segment. If the initial length of a segment positioned at

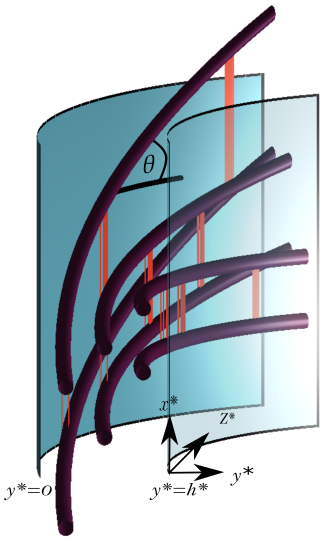


Figure 3.1: A segment of the cell wall. The two curved (light blue) surfaces are the two boundaries for the cell wall. The thick (purple) rods represent the cellulose molecules, and the groups of thin (orange) fibres represent the hotspots where both become increasingly stretched as they traverse to the outside of the cell. The equation (3.2.1) imposes this movement and deformation in the model's domain of the x-y plane.

$y^* = y_i^*$ at time $t^* = \tau^*$ is L_i^*, the segment length evolves according to $L^* = L_i^* e^{\alpha^*(t^*-\tau^*)}$ on the characteristic $y^* = y_i^* e^{-\alpha^*(t^*-\tau^*)}$ (from equation 3.2.2). The evolving segment length is then related to its position in the cell wall by $L^* = \frac{L_i^* y_i^*}{y^*}$, encoding both its extension and trajectory.

We assume that at the inner surface of the cell wall, material is deposited such that constant cell wall thickness is maintained. This new wall material then gets pushed through the wall towards the outer surface via the flow (3.2.1). We find that wall density remains uniform for all time, assuming appropriate initial conditions (see appendix A.1.1 for details)

3.2.2 Principal equations

3.2.2.1 Stress resultant from the composite cell wall

The total stress resultant from the composite cell wall in the axial direction depends on the mechanical properties of each constitutive (and evolving) part: the CMF which are bound together by both the BH and other cell wall components, the hemicellulose within the BH and the surrounding pectin ground matrix. We assume a Kelvin-Voight standard linear system, so the total stress σ^* is the sum of the stress arising from the biological hotspots $\tilde{\sigma}^*_H$ and the cellulose molecules σ^*_C.

We let σ^*_H be the stress held in a hemicellulose fibre which we assume to be characterised by a Maxwell element where the hemicellulose strain, s_H, is equal to the wall strain, $s = s_H$. The Maxwell assumption means that the hemicellulose strain is the sum of the elastic and viscous contributions, $s_H = s_{H,e} + s_{H,v}$, with the hemicellulose stress being equal to its elastic and viscous stress, $\sigma^*_H = \sigma^*_{H,e} = \sigma^*_{H,v}$. This implies that

$$\frac{1}{\nu^*_H}\frac{\partial \sigma^*_H}{\partial t^*} + \frac{1}{\mu^*}\sigma^*_H = \frac{\partial s}{\partial t^*}, \tag{3.2.3}$$

with the boundary and initial conditions of, $\sigma^*_H(h^*, \tau^*) = \sigma^*_H(y^*, 0) = 0$ where the constant τ^* is the time the fibre is deposited (so for a fibre that just been deposited $\tau^* = t^*$), h^* the wall thickness, ν^*_H the hemicellulose Young's modulus and μ^* the material constant of viscosity. As each BH is a compact collection of hemicellulose fibres, we assume the stress arising from the BH, $\tilde{\sigma}_H$, is then the sum of the hemicellulose stresses contained within it, meaning $\tilde{\sigma}^*_H = n^*\sigma^*_H$.

Assuming the cellulose molecules are elastic, the stress term for the CMF in the axial direction is then

$$\sigma^*_C = \nu^*_C s_C \sin\theta, \tag{3.2.4}$$

where ν^*_C is the Young's modulus, θ the fibre angle, $\sin\theta$ a modifier that changes the

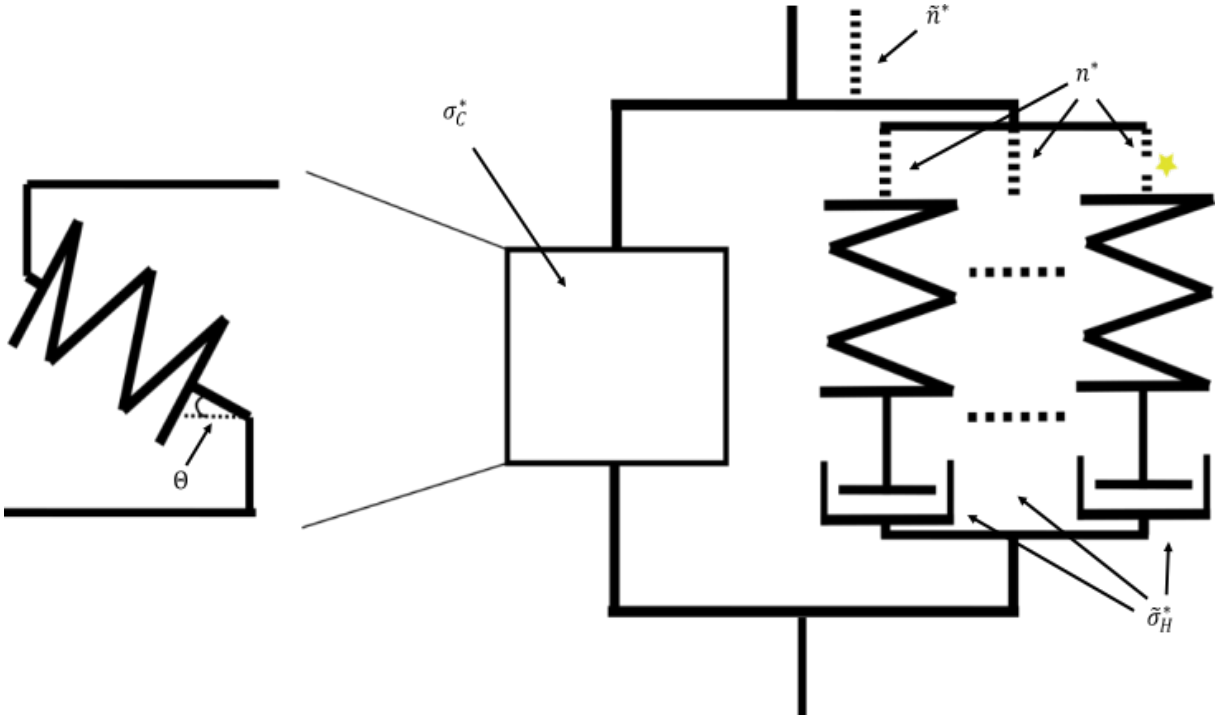


Figure 3.2: Depiction of a single unit of the continuum model with the cellulose (see A) and hotspot (see B) contributions to the stress joined in parallel. The hotspot stress $\tilde{\sigma}_H^*$ arises from a collection of hemicelluloses represented as maxwell elements, crosslinked with bond density n^* (where the yellow star represents a bond breakage). The cellulose stress σ_C^* is represented by a box that resists the strain elastically proportionally to the cellulose's angle θ. The whole unit's stress is then dependant on the biological hotspot density $\tilde{n}^*$ such that when it is zero, the only contribution is coming from cellulose crosslinked by other molecules.

cellulose stress as they become increasingly reoriented to the axial direction, and s_C the strain of cellulose fibre, such that

$$s_C = \frac{L_C^*}{L_{C,0}^*} - 1. \tag{3.2.5}$$

where $L_{C,0}^*$ is the cellulose resting length.

The cellulose fibre angle θ and length L_C^* are orientated and deformed by the flow $\mathbf{u}^*$. Letting $\mathbf{a}$ be the cellulose direction vector, we shall assume the cellulose network is uniform in the x^* and z^*-direction as they are in the plane of the wall, thus $\mathbf{a} = (\sin\theta, 0, \cos\theta)$. Assuming the cell wall is a composite material with a preferred direction under an incompressible, transversely isotropic viscous flow, the evolution of the fibre

director field, $\mathbf{a}$, can be described by [Green and Friedman, 2008],

$$\frac{\partial \mathbf{a}}{\partial t^*} + (\mathbf{u}^* \cdot \nabla^*)\,\mathbf{a} + \zeta^* \mathbf{a} = (\mathbf{a} \cdot \nabla^*)\mathbf{u}^*, \tag{3.2.6}$$

where $\zeta^* = \mathbf{a} \cdot \mathbf{e}^* \cdot \mathbf{a}$ represents the strain rate in the direction of the matrix, with $\mathbf{e}^* = \left(\nabla^* \mathbf{u}^* + \nabla^* \mathbf{u}^{*T}\right)/2$. We now have an expression that describes how cellulose fibres convect, stretch and reorient as they move through the cell wall via the flow, $\mathbf{u}^*$. Equation (3.2.6) can be re-expressed in terms of θ using the definition of $\mathbf{a}$ meaning $\zeta^* = \alpha^* \sin^2\theta$, and upon substituting in equation (3.2.6) we obtain

$$\cos\theta \frac{\partial \theta}{\partial t^*} - \alpha^* y^* \cos\theta \frac{\partial \theta}{\partial y^*} + \alpha^* \sin^3\theta = \alpha^* \sin\theta, \tag{3.2.7}$$

$$-\sin\theta \frac{\partial \theta}{\partial t^*} - \alpha^* y^* \sin\theta \frac{\partial \theta}{\partial y^*} + \alpha^* \sin^2\theta \cos\theta = 0. \tag{3.2.8}$$

Computing $\sin\theta \times (3.2.7) + \cos\theta \times (3.2.8)$ and dividing the result by $\sin\theta\cos\theta$ yields

$$\frac{\partial \theta}{\partial t^*} - \alpha^* y^* \frac{\partial \theta}{\partial y^*} - \alpha^* \sin\theta \cos\theta = 0, \tag{3.2.9}$$

with boundary and initial conditions respectively being $\theta(h^*, \tau^*) = \theta(y^*, 0) = \theta_0$ (note $\theta_0 \neq 0$, else the solution is simply $\theta = 0$ for all $t^* > 0$).

From equation (3.2.6) derivation we also have an expression that describes the evolution of the cellulose length L_C^* when stretched via the flow as

$$\frac{1}{L_C^*} \frac{dL_C^*}{dt^*} = \mathbf{a} \cdot \left((\mathbf{a} \cdot \nabla^*)\,\mathbf{u}^*\right) = \alpha^* \sin^2\theta, \tag{3.2.10}$$

with boundary and initial conditions being $L_C^*(h^*, \tau^*) = L_C^*(y^*, 0) = L_{C,0}^*$.

Finally, the total stress resultant in the cell wall is then the sum of the stress of all components when crosslinked in each "layer" of the cell wall, i.e. integrating over the

thickness of the wall, which gives

$$\Sigma^* = \int_0^{h^*} \rho^*(1 + A^*\tilde{n}^*)\sigma_C^* + \tilde{n}^*\tilde{\sigma}_H^* \, dy^* + \Gamma^*\alpha^*, \tag{3.2.11}$$

where ρ^* is the density of cellulose and $A^*\tilde{n}^*$ is the modification of the cellulose stress due to hotspot crosslinking. The integral is the contribution from the CMF and the BHs while the final term is the pectin matrix contribution with Γ^* being the stiffness density of the matrix.

3.2.2.2 Bond density evolution equation

We now introduce equations that describe the BH and hemicellulose density, $\tilde{n}^*$ and n^* respectively. Assuming that the CMF do not break before the BHs, it is then the BH connections that rupture to allow slippage of the cell wall components. The BHs and the hemicellulose fibers within them are advected through the cell wall according to a Smoluchowski equation [Dembo et al., 1988], with both $\tilde{n}^*$ and n^* undergoing energy-dependant breakage:

$$\frac{\partial \tilde{n}^*}{\partial t^*} - \alpha^* y^* \frac{\partial \tilde{n}^*}{\partial y^*} = -\tilde{k}_{\text{off}}^* \tilde{n}^*, \tag{3.2.12}$$

$$\frac{\partial n^*}{dt^*} - \alpha^* y^* \frac{\partial n^*}{\partial y^*} = -k_{\text{off}}^* n^*, \tag{3.2.13}$$

where $\tilde{n}^*(h^*, \tau^*) = \tilde{n}^*(y^*, 0) = \tilde{n}_0^*$, and $n^*(h^*, \tau^*) = n^*(y^*, 0) = n_0^*$, with the breakage rates defined as

$$\tilde{k}_{\text{off}}^* = \tilde{k}_0^* \exp\left(\frac{\hat{\beta}^2}{k_b^* T^*}\tilde{U}^*\right), \tag{3.2.14}$$

$$k_{\text{off}}^* = k_0^* \exp\left(\frac{\gamma^2}{k_b^* T^*}U^*\right). \tag{3.2.15}$$

In equations (3.2.14) and (3.2.15), $k_b^* T^*$ is the thermal energy (k_b^* being the Boltzmann's constant and T^* the absolute temperature), $\tilde{k}_0^*$ and k_0^* are the breakage rates when the

fibres are unstressed, $\tilde{U}^*$ and U^* the deformation free energies and $\hat{\beta}$ and γ are parameters controlling how strongly the energies affect the breakage rates. This formulation entails a direct relationship between the stress held in the fibres and the breakage rates, and has been used successfully in other models of adhesion dynamics [Li et al., 2015, Groot et al., 1996, Bell et al., 1984, Zhu, 2000]. To ensure that the crosslinks stretch a significant length before breaking [Dyson et al., 2012], we take $\hat{\beta}, \gamma \ll 1$; alternatively, taking larger values of these parameters allows us to model increased breakage rates caused by, for example, heightened hydrolysis action. As hemicellulose bonds break, the BHs become easier to rupture, and as a result, we take $\hat{\beta}^2 = (\frac{n_0}{n^*} - 1)\beta^2$. We also assume that the hotspots are stronger than the hemicellulose crosslinks, so $\beta < \gamma$.

To calculate the free energy potential in a single fibre, we consider the force $\mathbf{F}^*$ on a fibre as it moves along the trajectory $\mathbf{x}^*(t^*) = (x^*(t^*), y^*(t^*), z^*(t^*))$. We set $y^*(t) = z^*(t) = 0$ as the molecules are only being extended in the axial direction, so

$$x^*(t^*) = s^*_{H,e},$$

with $s^*_{H,e}$ being the elastic extension. The work done by $\mathbf{F}^*$ is then

$$W^* = \int_0^{s^*_{H,e}} F^*_x \, dx^*.$$

We assume that the wall strain is uniformly distributed across all the fibres. Since the fibre breakage is dependent on elastic strain, the force is also elastic, meaning $F^*_x = -\kappa^* x^*$ where κ^* is the stiffness of the springs and is equal to the area multiplied by ν^*_H divided by the length of the cellulose molecules. Since temperature is constant, the free energy equals the potential and so $U^* = \frac{\kappa^*}{2}\left(s^*_{H,e}\right)^2$. For the hotspot density potential, the force applied is $F^*_x = -\tilde{\kappa}^* x^*$ for some stiffness $\tilde{\kappa}^*$ which should be affected by the number of intact fibres in the hotspot, n^*; we therefore take $\tilde{\kappa}^* = n^* \kappa^*$, as the springs are in parallel

so stiffness is additive and hence $F_x^* = -\kappa^* n^*(y^*, t^*)x^*$. Then it follows that

$$W^* = \int_0^{s^*_{H,e}} F_x^* \, dx^* = -\frac{\kappa^*}{2} n^*(y^*, t^*)(s^*_{H,e})^2, \tag{3.2.16}$$

and $\tilde{U}^* = \frac{\kappa^*}{2} n^*(y^*, t^*)(s^*_{H,e})^2$; therefore,

$$\tilde{k}^*_{\text{off}} = \tilde{k}_0 \exp\left(\frac{\kappa^* \beta^2 n_0^* \left(1 - \frac{n^*}{n_0^*}\right)}{2 k_b^* T^*} (s^*_{H,e})^2 \right).$$

3.2.2.3 Enzyme action

Here we describe a simple model of enzyme action. Recall that the enzymes Cel12A and XTH perform hydrolysis/cutting action, where Cel12A targets the hotspots junctions (cutting both cellulose and hemicellulose) and XTH targets the hemicellulose fibres. We simulate the Cel12A and XTH actions by increasing β and γ respectively in equations (3.2.14) and (3.2.15).

Due to the lack of consensus on how expansin works, we try two different simple methods of enzyme action. As mentioned in section 2.1.1, expansin may work by allowing slippage in the fibres [Arsuffi and Braybrook, 2017]. We implement this by firstly decreasing the viscosity of the dashpots, i.e. decreasing their resistance to the flow. This effect is modelled by the equation

$$\frac{d\mu^*}{dt^*} = E^* \mu^* \left(1 - \frac{\mu^*}{\mu_1^*}\right), \tag{3.2.17}$$

with the conditions $\mu^*(h^*, \tau^*) = \mu^*(y^*, 0) = \mu_0^*$, where E^* is the expansin action rate, μ_0^* the initial viscosity and μ_1^* the target viscosity with $\mu_1^* < \mu_0^*$. We choose this form to keep the model as simple as possible while ensuring that μ^* decreases and that $\mu^* \neq 0$.

Secondly, we can also impose expansin action by increasing the resting length of the springs in the system allowing for stress relaxation. We assume that the resting length growth rate depends on the strain of the spring, rather than the extension; this assumption

avoids the resting length exceeding the actual length. Thus,

$$\frac{dL_0^*}{dt^*} = E^* \left(\frac{L^*}{L_0^*} - 1 \right), \tag{3.2.18}$$

with the boundary and initial conditions, $L_0(h^*, \tau^*) = L_0^*(y^*, 0) = l_0^*$.

3.2.3 Nondimensionalisation

We nondimensionlise the system according to

$$t^* = \frac{t}{\tilde{k}_0^*},\ \tau^* = \frac{t}{\tilde{k}_0^*},\ \tilde{n}^* = \tilde{n}_0^* \tilde{n},\ n^* = n_0^* n,\ y^* = h^* y,\ y_i^* = h^* y_i,\ L^* = L_0^* L,\ L_C^* = L_{C,0}^* L_C,$$
$$\Sigma^* = \mathcal{E}^* \Sigma,\ \alpha^* = \tilde{k}_0^* \alpha,\ \tilde{k}_{\text{off}}^* = \tilde{k}_0^* \tilde{k}_{\text{off}},\ k_{\text{off}}^* = \tilde{k}_0^* k_{\text{off}},\ \sigma_H^* = \nu_H^* \sigma_H,\ \sigma_C^* = \nu_C^* \sigma_C,\ L_0^* = l_0^* L_0,$$
$$\Gamma^* = \frac{\mathcal{E}^* \Gamma}{\tilde{k}_0^*},\ \mu^* = \mu_0^* \mu \text{ and } E^* = \tilde{k}_0^* E \text{ (for equation 3.2.17) or}$$
$$E^* = \tilde{k}_0^* l_0^* E \text{ (for equation 3.2.18).}$$

where we define $\mathcal{E}^* = \nu_C^* h^* \rho^*$. Equations (3.2.2)-(3.2.18) are simplified as follows. The wall length equation (3.2.2) becomes,

$$\frac{dL}{dt} = \alpha L, \tag{3.2.19}$$

with $L(1, \tau) = L(y, 0) = 1$. For the hemicellulose stress equations (3.2.3), after nondimensionlisation we have,

$$\frac{\partial \sigma_H}{\partial t} + \omega \sigma_H = \frac{\partial s}{\partial t}, \tag{3.2.20}$$

with $\sigma_H(1,\tau) = \sigma_H(y,0) = 0$, where $\omega = \frac{\nu_H^*}{\mu_0^* \mu \tilde{k}_0}$ and $s = \frac{L}{L_0} - 1$ (where $L_0 = 1$ when expansin is not acting upon it). The cellulose stress equation (3.2.4), is then simply

$$\sigma_C = s_C \sin\theta, \tag{3.2.21}$$

where $s_C = L_C - 1$. The length of the cellulose fibres equation (3.2.10) is then

$$\frac{1}{L_C}\frac{dL_C}{dt} = \alpha \sin^2\theta, \tag{3.2.22}$$

where $L_C(1,\tau) = L_C(y,0) = 1$. Equation (3.2.9) describing the cellulose angle becomes,

$$\frac{\partial\theta}{\partial t} - \alpha y \frac{\partial\theta}{\partial y} - \alpha \sin\theta\cos\theta = 0, \tag{3.2.23}$$

with $\theta(1,\tau) = \theta(y,0) = \theta_0$. The evolving BH and hemicellulose bond density equations (3.2.12) and (3.2.13) are now,

$$\frac{\partial\tilde{n}}{\partial t} - \alpha y \frac{\partial\tilde{n}}{\partial y} = -\tilde{k}_{\text{off}}\tilde{n} \text{ where } \tilde{k}_{\text{off}} = \exp\left(\tilde{\beta}^2\tilde{\varsigma}(1-n)s_{H,e}^2\right), \tag{3.2.24}$$

$$\frac{\partial n}{\partial t} - \alpha y \frac{\partial n}{\partial y} = -k_{\text{off}} n \text{ where } k_{\text{off}} = \breve{k}_0 \exp\left(\gamma^2 \varsigma s_{H,e}^2\right), \tag{3.2.25}$$

with $\tilde{n}(1,\tau) = \tilde{n}(y,0) = 1$, $n(1,\tau) = n(y,0) = 1$, $\tilde{\beta} = \sqrt{n_0^*}\beta$, $\sigma_H = s_{H,e}$, $\breve{k}_0 = \frac{k_0^*}{\tilde{k}_0^*}$ and $\tilde{\varsigma} = \varsigma = \frac{\kappa^* L_0^{*2}}{2k_b^* T^*}$.

Enzyme action on the viscosity on the dashpot (3.2.17) is now,

$$\frac{d\mu}{dt} = E\mu\left(1 - \mathcal{M}\mu\right), \tag{3.2.26}$$

with $\mu(1,\tau) = \mu(y,0) = 1$ where $\mathcal{M} = \frac{\mu_0}{\mu_1}$. The enzyme action on the resting length (3.2.18) becomes,

$$\frac{dL_0}{dt} = E\left(\frac{L}{L_0} - 1\right), \tag{3.2.27}$$

with $L_0(1,\tau) = L_0(0,y) = 1$.

Finally, the stress resultant equation (3.2.11) is now,

$$\Sigma = \int_0^1 (1 + a_1\tilde{n})\sigma_C + a_2 n\tilde{n}\sigma_H \; dy + \Gamma\alpha, \tag{3.2.28}$$

where $a_1 = A^*\tilde{n}_0^*$ is the modification of the cellulose stress due to hotspot crosslinking, and $a_2 = \frac{n_0^*\tilde{n}_0^*\nu_H^*}{\rho^*\nu_C^*}$ is the ratio of the cellulose and hemicellulose stiffness densities. We therefore have a closed system of 10 equations (3.2.19)-(3.2.28) with a total of 10 unknowns, Σ, $\tilde{n}$, n, σ_C, $\tilde{\sigma}_H$, L_0, μ, s, s_C and θ. From Dyson et al. [2012] framework, we have expanded into viscoelasticity, incorporated biological hotspot dynamics (where the previous setup assumed the tethered network hypothesis), included cellulose reorientation and its contribution to the cell wall stress and enzyme loosening mechanisms.

3.3 Model analysis

To evaluate the effect of the BHs and enzyme action on the stress resultant, and hence the overall mechanical behaviour, we proceed to analyse the model as described in section 3.2.2. The equations may be solved via a (lengthy) semi-analytic method; we merely state the solutions in 3.3.1 and leave full details to the Appendices A.1.2, A.1.3 and A.1.4. Since breakage rates are assumed to be small, we also employ asymptotic expansions to determine the leading-order behaviour of the cell wall, as shown in section 3.3.2; as before full details are consigned to A.1.5 for brevity.

3.3.1 Semi-analytical solutions

Throughout the analysis, we recognise two contrasting regions of cell wall material: the thinning region $0 \leq y \leq e^{-\alpha t}$ contains material already present at $t = 0$, while the expanding $e^{-\alpha t} < y \leq 1$ region contains newly-deposited material which has been added to the $y = 1$ surface at some $t > 0$. Material deposited at time $t = \tau$ lies on a characteristic

$y = y_i e^{-\alpha \bar{t}}$, where $\bar{t} = t - \tau$. For the initially-present material, the deposition time is $\tau = 0$, the initial position is $0 \leq y_i \leq 1$ and the extension is described by $L = e^{\alpha t}$. For the later-deposited material, we have $\tau > 0$ and $y_i = 1$, and the extension is given in terms of position in the wall as $L = \frac{1}{y}$.

In the absence of enzymatic action, L_0 and μ are constant, and hence equation (3.2.20) may be solved using an integrating factor to find the axial hemicellulose stress,

$$\sigma_H = \frac{\alpha}{\alpha + \omega} \left(L - L^{-\frac{\omega}{\alpha}} \right). \tag{3.3.1}$$

In contrast, when enzyme action is incorporated, L_0 and μ are no longer constant and hence the solution (3.3.1) is invalid. To solve for variable spring rest length we first divide equation (3.2.27) by $\frac{dy}{dt} = -\alpha y$ to reformulate the differential equation for L_0 in terms of y. This equation does not have an analytical solution, and hence we proceed to derive a (forward) finite difference expression for L_0 which can be used for solving equation (3.2.20) with an integrating factor, yielding

$$\sigma_H = L^{-\frac{\omega}{\alpha}} \int_0^{\bar{t}} L^{\frac{\omega}{\alpha}} \left(\frac{\alpha L}{L_0(L)} - \frac{L}{L_0^2(L)} \frac{dL_0(L)}{d\hat{t}} \right) \, d\hat{t}, \tag{3.3.2}$$

where L_0 is treated as a function of L.

For expansin action on the viscosity, μ, we begin by solving equation (3.2.26) using separation of variables to get

$$\mu = \frac{1}{\mathcal{M} + (1 - \mathcal{M}) e^{-Et}},$$

which means that $\omega = \omega_0 \left(\mathcal{M} + (1 - \mathcal{M}) e^{-Et} \right)$ where $\omega_0 = \frac{\nu_H^*}{\mu_0^* k_0^*}$. We can then solve equation (3.2.20) to find

$$\sigma_H = y^{\frac{\omega_0 \mathcal{M}}{\alpha}} \exp\left(\frac{\omega_0}{E} (1 - \mathcal{M}) y^{\frac{E}{\alpha}} \right) \int_y^1 \alpha y^{-2 - \frac{\omega_0 \mathcal{M}}{\alpha}} \exp\left(-\frac{\omega_0}{E} (1 - \mathcal{M}) y^{\frac{E}{\alpha}} \right) \, d\hat{t}, \tag{3.3.3}$$

To determine the evolving bond densities, we solve (3.2.25) for n using the method of characteristics and combining equation (3.2.19) and (3.2.25) we derive

$$n = \exp\left(-\frac{\breve{k}_0}{\alpha} G\left(\frac{1}{L}\right)\right) \text{ with} \tag{3.3.4}$$

$$G(y) = \int_y^1 \frac{\exp(\gamma^2 \varsigma s_{H,e}^2)}{\hat{y}}\, d\hat{y}. \tag{3.3.5}$$

Similarly from equation (3.2.24),

$$\tilde{n} = \exp\left(-\frac{1}{\alpha}\tilde{G}\left(\frac{1}{L}\right)\right) \text{ with} \tag{3.3.6}$$

$$\tilde{G}(y) = \int_y^1 \frac{\exp\left(\tilde{\beta}^2 \tilde{\varsigma}\left(1 - \exp\left(-\frac{\breve{k}_0}{\alpha} G(\hat{y})\right)\right) s_{H,e}^2\right)}{\hat{y}}\, d\hat{y}. \tag{3.3.7}$$

Solving equation (3.2.23) gives the cellulose angle from the horizontal,

$$\theta = \arctan\left(\tan\theta_0 L\right), \tag{3.3.8}$$

and thus the cellulose extension length is,

$$L_C = \exp\left(\alpha \int_0^{\bar{t}} \sin^2\theta(\hat{t})\, d\hat{t}\right). \tag{3.3.9}$$

The stress resultant is hence constructed by separating the domain into two regions $\epsilon \leq y \leq e^{-\alpha t}$ and $e^{-\alpha t} < y \leq 1$, to give

$$\begin{aligned}
\Sigma = \left(e^{-\alpha t} - \epsilon\right) & \left(\left(1 + a_1 \exp\left(-\frac{1}{\alpha}\tilde{G}\left(e^{-\alpha t}\right)\right)\right)\left(\exp\left(\alpha \int_0^t \sin^2\theta(\hat{t}) d\hat{t}\right) - 1\right)\right. \\
& \times \sin\left(\arctan\left(\tan(\theta_0) e^{\alpha t}\right)\right) + a_2 \exp\left(-\tfrac{k_0}{\breve{k}_0}\tfrac{1}{\alpha} G\left(e^{-\alpha t}\right)\right) \exp\left(-\tfrac{1}{\alpha}\tilde{G}\left(e^{-\alpha t}\right)\right) \sigma_H(t)\Big) \\
& + \int_{e^{-\alpha t}}^1 \left(1 + a_1 \exp\left(-\frac{1}{\alpha}\tilde{G}\left(y\right)\right)\right)\left(\exp\left(\int_y^1 \frac{\sin^2\theta(\hat{y})}{y} d\hat{y}\right) - 1\right) \\
& \times \sin\left(\arctan\left(\tfrac{\tan(\theta_0)}{y}\right)\right) + a_2 \exp\left(-\tfrac{k_0}{\breve{k}_0}\tfrac{1}{\alpha} G\left(y\right)\right) \exp\left(-\tfrac{1}{\alpha}\tilde{G}\left(y\right)\right) \sigma_H\left(y\right)\, dy + \Gamma\alpha.
\end{aligned} \tag{3.3.10}$$

where σ_H is given by equation (3.3.1), (3.3.2) or (3.3.3) for the different expansin mechanisms. The small parameter ϵ denotes a cut-off for the outer region of the cell wall; this ensures the cellulose stress does not go to infinity and that the molecules will eventually break rather than becoming infinitely long. The steady-state stress resultant as $t \to \infty$ is

$$\Sigma^{\infty} = \int_{\epsilon}^{1} \left(1 + a_1 \exp\left(-\frac{1}{\alpha}\tilde{G}\left(y\right)\right)\right)\left(\exp\left(\int_{y}^{1} \frac{\sin^2\theta(\hat{y})}{y} d\hat{y}\right) - 1\right) \\ \times \sin\left(\arctan\left(\tfrac{\tan(\theta_0)}{y}\right)\right) + a_2 \exp\left(-\tfrac{k_0}{\breve{k}_0}\tfrac{1}{\alpha}G\left(y\right)\right)\exp\left(-\tfrac{1}{\alpha}\tilde{G}\left(y\right)\right)\sigma_H(y)\, dy + \Gamma\alpha. \quad (3.3.11)$$

where the contributions from the fibres present at $t = 0$ have now disappeared.

3.3.2 Leading-order cell wall behaviour

An asymptotic expansion simplifies the model and extracts the leading-order components of the stress resultant integral when expansin is neglected. Since both $\gamma,\ \beta \ll 1$ by definition, we can expand the steady-state solution (3.3.11) with no expansin action (i.e. taking σ_H from equation 3.3.1).

We first expand the integral G (equation 3.3.4) considering the respective regions $\gamma \ll y \leq 1$ and $\epsilon \leq y \ll \gamma$. By bounding the integral for G, integrating by parts, and neglecting higher-order terms, we find

$$G(y) \approx \begin{cases} \frac{y^2}{2\breve{\alpha}^2\gamma^2}\exp\left(\breve{\alpha}^2\frac{\gamma^2}{y^2}\right), & \epsilon \leq y \ll \gamma \\ \ln\left(\frac{1}{y}\right), & \gamma \ll y \leq 1, \end{cases} \quad (3.3.12)$$

where we define $\breve{\alpha} = \frac{\alpha}{\alpha+\omega}$ for notational simplicity. From equation (3.3.4) the asymptotic approximation of n is then,

$$n = \begin{cases} \exp\left(-\frac{\breve{k}_0}{\alpha}\frac{y^2}{2\breve{\alpha}^2\gamma^2}e^{\breve{\alpha}^2\frac{\gamma^2}{y^2}}\right), & \epsilon < y \ll \gamma \\ y^{\frac{\breve{k}_0}{\alpha}}, & \gamma \ll y \leq 1. \end{cases} \quad (3.3.13)$$

The expansion of $\tilde{G}$ proceeds similarly to give

$$\tilde{G}(y) \approx \begin{cases} \frac{y^2}{2\breve{\alpha}^2\tilde{\beta}^2} \exp\left(\breve{\alpha}^2 \frac{\tilde{\beta}^2}{y^2}\right), & \epsilon < y \ll \tilde{\beta} \\ \ln\left(\frac{1}{y}\right), & \tilde{\beta} \ll y \leq 1. \end{cases} \tag{3.3.14}$$

Combining, we find

$$\tilde{n} = \begin{cases} \exp\left(-\frac{1}{\alpha} \frac{y^2}{2\breve{\alpha}^2\tilde{\beta}^2} e^{\breve{\alpha}\frac{\tilde{\beta}^2}{y^2}}\right), & \epsilon < y \ll \tilde{\beta} \\ y^{\frac{1}{\alpha}}, & \tilde{\beta} \ll y \leq 1. \end{cases} \tag{3.3.15}$$

Notice that the simplification of $\tilde{n}$ is not dependant on n. To complete the approximations for all y, we find switch-over values where the asymptotic behaviour of n and $\tilde{n}$ changes from one regime to another (denoted χ and $\tilde{\chi}$ for the hemicellulose and BH bond densities respectively). These are the y-values close to γ or $\tilde{\beta}$ such that the derivatives of the dominant exponents in n and $\tilde{n}$ exceed some threshold Q, causing n and $\tilde{n}$ to rapidly decrease. Thus,

$$\chi = \sqrt{\frac{\gamma^2\breve{\alpha}^2}{\ln\left(\frac{\alpha}{\bar{k}_0}Q\right)}} \text{ and } \tilde{\chi} = \sqrt{\frac{\tilde{\beta}^2\breve{\alpha}^2}{\ln(\alpha Q)}}. \tag{3.3.16}$$

Approximations of the trigonometric term describing how much cellulose contributes to the axial stress and the cellulose extension are also required. To balance simplicity and accuracy the following expansions are taken to such an order that they achieve a mean squared error of $\approx 10^{-3}$ with respect to the numerical solution, and the domain is split into three regions corresponding to $\frac{\tan\theta_0}{y} \gtrsim, \approx, \lesssim 1$. In the first region, $\tan\theta_0 + \delta < y \leq 1$, where δ is a small number of our choosing to optimise the expansion's overall accuracy, we Taylor expand sin and arctan in equation (3.3.11), where θ is described by equation (3.3.8). In the second and third regions, where $\frac{\tan\theta_0}{2} < y \leq \tan\theta_0 + \delta$ and $\epsilon \leq y \leq \frac{\tan\theta_0}{2}$, we use the expression $\sin\left(\arctan\left(\tan\theta_0 \frac{1}{y}\right)\right) = \frac{\tan\theta_0}{\sqrt{\tan^2\theta_0 + y^2}}$ and Taylor expand around

$y = \tan\theta_0$ and $y = 0$ respectively. Hence,

$$\sin\left(\arctan\left(\tan(\theta_0)\frac{1}{y}\right)\right) = \begin{cases} \frac{\tan\theta_0}{y} - \frac{1}{2}\frac{\tan^3\theta_0}{y^3} + \frac{3}{8}\frac{\tan^5\theta_0}{y^5} - \frac{5}{16}\frac{\tan^7\theta_0}{y^7}, & \tan\theta_0 + \delta < y \leq 1, \\ \frac{1}{\sqrt{2}} - \frac{y-\tan\theta_0}{2\sqrt{2}\tan\theta_0} + \frac{(y-\tan\theta)^2}{8\sqrt{2}\tan^2\theta_0} + \frac{(y-\tan\theta)^3}{16\sqrt{2}\tan^3\theta_0} - \frac{13(y-\tan\theta_0)^4}{128\sqrt{2}\tan\theta_0^4}, & \frac{\tan\theta_0}{2} < y \leq \tan\theta_0 + \delta \\ 1 - \frac{y^2}{2\tan^2\theta_0} + \frac{3y^4}{8\tan^4\theta_0} - \frac{5y^6}{16\tan^6\theta_0}, & \epsilon < y \leq \frac{\tan\theta_0}{2}. \end{cases} \tag{3.3.17}$$

By substituting equation (3.3.17) into equation (3.3.9), integrating and Taylor expanding the exponential, we find the leading orders terms of L_C to be,

$$L_C(y) = \begin{cases} b_1\left(1 + \frac{\tan^2\theta_0}{2\hat{y}^2}\right), & \tan\theta_0 + \delta < y \leq 1, \\ \frac{b_2}{y^{\frac{34969}{32768}}}(1 - H(y) + \frac{H(y)^2}{2}), & \frac{\tan\theta_0}{2} < y \leq \tan\theta_0 + \delta, \\ \frac{b_3}{y}\left(1 + \frac{y^2}{2\tan^2\theta_0}\right), & \epsilon \leq y \leq \frac{\tan\theta_0}{2}, \end{cases} \tag{3.3.18}$$

where b_0, b_1, b_2 and b_3 are constants and $H(y)$ is a function of the form $\sum_i p_i \left(\frac{y}{\tan\theta_0}\right)^{q_i}$, with q_i being integers; all b_i, p_i, q_i and H are defined in appendix A.1.5.

The stress resultant consists of three terms each representing a physical effect. Firstly, the cellulose contribution independent of the BH connections is

$$\Sigma_1^\infty = \int_\epsilon^1 (L_c - 1)\sin\theta \; dy = \sum_i c_i, \tag{3.3.19}$$

where c_i are constants dependent on $\tan\theta_0$ or ϵ (defined in table A.1). Secondly, the

cellulose contribution when crosslinked by the BH is

$$\begin{aligned}\Sigma_2^{\infty} &= \int_{\epsilon}^{1} a_1 \tilde{n}(L_c - 1)\sin\theta \; dy \\ &= a_1 \left(\left(\sum_i d_{1,i}(\alpha) \right) + \tan_0 (b_1 - 1)\,\alpha + \left(\sum_i d_{2,i}(\alpha) \right) (\delta + \tan\theta_0)^{\frac{1}{\alpha}} \right. \\ &+ \tan\theta_0 (1 - b_1)\,\alpha(\delta + \tan\theta_0)^{\frac{1}{\alpha}} + \left(\sum_i d_{3,i}(\alpha) \right) \left(\frac{\tan\theta_0}{2} \right)^{\frac{1}{\alpha}} \\ &\left. + b_3\alpha \left(\frac{\tan\theta_0}{2} \right)^{\frac{1}{\alpha}} + \left(\sum_i d_{4,i}(\alpha) \right) (\tilde{\chi})^{\frac{1}{\alpha}} - b_3\alpha(\tilde{\chi})^{\frac{1}{\alpha}} \right). \end{aligned} \tag{3.3.20}$$

The generic form of the constants $d_{j,i}$ is $\frac{w_1}{w_2\left(\frac{1}{\alpha}+w_3\right)}$, where w_1, w_2 and w_3 are known constants often dependant on $\tan\theta_0$, δ and $\tilde{\chi}$ (see table A.2). Lastly, the contribution from the hotspots is then

$$\begin{aligned}\Sigma_3^{\infty} &= \int_{\epsilon}^{1} a_2 n \tilde{n} \sigma_H \; dy \\ &= a_2 \breve{\alpha} \left(\frac{\alpha}{\breve{k}_0 + 1} \left(1 - \chi^{\frac{\breve{k}_0+1}{\alpha}} \right) - \frac{1}{\frac{1}{\alpha}\left(\breve{k}_0 + \omega + 1 \right) + 1} \left(1 - \chi^{\frac{\breve{k}_0+\omega+1}{\alpha}+1} \right) \right). \end{aligned} \tag{3.3.21}$$

Further simplifications to the stress resultant can be made by examining the cases for small and large strain-rate, $\alpha \ll 1$ and $\alpha \gg 1$ respectively. When $\alpha \ll 1$, all terms of the form $\mathcal{Z}^{\frac{1}{\alpha}}$ that appear in the expansions are negligible, since $\mathcal{Z}$ is less than one for all such expressions. When $\alpha \gg 1$ all the terms of the form $\frac{w_1}{w_2\left(\frac{1}{\alpha}+w_3\right)}\mathcal{Z}^{\frac{1}{\alpha}}$ tend to a constant, and are smaller in magnitude compared to terms of the form $\alpha\mathcal{Z}^{\frac{1}{\alpha}}$ and consequently can also be neglected. As a result,

$$\Sigma^{\infty} = \begin{cases} \sum_i c_i + a_1\alpha\tan\theta_0 (b_1 - 1) + a_2\breve{\alpha}\left(\frac{\alpha}{\breve{k}_0+1} - \frac{1}{\frac{1}{\alpha}(\breve{k}_0+\omega+1)+1} \right), & \alpha \ll 1, \\ \sum_i c_i + a_1\alpha \left(\tan\theta_0 (b_1 - 1) + \tan\theta_0 (1 - b_1)(\delta + \tan\theta_0)^{\frac{1}{\alpha}} + b_3 \left(\frac{\tan\theta_0}{2} \right)^{\frac{1}{\alpha}} \right. & \\ \qquad \left. - b_3(\tilde{\chi})^{\frac{1}{\alpha}} \right) + a_2\breve{\alpha}\left(\frac{\alpha}{\breve{k}_0+1}\left(1 - \chi^{\frac{\breve{k}_0+1}{\alpha}} \right) - \frac{1}{\frac{1}{\alpha}\left(\breve{k}_0+\omega+1\right)+1} \right), & \alpha \gg 1. \end{cases} \tag{3.3.22}$$

Equation (3.3.22) gives the leading-order terms that control the dominant cell wall be-

haviour for small and large strain-rates, neglecting the effect of expansin action. This expression is used to validate the numerical scheme presented in section 3.4, where the biological implications are also discussed.

3.4 Results and discussion

The complexity of the plant cell wall and its growth process presents many modelling challenges. A simple model has therefore been created to focus attention on the cell wall structure and its implications on possible enzyme action

The system of equations (3.3.4)-(3.3.10) are solved for the bond densities n and $\tilde{n}$, the CMF angle θ, and the stress resultant Σ, subject to a choice of expansin action where σ_H is determined by one of (3.3.1)-(3.3.3). Where the steady-state stress resultant is required, we use (3.3.11) instead of (3.3.10). The asymptotically simplified expressions (3.3.19)-(3.3.22) for the steady-state stress resultant are used where applicable. This study focusses on the cellulose crosslinking dynamics, hence the effect of pectin on the cell wall dynamics is neglected by setting $\Gamma = 0$ throughout. All other fixed parameters values are listed in table 3.1. All solutions are obtained using MATLAB; in particular, the integrals are computed numerically using the Legendre-Gauss Quadrature code by von Winckel [2021].

The discussion of the results are begun, by first analysing the model's implications on the cell wall structure and yield threshold in section 3.4.1. Secondly, possible enzyme mechanisms and the likelihood of BH structures in the cell wall are explored in section 3.4.2. The section is then finished of with some final remarks and possible future directions in section 3.4.3.

3.4.1 Cell wall structural implications

It is first described how the stress resultant links to the cell wall yield threshold. A fixed turgor pressure will result in a specific cell wall tension. When expansin acts on the

Parameter	Value	Reference
ν_C^*	140Gpa	[Moon et al., 2011, Gindl and Schöberl, 2004] [Gassan et al., 2001, Iwamoto et al., 2009]
ν_H^*	7Gpa	[Moon et al., 2011, Gindl and Schöberl, 2004] [Gassan et al., 2001, Iwamoto et al., 2009]
θ_0	0.1	Huang et al. [2018]
$\breve{k}_0$	1	
ς_n	1	Dyson et al. [2012]
ς_m	1	Dyson et al. [2012]
$\frac{\tilde{n}_0^* n_0^*}{\rho^*}$	0.5	[Wilson et al., 2021, Ye et al., 2020]
μ^* & μ_0^*	0.15	Fozard et al. [2013]
ϵ	0.0001	
δ	0.06	

Table 3.1: Model parameter values. In the model, the relevant parameters for the roots of *Arabidopsis thaliana* are used. It is assumed that $\breve{k}_0 = \frac{k_0^*}{\tilde{k}_0^*} \approx 1$ so that the breakage rates of the hotpsots and the hemicellulose fibres at rest are approximately the same. We set $a_1 = 0.1$ in most simulations as this number does not affect the results apart from the expansin action simulations where this parameter's effect and implications are commented on in section 3.4.2. The table values mean that $a_2 = 0.025$

BH resting length, L_0, the same cell-wall stress/turgor pressure produces different strain rates (figure 3.3a, solid line versus dashed line); equation (1.1.1) then implies that the yield threshold has changed. Further analysis of the stress-strain-rate relationship and the crosslinks' influence on the cell-wall yield threshold can be found in Dyson et al. [2012].

In the collective results some general trends can first be noticed. As the strain rate increases, the stress resultant is seen to plateau (e.g. figure 3.3). This behaviour arises despite the inclusion of linear elasticity due to the relationship the bond densities, n and $\tilde{n}$, have with α. Specifically, for low values of α, the bond density $\tilde{n}$ remains low for much of the domain (see figure 3.6b). However, when this value is increased, the bonds become increasingly loaded and remain intact for longer (increasing the overall stress held in the cell wall) before finally breaking. Upon furthers increases to α, the BHs reach a limit as to how much stress they can withstand without breaking, and the bond density eventually drops to 0 when $y \approx 0$ (meaning the amount of stress held across the cell wall has reached capacity)(figure 3.6b). This limit on the bond densities capacity consequently limits further increases to the stress resultant, implying that the cell wall's yield threshold

has a maximum, where increasing the growth rate has little further effect. Even though it is the CMF that resists the majority of the turgor imposed tension, this limit demonstrates that it is how the cellulose molecules are crosslinked, which caps cell wall strength.

The effect cellulose re-orientation during growth has on the stress resultant is now examined. For lower strain rates, the stress resultant is found to increase as time progresses (figure 3.7a) due to a combination of all the fibres being increasingly strained and the cellulose progressively re-orientating. The stress difference between the varying times gets negated for large strains because of the increase in the rate of re-orientation (it's dependant on $e^{\alpha t}$), allowing the fibres to converge to the same distribution of orientations. A sharp point in the lines for lower times is also witnessed (figure 3.7a). This peak occurs because as the strain rate increases (equivalent to time progressing due to dependence on $e^{\alpha t}$) the fibres present at $t = 0$ are stretched and re-orientated uniformly. For fibres deposited at $t > 0$, they are progressively stretched and rearranged as they move to the outside of the wall, thus for certain times, the sum of the stress arising in this family of fibres is less than those present at $t = 0$. This raised stress resultant doesn't last where the crosslinks present at $t = 0$ eventually break and causes a rapid decrease in the cell wall strength, producing a sharp peak in the simulations (figure 3.7a). The effect of cellulose re-orientation can also be seen when the initial fibre angle, θ_0 is increased (figure 3.7b). As can be noted in equation (3.3.8), when θ_0 is increased with the fibre position in the cell wall, y remaining constant, the cellulose fibres get increasingly re-oriented. Consequently, increasing θ_0 also significantly increases the stress resultant (figure 3.7b). From these results, it can be concluded that cellulose re-orientation leads to a higher stress resultant in the plant cell wall and, subsequently, increases the cell wall yield threshold. The yield threshold increasing due to cellulose re-orientation could provide a possible mechanism for growth slow down and hence the beginning of the cells secondary wall structure. An idea that has been previously hypothesised Anderson et al. [2010]. Cellulose re-orientation reducing axial growth has been previously reported in other mathematical models [Dyson and Jensen, 2010, Ptashnyk and Seguin, 2016].

Major agreement between the different sets of asymptotic expansions and the numerical results can be seen for all three combinations of $\tilde{\beta}$ and γ (figure 3.8) where there is some error as a result of neglecting the lower order terms. There is also little difference in the accuracy between the full asymptotic equations (3.3.19)-(3.3.21) (dashed line) and the further simplified expansion, (equation (3.3.22)) (dotted line) (where the lines are overlapping due to their very similar values) demonstrating that it is these terms, in equation (3.3.22), that characterise the cell wall yield threshold's behaviour. From equations (3.3.19), and (3.3.20) the values of the sets of constants, c and d in the cellulose's contribution to the cell wall strength are seen to be dependent on $\tan\theta_0$ meaning it can be explicitly observed that increasing this value will increase the stress held in the cell wall. When combined with the fact that $a_2 < a_1$, and the results discussed above shows that the main control of the cell wall yield threshold in the axial direction is the cellulose orientation. This result matches with the fact that it is the cellulose direction that controls growth direction in most plant cells [Geitmann, 2010].

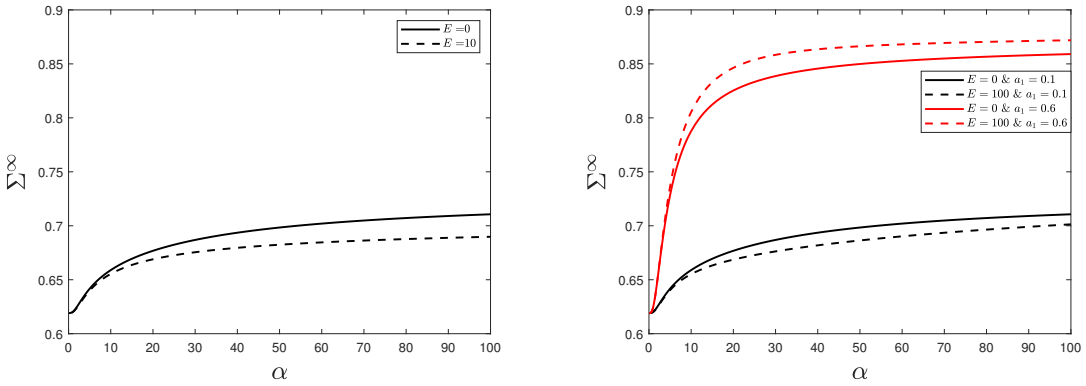
The main terms characterising the cell wall stress behaviour can be seen from the further reduced asymptotic expansion (equation 3.3.22). The BH bond density's contribution (the $\tilde{\chi}$ term) is controlled by b_3, which is the coefficient controlling the slope of the extension curve of the cellulose molecules, L_C, as they rapidly extend close to $y = 0$ where they are most stressed. This control implies that the leading order stress behaviour when the hotspots are targeted (changing $\tilde{\beta}$) is the result of targeting the smaller group of significantly stressed cellulose molecules. From this expression, the reason behind the stress resultant plateauing can also been seen. The terms of the form $(\bullet)^{\frac{1}{\alpha}}$ converges towards 1 as α increases. However as χ & $\tilde{\chi} < \tan\theta_0$, when α is smaller, $\chi^{\frac{1}{\alpha}}$ & $\tilde{\chi}^{\frac{1}{\alpha}} < \left(\frac{\tan\theta_0}{2}\right)^{\frac{1}{\alpha}}$ & $(\tan\theta_0 + \delta)^{\frac{1}{\alpha}}$, but as α increases they converge to the same value. As the coefficients of χ and $\tilde{\chi}$ are negative, this means the gradient of the stress resultant curve decreases as α grows. So this plateauing occurs due to the bond breakage terms increasing more relative to the other terms as they reach their limit as to how much more stress the bonds can hold. It is also noted that for $\alpha \ll 1$, the stress resultant is not

controlled by χ and $\tilde{\chi}$ at all. This implies for low levels of turgor pressure, enzyme action on the cell wall is ineffective at controlling the growth rate and that it is solely controlled by the orientation and concentration of fibres.

3.4.2 Enzyme action on the cell wall

Different modes of enzyme action are now examined beginning with expansin. As previously mentioned in section 2.1.1 expansin causes wall loosening without reducing the strength of the cell wall by possibly allowing the slippage of fibres within the hotspot. Expansin's hypothesised action is simulated via two methods; decreasing the viscosity of the dashpot and increasing the spring resting length by equations characterised in section 3.2.2.3. Simulations of expansin's theorised fibre slippage action on the resting length (equation 3.3.2) reveal a decrease in the stress resultant (figure 3.3a) while ensuring the bond density does not reach zero (figure 3.4a). Similarly, expansin's slippage action on the viscosity of the dashpot (equation 3.3.3) decreases the stress resultant if BH cellulose crosslinking is small (figure 3.3b) and increases the bond density (figure 3.4b). This bond density increase arises due to stress relaxation via either extension of the resting lengths or a decrease in viscosity; both mechanisms reduce the elastic strain imposed on the fibres which are therefore less likely to break. Both of these methods have therefore been found to decrease the axial stress resultant for all strain rates (figure 3.3) meaning both methods are effective mechanisms for inducing growth. The BH bond densities $\tilde{n}$ are also seen to have increased for both enzyme action pathways (figure 3.4) implying that the cell wall has strengthened upon their action. Allowing the fibres to flow in the dashpots or loosen due to an increased resting length allows the fibres to relax and decreases the likelihood of the bonds breaking. Thus we have explained experimental behaviour and have provided evidence for this slippage theory. This result is dependant on the parameter, a_1, where when this value is increased, expansin action causes the yield threshold to increase (figure 3.3b) despite the loosening. This is because two opposing effects contribute to the overall stress resultant: stress relaxation from the BH, combined with the inclusion of more, in-

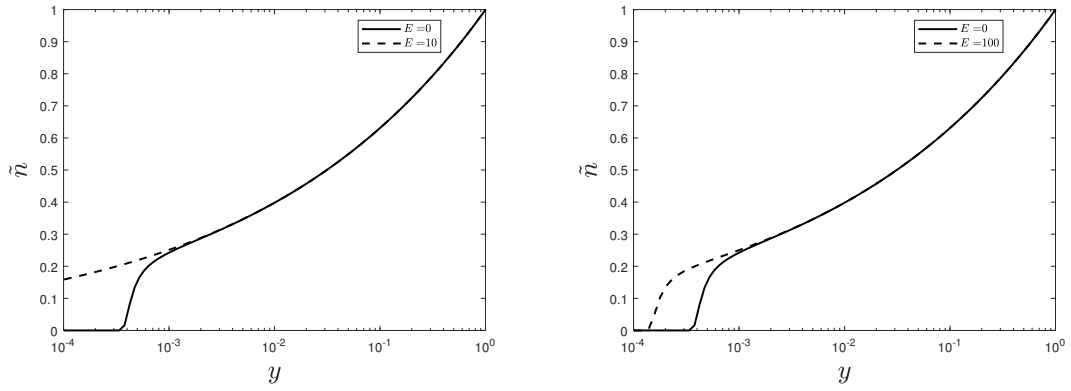
creasingly stretched, CMF molecules towards the outer boundary of the cell wall. When the BH-cellulose crosslinking is sufficiently large to counteract the BH stress relaxation, the stress resultant increases with expansin action due to the increased contribution of the CMF (figure 3.3b). This result can be biologically explained. Plants that lack xyloglucan have been shown to have only a small amount of growth reduction, and alterations in cell wall structure [Park and Cosgrove, 2015, Kuki et al., 2020]. This observation has led to suggestions that when xyloglucan is present, it is concentrated in these compact biological hotspots. The model seems to supports this theory as when we increase a_1, the cellulose contribution to the cell wall strength when crosslinked by xyloglucan/BH's increases and, expansin's experimental behaviour can no longer be recreated.



(a) (b)

Figure 3.3: The effect on the stress resultant of expansin acting on (a) the resting length, L_0; or (b) the viscosity, μ, where the small (large) a_1 value represents reduced (enhanced) cellulose crosslinking by the BHs. Other parameters: $\tilde{\beta} = 0.01$ and $\gamma = 0.05$.

Continuing the investigation of hypothesised enzyme action, XTH and Cel12A are now focussed on. As detailed in section 2.1.1, XTH hydrolyses hemicellulose and Cel12A hydrolyses the hotspots. Recall that this cutting action was recreated by increasing the breakage rate of the hemicellulose fibres, γ, to model XTH, and increasing the hotspot breakage rate, $\tilde{\beta}$, to model Cel12A action. By testing a range of values for both parameters it is discovered that $\tilde{\beta}$ significantly affects the stress resultant compared to γ (figure 3.5a). These results agree with previous work, which also finds the yield threshold to be controlled by the rate of dissociation of tethering crosslinks [Sridhar et al., 2018]. The

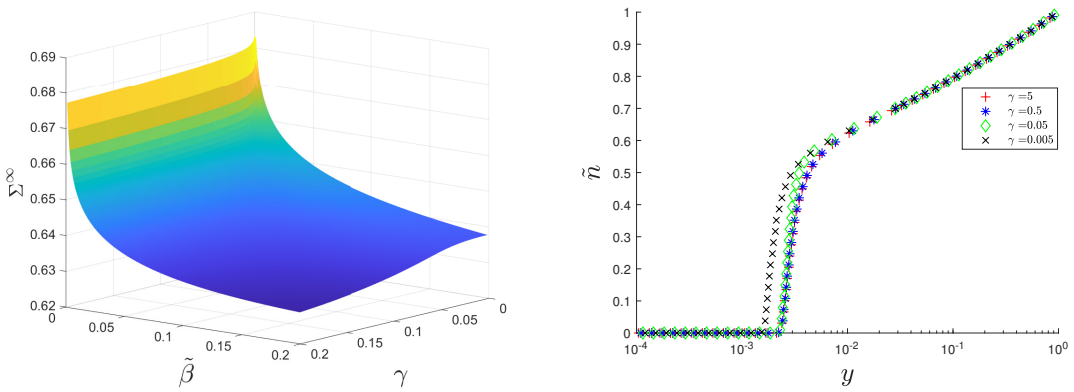


(a) (b)

Figure 3.4: The effect on the BH density of expansin acting on (a) the resting length, L_0; or (b) the viscosity, μ, with $\alpha = 5$, $\tilde{\beta} = 0.01$ and $\gamma = 0.05$.

effect of γ on the hotspot bond density, $\tilde{n}$, is also negligible (figure 3.5b). In contrast, an increased $\tilde{\beta}$ leads to a considerable decrease in $\tilde{n}$ (figure 3.6a). As the fibres move towards the outer $y = 0$ boundary their lengths increase sharply ($L = \frac{1}{y}$), leading to significantly larger stresses; the stress resultant is therefore highly sensitive to small changes in the transition location $\tilde{\chi}$ in the region $0 < y < 0.1$ where $\tilde{n}$ drops rapidly. This effect implies increasing the breakage rate of the hemicellulose fibres (increasing γ) is ineffective when compared to targeting the hotspots themselves (increasing $\tilde{\beta}$). With simulating XTH action, minimal reductions in the stress resultant and the BH density are seen implying due to its limited wall loosening ability, minimal growth is induced, as observed in experiments [Cosgrove, 2016]. This effect occurs despite a natural assumption that the hydrolysis of bonds by some members of the XTH family could cause wall loosening [Cosgrove, 2016, Yuan et al., 2001]. The model suggests that either when hemicellulose fibres are cut, the hotspots can maintain their integrity and remain intact or possibly because if the BH's are compact and inaccessible, hydrolysing hemicellulose could be ineffective at breaking BH's down. Interestingly from the asymptotic expansions it is $\tilde{\beta}$ not γ (in the form of $\tilde{\chi}$) that helps control the leading order terms of cellulose's contribution. So as a consequence of the modelling choices, it is explicitly seen that if XTH's ability to break down the hotspots is ineffective, observed experimental behaviour is recreated.

By recreating Cel12A hypothesised hotspot cleaving action, it is seen that it weakens the cell walls by decreasing the BH density, which decreases the stress resultant and induces growth. This result is the same effect Cel12A has in biological experiments [Cosgrove, 2016]. This effect would not occur if we assumed a tethered network setup, meaning if the model had just one bond density that is not dependent on another (in a similar manner to Dyson et al. [2012]). This is because we wouldn't have two separate breakage rates, leaving us unable to distinguish between Cell12A and XTH's action. Therefore through analysis of the breakage rates and the model's assumption of the BH hypothesis, we have recreated experimental enzyme behaviour.

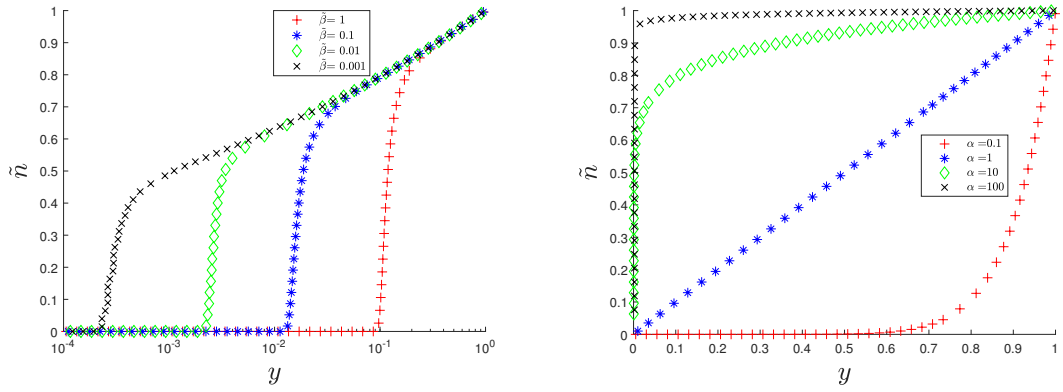


(a) (b)

Figure 3.5: Enzyme cutting action with $\tilde{\beta}$ and γ representing cel12a and XTH's action respectively on (a) the stress resultant with $\alpha = 50$ and (b) XTH's action on the BH density $\tilde{n}$ with $\beta = 0.1$ and $\alpha = 10$.

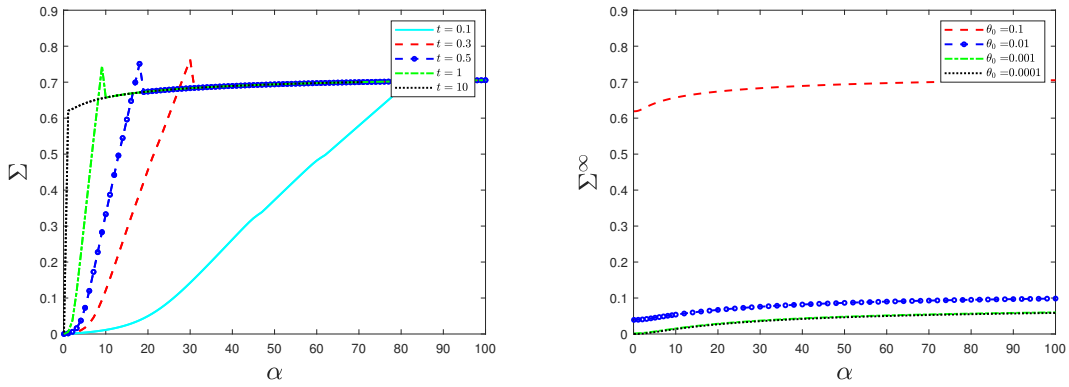
3.4.3 Closing remarks and future work

The results presented play into the theory that plant cell walls undergoing growth seem to undergo a glass transition. A theory that suggests, that hemicellulose is not the primary stress-bearing component (as a_1 is small), but the stress relaxation imposed on them by the digestion or slippage of the hotspots could be enough to cause the stress to then be placed on other cell wall components such as pectin intertwined with the cellulose to induce growth. With the cell wall extending, other hotspots could begin to be stressed,



(a) (b)

Figure 3.6: The effect of varying (a) Cel12a's action with $\alpha = 10$ and (b) α with $\tilde{\beta} = 0.01$, on the BH bond density $\tilde{n}$, both with $\gamma = 0.05$.



(a) (b)

Figure 3.7: Changes in the stress resultant as we affect the cellulose fibre orientation by changing (a) the time point and (b) θ_0 with $\beta = 0.01$ and $\gamma = 0.05$.

where they then raise the yield threshold again.

These results depend on the inclusion of the cellulose contributing to the axial stress. Even though on average, the cellulose molecules are perpendicularly oriented to the growth axis [Kafle et al., 2014], our findings show the importance of including cellulose re-orientation or having them in a variety of angles in mathematical models of growth.

There are possibilities to extend this model further. One improvement that could be made is to increase the dimensionality of the model. Radial expansion could then be examined by looking at the stress held in the normal direction to the cell wall (radial direction/y direction). This improvement would allow an understanding of how enzyme

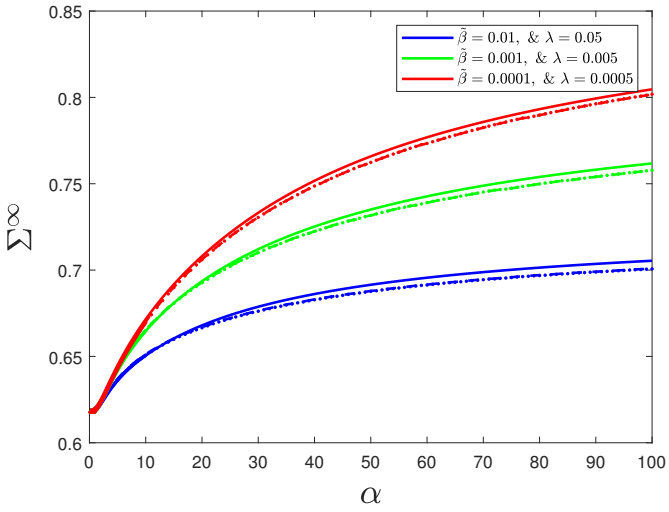
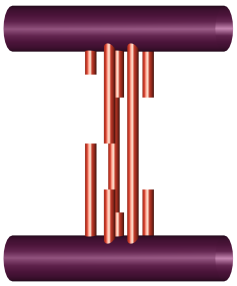
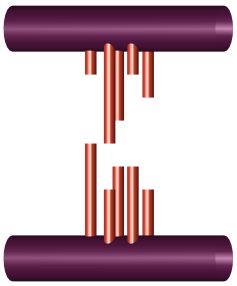


Figure 3.8: Comparison between the axial stress resultant's numerical solution (solid line) to our asymptotic approximations, equation (3.3.19)-(3.3.21) (dashed line) and equation (3.3.22) (dotted line) both plotted for different values of $\tilde{\beta}$ and γ.

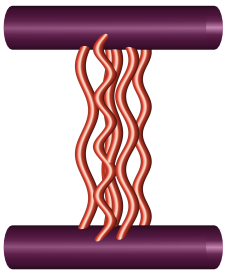
action does not necessarily lead to radial growth and the consequences of cellulose re-orientation, as it has been observed a reduction in anisotropy can lead to radial swelling [Crowell et al., 2011]. Expansin has been shown to induce growth as soon as it is applied, while Cel12A induced growth is delayed after application [Zhang et al., 2019]. The model cannot explain this time delay phenomenon, meaning we could benefit from further work on the crosslinking dynamics to understand this process. Many experiments are done on a tissue level, while the model examines only a small cell wall section. Therefore, there could be advantages to constructing a tissue-scale model for cells, including their interactions and the different cell layers to match with experiments. Growth in many tissues occurs as a whole, for example, in plant stems, the outer cells are considered to be load-bearing with longitudinally arranged CMF (therefore restricting growth), and the inner cells (which are being restricted) having thinner, more pliant cell walls with the CMF arranged horizontally [Creff et al., 2015, Derbyshire et al., 2007, Baskin and Jensen, 2013]. An expanded model could help us to understand the significance of differing cellulose orientations and how a plant tissue grows as a whole.



(a) XTH action



(b) Cel12A action



(c) Expansin action

Figure 3.9: Hypothesised enzyme action. The purple rods represent cellulose molecules, and the red rods are the hemicellulose fibres in a hotspot. a) XTH hydrolysis action only cutting a select amount of hemicellulose fibres. b) Cel12A hydrolysis action cutting the whole hotspot. c) Expansin loosening action allowing the hotspot to be intact while allowing extension.

3.5 Conclusion and summary

It can be concluded, firstly, that cellulose re-orientation during cell wall extension leads to a decrease in the axial growth rate and its orientation is the primary control for cell growth and the yield threshold. Secondly, experimentally observed enzyme behaviour has been explained by assuming the biological hotspot hypothesis and thus provides evidence for the theory. Thirdly, we propose the following enzyme mechanisms which are in line with experimental observations (figure 3.9). XTH only cuts individual hemicellulose fibres, meaning as a result of the hotspots remaining inaccessible or hemicellulose scissoring being ineffective in breaking the full hotspot down, XTH does not provide sufficient wall loosening to induce growth. On the other hand, Cel12A can cleave the whole hotspot allowing the cell to grow where it also weakens the cell wall. Expansin action causes fibre

slippage, permitting stress relaxation, enabling cell wall extension without weakening the cell wall . We have therefore presented a mechanistic understanding of potential enzyme action, which matches observed experimental mechanical behaviour.

Enzyme action on the cell wall is an under-researched area of plant growth which modellers have particularly overlooked. By not understanding how cell wall modifying enzymes work, we do not truly understand how plants grow. We hope this work is a stepping stone on the path to our understanding of how these enzymes work.

As growth on the microscale has now be examined, if growth control is to be fully understood, larger scale dynamics now needs to be investigated. In the subsequent chapters we consider pavement cells to understand growth control at a cell level where due to their complex shape, pavement cells offer a great case study.

Chapter 4

Experimental methods to understand pavement cell development

4.1 Introduction and experimental aims

We now investigate how pavement cell growth is controlled, specifically how pavement cell lobes are initiated. We first present experimental results undertaken while visiting Dr Siobhan Braybrook's Lab at the University of California, Los Angeles, funded by a Travelling Fellowship grant from Development and The Company of Biologists. This will be followed with theoretical modelling studies in chapters 5-7.

There are several tasks we wanted to complete with the experiments. Firstly we wish to obtain actual pavement cell shapes for the modelling simulations in chapters 5-7. Secondly, we want to validate some past experiments and repeat these same experiments in early pavement cells before their lobes are fully developed, as in some cases, young pavement cells have not been examined. Specifically, we will test the claims of microtubules and actin filaments localising to the indents and lobes respectively and check how early this localisation occurs to see if they could initiate lobes. Finally, we also wish to investigate cell wall material properties in young pavement cells, specifically the Youngs modulus/stiffness, to see where and if this varies early on.

Our experimental objectives highlighted above will enable us to see any evidence of early cytoskeleton localisation or differing stiffnesses in very small lobes and/or along straight walls (meaning a possible lobe/indent precursor site). Because chemical signalling pathways would most likely cause these patterns of cytoskeletal localisation and stiffnesses heterogeneities, evidence of such features in young pavement cells could imply chemical signalling lobe initiation. To clarify, if buckling mechanisms initiated lobes, the features mentioned above would not necessarily be needed in this early stage of development.

In this chapter, the imaging and experimental procedures are described in section 4.2 where the results are presented and discussed in section 4.3. This chapter is then summarised in section 4.4.

4.2 Experimental methods

Here is described the experimental methods as to how the plant cell outlines, cytoskeleton and cell wall stiffnesses are captured. In the vast majority of the experiments, *Arabidopsis thaliana* is used where *Nicotiana benthamiana* is also used for the mature pavement cell outlines as they are easy to grow, have a very similar pavement cell phenotype and provide high-quality images that feature less prominent stomata to disrupt the pavement cells outlines.

This section is begun with the description of how the plants were grown and maintained in section 4.2.1 which is followed by an explanation of how the plants were processed and imaged in section 4.2.2. It is then detailed as to how these images were edited and processed for use in the later chapters in section 4.2.3. Finally, this section is finished by detailing how the plant cell wall's stiffness values are obtained using an instrument called an atomic force microscope (AFM) in young pavement cells in section 4.2.4.

4.2.1 Plant seeding and maintenance

Arabidopsis thaliana seeds are selected and mixed in 70% ethanol for 5 minutes, occasionally shaking, to decontaminate and then rinsed in 100% ethanol. The seeds are then placed in Petri dishes with 25ml of MS (Murashige and Skoog) growth media (see below for details) in a laminar flow hood to reduce the risk of contamination. After this step, the seeds are placed in the fridge at $4°C$ and wrapped in foil to block any light for 72 hours for them to undergo stratification (meaning the breakage of seed dormancy to promote germination). The Petri dishes are then taken out and put in a growth chamber set at $20°C$ on a long day cycle (18 hours of light and 6 hours of dark) for a prescribed number of days (varies per experiment).

The Petri dishes containing the growth media are prepared by first making a mixture of media with 2.2g/l of MS powder (where MS powder contains all the nutrients the seeds need to grow and develop). The MS powder is diluted with Milli-Q water (pure water,

deionised), and using potassium hydroxide (an Alkali/base), the pH of the mixture is adjusted to 5.7 ($5.7 - 5.8$), which is the optimum pH for *Arabidopsis thaliana* to grow (as the water-MS solution will be too low otherwise). Lastly, plant agar is added at 8g/L, noting that any changes to this concentration will affect the osmotic potential of the media and consequently the turgor pressure in the plant cells. The mixture is then placed in an autoclave for decontamination, where upon completion, the mixture is then poured into Petri dishes in a laminar flow hood to prevent contamination. They are then left for 20 minutes for the agar to solidify, where they are then sealed and must be allowed to cool down before use.

The process of growing *Nicotiana benthamiana* is different due to their size. Multiple tobacco seeds are planted in pots containing fertiliser, where after a week, they are transferred to individual bigger pots also containing fertiliser to allow further growth. For optimum growth conditions, the *Nicotiana benthamiana* plants are grown in a greenhouse held at around $27°C$.

4.2.2 Imaging pavement cells

Pavement cells are imaged using a confocal microscope which scans an object with lasers that excite fluorescent particles, which then emit a light that is measured by the microscope [Prasad et al., 2007]. There are several options and parameters to choose from when using a confocal microscope. The first choice to make is the emission range of the laser, so that it only excites the molecules that we want to observe (for example, care needs to be taken not to detect chloroplasts, which emit light when hit in a specific emission range). Secondly, the laser power also needs to be changed (if it is too low, the microscope will struggle to detect anything, and if it is too high, it can cause photobleaching) and the gain (i.e. the sensitivity). These parameters are specified in each experiment. Confocal microscopes can also perform an operation called a z stack, which scans multiple layers. Z stacks allow us to capture the concentrations of specific molecules not just in one layer but across the whole cell depth.

The confocal microscope used for the experiments was the Zeiss LSM 710 using the software Zeiss zen black. The objective details that are used are 10X/0.3, 20X/0.8, 40X/1.30 oil, and 63X/1.40 oil.

How the plants' cell walls were imaged is described in section 4.2.2.1. As mentioned in the introduction, some experiments are to be done on young pavement cells meaning the cotyledons (embryonic leaves) have to be removed from their seeds. How this is done is explained in section 4.2.2.2. Lastly, how the GFP transgenic lines to capture the cytoskeleton were chosen and imaged is detailed in section 4.2.2.3.

4.2.2.1 Imaging and preparing the leaves/cotyledons for cell wall imaging

In order to observe the cell walls to obtain pavement cell outlines, a fluorescent chemical compound called propidium iodide (PI) is used. When plant cells are correctly treated with PI, it attaches to de-methylated pectin in the cell wall [Bidhendi et al., 2020a] such that when it is hit by the confocal microscope's laser (under a specific emission range, specified in section 4.3) it emits light and allows us to visualise and image the cell walls. Below is a detailed description of how the cell walls are stained with PI.

The PI solution is first diluted to $(1-3)\mu L$ (we used 3) per $100\mu L$ of tap water. Tap water is used as it contains other chemicals meaning it will have around the same osmotic potential as the plant cells. This osmotic balance is important as otherwise the plant cells will become plasmolysed (where the plant cells lose their water) or they might burst. The plants to be imaged are then retrieved and using forceps scissors, the parts to be pictured are then cut off, i.e. the leaves or the cotyledons. This scissoring is done using a light microscope to examine the cutting procedure closely.

For *Arabidopsis thaliana*, $100\mu L$ of the diluted PI solution is pipetted in the middle of a slide with the objects to be imaged placed on top. A coverslip is then placed on top where the cotyledon/leaves are now ready to be imaged. The time it takes to get to the confocal microscope is sufficient to allow the PI to diffuse in and stain the cell walls.

The process of imaging *Nicotiana benthamiana* requires a different protocol because

(as a result of their different and larger leaves) the method above for *Arabidopsis thaliana* did not stain their cell walls properly. First, *Nicotiana benthamiana* leaves are placed in a syringe containing enough PI to cover them. Secondly, the plunger is moved so that there is no air in the syringe, where the tip of the syringe is then covered with a finger to block the airflow. Thirdly, by pulling back on the plunger, the air is then pulled out of the leaves, allowing the PI to infiltrate the air gaps and successfully stain the cell walls. After repeating the last two steps several times, these leaves are lastly placed on a slide (sometimes using a scalpel to cut off smaller sample pieces of a leaf) with a coverslip on top, allowing them to then be imaged.

4.2.2.2 Cotyledon removal from seed

In several experiments, we wanted to observe young *Arabidopsis thaliana* pavement cells before germination, i.e. ones that were only $0-2$ days old after stratification meaning the seeds have to be dissected in order to remove their cotyledons.

This dissection was done using a light microscope and placing the seeds underneath the objective on a damp piece of filter paper using a transfer pin. The seeds are first examined to see which side is bigger and smaller, as the cotyledons are on the bigger side and the root/hypocotyl (the embryonic stem) is on the smaller side. Two pins are used for this procedure, one with a sharp end and one with a blunt end. By using the blunt-ended pin to hold the seed in place and using the sharp-ended pin to scratch the root/hypocotyl side (the side we do not care about damaging) to remove part of the seed coat, the blunt-ended pin can then be used again to squeeze on the cotyledon side to push the embryo out. Following this procedure, a scalpel is used to cut the hypocotyl off and to separate the two cotyledons. The PI staining procedure for *Arabidopsis thaliana* is then repeated (section 4.2.2.1) to image their cell walls.

4.2.2.3 Imaging GFP Transgenics

To observe the cytoskeleton, transgenic plants that have GFP markers attached to actin or tubulin dimers were grown (see section 4.2.1 for details). Here it is described how the transgenic lines were chosen as there were several different options.

The limited studies that have visualised actin in pavement cells all used different transgenic lines from one another, as a result, numerous GFP expressing actin lines were examined to inspect which one is best. The GFP lines that were checked are, Lifeact:VENUS [Era et al., 2009], GFP:mTalin [Mathur et al., 2002], Lifeact:Eos [Mathur et al., 2010], 35S::GFP:ABD2:GFP, [Wang et al., 2008], 35S::YFP:ABD2:YFP, [Dyachok et al., 2014], ABD2:GFP mCherry:TUA5 [Sampathkumar et al., 2011], GFP:ABD2, [Higaki et al., 2010] and GFP:Talin [Kwok and Hanson, 2004]. As a GFP marker is not a natural part of a protein, it can sometimes alter its expression. Therefore, each line is observed to see if the cytoskeleton looks normal and if there are any alterations in pavement cell size and shape. Some lines also do not express their marker as much in pavement cells. From examining each of the lines, we chose to use 35S::GFP:ABD2:GFP, as this produced the clearest images and displayed a normal pavement cell phenotype.

To observe microtubules, the line GFP:MAP4 [Marc et al., 1998] was chosen, as this transgenic has been established as a good line to use in pavement cells [Bidhendi et al., 2019].

With the lines chosen, before imaging, the cell walls are stained with PI (see section 4.2.2.1) as it is important to be able to see where the cell walls are. Also, when imaging cytoskeletal elements, the leaves must not be squashed as any mechanical perturbation could damage and alter the arrangement of the molecules [Sampathkumar et al., 2014]. As a result, the transgenic cotyledons/leaves are placed on the slides in the middle of a gene frame, and as this frame is raised, it prevents any potential flattening when placing the coverslip. In the confocal microscope, two lasers are used, one for capturing PI and the other for the GFP signal, as imaging them separately produces a better signal, where the emission ranges are set so that they do not overlap. When taking the GFP marked

cytoskeleton images, z stacks are taken to capture the whole cytoskeleton in the cells. Care has to be taken on high laser powers because high levels can increase the likelihood of photobleaching the GFP markers.

4.2.3 Image processing

The captured confocal microscopy images now need to be processed to convert them to a usable format, improve the clarity, and extract the pavement cell outlines for use in later chapters. The methodology to convert and edit the images is detailed in section 4.2.3.1 and how the pavement cell shape outlines are extracted is explained in section 4.2.3.2.

4.2.3.1 Editing the images

The images are processed and converted using ImageJ, which has several inbuilt features to ensure the images are clear and can save them in any file format required (e.g. tiff). This editing is essential for extracting pavement cell outlines as if the outlines are not prominent enough, the later steps will not work. To improve the clarity of the images, the brightness and contrast are adjusted, as well as sometimes using the subtract background tool, which helps reduce noise.

The GFP tagged cytoskeleton z stack images are also processed using ImageJ by combining all the z stack layers into one image using the max intensity projection (takes the maximum signal from each layer and uses it in the final image), as this produces the best image. The PI stained cell walls and the GFP marked cytoskeleton images are then merged as it is important to see the cell walls.

4.2.3.2 Pavement cell shapes extraction

After editing, the now clear pavement cell outline coordinates can be extracted. For full details on how this extraction is performed, see appendix A.2.1.

The software CellSeT [Pound et al., 2012] is used to segment the images where the

MorphopLibJ's morphological segmentation tool in ImageJ is then utilized to extract the pavement cell shapes. The extracted shapes are imported into MATLAB and using the functions `im2bw` and `bwtraceboundary` the outline coordinates, $\mathbf{X}_B^*$ with $\mathbf{X}_B^*=(\mathbf{x}_B^*, \mathbf{y}_B^*)$ are produced and then smoothed (which is necessary as the original extracted coordinates are pixelated). The cell outlines are now ready for use, where all of the experimental imaging procedures have now been outlined.

4.2.4 Atomic force microscopy

With the imaging protocols described, how the cell wall stiffness values are obtained is now described. Atomic force microscopes work by using a small cantilever with a tip at its end to prod an object with a specific force. Indenting a surface causes the cantilever to bend, which the microscope measures to create a curve of the deflection of the cantilever versus the indentation depth. By combining this curve with the known indentation force and stiffness of the cantilever, parameters such as the Youngs modulus/stiffness can be estimated. This parameter calculation is done by inputting the data into software that makes certain modelling assumptions about the surface's elastic (and possibly viscous) behaviour when indented. Using this instrument, we can find how the stiffness/Youngs modulus values spatially vary across the pavement cell walls when in an early stage of development.

There are some issues with AFM experiments as a whole that need to be mentioned. AFM does not measure the plant cell wall's actual stiffness/Young's modulus as many factors affect the measurements. For example, the AFM probe pokes the cell wall vertically, so it is finding the stress response in the normal direction, meaning the output values may not be the actual stiffnesses to which the cell wall is resisting expansion [Sampathkumar et al., 2014]. These indentation experiments can also be affected by the stiffness values in the cell layers below [Zhang et al., 2019]. As a result, from now on, the term, indentation modulus is used instead of using the terms stiffness and Young's modulus to distinguish our values from the true values of these parameters [Daher et al., 2018]. Even though we

are not getting the actual plant cell wall stiffness values, the indentation modulus is still an excellent indicator of how the cell wall properties spatially change.

How the slides are prepared for AFM and then used in the AFM are described in sections 4.2.4.1 and 4.2.4.2 respectively.

4.2.4.1 Preparing the slide

1-day old *Arabidopsis thaliana* plants are selected and their cotyledons removed to sample (see section 4.2.2.2 for details) quickly to ensure that they do not dry out. The cotyledons are placed on double-sided tape on the slides (using kimtech wipes to dry the cotyledons first and then place them on tape as their dampness prevented them from sticking), applying gentle force to ensure that they are stuck. This step prevents the cotyledons from moving while performing the AFM experiments, ensuring reliable results. When transporting the cotyledons to the microscope, it is important to place them in a water solution with similar osmotic conditions as they were grown in, as changing the turgor pressure now, would affect the measurements. The cotyledons on the slide are now ready for AFM.

4.2.4.2 Using the atomic force microscope

The Atomic force microscope is first set up using the instrument's instructions and correctly calibrated. The AFM experiments use the JPK Nanowizard 4 software with the indention being done with a paraboloid tip head with a 5nm radius on a cantilever with stiffness, 28.813N/m and sensitivity 25.93 nm/V. The indentation force and the Z length (the range of the deflection depth curve) varies per sample from 250nN to 500nN and 5 to 10 respectively, with the pixelation also changing (the density of indents) and shall be specified in each sample in section 4.3.4.

After setting up the AFM, the water solution is removed from the slide, and the cotyledons are submerged in 0.6mol Mannitol solution. This solution plasmolyses (water removed from the cell) the cells, ensuring the wall indentation moduli values are unaffected

by the turgor pressure. It is important to note that removing turgor pressure from the system can alter the stress patterns and the mechanical state of the cell walls [Cosgrove, 2015].

After using the AFM, the deflection versus depth curves are analysed using JPK SPM Data Processing software (JPK Instruments, DE; v. spm 5.0.69) using a Hertzian indentation model and a paraboloid tip shape (see appendix A.2.2 for details). All the settings and options chosen here are in line with previous research on measuring plant cell wall indentation moduli [Daher et al., 2018].

4.3 Experimental results and discussion

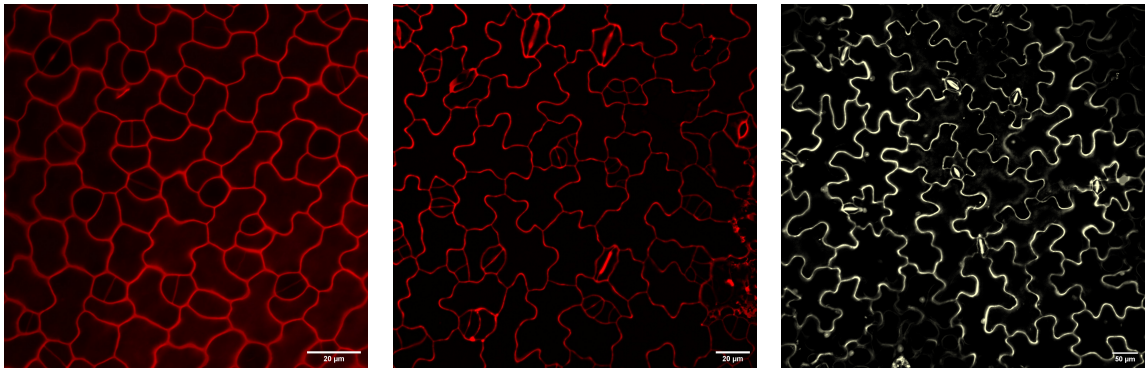
The experimental results are now displayed and examined. As discussed in the chapter's introduction, we have several specific aims, which are now discussed in more detail. The first aim was to obtain images of pavement cells at different stages of growth, in order to extract their outlines for use in later chapters. The second aim was to examine the cell cytoskeleton to test past experimental claims. For the microtubules, we wanted to confirm previous reports that they localise and fan out from the indents [Armour et al., 2015, Qian et al., 2009, Altartouri et al., 2019, Kotzer and Wasteneys, 2006, Bidhendi et al., 2019]. Young pavement cells are also examined to see if there are any early examples of microtubule localisation, as Armour et al. [2015] found that microtubule localisation on straight pavement cell walls predicted indent sights. Additionally, actin localisation to the lobes warranted further investigation as previous reports claiming to observe such localisation were not entirely persuasive [Fu et al., 2002, Xu et al., 2010] and contradictory Armour et al. [2015] say they found no evidence of the phenomenon. The final aim was to check for wall stiffness heterogeneities in young pavement cells as such variations had been previously found in the anticlinal [Sampathkumar et al., 2014, Majda et al., 2017] and periclinal wall [Sampathkumar et al., 2014] in older pavement cells with established lobes, but in our knowledge, only one study has found such heterogeneities in young pavement

cells [Altartouri et al., 2019]. Examining young pavement cells allows us to see how early on cytoskeletal localisation and wall stiffness variations occur, which would result from chemical signalling suggesting chemical lobe initiation.

The pavement cell outlines results are presented and discussed in section 4.3.1, the GFP marked microtubule and actin filaments images are displayed and examined in section 4.3.3 and 4.3.2 respectively, and the AFM experimental results are shown and reviewed in section 4.3.4.

4.3.1 Pavement cell outlines

For use in later chapters, pavement cell outlines *Arabidopsis thaliana* and *Nicotiana benthamiana*'s were obtained at three different stages of growth; firstly, ones that are just beginning their development, secondly, those that have developed lobes but are still growing in amplitude and number, and thirdly mature pavement with well developed lobes.



(a) (b) (c)

Figure 4.1: Pavement cells with PI stained cells walls at different stages of development (all pictures are in different cotyledons). a) 2 day old *Arabidopsis thaliana* abaxial pavement cells. b) 4 day old *Arabidopsis thaliana* abaxial pavement cells c) 2 weeks old *Nicotiana benthamiana* adaxial pavement cells.

To capture these three different stages images were took of 1 to 2 days old (figure 4.1 a), and 3 to 4 days old wildtype *Arabidopsis thaliana* cotyledons (figure 4.1b) and 2 week old wildtype *Nicotiana benthamiana* leaves (figure 4.1c). These images were all taken using a 561nm laser with the powers set to 100%, 12% and 100% and PI gain of 456,

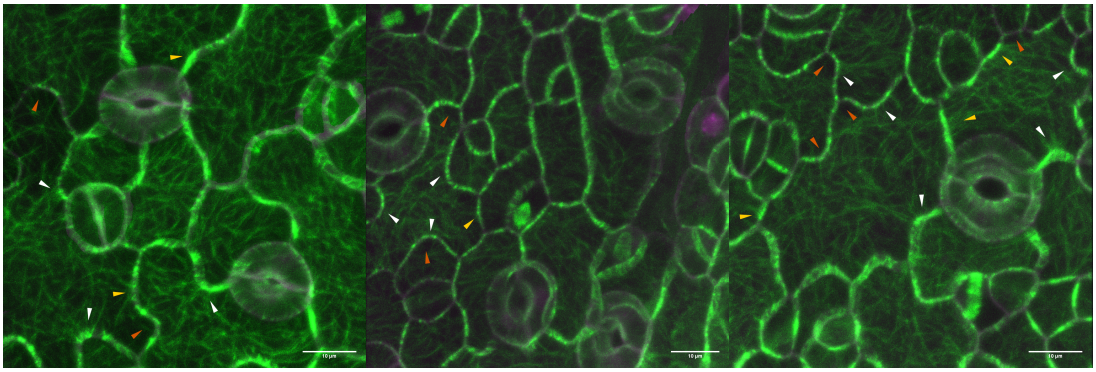
573 and 409 respectively, where both the *Arabidopsis thaliana* images used a PI emission range of $578-594$nm and *Nicotiana benthamiana* images used the range of $578-649$nm. The pavement cell outline coordinates were then extracted via the process detailed in section 4.2.3.2

The extracted pavement cell outline coordinates need to be at the right scale to ensure modelling accuracy in the next chapters. Therefore using ImageJ, measurements of both the long axis and the axis perpendicular to it (identified by observation) were taken to estimate the average pavement cell sizes at the three different stages of growth. For the older more developed *Nicotiana benthamiana*, the less developed and young *Arabidopsis thaliana* pavement cells, measurements were taken of 21, 16 and 20 cells from 3, 2 and 3 leaves/cotyledons, respectively, to get their sizes to be of the order of $100\mu m$, $50\mu m$ and $10\mu m$ in length. All of the pavement cell outlines can now be correctly scaled for use in the chapters 5, 6 and 7.

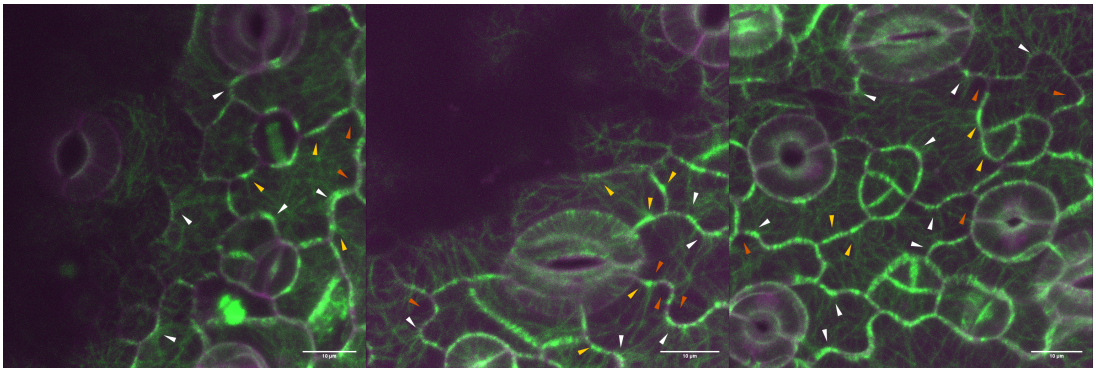
4.3.2 The microtubule cytoskeleton

The confocal images of GFP marked microtubules are now displayed to examine if microtubule indent localisation can be confirmed and to see if there is any evidence of localisation in young pavement cell development before lobeing. For this, images were taken of five 9 day old leaves where 20 usable z stacks were obtained. The confocal microscope settings for PI were, emission range between $578-627$nm with 100% laser power using a 561nm laser, and gain 441, and for the GFP markers, the emission range was set to $492-548$nm with laser power 40% using the 488nm laser and gain 741. Arrows are placed in the images by observing where there is prominent high or low fluorescence localisation matched with opposing low or high fluorescence respectively on the other side of the cell wall. Note that thick green fluorescence appears at the anticlinal walls as numerous microtubules can run along and up the anticlinal walls, and as these images are z stacks, their signal gets grouped together.

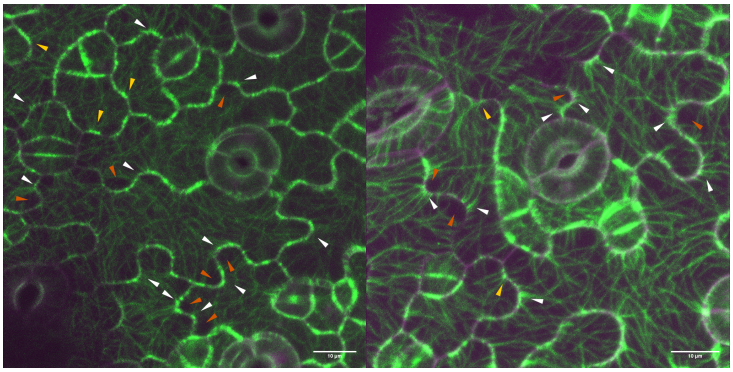
By examining the white and orange arrows (figure 4.2) numerous examples can be



(a) (b) (c)



(d) (e) (f)



(g) (h)

Figure 4.2: Confocal microscope images of GFP marked microtubules (shown in green) in *Arabidopsis thaliana* combined with PI stained cell walls (shown in magenta). The meanings of the different coloured arrows are defined in the main text.

observed of both microtubule localisation to the indents where there are seen to fan out and low microtubule fluorescence in the lobe regions, respectively. We have therefore confirmed the previous findings [Armour et al., 2015, Qian et al., 2009, Altartouri et al., 2019, Kotzer and Wasteneys, 2006, Bidhendi et al., 2019] that microtubule localise and fan out from the indents, where they then can reinforce the indents through cellulose

deposition.

Indicated by the yellow arrows are examples of microtubules bundling and localising on slightly curved and straight walls, a phenomena also observed by Armour et al. [2015]. Microtubule localisation to the slightly curved walls demonstrate how early localisation can occur, and the localisation on the straight walls could indicate indent precursor sites. Chemical pathways could cause this early localisation as these regions would not necessarily be areas of increased stress yet, which is also known to make microtubules localise. However, other timelapse studies have found these early microtubule localisation sites to be unstable [Lin and Yang, 2020] and for the demethylated pectin to localise before the microtubules [Altartouri et al., 2019].

This work demonstrates that more research still needs to be done. We have confirmed that microtubules localise to developed indents, but what microtubules do in early lobe development is the contentious issue. As detailed in section 2.1.4.2, there seems to be much conflicting evidence over the microtubules' role in pavement cell development. Some studies have shown that no lobes form if you disrupt the network, whereas other reports show you only get a weaker lobeing phenotype (similarly for cellulose), suggesting that microtubules may not be essential for lobe formation. More evidence needs to be presented for either microtubules causing indent initiation or against it, as there is yet to be significant proof for either side of the argument. This evidence will have to come in the form of timelapse images to see how stable the microtubules are and to check whether their localisation sites predicts an indent site. These observations should be complemented by examining other cell wall materials such as pectin to get an explicit time-scale as to when possible differing concentrations occur, similarly to Altartouri et al. [2019].

4.3.3 The actin cytoskeleton

Here the GFP marked actin images are shown to see if there is any evidence of early localisation in young pavement cells, which (to our knowledge) has never been tested and to check the previous findings that actin localises to the lobes in developed pavement

cells. The confocal microscope settings for PI were, emission range of $578 - 627$nm with 100% laser power using the 561nm laser and gain 727 and the GFP settings were, emission range of $492 - 548$nm with laser power 27% using the 488nm laser and gain 491.

To observe the actin cytoskeleton in young pavement cells, 9 days old leaves were imaged, and to examine developed pavement cells, 14-15 days old leaves that were around $5000\mu m$ in length were examined so that we could accurately compare our results to previous work [Fu et al., 2002]. The data set for this experiment was six 9 days old leaves and four 14 days old leaves, which produced 23 and 18 usable confocal z stack images, respectively. The arrows are placed by observing when the fluorescence in the lobes/indents clearly exceeds that of the indents/lobes on the opposite side of the cell wall.

By examining the white and red arrows in the images (figure 4.3), examples can be seen of both high and low actin expression and localisation to the lobes, respectively. Furthermore, as shown by the blue arrows, instances of actin indent localisation can also be observed, which Armour et al. [2015] also reported seeing. Therefore, from these images, actin's lobe localisation does not appear entirely consistent, with it being unclear and sometimes non-existent in multiple lobes. By also comparing these images to those that were shown in the last section (section 4.3.2), as a whole, there is little actin localisation that is as convincing and consistent as the GFP marked microtubules (figure 4.2).

When examining young pavement cells (figures 4.3a-f), no evidence is found of actin localisation on any straight walls that could be lobe initiation sites. In all of these young pavements, the actin arrays look almost evenly distributed across the cell and along the cell wall boundaries.

From the analysis of the results, we conclude that there is insufficient evidence to suggest that actin localises to the lobes. This localisation is a widely stated phenomenon in pavement cell development, appearing in much of the literature (for example [Sapala et al., 2018, Lin and Yang, 2020]). Actin also does not seem to localise early in young pavement cells, suggesting that if chemical pathways initiate lobes, they may not do

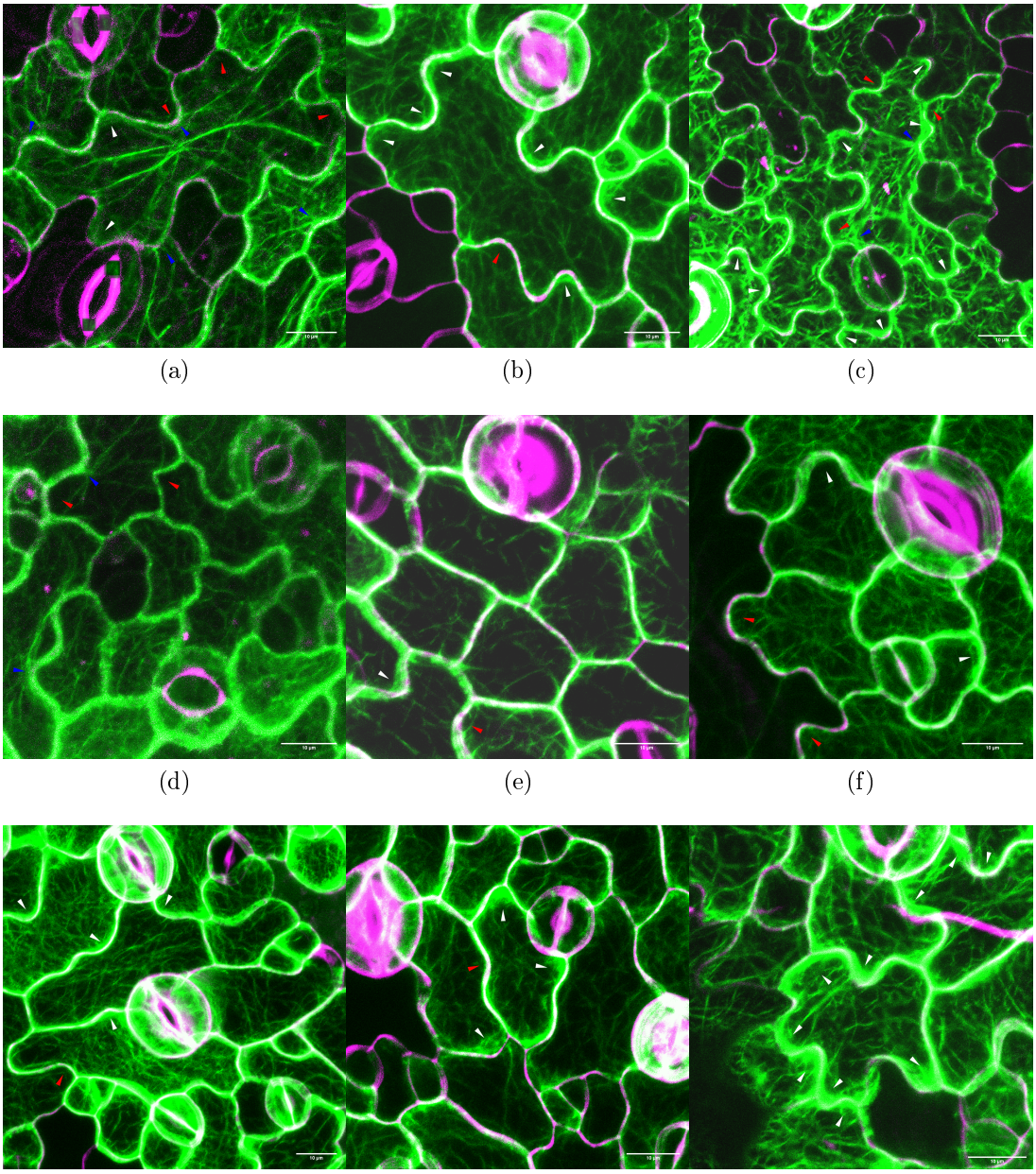


Figure 4.3: Confocal microscope images of GFP marked actin (shown in green) combined with PI stained cell walls (shown in magenta)

so through actin. If actin does not localise, this leads to the question of RIC4 and ROP2's purposes in localising to the lobes. Maybe these signalling proteins could have other effects, such as changing the PH of the cell walls in the lobes, which can lead to increased cell wall loosening [Cosgrove, 2005, Hocq et al., 2021]. In other words, it would be interesting to examine if there is any evidence of increased enzyme activity in the

lobes to see what causes their higher growth rates, as in the absence of actin localisation, something must be causing their observed wall softening. Furthermore, as detailed in section 2.1.4.3 PIN1 molecules through actin's stabilisation are said to localise to the lobes and help them to develop. Therefore, if actin does not localise to the lobes, what stops PIN1 from undergoing endocytosis there; could this phenomenon be maintained by ROP2 instead, or are there some other unknown mechanisms in play?

However, Lin and Yang [2020] comment that actin is tricky to image, for example, in pollen tubes, there were initial disagreements over the now confirmed actin localisation to the tip. More work needs to be done on actin's role in pavement cell morphology as mutants affecting actin have shown them to affect pavement cell shape. To our knowledge, all previous work of imaging actin in pavement cells have all been singular snapshots that may be capturing moments where the actin molecules are not localising to the lobes. If time-lapse images could be pictured, we could see how the cytoskeleton changes over time, allowing us to learn how persistent any localisation to the lobes (or any straight cell walls) is.

4.3.4 Atomic force microscopy results

Atomic force microscopy experiments were performed to investigate cell wall stiffness heterogeneities in young pavement cells. These AFM experiments were conducted on three 1 day old cotyledons where the results from these experiments are displayed below (figure 4.4) where the z length, the size of the scan and the number of pixels is stated for each image. Note that in the results we use the rainbow colour map. However, this is not good practice, as it is inaccessible to some of the population with vision deficiencies and also distorts the data due to its non-smooth mapping from data to colours which can give the impression of artificial boundaries (see [Heron et al., 2021] for a detailed explanation).

By analysing the AFM results, it can be observed that these young pavement cells display large amounts of indentation moduli heterogeneities along each individual cell's anticlinal walls (most obviously seen in figure 4.4a). These variations in the anticlinal wall

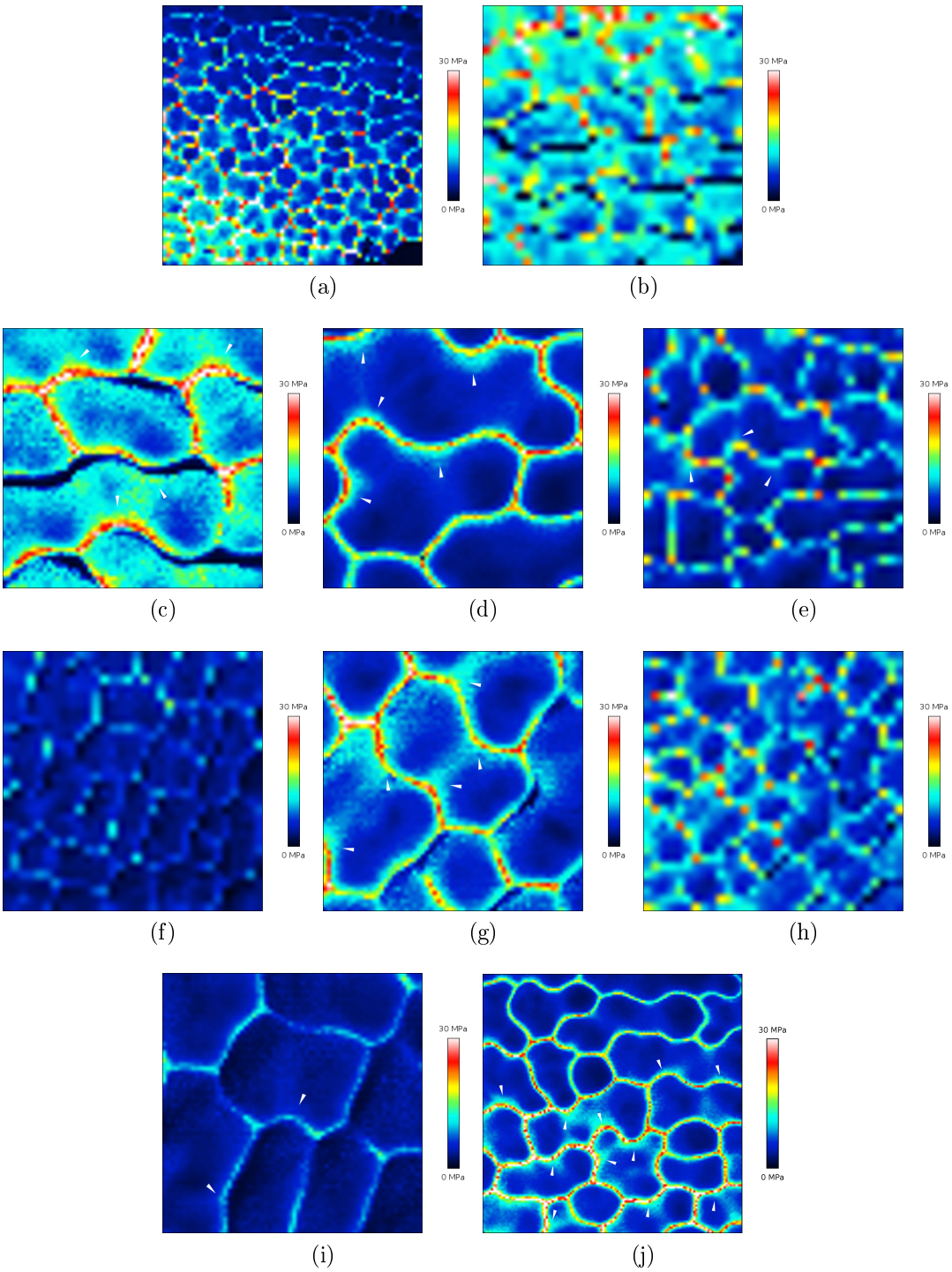


Figure 4.4: Atomic force microscopy on cotyledons using $500nN$ of force where the experimental details are (where Z and then a number shows the z length) a) Z10 64 pixel $100\mu m$ b) Z5 32 pixel $50\mu m$ c)Z5 64 pixel $25\mu m$ d)Z5 64 pixel $25\mu m$ e) Z5 32 pixel $50\mu m$ f)Z5 32 pixel $50\mu m$ g) Z5 64 pixel $25\mu m$ h)Z5 32 pixel $50\mu m$ i) Z5 64 pixel $25\mu m$ j) Z5 128 pixel $50\mu m$

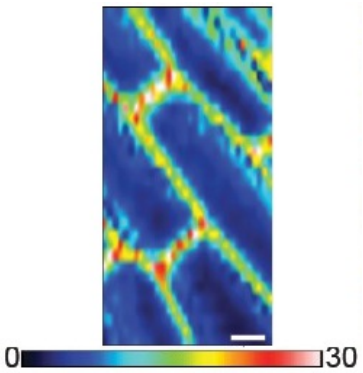


Figure 4.5: Example AFM image from Daher et al. [2018] showing consistent stiffness values across the longitudinal and horizontal walls.

stiffness have previously been found in older pavement cells [Sampathkumar et al., 2014, Majda et al., 2017]. We can compare our images to the AFM images in plant stems which display consistent indentation moduli values along the axial and traverse walls [Daher et al., 2018] (figure 4.5). Local consistency in the wall indentation moduli can also be seen in individual cells and small tissue areas in the plant apical meristem [Braybrook and Peaucelle, 2013, Peaucelle et al., 2011]. These observations seem to suggest that the indentation moduli heterogeneities in pavement cells are quite unique.

The AFM experiments also reveal wall indentation moduli heterogeneities on the periclinal wall, where as shown by the white arrows, the indentation modulus is higher in the developing indent regions when compared to their neighbouring lobes on the opposite side of the cell wall. We have therefore matched the findings of Altartouri et al. [2019] and Sampathkumar et al. [2014] who find similar results in young and developed pavement cells, respectively. These indents with high indentation moduli have stiffer periclinal walls, restricting growth and permitting the development of the indentations and lobes.

These indentation moduli heterogeneities in the anticlinal and periclinal walls in young pavement cells with very little lobeing are interesting as they may arise due to differing wall properties caused by locally varying chemical signalling, suggesting that such signalling occurs early on in development. If these indentation moduli variations were not observed it would provide evidence against the chemical initiation hypothesis, as these small lobes

would likely have to be initiated by some other possible mechanical mechanism. However, as these early variations are happening, it could suggest that lobes are not initiated through mechanical buckling mechanisms.

As this is one of the first studies to examine varying indentation modulus values in young pavement cells, to develop this idea further would require more AFM experiments to increase the data size and support the theory. Experiments could even be performed in even younger pavement cells to see how early on these heterogeneities happen. In particular, observations could be made to check for heterogeneities on periclinal walls on either side of a straight anticlinal cell wall segment to find possible lobe/indent precursor sites, as at the moment, only lobes that have been already initiated are being examined. This procedure would present evidence of lobes initiating via chemical pathways.

4.4 Summary

In this chapter, firstly, pavement cell outlines were obtained for use in the simulations to follow. Secondly, we have confirmed previous findings that microtubules localise to the indents, and by looking at young pavement cells, we suggest that microtubule could localise early to initiate indents. Thirdly, by observing GFP marked actin, we found that actin does not consistently localise to the lobes and by examining young pavement, found no evidence that actin localises early in lobe development. However, no solid conclusions can be made on these last two findings due to many opposing ideas in the surrounding literature. Lastly, by performing AFM experiments, we found that the cell walls' indentation moduli appears to display variations in value very early on in pavement cell development. Overall, the first chapter on pavement cell growth control has led to suggestions of chemical signalling initiation.

In the next chapter, we start the pavement cell modelling process by building a microtubule model. We know microtubules play a fundamental role in pavement cell dynamics, so this model will allow us to understand how they organise.

Chapter 5

Building and validating a microtubule stochastic model

5.1 Introduction

In this chapter, the theoretical work to understand how pavement cells develop and initiate their lobes is begun. Specifically, this modelling process is started by building and validating a model of the important microtubule dynamics, which are an essential part of the pavement cell signalling network and are vital in controlling pavement cell wall mechanical properties and consequently have a massive role in controlling their shape.

In particular, this model is built to explore how the ROPs and the RICs that directly interact with the cytoskeleton and vice versa form an alternating pattern of microtubule and ROP2 localisation to develop and/or initiate pavement cells indents and lobes, respectively. Thus, in the next chapter, if a model of the signalling pathways that influence pavement cell shape (chapter 6) is going to be built, it is vital to include microtubule behaviour (which can not be assumed constant over time in the reaction-diffusion model).

Therefore, to simulate microtubule behaviour, a 2D stochastic microtubule model is created that incorporates microtubule interactions with one another, and as this model will be incorporated with the reaction-diffusion dynamics, one of the aims is to keep it as simple as possible to ensure reasonable computation time. As a result of this aim, the validation of this model is an essential step to ensure accuracy, as the model shall be missing certain microtubule features to achieve this goal.

This chapter is begun in section 5.2 by describing the basics of the model and what microtubule features are incorporated, and why. Full details of how the model is programmed can be found in appendix A.3.1. This section is then followed by a brief discussion and the presentation of the model parameters in section 5.3. We then display and discuss the results of the validation simulations as well as some other interesting findings in section 5.4. Concluding remarks about the model and possible future directions are then made in section 5.5.

5.2 Model set up, assumptions and analysis methods

To model pavement cell development, a simple numerical model of the microtubule dynamics is built. How this model is programmed, what is included and why is briefly described in section 5.2.1 with the details left to appendix A.3.1. The model simulations will also need to be analysed, meaning the order of the microtubule array overtime needs to be known. How the order is measured is described in section 5.2.2 where the full description of its derivation can be found in appendix A.3.2.

5.2.1 Microtubule model implementation principles

One of the model aims is to keep it as simple as possible while still maintaining realism meaning the included microtubule features have to be carefully chosen and limited. These exclusions are also in place as finding accurate parameters for some microtubule features is also difficult, a perspective echoed by Allard et al. [2010a] who comment that making their model more accurate would rely on non-measurable parameters (with Gomez et al. [2016] also mentioning similar problems). For a detailed description of microtubule dynamics, please refer back to section 2.1.2.

We are building up a stochastic model meaning every event and interaction has a probability of occurrence. All of the microtubules are represented as lines modelled with space curves that describe their path in the cell domain (figure 5.2). Microtubules are spawned at singular points in random places in the cell domain Ω (with m_{max} being the max number of microtubules in the system and m the current number of microtubules in the system) where they begin to grow in a random direction. At each time step, Δt^*, they continue to grow in the same direction with the microtubule $\imath$ line coordinates being expressed as $(\mathbf{x}^*_{M,(\imath,1)}, \cdots, \mathbf{x}^*_{M,(\imath,\jmath)}, \cdots \mathbf{x}^*_{M,(\imath,l_\imath)})$ where $l_\imath$ is the number of points in the $\imath$th microtubule's line coordinates and $\jmath$ a certain point along its space curve. We store each microtubule point's growth direction in the matrix Θ, where the entry $\Theta_{\imath,\jmath}$ is the growth direction of microtubule $\imath$ at point $\jmath$ along its space curve. Plus-end and minus-end (the

"front" and "back" end of the microtubules) dynamic instability is not included as on average, microtubule plus ends are growing (with speed v^*_{gr}), and their minus ends are shrinking (with speed v^*_{shr}) [Chakrabortty et al., 2018, Mirabet et al., 2018, Eren et al., 2015] where this exclusion also helps to keep the model simple and limits the number of parameters we need. Allard et al. [2010b] tested the effect of minus-end dynamic instability and found it not to affect microtubule organisation (in wild-type simulations), making the exclusion of such a feature reasonable. In the model, a microtubule at any time point can also undergo a random catastrophe (with probability $\mathcal{P}_{RC}$) where they start breaking down from their minus end. As a consequence of the previous assumption, no rescue events are considered such that when the minus end starts to break down and retract, it continues to do so for the rest of that microtubule's lifetime. As they have been shown to be important in modelling microtubules in pavement cells, edge induced catastrophes are included [Chakrabortty et al., 2018] where the microtubule start to retract from their plus end when they hit the cell wall boundary (with probability $\mathcal{P}_{EC}$). Microtubules are then removed from the system when its plus-end or minus-end retracts enough to catch up with the other. The dynamics of microtubule anchoring to the cell membrane are also not considered as Allard et al. [2010a] found that once an anchor is attached, on average it will stay attached for a week which is above the time scale of the model.

The microtubules in the model can also importantly interact with one another (when the plus end is in a certain range, r^*_I of another microtubule) in an angle dependent manner to match with the biology (figure 5.2). Upon collision, a microtubule can undergo a collision-induced catastrophe at its plus end (with probability $\mathcal{P}_{CC}$) when the angle of interaction is above some critical threshold, θ_{crit} or bundle up with the other microtubule (with probability $\mathcal{P}_B$) when the angle of interaction is below the critical threshold (figure 5.1). The matrix Θ is used to easily calculate the angle of interactions. If the microtubule does not bundle or undergo collision-induced catastrophe, the microtubule will just crossover meaning the microtubule will continue growing in the same direction.

Other possible interaction scenarios are not included, such as buckling on collision, and microtubule direction perturbation, as no probability values of such events occurring could be found. Furthermore, for simplicity, pauses after microtubules first interact with one another are also omitted. Dixit and Cyr [2004] showed that parallel organisation was not dependant on the contact time difference on bundling between longitudinally and transversally orientated microtubules, demonstrating that these pauses are not a major microtubule feature that needs to be included. Lastly, for simplicity, microtubules branching events are also not included.

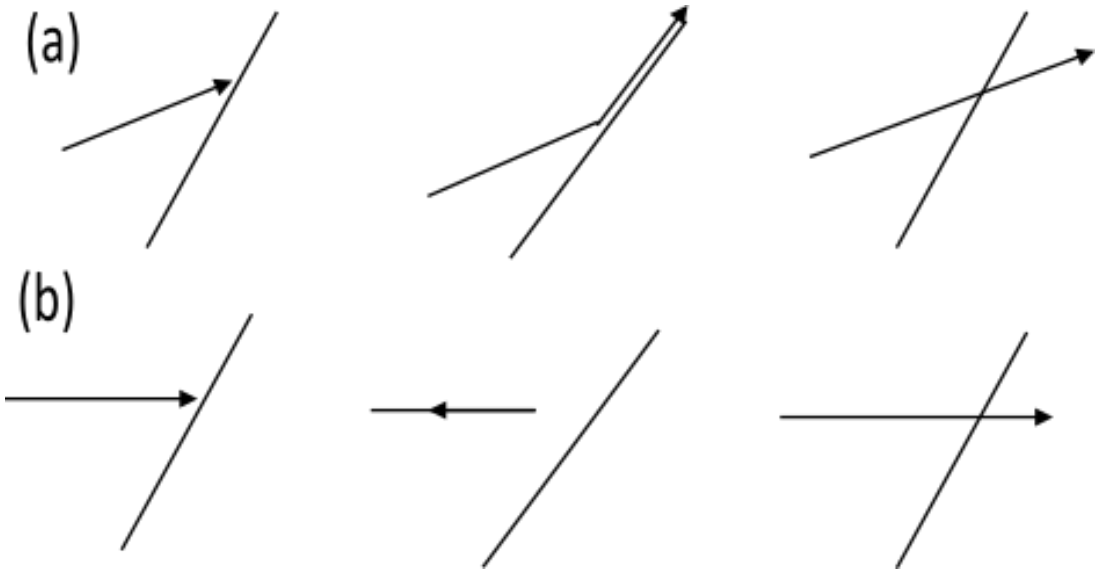
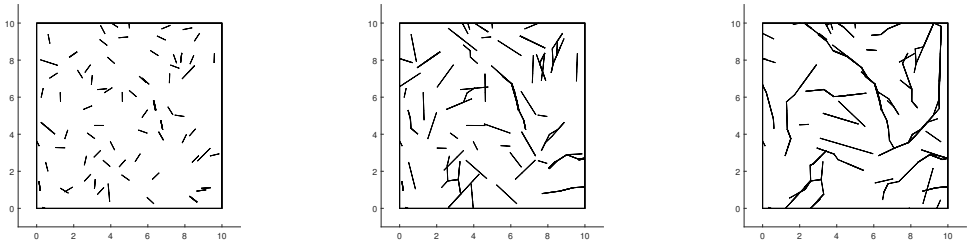


Figure 5.1: Diagram illustrating microtubule interaction principles upon microtubule collision with another. The lines represent microtubules, and the arrows their growth direction. a) When the angle of interaction is small, the microtubule can bundle up and begin to grow in the same direction as the other or simply crossover. b) When the angle of interaction is big, this can cause a collision-induced catastrophe, causing the microtubule to shrink from its plus end, or it can simply crossover.

In the pavement cells outline simulations, it is important to include the effect of stress, as this has been shown to cause microtubule localisation to the indents [Sampathkumar et al., 2014] (see section 5.4.3 for further details). As discussed in section 2.1.2, as microtubules are said to be stabilised by the stress and the indents are known to be areas of increased stress, to recreate this microtubule indent localisation behaviour, the probability of a microtubule undergoing a random catastrophe is changed depending on where



(a) (b) (c)

Figure 5.2: Snapshots from an example microtubule simulation progressing in time where the thickness of the line represents the number of microtubules in that bundle.

the ends of the microtubules are located. We first need to identify where the lobes and indents are in the pavement cell outlines. For this identification, a parameter called the lobe indicator function denoted as $\tilde{\kappa}$ is calculated, which uses the pavement cell outline's curvature to assign a value between -1 and 1 to each point along the boundary coordinates, $\mathbf{X}_B^*$ to indicate whether the coordinate point is in a lobe or indent (assigned a positive or negative value respectively) and where in the lobe it is (assigns high/low values the closer to the lobe tip/indent centre point you are and decreases/increases to 0 when you move away from this point). For full details on how $\tilde{\kappa}$ is derived, please see appendix A.3.4. The stress stabilisation of the microtubules uses $\tilde{\kappa}$ by decreasing the probability of a random catastrophe when a microtubule hits an indent ($\tilde{\kappa} < 0$) and increases the probability when a microtubule hits a lobe ($\tilde{\kappa} > 0$). This behaviour is implemented by using the logistic function (and shifting it down the y axis by a $\frac{1}{2}$, so it takes negative and positive values), which is used due to its simplicity and the fact that it plateaus, so its effect is limited. The probability of microtubule $\imath$ undergoing a random catastrophe is therefore,

$$\mathcal{P}_{RC,\imath} = a_1 \left(\frac{1}{1 + e^{-b_1 \tilde{\kappa}_\imath}} - \frac{1}{2} \right) + \bar{\mathcal{P}}_{RC}, \tag{5.2.1}$$

where a_1 is the max effect this function has, $\tilde{\kappa}_\imath$, is the lobe/indent indicator value at the microtubule endpoint, b_1 affects how quickly the function reaches its maximum or minimum value and $\bar{\mathcal{P}}_{RC}$ is the base catastrophe rate. However, when this stress effect

is first implemented, some microtubules hit the indents tangentially and stabilised. In actual pavement cells, microtubules are observed to fan out in the normal direction to the indents, mirroring the stress fields of the cell. To get rid of this unrealistic behaviour, the angle the microtubule hits the boundary is calculated, and if this angle is within $\frac{\pi}{4}$ radians of the boundary's inward pointing normal direction, the microtubule's random catastrophe rate is changed via equation (5.2.1).

To summarise, the following features are including in the model.

- Microtubules spawn at random points and start to grow in a random direction.
- Microtubules can suffer from a random catastrophe at any time.
- When microtubules collide they can interact with one another in a angle dependant manner, where below or above a critical angle they can bundle up or suffer a catastrophe respectively upon collision.
- Microtubules can undergo a catastrophe when hitting the cell boundary.
- Microtubules can be stabilised when in a region of increased stress.

All simulations were performed in MATLAB using the University of Birmingham's BlueBEAR HPC service, which provides a flexible resource for intensive computational work to the University's research community. See http://www.birmingham.ac.uk/bear for more details.

5.2.2 Model analysis methods

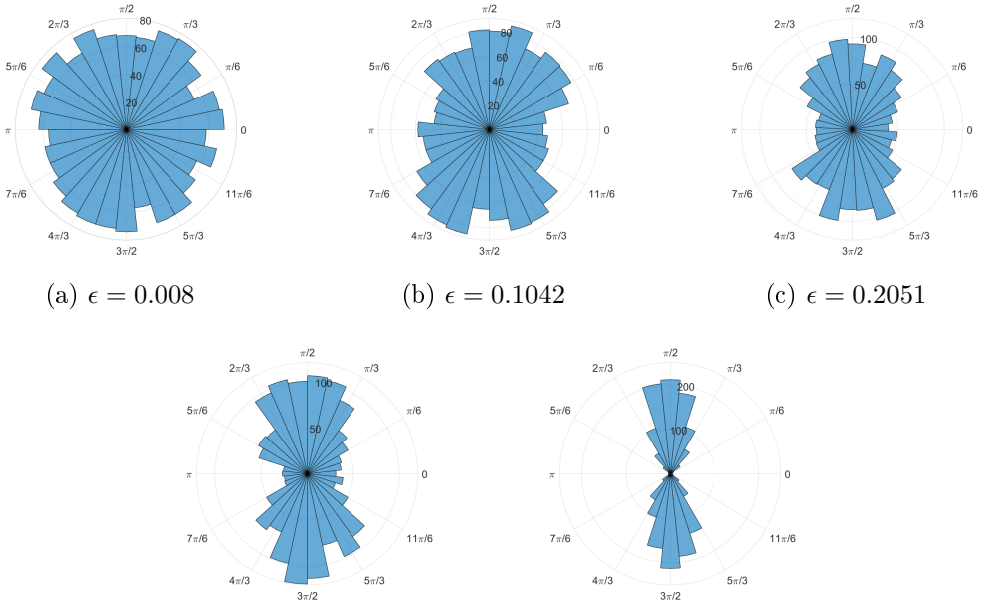
In analysing the simulations, to validate the model, there is a need to know the order of the system/how organised the system is over time. Reference is made to the microtubules forming an ordered array when they organise and align themselves in a particular mean/bias direction. The organisation in the system is found by examining the microtubules' angles in the matrix Θ, where the directional bias needs to be calculated first.

This is done by transforming the angle data to non-polar form so that all the angles are between 0 and π (for example, the angles $-\frac{\pi}{4}$ and $\frac{3\pi}{4}$ are identified as the same direction), where they are then redistributed so that the total angle distribution looks like a bell shaped curve (where all the angles are now stored in a vector labelled as $\hat{\bar{\Theta}}$). Briefly, transforming the angles solves the issue of finding the mean direction when microtubules are growing in the same bias but opposite direction (e.g. the mean direction of $\frac{\pi}{2}$ and $-\frac{\pi}{2}$ would be 0 and not $\frac{\pi}{2}$ which we want) and redistribution ensures the mean is not skewed when the bias is close to 0 or π. Consequently, this process allows us to calculate an accurate value for the mean/bias direction of the microtubules, which is called, $\hat{\bar{\theta}}$. For full details of how the bias in direction is calculated and why it is done in this way, refer to the appendix A.3.2. Finally, for the measure of order, we choose not to use the standard deviation but instead adopt the order parameter used by Allard et al. [2010b] defined as,

$$\epsilon = \frac{\sum_J \cos^2\left(\hat{\bar{\Theta}}_J - \hat{\bar{\theta}}\right) - \sin^2\left(\hat{\bar{\Theta}}_J - \hat{\bar{\theta}}\right)}{\sum_J 1}, \tag{5.2.2}$$

where it sums over all of the microtubules' current angles. This order parameter, ϵ, ranges between 0 and 1 and is ≈ 0 when the distribution of angles is uniform and is ≈ 1 when the distribution is highly organised.

To illustrate the value of this parameter at different degrees of organisation, dummy angle distributions were created by using the normal distribution (data set of 2000 values) with a bias in the $\frac{\pi}{2}/-\frac{\pi}{2}$ direction and varying the standard deviation (figure 5.3). When $\epsilon \approx 0$, the distribution of angles is uniform (figure 5.3a), meaning the array is not organised at all. When $\epsilon \approx 0.1$, weak directional bias can be seen (figure 5.3b), and thus the array is slightly organised, while when $\epsilon \approx 0.2$ a definite directional bias can be observed (figure 5.3c) meaning the array is becoming more organised. When the order parameter further increases, the angle distribution becomes increasingly organised where when $\epsilon \approx 0.7$ the angles are highly biased in one direction (figure 5.3e).



(a) $\epsilon = 0.008$ (b) $\epsilon = 0.1042$ (c) $\epsilon = 0.2051$

(d) $\epsilon = 0.3024$ (e) $\epsilon = 0.7364$

Figure 5.3: Example angle distributions of varying organisation with a bias in the vertical direction

5.3 Model parameters

The model parameters that can be fixed are stated in table 5.1 with their relevant references.

Table 5.1: Microtubule model parameters

Paramater	Value	Reference
v_{gr}^*	5μm min^{-1}	[Allard et al., 2010a, Eng and Wasteneys, 2014] [Dixit and Cyr, 2004, Chakrabortty et al., 2018]
v_{sh}^*	8μm min^{-1}	[Allard et al., 2010a, Eng and Wasteneys, 2014] [Dixit and Cyr, 2004, Chakrabortty et al., 2018]
$\mathcal{P}_{RC}$ & $\bar{\mathcal{P}}_{RC}$	0.2 per minute	[Allard et al., 2010a, Eng and Wasteneys, 2014], [Chi and Ambrose, 2016]
θ_{crit}	$\frac{2}{9}\pi$	[Dixit and Cyr, 2004, Chi and Ambrose, 2016], [Allard et al., 2010b]
$\mathcal{P}_{EC}$	0.26	[Chakrabortty et al., 2018]
r_I^*	0.5μm	
ϱ^2	1	
a_1	0.2	
b_1	7	

However, there are some parameters for which their value is uncertain. Firstly, the interaction probabilities display a wide range of possible values, for example, $\mathcal{P}_B$ ranges between 0.02 to 0.9 in the surrounding literature [Dixit and Cyr, 2004, Allard et al., 2010b, Chakrabortty et al., 2018, Gomez et al., 2016]. Consequently, in the next section (section 5.4) a parameter sweep is performed to investigate the effect of these probabilities. The effect of the max microtubule number, m_{max}, is also tested in the parameter sweep, as this value is also unknown. Note that the value of Δt^* is chosen so that during one time step, the microtubules cannot move a distance further than r_I^* meaning $\Delta t^* = 0.99 \times \frac{r_I^*}{v_{gr}^*}$ minutes ensuring no possible interactions are missed. The value of a_1 is set such that the microtubule random catastrophe rate ranges between $0.1 - 0.3$ per min so that the random catastrophe rate remains in a realistic range

5.4 Microtubule model results, validation and discussion

There are several objectives to complete with the simulations. One of the primary objectives is to validate the simple model by replicating the main results of past studies that have examined microtubule dynamics and to test the effect of certain parameters on the system. The model is also run in pavement cell outlines to understand how the system works independently of any other interactions with signalling proteins.

These verifying simulations come in two forms. Firstly, a key features that has to be replicated, is that the microtubules must be able to organise as a result of their basic interactions (bundling and collision induced catastrophes), meaning the microtubules start of randomly but then become increasingly ordered and form an organised array in one direction. This result is in order to find agreement with Allard et al. [2010b] Dixit and Cyr [2004] and Mirabet et al. [2018] who say that this is an essential microtubule characteristic that is needed for basic cell function. These test simulations are run in square domains where both the domain size and interaction probabilities are varied to see when/if we get microtubule alignment. Secondly, the model is tested to see whether it can replicate the results of Gomez et al. [2016] who find that microtubules increasingly organise as the aspect ratio (height of the cell divided by the width of the cell) increases and that microtubules align with the long axes. These validation simulations are run in rectangular domains of varying aspect ratio where once again the interaction probabilities are varied to investigate their possible effect. To measure the order of the system, the parameter ϵ is calculated at each time step (see section 5.2.2 for details) which allows us to see the emergent properties arising as a result of microtubules interacting with one another.

If the model passes these verification tests, initial simulations are then run in actual pavement cell shapes. As described in section 2.1.4.2, and from the observations of GFP marked microtubules in section 4.3.2 it is known that microtubules localise to the indents and are low in concentration in the lobes. The 3D microtubule simulations of Chakrabortty et al. [2018] recreated this phenomenon where they found the microtubules to localise to the indents. However, they comment that this localisation was not consis-

tent. As a result of these observations and past simulations, microtubule localisation to the indents is another property that needs to be replicated in the simulations here.

For the tests in square and rectangular domains, we perform 50 simulations and plot the mean order parameter (the black line) and the standard deviation (grey region) against time (see section 5.2.2 for details) where the steady-state mean order values after the systems have stabilised/plateaued are also displayed (the straight black line). The value of the steady-state mean order is found by first calculating the fluctuations in ϵ's mean value (by finding the maximum minus the minimum ϵ value in the past 30 time steps for every time point), and secondly by then calculating the average of the mean ϵ values once the fluctuations decrease past a certain threshold (in a similar manner to Ellis and Petrovskaya [2020]).

The results of the simulations in square domains are displayed and discussed in section 5.4.1, the findings from tests run in rectangular domains are shown and examined in section 5.4.2, and the results from simulations run in actual pavement cells are analysed in section 5.4.3.

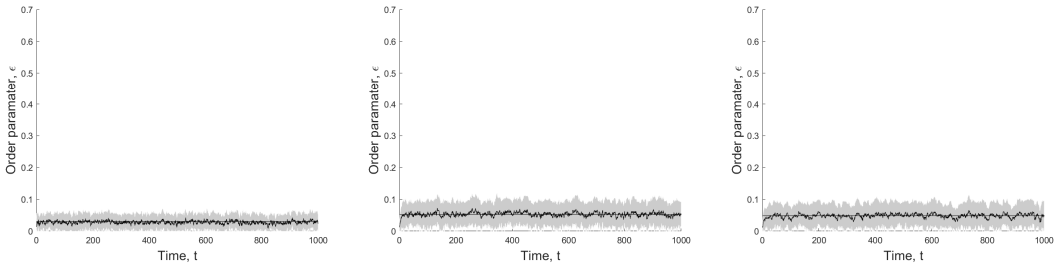
5.4.1 Square domain simulations

The results of the various simulations run in square domains are now displayed to check when/if microtubule alignment occurs. Specifically, these simulations are run in the square domains of length and height of 10μm, 50μm, and 100μm, where these sizes have been taken from actual plant cells (see section 4.3.1). The different probabilities that are tested in each cell size are $\mathcal{P}_{CC} = \mathcal{P}_B = \{0.1, 0.2, 0.3, 0.4, 0.5, 0.6, 0.7, 0.8\}$ with the max microtubule number set at $m_{max} = 1000$ and run for 1000 minutes. Simulations are also performed in the square domain of size 50μm to investigate the effect of the max microtubule number, by setting $m_{max} = 100,\ 500,\ 1000,\ 2000$, and 3000 and running for 2000 minutes. Note that similar parameter sets to previous modelling attempts are being compared to validate the model, for example, Allard et al. [2010b] set $\mathcal{P}_{CC} = 0.6$, $\mathcal{P}_B = 1$, the cell length and height equal to 10μm and $m_{max} = 1000$.

Beginning with the simulations with $\mathcal{P}_{CC} = \mathcal{P}_B = 0.1$ and $\mathcal{P}_{CC} = \mathcal{P}_B = 0.2$, for low interaction probabilities the system order value do not increase beyond 0.1 (figures 5.4 and 5.5), demonstrating that when microtubule interactions are limited, order does not arise. This lack of order can be directly seen in the microtubule array, where when $\mathcal{P}_{CC} = \mathcal{P}_B = 0.1$ (figure 5.9a), the array is randomly organised with no bias direction. However, when $\mathcal{P}_{CC} = \mathcal{P}_B = 0.3$ and the domain size is 50μm, the system plateaus around a steady-state order value of 0.1 (figure 5.6b), implying the microtubule arrays are weakly organised (see figure 5.3). Thus order can arise when the interaction probabilities are low. In this same parameter set, order is limited in both cells of size 10μm (figure 5.6a) and 100μm (figure 5.6c) possibly because in the smaller domain, there is less space for interactions to occur as the microtubules will reach their full length quickly (and consequently can no longer interact with any other microtubules) and in the larger domain, the microtubules will be more diluted, meaning fewer interaction opportunities.

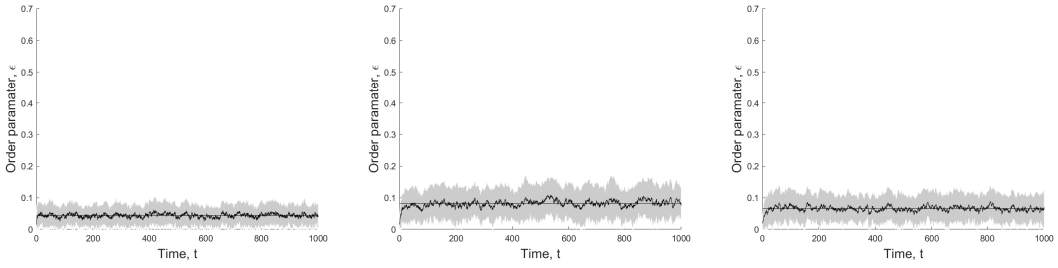
Continuing, when $\mathcal{P}_{CC} = \mathcal{P}_B = 0.4$, the microtubules for all cell sizes have become organised with $\epsilon > 0.1$ (figure 5.7). Upon examining an example microtubule array (figure 5.9b), a weakly organised system is observed with them being biased towards the diagonal. When $\mathcal{P}_{CC} = \mathcal{P}_B = 0.5$ and $\mathcal{P}_{CC} = \mathcal{P}_B = 0.6$ a trends begins to appear, of as the interaction probabilities increase, the order in the system increases (figure 5.8 and 5.10) for all cell sizes where when $\mathcal{P}_{CC} = \mathcal{P}_B = 0.6$ the steady-state mean order values are now all > 0.2 (figure 5.10), which means they have a clear bias in a particular direction (figure 5.3). This trend continues upon further increase to the interaction probabilities (figures 5.11 and 5.12) where when $\mathcal{P}_{CC} = \mathcal{P}_B = 0.8$, $\epsilon > 0.3$, informing us the microtubules are forming highly anisotropic arrays which can also be evidenced when the microtubule array is examined (figure 5.9c), where many microtubules are bundled up and are strongly aligned to the diagonal. This trend demonstrates that as the probability of microtubule interaction increases, the microtubules will become increasingly organised. Unlike the simulations with low interaction probabilities, the cells of size 10μm now display the highest mean order, and those of cell size 100μm, the lowest. This phenomenon is possibly

because all the simulations have the same microtubule number, meaning the density of microtubules is higher in the smaller cells, allowing for more microtubule interactions, leading to a higher degree of anisotropy. We have therefore gained an understanding of the effect of cell size on the microtubule simulations. Also, note that in nearly all of the simulations, the order parameter starts ≈ 0 and increases over time, where it then plateaus at a value > 0.1 (most obviously seen in figure 5.10a and 5.11a). This behaviour shows that microtubule organisation is an emergent property of the system occurring as a result of the microtubules interacting with one another, meaning the simple model successfully fulfils the needed requirements and is validated [Dixit and Cyr, 2004].



(a) 10μm (b) 50μm (c) 100μm

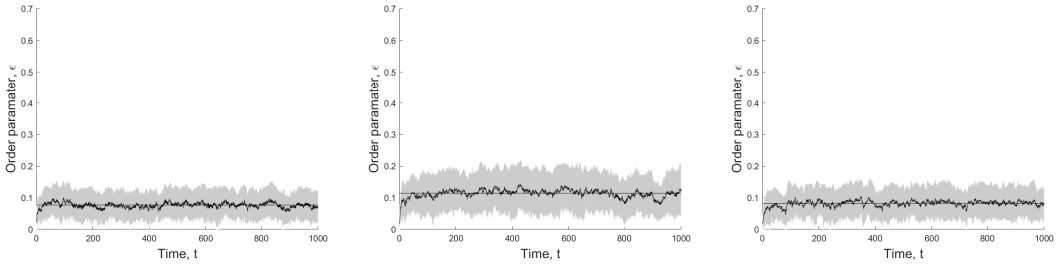
Figure 5.4: How the order parameter changes with time for simulations with probability $\mathcal{P}_{CC} = 0.1$ and $\mathcal{P}_B = 0.1$ with the simulation domain's length and height stated in the figure subcaptions



(a) 10μm (b) 50μm (c) 100μm

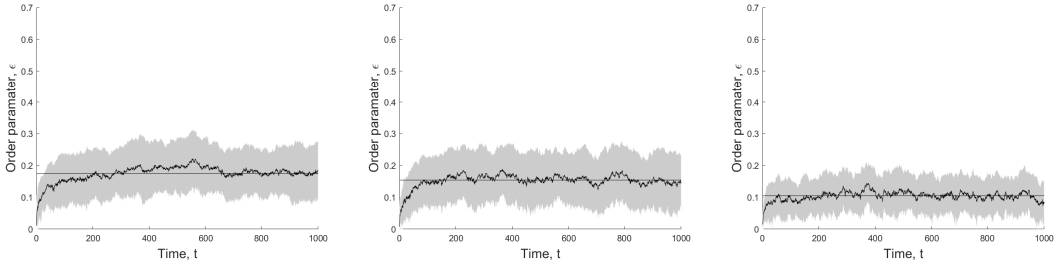
Figure 5.5: How the order parameter changes with time for simulations with probability $\mathcal{P}_{CC} = 0.2$ and $\mathcal{P}_B = 0.2$ with the simulation domain's length and height stated in the figure subcaptions

It is important to also understand the effect of increasing the number of microtubules in the system where we set $\mathcal{P}_{CC} = 0.7$ and $\mathcal{P}_B = 0.7$ (figure 5.13). When $m_{max} = 100$,



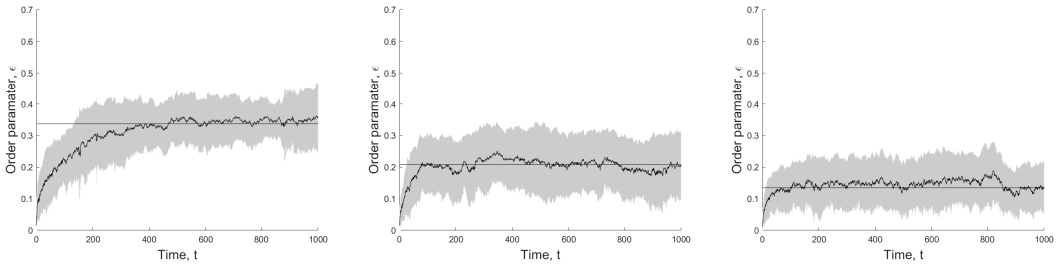
(a) 10μm (b) 50μm (c) 100μm

Figure 5.6: How the order parameter changes with time for simulations with probability $\mathcal{P}_{CC} = 0.3$ and $\mathcal{P}_B = 0.3$ with the simulation domain's length and height stated in the figure subcaptions



(a) 10μm (b) 50μm (c) 100μm

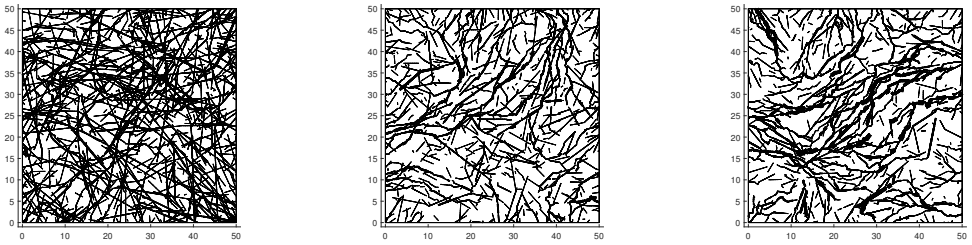
Figure 5.7: How the order parameter changes with time for simulations with probability $\mathcal{P}_{CC} = 0.4$ and $\mathcal{P}_B = 0.4$ with the simulation domain's length and height stated in the figure subcaptions



(a) 10μm (b) 50μm (c) 100μm

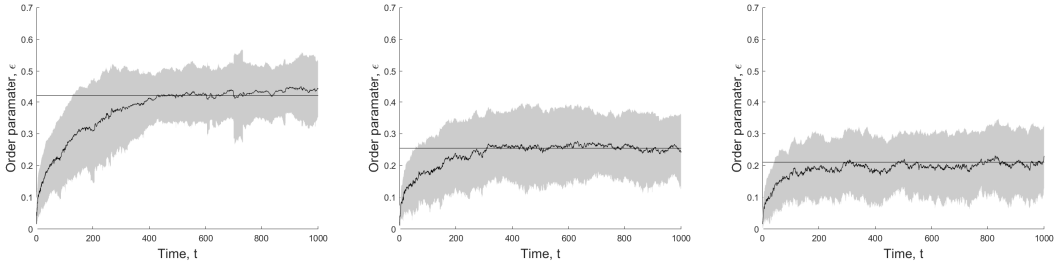
Figure 5.8: How the order parameter changes with time for simulations with probability $\mathcal{P}_{CC} = 0.5$ and $\mathcal{P}_B = 0.5$ with the simulation domain's length and height stated in the figure subcaptions

it can be seen that order quickly arises but ϵ displays large variations, ranging between 0.2 to 0.3 (figure 5.13a). However, when $m_{max} = 500$ and $m_{max} = 1000$, the order in the system slightly increases but also becomes increasingly stable, where it plateaus around 0.3 (figure 5.13b and c). Further increases to the number of microtubules in the system to



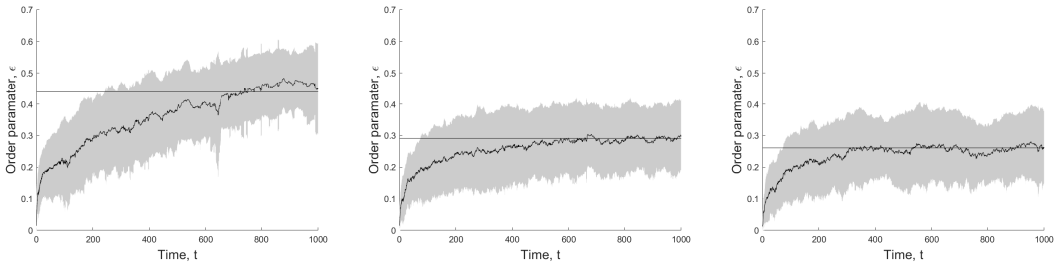
(a) $\mathcal{P}_{CC} = \mathcal{P}_B = 0.1$ (b) $\mathcal{P}_{CC} = \mathcal{P}_B = 0.4$ (c) $\mathcal{P}_{CC} = \mathcal{P}_B = 0.8$

Figure 5.9: Microtubule arrays with different interaction probabilities of size $50\mu m$, where the thickness of the lines represent how many microtubules are in that bundle with the simulation's interactions probabilities stated in the figure subcaptions



(a) 10μm (b) 50μm (c) 100μm

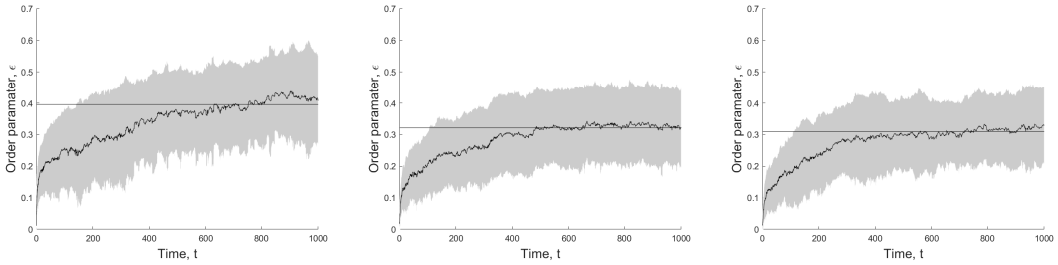
Figure 5.10: How the order parameter changes with time for simulations with probability $\mathcal{P}_{CC} = 0.6$ and $\mathcal{P}_B = 0.6$ with the simulation domain's length and height stated in the figure subcaptions



(a) 10μm (b) 50μm (c) 100μm

Figure 5.11: How the order parameter changes with time for simulations with probability $\mathcal{P}_{CC} = 0.7$ and $\mathcal{P}_B = 0.7$ with the simulation domain's length and height stated in the figure subcaptions

$m_{max} = 2000$ and $m_{max} = 3000$ reduces the order in the system where it also takes longer for the system to plateau (figure 5.13d and e). From these results, it is concluded that there is a possible optimum value for m_{max} where microtubules can easily form robust, organised arrays. Setting m_{max} lower than this value results in a system with fewer



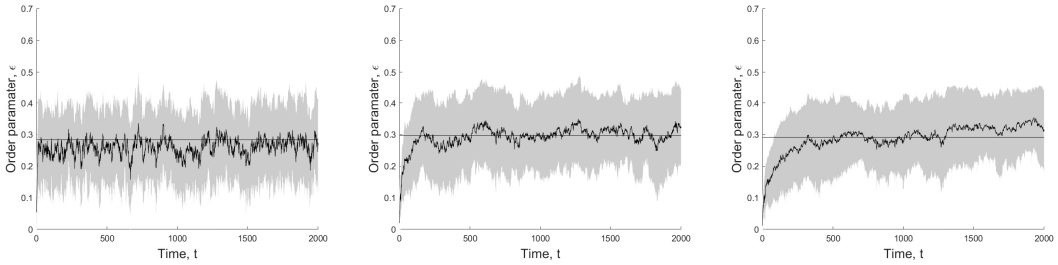
(a) 10μm (b) 50μm (c) 100μm

Figure 5.12: How the order parameter changes with time for simulations with probability $\mathcal{P}_{CC} = 0.8$ and $\mathcal{P}_B = 0.8$ with the simulation domain's length and height stated in the figure subcaptions

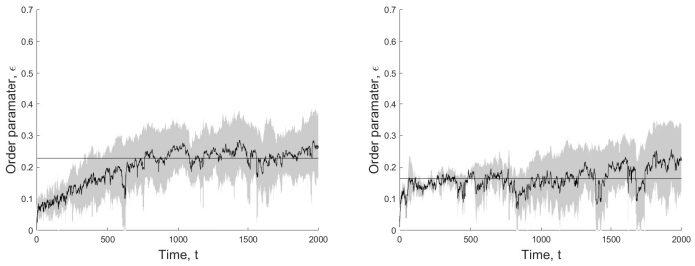
interactions occurring as there are fewer microtubules to interact with and thus reduces the order in the system. On the other hand, setting m_{max} higher than this critical value reduces the order in the system, possibly because there are too many interactions leading to the microtubules struggling to establish a single bias in direction. Consequently, in the simulations in pavement cells, we need to be mindful not to add too little or too many microtubules. Importantly, order did still arise in all of these simulations, demonstrating that the model still has the needed emergent features no matter the parameter's value.

5.4.2 Rectangular domain simulations

To further validate the model, whether microtubule order increases with cell eccentricity and if the microtubules align to the long axis when under the right parameter set are now tested. As a result, simulations are firstly performed in rectangular domains of varying aspect ratios, 1, 2, 3, 4 and 5 which have a width of 10μm and varying heights of 10μm, 20μm, 30μm, 40μm and 50μm respectively, all with $\mathcal{P}_{CC} = 0.4$ and $\mathcal{P}_B = 0.4$. Secondly, simulations are run in a rectangular domain of aspect ratio 5 with $\mathcal{P}_{CC} = 0.01$ and $\mathcal{P}_B = 0.9$ to match with Gomez et al. [2016]'s simulations. Simulations are also run in this same rectangular domain to test the effect of the interactions probabilities on microtubule organisation by setting their values to $\{0.01, 0.1, 0.2, 0.3, 0.5, 0.7, 0.9\}$ where $\mathcal{P}_{CC} = \mathcal{P}_B$. These simulations are all run with $m_{max} = 500$ and for 500 minutes. In this



(a) $m_{max} = 100$ (b) $m_{max} = 500$ (c) $m_{max} = 1000$



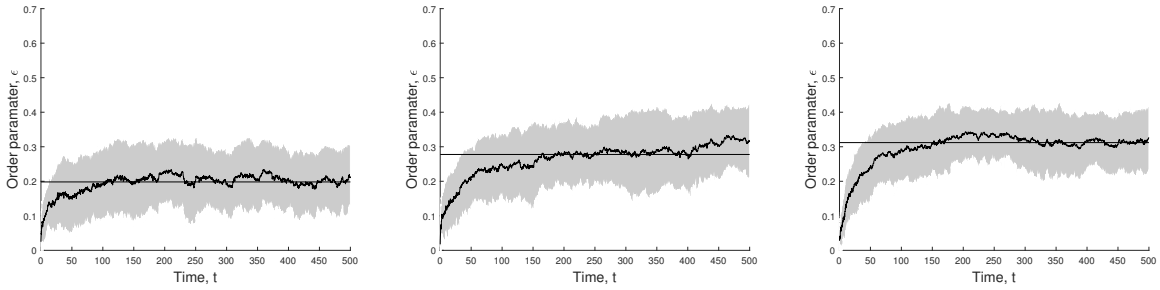
(d) $m_{max} = 2000$ (e) $m_{max} = 3000$

Figure 5.13: How the order parameter changes with time for simulations with varying max microtubule number all with size size $50\mu m$ and probabilities $\mathcal{P}_{CC} = 0.7$ and $\mathcal{P}_B = 0.7$ with the simulation's max microtubule number stated in the figure subcaptions

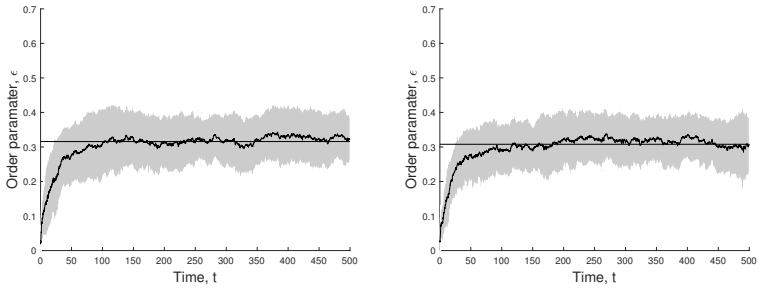
section, for each test scenario, as well as plotting the order parameter against time, we also display the cumulative sum of the 50 simulation's angle distribution at the final time step.

To begin examining the effect of the aspect ratio, when it is 1 (a square domain), the system does become organised with the order parameter plateauing around 0.2 (figure 5.14a), but the cumulative angle distribution is approximately uniform (figure 5.15a), demonstrating that the microtubules are not consistent in their bias direction. As the aspect ratio increases to 2 and 3, the microtubule array becomes increasingly organised (figure 5.14b and c), where the order value plateaus around 0.29 and 0.31 respectively. However, further increases to the aspect ratio to 4 and 5 does not increase the order parameter more, but it does decrease the time it takes for the system to stabilise (figure 5.14d and e). This trend can also be seen in the cumulative angle distributions where when the aspect ratio increases, the microtubules increasingly arrange transversely to the long axis (figure 5.15). We can conclude that microtubule alignment/order increases with

eccentricity (up to a point), and thus have produced similar results to Gomez et al. [2016], helping validate the model.



(a) Aspect ratio 1 (b) Aspect ratio 2 (c) Aspect ratio 3

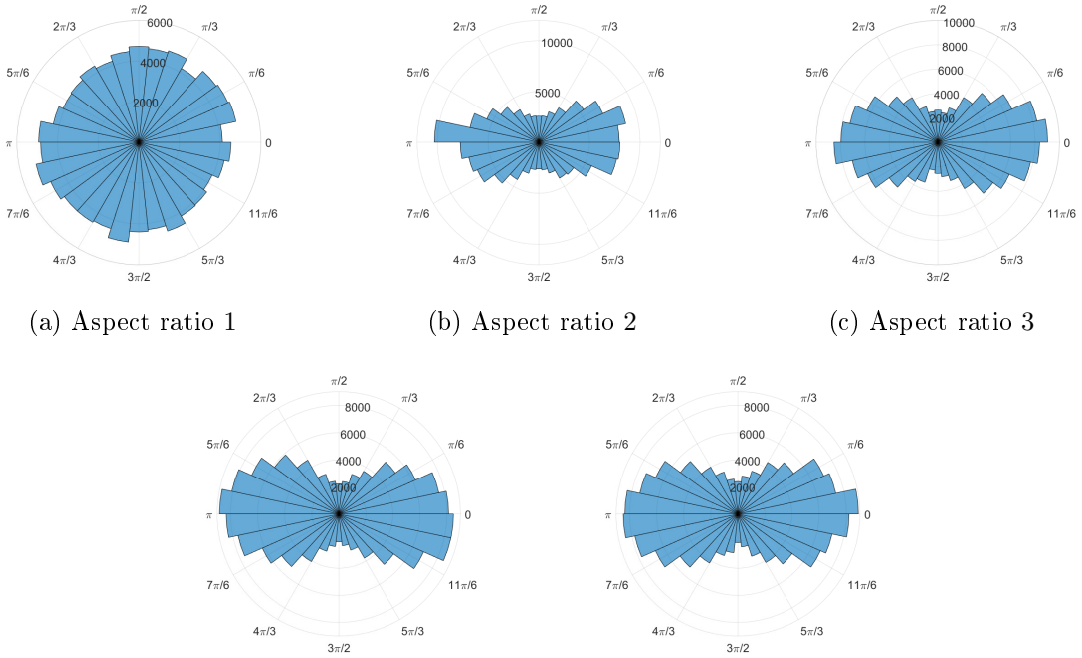


(d) Aspect ratio 4 (e) Aspect ratio 5

Figure 5.14: How the order parameter changes with time for simulations with probabilities $\mathcal{P}_{CC} = 0.5$ and $\mathcal{P}_B = 0.5$ and varying aspect ratios where the subcaptions state the aspect ratios.

To continue the validation experiments, microtubule alignment direction in rectangular domains of aspect ratio 5 is now examined. When $\mathcal{P}_{CC} = 0.01$ and $\mathcal{P}_B = 0.9$, the interaction probabilities used by Gomez et al. [2016], order arises with it plateauing around $\epsilon = 1.5$ (figure 5.16a) where the microtubule arrays are observed to align themselves in the longitudinal direction (figure 5.17a). Our simple model has therefore recreated the results of Gomez et al. [2016], Mirabet et al. [2018] and Lagomarsino et al. [2007] (with the latter two performing their simulations in 3D).

The effect of the different interaction probabilities on microtubule alignment is now tested in the rectangular domain of aspect ratio 5. When the probabilities are low, $\mathcal{P}_{CC} = \mathcal{P}_B = 0.01$ and $\mathcal{P}_{CC} = \mathcal{P}_B = 0.1$, the microtubules once again align with the long axis (figure 5.17b and c), where the alignment is stronger in the first case with the



(a) Aspect ratio 1 (b) Aspect ratio 2 (c) Aspect ratio 3

(d) Aspect ratio 4 (e) Aspect ratio 5

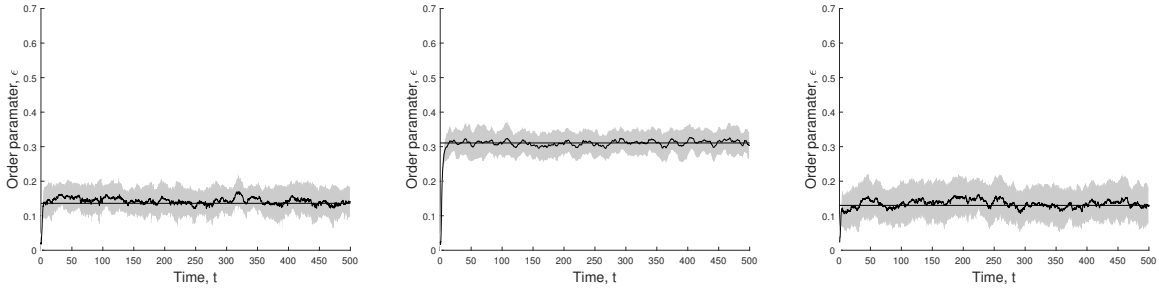
Figure 5.15: The aspect ratio's effect on the cumulative angle distribution for simulations with probability $\mathcal{P}_{CC} = 0.5$ and $\mathcal{P}_B = 0.5$ where the subcaptions state the aspect ratios.

steady-state order parameters respectively being around 0.31 and 0.13 (figure 5.16b and c). However, as the interaction probabilities increase further, something interesting happens: the microtubules' alignment transitions from a longitudinal to a transverse directional bias. This transition occurs approximately when $\mathcal{P}_{CC} = \mathcal{P}_B = 0.2$, where the mean order in the system is low ($\epsilon \approx 0.09$) (figure 5.16d) and the cumulative angle distribution is uniform (figure 5.17d). When the interaction probabilities increase further, with $\mathcal{P}_{CC} = \mathcal{P}_B = 0.3$, weak alignment in the transverse direction can be seen (figure 5.17e) with the steady-state order parameter rising to 0.2 (figure 5.16e). This transverse alignment and microtubule order increases with further increases to the interaction probabilities (figure 5.16f, g and h and figures 5.17f, g and h) where when $\mathcal{P}_{CC} = \mathcal{P}_B = 0.9$ the steady-state order parameter is around 0.4 (figures 5.16 h). This alignment transition truly demonstrates the importance of carefully selecting the parameters for the pavement cell simulations, as certain values could change the system's behaviour.

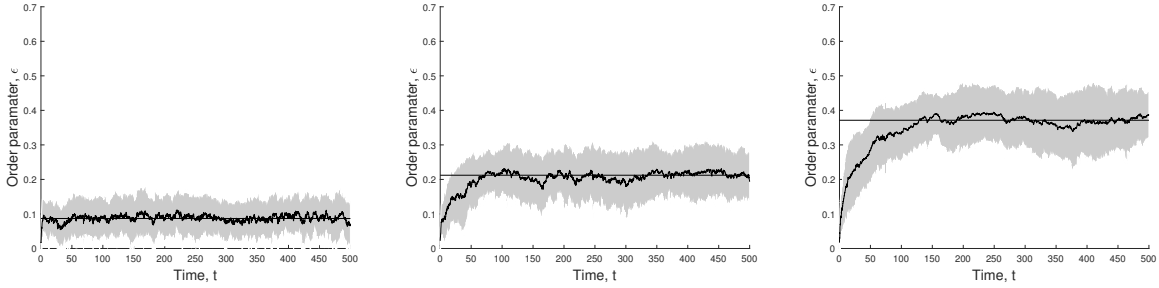
This microtubule alignment transition caused by varying the interaction probabili-

ties is an exciting result, which to our knowledge, has never been previously reported. The transverse alignment could be a more realistic outcome compared to longitudinal alignment, as it has been reported that microtubules often orientate transversally to the elongation axis in actual plant cells [Dixit and Cyr, 2004, Mirabet et al., 2018]. However, this is not the complete picture as it has been observed that in plant stems, the outer cells have longitudinally oriented microtubules and the inner cells have transversally oriented microtubules [Baskin and Jensen, 2013]. Our results could allude to a possible mechanism as to how this arrangement and generally how microtubule alignment control occurs. Suppose in the plant stem some external signalling factor could control the microtubule interaction probabilities so that they are higher in the internal tissues and lower in the outer tissue, causing the microtubules to align transversally and longitudinally, respectively.

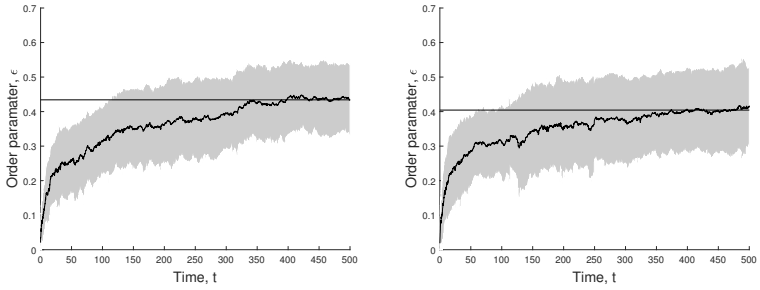
However, other studies have found other mechanisms to cause microtubule alignment transition. Colin et al. [2020] found that microtubules align with the long axis in low-stress conditions and reorient transversally when cortical tension is increased. Also, to our knowledge, differential microtubule interaction probabilities within tissues have not been previously reported in biological scenarios. We note that it is the preliminary analysis that suggests that the change in interaction probabilities directly causes this transition behaviour, but other mechanisms could be at play. For example, increasing $\mathcal{P}_{CC}$ could increase the overall number of catastrophe events allowing for more microtubule turnover and reducing the average microtubule length in the system. As a result, the idea of the interaction probabilities helping control microtubule alignment requires more work where any future studies would have to incorporate the effect of stress, which microtubules are undoubtedly affected by [Szymanski and Cosgrove, 2009, Hamant et al., 2019, Mirabet et al., 2018, Colin et al., 2020].



(a) $\mathcal{P}_{CC} = 0.01$ and $\mathcal{P}_B = 0.9$ (b) $\mathcal{P}_{CC} = 0.01$ and $\mathcal{P}_B = 0.01$ (c) $\mathcal{P}_{CC} = 0.1$ and $\mathcal{P}_B = 0.1$



(d) $\mathcal{P}_{CC} = 0.2$ and $\mathcal{P}_B = 0.2$ (e) $\mathcal{P}_{CC} = 0.3$ and $\mathcal{P}_B = 0.3$ (f) $\mathcal{P}_{CC} = 0.5$ and $\mathcal{P}_B = 0.5$

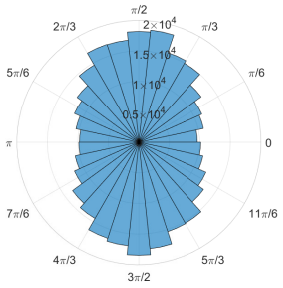


(g) $\mathcal{P}_{CC} = 0.7$ and $\mathcal{P}_B = 0.7$ (h) $\mathcal{P}_{CC} = 0.9$ and $\mathcal{P}_B = 0.9$

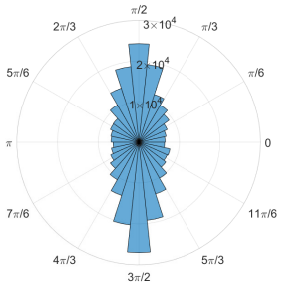
Figure 5.16: How the order parameter changes with time for the simulations run in a rectangular domain with aspect ratio 5 when testing the effect of different interaction probabilities

5.4.3 Pavement cell simulations

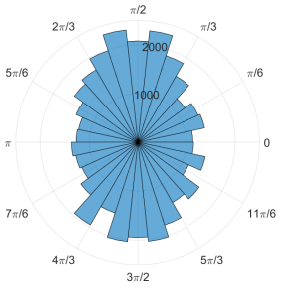
With the model validated, test simulations in pavement cells can now be run using the outlines extracted from the confocal images (see section 4.3.1). As already stated, to match with the biology and previous studies, the model should be able to reproduce microtubule alignment/localisation to the indents where they fan out in the normal direction. In order to know if this alignment is happening, the number of instances of when a microtubule's endpoint hits a lobe or an indent is recorded, where $\tilde{\kappa}$ is used to know where



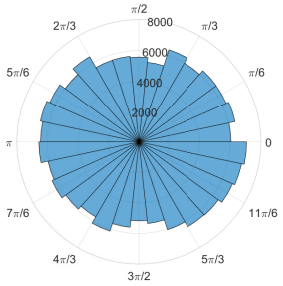
(a) $\mathcal{P}_{CC} = 0.01$ and $\mathcal{P}_B = 0.9$



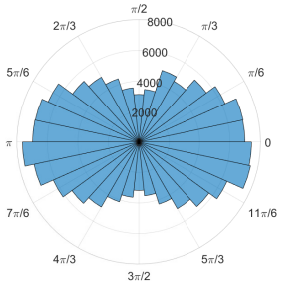
(b) $\mathcal{P}_{CC} = 0.01$ and $\mathcal{P}_B = 0.01$



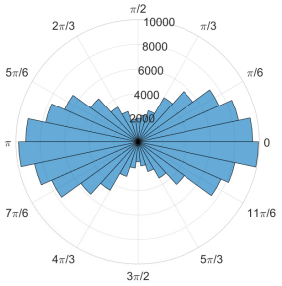
(c) $\mathcal{P}_{CC} = 0.1$ and $\mathcal{P}_B = 0.1$



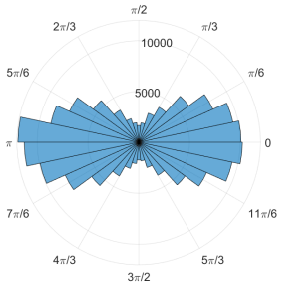
(d) $\mathcal{P}_{CC} = 0.2$ and $\mathcal{P}_B = 0.2$



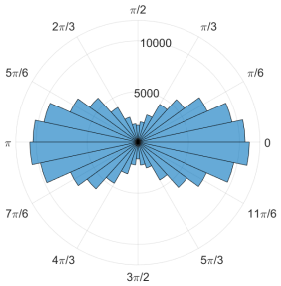
(e) $\mathcal{P}_{CC} = 0.3$ and $\mathcal{P}_B = 0.3$



(f) $\mathcal{P}_{CC} = 0.5$ and $\mathcal{P}_B = 0.5$



(g) $\mathcal{P}_{CC} = 0.7$ and $\mathcal{P}_B = 0.7$



(h) $\mathcal{P}_{CC} = 0.9$ and $\mathcal{P}_B = 0.9$

Figure 5.17: The angle distributions for the simulations run in a rectangular domain with aspect ratio 5 when testing the effect of different interaction probabilities.

the microtubules are hitting. Furthermore, confirmation of whether the microtubules are behaving correctly or not can arise by also directly observing the microtubule array in the pavement cells. The simulations are in 10 different mature pavement cell outlines of varying shapes where each shape is run 10 times (50 simulations in total), allowing us to plot the mean and standard deviation of the sum of the lobe and indent localisation instances. The number of microtubule indent localisation instances to a lobe or indent is measured by totalling up the number of microtubules that have hit the boundary and seeing where on the boundary they are using $\tilde{\kappa}$ at each time step. We let $\mathcal{P}_{CC} = 0.2$ and

$\mathcal{P}_B = 0.1$ in order to coincide with observations made in pavement cells and other values stated in the surrounding literature [Dixit and Cyr, 2004, Allard et al., 2010a,b, Chi and Ambrose, 2016, Gomez et al., 2016, Chakrabortty et al., 2018] where the simulations are run for 1000 minutes and $m_{max} = 4000$.

From the simulations, it can be observed that there is a slight bias in the number of microtubules localising to the indents when compared to the number of lobe localisation instances (figure 5.18a); however, the standard deviations of the localisation instances overlap meaning that this difference is insignificant. By also examining the microtubule array in an example pavement cell outline (figure 5.18c), the microtubules do not appear to fan out from the indents as experimentally observed. Consequently, we are not satisfied with this result, however the model is currently missing a critical feature.

Microtubules have been repeatably observed to align with the direction of maximal tensile stress (see section 2.1.2). This microtubule stress response and alignment has been directly observed in pavement cells; for example, when the stomata pop out of the epidermis imposing tissue tensions, microtubules form rings in the predicted stress patterns and squashing pavement cells using a coverslip and other mechanical perturbations has also been shown to alter microtubule arrangement [Jacques et al., 2013, Sampathkumar et al., 2014]. Importantly the indents have been shown to be areas of increased stress where the microtubules have been observed to align with the stress fields and localise to the indents [Sampathkumar et al., 2014]. As discussed in section 2.1.2, microtubules are said to be stabilised by stress, as a result, this behaviour is implemented in the model by changing the probability of a microtubule undergoing a random catastrophe, $\mathcal{P}_{RC}$, decreasing its value when a microtubule hits an indent and increasing it when it hits a lobe (see section 5.2 for details). We feel confident in adding this effect as from Chakrabortty et al. [2018]'s microtubule simulations in pavement cells, they comment that there needs to be some kind of forcing term as microtubules do not localise to the indents naturally.

With this stabilisation effect, the 50 simulations are rerun in the pavement cell outlines. From the tests, the mean cumulative sum of the microtubules localising to the indents

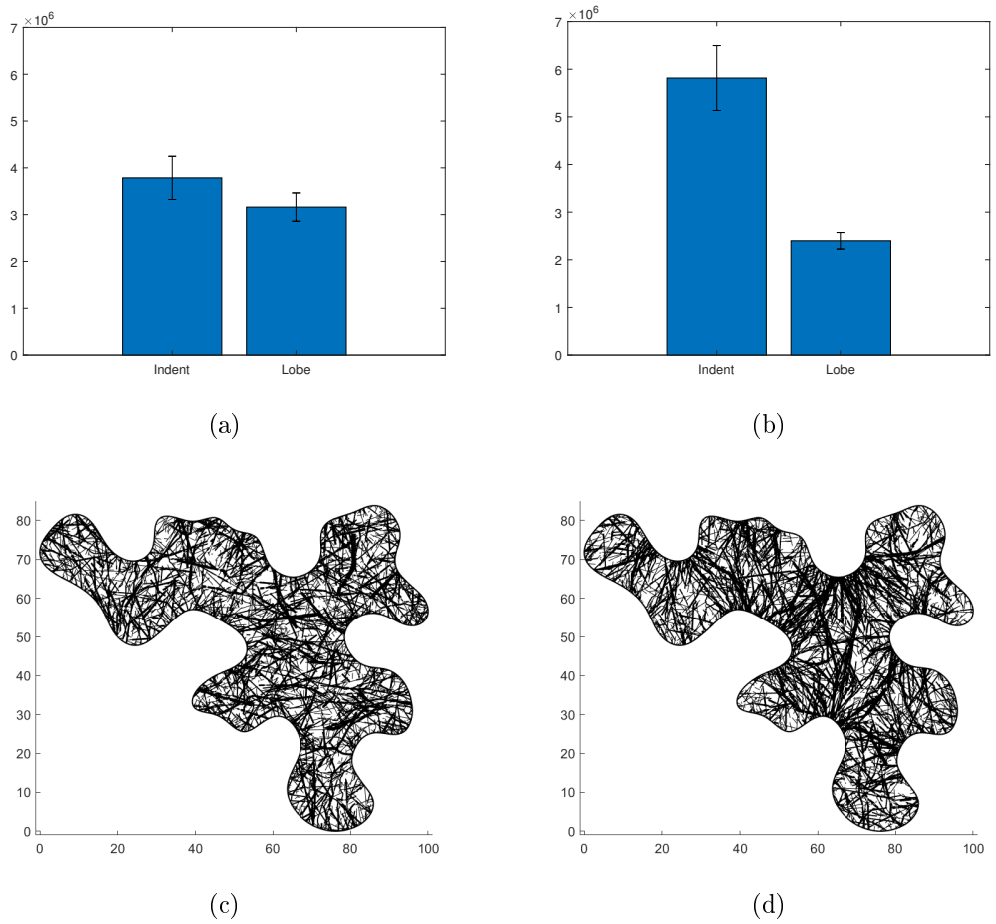


Figure 5.18: The results of running the model in pavement cells with (b and d) and without the (a and c) stress stabilisation with the bar charts (a and b) showing the cumulative microtubule lobe and indent localisation instances and the microtubule diagrams (c and d) showing the microtubule arrays in the pavement cell outlines.

is higher than that of the lobes (figure 5.18b) where, unlike the previous simulations, there is no overlap in the error bars demonstrating that this difference is significant. The microtubule array is now also observed to (figure 5.18d) localise and bundle together while also fanning out in the normal direction at the indents, while the lobes show lower concentrations of microtubules. The same microtubule array behaviour can be seen in the other pavement cell outlines displayed in appendix A.3.3. The pavement cell simulations therefore display the correct phenotype and features.

5.5 Microtubule model conclusions, further remarks and summary

In this chapter, we have demonstrated that the simple microtubule model possesses the key features that ensure its validity. In section 5.4.1 it was first proved that order could arise just from the microtubules interacting with one another, an essential feature. Secondly, in section 5.4.2, past results were replicated by showing both the microtubules aligning with the long axis in a rectangular domain (under certain parameter choices) and that the order in the system increases with the eccentricity of the domain. It was also interestingly discovered that microtubules in a rectangular domain change their alignment (longitudinally or transversally) when the interaction probabilities are varied. Also, realistic microtubule arrays were recreated by running the model in actual pavement cell outlines and including microtubule stress stabilisation. This microtubule model is therefore ready for further use.

However, in keeping the model as simple as possible, features that could affect microtubule behaviour have been missed out. Examples of such features are microtubule rescue after catastrophe (and dynamic instability as a whole), which could allow the microtubule lifetime to increase and pauses after microtubules interact with one another, which could affect the convergence time to an ordered system. An additional feature not included was the microtubule spawning/branching of other microtubules. This phenomenon may cause different microtubule organisational properties, as aligned microtubule arrays could spawn more microtubules, possibly helping promote further alignment. Including such features in future models could make the system more realistic, enabling us to make more believable conclusions from the results.

Modelling in 2D could also restrict the realism of the model. Microtubules in real life grow along the plasma membrane surface (sometimes moving into the cytoplasm), where they can circle around the cell allowing for more possible interactions, unlike the model created here, where the microtubules stop when they hit the cell boundary. Microtubule mechanical properties are also ignored, like their bending stiffness. However, Lagomarsino et al. [2007] who include this feature state that they are assuming the bending energy to

characterise microtubule dynamics, where in real life, it is unknown as to how much the bending stiffness dominates microtubule behaviour.

In the pavement cells simulations, the curvature of the pavement cell outlines is used rather than the actual tissue stresses to impose microtubule stabilisation. This stabilisation implementation also means that the microtubules that do not hit the boundary but are near and aligned with the stress fields will not be affected. To improve on this and increase the realism, the stress fields could somehow be estimated and used to stabilise the microtubules instead.

Despite these missing features, we still feel confident in our model as it has been successfully validated in several ways. Importantly our implementation allows for quick microtubule simulations, which is favourable to us when incorporating this microtubule model with the reaction-diffusion signalling dynamics system in the next chapter (chapter 6), allowing us to understand how the ROPs and RICs network work to control pavement cell growth.

Chapter 6

Getting to know the ROPS: a partial differentiable reaction diffusion system to understand pavement cell signalling pathways

6.1 Introduction

Signalling proteins in a plant cell control the cell cytoskeleton and consequently control the deposition of new cell wall material and wall loosening enzymes. Therefore, the signalling protein dynamics must be known to understand how growth is controlled in a pavement cell. As detailed in section 2.1.4.3 there are several relevant proteins in pavement cell lobe formation, mainly ROP6, ROP2, RIC1 and RIC4, which all interact with one another and with the microtubules and actin filaments.

In this chapter, we investigate this network of interacting proteins and cytoskeletal components as depicted in figure 2.1 which contains all of the known main relevant substances and interactions that influence pavement cell growth. This network is hypothesised to set up alternating patches of ROP2 and microtubule expression that can sustain/further develop and initiate pavement cell lobeing. Building up a model of their dynamics will allow us to test this hypothesis and discern if there are any missing interactions.

To model the pavement cell signalling dynamics a reaction-diffusion system solved via finite element methods is built that reacts to the evolving microtubule array in real-time. Using this model in mature pavement cells, first to be tested is the hypothesis that this signalling network is capable of controlling/sustaining the further development of pavement cell lobes and indents. Secondly, by changing model parameters and simulating in less developed pavement cells, this network is further examined by attempting to recreate experimental observations of pavement cell mutants. Both of these simulations, if successful, can also help to validate the model. Lastly, whether this network can initiate lobes is tested by running the model in young small pavement cells. For simplicity and to ensure reasonable computation time, only one cell will be modelled at a time, and due to the different timescales explained in section 1.2 the domain is also non-growing.

Beginning in section 6.2 needed preliminary mathematical definitions to understand the reaction-diffusion equations and their eventual solutions are stated. Next, what is included in the model and why is then outlined, followed by the formulation of the system equations and boundary conditions in section 6.3. The method for solving the system is

then implemented and shown in section 6.4. The results from the model are displayed and discussed in section 6.5 with the chapter then finished up with some concluding remarks in section 6.6.

6.2 Mathematical preliminaries

In order to understand the equations and how they are solved using finite element methods, some terms first need to be defined.

The first definition is the space of functions labelled $\mathcal{L}_2(\Omega)$ that are square integrable in a domain Ω. An arbitrary function f belongs in this space if it has the following property

$$||f(\mathbf{x}^*)||_2 = \left(\int_\Omega |f(\mathbf{x}^*)|^2 dV\right)^{\frac{1}{2}} < \infty, \tag{6.2.1}$$

where $|\ |$ represents the absolute value. The reaction diffusion equations in the next section are required to be square integrable and to also have square integrable derivatives [Donea and Huerta, 2003].

Secondly a Sobolev space, over the domain Ω labelled $\mathcal{H}^k(\Omega)$ is defined to be the space of functions that are square integrable and have square integrable derivatives of up to order k. Specifically, given a n tuple $\boldsymbol{\alpha} = (\alpha_1, \alpha_2, \ldots, \alpha_n)$ with $\alpha_i \in \mathbb{N}\ \forall\ i = 1, 2 \ldots n$, this space is written (in n dimensional space) as

$$\mathcal{H}^k(\Omega) = \left\{ f \in \mathcal{L}_2(\Omega) | \frac{\partial^{|\boldsymbol{\alpha}|} f}{\partial x_1^{*\alpha_1} \partial x_2^{*\alpha_2} \ldots \partial x_n^{*\alpha_n}} \in \mathcal{L}_2(\Omega)\ \forall\ |\boldsymbol{\alpha}| \leq k \right\}, \tag{6.2.2}$$

where $|\boldsymbol{\alpha}| = \alpha_1 + \alpha_2 + \cdots + \alpha_n$. The third space of functions to be defined, denoted by $\mathcal{V}$, is a subset of $\mathcal{H}^k(\Omega)$ where the functions vanish on the boundary, specifically

$$\mathcal{V} = \{ f \in \mathcal{H}^k(\Omega) | f(\mathbf{x}^*) = 0 \text{ where } \mathbf{x}^* \in \partial\Omega \}. \tag{6.2.3}$$

$\mathcal{T}(\Omega)$ is also defined to be the partition of the space, Ω called the triangulation which is built up of N triangular subdomains labelled τ_u for $u = 1, 2 \ldots N$ such that,

$$\hat{\Omega} = \cup_{u=1}^{N} \tau_u \text{ with } \tau_u \cap \tau_{\tilde{u}} = \emptyset \text{ for } u \neq \tilde{u}. \tag{6.2.4}$$

The characteristic mesh/triangulation size, labelled h^* is defined to be,

$$h^* = \sup_{\tau_u \in \mathcal{T}} H(\tau_u), \text{ where} \tag{6.2.5}$$

$$H(\tau_u) = \text{the longest element in the triagle } \tau_u. \tag{6.2.6}$$

A subspace of $\mathcal{V}$ labelled $\mathcal{V}^{h^*}$ can then be defined to be,

$$\mathcal{V}^{h^*} = \{f \in \mathcal{H}^k(\Omega) |\ f|_{\tau_u} \in \mathcal{P}_m(\tau_u)\ \forall \tau_u \in \mathcal{T} \text{ and } f(\mathbf{x}^*) = 0 \text{ where } \mathbf{x}^* \in \partial\Omega\}, \tag{6.2.7}$$

where $\mathcal{P}_m$ is the finite element interpolating space which can be the set of polynomials of total degree $\leq m$. With these definitions in place the model can now be setup.

6.3 Signalling protein and microtubule network model outline and description

In this section, the system equations are both explained and defined. To thoroughly test the signalling network, the model includes nearly all of the main relevant substances and features that are claimed to determine pavement cell growth (as shown in figure 2.1), however certain interactions are excluded when the current biological understanding is questionable. All the interactions are assumed to be linear to ensure the system is as simple as possible and that no Turing patterning is imposed on the system.

The influential signalling proteins to be modelled are the active forms of ROP6, ROP2, RIC1 and RIC4, as well as including the important microtubules that are constantly changing and evolving as described in chapter 5. The actin cytoskeleton is excluded

because, as detailed in section 4.3.3 it is not known whether the actin localises to the lobes or not, making their role uncertain. For simplicity, auxin is not directly included, as it affects and is affected by many things, instead, auxin's promotion of ROP2 and ROP6 is incorporated through specific parameters. On top of this, TOPP4, SPK1, SCAR, gibberellic acid and brassinosteroid are not considered as their inclusion would further complicate an already complex system (leading to parametrisation difficulties) and some of their interactions are also not fully known biologically.

The concentrations of these signalling proteins are written as $[ROP6]^* = R_6^*$, $[ROP2]^* = R_2^*$, $[RIC4]^* = R_4^*$ and $[RIC1]^* = R_1^*$ with M^* representing the "concentration" of microtubules at a point (which is determined from the number of local microtubule line coordinates at each point in the domain as described in more detail in section 6.4.4.1). Ω is set to be the pavement cell domain and $\partial\Omega$ to be the boundary where $\hat{\Omega}$ is the closure of Ω with $\hat{\Omega} = \Omega \cup \partial\Omega$ and $T = [0, t^*_{max}]$ is the time interval of interest with $t^*_{max} > 0$. As R_6^*, R_4^* R_2^* all diffuse and interact in the cell membrane, their concentrations are characterised with a set of coupled reaction diffusion equations, meaning $R_6^*(\mathbf{x}^*, t^*), R_4^*(\mathbf{x}^*, t^*), R_2^*(\mathbf{x}^*, t^*) \in \mathcal{H}^1(\Omega)$ where $\mathbf{x}^* \in \hat{\Omega}$ and $t^* \in T$. On the other hand, as RIC1 binds to the microtubules in their activated forms (so no diffusion) every microtubule coordinate is assigned a RIC1 concentration, $R^*_{1,(\imath,\jmath)}(t^*)$ where $\imath = 1, \cdots m$ and $\jmath = minus_\jmath^k \cdots plus_\imath^k$ (where m is the number of microtubules currently in the system and $minus_\imath^k$ and $plus_\imath^k$ are the starting and ending indices of microtubule $\imath$ at time step k).

From the background (see section 2.1.4.3 for details), the following network interactions are included in the reaction-diffusion system: the microtubules inhibition of ROP2, ROP2's promotion of RIC4, and ROP2's inhibition and ROP6's promotion of RIC1, where both RIC1 and the stress promote microtubule order (figure 2.1). As a result the system

equations with $\mathbf{x}^* \in \hat{\Omega}$ and $t^* \in T$ are,

$$\frac{\partial R_2^*}{\partial t^*} = D_2^* \nabla^{*2} R_2^* - \delta_2^* R_2^* + \lambda_2^* - k_{M2}^* M^* R_2^*, \tag{6.3.1}$$

$$\frac{\partial R_4^*}{\partial t^*} = D_4^* \nabla^{*2} R_4^* - \delta_4^* R_4^* + k_{24}^* R_2^*, \tag{6.3.2}$$

$$\frac{\partial R_6^*}{\partial t^*} = D_6^* \nabla^{*2} R_6^* - \delta_6^* R_6^* + \lambda_6^*, \tag{6.3.3}$$

$$\frac{dR_{1,(\imath,\jmath)}^*}{dt^*} = k_{61}^* R_{6,(\imath,\jmath)}^* - k_{21}^* R_{2,(\imath,\jmath)}^* R_{1,(\imath,\jmath)}^* - \delta_1^* R_{1,(\imath,\jmath)}^*, \tag{6.3.4}$$

$$\mathcal{P}_{\imath,RC} = g(\tilde{\kappa}_\imath, R_1^*) + \bar{\mathcal{P}}_{RC}, \tag{6.3.5}$$

where $\nabla^{*2} = \frac{\partial^2}{\partial x^{*2}} + \frac{\partial^2}{\partial y^{*2}}$, λ_I^*, $(I = 2, 6)$ are R_2^* and R_6^*'s production rates interpreted as their activation rate from the cytoplasm into the plasma membrane promoted by auxin, δ_I^*, $(I = 1, 2, 4, 6)$ are the natural decay rates, D_I^* $(I = 2, 4, 6)$ are the diffusion rates, k_{M2}^* is the microtubule inhibition rate of R_2^* (where the inhibition term $-k_{M2}^* M R_2^*$ is also dependant on R_2^* so that there are no negative concentrations), k_{24}^* is R_2^*'s promotion rate of R_4^*, and k_{61}^* and k_{21}^* are R_6^* and R_2^* promotion and inhibition rate of R_1^* respectively where $R_{2,(\imath,\jmath)}^*$ and $R_{6,(\imath,\jmath)}^*$ are R_2^* and R_6^*'s concentrations on each microtubule point respectively and $g(\tilde{\kappa}_\imath, R_1^*)$ is the microtubule stabilising function dependant on both the stress and the RIC1 concentration (see 6.4.4.2).

Since the signalling proteins do not leave the cell, R_2^*, R_6^* and R_4^* all have no-flux boundary conditions such that for $\mathbf{x}^* \in \partial\Omega$, and $t^* \in T$,

$$\nabla^* R_2^*(\mathbf{x}^*, t^*) \cdot \mathbf{n} = 0, \tag{6.3.6}$$

$$\nabla^* R_4^*(\mathbf{x}^*, t^*) \cdot \mathbf{n} = 0, \tag{6.3.7}$$

$$\nabla^* R_6^*(\mathbf{x}^*, t^*) \cdot \mathbf{n} = 0, \tag{6.3.8}$$

where $\mathbf{n}$ is the unit normal vector and $\nabla^* = \frac{\partial}{\partial x^*} + \frac{\partial}{\partial y^*}$. To ensure any possible steady

state solution is an emergent property of the system, the initial conditions are,

$$R_2^*(\mathbf{x}^*, 0) = 0, \tag{6.3.9}$$

$$R_4^*(\mathbf{x}^*, 0) = 0, \tag{6.3.10}$$

$$R_6^*(\mathbf{x}^*, 0) = 0, \text{all for } \mathbf{x}^* \in \hat{\Omega} \text{ and} \tag{6.3.11}$$

$$R_{1,(\imath,\jmath)}^*(0) = 0, \text{ for } \imath = 1, \cdots m \text{ and } \jmath = minus_\imath^k \cdots plus_\imath^k. \tag{6.3.12}$$

To ensure we have included every feature, ROP2's promotion of ROP6 on the opposite side of the cell wall is implemented as part of the computational algorithm of the system and is explained in section 6.4.2.

We therefore have a set of equations (equations 6.3.1-6.3.5) with corresponding boundary conditions (equations 6.4.48-6.3.8) and initial conditions (equations 6.3.9-6.3.12) which characterise the reaction diffusion microtubule model with 4 unknowns, R_6^*, R_4^* R_2^* and R_1^* with $\mathcal{P}_{\imath,RC}$ for each microtubule $\imath$ also to be determined.

6.4 Solving the system and the model implementation

With the system equations now outlined, the model can now be solved and implemented. First the reaction-diffusion solutions are found (equations (6.3.1)-(6.3.3)) using finite element methods in section 6.4.1 followed by the description of how ROP6's boundary conditions are implemented (equation (6.4.48)) in section 6.4.2. The differential equation describing RIC1 is then solved in section 6.4.3. Next, how the microtubule model is incorporated with the reaction-diffusion system is described in section 6.4.4. This section is finished by stating the model parameters and outlining how their values are found in section 6.4.5.

6.4.1 Solving the reaction diffusion equations

As the partial differential equations cannot be solved analytically, numerical approximations are used, specifically, finite element approximations which have a history of success of solving structural, mechanical and other partial differential equation systems like heat conduction [Donea and Huerta, 2003]. Briefly, the finite element method works by discretising the domain into smaller subspaces, creating a system of nodes connected by elements (figure 6.1). By then integrating the reaction diffusion equations, creating a weak solution, substituting in approximations for the concentrations, values for the concentrations can then be found at each node by approximating the integrals in each subdomain.

Therefore to find the solutions, the weak solutions to the equations are found in section 6.4.1.1, followed by the domain discretisation and the calculation of the finite element solutions in section 6.4.1.2. Finally, the equations are solved and the final concentrations obtained over the triangulated mesh in section 6.4.1.3.

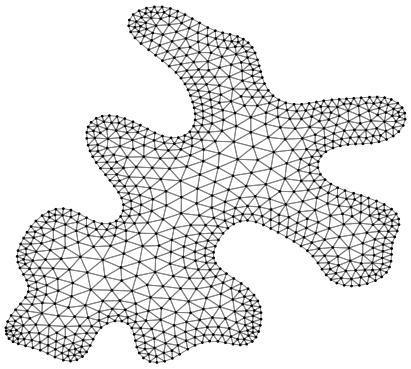


Figure 6.1: Example mesh of one of the pavement cell outlines where the dots represent the nodes and the lines represent elements

6.4.1.1 Obtaining the weak solution

In order to find the weak solution the equations are multiplied (6.3.1)-(6.3.3) by an arbitrary weight function $w^*(\mathbf{x}^*) \in \mathcal{V}^{h^*}$, the diffusion terms moved to the other side and the equations integrated over

the domain Ω to get,

$$\int_\Omega w^*(\mathbf{x}^*)\left(\frac{dR_2^*}{dt^*} - D_2^*\nabla^{*2}R_2^*\right)\ dV^* = \int_\Omega w^*(\mathbf{x}^*)\left(-\delta_2^*R_2^* + \lambda_2^* - k_{M2}^*MR_2^*\right)\ dV^*, \quad (6.4.1)$$

$$\int_\Omega w^*(\mathbf{x}^*)\left(\frac{dR_4^*}{dt^*} - D_4^*\nabla^{*2}R_4^*\right)\ dV^* = \int_\Omega w^*(\mathbf{x}^*)\left(-\delta_4^*R_4^* + \lambda_4^*R_2^*\right)\ dV^*, \quad (6.4.2)$$

$$\int_\Omega w^*(\mathbf{x}^*)\left(\frac{dR_6^*}{dt^*} - D_6^*\nabla^{*2}R_6^*\right)\ dV^* = \int_\Omega w^*(\mathbf{x}^*)\left(-\delta_6^*R_6^* + \lambda_6^*\right)\ dV^*. \quad (6.4.3)$$

For an arbitrary function $u^*(x^*)$ and using the chain rule, the following useful expression can be derived,

$$\begin{aligned} \frac{\partial}{\partial x^*}\left(w^*\frac{\partial u^*}{\partial x^*}\right) &= \frac{\partial w^*}{\partial x^*}\frac{\partial u^*}{\partial x^*} + w^*\frac{\partial^2 u^*}{\partial x^{*2}} \\ \Rightarrow -\frac{\partial^2 u^*}{\partial x^{*2}} &= -\frac{\partial}{\partial x^*}\left(w^*\frac{\partial u^*}{\partial x^*}\right) + \frac{\partial w^*}{\partial x^*}\frac{\partial u^*}{\partial x^*}. \end{aligned} \quad (6.4.4)$$

Upon using equation (6.4.4) in the left hand side of the above equations (6.4.1)-(6.4.3) to convert the Laplacian, it is found,

$$\int_\Omega w^*(\mathbf{x}^*)\left(\frac{dR_I^*}{dt^*} - D_I^*\nabla^{*2}R_I^*\right)\ dV^* = \quad (6.4.5)$$

$$\int_\Omega w^*(\mathbf{x}^*)\frac{dR_I^*}{dt^*} + D_I^*\left(-\nabla^*\left(w^*(\mathbf{x}^*)\nabla^*R_I^*\right) + \nabla^*w^*(\mathbf{x}^*)\cdot\nabla^*R_I^*\right)\ dV^*, \quad (6.4.6)$$

for $I = 2, 4, 6$. This step is also sometimes called the integration by parts step and is an important one as it is the reason why we can assume the functions are in $\mathcal{H}^1(\Omega)$ and not necessarily in $\mathcal{H}^2(\Omega)$ [Brenner and Scott, 2008]. Using the Gauss divergence theorem the middle term of equation (6.4.6) becomes,

$$\int_\Omega \nabla^*\left(w^*(\mathbf{x}^*)\nabla^*R_I^*\right)\ dV^* = \int_{\partial\Omega} w^*(\mathbf{x}^*)\left(\mathbf{n}\cdot\nabla^*R_I^*\right)\ dS^*, \quad (6.4.7)$$

where $\mathbf{n}$ is the unit normal vector and from the no flux boundary conditions (equations (6.3.6)-6.3.8) the integrand and therefore the resulting integral is zero. The equations

(6.4.1)-(6.4.3) are now

$$\int_\Omega w^*(\mathbf{x}^*)\frac{dR_2^*}{dt^*} + D_2^*\nabla^* w^*(\mathbf{x}^*)\cdot\nabla^* R_2^*\ dV^* = \int_\Omega w^*(\mathbf{x}^*)\left(-\delta_2^* R_2^* + \lambda_2^* - k_{M2}^* M^* R_2^*\right)\ dV^*, \tag{6.4.8}$$

$$\int_\Omega w^*(\mathbf{x}^*)\frac{dR_4^*}{dt^*} + D_4^*\nabla^* w(\mathbf{x}^*)\cdot\nabla^* R_4^*\ dV^* = \int_\Omega w^*(\mathbf{x}^*)\left(-\delta_4^* R_4^* + \lambda_4^* R_2^*\right)\ dV^*, \tag{6.4.9}$$

$$\int_\Omega w^*(\mathbf{x}^*)\frac{dR_6^*}{dt^*} + D_6^*\nabla^* w^*(\mathbf{x}^*)\cdot\nabla^* R_i^*\ dV^* = \int_\Omega w^*(\mathbf{x}^*)\left(-\delta_6^* R_6^* + \lambda_6^*\right)\ dV^*. \tag{6.4.10}$$

With these integral expressions found, time can now be discretised. Time is partitioned with the set $\mathcal{K} = \{t_k^*, k = 1,\ldots,K\}$ with $\Delta t_k^* = t_k^* - t_{k-1}^*$ where the k is dropped and it is assumed that $\Delta t_k^* = \Delta t^*$ is constant. If the concentrations are expressed as $R_I^*(\mathbf{x}^*, t_k^*) = R_I^{*k}(\mathbf{x}^*)$ the time derivatives can then be discretised using the backward euler method to get,

$$\frac{\partial R_I^*}{\partial t^*} = \frac{R_I^{*k} - R_I^{*k-1}}{\Delta t^*}, \tag{6.4.11}$$

where upon using implicit differentiation, so that all other R_I^* terms appear as R_I^{*k} and not R_I^{*k-1} the left hand side of equations (6.4.8)-(6.4.10) now become

$$\int_\Omega w^*(\mathbf{x}^*)\left(\frac{R_I^{*k} - R_I^{*k-1}}{\Delta t^*}\right) + D_I^*\nabla^* w^*(\mathbf{x}^*)\cdot\nabla^* R_I^{*k}\ dV^*, \tag{6.4.12}$$

for $I = 2, 4, 6$. The backward euler method is used, as unlike the forward euler method it is unconditionally stable meaning that the stability of the solver does not rely on the

step size Δt^* being small [Chen, 2005]. The final weak solutions are

$$\int_\Omega w^*(\mathbf{x}^*)\frac{R_2^{*k}}{\Delta t^*} - w^*(\mathbf{x}^*)\frac{R_2^{*k-1}}{\Delta t^*} + D_2^*\nabla^* w^*(\mathbf{x}^*)\cdot\nabla^* R_2^{*k}\ dV^*$$
$$= \int_\Omega -\delta_2^* w^*(\mathbf{x}^*)R_2^{*k} + \lambda_2^* w^*(\mathbf{x}^*) - k_{M2}^* M^{*k-1} R_2^{*k} w^*(\mathbf{x}^*)\ dV^*, \tag{6.4.13}$$

$$\int_\Omega w^*(\mathbf{x}^*)\frac{R_4^{*k}}{\Delta t^*} - w^*(\mathbf{x}^*)\frac{R_4^{*k-1}}{\Delta t^*} + D_4^*\nabla^* w^*(\mathbf{x}^*)\cdot\nabla R_4^{*k}\ dV^*$$
$$= \int_\Omega -\delta_4^* w^*(\mathbf{x}^*)R_4^{*k} + \lambda_4^* w^*(\mathbf{x}^*)R_2^{*k-1}\ dV^*, \tag{6.4.14}$$

$$\int_\Omega w^*(\mathbf{x}^*)\frac{R_6^{*k}}{\Delta t^*} - w^*(\mathbf{x}^*)\frac{R_6^{*k-1}}{\Delta t^*} + D_6^*\nabla^* w^*(\mathbf{x}^*)\cdot\nabla^* R_6^{*k}\ dV^*$$
$$= \int_\Omega -\delta_6^* w^*(\mathbf{x}^*)R_6^{*k} + \lambda_6^* w^*(\mathbf{x}^*)\ dV^*. \tag{6.4.15}$$

Note that when a concentration R_I^*, $I = 2, 4, 6$ is dependant on another R_J^*, $J = 2, 4, 6$ with $J \neq I$, the previous time step's values, R_J^{*k-1} are used.

6.4.1.2 Space discretisation and obtaining the finite element solutions

With the weak solutions found, the space Ω can now be descretised by splitting the domain up into non-overlapping simple polygonal shapes (triangles are used here).

This triangulation is created by meshing the pavement cell outlines (see section 4.2.3 for details). The meshing is done in MATLAB using the existing code, `MESH2D` which creates a fine Delaunay-based unstructured triangulation [Engwirda, 2014]. An unstructured mesh means that the number of elements connected to a node may vary from node to node, while a Delaunay-based algorithm works to maximise each triangle's minimum angle. Producing a fine mesh with triangles containing no small angles helps ensure the accuracy of the finite element approximations and reduces the error which can come from small angles [Felippa, 2004].

This triangulation is used to calculate the concentrations at each node by approximating the values of the integrals in every triangle $\tau_u \in \mathcal{T}(\Omega)$. The matrix listing the nodes in the descretised space is denoted $\mathbf{X}^* = (\mathbf{x}_1^*, \mathbf{x}_2^*, \ldots, \mathbf{x}_M^*)^T$ where $\mathbf{x}_i^* = (x_i^*, y_i^*)$ for $i = 1, \ldots, M$ and M is the number of nodes.

In order to carry out the finite element approximations, a set of piecewise linear basis functions is defined as $\{\phi_i^*\}_{i=1}^M \in \mathcal{V}^{h^*}$ (also called hat functions) where,

$$\phi_i^*(\mathbf{x}^*) = \begin{cases} 1, \ \mathbf{x}^* = \mathbf{x_i}^* \\ 0, \ \mathbf{x}^* = \mathbf{x_j}^*, \ \text{where } j \neq i, \end{cases} \qquad \forall i = 1, \ldots, M. \tag{6.4.16}$$

The indices of the three nodes referred to in the triangle τ_u are labelled as $\tau_{u,1}$, $\tau_{u,2}$ and $\tau_{u,3}$. For the basis functions on these nodes we assume that $\phi^*_{\tau_{u,v}} \in \mathcal{P}_1(\tau_u)$, for $v = 1, 2, 3$ and as they are also linear the functions in the triangles are defined as,

$$\phi^*_{\tau_{u,v}} = a + bx^* + cy^*, \ \text{for } \mathbf{x}^* = (x^*, y^*) \in \tau_u, \tag{6.4.17}$$

for $a, b, c \in \mathbb{R}$ [Chen, 2005].

Using (6.4.15) and setting w^* to ϕ_i^*, the equations are then re-expressed as,

$$\begin{aligned}
\int_\Omega \phi_i^* \frac{R_2^{*k}}{\Delta t^*} - \phi_i^* \frac{R_2^{*k-1}}{\Delta t^*} + D_2^* \nabla^* \phi_i^* \cdot \nabla^* R_2^{*k} \ dV^* &= \int_\Omega -\delta_2^* \phi_i^* R_2^{*k} + \lambda_2^* \phi_i^* - k_{M2}^* M^{*k-1} R_2^{*k} \phi_i^* \ dV^*, \\
\int_\Omega \phi_i^* \frac{R_4^{*k}}{\Delta t^*} - \phi_i^* \frac{R_4^{*k-1}}{\Delta t^*} + D_4^* \nabla^* \phi_i^* \cdot \nabla^* R_4^{*k} \ dV^* &= \int_\Omega -\delta_4^* \phi_i^* R_4^{*k} + \lambda_4^* \phi_i^* R_2^{*k-1} \ dV^*, \\
\int_\Omega \phi_i^* \frac{R_6^{*k}}{\Delta t^*} - \phi_i^* \frac{R_6^{*k-1}}{\Delta t^*} + D_6^* \nabla^* \phi_i^* \cdot \nabla^* R_6^{*k} \ dV^* &= \int_\Omega -\delta_6^* \phi_i^* R_6^{*k} + \lambda_6^* \phi_i^* \ dV^*.
\end{aligned} \tag{6.4.18}$$

As any function in $\mathcal{V}^{h^*}$ has the unique representation [Chen, 2005]

$$R_I^{*k}(\mathbf{x}^*) = \sum_{j=1}^{M} c_{I,j}^{*k} \phi_j^*(\mathbf{x}^*), \ \forall \ \mathbf{x}^* \in \hat{\Omega} \text{ for } I = 2, 4, 6, \tag{6.4.19}$$

and if $c_{M,j}^{*k}$ is set as the "concentration" of the microtubles on $\mathbf{x}_j^*$, upon substituting these

expressions into equation (6.4.18) it is derived,

$$\sum_{j=1}^{M}\left[c_{2,j}^{*k}\int_{\Omega}\frac{\phi_i^*\phi_j^*}{\Delta t^*}+D_2^*\nabla^*\phi_i^*\cdot\nabla^*\phi_j^*\;dV^*-c_{2,j}^{*k-1}\int_{\Omega}\frac{\phi_i^*\phi_j^*}{\Delta t^*}\;dV^*\right]$$
$$=\sum_{j=1}^{M}\left[c_{2,j}^{*k}\int_{\Omega}-\delta_2^*\phi_i^*\phi_j^*\;dV^*+\int_{\Omega}\lambda_2^*\phi_i^*\;dV^*+c_{M,j}^{*k-1}c_{2,j}^{*k}\int_{\Omega}-k_{M2}^*\phi_i^*\phi_j^*\;dV^*\right], \tag{6.4.20}$$

$$\sum_{j=1}^{M}\left[c_{4,j}^{*k}\int_{\Omega}\frac{\phi_i^*\phi_j^*}{\Delta t^*}+D_4^*\nabla^*\phi_i^*\cdot\nabla^*\phi_j^*\;dV^*-c_{4,j}^{*k-1}\int_{\Omega}\frac{\phi_i^*\phi_j^*}{\Delta t^*}\;dV^*\right]$$
$$=\sum_{j=1}^{M}\left[c_{4,j}^{*k}\int_{\Omega}-\delta_4^*\phi_i^*\phi_j^*\;dV^*+c_{2,j}^{*k-1}\int_{\Omega}\lambda_4^*\phi_i^*\phi_j^*\;dV^*\right], \tag{6.4.21}$$

$$\sum_{j=1}^{M}\left[c_{6,j}^{*k}\int_{\Omega}\frac{\phi_i^*\phi_j^*}{\Delta t^*}+D_6^*\nabla^*\phi_i^*\cdot\nabla^*\phi_j^*\;dV^*-c_{6,j}^{*k-1}\int_{\Omega}\frac{\phi_i^*\phi_j^*}{\Delta t^*}\;dV^*\right]$$
$$=\sum_{j=1}^{M}\left[c_{6,j}^{*k}\int_{\Omega}-\delta_6^*\phi_i^*\phi_j^*\;dV^*+\int_{\Omega}\lambda_6^*\phi_i^*\;dV^*\right].. \tag{6.4.22}$$

Equations (6.4.20)-(6.4.22) are simplified by first defining the matrices,

$$A_{ij}^*=\int_{\Omega}\nabla^*\phi_i^*\cdot\nabla^*\phi_j^*\;dV^*, \tag{6.4.23}$$
$$M_{ij}^*=\int_{\Omega}\phi_i^*\phi_j^*\;dV^*, \tag{6.4.24}$$
$$H_{ij}^*=\int_{\Omega}\phi_i^*\;dV^*, \tag{6.4.25}$$

where $\mathbf{A}^*$ is called the stiffness matrix, $\mathbf{M}^*$ is the mass matrix and $\mathbf{H}^*$ the load vector. By writing in vector format, such that $\mathbf{c}_I^{*k}=\left(c_{I,1}^{*k},c_{I,2}^{*k},\ldots,c_{I,M}^{*k}\right)^T$ and rearranging, it is finally found,

$$\left(\frac{1}{\Delta t^*}\mathbf{M}^*+D_2^*\mathbf{A}^*+\delta_2^*\mathbf{M}^*+k_{M2}^*\mathbf{c}_M^{*k-1}\mathbf{M}^*\right)\mathbf{c}_2^{*k}=\frac{1}{\Delta t^*}\mathbf{M}^*\mathbf{c}_2^{*k-1}+\lambda_2^*\mathbf{H}^*, \tag{6.4.26}$$
$$\left(\frac{1}{\Delta t^*}\mathbf{M}^*+D_4^*\mathbf{A}^*+\delta_4^*\mathbf{M}^*\right)\mathbf{c}_4^{*k}=\frac{1}{\Delta t^*}\mathbf{M}^*\mathbf{c}_4^{*k-1}+\lambda_4^*\mathbf{M}^*\mathbf{c}_2^{*k-1}, \tag{6.4.27}$$
$$\left(\frac{1}{\Delta t^*}\mathbf{M}^*+D_6^*\mathbf{A}^*+\delta_6^*\mathbf{M}^*\right)\mathbf{c}_6^{*k}=\frac{1}{\Delta t^*}\mathbf{M}^*\mathbf{c}_6^{*k-1}+\lambda_6^*\mathbf{H}^*. \tag{6.4.28}$$

From the initial conditions (equations 6.3.9-6.3.12), $\mathbf{c}_I^{*0}=\mathbf{0}$, so to find the final concen-

trations from the recursive relations above (equations 6.4.26-6.4.28) all that is left is to approximate the integrals (equations 6.4.23-6.4.25) over the mesh.

6.4.1.3 Approximating the integrals and obtaining the concentration values

To find the entry values of the matrices $\mathbf{A}^*$, $\mathbf{H}^*$ and $\mathbf{M}^*$ over the triangle mesh the integral equations are reexpressed by splitting them up into the sum of their parts i.e. summing over the triangles, meaning $\forall 1 \leq i, j \leq M$,

$$A^*_{ij} = \int_\Omega \nabla^* \phi^*_i \cdot \nabla^* \phi^*_j \, dV^* = \sum_{\tau_u \in \mathcal{T}} \int_{\tau_u} \nabla^* \phi^*_i \cdot \nabla^* \phi^*_j \, dV^* = \sum_{\tau_u \in \mathcal{T}} A^{*\tau_u}_{ij}, \tag{6.4.29}$$

$$M^*_{ij} = \int_\Omega \phi^*_i \phi^*_j \, dV^* = \sum_{\tau_u \in \mathcal{T}} \int_{\tau_u} \phi^*_i \phi^*_j \, dV^* = \sum_{\tau_u \in \mathcal{T}} M^{*\tau_u}_{ij}, \tag{6.4.30}$$

$$H^*_{ij} = \int_\Omega \phi^*_i \, dV^* = \sum_{\tau_u \in \mathcal{T}} \int_{\tau_u} \phi^*_i \, dV^* = \sum_{\tau_u \in \mathcal{T}} H^{*\tau_u}_{ij}, \tag{6.4.31}$$

where the integrals in the sum are called, the local stiffness matrix, $A^{*\tau_u}_{ij}$, the local mass matrix, $M^{*\tau_u}_{ij}$, and the load vector, $H^{*\tau_u}_{ij}$. With this decomposition, all that remains to do is to calculate the integrals in each triangle, τ_u. These integrals could be immediately approximated over these triangular domains, however doing so would involve having to find the values of a, b and c in equation (6.4.17) for each node in each triangle. It is therefore simpler to first transform each integral onto a reference triangle where equation (6.4.17) is simple and known, which then allows the integrals to be easily approximated using quadrature rules.

The reference triangle, denoted $\hat{\tau}$, has corner co-ordinates $\hat{\mathbf{x}}^*_{\hat{\tau}_1} = (1, 0)$, $\hat{\mathbf{x}}^*_{\hat{\tau}_2} = (0, 1)$ and $\hat{\mathbf{x}}^*_{\hat{\tau}_3} = (0, 0)$. An arbitrary triangle τ_u with corner corner co-ordinates $\mathbf{x}^*_{\tau_{u,1}} = (x^*_{\tau_{u,1}}, y^*_{\tau_{u,1}})$, $\mathbf{x}^*_{\tau_{u,2}} = (x^*_{\tau_{u,2}}, y^*_{\tau_{u,2}})$ and $\mathbf{x}^*_{\tau_{u,3}} = (x^*_{\tau_{u,3}}, y^*_{\tau_{u,3}})$ is transformed onto the reference triangle using the affine map $F : \hat{\tau} \mapsto \tau$. This map takes the form of

$$F^*(\mathbf{x}^*) = B^*(\mathbf{x}^*) + \mathbf{c}^*, \tag{6.4.32}$$

where the value of $B^*(\mathbf{x})^* = \begin{pmatrix} B_{11}^* & B_{12}^* \\ B_{21}^* & B_{22}^* \end{pmatrix}$ and $\mathbf{c}^* = \begin{pmatrix} c_1^* \\ c_2^* \end{pmatrix}$ is calculated by using the known mapping,

$$\begin{pmatrix} x_{\tau_u,1}^* \\ y_{\tau_u,1}^* \end{pmatrix} = \begin{pmatrix} B_{11}^* & B_{12}^* \\ B_{21}^* & B_{22}^* \end{pmatrix} \begin{pmatrix} 1 \\ 0 \end{pmatrix} + \begin{pmatrix} c_1^* \\ c_2^* \end{pmatrix}, \tag{6.4.33}$$

$$\begin{pmatrix} x_{\tau_u,2}^* \\ y_{\tau_u,2}^* \end{pmatrix} = \begin{pmatrix} B_{11}^* & B_{12}^* \\ B_{21}^* & B_{22}^* \end{pmatrix} \begin{pmatrix} 0 \\ 1 \end{pmatrix} + \begin{pmatrix} c_1^* \\ c_2^* \end{pmatrix}, \tag{6.4.34}$$

$$\begin{pmatrix} x_{\tau_u,3}^* \\ y_{\tau_u,3}^* \end{pmatrix} = \begin{pmatrix} B_{11}^* & B_{12}^* \\ B_{21}^* & B_{22}^* \end{pmatrix} \begin{pmatrix} 0 \\ 0 \end{pmatrix} + \begin{pmatrix} c_1^* \\ c_2^* \end{pmatrix}, \tag{6.4.35}$$

which can be solved to find,

$$B = \begin{pmatrix} x_{\tau_u,1}^* - x_{\tau_u,3}^* & y_{\tau_u,1}^* - y_{\tau_u,3}^* \\ x_{\tau_u,2}^* - x_{\tau_u,3}^* & y_{\tau_u,2}^* - y_{\tau_u,3}^* \end{pmatrix} \text{ and } \mathbf{c} = \begin{pmatrix} x_{\tau_u,3}^* \\ y_{\tau_u,3}^* \end{pmatrix}. \tag{6.4.36}$$

This transformation is then used in the calculation for the local stiffness matrix using the fact that $\hat{\phi}_i^*(\hat{\mathbf{x}}^*) = \phi_i^*(F^*(\hat{\mathbf{x}}^*))$, so that $\hat{\nabla}^*\hat{\phi}_i^* = B^*\nabla^*\phi_i^*$ and $dV^* = |\det(B^*)|\, d\hat{V}^*$, thus

$$A_{ij}^{*\tau_u} = \int_{\tau_u} \nabla^*\phi_i^* \cdot \nabla^*\phi_j^*\, dV^* = \int_{\hat{\tau}} \left(B^{*-1}\hat{\nabla}^*\hat{\phi}_i^*\right) \cdot \left(B^{*-1}\hat{\nabla}^*\hat{\phi}_j^*\right) |\det(B^*)|\, d\hat{V}^*. \tag{6.4.37}$$

Repeating the same transformation procedure for the local mass matrix and load vector, it is derived,

$$M_{ij}^{*\tau_u} = \int_{\hat{\tau}} \hat{\phi}_i^*\hat{\phi}_j^* |\det(B^*)|\, d\hat{V}^*, \tag{6.4.38}$$

and

$$H_{ij}^{*\tau_u} = \int_{\hat{\tau}} \hat{\phi}_i^* |\det(B^*)|\, d\hat{V}^*. \tag{6.4.39}$$

Quadrature rules can now be used to approximate the integrals, which can be expressed in the general form

$$\int_{\tau_u} f^*(x^*)dV^* \approx \sum_{i=1} w_i^* f^*(\mathbf{x}_\mathbf{i}^*), \tag{6.4.40}$$

where $w_i^* > 0$ and $\mathbf{x}_i^*$ are certain weights and points in the domain τ_u, respectively [Chen, 2005]. Over the reference triangle the following two quadrature approximations are utilised,

$$\int_{\hat{\tau}} f^*(\mathbf{x}^*)dV^* \approx |\hat{\tau}| f^*(m_0^*), \tag{6.4.41}$$

where m_0^* is the center of gravity of the area and $|\hat{\tau}|$ is the area of the triangle and

$$\int_{\hat{\tau}} f^*(\mathbf{x}^*)dV^* \approx \frac{|\hat{\tau}|}{3}\left(f^*(m_{12}^*) + f^*(m_{23}^*) + f^*(m_{13}^*)\right), \tag{6.4.42}$$

where $m_{v\tilde{v}}^*$ is the midpoint of the element connecting the nodes $\hat{\tau}_v$ and $\hat{\tau}_{\tilde{v}}$. Returning to the calculation of $A_{ij}^{*\tau_u}$, from equation (6.4.17), for the reference triangle $\hat{\phi}_{\hat{\tau}_1}^* = \hat{x}^*$, $\hat{\phi}_{\hat{\tau}_2}^* = \hat{y}^*$ and $\hat{\phi}_{\hat{\tau}_3}^* = 1 - \hat{x}^* - \hat{y}^*$, thus,

$$\hat{\nabla}^*\hat{\phi}_{\hat{\tau}_1}^* = \begin{pmatrix} 1 \\ 0 \end{pmatrix}, \ \hat{\nabla}\hat{\phi}_{\hat{\tau}_2}^* = \begin{pmatrix} 0 \\ 1 \end{pmatrix}, \text{ and } \hat{\nabla}\hat{\phi}_{\hat{\tau}_3}^* = \begin{pmatrix} -1 \\ -1 \end{pmatrix}. \tag{6.4.43}$$

To finally evaluate the integral for the local stiffness matrix, the first quadrature approximation is used (equation 6.4.41) on equation (6.4.37) and as the area of the unit triangle is $|\hat{\tau}| = \frac{1}{2}$, is it found

$$A_{ij}^{*\tau_u} = \frac{1}{2}|\det(B^*)| \left(B^{*-1}\hat{\nabla}^*\hat{\phi}_{\hat{\tau}_i}^*\right) \cdot \left(B^{*-1}\hat{\nabla}^*\hat{\phi}_{\hat{\tau}_j}^*\right). \tag{6.4.44}$$

To approximate the local mass matrix (equation 6.4.38) the second quadrature rule is

used (equation 6.4.42) to get,

$$M_{ij}^{*\tau_u} = \tfrac{1}{6}|\det(B^*)| \left(\hat{\phi}^*_{\hat{\tau}_i}(\hat{m}^*_{12})\hat{\phi}^*_{\hat{\tau}_j}(\hat{m}^*_{12}) + \hat{\phi}^*_{\hat{\tau}_i}(\hat{m}^*_{23})\hat{\phi}^*_{\hat{\tau}_j}(\hat{m}^*_{23}) + \hat{\phi}^*_{\hat{\tau}_i}(\hat{m}^*_{13})\hat{\phi}^*_{\hat{\tau}_j}(\hat{m}^*_{13}) \right), \tag{6.4.45}$$

where $\hat{m}^*_{23} = (0, \frac{1}{2})$, $\hat{m}^*_{13} = (\frac{1}{2}, 0)$ and $\hat{m}^*_{12} = (\frac{1}{2}, \frac{1}{2})$. Lastly, the load vector (equation 6.4.39) can be similarly approximated using the second quadrature rule (equation 6.4.42) to find

$$H_{ij}^{*\tau_u} = \frac{1}{6}|\det(B^*)| \left(\hat{\phi}^*_{\hat{\tau}_i}(\hat{m}^*_{12}) + \hat{\phi}^*_{\hat{\tau}^*_i}(\hat{m}^*_{23}) + \hat{\phi}^*_{\hat{\tau}_i}(\hat{m}^*_{13}) \right). \tag{6.4.46}$$

With the local matrices found and by summing over all the triangles in the domain (using equations (6.4.29)-(6.4.31)) the matrices $\mathbf{A}^*$, $\mathbf{M}^*$ and $\mathbf{H}^*$ can all be calculated. When this method is implemented in MATLAB, both $\mathbf{A}^*$ and $\mathbf{M}^*$ are stored as sparse matrices which takes advantage of the fact that the majority of their entries are zero. Operations on sparse matrices require less computational power and uses less memory which consequently helps the computation time of the model.

Upon the evaluation of the matrices, using equations (6.4.26)-(6.4.28) and rearranging the concentrations $\mathbf{c_2}^*$, $\mathbf{c_4}^*$, and $\mathbf{c_6}^*$ are obtained to be,

$$\begin{aligned}
&\mathbf{c}_I^{*k} = \left(\mathbf{D}_I^{*k}\right)^{-1} \mathbf{q}_I^{*k}, \text{ for } I = 2, 6, 4 \text{ where,} \qquad (6.4.47)\\
&\mathbf{D}_2^{*k} = \left(\frac{1}{\Delta t^*}\mathbf{M}^* + D_2^*\mathbf{A}^* + \delta_2^*\mathbf{M}^* + k_{M2}^*\mathbf{c}_M^{*k-1}\mathbf{M}^* \right) \text{ and } \mathbf{q}_2^{*k} = \mathbf{c}_2^{*k-1}\frac{1}{\Delta t^*}\mathbf{M}^* + \lambda_2^*\mathbf{H}^*,\\
&\mathbf{D}_4^{*k} = \left(\frac{1}{\Delta t^*}\mathbf{M}^* + D_4^*\mathbf{A}^* + \delta_4^*\mathbf{M}^* \right) \text{ and } \mathbf{q}_4^{*k} = \mathbf{c}_4^{*k-1}\frac{1}{\Delta t^*}\mathbf{M}^* + \lambda_4^*\mathbf{c}_2^{*k-1}\mathbf{M}^*,\\
&\mathbf{D}_6^{*k} = \left(\frac{1}{\Delta t^*}\mathbf{M}^* + D_6^*\mathbf{A}^* + \delta_6^*\mathbf{M}^* \right) \text{ and } \mathbf{q}_6^{*k} = \mathbf{c}_6^{*k-1}\frac{1}{\Delta t^*}\mathbf{M}^* + \lambda_6^*\mathbf{H}^*.
\end{aligned}$$

Using finite element methods expressions for the concentrations have now been found.

6.4.2 ROP6 boundary conditions

ROP2's promotion of ROP6 on the opposite side of the cell wall (if ROP2 localises to the lobes ROP6 is promoted on the indent boundary) is included as part of the computational algorithm and takes the form of a nonlocal source term on the boundaries, thus

$$R_6^*(\mathbf{x}^*, t^*) = \lambda_{B,6}^*(R_2^*), \text{for } \mathbf{x}^* \in \partial\Omega, \quad \text{and for } t^* \in T, \tag{6.4.48}$$

where the function $\lambda_{B,6}^*(R_2^*)$ is the source term.

Before detailing this boundary source, the reasons behind its form are first explained. As detailed in the biological background (section 2.1.4.3), ROP2 stabilises PIN1 in the lobes which exports auxin (which diffuses back into the lobes and indents from outside the cell), and thus promotes both ROP6 and itself in the indents and the lobes respectively. However, there seems to be a few unknowns in the literature that would affect the model.

Firstly, it is unclear whether when auxin diffuses back into the lobes/indents after exportation, does it just promote ROP2/ROP6 respectively or both? If it promotes both (which auxin has generally been found to do), it could disrupt the ROP2 and microtubule localisation to the lobes and indents, respectively (and also contradicts the impression the surrounding literature gives). Secondly, when auxin is exported from the lobes by PIN1, we do not know whether this causes a drop in the auxin levels in the lobes, which could be expected [Adamowski and Friml, 2015]. This drop in auxin could lead to a negative feedback loop where ROP2 localisation to the lobes causes auxin exportation, meaning there will be less auxin to promote ROP2, a phenomenon not mentioned in the literature in relation to pavement cells.

With these looming questions and uncertainty, it is decided that only ROP2's promotion of ROP6 on the opposite side of the cell wall boundary will be included. As a result, a feature missing from the model is a possible feedback loop between ROP2 and itself, which may just affect the time it takes to reach a steady state.

Algorithmically, ROP2's promotion of ROP6 is implemented through the boundary

conditions, $\lambda^*_{B,6}(R^*_2)$, such that when ROP2 starts to localise, ROP6's production is stimulated on the "opposite" side of the boundary, i.e. if ROP2 is localising to the lobes, this expression is mirrored for ROP6 in the indents. This mirroring has to be done as only one cell is being simulated, so it is being assumed that if ROP2 localises in this cell, it is also localising in the neighbouring cells. To go into more detail, to do this mirroring the concentrations of ROP2 along the cell boundary need to be known. For this the lobe indicator variable, $\tilde{\kappa}$ (see appendix A.3.4) is used and partitioned into W regions, for example $\mathcal{I} = \{[-1, -1+\delta], (-1+\delta, -1+2\delta], \ldots, (0, 0+\delta], \ldots, (1-\delta, 1]\}$ where $\delta = \frac{2}{W}$ is the width of the regions (where each region represents a different section of a lobe or indent). The average concentration of ROP2 in each lobe indicator region can then be found by using the ROP2 concentration along the cell boundary $\mathbf{X}^*_B$ and the $\tilde{\kappa}$ values allocated to each boundary point. Upon scaling with $\frac{\lambda^*_2}{\delta^*_2}$ (the max ROP2 concentration), a vector called, $\bar{R}_{2,\tilde{\kappa}}$ is found which contains values ranging between 0 and 1 which informs us how much ROP2 is localising to each section of a lobe or indent.

As already mentioned, ROP2's expression needs to be mirrored. To do this, the vector $\bar{R}_{2,\tilde{\kappa}}$ is flipped to create another vector $\bar{R}_{6,\tilde{\kappa}}$ so that the entries for the negative intervals are now the entries for the positive intervals in reverse and vice a versa. To implement the boundary conditions, the logistic equation is used again (as the effect is required to plateau with the logistic function's midpoint $\frac{1}{2}$, being taken away so that it takes both negative and positive values) to allocate a concentration of ROP6 to each $\tilde{\kappa}$ region, thus

$$R^*_{6,\tilde{\kappa}} = a^*_2 \left(\frac{1}{2\left(1 + e^{b_2\left(\bar{R}_{6,\tilde{\kappa}} - c_2\right)}\right)} - \frac{1}{2} \right), \tag{6.4.49}$$

where a^*_2 is the max value, b_2 affects how quickly the function reaches its maximum or minimum value and c_2 is the threshold value of $\bar{R}_{6,\tilde{\kappa}}$ in which it needs to be higher than for the logistic function to take positive values (as we only want R^*_6 being produced on parts of the boundary where R^*_2 is high enough on the mirrored side). The values in $R^*_{6,\tilde{\kappa}}$ are then used to set the R^*_6 values along the boundary $\mathbf{X}^*_B$. Note that if the value of $R^*_{6,\tilde{\kappa}}$

is less than the R_6 value at a boundary point its value is left unchanged (as it would be unrealistic for these boundary conditions which promote ROP6 to decrease its value).

From initial simulations, this boundary condition created some unrealistic features. When the simulations started and the ROP2 concentration was low, unorganised and sporadic, it caused ROP6 to be produced along the boundary in random places and in sudden bursts. As a result, a_2^* is scaled, with a variable we call $\hat{a}_2$, such that it is close to or is 1 when the ROP2 concentration shows variety and is close to 0 otherwise; meaning the boundary conditions are only effective when there are regions of both high and low concentrations of ROP2. This modelling assumption has the biological justification that PIN1 only starts to export auxin to promote ROP6 on the opposite side of the boundary when ROP2 is both stable and localised. $\hat{a}_2$ is defined to be the standard deviation of the c_2^{*k} boundary values divided by the standard deviation of the "perfectly" varied and localised c_2^{*k} boundary values. These perfectly localised c_2^{*k} boundary values are calculated by setting the value of c_2^{*k} on the boundary to the max steady state $\frac{\lambda_2^*}{\delta_2^*}$ when its corresponding $\tilde{\kappa}$ value is 1 and decreasing its value linearly to 0 when $\tilde{\kappa}$ is -1. All of the reaction-diffusion equations solutions and boundary conditions have now been defined.

6.4.3 Solving the RIC1 equation

The procedure to solve equation (6.3.4) which describes RIC1's behaviour is a lot easier than that for the ROP2, ROP6 and RIC4 dynamics, as only a differential equation needs to be solved. By first discretising time and once again using a modified backwards Euler method to account for non-linearities [Chen, 2005] (equation 6.4.19), it is found,

$$\frac{R_{1,(\imath,\jmath)}^{*k} - R_{1,(\imath,\jmath)}^{*k-1}}{\Delta t^*} = k_{61}^* R_{6,(\imath,\jmath)}^{*k-1} - k_{21}^* R_{2,(\imath,\jmath)}^{*k-1} R_{1,(\imath,\jmath)}^{*k} - \delta_1^* R_{1,(\imath,\jmath)}^{*k}, \tag{6.4.50}$$

and rearranging yields,

$$R^{*k}_{1,(\imath,\jmath)} = \frac{\Delta t^* k^*_{61} R^{*k-1}_{6,(\imath,\jmath)}}{1 + \Delta t^* \left(\delta^*_1 + k^*_{21} R^{*k-1}_{2,(\imath,\jmath)}\right)}. \tag{6.4.51}$$

As expressions for all of the concentrations have now been found (equations 6.4.47 and 6.4.51), the next step is to incorporate the microtubule dynamics.

6.4.4 Combining the reaction diffusion system with the microtubule network

A crucial part of the model is linking the microtubule dynamics to the signalling proteins and vice versa. First, the method for how the ROP6 and ROP2 concentration on each microtubule point, $R^*_{6,(\imath,\jmath)}$ and $R^*_{2,(\imath,\jmath)}$, and the microtubule concentration, M^* are found is explained in section 6.4.4.1. Second, how the signalling proteins affect the microtubules (through $\mathcal{P}_{RC}$) is then detailed in section 6.4.4.2.

6.4.4.1 Combining the triangulation mesh and microtubule co-ordinates

To find the ROP2 and ROP6 concentrations on microtubule $\imath$ at point $\jmath$ along its trajectory which has coordinates $(x^*_{M,(\imath,\jmath)}, y^*_{M,(\imath,\jmath)})$ both the three closest mesh coordinates (using the Euclidean norm), labelled $\mathbf{x}^*_{\eta_1}$, $\mathbf{x}^*_{\eta_2}$ and $\mathbf{x}^*_{\eta_3}$, and the weighted average ROP2 and ROP6 concentrations between these co-ordinates at the microtubule point are found. The weighted average allows accurate concentration values to be found at the microtubule points as the mesh coordinates closer to the microtubule point contribute more to the average. Thus,

$$R^{*k}_{I,(\imath,\jmath)} = \frac{c^{*k}_{I,\eta_1} w_1 + c^{*k}_{I,\eta_2} w_2 + c^{*k}_{I,\eta_1} w_3}{w_1 + w_2 + w_3}, \ I = 2, 6, \tag{6.4.52}$$

with weights defined by,

$$w_J = \frac{d^*_J}{d^*_1 + d^*_2 + d^*_3}, \ J = 1, 2, 3, \tag{6.4.53}$$

where d_J^* represents the distances from the mesh points to the microtubule coordinates and are calculated by,

$$d_J^* = \sqrt{\left(x_{\eta_J}^* - x_{M,(\imath,\jmath)}^*\right)^2 + \left(y_{\eta_J}^* - y_{M,(\imath,\jmath)}^*\right)^2} \text{ for } J = 1, 2, 3. \tag{6.4.54}$$

To save computation time, for each microtubule coordinate, the indices η_1, η_2 and η_3 are saved so that they do not need to found again for each time step.

To find the microtubule concentration $c_{M,i}^{*k}$ on a node i all the microtubule coordinates within a certain radius, r_M^* of the node are found and their total effect summed up. Here it is assumed that each microtubule coordinate has an area of effect characterised by the Gaussian distribution (as it is rotationally symmetric) such that if the microtubule point is at the exact same position as the mesh node, its effect is 1, but decreases to 0 as the node gets further away. The microtubule concentration is therefore,

$$c_{M,i}^{*k} = \sum_{\imath} \sum_{\jmath | d_{\imath,\jmath}^* < r_M^*} e^{-b_3^* d_{\imath,\jmath}^*}, \tag{6.4.55}$$

$$\text{where } d_{\imath,\jmath}^* = \sqrt{\left(x_i^* - x_{M,(\imath,\jmath)}^*\right)^2 + \left(y_i^* - y_{M,(\imath,\jmath)}^*\right)^2}, \tag{6.4.56}$$

which is summed over all microtubule points within range, where b_3 is the area of effect of the microtubule point. For each node coordinate, i the microtubule indices $\imath$ and $\jmath$ that are affecting this coordinate are saved to once again save computation time. This stored information is changed when required (likewise for η_1, η_2 and η_3) as a result of the ever-changing microtubule array (e.g. because of microtubules spawning, bundling events that cause microtubules to change direction and catastrophes events that remove microtubules from the system). Note that linking the microtubule dynamics to the mesh and vice versa is one of the most computationally expensive steps where entries in the stored information (which are stored in large matrices) will need to be found and then changed or deleted for each time step where numerous norms have to also be calculated.

Methods to calculate $\mathbf{c}_M^*$ which influences $\mathbf{c}_2^*$ and $R_{2,(\imath,\jmath)}^*$ and $R_{6,(\imath,\jmath)}^*$ which affects $R_{1,(\imath,\jmath)}^*$

in equations (6.4.47) and (6.4.51) respectively have now been found.

6.4.4.2 Signalling proteins effect on the catastrophe rate probability

The implementation of RIC1's effect on the microtubules is now described. As detailed in section 2.1.4.3 there is some uncertainty as to how exactly RIC1 promotes microtubules localisation to the indents. However, as RIC1 promotes order, it is assumed that high/low concentrations of RIC1 stabilises/destabilises the microtubules by decreasing/increasing their probability of a random catastrophe. This effect is included in combination with stress's stabilisation effect on the microtubules (see 5.2 for details). As it is unknown if either RIC1 or stress has the dominant effect on microtubule behaviour, it is assumed that they both contribute equally. Therefore, from equation (6.3.5),

$$g = a_4 \left(\frac{1}{2} g_{R_1} + \frac{1}{2a_1} g_\sigma \right), \tag{6.4.57}$$

where g_{R_1} is the RIC1 stabilisation term and g_σ is the stress stabilisation term characterised by equation 5.2.1 (and divided by a_1 so it now ranges between -1 and 1).

To derive g_{R_1} a single RIC1 concentration value called $\bar{R}^*_{1,i}$ is required for each microtubule i. This value is calculated using the weighted average R_1 concentration on each microtubule where higher valued weights are applied when $R^*_{6,(\imath,\jmath)}$ is higher in value to shift the average. When using the normal average in initial simulations, ROP6's stabilisation effect on the microtubules got drowned out as a result of there being only a few high RIC1 values due to ROP6 being concentrated around the indents. Thus the weighted average is used, with the weights defined as,

$$w(\imath,\jmath) = \vartheta \frac{R^*_{6,(\imath,\jmath)}}{\sup_{\imath=1\cdots m \ \&\ \jmath=minus_\imath^k \cdots plus_\imath^k}(R^*_{6,(\imath,\jmath)})} + (1-\vartheta), \tag{6.4.58}$$

where the first term takes a value ranging from 0 to 1 and is higher when the ROP6 concentration is higher and ϑ also ranges from 0 to 1 and scales the extra weight given to a point with a high ROP6 value. Thus if $\vartheta = 0$ this equation is the normal average and if

$\vartheta = 1$ all the weights are completely determined by the scaled ROP6 concentration. The weighted average RIC1 concentration per microtubule is then,

$$\bar{R}^*_{1,\imath} = \frac{\sum_{\jmath=minus^k_\imath \cdots plus^k_\imath} R^*_{1,(\imath,\jmath)} w(\imath,\jmath)}{\sum_{\jmath=minus^k_\imath \cdots plus^k_\imath} w(\imath,\jmath)}. \tag{6.4.59}$$

With $\bar{R}^*_{1,\imath}$ being the shifted RIC1 average on microtubule $\imath$. Once again using the logistic function, due to its plateauing nature RIC1's effect it characterised by,

$$g_{R_1} = \frac{1}{1 + e^{b^*_4(\bar{R}^*_{1,\imath} - c^*_4)}} - \frac{1}{2}, \tag{6.4.60}$$

where b^*_4 affects how quickly the function reaches its maximum or minimum value and c^*_4 is the threshold value for which $\bar{R}^*_{1,\imath}$ needs to be higher than for the logistic function to take positive values.

All the characterising equations for the signalling network model have now been obtained. How the system is implemented is summarised in the flow diagram (see figure 6.2) which illustrates what happens in each time step.

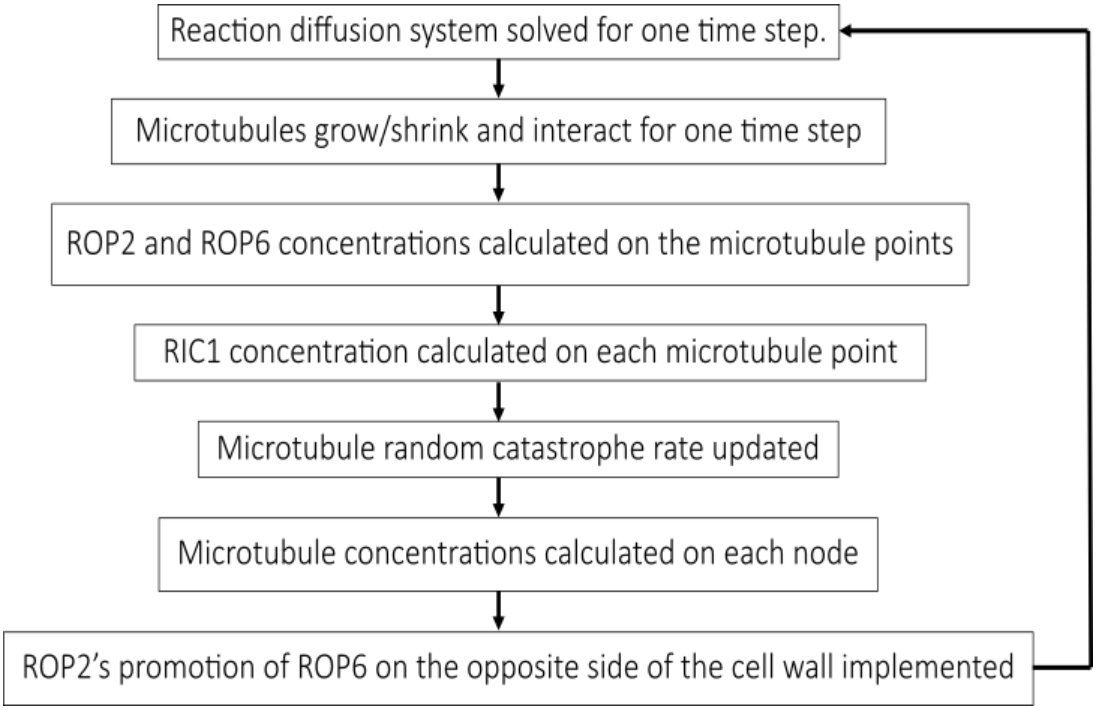


Figure 6.2: Flow diagram illustrating how the system is solved.

6.4.5 Model parameters

Unlike the microtubule model, where realistic values could be found for the majority of the parameters, for the signalling network model, the parameters have to be estimated by finding realistic bounds and performing test simulations. The parameters are displayed below (table 6.1) with the full details of how they are estimated left to the appendix A.4.1.

The diffusion rates can however be fixed as the active forms of the ROPS diffuse in the plasma membrane and, as a result, diffuse slower than if there were in the cytoplasm [Payne and Grierson, 2009, Jilkine et al., 2007, Postma et al., 2004]. The parameters that were not first introduced in this chapter, like the time-stepping value, Δt^*, are the same as in the microtubule model as stated in section 5.3 in table 5.1.

Table 6.1: All parameters values for the signalling network model

Paramater	Value	Paramater	Value
$D_i^*\ i = 2, 6, 4$	$0.1\mu\text{m}^2\text{s}^{-1}$	λ_2^*	10mol min^{-1}
λ_6^*	0.1mol min^{-1}	δ_2^*	0.5min^{-1}
δ_6^*	0.5min^{-1}	δ_4^*	10min^{-1}
δ_1^*	1min^{-1}	k_{21}^*	$0.3\text{mol}^{-1}\text{min}^{-1}$
k_{M2}^*	$0.0074\text{mol}^{-1}\text{min}^{-1}$	k_{61}^*	50min^{-1}
k_{24}^*	10min^{-1}	a_2^*	1000mol
b_2	15	c_2	0.6
b_3^*	$0.5\mu\text{m}^{-1}$	ϑ	0.86
a_4	a_1	b_4^*	0.1mol
c_4^*	21mol		

6.5 Results and discussion

A model that includes every known and relevant interaction hypothesised to determine pavement cell shape (apart from ROP2's possible promotion of itself) has been established.

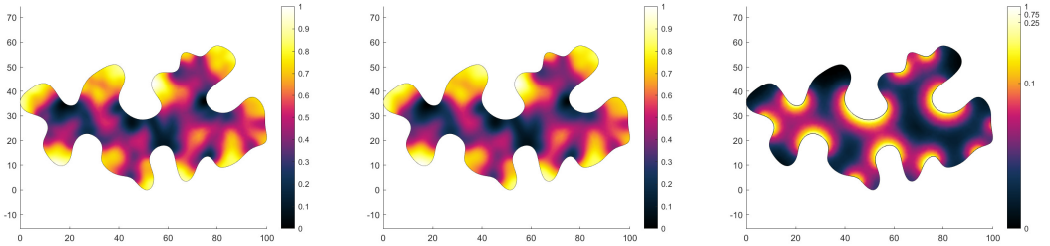
Therefore simulations can now be performed to test the validity of the theory that this signalling network sustains/further develops and initiates pavement cell lobeing.

The first aspect of this theory to be tested, is that this network of interactions and feedback loops are enough to establish a steady-state, where ROP2/RIC4 and microtubule localise to the lobes and indents, respectively, to allow pavement cells to further develop their morphology. These simulations are done in mature pavement cell outlines that have well-developed lobes and are displayed and analysed in section 6.5.1. Secondly, the robustness of this signalling network is tested by performing simulations in perturbed scenarios. Specifically, the pavement cell mutants CA ROP2, CA ROP6, DN ROP2, and DN ROP6 are simulated and by comparing to experimental results, the signalling network and model could both be validated or the network could be shown to have missing information. These mutant simulations are done in less developed pavement cells (as the effect of these mutations occurs early on in pavement cell development, but still wish to see if any indent or lobe localisation occurs) and are shown and discussed in section 6.5.2. Lastly, by examining simulations for signs of microtubule or ROP2/RIC4 localisation on straight wall segments it is investigated whether the signalling network can initiate lobes or indents. These simulations are run in small pavement cells with very little lobeing and are presented and examined in section 6.5.3.

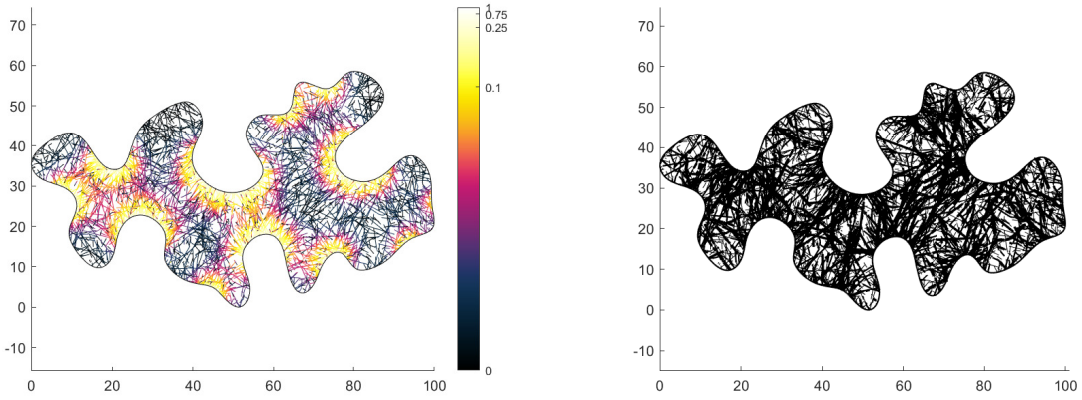
For all simulations, the normalised concentrations are shown, so that they are all ranging between 0 and 1 to allow easy comparison between different figures. This normalisation is mainly because of the simulations in young pavement cells in section 6.5.3, where the concentration ranges in the different outlines are all different from one another. Also, for simplicity and clarity, for each simulation set, the results (the ROP2, ROP6, RIC4, and RIC1 concentrations and the microtubule array) of only one pavement cell outline are shown with the rest presented in the appendix A.4.

6.5.1 Testing the signalling protein and microtubule network localisation establishment

This section aims to examine whether the signalling network is enough to help further develop pavement cells. As detailed in section 2.1.4.3, it is hypothesised that as a result of the signalling protein and microtubule network, ROP2 localises to the lobes helping promote growth, and the microtubules localise to the indents where they restrict growth. Examining the results will allow us to present evidence for or against this hypothesis. The simulations are run in the 10 different mature pavement cells, which we set to be of order $100\mu m$ in length (see section 4.3.1) for 5000 time steps with $m_{max} = 4000$.



(a) ROP2 (b) RIC4 (c) ROP6



(d) RIC1 (e) Microtubule array

Figure 6.3: Reaction diffusion model results in the 6th mature pavement cell outline where figures a b c and d show the different signalling protein concentrations and e shows the microtubule array where the lines increase in thickness as more microtubules are contained in that bundle. Figures c and d have nonlinear scalebar in order to see concentration variations clearly.

The analysis of the results begin by examining the ROP2 concentration. In the simu-

lations, ROP2 can be observed to consistently localising to the lobes (figure 6.3a) with low concentrations in the indents. As ROP2 promotes RIC4, RIC4 is also seen to localise to the lobes and excluded from the indents (figure 6.3b). Both ROP2 and RIC4's localisation is also robust with this phenomenon is witnessed in all of the differently shaped pavement cells (figures A.6-A.22a). ROP2 and RIC4 have both been biologically observed to localise to the lobes, corroborating the model outputs. However, some examples of weak or lack of localisation in some smaller sized lobes can be seen (e.g the top right of figure A.10a).

When ROP6 is observed (figure 6.3c), consistent localisation to the indents can be seen due to the effect of the boundary conditions, which is mirroring ROP2's localisation to the lobes. ROP6 has been biologically observed to localise to the indents, authenticating the model results. When RIC1 is also examined in the simulations, high concentrations along the microtubules at the indents and low concentrations in the lobes are observed (figure 6.3d). This variation results from the different ROP2 and ROP6 concentrations inhibiting and promoting RIC1 in the indents and lobes, respectively. These differing concentrations of RIC1 will stabilise the microtubules along the indents and vice versa in the lobes to help promote microtubule patterning.

Consistent microtubule localisation to the indents can be seen in all the pavement cells shapes where they bundle up and fan out which is complemented by a lack of microtubules in the lobes. The microtubule localisation to the indents will then inhibit ROP2, preventing ROP2 localisation to the indents and on the other hand, the ROP2 localisation to the lobes through its inhibition of RIC1 helps prevent microtubule localisation to the lobes. This microtubule behaviour directly agrees with what is experimentally observed (see section 4.3.2), demonstrating the realistic results of the model.

The model results have therefore managed to strongly match to the biological observations. Each signalling protein starts at a concentration of 0, with all the microtubules also starting at a singular random point and growing in a random direction. The localisation of the various proteins and the microtubules is therefore an emergent property of the system where the microtubules will then be able to stiffen the indenting regions, and the

ROP2/RIC4 pathway can soften the lobeing regions. All the relationships between the signalling proteins are simple, meaning we are not forcing this behaviour as no Turing patterning mechanisms are included, which are known to cause spatial heterogeneous protein expression. Therefore, we have provided evidence for the hypothesis that this signalling network is sufficient to control the further development of pavement cell lobes. The proof of this hypothesis is not yet complete, as it is still to be shown whether the signalling network's effect on the wall properties actually leads to the further development of pavement cells. This proof will be done using the vertex element model in the next chapter. Nonetheless, this result still helps to validate the model as a biological phenomenon has been successfully recreated.

There are also questions remaining in pavement cell development. Pavement cells only grow in 2 dimensions as they need to maintain a constant height to make sure the leaves stay thin. To ensure their height is maintained, the adaxial pavement cell periclinal walls are 10 times thicker to resist expansion as the top periclinal wall has no other neighbouring cells to balance out the turgor forces [Szymanski, 2014]. Discussion around this signalling network examines how the microtubules localise to develop and initiate lobing, but not how they are organised to deposit cellulose to resist axial strain. This arrangement is an essential pavement cell feature that has seemed to be ignored and should be investigated further to fully understand how pavement cell development works.

6.5.2 The signalling network in mutant pavement cells

With the model working and matching the observations made in wildtype, more simulations are now performed in mutants. Recreating experimentally observed biological behaviour will help to validate the model further or alternatively if the results do not match, missing parts of this signalling network may be revealed. The mutant simulations we are performing are CA ROP2, CA ROP6, DN ROP2 and DN ROP6.

From biological experiments, the following observations have been made of these mutants (see section 2.1.4 for details). For CA ROP2, both actin and RIC4 were found to be

evenly distributed throughout the cell, where the organisation of the microtubule array was also delayed with little microtubule localisation to the indents [Fu et al., 2005, 2002, Panteris and Galatis, 2005]. Observations of CA ROP6 found the microtubules to form traverse arrays that were perpendicular to the elongation axis [Fu et al., 2009]. By examining DN ROP2, pavement cells were found to form lobes with small amplitudes with very little actin localisation to the lobes, where the microtubules were also found to form more and thicker bundles [Fu et al., 2005, 2002]. Finally, regarding DN ROP6, observations found the mutant to form wide lobes due to fewer microtubules that were more disorganised and less bundled [Fu et al., 2009]. When examining the results, actin expression is expected to be mirrored by ROP2 (as actin is supposedly downstream from ROP2) such that when there is little actin or when it is uniformly distributed as mentioned in the experiments above, ROP2 will follow a similar pattern.

To simulate the CA mutants, the base production rates are increased, and for the DN mutants, these rates are decreased and additionally, for DN ROP6, the effectiveness of the boundary conditions are decreased. Thus for the CA ROP2 simulations $\lambda_2^* = 100$, the CA ROP6 simulations $\lambda_6^* = 100$, the DN ROP2 simulations $\lambda_2^* = 0.1$ and the DN ROP6 simulations $\lambda_6^* = 0.01$ and $a_2^* = 10$ where all these simulations are run for 3000 time steps with $m_{max} = 3000$.

Simulations were run in 9 different cell shapes where all the mutants are presented next to their control simulations with a matching colour bar (figures 6.4-6.13). The numbers presented on the colour bars are the critical numbers which are the maximum values of the control and the mutant concentrations (where most of the colour bar scalings are non-linear to highlight concentration variations).

6.5.2.1 CA ROP2

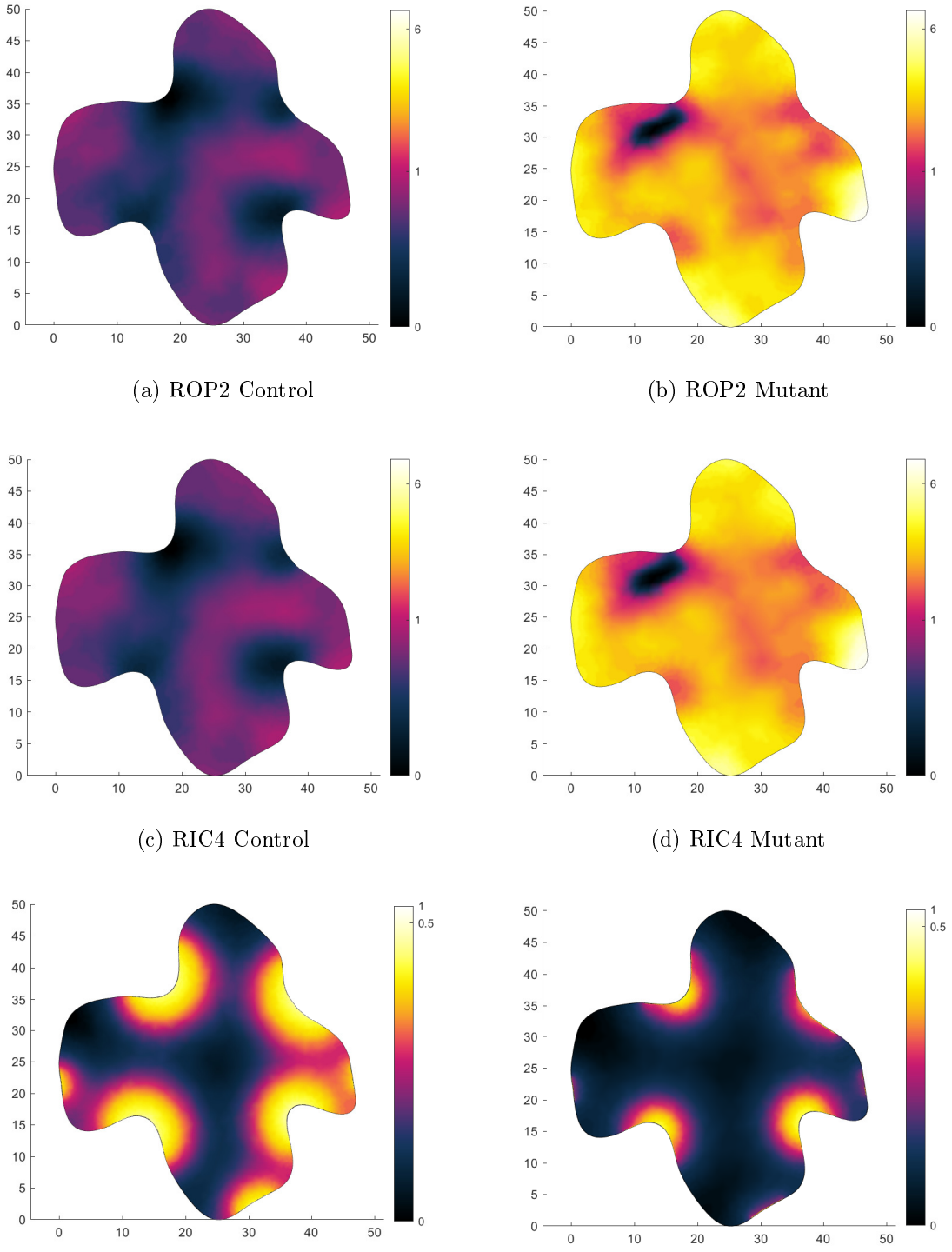
The mutant analysis is begun with the CA ROP2 simulations. As a result of the increase in ROP2's production the concentration of ROP2 has generally increased (figure 6.4a and b). This effect has then led to an increase in RIC4 in all simulations (figure 6.4c

and d) where the RIC4 concentration distribution seems less localised to the lobes and is increasingly uniform with high rates of expression when compared to the control, an effect seen in biological experiments. On top of this, as a result of ROP2 being less localised, its mirroring effect on ROP6's boundary conditions is lessened causing a decrease in ROP6's expression (figure 6.4e and f) to the indents.

ROP2's over expression also majorly decreases RIC1's concentration along the microtubules (figure 6.5a and b), which will consequently destabilise the microtubules and cause the microtubule random catastrophe rates $\mathcal{P}_{RC}$ to increase. As a result of this destabilisation effect disorganised microtubule arrays are observed (figures 6.5c and d) with the microtubules becoming less localised to the indents. CA ROP2's effect on the microtubule array can be seen quantitatively (figure 6.6) where the number of indent localisation instances is decreased in the mutants in all in the different pavement cell outline simulations with this difference being significant in all but one of the cases (see section 5.4.3 for details of how the localisation instances is measured). The simulations have therefore recreated biological observations of both the microtubule array and of RIC4's concentration distribution demonstrating the accuracy of the model.

6.5.2.2 CA ROP6

The results of the CA ROP6 simulations are now examined. Firstly, the protein distribution of both RIC4 and ROP2 seems largely unaffected. However, in some cases, both an increase and decrease in localisation to the lobes can be observed due to the microtubules strongly associating with the indents and because of the changed microtubule array respectively (figure 6.7a, b, c and d). Secondly, a significant increase in the ROP6 levels across the cell can be seen (figure 6.7e and f) which in turn has caused an increase in RIC1's concentration along all the microtubules (figure 6.8a and b) leading to a decrease of $\mathcal{P}_{RC}$ which helps to stabilise them (and not just those that are localised to the indents as in the control). Consequently, in nearly all cases, the microtubule array has changed (figures 6.8b and c). To display this rearrangement more obviously, the microtubule angle



(a) ROP2 Control

(b) ROP2 Mutant

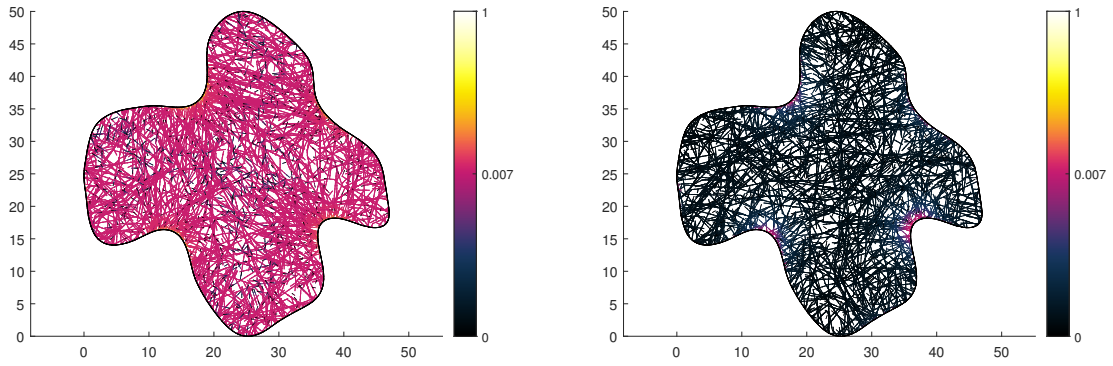
(c) RIC4 Control

(d) RIC4 Mutant

(e) ROP6 Control

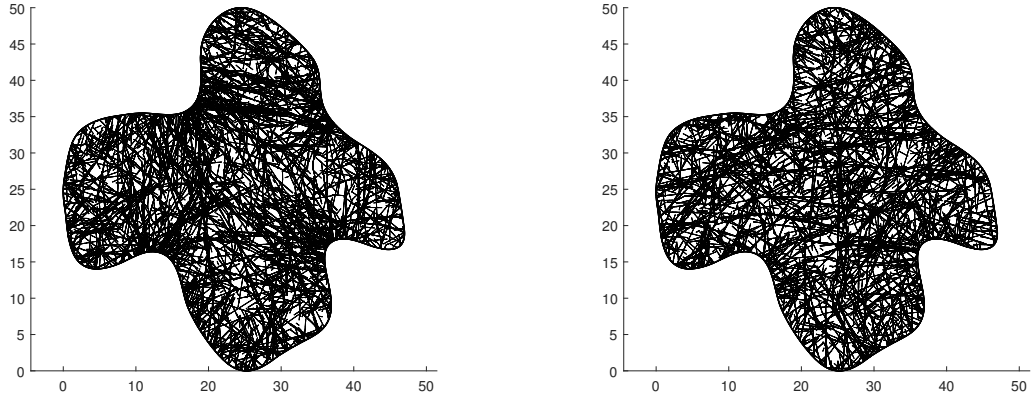
(f) ROP6 Mutant

Figure 6.4: Reaction diffusion model results in the 8th less developed pavement cell outline where each figure shows the different signalling protein concentrations where figures a c and e are the results from the control simulations and b, d and f show the result from the CA ROP2 simulations



(a) RIC1 Control

(b) RIC1 Mutant



(c) Microtuble array control

(d) Microtubule array mutant

Figure 6.5: Reaction diffusion model results in the 8th less developed pavement cell outline where figures a and b shows the RIC1 concentrations and c and d show the microtubule arrays where the lines increase in thickness as more microtubules are contained in that bundle. Figures a and c show the control simulation results and b and d show the CA ROP2 simulations results.

distributions are displayed with a black line showing the long axis direction found by fitting an ellipse onto the cell outlines [Ohad, 2021]. Upon examination, the microtubule angle distributions (figures 6.8d and e) are increasingly orientated transversely to the long axis, a phenomenon observed experimentally.

One of the big questions that arises from these simulations is why do the microtubules rearrange as a result of the microtubule's random catastrophe rates decreasing (from the raised ROP6 and RIC1 levels)?. This effect is interesting as it links to the microtubule simulations in chapter 5 where the microtubules are found to increasingly align transver-

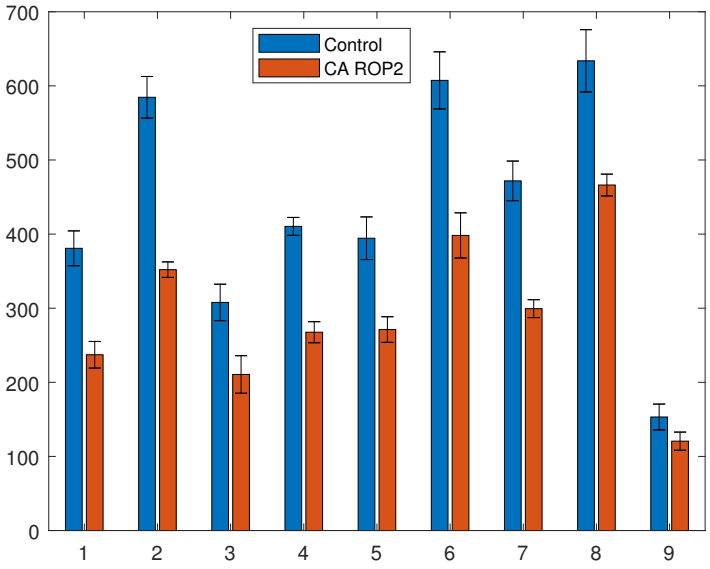
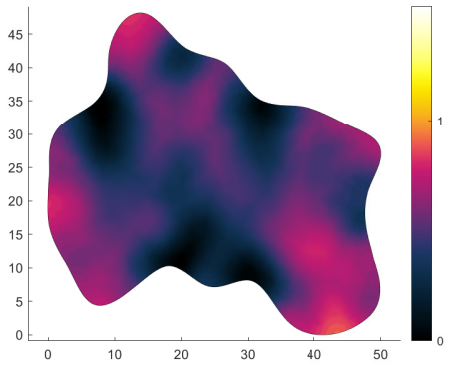


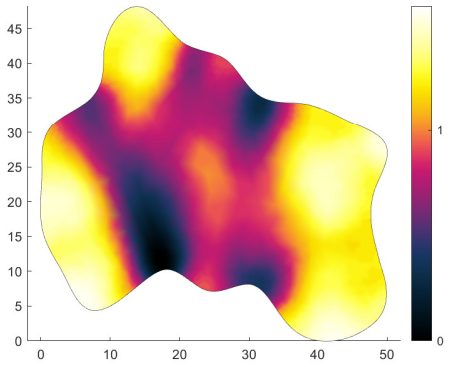
Figure 6.6: The average number of microtubule indent localisation instances with standard deviation error bars over all pavement cell outlines calculated from the 3000, 2000, 1500, 1000 and 500 time steps

sally to the long axis as the interaction probabilities are increased. Perhaps in both cases there is some underlying principle as to why this happens. In a rectangular-like domain, the microtubules growing transversally (the short axis) have to cover less distance to reach the boundary, meaning fewer opportunities for them to suffer a collision-induced catastrophe compared to the longitudinally growing microtubules and once at the boundary, they can stay there. So conceivably in the pavement cell control case, there is a natural bias to the short axis, but in the mutant case, where the microtubules have a lower random catastrophe rate, the transversally orientated microtubules now stay around for longer and present more barriers for the microtubules growing longitudinally making them more likely to suffer from a collision-induced catastrophe. This principle could be the same fundamental process when the interaction probabilities are changed in the last chapter. The microtubule array increasingly orients transversally as $\mathcal{P}_{CC}$ is increased, as longitudinally growing microtubules possibly become decreasingly likely to make it across the whole cell distance. We can, therefore, hypothesise that signalling proteins could control the microtubule array and hence the growth direction simply through the microtubule

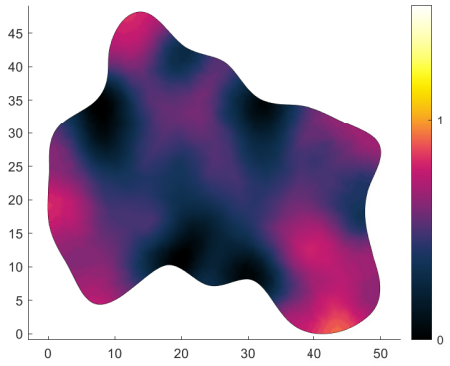
catastrophe rates.



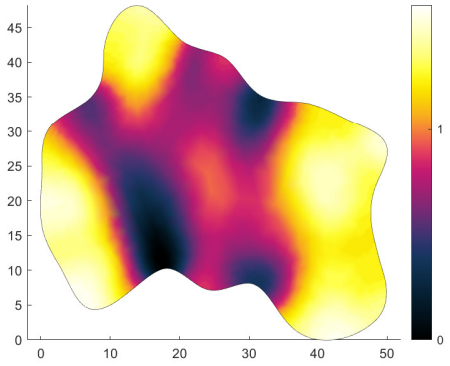
(a) ROP2 Control



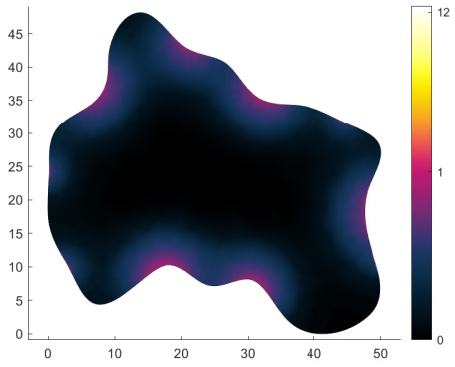
(b) ROP2 Mutant



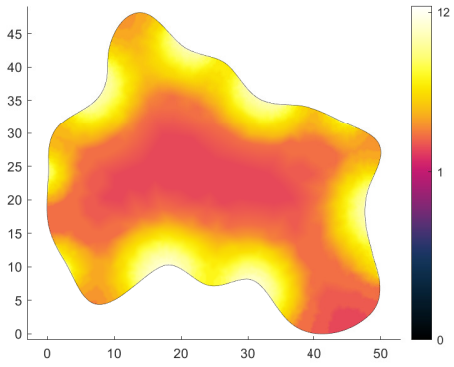
(c) RIC4 Control



(d) RIC4 Mutant

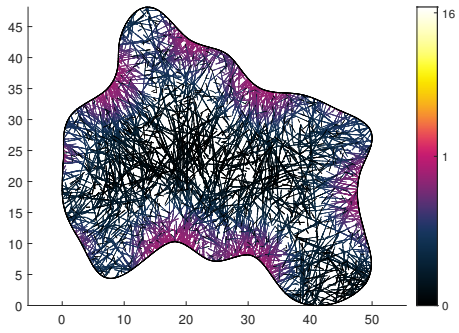


(e) ROP6 Control

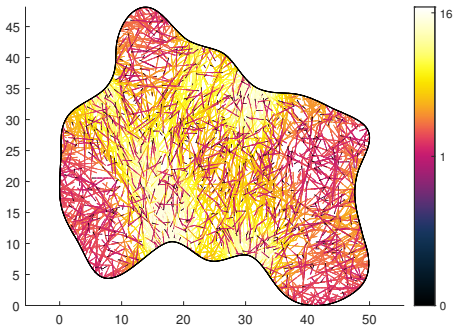


(f) ROP6 Mutant

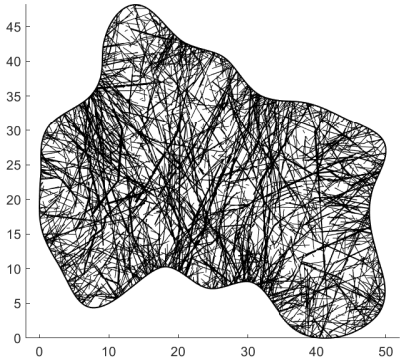
Figure 6.7: Reaction diffusion model results in the 5th less developed pavement cell outline where each figure shows the different signalling protein concentrations where figures a c and e are the results from the control simulations and b, d and f show the result from the CA ROP6 simulations



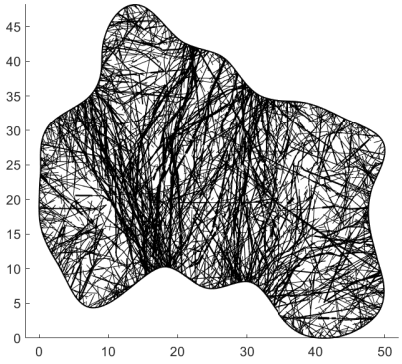
(a) RIC1 Control



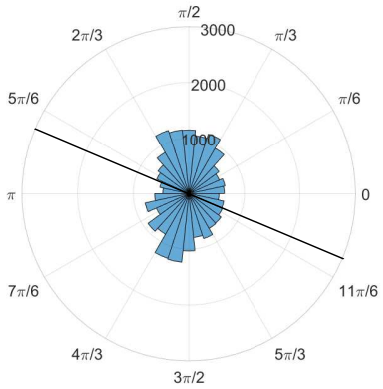
(b) RIC1 Mutant



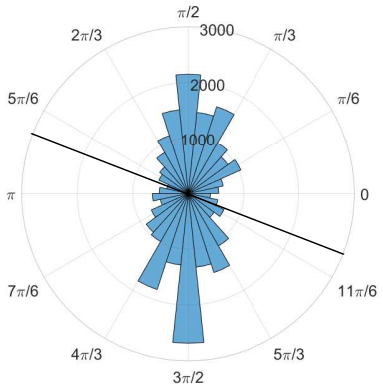
(c) Microtuble array control



(d) Microtubule array mutant



(e) Microtuble array distribution control



(f) Microtubule array distribution mutant

Figure 6.8: Reaction diffusion model results in the 5th less developed pavement cell outline where figures a and b shows the RIC1 concentrations, c and d show the microtubule arrays where the lines increase in thickness as more microtubules are contained in that bundle and e and f showing the microtubule arrays angle distribution with the black line showing the long axis direction. Figures a c, and e show the control simulation results and b, d and f show the CA ROP6 simulations results.

6.5.2.3 DN ROP2

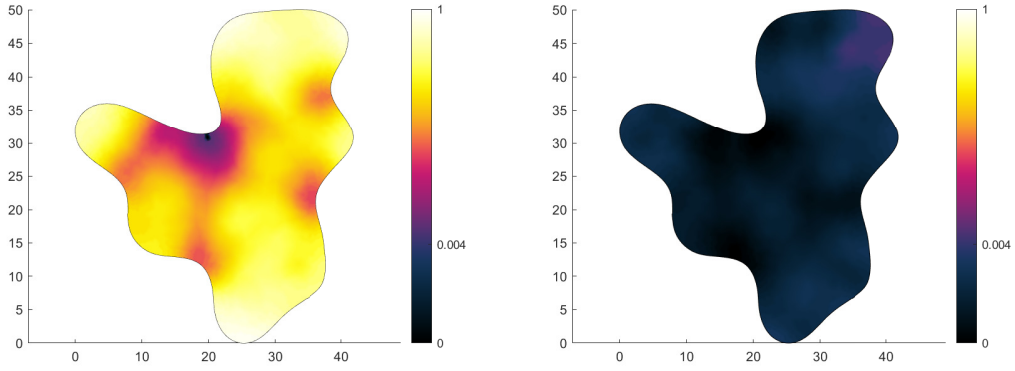
The dominant negative mutants are now examined, beginning with ROP2. Upon analysing the results, a general reduction in the ROP2 levels throughout the cellular domains (figures 6.9a and b) and a reduction in ROP2 localisation to the lobes can be seen. As a consequence of this decrease in ROP2, the exact same expression pattern for RIC4 can be observed (figure 6.9 c and d) which means actin could follow a similar pattern. This finding matches experimental observations that observed little actin localisation to the lobes. When ROP6 is examined, its expression is dramatically decreased as a result of ROP2 no longer being able to promote its production on the opposite side of the cell wall (figure 6.9e and f). As a result of the reduced ROP2, RIC1's concentration along the microtubules have become generally higher, and due to the reduced ROP6 levels at the boundaries, RIC1's concentrations have become more evenly distributed. In consequence of the raised RIC1 levels, the microtubules are being increasingly stabilised and are consequently bundling more (figure 6.11) for all cell outlines simulations (wherein several cases this difference is significant). Increased microtubule bundling has been experimentally observed in this mutant, meaning experimental behaviour has once again been experimentally recreated. It is also noted that because of RIC1's even distribution (and from the lack of ROP6 localisation to the indents), the microtubule array has become disrupted with less microtubule localisation to the indents (figure 6.10c and d).

This lack of ROP6 and microtubule localisation to the indents is an interesting phenomenon as it is here that the model results differ from observed behaviour. DN ROP2 mutants have been seen to have lobes with reduced amplitude but not necessarily wider necks, which are observed when the microtubule array is disrupted (lack of microtubule localisation) [Armour et al., 2015, Szymanski, 2014]. To our knowledge, we have not seen any reference to the disruption of the ROP6 or microtubule localisation in the DN ROP2 mutants in the literature. This result suggests that something is missing from the current understanding of how this signalling network works. Without ROP2's stimulation of ROP6 through the boundary conditions, there is nothing else to promote ROP6's

indent localisation, which is needed to promote microtubule localisation to the indents. The model has therefore demonstrated the limitations of the current signalling network hypothesis. Some interesting papers which have yet to be peer-reviewed could fill in this missing information [Lin et al., 2018, Yang et al., 2021]. It has been suggested that cell wall receptors attached to pectin in the cell wall, sense stress, which can then activate ROP6, stabilising the microtubules in these stressed regions. Thus this mechanosensing could be what is missing from the model. There is, therefore, a need for further work to explore the feasibility behind this idea, where future modelling effort should include this mechanosensing to see whether the observed realistic phenotype could be recovered.

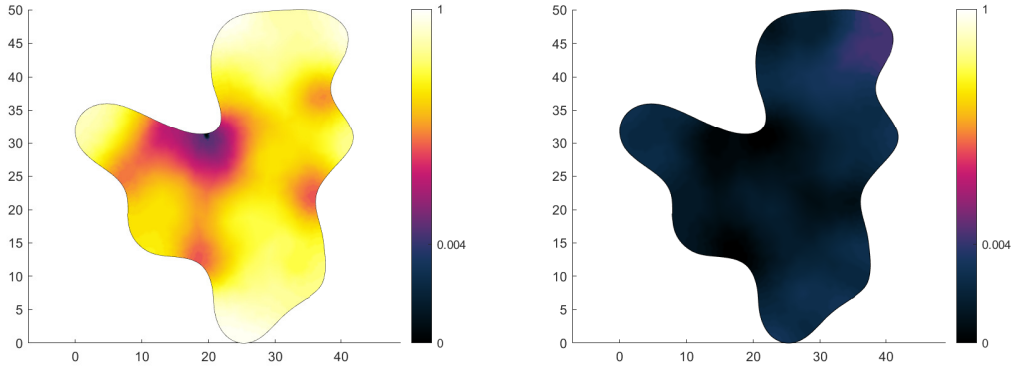
6.5.2.4 DN ROP6

The last mutant to be examined is DN ROP6. From observations, the ROP6's concentration has significantly reduced (figures A.154e and f), which has caused a drop in RIC1's concentration along the microtubules (figures 6.13a and b). The drop in RIC1's concentration then destabilises the microtubules, causing the array to be significantly disrupted with little localisation to the indents (figures 6.13c and d). Biological experiments have observed the exact same phenomenon demonstrating the accuracy and the validity of the model. However, microtubules are seen to be increasingly bundled up in the mutant simulations which contradicts what has been seen in experiments (figure 6.14). This result could be occurring as a result of the lack of microtubule indent localisation allowing the microtubules to form increasingly aligned arrays which could promote bundling (figure 6.13). This result is not too concerning as the central feature of microtubule disruption in the mutants has been reproduced. Both ROP2 and RIC4's concentrations are seen to be reduced with less localisation to the indents (figures A.154a, b, c and d). This reduction is due to the microtubule array being more evenly disrupted, so ROP2 is being inhibited throughout the cellular area.



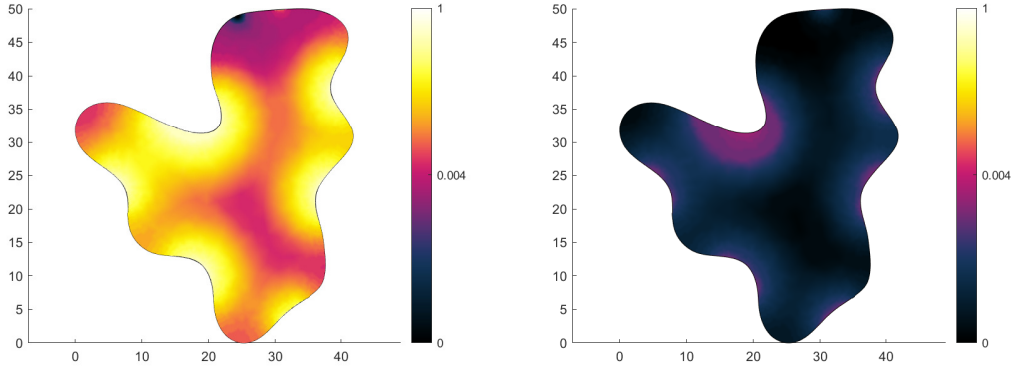
(a) ROP2 Control

(b) ROP2 Mutant



(c) RIC4 Control

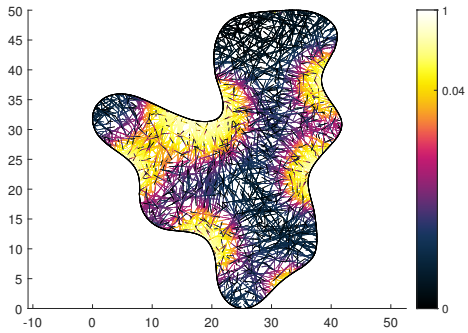
(d) RIC4 Mutant



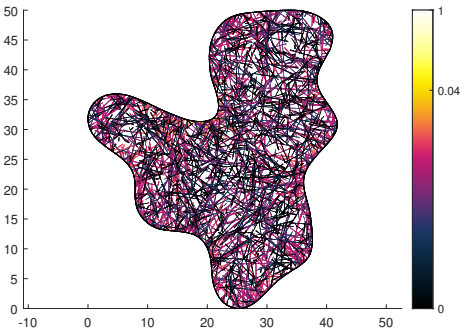
(e) ROP6 Control

(f) ROP6 Mutant

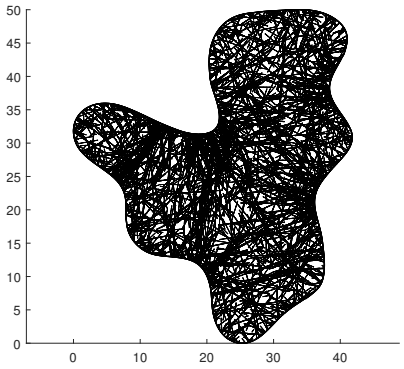
Figure 6.9: Reaction diffusion model results in the 2nd less developed pavement cell outline where each figure shows the different signalling protein concentrations where figures a c and e are the results from the control simulations and b, d and f show the result from the DN ROP2 simulations.



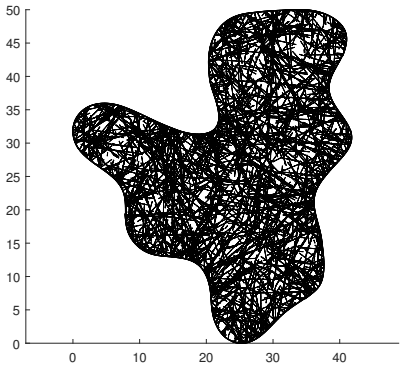
(a) RIC1 Control



(b) RIC1 Mutant



(c) Microtuble array control



(d) Microtubule array mutant

Figure 6.10: Reaction diffusion model results in the 2nd less developed pavement cell outline where figures a and b shows the RIC1 concentrations and c and d show the microtubule arrays where the lines increase in thickness as more microtubules are contained in that bundle. Figures a and c show the control simulation results and b and d show the DN ROP2 simulations results.

6.5.3 Can the signalling network initiate lobes?

With the model validated, we now test whether the signalling network can set up an alternating pattern of ROP2 and microtubule localisation sites to initiate lobes and indents, respectively. However, we first analyse if the signalling network can help further develop the existing pavement cell lobes at this scale. Simulations are run in 13 different pavement cell outlines with $m_{max} = 1200$ for 3000 time steps.

Examinations of the simulations begin by looking for any evidence of ROP2 and microtubule lobe and indent localisation patterning. From the results, in the larger lobes

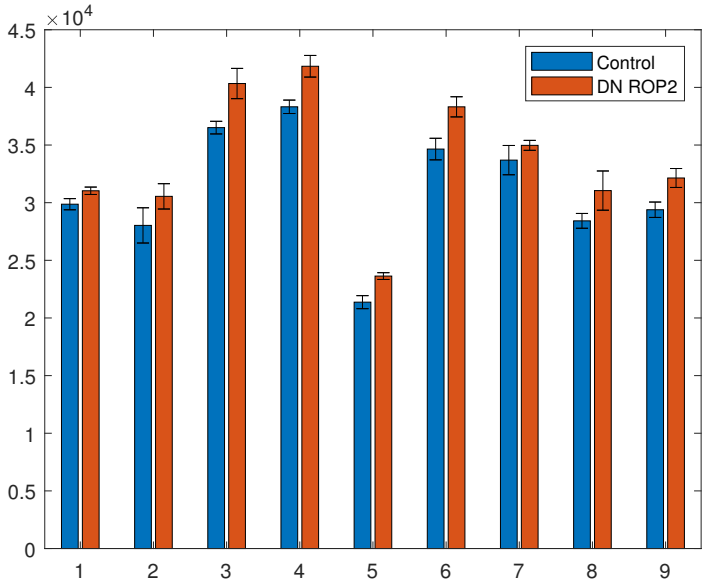
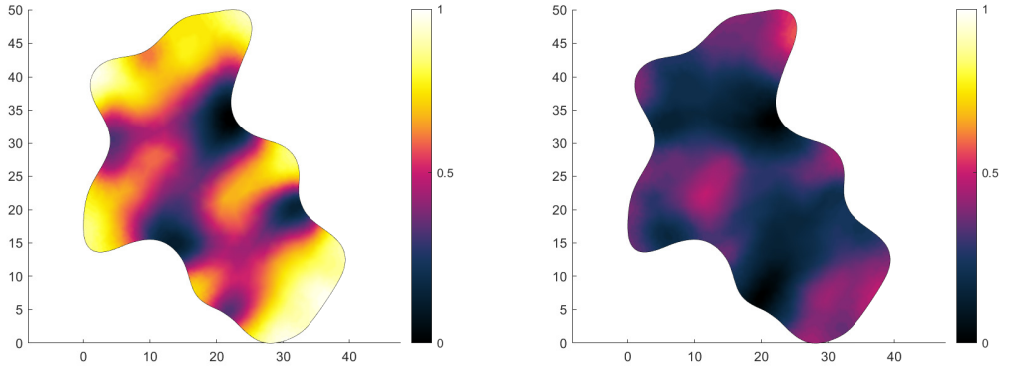


Figure 6.11: The average number of microtubule co-ordinate points contained in bundles for each cell outline averaged over the 500, 1000, 1500, and 2000, 3000th time steps with standard deviation bars.

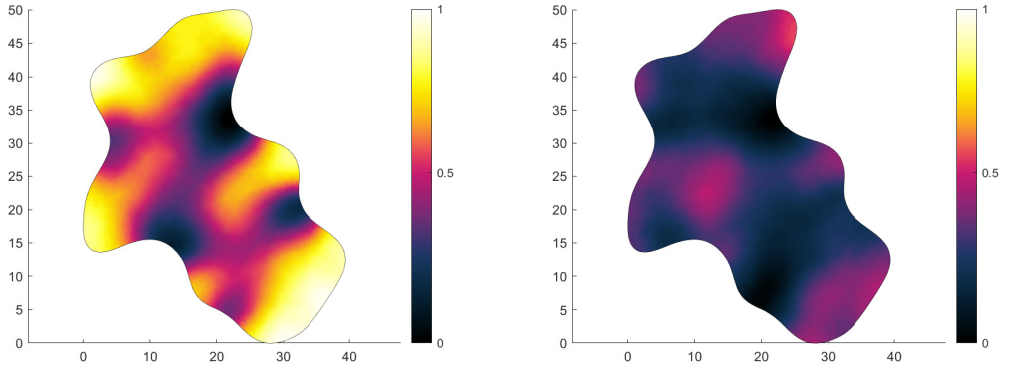
and indents some ROP2 and microtubule localisation, respectively, can be seen (figure 6.15a), but as a whole, little localisation of the two is observed in the smaller indents and lobes. The model does not seem to work at this scale. These simulations are also run with different parameters to ensure that they were not the issue. To make sure the microtubules can interact with one another so organisation can occur in the smaller domains, the interaction probabilities are set to $\mathcal{P}_{CC} = 0.5$ and $\mathcal{P}_B = 0.4$ (using the simulations in section 5.4.1 to inform the decision), the range of effect of the microtubules is also decreased by setting $b_3^* = 10$ and the ROP2 sensitivity to the microtubules is also increased by setting $k_{M2}^* = 0.0517$. However, even with these changes, lobe and indent localisation could still not be obtained. The model has been shown to be accurate, with validation simulations run in both large wildtype pavement cells (section 6.5.1) and several mutant types in medium-sized pavement cells (section 6.5.2). For it not to work at this scale, there could be something missing from the signalling network.

The signalling proteins have inactive forms which diffuse quickly in the cytoplasm. Champneys et al. [2021] included these inactive forms in their model and got periodic



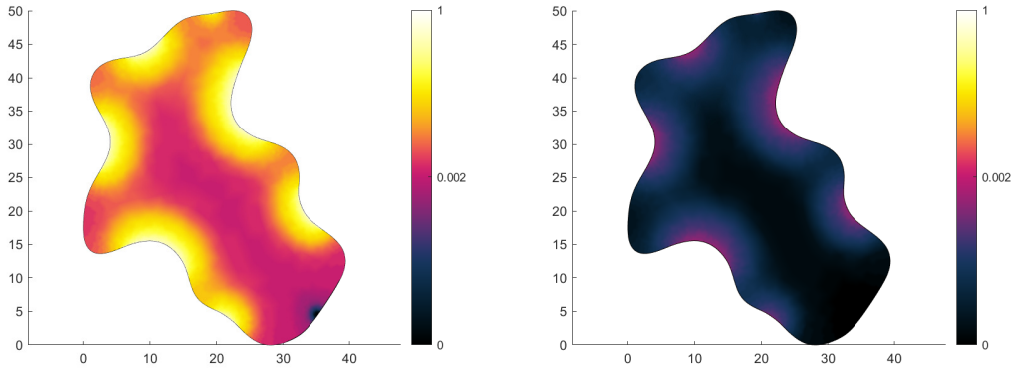
(a) ROP2 Control

(b) ROP2 Mutant



(c) RIC4 Control

(d) RIC4 Mutant

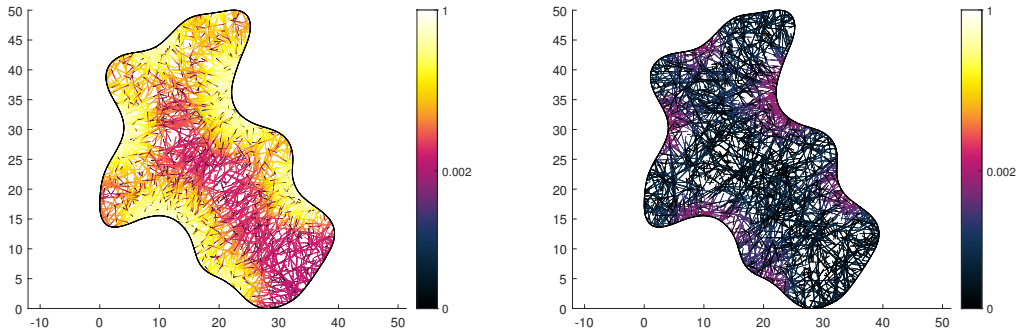


(e) ROP6 Control

(f) ROP6 Mutant

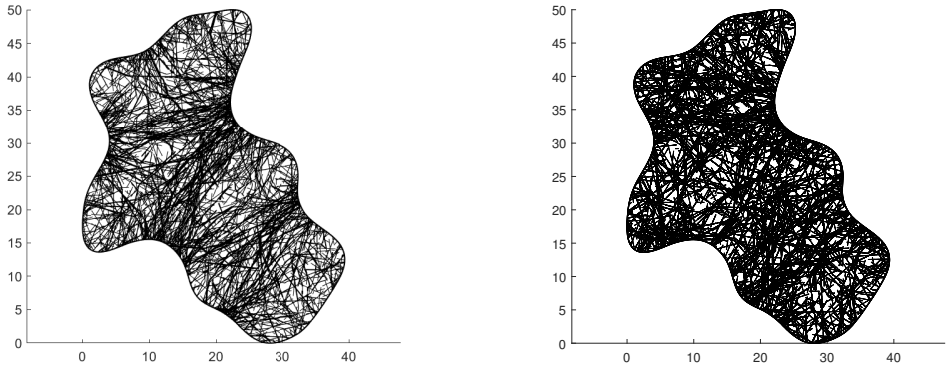
Figure 6.12: Reaction diffusion model results in the 10th less developed pavement cell outline where each figure shows the different signalling protein concentrations where figures a c and e are the results from the control simulations and b, d and f show the result from the DN ROP6 simulations.

patterns of ROP2 and ROP6 expression. So possibly in this length scale, the inclusion of the inactive forms becomes important. Other proteins could also be essential at this



(a) RIC1 Control

(b) RIC1 Mutant



(c) Microtuble array control

(d) Microtubule array mutant

Figure 6.13: Reaction diffusion model results in the 10th less developed pavement cell outline where figures a and b shows the RIC1 concentrations and c and d show the microtubule arrays where the lines increase in thickness as more microtubules are contained in that bundle. Figures a and c show the control simulation results and b and d show the DN ROP6 simulations results.

scale, such as SCAR, which has been hypothesised to promote lobe formation through actin [Qian et al., 2009].

Alternatively, maybe the issue is with the microtubule model. As a result of this small domain, microtubules grow and reach the boundary quicker (where they remain there until they suffer a random catastrophe) when compared to the other simulations in larger domains, meaning they have fewer opportunities to interact. This feature could limit the microtubules' ability to organise to the indents. So in the smaller domain simulations, the limitations of modelling in 2D could be more prevalent. Future work on this signalling network should delve into these issues by including the inactive forms and

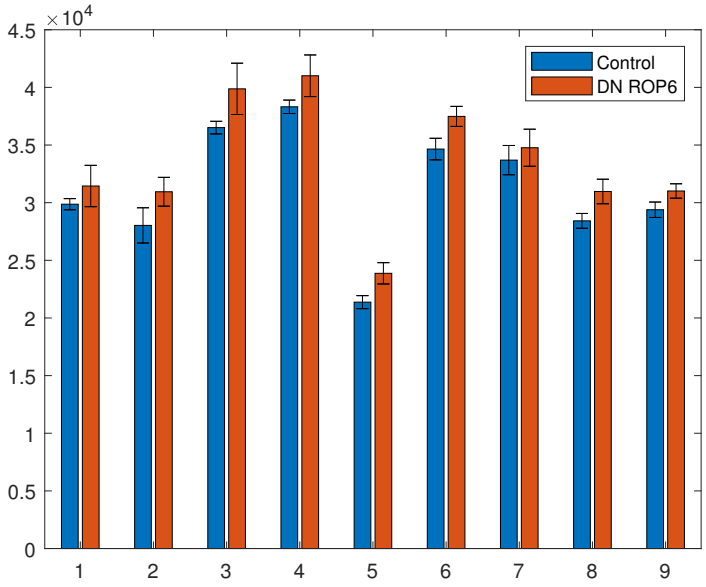


Figure 6.14: The average number of microtubule coordinate points contained in bundles for each cell averaged over the 500, 1000, 1500, 2000 and 3000th time steps with standard deviation bars

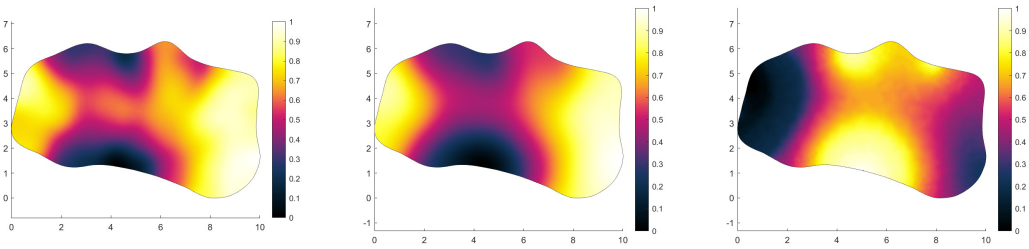
possibly modelling in 3D.

Despite the apparent negatives of these findings, the lack of ROP2 and microtubule localisation remains an interesting result, as in the model, every interaction that the literature declares to be important has been included, thus this network has been shown to be insufficient to explain dynamics in young pavement cells.

We now investigate if there is any evidence that this signalling network sets up lobe or indent initiation sites. From examining the different simulations, no consistent proof of alternating microtubule and ROP2 localisation patterning on the straight wall segments can be seen which could be lobe or indent initiation sites (figures 6.16b). On top of this, in actual pavement cells, lobes get initiated in mature cells as well [Zhang et al., 2011], meaning possible initiation sights should have appeared in the simulations in section 6.5.1, however nothing convincing was seen. This suggests that this network of signalling proteins can not cause lobe initiation. If lobes are chemically initiated there must be some other pathways that are currently unknown and therefore missing from the model that helps create the alternating patterning of ROP2 and microtubules.

These pathways may have already been revealed by Champneys et al. [2021] who assumed that the ROP2 ROP6 with their active and inactive forms behave like a Turing system and found them to form alternating patterns of expression in a 1D domain. Extending this model to a 2D system could give us clues as to how lobes could be chemically initiated. A good way to test this potential model would be to see the effect and sensitivity of the parameters on the number of lobes initiated as similar species exhibit different lobeyness scales [Vőfély et al., 2018]. Another theory as to how lobes get initiated which warrants further investigation is the nanoclustering of ROP6 [Platre et al., 2019] (see section 2.1.4.3).

Lastly we note that in some of the simulations the polarisation of ROP2 can be seen (figures 6.15a), meaning that ROP2 appears in both ends of the cell. This possibly occurs due to the microtubule arrays naturally forming transversally to the long axis and therefore inhibiting ROP2 expression on the sides and middle but not at the ends. This is interesting as it alludes to a possible mechanism as to how spatial protein arrangements could emerge.

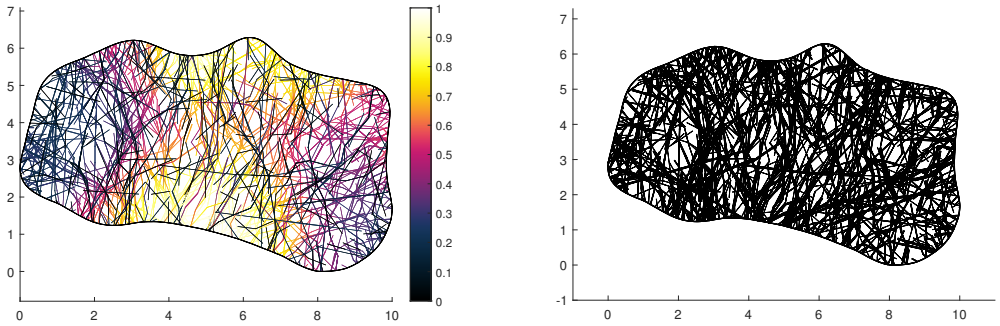


(a) ROP2 concentration (b) RIC4 concentration (c) ROP6 concentration

Figure 6.15: Reaction diffusion model results in our 7th young pavement cell outline where each figure shows the different signalling protein concentrations.

6.6 Concluding remarks

In this chapter, we have shown that the hypothesised signalling network of proteins and microtubules is sufficient to explain ROP2 and microtubule's localisation to the lobes and



(a) RIC1 concentration

(b) Microtubule array

Figure 6.16: Reaction diffusion model results in our 7th young pavement cell outline where figure a shows the RIC1 concentrations and b shows the microtubule array where the lines increase in thickness as more microtubules are contained in that bundle.

indents to help further develop their shape. Experimental observations were also recreated through the simulations in perturbed mutant scenarios, validating the model and assuring its results and their use in the next chapter. Intriguingly, from the DN ROP2 and young pavement cells simulations, it was also discovered that the hypothesised signalling network is not complete and can not explain chemical lobe initiation. Therefore we conclude that the lobe triggering mechanism are different from the developmental mechanisms.

Similarly, the modelling process also demonstrated that there are missing bits of information in the signalling network. Specifically, further work needs to be on the questions presented in section 6.4.2 on how exactly ROP2 promotes itself and how this exportation of auxin by the PIN1 molecules does not promote both ROP2 and ROP6 in both the lobes and indents.

There are also some general questions remaining in pavement cell signalling dynamics. Upon examining pavement cells over time Zhang et al. [2011] found that they develop in waves (lasting days) where one wave type consists of both growth and lobe initiation and the other of just isotropic growth with very little lobe initiation. This phenomenon presents many further queries, for example, what causes these different waves and what happens to the signalling network? Specifically, how are the different proteins and cytoskeletal components arranged/localised (if any) in these different waves? These waves

could be especially relevant when observing the actin cytoskeleton as potentially the observations in chapter 4 were made in the isotropic growth stage, which could explain why no lobe localisation was observed.

Included in the further questions is the uncertainty surrounding how RIC1 promotes order. Lin et al. [2013]'s found that RIC1 works by promoting the protein katanin, which severs microtubules branching from other microtubules. They theorise that this severing could induce a densely packed and aligned array by removing nonaligned microtubules and increasing the number of microtubules there. This theory seems quite promising and has arisen from the first proper experimental observations of RIC1's effect. There are, however, some remaining key unknowns (and the reason why this mechanism wasn't included in the model) such as, do the microtubules reorient themselves after being severed so that they become parallel to their neighbours, which may need to happen if an ordered array is to form and if this does happen, how does it occur? RIC1 and katanin also increase the general severing activity, leading to shorter microtubules, so it is also unknown how this apparent destabilisation of the microtubules can promote order and consistent localisation to the indents. It would therefore be interesting in future investigations to use the microtubule model to simulate the effect of this phenomenon to try to understand how order is promoted.

There are further improvements that could be made to the signalling network model. One such improvement is that we could simulate multiple pavement cells at once. This refinement would permit us to fully model pavement cell interactions instead of simulating this feature through the boundary conditions, allowing for more realistic simulations. Including multiple cells would allow us to test the questions about how ROP2 promotes itself through its activation of PIN1 presented in section 6.4.2. How neighbouring cells have different growth rates, which can be around $\approx 2-6$ fold different [Szymanski, 2014] could also be researched by performing tissue simulations.

Another improvement would be to build this model in 3D, which would allow for more realistic simulations. This higher dimensional model would also permit us to investigate

the signalling dynamics behind how pavement cells create a thickened periclinal wall and arrange their microtubules in order to resist axial strain in order to maintain a constant height (first mentioned in section 6.5.1).

With the examination of the signalling dynamics behind growth control now finished, the mechanical control of pavement cell growth now needs to be understood. To gain this understanding, in the next chapter, a vertex element visco-elastic model is built where the results of this chapter are used to determine certain parameter choices.

Chapter 7

A visco-elastic vertex element model to simulate pavement cell growth

7.1 Introduction

As described in chapter 1, cell growth is a highly mechanical process with the cell wall under a lot of turgor-imposed stress. In order to fully comprehend how growth is controlled on a cellular level, the mechanics of how pavement cells grow needs to be examined.

Specifically, in this chapter we aim to understand the mechanisms behind lobe development and initiation. Firstly, it needs to be known how each cell wall material/property contributes to the further development of pavement cell lobes. Therefore, individual pavement cells shall be simulated and by using the results from the previous chapter (chapter 6) to inform the parameters, a complete understanding of how each component of the signalling network influences morphology can be achieved. Secondly, different chemical and mechanical lobe initiation mechanisms are explored by simulating multiple connected cells, which could help rule out or provide evidence for different initiation strategies.

To achieve the goals, we use a simplified version of a 2D+1D vertex element viscoelastic model created by Fozard et al. [2013] (with some additional features) who managed to accurately capture plant growth behaviour by modelling *Arabidopsis* root growth. As well as its accuracy, this model was chosen as it includes turgor-induced growth as well as being part of a limited group of plant growth models that captures both viscous and elastic behaviour [Smithers et al., 2019] while also including anisotropy. These features are essential for capturing the effect of each cell wall component. This model also benefits from incorporating aspects of a 3D system.

This chapter begins by detailing the vertex element model and its numerical implementation in section 7.2. Simulations are then performed using this model to explore pavement cell development and lobe initiation in section 7.3. Finishing off, the chapter is summarised in section 7.4.

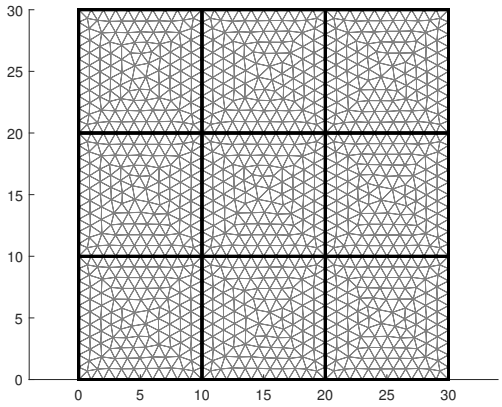


Figure 7.1: An example vertex element setup with 9 cells where the bold black lines represent the cell walls between neighbouring cells, the anticlinal walls, and the grey triangulation represent the cell walls in the plane of the simulation, the periclinal walls.

7.2 Vertex element modelling of pavement cell growth

A vertex element model is a system of nodes (a set of coordinates) connected to other nodes via their elements (a set of lines). The movement of these nodes represents the system growing and is controlled by the vertexes and elements viscous, anisotropic and elastic properties.

This section begins by setting up the system and stating the principle equations in section 7.2.1. The system is then discretised over the meshed surface in section 7.2.2 followed by the nondimensionalisation of the equations in section 7.2.3. The model is then parametrised using the results from the previous chapter in section 7.2.4 with the numerical methods to solve the system then outlined in section 7.2.5.

7.2.1 Setting up the vertex element model

The model here attempts to model a 3D system in 2D. This model counters this potential inaccuracy by distinguishing between two different kinds of walls, both of which will have different stress terms. First to be considered are walls in the plane of the simulation (the periclinal walls), and secondly, those orthogonal to the plane (anticlinal walls) (figure 7.1).

Each node $\mathbf{x}_i^{*k}$ $i = 1, \ldots, M$ at time step t_k^* where M is the number of nodes, moves in the simulation by balancing the forces at each vertex at each time step (where time is discretised in the same manner as section 6.4.1.1). Here it is assumed that due to the small length scale, inertia is negligible. Turgor acts as a pushing force on the anticlinal wall nodes, which is counteracted by the elastic stretching of the elements, restricting expansion. Also included are the isotropic viscous forces, which reduce the extension rate and the anisotropic viscous forces, that resist growth in certain defined directions. How each feature is implemented is described below.

Turgor pressure is an isotropic force that provides the power behind cell wall extension which is assumed to be constant in each cell (see Fozard et al. [2013] for justification). In order to model the pressure on an individual node, an element, e, between two vertices $\mathbf{x}_i^{*k}$ and $\mathbf{x}_j^{*k}$ is considered. The force on the element is proportional to its length and directed outwards i.e.

$$p_m^* \|\mathbf{x}_j^{*k} - \mathbf{x}_i^{*k}\| \mathbf{n}_{ij}, \tag{7.2.1}$$

where $\|\ \ \|$ is the euclidean norm, p_m^* is the turgor pressure in cell m and $\mathbf{n}_{ij}$ is the outward pointing normal vector for the edge. We define, $\|\mathbf{x}_j^{*k} - \mathbf{x}_i^{*k}\| \mathbf{n}_{ij} = \mathbf{R}^*(\mathbf{x}_j^{*k} - \mathbf{x}_i^{*k})$ with $\mathbf{R}^*(\mathbf{x}^*) = \mathbf{x}^* \times \mathbf{k}$ where $\mathbf{k}$ is the unit vector pointing out of the plane, meaning this function corresponds to a in plane rotation by $-\frac{\pi}{2}$. The pressure on this element is equally distributed between $\mathbf{x}_i^{*k}$ and $\mathbf{x}_j^{*k}$, thus from equation (7.2.1) the pressure on $\mathbf{x}_i^*$ is,

$$\frac{p_m^*}{2} \mathbf{R}^*(\mathbf{x}_j^{*k} - \mathbf{x}_i^{*k}). \tag{7.2.2}$$

Using these principles the total pressure on the node $\mathbf{x}_i^{*k}$ is then the sum of the pressure coming from each connecting cell,

$$\mathbf{T}_i^* = \sum_{m | i \in B_i(m)} \frac{p_m^*}{2} \mathbf{R}^*(\mathbf{x}_{m_+(i)}^{*k} - \mathbf{x}_{m_-(i)}^{*k}), \tag{7.2.3}$$

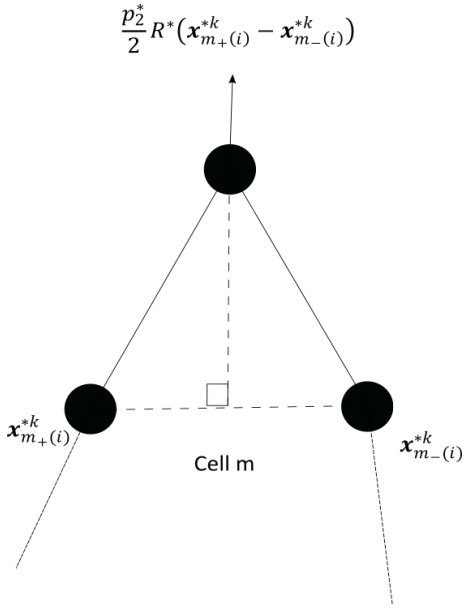


Figure 7.2: Model principles behind equation (7.2.3) where a network of nodes and anticlinal wall elements can be seen demonstrating the total force on vertex $\mathbf{x}_i^{*k}$ from the pressure in cell m.

where $B_i(m)$ is the set of cells for which the node $\mathbf{x}_i^{*k}$ is part of the boundary wall and $\mathbf{x}^{*k}_{m_+(i)}$ and $\mathbf{x}^{*k}_{m_-(i)}$ are the previous and next nodes to vertex $\mathbf{x}_i^{*k}$ in cell m in a anticlockwise direction (figure (7.2)).

The turgor action pushes nodes outwards, straining the elements that create stress due to the anisotropic viscoelastic properties given to the edges. The wall stress, σ^* on an element is found by letting,

$$\sigma^* = \sigma_y^* + \sigma_a^* + \sigma_e^*, \tag{7.2.4}$$

where σ_y^* is the isotropic viscous stress, σ_a^* the anisotropic viscous stress, and σ_e^* the elastic stress. Different combinations of these terms are summed for the different wall types mentioned above (anticlinal or periclinal walls). Note that as the different stresses are being added, the elements are being represented by a Kelvin-Voigt model, which implies the spring and dashpot are connected in parallel. The form the elastic stress takes is detailed in section 7.2.2

The isotropic viscous stresses are modelled by defining,

$$\sigma_y^* = \mu_y^* \mathbf{E}^*, \tag{7.2.5}$$

where μ_y^* is the isotropic viscosity of the pectin matrix (and hemicellulose crosslinks) and $\mathbf{E}^*$ is the rate of strain tensor.

Anisotropy arises in cells due to the arrangement of cellulose molecules restricting growth in their aligned direction. If the cellulose direction $\mathbf{a}$ is considered, the anisotropic viscous stress is then,

$$\sigma_a^* = \mu_a^* \left(\mathbf{a} \cdot \mathbf{E}^* \mathbf{a}\right) \mathbf{a} \otimes \mathbf{a}, \tag{7.2.6}$$

where $\otimes$ is the outer product of two vectors i.e $\mathbf{a} \otimes \mathbf{b} = \mathbf{a}\mathbf{b}^T$. This term represents the additional stress arising from the strain in the fibre direction with viscosity μ_a^*. The scalar $\mathbf{a} \cdot \mathbf{E}\mathbf{a}$ is the strain rate in the direction of the fibres and the matrix $\mathbf{a} \otimes \mathbf{a}$ is a tensor representing the direction of the fibres. With the system equations outlined, how the system is solved in the triangulation of the cellular domain is described next.

7.2.2 Discretisation

The discretisation of the stresses begins with the walls in the plane of the simulation (the periclinal walls), which according to Fozard et al. [2013] have an important role in preventing transverse swelling and deciding the rate of elongation. For these walls they suggest making the assumption that $\sigma^* = \sigma_a^* + \sigma_y^*$. To solve the system, the domain is decomposed into triangular elements in the same manner as section 6.4.1.2. Here the procedure to calculate the forces acting on each vertex in a single triangle element is described. Each vertex is part of several different triangles, so the total force on that node is the sum of the contribution from each triangle it is associated with.

Every element is associated with a fibre direction which has direction $\mathbf{A}$ in the reference

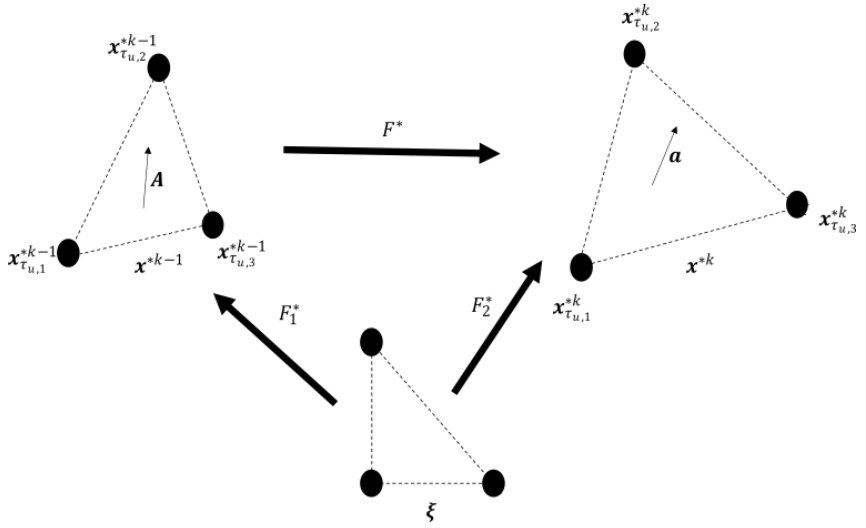


Figure 7.3: The reference triangle with coordinates $\mathbf{x}^{*k-1}_{\tau_{u,1}}, \mathbf{x}^{*k-1}_{\tau_{u,2}}, \mathbf{x}^{k-1}_{\tau_{u,3}}$ is mapped onto the current configuration with coordinates $\mathbf{x}^{*k}_{\tau_{u,1}}, \mathbf{x}^{*k}_{\tau_{u,2}}, \mathbf{x}^{*k}_{\tau_{u,3}}$ via the deformation gradient F^*. The deformation gradient is calculated by $F^* = F_2^* F_1^{*-1}$ where F_1^* is the gradient map to the reference configuration and F_2^* the gradient map to the current configuration both from the unit triangle. The reference triangle has fibre direction $\mathbf{A}$ where the fibres is embedded within the material and is deformed with the triangle to the fibre direction $\mathbf{a}$.

configuration and is mapped to the current configuration via,

$$\mathbf{a} = \frac{F^*\mathbf{A}}{|F^*\mathbf{A}|}, \text{ where } F^* = F_2^* F_1^{*-1}, \tag{7.2.7}$$

where F_1^* and F_2^* are the gradients of the maps from the unit triangle, denoted $\hat{\tau}$ (a triangle with vertices $(0,0),\ (1,0)$ and $(0,1)$) to the reference and current configuration respectively in the triangle τ_u. The reference configuration coordinates are the coordinates at the start of each time step (i.e the co-ordinates at time $k-1$) and labelled $\mathbf{x}^{*k-1}_{\tau_{u,1}}, \mathbf{x}^{*k-1}_{\tau_{u,2}}, \mathbf{x}^{*k-1}_{\tau_{u,3}}$ and the current coordinates, which are unknown and will be solved for, are labelled $\mathbf{x}^{*k}_{\tau_{u,1}}, \mathbf{x}^{*k}_{\tau_{u,2}}, \mathbf{x}^{*k}_{\tau_{u,3}}$ (see figure 7.3). The position vectors in the two configurations can be given by linear interpolation as

$$\mathbf{x}^{*k-1}(\xi) = \sum_{I=1}^{3} \mathbf{x}^{*k-1}_{\tau_{u,I}} N_I(\xi), \text{ and } \mathbf{x}^{*k}(\xi) = \sum_{I=1}^{3} \mathbf{x}^{*k}_{\tau_{u,I}} N_I(\xi), \tag{7.2.8}$$

where $\xi = (\xi_1, \xi_2)$ parametrises each point in the unit triangle. The shape functions are

then defined as,

$$N_1 = 1 - \xi_1 - \xi_2,\ N_2 = \xi_1,\ N_3 = \xi_2. \tag{7.2.9}$$

The gradients F_1^* and F_2^* are calculated via,

$$(F_1)^*_{\alpha\beta} = \frac{\partial x^{*k-1}_\alpha}{\partial \xi_\beta} = \sum_{I=1}^{3} x^{*k-1}_{I\alpha} N_{I,\beta}(\xi), \tag{7.2.10}$$

$$(F_2)^*_{\alpha\beta} = \frac{\partial x^{*k}_\alpha}{\partial \xi_\beta} = \sum_{I=1}^{3} x^{*k}_{I\alpha} N_{I,\beta}(\xi), \tag{7.2.11}$$

where $N_{I,\beta}(\xi) = \frac{\partial N_I}{\partial \xi_\beta}$ and $x^{*k-1}_{\tau_{u,I}\alpha}$ denotes the α component of $\mathbf{x}^{*k-1}_{\tau_{u,I}}$. The velocity $\mathbf{v}^*$ is given by

$$\mathbf{v}^* = \sum_{I=1}^{3} \mathbf{v}^*_{\tau_{u,I}} N_I(\xi), \tag{7.2.12}$$

where $\mathbf{v}^*_{\tau_{u,I}} = \frac{\partial \mathbf{x}^*_{\tau_{u,I}}}{\partial t^*}$ is the velocity of the vertex $\mathbf{x}^*_{\tau_{u,I}}$. The rate of strain tensor is defined as,

$$E^* = \frac{1}{2}\left(\nabla^* \mathbf{v}^* + (\nabla^* \mathbf{v}^*)^T\right), \tag{7.2.13}$$

where in terms of the maps the velocity gradient is,

$$(\nabla^* \mathbf{v}^*)_{\alpha\beta} = \sum_{I=1}^{3}\sum_{J=1}^{2} v^*_{\tau_{u,I}\alpha} N_{I,J}(\xi)(F_2^{*-1})_{J\beta}. \tag{7.2.14}$$

Now, with the ability to calculate the stress, σ^* in each triangle the forces $f^*_{K,12}$, $f^*_{K,23}$ and $f^*_{K,31}$, where $K = a, y$ are defined on each element of the triangle as (figure 7.4),

$$\mathbf{f}^*_{K,12} = -\sigma^*_K \cdot \mathbf{n}_{12}|\mathbf{x}^*_2 - \mathbf{x}^*_1|,\ \mathbf{f}^*_{K,23} = -\sigma^*_K \cdot \mathbf{n}_{12}|\mathbf{x}^*_3 - \mathbf{x}^*_2|,\ \mathbf{f}^*_{K,31} = -\sigma^*_K \cdot \mathbf{n}_{31}|\mathbf{x}^*_1 - \mathbf{x}^*_3|. \tag{7.2.15}$$

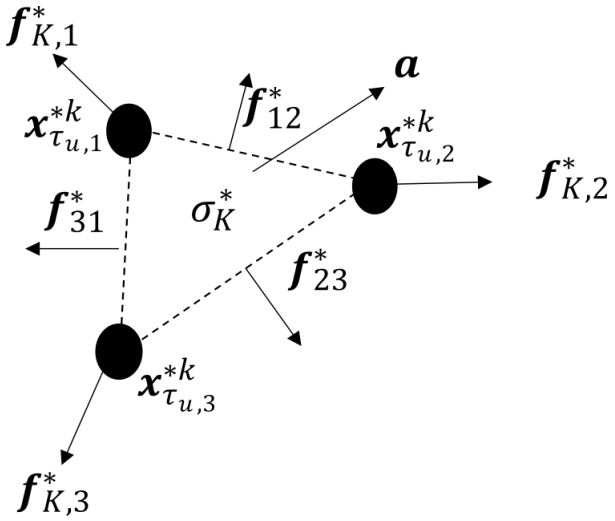


Figure 7.4: Evaluation of the viscous stress in a example periclinal wall triangle with the dashed lines representing the periclinal elements

The forces on each node are then,

$$\mathbf{f}^*_{K,1} = \frac{1}{2}(\mathbf{f}^*_{K,12} + \mathbf{f}^*_{K,31}),\ \mathbf{f}^*_{K,2} = \frac{1}{2}(\mathbf{f}^*_{K,23} + \mathbf{f}^*_{K,12}),\ \mathbf{f}^*_{K,3} = \frac{1}{2}(\mathbf{f}^*_{K,31} + \mathbf{f}^*_{K,23}), \tag{7.2.16}$$

and are summed over all triangles to calculate the total viscous or anisotropic force, $\mathbf{f}^*_{i,K}$, on each node, i, so that for each periclinal wall node the total force is $\mathbf{f}^{*k}_i = \mathbf{f}^*_{i,a} + \mathbf{f}^*_{i,y}$.

Considering the walls that are perpendicular to the simulation (anticlinal walls), Fozard et al. [2013] recommend that the stress can be expressed as $\sigma^* = \sigma^*_y + \sigma^*_e$. As the viscous forces on each of these nodes have already been calculated (see above), all that remains is to derive the elastic forces. The elastic stresses are evaluated along the line elements of the perpendicular walls and not in the triangles. The elastic stress on a wall element, e is,

$$\sigma^*_e = \lambda^*_e \left(\frac{l^*_e}{l^*_{0,e}} - 1 \right), \tag{7.2.17}$$

where l^*_e and $l^*_{0,e}$ are the current and resting length's of the element respectively, and λ^*_e is the extensibility of the edge. The forces on the nodes $\mathbf{x}^*_i$ and $\mathbf{x}^*_j$ which are connected

by the edge, e are then (figure 7.5),

$$\mathbf{f}^*_{e,i} = +\sigma^*_e \frac{\mathbf{x}^*_j - \mathbf{x}^*_i}{\|\mathbf{x}^*_j - \mathbf{x}^*_i\|}, \text{ and } \mathbf{f}^*_{e,j} = -\sigma^*_e \frac{\mathbf{x}^*_j - \mathbf{x}^*_i}{\|\mathbf{x}^*_j - \mathbf{x}^*_i\|}. \tag{7.2.18}$$

So for each anticlinal wall node all the elastic and viscous forces are summed together, such that $\mathbf{f}^{*k}_i = \mathbf{f}^*_{i,e} + \mathbf{f}^*_{i,y}$. All features to be listed below are now our own additions to the model.

In some simulations, for realism, the anticlinal walls need to be able to grow. To implement this growth, this model follows in the footsteps of other plants models [Smithers et al., 2019] by using plastic spring growth, meaning that the elements resting length's are extended proportional to their extension. Thus,

$$l^*_{0,e} = l^*_{0,e} + \upsilon_e G_{sr}(l^*_e - l^*_{0,e}), \tag{7.2.19}$$

where υ_e is the cell wall material deposition rate and G_{sr} is the general spring growth rate of the system and ranges between 0 and 1.

Boundary forces are also imposed on the system to replicate the effect of neighbouring cells. This feature is included to ensure realism as pavement cells are immersed in a plant tissue but simulating the whole leaf would be too computationally expensive. Through trial and error, it is found that the most suitable boundary conditions is to assume that there are boundary nodes (labelled $\mathbf{x}^*_c$) which are connected to the outside anticlinal walls via linear elastic springs, which oppose turgor induced growth. We also found that it is best to connect three boundary nodes to each anticlinal wall node to reduce the degrees of freedom (figure 7.6). For a node i that is connected to the boundary nodes $c(i)$, $c_-(i)$ and $c_+(i)$ the boundary force is,

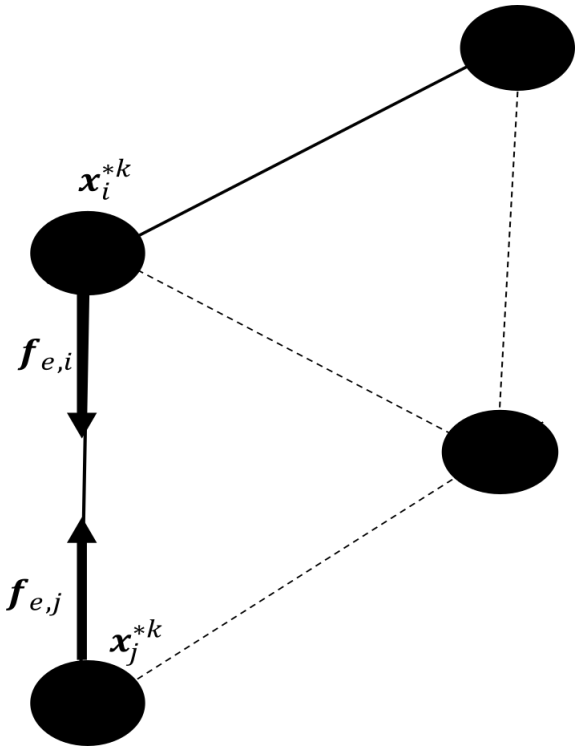


Figure 7.5: Evaluation of the edge stress in a example anticlinal wall, where the bold lines represent the anticlinal walls and the dash lines the periclinal walls

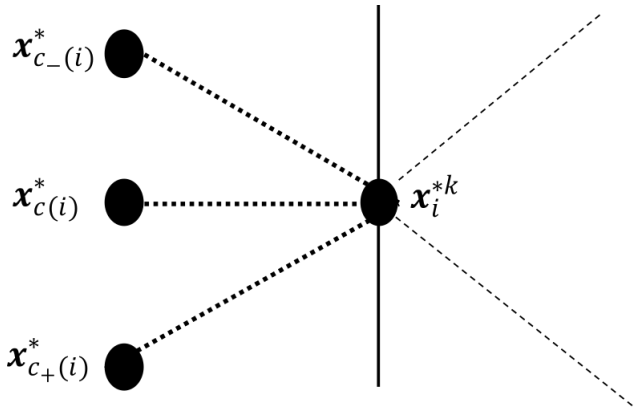


Figure 7.6: Depiction of the boundary elements shown as dotted lines connected to the boundary anticlinal wall node $\mathbf{x}_i^*$ where the black lines represent the anticlinal wall elements, and the dashed lines represent the periclinal wall elements

$$\mathbf{f}^*_{i,c} = \lambda^*_c \left(\left(\frac{l^*_{c,e}}{l^*_{c,0}} - 1 \right) \mathbf{u}_c + \left(\frac{l^*_{c_-,e}}{l^*_{c_-,0}} - 1 \right) \mathbf{u}_{c_-} + \left(\frac{l^*_{c_+,e}}{l^*_{c_+,0}} - 1 \right) \mathbf{u}_{c_+} \right), \text{ where} \tag{7.2.20}$$

$$l^*_{c,e} = \|\mathbf{x}^{*k}_i - \mathbf{x}^*_{c(i)}\|,\ l^*_{c_-,e} = \|\mathbf{x}^{*k}_i - \mathbf{x}^*_{c_-(i)}\|\ l^*_{c_+,e} = \|\mathbf{x}^{*k}_i - \mathbf{x}^*_{c_+(i)}\|, \tag{7.2.21}$$

$$\mathbf{u}_c = \frac{\mathbf{x}^{*k}_i - \mathbf{x}^*_{c(i)}}{l^*_{c,e}},\ \mathbf{u}_{c_-} = \frac{\mathbf{x}^{*k}_i - \mathbf{x}^*_{c_-(i)}}{l^*_{c_-,e}} \text{ and } \mathbf{u}_{c_+} = \frac{\mathbf{x}^{*k}_i - \mathbf{x}^*_{c_+(i)}}{l^*_{c_+,e}}, \tag{7.2.22}$$

where λ^*_c is the boundary spring stiffness, $l^*_{c,0}$ the middle boundary spring resting length, $l^*_{c_-,0}$ the left boundary spring resting length and $l^*_{c_+,0}$ the right boundary spring resting length going anticlockwise. So for a boundary anticlinal wall node the total force is $\mathbf{f}^{*k}_i = \mathbf{f}^*_{e,i} + \mathbf{f}^*_{i,y} + \mathbf{f}^*_{i,c}$.

As growth is being simulated, these boundary conditions also need to move to simulate the tissue as a whole growing. This is implemented algorithmically differently depending on the simulation that is running, but the main principle is that all the boundary nodes are allowed to move in the (outward-pointing) normal direction to the outside anticlinal wall node they are connected to by a distance that is proportional to their springs strain. For example, for each time step, we set,

$$\mathbf{x}^{*k+1}_c = \mathbf{x}^{*k}_c + G_{tr} \left(l^*_{c,e} - l^*_{c,0} \right) \mathbf{n}_i, \tag{7.2.23}$$

where $\mathbf{x}^{*k+1}_c$ is the new boundary node position, $\mathbf{x}^{*k}_c$ the old boundary node position, $\mathbf{n}_i$ the outward pointing normal vector at node $\mathbf{x}^*_i$ and G_{tr} the tissue growth rate, ranging between 0 and 1 (where when $G_{tr} = 0$ there is no growth and when $G_{tr} = 1$ the boundary nodes match the growth rate of the tissue).

In some later simulations, to ensure realism, the bending stiffness needs to be included [Dreyer and Van Vuuren, 1999], a feature which Sapala et al. [2018], Higaki et al. [2016] also included in their 2D pavement cell models. For the anticlinal walls, the total force is now $\mathbf{f}^{*k}_i = \mathbf{f}^*_{e,i} + \mathbf{f}^*_{i,y} + \mathbf{f}^*_{i,b}$ where $\mathbf{f}^*_{i,b}$ is the correcting force trying to enforce a straight wall by moving the wall nodes. For a node $\mathbf{x}^*_i$ the first step in calculating this force, is to define the unit vectors directed from node i to its neighbouring nodes $m_-(i)$ and $m_+(i)$,

which gives,

$$\mathbf{u}_1 = \frac{\mathbf{x}^*_{m-(i)} - \mathbf{x}^*_i}{\|\mathbf{x}^*_{m-(i)} - \mathbf{x}^*_i\|}, \text{ and } \mathbf{u}_2 = \frac{\mathbf{x}^*_{m+(i)} - \mathbf{x}^*_i}{\|\mathbf{x}^*_{m+(i)} - \mathbf{x}^*_i\|}. \tag{7.2.24}$$

Secondly, to find how much the wall is bending the angle, θ, between these vectors is found, by calculating,

$$\theta = \cos^{-1}\left(\mathbf{u}_1 \cdot \mathbf{u}_2\right). \tag{7.2.25}$$

Thirdly, to calculate the force direction the two unit vectors are summed,

$$\mathbf{u} = \frac{\mathbf{u}_1 + \mathbf{u}_2}{\|\mathbf{u}_1 + \mathbf{u}_2\|}. \tag{7.2.26}$$

The bending stiffness is then

$$\mathbf{f}^*_{b,i} = \lambda^*_b \left(\pi - \theta\right) \mathbf{u}, \tag{7.2.27}$$

where λ^*_b is the bending stiffness constant. This term increases in magnitude as the angle between the two vectors gets further away from π ($\theta = \pi$ when the wall is straight) and is directed in the concave-pointing normal direction.

7.2.3 Nondimensionlisation

The system can now be nondimensionalised in order to simplify the equations. We set,

$$t^* = t^*_{max} t, \text{ and } \mathbf{x}^* = L^* \mathbf{x}, \tag{7.2.28}$$

where t^*_{max} is the time scale, and L^* is the length scale of the cells. Consequently, $v^*_I = v_I \frac{L^*}{t^*_{max}}$ where $v_I = \frac{d\mathbf{x}_I}{dt}$ and thus the principal equation now becomes,

$$\sigma^*_y = \frac{\mu^*_y}{t^*_{max}}\sigma_y, \text{ where } \sigma_y = \mathbf{E}, \text{ with } \mathbf{E} = \frac{1}{2}\left(\nabla v + (\nabla v)^T\right), \tag{7.2.29}$$

$$\sigma^*_a = \frac{\mu^*_a}{t^*_{max}}\sigma_a \text{ where } \sigma_a = (\mathbf{a}\cdot\mathbf{E}\mathbf{a})\,\mathbf{a}\otimes\mathbf{a}, \tag{7.2.30}$$

$$\sigma^*_e = \lambda^*_e\sigma_e, \text{ where } \sigma_e = \left(\frac{l_e}{l_{0,e}} - 1\right), \tag{7.2.31}$$

$$\mathbf{T}^*_i = p^*_m L^* \mathbf{T}_i \text{ where } \mathbf{T}_i = \sum_{m|i\in B_i(m)} \frac{1}{2} R(\mathbf{x}_{m_+(i)} - \mathbf{x}_{m_-(i)}) \tag{7.2.32}$$

$$\mathbf{f}^*_{i,c} = \lambda^*_c \mathbf{f}_{i,c} \text{ where } \mathbf{f}_{i,c} = \left(\left(\frac{l_{c,e}}{l_{c,0}} - 1\right)\mathbf{u}_c + \left(\frac{l_{c_-,e}}{l_{c_-,0}} - 1\right)\mathbf{u}_{c_-} + \left(\frac{l_{c_+,e}}{l_{c_+,0}} - 1\right)\mathbf{u}_{c_+}\right) \tag{7.2.33}$$

$$\mathbf{f}^*_{i,b} = \lambda^*_b \mathbf{f}_{i,b} \text{ where } \mathbf{f}_{i,b} = (\pi - \theta)\,\mathbf{u}. \tag{7.2.34}$$

If $\mathbf{f}^{*k}_i = \frac{\mu^* L^*}{t^*_{max}}\mathbf{f}^k_i$, the total force on each element is then,

$$\mathbf{f}^k_i = \frac{p^*_m t^*_{max}}{\mu^*_y}\mathbf{T}_i + \mathbf{f}_{i,y} + \frac{\mu^*_a}{\mu^*_y}\mathbf{f}_{i,a} + \frac{\lambda^*_e t^*_{max}}{\mu^*_y L^*}\mathbf{f}_{i,e} + \frac{\lambda^*_b t^*_{max}}{\mu^*_y L^*}\mathbf{f}_{i,b} + \frac{\lambda^*_c t^*_{max}}{\mu^*_y L^*}\mathbf{f}_{i,c}, \tag{7.2.35}$$

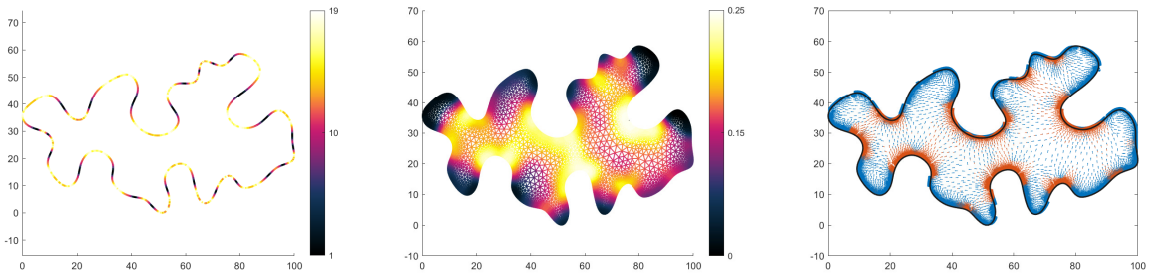
where the respective force terms are ignored depending on if node i is a anticlinal, periclinal or boundary wall node. To solve the system the co-ordinates $\mathbf{X}^k$ for which each $\mathbf{f}^k_i$ is zero for each time step needs to be found. In vector form if $\mathbf{F^k} = (\mathbf{f}^k_1, \mathbf{f}^k_2, \cdots, \mathbf{f}^k_M)^T$, then the equation $\mathbf{F}(\mathbf{X}^k) = \mathbf{0}$ needs to be solved.

7.2.4 Fixing the parameters and using the signalling protein and microtubule dynamics results to influence their values

With the model equations established the parameters can now be fixed. For the base parameters the same values as Fozard et al. [2013] used are chosen which are listed in table 7.1. λ^*_b is fixed by setting it to be proportional to the turgor pressure (so that on an element of length $1\mu m$ its boundary resistance force is equal to the turgor pressure when its boundary spring's length is half of its resting length) and λ^*_c is found through trial and error.

Parameter	Value
p_m^*	0.3 MPa
μ_y^*	0.15 MPa hr
μ_a^*	20 MPa hr
λ_e^*	10MPa μm
λ_b^*	0.6MPa μm
λ_c^*	20MPa μm

Table 7.1: Vertex element base parameter values



(a) (b) (c)

Figure 7.7: Parameter values in the pavement cells. a) the stiffness values, b) the viscosity values, c) the anisotropy directions and magnitude where the blues arrow show the normalised directions and the orange arrows represent the anisotropy directions and their scaling with the microtubule concentration.

As previously mentioned, it shall be tested whether the signalling network leads to the further development of pavement cell shape, as is hypothesised. In order to investigate this theory, data from the last chapter's simulations in mature pavement cells in section 6.5.1 are used to inform how the parameters vary across the domain.

Firstly, from section 2.1.4, it is theorised that the localisation of the ROP2 through RIC4 to the lobes can stabilise actin which can lead to the deposition of methylated pectin and wall loosening enzymes (or possibly via some other mechanism). Pectin in this form is less viscous, and when combined with the effect of the wall loosening enzymes, it is assumed that where and when RIC4 is localised and higher in concentration, the viscosity parameter μ_y^*, is lower. To implement this behaviour, the logistic function is used (so the effect is limited) such that on a node i, the higher the RIC4 concentration, the lower its

viscosity $\mu^*_{y,i}$, thus

$$\mu^*_{y,i} = a^*_5 \left(\frac{1}{1 + e^{b^*_5 (c^{*K}_{4,i} - c^*_5)}} - \frac{1}{2} \right) + \bar{\mu}^*_y, \tag{7.2.36}$$

where a^*_5 is the max effect, b^*_5 controls how quickly it reaches it's maximum, $c^{*K}_{4,i}$ is the RIC4 concentration on i at the last time step K, c^*_5 is the threshold value for which $c^{*K}_{4,i}$ needs to be higher than for the viscosity to decrease and $\bar{\mu}^*_y$ is the mean viscosity (with its value stated in table 7.1) as well as a $\frac{1}{2}$ being taken away to allow the logistic part of the function to take both positive and negative values. The μ^*_y values for an element is then found by just calculating the mean of the two $\mu^*_{y,i}$ values on the nodes that this element connects. When the results of this implementation are examined (figure 7.7b) lower viscosity values can be seen in the lobes and higher viscosity values in the indents, which match to the experimental observations made of methylated and demethylated pectin's distributions in pavement cells. As only a single viscosity value, μ^*_{y,τ_u}, is needed in equation (7.2.5), for each triangle the mean viscosity value from the elements in the triangle is calculated and used.

Secondly, anisotropy needs to be incorporated where and when the microtubules are localised and high in concentration as they are known to deposit cellulose in these locations. Therefore for a node i the anisotropy direction $\mathbf{a}_i$ is determined by finding the mean microtubule direction (where this is the non-polarised direction found using the procedure in section 5.2) from the microtubule points within a certain radius (which are already known from section 6.4.4.1). The anisotropy direction are then scaled with how localised the microtubules are using the microtubule concentration, $c^{*K}_{M,i}$, on node i. This is completed once again using the logistic function, which is ranging between 0 and 1, with it being close to 1 when $c^{*K}_{M,i}$ is higher and close to 0 otherwise, thus

$$\mu^*_{a,i} = \bar{\mu}^*_a \left(\frac{1}{1 + e^{-b^*_6 (c^{*K}_{M,i} - c^*_6)}} \right), \tag{7.2.37}$$

where b^*_6 effects how quickly it reaches its maximum value, c^*_6 is the threshold value and

$\bar{\mu}_a^*$ is the mean anisotropy viscosity and has value stated in table 7.1. The μ_a^* values for an element is then found by just calculating the average of the two $\mu_{a,i}^*$ values of the nodes that this element connects. Upon analysing the results of this process (figure 7.7c), the anisotropy directions look nearly identical to the pavement cell stress fields found by Sampathkumar et al. [2014] and as the microtubules align with stress, this helps to further validate the signalling network model results. For use in equation (7.2.6) in a triangle τ_u the average anisotropy direction of the three elements in the triangle is used.

Lastly, the anticlinal wall stiffnesses would be affected by both the microtubules' deposition of cellulose and ROP2's effect on the wall properties, such that when $c_{M,i}^{*K}$ is high and $c_{2,i}^{*K}$ is low on an anticlinal wall node, the stiffness will be high and vice versa. As the anticlinal wall is shared by neighbouring cells, a lobe for the current cell is an indent for the neighbouring cell, thus if $c_{M,i}^{*K}$ is high along the indents meaning high stiffness values, then the tips of the lobes will also be stiffer. Consequently, as only one cell is being simulated, care needs to be taken to ensure this effect is included. To find the stiffness values, the lobe indicator variable, $\tilde{\kappa}$ is used in a very similar manner to how ROP6's boundary conditions are implemented in section 6.4.2. By splitting up $\tilde{\kappa}$ into different regions (where each region represents a different section of a lobe or indent) and calculating the mean microtubule concentration in each region (for simplicity, the ROP2 concentration are not incorporated in this calculation as it has the same localisation pattern meaning it wouldn't have any additional effect) a vector called $\bar{M}_{\tilde{\kappa}}^*$ can be found which lists the mean concentration in each lobe region. Now to ensure the stiffening effect of the neighbouring cells are included a new vector $\hat{\bar{M}}_{\tilde{\kappa}}^*$ is created which is the sum of $\bar{M}_{\tilde{\kappa}}^*$ and $\bar{M}_{\tilde{\kappa}}^*$ again but in reverse (so that its jth entry is $\bar{M}_{\tilde{\kappa},W-j}^*$, where W is the number of lobe regions $\tilde{\kappa}$ has been split into). So if a boundary node i lies in the $\tilde{\kappa}$ region j we have,

$$\lambda_{e,i}^* = a_7^* \left(\frac{1}{1 + e^{b_7^* \left(\hat{\bar{M}}_{\tilde{\kappa},j}^* - c_7^* \right)}} - \frac{1}{2} \right) + \bar{\lambda}_e^*, \tag{7.2.38}$$

where a_7^* is the max effect, b_7^* controls how quickly it reaches its maximum, c_7^* is the

Parameter	Value	Parameter	Value
a_5^*	0.2 MPa hr	b_5^*	3.6mol^{-1}
c_5^*	9 mol	b_6^*	0.19mol^{-1}
c_6^*	85 mol	a_7^*	$18\text{MPa}\mu\text{m}$
b_7^*	0.34mol^{-1}	c_7^*	97mol

Table 7.2: Further vertex element parameter values

threshold value for which $\hat{\bar{M}}^*_{\tilde{\kappa},j}$ needs to be higher than for the $\lambda^*_{e,i}$ to increase and $\bar{\lambda}^*_m$ is the mean stiffness and has value stated in table 7.1. The λ^*_e value for an element is then found by calculating the mean of the two $\lambda^*_{e,i}$ values of the nodes that this element connects.

When plastic spring growth needs to be incorporated (equation 7.2.19), for an edge e the υ_e values are set using λ^*_e via,

$$\upsilon_e = 1 - \frac{\lambda^*_e}{\frac{a^*_7}{2} + \bar{\lambda}^*_e}, \tag{7.2.39}$$

where $\frac{a^*_7}{2} + \bar{\lambda}^*_e$ is the maximum possible λ^*_e value so that the whole term above varies between 0 and 1 and is 0 when the stiffness is high and increases to 1 as the stiffness decreases. Equation (7.2.39) take this form as the areas of maximum growth mirror the areas which are not as stiff because that is where there is less cellulose and demethylated pectin and more deposition of methylated pectin and wall loosening enzymes.

7.2.5 Numerical implementation

The simulations are performed in MATLAB, again using the University of Birmingham's BlueBEAR HPC service. In order to solve the system of equations, several numerical techniques are used to solve for time and calculate the force balance which need to be both accurate and non computationally expensive. Included in the efforts to maintain accurate results is the need to periodically remesh the domain to ensure no triangles have small angles, which can otherwise lead to errors. The numerical methods also need to be robust, meaning that they can find a solution to the problem in various simulation

scenarios.

This subsection begins by outlining the differentiation methods in section 7.2.5.1 followed by the description of how the coordinates are calculated in order to find the force balance in section 7.2.5.2. How these numerical methods are optimised is then examined in section 7.2.5.3. How the domain is remeshed is then described in section 7.2.5.4. These descriptions are then followed up by additional methods that helped produce robust and efficient solvers in section 7.2.5.5.

7.2.5.1 Differentiation methods

To solve the system with respect to time an implicit-explicit derivative method is used, meaning, the only points in the equations that are dependant on the previous time steps, $\mathbf{X}^{k-1}$ are in the derivative and the turgor pressure forces, with the rest dependant on $\mathbf{X}^{k}$. This choice is made as the backward Euler method is known to be more stable and because a fixed turgor force in a specific direction on every node at each time step is found to help the stability of the solver. To increase the stability of the solver, the 2nd and 3rd backward differentiation formulas are used as they have the advantage of a larger area of absolute stability as a result of being dependant on the previous two and three time steps, respectively, [Süli and Mayers, 2003]. These formulas are utilized in the approximations of the velocities such that when $k = 1$, for each node,

$$\mathbf{v}_i = \frac{\mathbf{x}_i^k - \mathbf{x}_i^{k-1}}{\Delta t}, \tag{7.2.40}$$

when $k = 2$,

$$\mathbf{v}_i = \frac{\frac{3}{2}\mathbf{x}_i^k - 2\mathbf{x}_i^{k-1} + \frac{1}{2}\mathbf{x}_i^{k-2}}{\Delta t}, \tag{7.2.41}$$

and when $k \geq 3$,

$$\mathbf{v}_i = \frac{\frac{11}{6}\mathbf{x}_i^k - 3\mathbf{x}_i^{k-1} + \frac{3}{2}\mathbf{x}_i^{k-2} - \frac{1}{3}\mathbf{x}_i^{k-3}}{\Delta t}. \tag{7.2.42}$$

By substituting these expressions into equation (7.2.12), equation (7.2.35) can then be reexpressed in terms of $\mathbf{X}^k$ and its previous time steps. The system can now be solved for $\mathbf{X}^k$ in order to find the force balance.

7.2.5.2 Finding the solution: Newton's method

The next task is to find $\mathbf{X}^k$ such that $\mathbf{F}(\mathbf{X}^k) = \mathbf{0}$ which in other words is a root finding problem. To find the root, Newton's method is used as it typically converges quickly when compared to different methods [Schoeller et al., 2021]. Newton's method works through iterations where it supposedly gets closer to the solution in each step where these iterations are labelled k_I with the starting coordinates set to $\mathbf{X}^{k_0} = \mathbf{X}^{k-1}$.

Newtons method is used by re-expressing the coordinate and force matrices as vectors letting $\tilde{\mathbf{X}}^{k_I} = \left(x_1^{k_I}, x_2^{k_I}, \ldots, x_M^{k_I}, y_1^{k_I}, y_2^{k_I}, \ldots, y_M^{k_I}\right)$ and

$$\tilde{\mathbf{F}}(\mathbf{X}^{k_I}) = \left(f_{11}^{k_I}(\mathbf{X}^{k_I}), f_{21}^{k_I}(\mathbf{X}^{k_I}), \ldots, f_{M1}^{k_I}(\mathbf{X}^{k_I}), f_{12}^{k_I}(\mathbf{X}^{k_I}), f_{22}^{k_I}(\mathbf{X}^{k_I}), \ldots, f_{M2}^{k_I}(\mathbf{X}^{k_I})\right)$$

and then iterating using the following formula,

$$\tilde{\mathbf{X}}^{k_{I+1}} = \tilde{\mathbf{X}}^{k_I} - \mathbf{J}^{-1}(\tilde{\mathbf{X}}^{k_I})\tilde{\mathbf{F}}(\mathbf{X}^{k_I}), \tag{7.2.43}$$

where $\mathbf{J}$ is the Jacobian and defined as $J_{ij}(\tilde{\mathbf{X}}^{k_I}) = \frac{\partial \tilde{\mathbf{F}}_i(\tilde{\mathbf{X}}^{k_I})}{\tilde{\mathbf{X}}_j^{k_I}}$ where $J^{-1} \neq 0$ [Süli and Mayers, 2003] and $\tilde{\mathbf{F}}$ is differentiable in a neighbourhood around the root of the problem, $\mathbf{X}_M^k$. These iterations are repeated until the condition

$$||\mathbf{F}(\mathbf{X}^{k_I})|| < \epsilon_N, \tag{7.2.44}$$

is met where, ϵ_N is a very small tolerance (we set $\epsilon_N = 10^{-12}$).

The calculation of the Jacobian is done using the finite difference method, so that,

$$J_{ij}(\tilde{\mathbf{X}}^{k_I}) = \frac{\tilde{\mathbf{F}}_i(\tilde{\mathbf{X}}^{k_I} + \boldsymbol{\delta}\mathbf{x}_j) - \tilde{\mathbf{F}}_i(\tilde{\mathbf{X}}^{k_I})}{\delta x}, \tag{7.2.45}$$

where $\boldsymbol{\delta}\mathbf{x}_j = (0, \ldots, \delta x, \ldots\ 0)^T$ i.e. it is a vector that is all zeros apart from the jth entry which has a value of δx (we set $\delta x = 10^{-6}\frac{h^*}{L^*}$). To allow for efficient computations in MATLAB the Jacobian is saved as a sparse matrix (as in section 6.4.1.3). Using this numerical solver the force balance can now be found for every time step.

7.2.5.3 Numerical solver optimisation

The numerics in their current form have a long computation time, especially when there are numerous nodes which are being solved for over several time steps. To make the numerical solver usable, it therefore has to be optimised.

The Jacobian calculation is first optimised by noticing that when a single co-ordinate is perturbed using $\boldsymbol{\delta}\mathbf{x}_j$, it only affects the force values of a small number of local co-ordinates meaning the majority of the values in $\mathbf{F}$ do not change. So when J_{ij} is computed, there is no need to recalculate every ith entry when substituting in the value $\tilde{\mathbf{X}}^{k_I} + \boldsymbol{\delta}\mathbf{x}_j$. As a result when the domain is meshed, $\tilde{\mathbf{F}}_i(\tilde{\mathbf{X}}^{k_I} + 100\boldsymbol{\delta}\mathbf{x}_j) - \tilde{\mathbf{F}}_i(\tilde{\mathbf{X}}^{k_I})$ is calculated ($100\boldsymbol{\delta}\mathbf{x}_j$ to ensure no nodes are missed) and for each $j = i, \cdots 2M$ the i indices for which this expression is non-zero are stored i.e the local affected coordinates. Thus when growth is simulated, when the jth column of the Jacobian is derived, the i entries which are known to be affected by the perturbation (using the stored information) are recalculated with the rest of the entries filled in using the already calculated $\tilde{\mathbf{F}}(\tilde{\mathbf{X}}^{k_I})$ from equation (7.2.43). This approximation significantly reduces computational complexity and hence the computation time of the solver is dramatically reduced (see appendix A.5.1 for details). This approximation also introduces little/no error as in test simulations when the exact Jacobian is compared with the approximated one, the difference between the two was of

the same order in magnitude as the base numerical error.

To further improve the computation time, in some simulations it is beneficial to use Broyden's quasi-newton method [Broyden, 1965, Gay, 1979, Ramli et al., 2010]. Broyden's method once again uses an iterative method similar to Newtons, but instead of recalculating the Jacobian each iteration, the Jacobian is updated based on the secant equation after its initial calculation in the first iteration. This procedure can significantly decrease the computation time as calculating the Jacobian is very computationally expensive [Schoeller et al., 2021] even when optimised (see appendix A.5.1 for details). In equation form, Broydens method works by still using newtons iterative formula (equations (7.2.43)) to find $\mathbf{X}^k$ but for $k \geq 1$ the Jacobian for the Ith iteration, $\mathbf{J}^{k_I}$ is,

$$\mathbf{J}^{k_I} = \mathbf{J}^{k_{I-1}} + \frac{\Delta\mathbf{F}^{k_I} - \mathbf{J}^{k_{I-1}}\Delta\mathbf{X}^{k_I}}{||\Delta\mathbf{X}^{k_I}||^2}\left(\Delta\mathbf{X}^{k_I}\right)^T \text{ where } \mathbf{J}^{k_0} = \mathbf{J}(\mathbf{x}_0), \tag{7.2.46}$$

where $\Delta\mathbf{F}^{k_I} = \mathbf{F}(\mathbf{X}^{k_I}) - \mathbf{F}(\mathbf{X}^{k_{I-1}})$ and $\Delta\mathbf{X}^{k_I} = \mathbf{X}^{k_I} - \mathbf{X}^{k_{I-1}}$. This is the good Broyden's method. The bad Broyden's method uses a similar formula but directly calculates $\left(\mathbf{J}^{k_I}\right)^{-1}$ using $\left(\mathbf{J}^{k_{I-1}}\right)^{-1}$ which saves on the computation cost of calculating the inverse but this is found to be less stable, so is not used. The numerical solver to find $\mathbf{X}^k$ is now optimised ensuring plant cell growth can be simulated in reasonable computation times.

7.2.5.4 Considering the mesh

When simulating pavement cell growth, care needs to be taken as to what is happening to the mesh. Due to the varying parameters, different areas grow at different rates, which can distort the mesh and the triangles within it. This distortion is problematic as when there are any small angles in the triangles and/or triangles with a large aspect ratio, it will cause the mesh quality to decrease, which can lead to an ill-conditioned Jacobian, which affects the accuracy and the robustness of the solver [You et al., 2015]. To solve this issue, the domain therefore needs to be periodically remeshed. First to be discussed is when to remesh, followed by an explanation of how the domain is remeshed where all

the parameter values need to be transferred onto the new mesh.

In order to know when to remesh, a parameter that measures the quality of the mesh is needed for which there are several options. For simplicity, for a triangle, τ_u, a scale invariant measure is chosen, which uses the area of the triangle A_{τ_u} and the root-mean-square edge length of an element l_{RMS}, and is defined as,

$$Q_{\tau_u} = \frac{A_{\tau_u}}{l_{RMS}^2}, \tag{7.2.47}$$

where,

$$A_{\tau_u} = \frac{1}{2}\left|\left(\det\left(\tilde{A}_\tau\right)\right)\right|, \tag{7.2.48}$$

$$\tilde{A}_\tau = \begin{pmatrix} x_{\tau_{u,1}} - x_{\tau_{u,3}} & x_{\tau_{u,2}} - x_{\tau_{u,3}} \\ y_{\tau_{u,1}} - y_{\tau_{u,3}} & y_{\tau_{u,2}} - y_{\tau_{u,3}} \end{pmatrix}, \tag{7.2.49}$$

and,

$$l_{RMS} = \sqrt{\frac{1}{3}\left(\|\mathbf{x}_{\tau_{u,1}} - \mathbf{x}_{\tau_{u,2}}\|^2 + \|\mathbf{x}_{\tau_{u,2}} - \mathbf{x}_{\tau_{u,3}}\|^2 + \|\mathbf{x}_{\tau_{u,3}} - \mathbf{x}_{\tau_{u,1}}\|^2\right)}, \tag{7.2.50}$$

where Q_{τ_u} is the triangle quality measure, and increases as the aspect ratio of the triangle increases/the angles get smaller in the triangle [Shewchuk, 2002]. The mesh is said to have reached an undesirable quality and needs to be remeshed when the following condition is met,

$$\sup_{\tau_u \in \mathcal{T}} Q_{\tau_u} \geq \epsilon_M, \tag{7.2.51}$$

where ϵ_M is the maximum measure value allowed before remeshing. Through trial and error this value is set as $\epsilon_M = 0.025$.

When remeshing, all the anticlinal wall nodes are kept as they are, as it is the growth patterns of these walls which are being inspected. Everything else is however remeshed

using the procedure outlined in section 6.4.1.2. After remeshing, the next problem is transferring the known parameter values, μ_y^*, μ_a^* and $\mathbf{a}$ onto the new set of nodes and elements. To do this, for each new node, the three closest old nodes are found and using the weighted average (weighted according to the distances from the old nodes to the new nodes) in the exact same manner as section 6.4.4.1, the parameter values are calculated on the new nodes, from their known values on the old mesh. From there, it is easy to calculate the parameter values on the new elements from the new node parameter value's (as done in section 7.2.4).

7.2.5.5 Newton method extensions, robustness issues

When Newton's method was run (with or without Broydens method) to simulate pavement cell growth, the solver suffered from robustness issues where the system would struggle to find a solution. Mehlmann and Richter [2017] who created a strongly nonlinear viscous-plastic sea ice model also encountered a very similar problem and found it to occur as a result of large variations in the viscosities in the system. These variations are also a problem in the system here, where both μ_y^* and μ_a^* spatially vary where sometimes μ_a^* can take a value 1000 times larger than the smallest μ_y^* value. Spatially varying the anisotropy directions, $\mathbf{a}$, is also found to (when comparing to simulations where the anisotropy is only in one direction) decreases the robustness of the system. These factors all contribute to the difficulty the numerical solver faces. Therefore, four changes are made to solve this issue, specifically: certain parameter values are changed, the degrees of freedom in the system are reduced, the condition number of the Jacobian is improved and the damped Newton's method is used. These all help improve the robustness of the solver and are explained in more detail below.

A lot of the robustness issues arise with the introduction of the viscous anisotropy forces, $\mathbf{f}_a$. Solving the system without this contribution is less problematic. Therefore a big difference to the robustness issues is made by decreasing the magnitude of the anisotropy parameter, μ_a^*, meaning $\mu_a^* = 2$. Decreasing this value further would help with

the robustness issues but would make the anisotropy effect negligible, meaning the effect of the cellulose fibres would not be simulated. Consequently, other methods to further increase the robustness of the solver are needed.

When the triangulation from the reaction-diffusion system is imported, there are many degrees of freedom (many nodes), making it increasingly difficult for the solver to find a solution. The pavement cells are therefore remeshed, creating another triangulation with fewer nodes and by using the method stated above (section 7.2.5.4), all the needed parameters values for each element and node can be found. This procedure made a difference to the robustness of the solver but more still needed to be done.

Another improvement to make is to improve the condition number of the Jacobian. The condition number of a matrix can represent how sensitive a matrix is to roundoff errors, meaning as this number increases, the errors in the numerical operations also increase. Reducing the condition number helps improve the accuracy of the numerical operations (like computing $\mathbf{J}^{-1}(\tilde{\mathbf{X}}^{k_I})\tilde{\mathbf{F}}(\tilde{\mathbf{X}}^{k_I})$ in equation (7.2.43)) which in turn helps the system converge to a solution. To improve the condition number, the LU decomposition is used, which decomposes the Jacobian into lower and upper triangular forms (which can be computed as long as the Jacobian diagonal entries exist). The system can therefore be rewritten as,

$$\mathbf{J} = \mathbf{L}\mathbf{U}, \tag{7.2.52}$$

where $\mathbf{L}$ is the lower triangular matrix and $\mathbf{U}$ is the upper triangular matrix where both matrices have smaller condition numbers than $\mathbf{J}$. These matrices are then used by rewriting equation (7.2.43) as

$$\tilde{\mathbf{X}}^{k_{I+1}} = \tilde{\mathbf{X}}^{k_I} + \mathbf{v} \text{ where} \tag{7.2.53}$$

$$\mathbf{v} = \mathbf{U}^{-1}\hat{\mathbf{v}} \text{ and } \hat{\mathbf{v}} = -\mathbf{L}^{-1}\tilde{\mathbf{F}}(\tilde{\mathbf{X}}^{k_I}). \tag{7.2.54}$$

Additionally, it is computationally favourable to decompose the Jacobian as MATLAB

can invert the lower and upper diagonal matrices quicker. There is an adapted Broyden's method that computes these upper and lower diagonal matrices directly, helping to further decrease the computation time [Bergamaschi et al., 2006] but this method was found to be unsuitable as the approximations of the matrices would lose their diagonal and sparse forms meaning the operations in equations (7.2.54) would take longer. With this change in place, one further improvement to the solver method is used.

The last change made to improve the robustness of the algorithm is to use the damped Newton's method. This method is used as it is said to significantly increase the robustness of a system [Lemieux et al., 2014] as Mehlmann and Richter [2017] also found. The basic formula for the damped Newton's method is,

$$\tilde{\mathbf{X}}^{k_{I+1}} = \tilde{\mathbf{X}}^{k_I} + \gamma \mathbf{v}, \tag{7.2.55}$$

where $\gamma \in (0, 1]$ is the damping parameter where when $\gamma = 1$, equation (7.2.55) is just the basic Newton's method. The parameter γ is made to satisfy the following statement,

$$\inf_{\gamma \in (0,1]} \left(\mathbf{F} \left(\mathbf{X}^{k_I} + \gamma \mathbf{v} \right) \right), \tag{7.2.56}$$

meaning the chosen γ value is the one that gets us closer to the root of the problem. To find this value, a simple linesearch is performed, which means a group of values in $(0, 1]$ are tested to see which one minimises equation (7.2.56). Mehlmann and Richter [2017] and Lemieux et al. [2014] suggest a linesearch be performed on the set of values,

$$\gamma \in \{1, (1-\omega), (1-\omega)^2, \ldots\}, \tag{7.2.57}$$

where they only check 4 values in this geometric series to save computation time. The choice of ω is important as it can affect the robustness of the solver. Mehlmann and Richter [2017] set $\omega = 0.75$ and Lemieux et al. [2014] set $\omega = 0.5$, with Mehlmann and Richter [2017] saying that their value allows for a more robust solver. Through experimentation,

when γ is set to take a smaller value like $\omega = 0.25$, the system converges faster, but as the robustness of the solver is the main problem, the choice of values when $\omega = 0.75$ are still needed. As the linesearch check is not the most computationally expensive part of the numerical solver, more values are checked to give the solver more choice, specifically,

$$\gamma \in \{1, 0.75, 0.5, (1-\omega), (1-\omega)^2, (1-\omega)^3, (1-\omega)^4\}, \tag{7.2.58}$$

with $\omega = 0.75$. By checking more values, both fast convergence and improved robustness can be achieved. It is also found that the damped Newton's method does not majorly increase the computation time and, even in some instances, decrease it (see appendix A.5.1 for details).

7.3 Results and Discussion

With the model equations and solver now established, simulations can finally be peformed. As mentioned in the introduction of this chapter two things shall be tested.

Firstly, as described in section 2.1.4, it is theorised that the signalling proteins and microtubule network, through their effect on the cell wall properties, lead to the further development of pavement cell lobes. This theory shall be investigated using the steady-state solutions of the signalling network found in chapter 6 that formed a pattern of expression of microtubule localisation to the indents and ROP2 localisation to the lobes, anisotropically stiffening and softening, respectively, where these spatially varying cell wall properties are reflected in the parameters values (see section 7.2.4). As part of this exploration, the roles of the different wall properties in growth also warrant investigation. Therefore, several test simulations are run which all involve different combinations of the mechanical features, spatially varying viscosity, elasticity, anisotropy, complimentary tissue parameters and spring growth.

Secondly, different theorised lobe initiation strategies are tested where both chemical

and mechanical initiation methods are examined. Chemical initiation is examined by seeing if spatially varying viscous properties or anisotropic properties can initiate lobes; Such simulations will investigate whether varying pectin properties/deposition or cellulose deposition, respectively, can cause lobe initiation. The first mechanical initiation strategy to be tested is whether experimentally observed differing growth rates between neighbouring cells can cause lobe initiation as a result of slower-growing cells forming an indent with their faster-growing neighbour to allow them in. The second and final mechanical initiation method to test is a possible buckling mechanism, which is theorised to occur because faster-growing pavement cells in the middle of the leaf are restricted and bounded by the slower-growing leaf rim.

Therefore how pavement cells further develop their lobes is tested in section 7.3.1 and how they possible initiate their lobes in section 7.3.2.

7.3.1 Pavement cell lobe development

Here the theory as to how pavement cells develop their lobes is investigated. As a fine mesh is required to simulate pavement cells, for modelling ease and as a result of some of the solver's robustness issues, only one cell is simulated at a time. However, this cell would realistically be embedded in a neighbourhood of pavement cells. So to ensure realism, the pavement cells are embedded in a tissue with similar parameters (taking the base values in table 7.1) and imposing the spring boundary conditions on the outside of this tissue (figure 7.8a). To also ensure realism in some cases complimentary tissue parameters are included as the indents and lobes of a pavement cell are always matched with an opposing lobe and indent, which would also have varying mechanical properties (figure 7.8b and c).

A complete understanding of the effect of each parameter on pavement cell growth is needed. As the growth rates G_{sr} and G_{tr} are unknown, a parameter sweep of both parameters is firstly completed by running simulations in one of the pavement cell outlines. Secondly, to gain a full understanding of the effect of each parameter, this parameter sweep is done in several different simulations scenarios which are as follows,

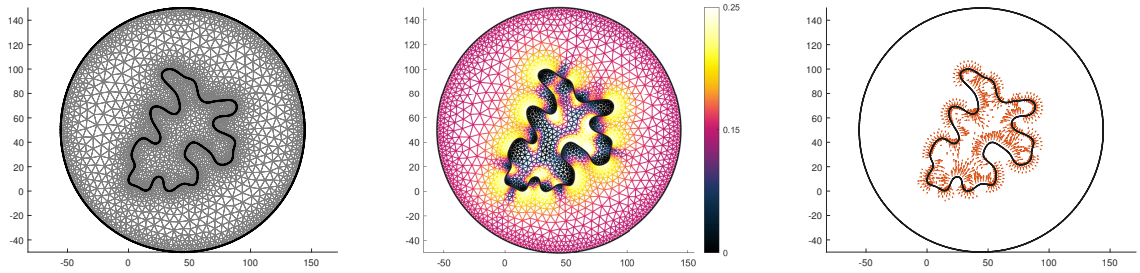
1. Sim 1: Includes spatially varying viscosity and elasticity,

2. Sim 2: Includes spatially varying viscosity, elasticity and anisotropy,

3. Sim 3: Includes spatially varying viscosity, elasticity, anisotropy and complimentary tissue parameters,

4. Sim 4: Includes spatially varying viscosity, elasticity, anisotropy, complementary boundary conditions and spring growth.

When the effect of the parameters is fully understood, simulations can then be performed in the rest of the pavement cell outlines to provide concrete evidence for or against the hypothesis that the signalling network can further develop pavement cell morphology. The parameter sweep simulations also are used to inform the growth rate parameter choices in these latter simulations.



(a) (b) (c)

Figure 7.8: Parameter values in an example pavement cell in an embedded tissue with complimentary tissue parameters. a) Example mesh of a pavement cell embedded in a tissue, b) viscosity values in a complementary tissue c) the scaled anisotropy directions in a complimentary tissue.

To quantify whether the pavement cell outlines in the growth simulations have further developed their lobes and become increasingly complex, a shape index measure is needed. There are several existing methods to quantify the complexity of pavement cell outlines [Altartouri et al., 2019, Vőfély et al., 2018, Sapala et al., 2018] including a very promising method from Nowak et al. [2021]. However, for simplicity and ease, the circularity is used, which is calculated by finding $4\pi \times \text{Area}/\text{perimeter}^2$ of the pavment cell outline which gives

a number between 0 and 1 and is 1 when the shape is perfectly circular and closer to 0 the more "complex" a shape is. This circularity index is used by calculating it at the start of the simulation and at the end, where the end value is then divided by the starting value to compare how it has changed. To ensure that this relative circularity index accurately informs us whether the lobes are developing further (increasing in amplitude), for the parameter sweep simulations, the relative average lobe aspect ratio is also calculated where it is found to agree with the relative circularity index (see appendix A.5.2 for details).

With the simulation principles in place, the parameter sweep simulations are displayed and discussed in section 7.3.1.1 followed by the full simulations in the rest of the pavement cell outlines which are shown and analysed in section 7.3.1.2.

7.3.1.1 Investigating the effect of different wall properties and parameters on pavement cell lobe development

To investigate the effect of the different parameters on lobe development, simulations are run for 500 time steps with $t^*_{max} = 20$hr and $\Delta t = 0.0001$ to allow enough time for all the different simulation types and their varying parameters to have their effect. It is important not to run these simulations for too long as the system will start to reach a steady-state where the elastic properties dominate, and the influence of the varying viscous parameter is lost.

The first observation made is that the growth rates G_{sr} and G_{tr} do not seem to affect the relative circularity index (tables 7.3 and 7.4). This result means that it does not matter what their values are set as for later simulations, as they do not significantly affect the results.

The effect of including the different varying wall properties can now be analysed. For the control simulations with no spatially varying parameters, all of the relative circularity indices are seen to be > 1 at the 50th and 500th time steps (table 7.3), which means the complexity of the pavement cell outline has decreased. This can also be observed

by comparing the final control outline with its original outline (figure 7.9a and b). This result implies that with no spatially varying mechanical wall properties, pavement cells cannot further develop their lobes and indeed lose their lobey shape. This phenomenon most likely happens as the pavement cells outline is attempting to reach its minimum energy steady state of a circle (like a soap bubble).

When both spatially varying elastic and viscous parameters are included (Sim 1), the pavement cell's relative circularity index is > 1 at the 500th time step (table 7.3), meaning the lobes have not further developed (figure 7.9c). However, the relative circularity index is < 1 at the 50th time step. This result implies that for shorter timescales, varying the isotropic properties can sustain and slightly develop pavement cell morphology. An implication of this result is that without anisotropy, pavement cells might have to continuously edit their cell walls to ensure this short timescale lobe sustaining behaviour continues. It is also noted that at the 500th time step, the relative circularity index is lower than the control, further demonstrating that the varying viscous parameters help sustain the lobes. From observations, the lobe width has also increased (figure 7.8c), which is consistent with biological observations in pavement cells where anisotropy is lost (see section 2.1.4.2 for details). Intriguingly, the impact of the spatially varying viscosities does not seem that significant, as at the 50th time step, the circulatory index is only smaller than the control by a factor of around 0.02. The range of the viscosity values set in section 7.2.4 could be increased to see if this could help further develop pavement cell lobes; however, this is not done for two reasons. Firstly, this would vary their values further away from the calculated viscosity value derived by Fozard et al. [2013] and secondly, increasing its value would put the isotropic viscosity at the same magnitude as the anisotropic viscosity, implying that the pectins' (and other cell wall components like hemicellulose) contribution to the cell wall strength is at the same magnitude as the cellulose molecules which is biologically unrealistic.

Next, when the anisotropy is added to the simulations (Sim 2), the relative circularity index is < 1 meaning the pavement cell lobes have further developed (figure 7.9d),

additionally, the index has decreased convincingly when compared to the control and the varying viscosity simulations. This result demonstrates the importance of anisotropy in pavement cell lobe formation as without such a feature, the lobes struggle to/do not further develop at longer timescales. This finding can be backed up by the biological observation that when microtubules are disrupted (so no anisotropy), no lobes form [Panteris and Galatis, 2005]. On the other hand, Altartouri et al. [2019] found that lobes could still form in pavement cell mutants where cellulose molecules were disorganised with no significant differences in cellulose anisotropy and microtubule concentration between neighbouring lobes and indents (see section 2.1.4.2 for details). There is, therefore, an open debate about cellulose's role in pavement cell development. However, combining the varying anisotropy results with the varying viscous results implies that anisotropy may not be essential for lobe development but makes a significant impact where its effect is also longer lasting.

Upon including complimentary tissue parameters (Sim 3), the relative circularity index can be seen to be < 1 (table 7.3) and is less than when no complimentary tissue parameters are included. This result demonstrates that complimentary tissue parameters on an opposing indent to a lobe and vice versa in neighbouring pavement cells helps to further develop pavement cell lobes. These complimentary tissue parameters would be present as a result of the ROP2-PIN1 signalling pathway (see section 2.1.4.3 for details), thus this result demonstrates the importance of such communication between cells.

Lastly, when all of these features with plastic spring growth are included (Sim 4), the relative circularity index is observed to be < 0.4 (table 7.3), demonstrating that this inclusion significantly helps pavement cells develop their lobes even further. This result shows the great effect of allowing growth and targeted cell wall material deposition on cell morphology. However, it is noted by observing the pavement cell outline that at the 500th time step (figure 7.9f), its shape has begun to look slightly unrealistic. This phenomenon results from the plastic spring growth feature allowing the cell to grow quicker than the others, and at this stage of growth, the parameter distributions have been distorted and

Simulation type \ Tissue growth rate	0.1	0.3	0.5	0.7	0.9
Control	1.6780 (1.0133)	1.8110 (1.0151)	1.8125 (1.0156)	1.8036 (1.0159)	1.8109 (1.0160)
Sim 1	1.3176 (0.9962)	1.3152 (0.9964)	1.3151 (0.9964)	1.3190 (0.9963)	1.3209 (0.9962)
Sim 2	0.8087	0.8093	0.8093	0.8107	0.8083
Sim 3	0.6810	0.6862	0.6858	0.6841	0.6846
Sim 4	0.3846	0.3785	0.3748	0.3750	0.3713

Table 7.3: Relative circularity shape index values at the 500th and 50th (shown in brackets) time step when varying the tissue growth rate G_{tr} and including different wall material properties.

Simulation type \ Spring growth rate	0.1	0.3	0.5	0.7	0.9
Sim 4	0.4879	0.4894	0.4813	0.4831	0.4767

Table 7.4: Relative circularity shape index values at the 300th time step when varying the tissue growth rate G_{sr} in our simulations that include varying viscosity, elasticity, anisotropy, complimentary tissue parameters and plastic spring growth.

may no longer be in the correct positions. For this reason, in the next section, the simulations are run for only 300 time steps. With these results now in place, the effect of including all these features are tested in the other pavement cell outlines.

7.3.1.2 Does the signalling protein and microtubule network further development pavement cell morphology?

Now that the effect of the different wall material properties and the different growth rates has been tested, simulations are run in the different pavement cell outlines for 300 time steps with $G_{sr} = 0.3$ and $G_{tr} = 0.5$.

From table 7.5 it is seen that for all pavement cell outlines, the relative circularity indices are < 1 meaning the lobes have further developed. This is a direct result of the varying parameters as when the control simulations are examined, the relative circularity indices are > 1 demonstrating that the pavement cell lobeyness has decreased. All of the parameters in these simulations were set from the results of the signalling network model in chapter 6. Therefore, the hypothesised signalling network is able to set up a pattern of microtubule and ROP2 localisation, which directly leads to the further development of pavement cell lobes.

The authentication of this hypothesised theory demonstrates the power of our novel

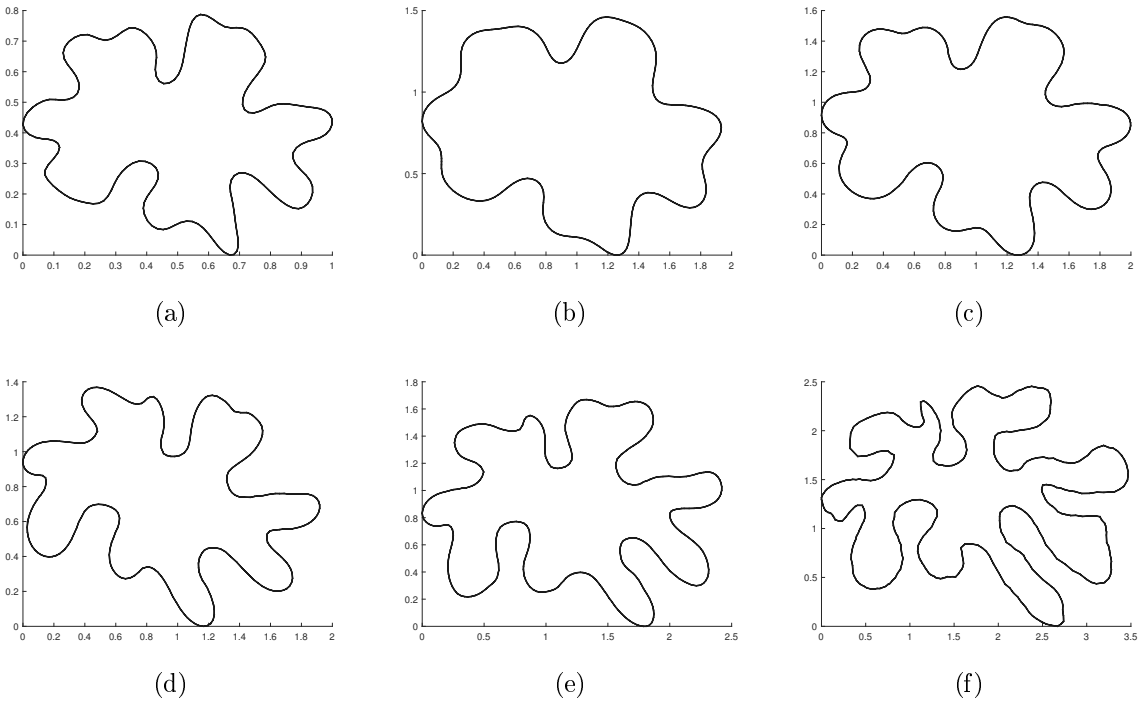


Figure 7.9: Pavement cell outlines for $G_{tr} = 0.5$ at the 500th time step (apart from a). a) Original pavement cell outline. b) Pavement cell outline from the control simulation. c) Pavement cell outline from the varying viscous and elastic properties simulation. d) Pavement cell outline from the varying viscous, elastic and anisotropic properties simulation. e) Pavement cell outline from the varying viscous, elastic, anisotropic with complimentary tissue parameters simulation. f) Pavement cell outline from the varying viscous, elastic, anisotropic, with complimentary tissue parameters and spring growth simulation with $G_{sr} = 0.3$.

model, where these results would not have been found without modelling all the microtubules, the signalling proteins, the growth mechanics and then combining them all. We have therefore set up a framework that future modelling efforts could adopt to make similar exciting discoveries.

7.3.2 Lobe initiation strategies

Now that it is understood how pavement cells sustain and further develop their lobes, how pavement cells initiate their lobes is now investigated. In this section, different chemical and mechanical theories first mentioned in sections 2.1.4.4 and 2.1.4.5 are tested. These different initiation strategies are tested in a bounded 16 cell tissue square set up (where

Simulation type \ Cell outline	1	2	3	4	5	6	7	8	9	10
Control	1.3104	1.3467	1.3456	1.3663	1.3474	1.3775	1.2972	1.3670	1.2830	1.3967
Sim 4	0.5288	0.5769	0.4457	0.5930	0.5482	0.4822	0.4384	0.4384	0.5174	0.5620

Table 7.5: Relative circularity shape index values at the 300th time step in the different cell outlines simulations that all include varying viscosity, elasticity, anisotropy, complimentary tissue parameters and plastic spring growth.

there are no existing lobes), where each cell has a width and height of 10μm (figure 7.10) with the mesh size set at $h^* = 0.5$. In the different simulations, the 4 inner cells of this tissue shall be examined for evidence of possible lobe initiation sites where we will be looking for lobes of any size, as a small indenting region could be enough to set up an area of increased stress which microtubules can localise to, to begin lobe development [Bidhendi et al., 2019]. Only the 4 inner cells are examined as these are the ones immersed in the tissue and therefore offer the most realistic results.

First to be investigated is possible chemical initiation theories. This theory claims that (by some unknown chemical signalling pathway), ROP2 or the microtubules through their deposition of wall loosening enzymes and pectin or cellulose set up a pattern of spatially varying isotropic or anisotropic cell wall mechanical properties that can lead to differential growth rates and directions which initiates lobes. This idea comes from biological observations in young pavement cells that have shown that there is a higher concentration of stiffer pectins in small indents and a lower concentration in their opposing lobes and microtubules to localise against straight wall segments that later become indents. This chemical initiation hypothesis is tested by simulating the growth of the 16 cells with spatially varying isotropic, μ_y and anisotropic parameters, μ_a (figures 7.10a and b) with it being assumed that the patterning of ROP2 will lead to regions of lower and higher isotropic viscosity and the microtubules will lead to regions of stiffer anisotropic viscosity as detailed in section 7.2.4. As it has been theorised that either the patterning of pectin or cellulose occurs first and initiates lobes by themselves, both isotropic or anisotropic initiation are tested independently.

Halfway between chemical and mechanical initiation is the theory that lobes form due

to differing growth rates between neighbouring cells that can cause cells to grow into their slower growing neighbour and form a lobe. Two different ways to implement this idea are simulated in the model. Firstly different spring growth rates are set for each cell (figures 7.10c), so that the anticlinal walls are growing at different rates (as higher values will allow the resting lengths to extend quicker) and secondly, varying viscosity values for each cell are set (figures 7.10d), so that the periclinal walls can grow at different rates (as lower viscosity values will allow the mesh triangles to resist expansion less).

The last initiation method tested is the mechanical buckling hypothesis. The idea behind this theory has come from reports that the leaf boundary grows at a slower rate than the inner tissues, restricting them, meaning if the inner tissue has a higher rate of cell wall material deposition (to cause this higher growth rate) causing excess growth with nowhere to expand into, then the pavement cell walls could be forced to buckle. The suggestion of buckling has also come from simply examining young pavement cells where they seem to form the perfect bend, which could be reasonably expected to be as a result of such a mechanism (figure 1.3). This hypothesis is simulated through restricting the 16 cells and only moving the boundary springs by a set distance at each time step and the inner cells excess growth is included via changing equation (7.2.19) to,

$$l_{0,e} = l_{0,e} + G_{sr}, \tag{7.3.1}$$

so that the resting lengths extend by a set amount at each time step. In this simulation, we also include bending stiffness as, without it, the anticlinal walls were found to form unrealistic shapes. Some stochastic noise is also added to the anticlinal wall coordinates by using the normal distribution with a mean of 0 and a standard deviation of 0.0075. This addition is as a result of in the initial simulations when $l_{0,e} > l_e$, the perfectly straight cell walls' (which is unrealistic) spring force propagated along the cells to the cell boundaries, accumulating excess force, causing them to erupt from their bounded domain.

The results of the isotropic initiation tests are displayed in section 7.3.2.1 and the

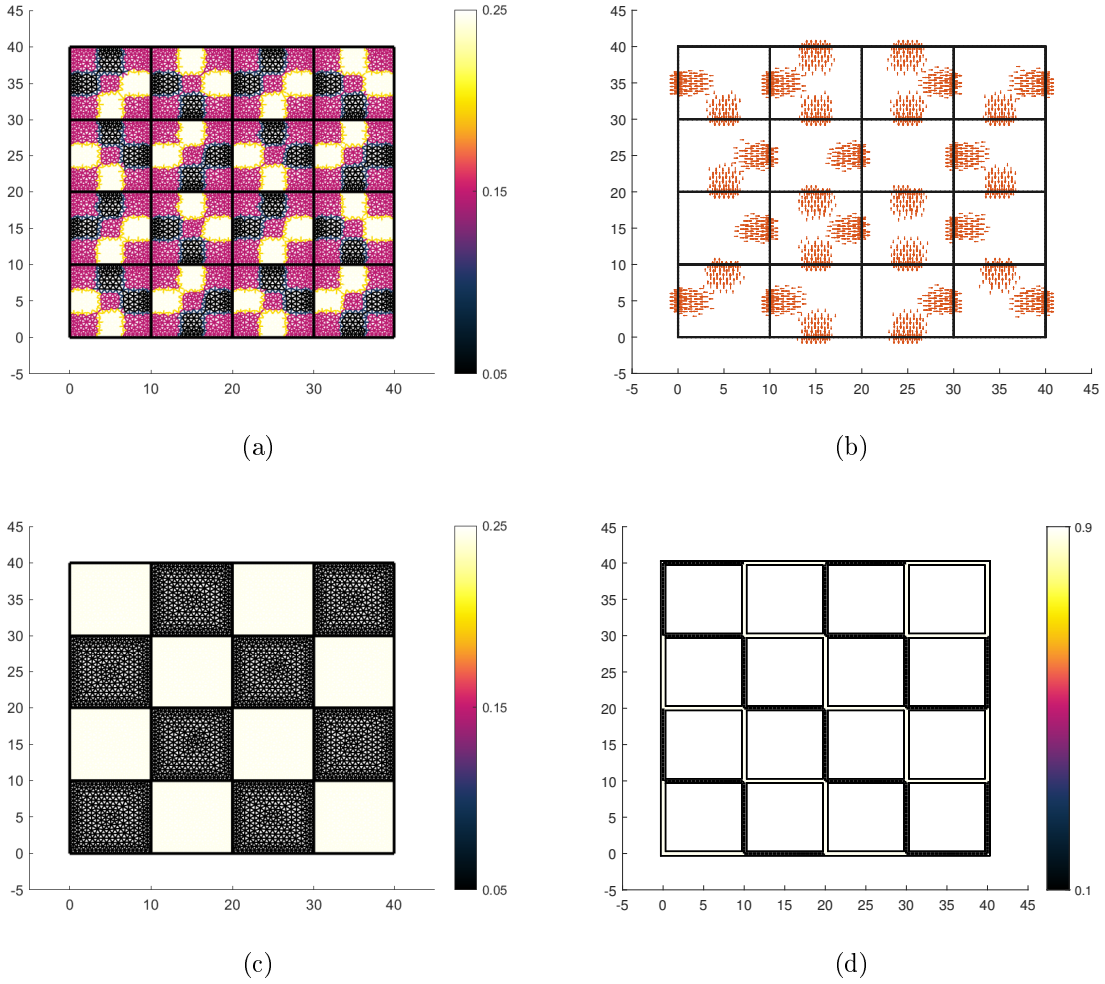


Figure 7.10: The parameters applied to the different simulations. a) The varying viscosity values in the isotropic initiation tests. b) The varying scaled anisotropy directions in our anisotropy initiation tests. c) The varying plastic spring growth rates for the first differential cell growth rates initiation test. d) The varying viscosity values for the second differential cell growth rates initiation test.

anisotropic initiation simulations in section 7.3.2.2. Following on from this, the results of the cell differential growth simulations are shown in section 7.3.2.3 and the restricted growth simulations in section 7.3.2.4. It should be noted that all the figures below show nondimensional lengths. The simulations are run until they reach a steady state where numerous time steps are checked where the time step with the most apparent lobeing is then displayed.

7.3.2.1 Chemically induced isotropic viscosity variation lobe initiation

Here the results from the isotropic initiation simulations are shown with $\Delta t = 0.01$ and $t^*_{max} = 20$hr with no anisotropy and $G_{tr} = 0.5$.

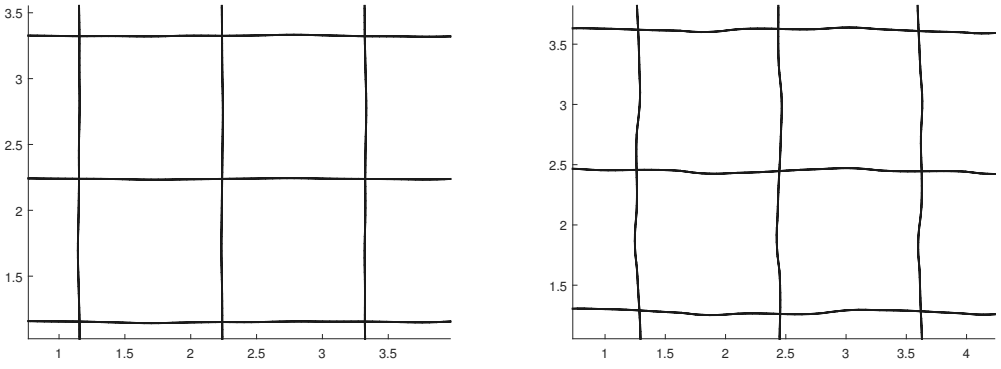
For the first simulation where μ^*_y is ranging between 0.05 and 0.25 (figures 7.11a), the cell anticlinal walls are not seen to have truly perturbed from the straight alignment they had at the start. This result implies that having regions of varying isotropic viscosity can not initiate lobes. However, to check this result's dependence on the parameter, μ^*_y, these simulations are rerun with μ^*_y ranging between 0.05 and 100. In this case, some bending along the anticlinal wall is observed, which could be lobe initiation sites (figures 7.11b). As discussed in section 7.3.1.1 we are cautious about increasing this parameter as it could be unrealistic for it to be this high, especially for it to be higher than the anisotropy parameter. Therefore, it is uncertain whether isotropic initiation is possible, meaning it is unknown if varying pectin's distribution can lead to lobes. However, this result is not conclusive as any small lobe could cause the feedback loop to be initiated to further develop the lobe.

Previous modelling work in 3D could dispute this result as Bidhendi et al. [2019] found that isotropic mechanical variations can initiate lobes, but this model assumed the cell wall was a hyperelastic material and not viscous, demonstrating how modelling choices can affect the results. Plants have been shown to behave both visco-elastically and hyperelastically (see Bidhendi et al. [2020b] and section 1.1.2 for details). Further modelling work is therefore needed, where by including all of these mechanical features, it could then be known if isotropic initiation is possible.

7.3.2.2 Chemically induced anisotropic viscosity variation lobe initiation

Now the simulations results are shown when spatially varying the anisotropic viscosities and directions with $\Delta t = 0.0001$, $t^*_{max} = 1$hr and $G_{tr} = 0.5$.

From the results clear bends in the anticlinal cell walls can be seen that could be potential lobe initiate sites (figure 7.12). It is also noted that these bends comes in a



(a) (b)

Figure 7.11: The 4 inner cells of the isotropic initiation simulations with a) the base viscosity values at the 10th time step b) the raised viscosity values at the 500th time step.

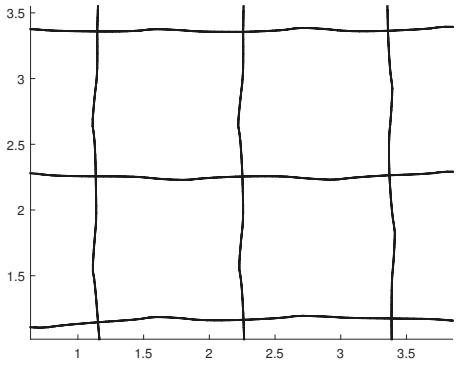


Figure 7.12: The 4 inner cells of the anisotropic initiation simulation at the 1596th time step

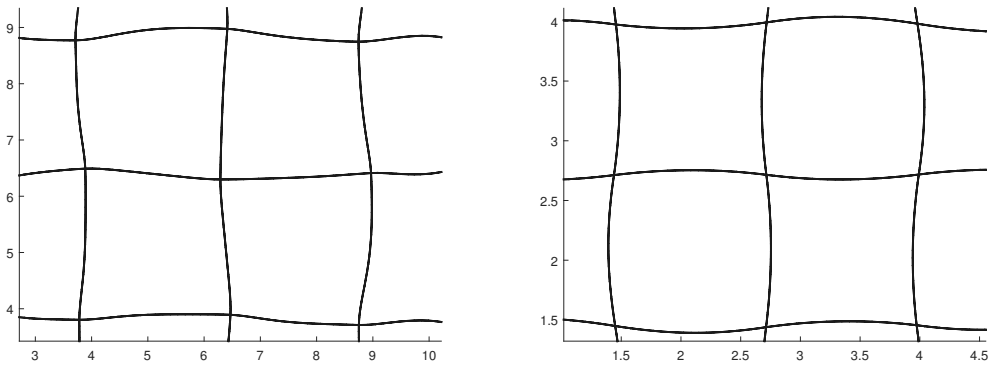
lot earlier than the isotropy induced lobes and for much lower parameter values. The results demonstrate that pavement cells would need to stiffen the cell walls less and possibly use less energy if they rely on anisotropy rather than isotropy. This clearly shows that microtubule localisation and consequently cellulose deposition is an effective way to initiate pavement cell lobes.

These anisotropy simulations however highlight the robustness problems with the numerical solver, as when this simulations went on for any longer the system would not converge. To further investigate anisotropy initiation a more robust method would have to be built. This is discussed in more detail in section 7.4.

7.3.2.3 Neighbouring cell differential growth lobe initiation

The results from the differential growth simulations are now displayed where $\Delta t = 0.01$, $t^*_{max} = 1$hr with no anisotropy in the system.

When the anticlinal walls' spring growth rates are varied, no true evidence of lobe initiation sites are seen (figure 7.13a). The anticlinal cell walls are not straight but do not look likes lobes/lobe initiation sites either. From this simulation, we then decided to model the differential growth rates between neighbouring cells differently by varying the isotropic viscosity values so that they are either 0.05 or 0.25 in each cell in a checkerboard pattern meaning the periclinal walls are assumed to be growing at different rates. From this simulation, exactly what was theorised can be seen, where the cells with higher growth rates have bulged into those with low growth rates forming an initial lobe (figure 7.13b), demonstrating that this could be a possible mechanism as to how pavement cells form lobes. However, this lobeing strategy only forms one lobe per side at a time. So to form multiple cell lobes with a neighbouring cell with this method, cells that have been bulged into could reinforce their current bulges via the signalling pathways ensuring they remain and then change their comparative growth rates with their neighbours to allow further bulges to form.



(a) (b)

Figure 7.13: The 4 inner cells from the differential cell growth rates simulations where the figures display a) the differential anticlinal wall spring growth rate simulation at the 180th time step and b) the differential periclinal wall viscosity simulation at the 100th time step.

To prove this as a possible lobe initiation mechanism, further simulations would need to be run where by stochastically varying the growth rates, reinforcing any bulges that form and allowing them to develop further and then continuing the simulation by changing the growth rates again, we could test whether multiple lobes can form. Experimental methods could also be used to investigate this theory as well, such as by applying a similar methodology to Elsner et al. [2012] and by making continuous observations, it could observed if neighbouring pavement cells repeatedly swap between being faster or slower growing than the other. Other modelling efforts could also bring some light to this process such as by producing a slow timescale Saffman–Taylor instability model [Saffman and Taylor, 1958].

These simulations also compliment the work by Bidhendi and Geitmann [2019] where we have similarly found that it is through the control of the periclinal wall not the anticlinal wall that lobes are initiated.

7.3.2.4 Inner tissue restricted growth buckling lobe initiation

Finally the results from the excess growth simulations are shown with $\Delta t = 0.01$, $t^*_{max} =$ 1hr and $G_{sr} = 0.02$

From the results, the cell anticlinal walls are seen to have clearly buckled, displaying many potential reasonably-sized lobe initiation sites. This finding demonstrates that if pavement cell growth is restricted possibly by the leaf margin, then this can cause numerous lobes to form. Interestingly, it has been suggested (through academic discussion [Robinson]) that as buckling is seen as quite a sudden dynamic process, it may not be able to occur over the scale of growth. This idea has, therefore, been rebuted as viscosity has been included in the model which would slow down any dynamic behaviour.

However, further work would need to be done to prove this theory more thoroughly. As mentioned in section 6.5.1 pavement cells only grow in 2D dimensions and maintain a constant height, so if this theory is true, then pavement cells would need some mechanism to ensure that this excess growth does not force the pavement cell to grow out

of plane, perhaps through significant axial cellulose reinforcement. Consequently, a 3D model would therefore be needed to test how this buckling mechanism truly works. Biological experiments could also be instrumental in investigating this theory further, where if the cell leaf's boundaries' growth rate could somehow be perturbed, it could be seen if this affects pavement cell lobeyness. As detailed in section 2.1.4.4 the buckling hypothesis comes from observations showing that the outer edge of the leaf grows slower than the inner. However, a question to ask is, do the cells buckle because the outer edge grows out more slowly, or does the outer edge move out more slowly because the cells inside are forming intricate puzzle-like shapes?

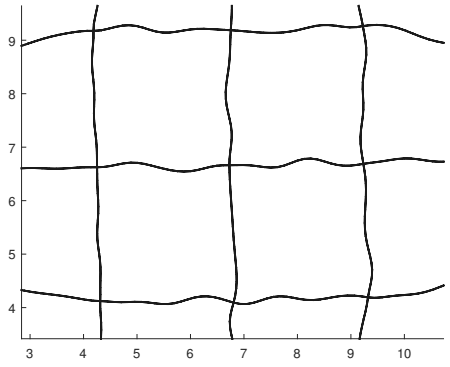


Figure 7.14: The 4 inner cells from the excess growth buckling simulations at the 10th time step.

7.4 Concluding remarks

In this chapter, a mechanical vertex element model to simulate pavement cell growth has been built that incorporates visco-elastic and anisotropic features. By combining the stochastic microtubule model, the signalling network model and the vertex element model, we have created a novel system to analyse pavement cell development. With this innovative model, it has been shown that the hypothesised signalling network's effect on the cell wall mechanical properties does indeed cause lobes to develop further and that anisotropy considerably contributes to this development. Different initiation strate-

gies were also tested. It was demonstrated that isotropic lobe initiation is only possible when the difference between varying viscosities is large (possibly unrealistically large), but anisotropic lobe initiation was found to be an effective way for pavement cells to initiate lobes. This finding suggested that it is a lot easier for pavement cells to initiate lobes through cellulose deposition than through pectin deposition. Secondly, by exploring mechanical initiation methods, differing periclinal wall growth rates between neighbouring cells were found to be able to initiate lobes, but neighbouring cells would have to switch between being slower and faster growing for this to be a valid method and thus this theory needs further study. If pavement cell growth is restricted it was also shown that, the anticlinal walls can buckle, forming numerous lobes. Therefore, we have presented no single method as to how pavement cells can form their lobes but have instead shown that there are numerous possibilities that need to be further researched. This exciting plant cell has, therefore, many secrets that remain to be revealed.

There are further improvements that could be made to this model. One problem already mentioned was the robustness of the solver, which greatly limited the degrees of freedom in the system, and thus restricted the mesh density and the number of cells we could simulate. This robustness issue was especially problematic upon the inclusion of anisotropy, limiting the use of this feature, which is an essential inclusion in a plant growth model. An example of this was in the anisotropy initiation simulation in section 7.3.2.2 which were cut short by such issues. Problems arising as a result of having parameter values at different magnitudes of scale have already been discussed in section 7.2.5.5. However, another potential problem is the lack of a unique solution for the equation $\mathbf{F}(\mathbf{X}^k) = \mathbf{0}$. Specifically, the viscous stresses calculated in a triangle seem to resist expansion by resisting an area increase, so that a force balance can be reached at numerous coordinate points. This phenomenon is a side effect of using the strain tensor (equations 7.2.13), which is solely dependent on the velocity, so it does not matter where the coordinates are, as the viscous stresses just resist the differences between the new and the previous coordinates, giving a full circle of values for the same velocity.

To move past these issues, it might be beneficial to adopt the methodology of the majority of plant cell models and only include elasticity where anisotropy can still be included through directional stiffnesses, similarly to Hamant et al. [2008]. This change would simplify the system and make it easier for the solver to find a solution. However, it is important to note that information could be lost, as through the inclusion of viscosity, differing results were found from a purely elastic model in section 7.3.2.1 and plant cell walls have been shown to be visco-elastic. Therefore, there is a need and a great opportunity for a new robust visco-elastic mechanical model to be built for plant biomechanical modelling.

Another improvement that could be is made is to model in 3D, which would allow a better understanding of pavement growth mechanics. For example, as already mentioned in section 7.3.2.4 a 3D model would enable further investigations of the possible buckling lobe initiation theory. A 3D model would also allow us to understand how pavement cells maintain their axial height while also forming lobes (first mentioned in section 6.5.1), an essential feature if pavement cells are to be the protective layer for plant leaves. The advantage of a 3D model can be seen through the work of Bidhendi et al. [2019]'s who found that stiffness variations in the anticlinal wall (on top of periclinal wall stiffness) increased lobeing, as well as showing that pavement cells experience vertical stress due to their thinness, results that the 2D model would not necessarily find.

Our model potentially also features some unrealistic properties. Linear elasticity has been used in the model, however, from experimental tests and finite element simulations on onion epidermises, it was shown that plant cell walls primarily follow hyperelastic laws [Bidhendi et al., 2020b]. Future modelling attempts should therefore stray away from linear behaviour where examining non-linear behaviour can also often yield interesting insights (such as Kierzkowski et al. [2012]). Despite these issues, we still trust the results, as the vertex element model has been shown to be accurate in the past [Fozard et al., 2013].

We have now built, analysed and discussed all of the models examining growth control

in this thesis. We now finish up our thesis in the next chapter with the conclusion (chapter 8).

Chapter 8

Conclusion

In this thesis, how plant cells control their growth has been examined. In order to gain an understanding of this complex process, a multiscale approach was taken by first looking at the microscale to see how plant cell walls are structured and loosened and secondly, on the cell level, it was examined how cells control their morphology through signalling networks and mechanical interactions. In the latter case, pavement cells were investigated due to their complex shape, where if their growth control mechanisms are unlocked, it could help us understand how growth is controlled in other plant cell types. We combined experimental measurements with a novel hybrid mathematical model to tackle these complex questions.

In chapter 3, a continuum model of the cell wall that incorporated crosslinking dynamics, cellulose reorientation and viscoelastic behaviour was built. With this model and through assuming the biological hotspot hypothesis, observed experimental behaviour was matched to and thus provided evidence for the theory. A mechanistic understanding of enzyme action was also presented with the following proposed mechanisms being able to produce observed biological behaviour: XTH hydrolysis action of hemicellulose fibres is unable to induce growth as it can not break down the biological hotspots, Cel12A can induce growth as it is able to break down the hotspot junctions, but in turn, weakens the cell wall, and expansin can induce growth while not weakening the cell wall and can even strengthen it by permitting the slippage of cell wall fibres. Through this modelling we have therefore presented novel understanding of cell wall enzyme action with our work being one of the only mathematical studies to do so. It was also confirmed that cellulose orientation is the primary control behind axial wall strength. Additionally the leading order behaviour was found to be dominated by the small group of significantly stressed fibres, and the celluloses' contribution was shown to be capped by the crosslinks ability to remain intact.

Pavement cell growth was next examined using a mix of experiments and a combined set of models to understand how they initiate and further develop their highly undulated shapes. Investigations began in chapter 4 using experimental methods. Specifically, by

making use of GFP marked proteins it was found that actin, despite previous claims, does not convincingly localise to pavement cell lobes, where on the other hand, microtubules were repeatedly observed to localise and fan out from the indents as previously reported. Our work has therefore highlighted the need for further experimental studies to investigate how ROP2 localisation causes a increase in growth rate. Using Atomic Force Microscopy, stiffness heterogeneities were found in very young pavement cells, including observing stiffer and softer areas in small indents and lobes, respectively, suggesting chemical signalling must occur very early on to initiate these variations.

In chapter 5, we derived, implemented and validated the first component of the combined pavement cell model, namely a stochastic model of the microtubule dynamics. We also found that microtubule alignment can change when the interaction probabilities are changed, alluding to a previously unreported possible microtubule orientation control mechanism.

To simulate the ROPs, and RICs' signalling network in a pavement cell, in chapter 6, the microtubule model is combined with a reaction-diffusion system. This signalling network included all the known and hypothesised protein and microtubule governing interactions. From the simulations, it was found that this theorised network is sufficient and capable of setting up an alternating pattern of ROP2 and microtubule localisation at the lobes and indents, respectively, allowing pavement cells to further develop their shape. By also simulating pavement cell mutants and comparing with experimental observations, the model was both validated and found to have possible missing parts suggesting the hypothesised signalling network also has missing interactions. Specifically, ROP6 may need some other mechanisms independent of ROP2 in order to localise to the indents. Furthermore, this signalling network was found to be unable to initiate lobes, further demonstrating that critical elements are missing from both the model and hence our biological understanding. Biological experimentation could find these missing links, such as by trying to find what is upstream from ROP6.

Lastly, in chapter 7, pavement cell growth was examined using a hybrid vertex ele-

ment visco-elastic model that included anisotropy and the effect of different interacting mechanisms to determine the cell wall properties. By incorporating the results from the signalling network and microtubule model, it was directly shown that the localisation patterning of the proteins and microtubules led to the development of pavement cell lobes where anisotropy was very important in this process. By also testing different initiation strategies, it was found that it could be a lot more feasible and efficient to initiate lobes through cellulose deposition rather than through pectin deposition and by testing mechanical initiation strategies, it was discovered that varying periclinal wall growth rates could initiate lobes and that pavement cells could form numerous lobes through buckling mechanisms if their growth is restricted. Therefore through our novel approach, we have shown new ways in which pavement cells can initiate lobes. However, more experimental and theoretical work needs to occur to confirm or disprove these mechanisms.

In this thesis, we have discovered many fascinating insights into how plant growth is controlled, where mathematics has proven to be a very effective tool in the research. There is, of course, much more work to do be done, for example, we were unable to explain why Cel12A's induced growth is delayed and expansins' is not, and we have just presented many possibilities as to how lobes could be initiated, and so the whole truth remains to be discovered. There are, therefore, many exciting mysterious to still be revealed in this fascinating and essential field.

Appendix A

Appendix

In this appendix we state the full derivation of certain equations and asymptotics expansions, supporting figures, and detailed methodology that were not suitable for the main text. The additional details for chapters 3, 4 5, 6 and 7 can be found in the appendix sections A.1, A.2 A.3, A.4 and A.5 respectively.

A.1 Biological hotspots

A.1.1 Proving constant density

The density at any point, $\rho(x^*, y^*, t^*)$ is described by

$$\frac{\partial \rho^*}{\partial t^*} + \mathbf{u}^* \cdot \nabla \rho^* = 0, \text{ with } \rho^*(x^*, h^*, t^*) = \rho_0^*, \tag{A.1.1}$$

where ρ_0^* is the density at which material is deposited. Using the total derivative, $\frac{D\rho^*}{DT^*} = 0$ on the characteristics $\frac{dx^*}{dt^*} = \alpha^* x^*$ and $\frac{dy^*}{dt^*} = -\alpha^* y^*$ which are from equation (3.2.1), the initial conditions $(x^*, y^*) = (x_0^*, h^*)$ at $t^* = \tau$ for some height up the cell, x_0^* and some time $\tau \geq 0$, we obtain $x^* = x_0^* e^{\alpha^*(t^*-\tau)}$ and $y^* = h^* e^{-\alpha^*(t^*-\tau)}$ for $t^* > \tau$. Therefore along the streamline $x^* y^* = x_0^* h^*$, we have $\rho^* = \rho_0^*$. Consequently if $\rho^*(x^*, y^*, 0) = \rho_0^*$ for $0 < y^* < h^*$, the density remains uniform for $t^* > 0$ meaning it can be assumed that the density of the cell wall components remain uniform for all time as well.

A.1.2 Solving stress terms

First equation (3.2.20) is solved to find the axial hemicellulose stress when not acted upon by any expansin action (L_0 and μ are constant). By using equation (3.2.19) we have $\frac{\partial s}{\partial t} = \frac{dL}{dt} = \alpha L$, and as a result equation (3.2.20) is rewritten as,

$$\frac{\partial \sigma_H}{\partial t} + \omega \sigma_H = \alpha L(t). \tag{A.1.2}$$

If we shift the time parameter so that $\bar{t} = t - \tau$ where the fibre is deposited at time $t = \tau$, we have that $\sigma_H(1, 0) = 0$. The above then becomes,

$$\frac{\partial \sigma_H}{\partial \bar{t}} + \omega \sigma_H = \alpha L(\bar{t}). \tag{A.1.3}$$

Using an integrating factor and integrating both sides it is derived,

$$\sigma_H = e^{-\omega\bar{t}} \int_0^{\bar{t}} \alpha L(\hat{t}) e^{\omega\hat{t}} \, d\hat{t}, \tag{A.1.4}$$

where on substituting $L = e^{\alpha\bar{t}}$ (using boundary conditions $L(0) = 1$) it is found,

$$\sigma_H = \frac{\alpha}{\alpha + \omega} e^{-\omega\bar{t}} \left(e^{(\alpha+\omega)\bar{t}} - 1 \right). \tag{A.1.5}$$

The fibres follow the trajectories $y = e^{-\alpha\bar{t}}$ (from section 3.2 using boundary condition $y(0) = 1$) and with $y = \left(e^{\omega\bar{t}}\right)^{-\frac{\alpha}{\omega}} = \frac{1}{L}$, the final form is calculated as,

$$\sigma_H = \frac{\alpha}{\alpha + \omega} \left(L - L^{-\frac{\omega}{\alpha}} \right). \tag{A.1.6}$$

For the expansin action on the spring resting length (equation (3.2.27)) we were unable to find an analytic expression, as a result forward finite differences are used to solve the equation. This expression is needed in terms of y so it is first divided by $\frac{dy}{d\bar{t}} = -\alpha y$ to get,

$$\frac{dL_0}{dy} = \frac{E}{-\alpha y} \left(\frac{1}{yL_0} - 1 \right). \tag{A.1.7}$$

The domain is partitioned such that $y = \{y_1, y_2, \ldots y_m\}$ where $y_1 = 0$ and $y_m = 1$ and $L_0(y_i) = L_{0,i}$ for $i = 1 \ldots m$ to get the recursive relation,

$$L_{0,i} = L_{0,i+1} + \frac{E}{\alpha y_{i+1}} (y_{i+1} - y_i) \left(\frac{1}{y_{i+1} L_{0,i+1}} - 1 \right) \text{ where } L_{0,m} = 1. \tag{A.1.8}$$

The calculated values of L_0 can the be used in equation (3.2.27) to find the derivative of L_0. The hotspot stress, σ_H is then derived which has non-constant resting length, so using the initial equation (equation 3.2.20), shifting time again and as $\frac{ds}{d\bar{t}} = \frac{1}{L_0}\frac{dL}{d\bar{t}} - \frac{L}{L_0^2}\frac{dL_0}{d\bar{t}}$, it can be derived,

$$\frac{\partial \sigma_H}{\partial \bar{t}} + \omega \sigma_H = \frac{\alpha L}{L_0} - \frac{L}{L_0^2} \frac{\partial L_0}{\partial \bar{t}}, \tag{A.1.9}$$

and using the same method as above and equation A.1.8 it is calculated,

$$\sigma_H = L^{-\frac{\omega}{\alpha}} \int_0^{\bar{t}} L^{\frac{\omega}{\alpha}} \left(\frac{\alpha L}{L_0(L)} - \frac{L}{L_0^2(L)} \frac{dL_0(L)}{d\hat{t}} \right) \, d\hat{t}, \tag{A.1.10}$$

which is the hemicellulose stress term for enzyme action on the resting length, L_0.

The same procedure is repeated for expansin action on the viscosity, μ. By solving equation (3.2.26) it can be obtained,

$$\mu = \frac{1}{\mathcal{M} + (1 - \mathcal{M})e^{-Et}}. \tag{A.1.11}$$

This means that $\omega = \frac{\nu_H^*}{\mu_0^* \tilde{\mu} \tilde{k}_0^*} = \omega_0 \left(\mathcal{M} + (1 - \mathcal{M})e^{-Et} \right)$ where $\omega_0 = \frac{\nu_H^*}{\mu_0^* \tilde{k}_0^*}$, so that substituting this into the non-dimensional stress term (equation (3.2.20)) and shifting time yields,

$$\frac{\partial \sigma_H}{\partial \bar{t}} + \omega_0 \left(\mathcal{M} + (1 - \mathcal{M})e^{-E\bar{t}} \right) \sigma_H = \alpha L, \tag{A.1.12}$$

where an integrating factor is used again and $L = e^{\alpha \bar{t}}$ to get,

$$\begin{aligned} &\exp\left(\omega_0 \left(\mathcal{M}\bar{t} - \frac{1}{E}(1 - \mathcal{M})e^{-E\bar{t}} \right) \right) \frac{\partial \sigma}{\partial \bar{t}} \\ &+ \left(\omega_0 \left(\mathcal{M} + (1 - \mathcal{M})e^{-E\bar{t}} \right) \right) \exp\left(\omega_0 \left(\mathcal{M}\bar{t} - \frac{1}{E}(1 - \mathcal{M})e^{-E\bar{t}} \right) \right) \sigma \\ &= \alpha e^{\alpha \bar{t}} \exp\left(\omega_0 \left(\mathcal{M}\bar{t} - \frac{1}{E}(1 - \mathcal{M})e^{-E\bar{t}} \right) \right). \end{aligned} \tag{A.1.13}$$

Upon integrating it is found,

$$\begin{aligned} \sigma_H = &\exp\left(-\omega_0 \left(\mathcal{M}\bar{t} - \frac{1}{E}(1 - \mathcal{M})e^{-E\bar{t}} \right) \right) \\ &\times \int_0^{\bar{t}} \alpha \exp\left(\alpha \hat{t} \right) \exp\left(\omega_0 \left(\mathcal{M}\hat{t} - \frac{1}{E}(1 - \mathcal{M})e^{-E\hat{t}} \right) \right) \, d\hat{t}, \end{aligned} \tag{A.1.14}$$

where the substitution $\hat{y} = e^{-\alpha \hat{t}}$ is made in the integral. This implies that $e^{-Et} = y^{\frac{E}{\alpha}}$ and

$dt = -\frac{1}{\alpha y} dy$ meaning,

$$\sigma_H = y^{\frac{\omega_0 \mathcal{M}}{\alpha}} \exp\left(\frac{\omega_0}{E}(1-\mathcal{M})y^{\frac{E}{\alpha}}\right) \int_y^1 \alpha y^{-2-\frac{\omega_0 \mathcal{M}}{\alpha}} \exp\left(-\frac{\omega_0}{E}(1-\mathcal{M})y^{\frac{E}{\alpha}}\right)\, d\hat{t}. \tag{A.1.15}$$

A.1.3 Solving the evolving bond densities

To determine the evolving bond densities, equation (3.2.25) is solved for n, using the method of characteristics with $\frac{dy}{dt} = -\alpha y$, $\frac{dx}{dt} = \alpha x$, and $\frac{\partial n}{\partial x} = 0$. The left hand side of equation (3.2.25) can then be rewritten to get,

$$\frac{\partial n}{\partial t} - \alpha y \frac{\partial n}{\partial y} + \alpha x \frac{\partial n}{\partial x} = \tag{A.1.16}$$

$$\frac{\partial n}{\partial t} + \frac{\partial y}{\partial t}\frac{\partial n}{\partial y} + \frac{\partial x}{\partial t}\frac{\partial n}{\partial x} = \frac{dn}{dt}, \tag{A.1.17}$$

the total derivative. As a result, equation (3.2.25) can be reexpressed as,

$$\frac{dn}{dt} = -\breve{k}_0 n \exp(\gamma^2 \varsigma s_{H,e}^2). \tag{A.1.18}$$

Combining equation (3.2.19) and (A.1.18) it is derived,

$$\frac{dn}{dL} = -\breve{k}_0 \frac{n}{\alpha L} \exp(\gamma^2 \varsigma s_{H,e}^2), \tag{A.1.19}$$

and integrating it is obtained,

$$n = \exp\left(-\frac{\breve{k}_0}{\alpha} \int_1^L \frac{\exp(\gamma^2 \varsigma s_{H,e}^2)}{\hat{L}}\, d\hat{L}\right), \tag{A.1.20}$$

which can be written as,

$$n = \exp\left(-\frac{\breve{k}_0}{\alpha} G\left(\frac{1}{L}\right)\right) \text{ with}$$
$$G(y) = \int_y^1 \frac{\exp(\gamma^2 \varsigma s_{H,e}^2)}{\hat{y}}\, d\hat{y}. \tag{A.1.21}$$

To find the hotspot bond density, $\tilde{n}$ (equation (3.2.24)) we repeat the same procedure using the total derivative and again using equation (3.2.19) we derive,

$$\frac{d\tilde{n}}{dL} = -\frac{\tilde{n}}{\alpha L} \exp\left(\tilde{\beta}^2 \tilde{\varsigma}\left(1 - \exp\left(-\frac{\breve{k}_0}{\alpha} G\left(\frac{1}{L}\right)\right)\right) s_{H,e}^2\right). \tag{A.1.22}$$

Continuing in the same manner, by once again integrating we calculate,

$$\tilde{n} = \exp\left(-\frac{1}{\alpha}\tilde{G}\left(\frac{1}{L}\right)\right) \text{ with} \tag{A.1.23}$$
$$\tilde{G}(y) = \int_y^1 \frac{\exp\left(\tilde{\beta}^2 \tilde{\varsigma}\left(1 - \exp\left(-\frac{\breve{k}_0}{\alpha} G(\hat{y})\right)\right) s_{H,e}^2\right)}{\hat{y}}\, d\hat{y}. \tag{A.1.24}$$

A.1.4 Solving the cellulose angle equation

To find the angle cellulose makes to the horizontal, θ, equation (3.2.23) is solved, by first rewriting the left hand side as the total derivative to get,

$$\frac{d\theta}{dt} = \alpha \sin\theta \cos\theta \text{ on } \frac{dy}{dt} = -\alpha y. \tag{A.1.25}$$

Beginning with the second group of fibres deposited at $y = 1$ for $t = \tau > 0$ with angle $\theta(\tau, 1) = \theta_0$, the parameter shift $\bar{t} = t - \tau$ is considered. Consequently on integrating $\frac{d\theta}{d\bar{t}} = \alpha \sin(\theta)\cos(\theta)$ it is found,

$$\int_{\theta_0}^{\theta} \frac{1}{\sin\theta' \cos\theta'}\, d\theta' = \int_0^{\bar{t}} \alpha\, d\tau'. \tag{A.1.26}$$

Making the substitution $v = \tan(\theta)$ it is calculated,

$$\int_{v_0}^{v} \frac{1}{v'}\, dv' = \alpha \bar{t}, \tag{A.1.27}$$

which is integrated to find,

$$\tan\theta(\bar{t}, y) = \tan\theta_0 \exp(\alpha \bar{t})\,. \tag{A.1.28}$$

Knowing $y = \exp(-\alpha \bar{t})$ using $y = 1$ at $\bar{t} = 0$ it is found,

$$\theta(t, y) = \arctan\left(\frac{\tan\theta_0}{y}\right) \text{ for } e^{-\alpha t} < y \leq 1. \tag{A.1.29}$$

Following the same procedure for the first group of crosslinks present at $t = 0$ positioned at $y = y_i$ with angle $\theta(t, y_i) = \theta_0$ it is derived,

$$\theta(t, y) = \arctan\left(\tan\theta_0 e^{\alpha t}\right) \text{ for } 0 \leq y \leq e^{-\alpha t}. \tag{A.1.30}$$

For the cellulose length the transformed co-ordinate $\bar{t}$ are once again used to get,

$$\frac{1}{L_C}\frac{dL_C}{d\bar{t}} = \alpha \sin^2(\theta(\bar{t}, y)), \tag{A.1.31}$$

using the separation of variables it is calculated,

$$\ln(L_C) = \int_0^{\bar{t}} \alpha \sin(\theta(\hat{t}, y)) d\hat{t}, \tag{A.1.32}$$

For the different domains it is then found,

$$L_C(t) = \exp\left(\alpha \int_0^{\bar{t}} \sin^2\theta(\hat{t})\; d\hat{t}\right) \text{ for } 0 \leq y \leq e^{-\alpha t}, \tag{A.1.33}$$

and,

$$L_C(y) = \exp\left(\int_y^1 \frac{\sin^2\theta(\hat{y})}{\hat{y}}\, d\hat{y}\right) \text{ for } e^{-\alpha t} < y \leq 1. \tag{A.1.34}$$

A.1.5 Asympototic expansion

Beginning with the asymptotic expansion of G, the two regions, $\gamma \ll y \leq 1$ and $\epsilon \leq y \ll \gamma$ are considered. In considering the first case it is known that $\left(\frac{1}{z} - z^{\frac{\omega}{\alpha}}\right) = \frac{1}{z}\left(1 - z^{\frac{\omega}{\alpha}+1}\right)$ and as $0 < z \leq 1$, and $\frac{\omega}{\alpha} > 0$ it is found $0 < z^{\frac{\omega}{\alpha}+1} \leq 1$ which implies the following bound, $0 < \left(1 - z^{\frac{\omega}{\alpha}+1}\right) \leq 1$. Using this it is derived,

$$G(y) = \int_y^1 \frac{\exp\left(\gamma^2 \breve{\alpha}^2 \left(\frac{1}{z} - z^{\frac{\omega}{\alpha}}\right)^2\right)}{z}\, dz \leq \int_y^1 \frac{\exp\left(\breve{\alpha}^2 \left(\frac{\gamma}{z}\right)^2\right)}{z}\, dz, \tag{A.1.35}$$

and as $\frac{\gamma}{y} \ll 1$, it is found

$$G(y) \approx \int_y^1 \frac{1}{z}\, dz = \ln\left(\frac{1}{y}\right). \tag{A.1.36}$$

Alternatively, for the second case, $\epsilon \leq y \ll \gamma$ we have $\frac{y}{\gamma} \ll 1$ where the upper bound of, $\left(1 - z^{\frac{\omega}{\alpha}+1}\right) \leq 1$ can be used to get,

$$G(y) \leq \int_y^1 \frac{\exp\left(\breve{\alpha}^2 \frac{\gamma^2}{z^2}\right)}{z}\, dz. \tag{A.1.37}$$

Using integration by parts and knowing that $\frac{d}{dz}\left(\exp\left(\breve{\alpha}^2\frac{\gamma^2}{z^2}\right)\right) = -\frac{2\gamma^2\breve{\alpha}^2}{z^3}\exp\left(\breve{\alpha}^2\frac{\gamma}{z^2}\right)$ it is calculated,

$$G(y) \leq \int_y^1 -\frac{z^2}{2\breve{\alpha}^2\gamma^2}\frac{d}{dz}\left(\exp\left(\breve{\alpha}^2\frac{\gamma^2}{z^2}\right)\right)\, dz \tag{A.1.38}$$

$$= \left[-\frac{z^2}{2\breve{\alpha}^2\gamma^2}\exp\left(\breve{\alpha}^2\frac{\gamma^2}{z^2}\right)\right]_y^1 + \int_y^1 \frac{z}{\breve{\alpha}^2\gamma^2}\exp\left(\breve{\alpha}^2\frac{\gamma^2}{z^2}\right)\, dz \tag{A.1.39}$$

$$= -\frac{1}{2\breve{\alpha}^2\gamma^2}\exp(\gamma^2\breve{\alpha}^2) + \frac{y^2}{2\breve{\alpha}^2\gamma^2}\exp\left(\breve{\alpha}^2\frac{\gamma^2}{y^2}\right)$$

$$- \int_y^1 \frac{z^4}{2\breve{\alpha}^4\gamma^4}\frac{d}{dz}\left(\exp\left(\breve{\alpha}^2\frac{\gamma^2}{z^2}\right)\right)\, dz. \tag{A.1.40}$$

Using the fact that γ is small causing the first term's exponential to be small, (compared to the others which have $\frac{\gamma}{y} \gg 1$) the first term can be ignored, and by repeatedly integrating by parts, the following sequence can be found

$$G(y) = \frac{y^2}{2\breve{\alpha}^2\gamma^2}\exp\left(\breve{\alpha}^2\frac{\gamma^2}{y^2}\right) + \frac{y^4}{2\breve{\alpha}^2\gamma^4}\exp\left(\breve{\alpha}^2\frac{\gamma^2}{y^2}\right) + \ldots. \tag{A.1.41}$$

As $\frac{y}{\gamma} \ll 1$ meaning $\frac{y^2}{\gamma^2} > \frac{y^k}{\gamma^k}$ where $k = 4, 6, 8, \ldots$ it is then found,

$$G(y) \approx \frac{y^2}{2\breve{\alpha}^2\gamma^2}\exp\left(\breve{\alpha}^2\frac{\gamma^2}{y^2}\right) + o\left(\frac{y^2}{2\breve{\alpha}^2\gamma^2}\exp\left(\breve{\alpha}^2\frac{\gamma^2}{y^2}\right)\right). \tag{A.1.42}$$

From equation (3.3.4) the asymptotic approximation of n is then,

$$n = \begin{cases} \exp\left(-\frac{\breve{k}_0}{\alpha}\frac{y^2}{2\breve{\alpha}^2\gamma^2}e^{\breve{\alpha}^2\frac{\gamma^2}{y^2}}\right), & \epsilon \leq y \ll \gamma \\ y^{\frac{\breve{k}_0}{\alpha}}, & \gamma \ll y \leq 1. \end{cases} \tag{A.1.43}$$

Writing $\breve{k}_0 = \frac{k_0}{\tilde{k}_0}$, the asymptotic expansion of $\tilde{G}$ can now be calculated. To find the approximation, the region $\gamma \ll y \leq 1$ and $\tilde{\beta} \ll y \leq 1$ is first considered, where upon using the expansion of n in this same region (equation (3.3.13)) and the upper bound of

the extension ($\left(1-z^{\frac{\omega}{\alpha}+1}\right)<1$) we get,

$$\tilde{G}(y)=\int_y^1 \frac{\exp\left(\tilde{\beta}^2\breve{\alpha}^2\left(1-z^{\frac{\check{k}_0}{\alpha}}\right)\left(\frac{1}{z}-z^{\frac{\omega}{\alpha}}\right)^2\right)}{z}\,dy \tag{A.1.44}$$

$$\leq\int_y^1 \frac{\exp\left(\tilde{\beta}^2\breve{\alpha}^2\frac{1}{z^2}\left(1-z^{\frac{\check{k}_0}{\alpha}}\right)\right)}{z}\,dy. \tag{A.1.45}$$

To find the leading order terms the exponential is Talyor expanded around $\tilde{\beta}=0$ to find,

$$=\int_y^1 \frac{1}{z}\left(1+\frac{\tilde{\beta}^2\breve{\alpha}^2}{z^2}\left(1-z^{\frac{\check{k}_0}{\alpha}}\right)+\frac{\tilde{\beta}^4\breve{\alpha}^4}{2z^4}\left(1-z^{\frac{\check{k}_0}{\alpha}}\right)^2+\ldots\right)\,dy. \tag{A.1.46}$$

Lets consider any term in the series, $\left(1-z^{\frac{\check{k}_0}{\alpha}}\right)^i$, with $i\in\mathbb{N}/\{0\}$. The biggest term in this bracket needs to be found. By assuming that 1 is the biggest term and using the fact that $\frac{\check{k}_0}{\alpha}>0$ and $0<z\leq 1$ it is found,

$$|1|\geq|z^{\frac{\check{k}_0}{\alpha}}|\Rightarrow 1\geq z^{\frac{\check{k}_0}{\alpha}}\Rightarrow 1\geq z. \tag{A.1.47}$$

So 1 is indeed the bigger term meaning $1-z^{\frac{\check{k}_0}{\alpha}}\leq 1$. It now needs to be shown that the 1st term in the integral (equation (A.1.46)) is greater than $\frac{\tilde{\beta}^{2i}\breve{\alpha}^{2i}}{i!z^{2i}}\left(1-z^{\frac{\check{k}_0}{\alpha}}\right)^i$ for each $i\in\mathbb{N}/\{0\}$. From the workings above, the ith term is known to be less than, $\frac{\tilde{\beta}^{2i}\breve{\alpha}^{2i}}{i!z^{2i}}$ so on assuming the first term, 1 is bigger than the other terms for any i, it is found $\frac{\tilde{\beta}^{2i}\breve{\alpha}^{2i}}{i!z^{2i}}<1\Rightarrow\left(\frac{\tilde{\beta}^2\breve{\alpha}^2}{i!z^2}\right)^i<1\Rightarrow\frac{\tilde{\beta}^2}{z^2}<\frac{i!}{\breve{\alpha}^2}$ and since $\frac{\tilde{\beta}}{z}\ll 1$, it is now known 1 is indeed the biggest term in the sequence. Therefore the higher order terms in equation (A.1.46) can now be ignored to get

$$\tilde{G}(y)\approx\int_y^1\frac{1}{z}\,dz=\ln\left(\frac{1}{y}\right). \tag{A.1.48}$$

Deriving the expansion for $\epsilon < y \ll \tilde{\beta}$ and $\epsilon < y \ll \gamma$ it is found that,

$$\begin{aligned}\tilde{G}(y) &= \int_y^1 \frac{\exp\left(\tilde{\beta}^2\breve{\alpha}^2\left(1-\exp\left(-\frac{\breve{k}_0}{\alpha}\frac{y^2}{2\breve{\alpha}^2\tilde{\beta}^2}e^{\tilde{\alpha_x}^2\frac{\tilde{\beta}^2}{y^2}}\right)\right)\left(\frac{1}{z}-z^{\frac{\omega}{\alpha}}\right)^2\right)}{z}\,dy \\ &\leq \int_y^1 \frac{\exp\left(\tilde{\beta}^2\breve{\alpha}^2\frac{1}{z^2}\right)}{z}\,dy, \end{aligned} \tag{A.1.49}$$

by using the upper bound of the extension again and the fact that if $\frac{y}{\tilde{\beta}} \ll 1$ then $e^{\frac{\tilde{\beta}^2}{y^2}} \gg 1$ and consequently $\exp\left(-\frac{\breve{k}_0}{\alpha}\frac{y^2}{2\breve{\alpha}^2\tilde{\beta}^2}e^{\frac{\tilde{\beta}^2}{y^2}}\right) \ll 1$. The procedure of solving equation (A.1.37) is repeated to derive,

$$\tilde{G}(y) = \frac{y^2}{2\breve{\alpha}^2\tilde{\beta}^2}\exp\left(\breve{\alpha}^2\frac{\tilde{\beta}^2}{y^2}\right) + o\left(\frac{y^4}{\gamma^4}\right). \tag{A.1.50}$$

The case $\tilde{\beta} < y < \gamma$ is a hybrid of the two methods. The exponential term can be ignored in a similar way to (A.1.49) and follow the same derivation for G in equation (A.1.36) to derive $\tilde{G} = \ln\left(\frac{1}{y}\right)$. Collecting the results together it is calculated,

$$\tilde{n} = \begin{cases} \exp\left(-\frac{1}{\alpha}\frac{y^2}{2\breve{\alpha}^2\tilde{\beta}^2}e^{\breve{\alpha}\frac{\tilde{\beta}^2}{y^2}}\right), & \epsilon \leq y \ll \tilde{\beta} \\ y^{\frac{1}{\alpha}}, & \tilde{\beta} \ll y \leq 1. \end{cases} \tag{A.1.51}$$

Notice that the simplification of $\tilde{n}$ is not dependant on n. It needs to be known exactly where the different asymptotic expansions in the different regions can be applied. Starting with n, the first boundary region, $0 < y \ll \tilde{\beta}$ applies when n has rapidly decreased. So if the value for y is found for when this happens the critical value for when the different expansions can be used can be discovered. This value is found by using the derivative of the dominate term of the exponent of n, which is $\frac{\breve{k}_0}{\alpha}\exp\left(\frac{\gamma^2\breve{\alpha}}{y^2}\right)$ and seeing when it exceeds a certain number, Q, as when this rapidly increases, n rapidly decreases. This value is

then,

$$\chi = \sqrt{\frac{\gamma^2 \breve{\alpha}^2}{\ln\left(\frac{\alpha}{k_0}Q\right)}} \tag{A.1.52}$$

where Q is a threshold value of our choice. The threshold value for $\tilde{n}$, similarly is,

$$\tilde{\chi} = \sqrt{\frac{\tilde{\beta}^2 \breve{\alpha}^2}{\ln(\alpha Q)}} \tag{A.1.53}$$

To be able to solve the limit stress resultant the trigonometric terms present,

$$\sin\left(\arctan\left(\tan(\theta_0)\frac{1}{y}\right)\right)$$

also need to be approximated. Note for $\tan\theta_0 < y \leq 1$ it is known that $\frac{\tan\theta_0}{y} < 1$. Using the Taylor expansions on both arctan and sin and ignoring higher order terms, it can be derived,

$$\begin{aligned}
\sin\left(\arctan\left(\tan(\theta_0)\tfrac{1}{y}\right)\right) &= \sin\left(\frac{\tan\theta_0}{y} - \frac{\tan^3\theta_0}{3y^3} + \frac{\tan^5\theta_0}{5y^5} - \frac{\tan^7\theta_0}{7y^7} + \dots\right) && \text{(A.1.54)}\\
&= \left(\frac{\tan\theta_0}{y} - \frac{\tan^3\theta_0}{3y^3} + \frac{\tan^5\theta_0}{5y^5} - \frac{\tan^7\theta_0}{7y^7} + \dots\right)\\
&\quad - \frac{1}{3!}\left(\frac{\tan\theta_0}{y} - \frac{\tan^3\theta_0}{3y^3} + \frac{\tan^5\theta_0}{5y^5} - \frac{\tan^7\theta_0}{7y^7} + \dots\right)^3\\
&\quad + \frac{1}{5!}\left(\frac{\tan\theta_0}{y} - \frac{\tan^3\theta_0}{3y^3} + \frac{\tan^5\theta_0}{5y^5} - \frac{\tan^7\theta_0}{7y^7} + \dots\right)^5\\
&\quad - \tfrac{1}{7!}\left(\tfrac{\tan\theta_0}{y} - \tfrac{\tan^3\theta_0}{3y^3} + \tfrac{\tan^5\theta_0}{5y^5} - \tfrac{\tan^7\theta_0}{7y^7} + \dots\right)^7 + \dots && \text{(A.1.55)}\\
&= \tfrac{\tan\theta_0}{y} - \tfrac{1}{2}\tfrac{\tan^3\theta_0}{y^3} + \tfrac{3}{8}\tfrac{\tan^5\theta_0}{y^5} - \tfrac{5}{16}\tfrac{\tan^7\theta_0}{y^7} + o\left(\tfrac{\tan^9\theta_0}{y^9}\right). && \text{(A.1.56)}
\end{aligned}$$

For the case $\gamma < y < \tan\theta_0$ the relation, $\sin\left(\arctan\left(\tan\theta_0\frac{1}{y}\right)\right) = \frac{\tan\theta_0}{\sqrt{\tan^2\theta_0+y^2}}$ is used. Noting that $\frac{y}{\tan\theta_0} < 1$ and using the Taylor expansion around $y = 0$ it is found,

$$\frac{\tan\theta_0}{\sqrt{\tan^2\theta_0 + y^2}} = 1 - \frac{y^2}{2\tan^2\theta_0} + \frac{3y^4}{8\tan^4\theta_0} - \frac{5y^6}{16\tan^6\theta_0} + o\left(\frac{y^8}{\tan^8\theta_0}\right). \tag{A.1.57}$$

Both of these approximations lose accuracy around $y = \tan_0$, the procedure above is therefore repeated but now Taylor expand around $y = \tan_0$ to get,

$$\begin{aligned}\frac{\tan\theta_0}{\sqrt{\tan^2\theta_0 + y^2}} =& \frac{1}{\sqrt{2}} - \frac{y - \tan\theta_0}{2\sqrt{2}\tan\theta_0} + \frac{(y-\tan\theta_0)^2}{8\sqrt{2}\tan^2\theta_0} \\ &+ \frac{(y-\tan\theta_0)^3}{16\sqrt{2}\tan^3\theta_0} - \frac{13(y-\tan\theta_0)^4}{128\sqrt{2}\tan\theta_0^4} + o\left(\frac{y^5}{\tan^5\theta_0}\right). \end{aligned} \tag{A.1.58}$$

The approximation for the trigonometric term is then defined by three different expansion in three different regions, such that,

$$\sin\left(\arctan\left(\tan(\theta_0)\tfrac{1}{y}\right)\right) = \begin{cases} \frac{\tan\theta_0}{y} - \frac{1}{2}\frac{\tan^3\theta_0}{y^3} + \frac{3}{8}\frac{\tan^5\theta_0}{y^5} - \frac{5}{16}\frac{\tan^7\theta_0}{y^7}, & \tan\theta_0 + \delta < y \leq 1, \\ \frac{1}{\sqrt{2}} - \frac{y-\tan\theta_0}{2\sqrt{2}\tan\theta_0} + \frac{(y-\tan\theta_0)^2}{8\sqrt{2}\tan^2\theta_0} + \frac{(y-\tan\theta_0)^3}{16\sqrt{2}\tan^3\theta_0} - \frac{13(y-\tan\theta_0)^4}{128\sqrt{2}\tan\theta_0^4}, & \frac{\tan\theta_0}{2} < y \leq \tan\theta_0 + \delta \\ 1 - \frac{y^2}{2\tan^2\theta_0} + \frac{3y^4}{8\tan^4\theta_0} - \frac{5y^6}{16\tan^6\theta_0}, & \epsilon < y \leq \frac{\tan\theta_0}{2}. \end{cases} \tag{A.1.59}$$

Where $\frac{\tan\theta_0}{2}$ and $\tan\theta_0 + \delta$ are interval values of our choosing to ensure accuracy. This expression is then used for the cellulose angle to find the leading terms that dominate the celluloses length's, L_C behaviour. Substituting in (A.1.59) it is found,

$$L_C(y) = \begin{cases} \exp\left(\int_y^1 \frac{\left(\frac{\tan\theta_0}{y} - \frac{1}{2}\frac{\tan^3\theta_0}{y^3} + \frac{3}{8}\frac{\tan^5\theta_0}{y^5} - \frac{5}{16}\frac{\tan^7\theta_0}{y^7}\right)^2}{y}\, d\hat{y}\right), & \tan\theta_0 + \delta < y \leq 1, \\ \exp\left(\int_{\tan\theta_0+\delta}^1 \sim\, d\hat{y} + \int_y^{\tan\theta_0+\delta} \frac{\left(\frac{1}{\sqrt{2}} - \frac{y-\tan\theta_0}{2\sqrt{2}\tan\theta_0} + \frac{(y-\tan\theta_0)^2}{8\sqrt{2}\tan^2\theta_0} + \frac{(y-\tan\theta_0)^3}{16\sqrt{2}\tan^3\theta_0} - \frac{13(y-\tan\theta_0)^4}{128\sqrt{2}\tan\theta_0^4}\right)^2}{y} d\hat{y}\right), & \tan\theta_0 + \delta < y \leq \frac{\tan\theta_0}{2} \\ \exp\left(\int_{\tan\theta_0+\delta}^1 \sim\, d\hat{y} + \int_{\frac{\tan\theta_0}{2}}^{\tan\theta_0+\delta} \sim\, d\hat{y} + \int_y^{\frac{\tan\theta_0}{2}} \frac{\left(1 - \frac{y^2}{2\tan^2\theta_0} + \frac{3y^4}{8\tan^4\theta_0} - \frac{5y^6}{16\tan^6\theta_0}\right)^2}{y}\, d\hat{y}\right), & \epsilon \leq y \leq \frac{\tan\theta_0}{2}, \end{cases} \tag{A.1.60}$$

where $\sim$ is used for simplicity to represent the integrand that appears in the previous line

for the same integral region. Upon evaluating the integral it is derived,

$$L_C(y) = \begin{cases} \exp\left(\left[-\frac{\tan^2\theta_0}{2\hat{y}^2} + \frac{\tan^4\theta_0}{4\hat{y}^4} - \frac{7\tan^6\theta_0}{54\hat{y}^6} + \frac{19\tan^8\theta_0}{576\hat{y}^8} - \frac{361\tan^{10}\theta_0}{51840\hat{y}^{10}}\right]_y^1\right), & \tan\theta_0 + \delta < y \leq 1, \\ e^{B_1(1)}e^{-B_1(\tan\theta_0+\delta)}\exp\Big(\Big[\frac{34969}{32768}\log(y) - \frac{935y}{4096\tan\theta_0} - \frac{7941y^2}{16384\tan^2\theta_0} + \frac{3235y^3}{12288\tan^3\theta_0} & \\ + \frac{67y^4}{65536\tan^4\theta_0} - \frac{245y^5}{4096\tan^5\theta_0} + \frac{1459y^6}{49152\tan^6\theta_0} - \frac{195y^7}{28672\tan^7\theta_0} + \frac{169y^8}{262144\tan^8\theta_0}\Big]_y^{\tan\theta_0+\delta}\Big), & \frac{\tan\theta_0}{2} < y \leq \tan\theta_0 + \delta, \\ e^{B_1(1)}e^{-B_1(\tan\theta_0+\delta)}e^{B_2(\tan\theta_0+\delta)}e^{-B_2\left(\frac{\tan\theta_0}{2}\right)}\exp\Big(\Big[\log(y) - \frac{y^2}{2\tan^2\theta_0} + \frac{y^4}{4\tan^4\theta_0} & \\ - \frac{y^6}{6\tan^6\theta_0} + \frac{29y^8}{512\tan^8\theta_0} - \frac{3y^{10}}{128\tan^{10}\theta_0} + \frac{25y^{12}}{3072\tan^{12}\theta_0}\Big]_y^{\frac{\tan\theta_0}{2}}\Big), & \epsilon \leq y \leq \frac{\tan\theta_0}{2}. \end{cases} \tag{A.1.61}$$

where,

$$B_1(y) = -\frac{\tan^2\theta_0}{2\hat{y}^2} + \frac{\tan^4\theta_0}{4\hat{y}^4} - \frac{7\tan^6\theta_0}{54\hat{y}^6} + \frac{19\tan^8\theta_0}{576\hat{y}^8} - \frac{361\tan^{10}\theta_0}{51840\hat{y}^{10}}, \tag{A.1.62}$$

$$\begin{aligned} B_2(y) =& \frac{34969}{32768}\log(y) - \frac{935y}{4096\tan\theta_0} - \frac{7941y^2}{16384\tan^2\theta_0} + \frac{3235y^3}{12288\tan^3\theta_0} \\ &+ \frac{67y^4}{65536\tan^4\theta_0} - \frac{245y^5}{4096\tan^5\theta_0} + \frac{1459y^6}{49152\tan^6\theta_0} \\ &- \frac{195y^7}{28672\tan^7\theta_0} + \frac{169y^8}{262144\tan^8\theta_0}, \end{aligned} \tag{A.1.63}$$

$$\begin{aligned} B_3(y) =& \log(y) - \frac{y^2}{2\tan^2\theta_0} + \frac{y^4}{4\tan^4\theta_0} \\ &- \frac{y^6}{6\tan^6\theta_0} + \frac{29y^8}{512\tan^8\theta_0} - \frac{3y^{10}}{128\tan^{10}\theta_0} + \frac{25y^{12}}{3072\tan^{12}\theta_0}. \end{aligned} \tag{A.1.64}$$

By ignoring the higher order terms and Taylor expanding the exponential the final form is then,

$$L_C(y) = \begin{cases} b_1\left(1 + \frac{\tan^2\theta_0}{2\hat{y}^2}\right), & \tan\theta_0 + \delta < y \leq 1, \\ \frac{b_2}{y\frac{34969}{32768}}(1 - H(y) + \frac{H(y)^2}{2}), & \frac{\tan\theta_0}{2} < y \leq \tan\theta_0 + \delta, \\ \frac{b_3}{y}\left(1 + \frac{y^2}{2\tan^2\theta_0}\right), & \epsilon \leq y \leq \frac{\tan\theta_0}{2}, \end{cases} \tag{A.1.65}$$

where $b_1 = e^{B_1(1)}$, $b_2 = e^{B_1(1)}e^{-B_1((\tan\theta_0+\delta))}e^{B_2(\tan\theta_0+\delta)}$ and

$b_3 = e^{B_1(1)}e^{-B_1((\tan\theta_0+\delta))}e^{B_2(\tan\theta_0+\delta)}e^{-B_2(\frac{\tan\theta_0}{2})}e^{B_3(\frac{\tan\theta_0}{2})}$ and $H(y) = B_2(2) - \dfrac{34969}{32768}\log(y)$.

All the needed approximations to calculate the stress resultant analytically have now been found. First, the cellulose contribution independent of the biological hotspots is calculated, with it being,

$$\Sigma_1^{\infty} = \int_{\epsilon}^{1} (L_c - 1)\sin\theta \; dy \tag{A.1.66}$$

$$\begin{aligned}
&= \int_{\tan\theta_0+\delta}^{1} \left(b_1\left(1+\frac{\tan^2\theta_0}{2\hat{y}^2}\right)-1\right)\left(\frac{\tan\theta_0}{y} - \frac{1}{2}\frac{\tan^3\theta_0}{y^3} + \frac{3}{8}\frac{\tan^5\theta_0}{y^5} - \frac{5}{16}\frac{\tan^7\theta_0}{y^7}\right)\; dy \\
&+ \int_{\frac{\tan\theta_0}{2}}^{\tan\theta_0+\delta} \left(\frac{b_2}{y^{\frac{34969}{32768}}}\left(1-H(y)+\frac{H(y)^2}{2}\right)-1\right)\left(\frac{1}{\sqrt{2}} - \frac{y-\tan\theta_0}{2\sqrt{2}\tan\theta_0} + \frac{(y-\tan\theta)^2}{8\sqrt{2}\tan^2\theta_0} + \frac{(y-\tan\theta)^3}{16\sqrt{2}\tan^3\theta_0} - \frac{13(y-\tan\theta_0)^4}{128\sqrt{2}\tan\theta_0^4}\right)\; dy \\
&+ \int_{\epsilon}^{\frac{\tan\theta_0}{2}} \left(\frac{b_3}{y}\left(1+\frac{y^2}{2\tan^2\theta_0}\right)-1\right)\left(1 - \frac{y^2}{2\tan^2\theta_0} + \frac{3y^4}{8\tan^4\theta_0} - \frac{5y^6}{16\tan^6\theta_0}\right)\; dy,
\end{aligned} \tag{A.1.67}$$

which we find to be,

$$\Sigma_1^{\infty} = \sum_i c_i, \tag{A.1.68}$$

where all the c_i values can be found in table A.1.

Table A.1: Asymptotic expansion constants for Σ_1^{∞}

Constant	**Value**	**Constant**	**Value**
c_1	$\frac{305\,b_3}{196608}$	c_2	ϵ
c_3	$\frac{766290879471899\,\tan\theta_0}{118219490218475520}$	c_4	$b_3\,\ln\left(\frac{\tan\theta_0}{2}\right)$
c_5	$\tan\theta_0\ln\left(\delta+\tan\theta_0\right)$	c_6	$-b_1\,\tan\theta_0\ln\left(\delta+\tan\theta_0\right)$
c_7	$-\frac{150077200448881\,b_2}{9758165696512\,(\delta+\tan\theta_0)^{2201/32768}}$	c_8	$-b_3\,\ln(\epsilon)$
c_9	$-\frac{b_1\tan^5\theta_0}{32}$	c_{10}	$\frac{b_1\tan^7\theta_0}{48}$
c_{11}	$\frac{5\,b_1\tan^9\theta_0}{256}$	c_{12}	$-\frac{\tan^3\theta_0}{4}$
c_{13}	$\frac{3\tan^5\theta_0}{32}$	c_{14}	$-\frac{5\tan^7\theta_0}{96}$

Continued on next page

Table A.1 – *Continued from previous page*

Constant	Value	Constant	Value
c_{15}	$\frac{-3\tan^5\theta_0}{32\,(\delta+\tan\theta_0)^4}$	c_{16}	$\frac{b_1\tan^5\theta_0}{32\,(\delta+\tan\theta_0)^4}$
c_{17}	$\frac{-2\,b_1\tan^7\theta_0}{96\,(\delta+\tan\theta_0)^6}$	c_{18}	$\frac{5\tan^7\theta_0}{96\,(\delta+\tan\theta_0)^6}$
c_{19}	$\frac{-5\,b_1\tan^9\theta_0}{576\,(\delta+\tan\theta_0)^8}$	c_{20}	$\frac{8\tan^3\theta_0\,(\delta+\tan\theta_0)^6}{32\,(\delta+\tan\theta_0)^8}$
c_{21}	$\frac{150077200448881\,b_2}{9758165696512\left(\frac{\tan\theta_0}{2}\right)^{2201/32768}}$	c_{22}	$-\frac{187\sqrt{2}\,(\delta+\tan\theta_0)}{256}$
c_{23}	$-\frac{\epsilon^3}{6\tan^2\theta_0}$	c_{24}	$\frac{3\,\epsilon^5}{40\tan^4\theta_0}$
c_{25}	$-\frac{5\,\epsilon^7}{112\tan^6\theta_0}$	c_{26}	$\frac{5\sqrt{2}\,(\delta+\tan\theta_0)^2}{128\,\tan\theta_0}$
c_{27}	$\frac{43\sqrt{2}\,(\delta+\tan\theta_0)^3}{384\tan^2\theta_0}$	c_{28}	$-\frac{15\sqrt{2}\,(\delta+\tan\theta_0)^4}{256\tan^3\theta_0}$
c_{29}	$\frac{13\sqrt{2}\,(\delta+\tan\theta_0)^5}{1280\tan^4\theta_0}$	c_{30}	$\frac{6020549791152521\,b_2\,(\delta+\tan\theta_0)^{30567/32768}}{44811695901638656\,\tan\theta_0}$
c_{31}	$\frac{7868723041398407\,b_2\,(\delta+\tan\theta_0)^{63335/32768}}{557100551561543680\tan^2\theta_0}$	c_{32}	$\frac{4402425010544735\,b_2\,(\delta+\tan\theta_0)^{96103/32768}}{1449138733222723584\tan^3\theta_0}$
c_{33}	$-\frac{81932115935621\,b_2\,(\delta+\tan\theta_0)^{128871/32768}}{19679883747655 68\tan^4\theta_0}$	c_{34}	$\frac{26825835184960 71\,b_2\,(\delta+\tan\theta_0)^{161639/32768}}{88861980001042432\tan^5\theta_0}$
c_{35}	$-\frac{7116713214246575\,b_2\,(\delta+\tan\theta_0)^{194407/32768}}{480943703297359872\tan^6\theta_0}$	c_{36}	$\frac{89993661700897\,b_2\,(\delta+\tan\theta_0)^{227175/32768}}{6917027650338816\tan^7\theta_0}$
c_{37}	$-\frac{1390888037066579\,b_2\,(\delta+\tan\theta_0)^{259943/32768}}{160768322470674432\tan^8\theta_0}$	c_{38}	$\frac{813773447008073\,b_2\,(\delta+\tan\theta_0)^{292711/32768}}{6336208227784458 24\tan^9\theta_0}$
c_{39}	$\frac{280915086652931\,b_2\,(\delta+\tan\theta_0)^{325479/32768}}{134200479411339264\tan^{10}\theta_0}$	c_{40}	$-\frac{5278606494654121\,b_2\,(\delta+\tan\theta_0)^{358247/32768}}{3101936844162465792\tan^{11}\theta_0}$
c_{41}	$\frac{3916342628302019\,b_2\,(\delta+\tan\theta_0)^{391015/32768}}{6771327241373614080\tan^{12}\theta_0}$	c_{42}	$-\frac{4112068129940143\,b_2\,(\delta+\tan\theta_0)^{423783/32768}}{11742049271075674521 6\tan^{13}\theta_0}$
c_{43}	$-\frac{1121251467598159\,b_2\,(\delta+\tan\theta_0)^{456551/32768}}{18447880144098951168\tan^{14}\theta_0}$	c_{44}	$\frac{1772224420073771\,b_2\,(\delta+\tan\theta_0)^{489319/32768}}{52725169158789005312\tan^{15}\theta_0}$
c_{45}	$-\frac{1694538362442335\,b_2\,(\delta+\tan\theta_0)^{522087/32768}}{168767973799942422528\tan^{16}\theta_0}$	c_{46}	$\frac{94162698713311\,b_2\,(\delta+\tan\theta_0)^{554855/32768}}{4782945069960475443 2\tan^{17}\theta_0}$
c_{47}	$-\frac{388717606998977\,b_2\,(\delta+\tan\theta_0)^{587623/32768}}{15196232515767458856 96\tan^{18}\theta_0}$	c_{48}	$\frac{1057140962472757\,b_2\,(\delta+\tan\theta_0)^{620391/32768}}{52154529959914841833472\tan^{19}\theta_0}$
c_{49}	$-\frac{2775672680954111\,b_2\,(\delta+\tan\theta_0)^{653159/32768}}{3707279049981556007370752\tan\theta_0{}^{20}}$	c_{50}	$-\frac{b_3\,\epsilon^4}{32\tan^4\theta_0}$
c_{51}	$\frac{b_3\,\epsilon^6}{48\tan^6\theta_0}$	c_{52}	$\frac{5\,b_3\,\epsilon^8}{256\tan^8\theta_0}$
c_{53}	$-\frac{6020549791152521\,b_2\left(\frac{\tan\theta_0}{2}\right)^{30567/32768}}{44811695901638656\,\tan\theta_0}$	c_{54}	$-\frac{7868723041398407\,b_2\left(\frac{\tan\theta_0}{2}\right)^{63335/32768}}{557100551561543680\tan^2\theta_0}$
c_{55}	$-\frac{4402425010544735\,b_2\left(\frac{\tan\theta_0}{2}\right)^{96103/32768}}{1449138733222723584\tan^3\theta_0}$	c_{56}	$\frac{81932115935621\,b_2\left(\frac{\tan\theta_0}{2}\right)^{128871/32768}}{1967988374765568\tan^4\theta_0}$
c_{55}	$-\frac{2682583518496071\,b_2\left(\frac{\tan\theta_0}{2}\right)^{161639/32768}}{88861980001042432\tan^5\theta_0}$	c_{58}	$\frac{7116713214246575\,b_2\left(\frac{\tan\theta_0}{2}\right)^{194407/32768}}{480943703297359872\tan^6\theta_0}$
c_{57}	$-\frac{89993661700897\,b_2\left(\frac{\tan\theta_0}{2}\right)^{227175/32768}}{6917027650338816\tan^7\theta_0}$	c_{60}	$\frac{1390888037066579\,b_2\left(\frac{\tan\theta_0}{2}\right)^{259943/32768}}{160768322470674432\tan^8\theta_0}$
c_{61}	$-\frac{813773447008073\,b_2\left(\frac{\tan\theta_0}{2}\right)^{292711/32768}}{6336208227784458 24\tan^9\theta_0}$	c_{62}	$-\frac{280915086652931\,b_2\left(\frac{\tan\theta_0}{2}\right)^{325479/32768}}{134200479411339264\tan^{10}\theta_0}$
c_{63}	$\frac{5278606494654121\,b_2\left(\frac{\tan\theta_0}{2}\right)^{358247/32768}}{3101936844162465792\tan^{11}\theta_0}$	c_{64}	$-\frac{3916342628302019\,b_2\left(\frac{\tan\theta_0}{2}\right)^{391015/32768}}{6771327241373614080\tan^{12}\theta_0}$

Continued on next page

Table A.1 – *Continued from previous page*

Constant	Value	Constant	Value
c_{65}	$\frac{4112068129940143\, b_2 \left(\frac{\tan\theta_0}{2}\right)^{423783/32768}}{11742049271075674521 6\tan^{13}\theta_0}$	c_{66}	$\frac{1121251467598159\, b_2 \left(\frac{\tan\theta_0}{2}\right)^{456551/32768}}{18447880144098951168\tan^{14}\theta_0}$
c_{67}	$-\frac{1772224420073771\, b_2 \left(\frac{\tan\theta_0}{2}\right)^{489319/32768}}{5272516915878900531 2\tan^{15}\theta_0}$	c_{68}	$\frac{1694538362442335\, b_2 \left(\frac{\tan\theta_0}{2}\right)^{522087/32768}}{16876797379994242252 8\tan^{16}\theta_0}$
c_{69}	$-\frac{94162698713311\, b_2 \left(\frac{\tan\theta_0}{2}\right)^{554855/32768}}{4782945069960475443 2\tan^{17}\theta_0}$	c_{70}	$\frac{388717606998977\, b_2 \left(\frac{\tan\theta_0}{2}\right)^{587623/32768}}{15196232515767458856 96\tan^{18}\theta_0}$
c_{71}	$-\frac{1057140962472757\, b_2 \left(\frac{\tan\theta_0}{2}\right)^{620391/32768}}{52154529959914841833472\tan^{19}\theta_0}$	c_{72}	$\frac{2775672680954111\, b_2 \left(\frac{\tan\theta_0}{2}\right)^{653159/32768}}{37072790499815560073707 52\tan^{20}\theta_0}$

The second term is the contribution from the cellulose fibres when crosslinked by the biological hotspots which is calculate to be,

$$\Sigma_2^{\infty} = \int_{\epsilon}^{1} a_1 \tilde{n}(L_c - 1)\sin\theta \; dy = \tag{A.1.69}$$

$$\begin{aligned}
&\textstyle\int_{\tan\theta_0+\delta}^{1} a_1 y^{\frac{1}{\alpha}} \left(b_1\left(1+\frac{\tan^2\theta_0}{2\hat{y}^2}\right)-1\right)\left(\frac{\tan\theta_0}{y}-\frac{1}{2}\frac{\tan^3\theta_0}{y^3}+\frac{3}{8}\frac{\tan^5\theta_0}{y^5}-\frac{5}{16}\frac{\tan^7\theta_0}{y^7}\right)\; dy \\
&+\textstyle\int_{\frac{\tan\theta_0}{2}}^{\tan\theta_0+\delta} a_1 y^{\frac{1}{\alpha}} \left(\frac{b_2}{y^{\frac{34969}{32768}}}(1-H(y)+\frac{H(y)^2}{2})-1\right)\left(\frac{1}{\sqrt{2}}-\frac{y-\tan\theta_0}{2\sqrt{2}\tan\theta_0}+\frac{(y-\tan\theta)^2}{8\sqrt{2}\tan^2\theta_0}+\frac{(y-\tan\theta)^3}{16\sqrt{2}\tan^3\theta_0}-\frac{13(y-\tan\theta_0)^4}{128\sqrt{2}\tan\theta_0^4}\right)\; dy \\
&+\textstyle\int_{\tilde{\chi}}^{\frac{\tan\theta_0}{2}} a_1 y^{\frac{1}{\alpha}} \left(\frac{b_3}{y}\left(1+\frac{y^2}{2\tan^2\theta_0}\right)-1\right)\left(1-\frac{y^2}{2\tan^2\theta_0}+\frac{3y^4}{8\tan^4\theta_0}-\frac{5y^6}{16\tan^6\theta_0}\right)\; dy \\
&+\textstyle\int_{\epsilon}^{\tilde{\chi}} a_1 \exp\left(-\frac{1}{\alpha}\frac{y^2}{2\tilde{\beta}^2}e^{\frac{\tilde{\beta}^2}{y^2}}\right)\left(\frac{b_3}{y}\left(1+\frac{y^2}{2\tan^2\theta_0}\right)-1\right)\left(1-\frac{y^2}{2\tan^2\theta_0}+\frac{3y^4}{8\tan^4\theta_0}-\frac{5y^6}{16\tan^6\theta_0}\right)\; dy,
\end{aligned} \tag{A.1.70}$$

which becomes,

$$\begin{aligned}
\Sigma_2^{\infty} =& a_1 \left(\left(\sum_i d_{1,i}(\alpha)\right) + \tan_0(b_1-1)\,\alpha + \left(\sum_i d_{2,i}(\alpha)\right)(\delta+\tan\theta_0)^{\frac{1}{\alpha}}\right. \\
&+\tan\theta_0\,(1-b_1)\,\alpha(\delta+\tan\theta_0)^{\frac{1}{\alpha}} + \left(\sum_i d_{3,i}(\alpha)\right)\left(\frac{\tan\theta_0}{2}\right)^{\frac{1}{\alpha}} \\
&\left.+b_3\alpha\left(\frac{\tan\theta_0}{2}\right)^{\frac{1}{\alpha}} + \left(\sum_i d_{4,i}(\alpha)\right)(\tilde{\chi})^{\frac{1}{\alpha}} - b_3\alpha(\tilde{\chi})^{\frac{1}{\alpha}}\right),
\end{aligned} \tag{A.1.71}$$

where the values of the coefficients $d_{1,i},\ldots,$,$d_{2,i},\ldots,$, $d_{3,i},\ldots,$, and $d_{4,i},\ldots,$ can be found in table A.2.

Table A.2: Asymptotic expansion constants for Σ_2^∞

Constant	Value	Constant	Value
$d_{1,1}$	$\frac{\tan^3\theta_0}{2(\frac{1}{\alpha}-2)}$	$d_{1,2}$	$-\frac{3\tan^5\theta_0}{8(\frac{1}{\alpha}-4)}$
$d_{1,3}$	$\frac{5\tan^7\theta_0}{16(\frac{1}{\alpha}-6)}$	$d_{1,4}$	$\frac{b_1\tan^5\theta_0}{8(\frac{1}{\alpha}-4)}$
$d_{1,5}$	$-\frac{b_1\tan^7\theta_0}{8(\frac{1}{\alpha}-6)}$	$d_{1,6}$	$-\frac{5b_1\tan^9\theta_0}{32(\frac{1}{\alpha}-8)}$
$d_{2,1}$	$\frac{\tan^3\theta_0}{2(2(\delta+\tan\theta_0)^2-\frac{(\delta+\tan\theta_0)^2}{\alpha})}$	$d_{2,2}$	$-\frac{3\tan^5\theta_0}{8(4(\delta+\tan\theta_0)^4-\frac{(\delta+\tan\theta_0)^4}{\alpha})}$
$d_{2,3}$	$\frac{5\tan^7\theta_0}{16(6(\delta+\tan\theta_0)^6-\frac{(\delta+\tan\theta_0)^6}{\alpha})}$	$d_{2,4}$	$\frac{b_1\tan^5\theta_0}{8(4(\delta+\tan\theta_0)^4-\frac{(\delta+\tan\theta_0)^4}{\alpha})}$
$d_{2,5}$	$-\frac{b_1\tan^7\theta_0}{8(6(\delta+\tan\theta_0)^6-\frac{(\delta+\tan\theta_0)^6}{\alpha})}$	$d_{2,6}$	$-\frac{5b_1\tan^9\theta_0}{32(8(\delta+\tan\theta_0)^8-\frac{(\delta+\tan\theta_0)^8}{\alpha})}$
$d_{2,7}$	$\frac{3916342628302019\,b_2\,(\delta+\tan\theta_0)^{\frac{391015}{32768}}}{2048\left(3306312129576960\tan\theta_0{}^{12}+\frac{2770769301995552\tan\theta_0{}^{12}}{\alpha}\right)}$	$d_{2,8}$	$-\frac{4112068129940143\,b_2\,(\delta+\tan\theta_0)^{\frac{423783}{32768}}}{131072\left(895847264944128\tan\theta_0{}^{13}+\frac{69269232549888\tan\theta_0{}^{13}}{\alpha}\right)}$
$d_{2,9}$	$-\frac{3363754402794477\,b_2\,(\delta+\tan\theta_0)^{\frac{456551}{32768}}}{4096\left(13511630964916224\tan\theta_0{}^{14}+\frac{969769255698432\tan\theta_0{}^{14}}{\alpha}\right)}$	$d_{2,10}$	$-\frac{5083615087327005\,b_2\,(\delta+\tan\theta_0)^{\frac{522087}{32768}}}{2048\left(247218711621009408\tan\theta_0{}^{16}+\frac{15516308091174912\tan\theta_0{}^{16}}{\alpha}\right)}$
$d_{2,11}$	$-\frac{2255234053275215\,b_2\,(\delta+\tan\theta_0)^{\frac{653159}{32768}}}{4294967296\left(7013241360220 16\tan\theta_0{}^{20}+\frac{35184372088832\tan\theta_0{}^{20}}{\alpha}\right)}$	$d_{2,12}$	$-\frac{737389043420589\,b_2\,(\delta+\tan\theta_0)^{\frac{128871}{32768}}}{32768\left(540524150784\tan\theta_0{}^{4}+\frac{137438953472\tan\theta_0{}^{4}}{\alpha}\right)}$
$d_{2,13}$	$\frac{7868723041398407\,b_2\,(\delta+\tan\theta_0)^{\frac{63335}{32768}}}{33554432\left(16602890240\tan\theta_0{}^{2}+\frac{8589934592\tan\theta_0{}^{2}}{\alpha}\right)}$	$d_{2,14}$	$\frac{2682583518496071\,b_2\,(\delta+\tan\theta_0)^{\frac{161639}{32768}}}{262144\left(338981552128\tan\theta_0{}^{5}+\frac{68719476736\tan\theta_0{}^{5}}{\alpha}\right)}$
$d_{2,15}$	$-\frac{187\sqrt{2}\,(\delta+\tan\theta_0)}{\frac{256}{\alpha}+256}$	$d_{2,16}$	$-\frac{15\sqrt{2}\,(\delta+\tan\theta_0)^4}{256\tan\theta_0{}^3+\frac{64\tan\theta_0{}^3}{\alpha}}$
$d_{2,17}$	$\frac{43\sqrt{2}\,(\delta+\tan\theta_0)^3}{384\tan\theta_0{}^2+\frac{128\tan\theta_0{}^2}{\alpha}}$	$d_{2,18}$	$\frac{13\sqrt{2}\,(\delta+\tan\theta_0)^5}{1280\tan\theta_0{}^4+\frac{256\tan\theta_0{}^4}{\alpha}}$
$d_{2,19}$	$\frac{3171422887418271\,b_2\,(\delta+\tan\theta_0)^{\frac{620391}{32768}}}{134217728\left(1165744586883072\tan\theta_0{}^{19}+\frac{61572651155456\tan\theta_0{}^{19}}{\alpha}\right)}$	$d_{2,20}$	$\frac{3198993443274073\,b_2\,(\delta+\tan\theta_0)^{\frac{227175}{32768}}}{32768\left(7503622963200\tan\theta_0{}^{7}+\frac{1082331758592\tan\theta_0{}^{7}}{\alpha}\right)}$
$d_{2,21}$	$\frac{7704243768453287\,b_2\,(\delta+\tan\theta_0)^{\frac{96103}{32768}}}{16777216\left(151156948992\tan\theta_0{}^{3}+\frac{51539607552\tan\theta_0{}^{3}}{\alpha}\right)}$	$d_{2,22}$	$\frac{5\sqrt{2}\,(\delta+\tan\theta_0)^2}{128\tan\theta_0+\frac{64\tan\theta_0}{\alpha}}$
$d_{2,23}$	$\frac{45154123433643 91\,b_2\,(\delta+\tan\theta_0)^{\frac{30567}{32768}}}{34359738368\left(978144\tan\theta_0+\frac{1048576\tan\theta_0}{\alpha}\right)}$	$d_{2,24}$	$-\frac{7116713214246575\,b_2\,(\delta+\tan\theta_0)^{\frac{194407}{32768}}}{32768\left(146772370391 04\tan\theta_0{}^{6}+\frac{2473901162496\tan\theta_0{}^{6}}{\alpha}\right)}$
$d_{2,25}$	$\frac{813773447008073\,b_2\,(\delta+\tan\theta_0)^{\frac{292711}{32768}}}{2048\left(309385167372288\tan\theta_0{}^{9}+\frac{34634616274944\tan\theta_0{}^{9}}{\alpha}\right)}$	$d_{2,26}$	$\frac{5899216819711551\,b_2\,(\delta+\tan\theta_0)^{\frac{325479}{32768}}}{8192\left(344019783647232\tan\theta_0{}^{10}+\frac{34634616274944\tan\theta_0{}^{10}}{\alpha}\right)}$
$d_{2,27}$	$-\frac{5278606494654121\,b_2\,(\delta+\tan\theta_0)^{\frac{358247}{32768}}}{8192\left(378654399922176\tan\theta_0{}^{11}+\frac{34634616274944\tan\theta_0{}^{11}}{\alpha}\right)}$	$d_{2,28}$	$\frac{1772224420073771\,b_2\,(\delta+\tan\theta_0)^{\frac{489319}{32768}}}{65536\left(804522234478592\tan\theta_0{}^{15}+\frac{53876069761024\tan\theta_0{}^{15}}{\alpha}\right)}$
$d_{2,29}$	$\frac{470813493566555\,b_2\,(\delta+\tan\theta_0)^{\frac{554855}{32768}}}{32768\left(7298194992005120\tan\theta_0{}^{17}+\frac{431008558088192\tan\theta_0{}^{17}}{\alpha}\right)}$	$d_{2,30}$	$-\frac{1390888037066579\,b_2\,(\delta+\tan\theta_0)^{\frac{259943}{32768}}}{1024\left(157000314912768\tan\theta_0{}^{8}+\frac{19791209299968\tan\theta_0{}^{8}}{\alpha}\right)}$
$d_{2,31}$	$-\frac{388717606998977\,b_2\,(\delta+\tan\theta_0)^{\frac{587623}{32768}}}{32768\left(4637522130055987 2\tan\theta_0{}^{18}+\frac{2586051348529152\tan\theta_0{}^{18}}{\alpha}\right)}$	$d_{2,32}$	$\frac{187\sqrt{2}\,b_2\,(\delta+\tan\theta_0)^{-\frac{2201}{32768}}}{\frac{256}{\alpha}-\frac{2201}{128}}$
$d_{3,1}$	$-\frac{3198993443274073\,b_2\left(\frac{\tan\theta_0}{2}\right)^{\frac{227175}{32768}}}{32768\left(7503622963200\tan\theta_0{}^{7}+\frac{1082331758592\tan\theta_0{}^{7}}{\alpha}\right)}$	$d_{3,2}$	$-\frac{3171422887418271\,b_2\left(\frac{\tan\theta_0}{2}\right)^{\frac{620391}{32768}}}{134217728\left(1165744586883072\tan\theta_0{}^{19}+\frac{61572651155456\tan\theta_0{}^{19}}{\alpha}\right)}$
$d_{3,3}$	$-\frac{7704243768453287\,b_2\left(\frac{\tan\theta_0}{2}\right)^{\frac{96103}{32768}}}{16777216\left(151156948992\tan\theta_0{}^{3}+\frac{51539607552\tan\theta_0{}^{3}}{\alpha}\right)}$	$d_{3,4}$	$-\frac{5\sqrt{2}\left(\frac{\tan\theta_0}{2}\right)^2}{128\tan\theta_0+\frac{64\tan\theta_0}{\alpha}}$
$d_{3,5}$	$-\frac{4515412343364391\,b_2\left(\frac{\tan\theta_0}{2}\right)^{\frac{30567}{32768}}}{34359738368\left(978144\tan\theta_0+\frac{1048576\tan\theta_0}{\alpha}\right)}$	$d_{3,6}$	$\frac{7116713214246575\,b_2\left(\frac{\tan\theta_0}{2}\right)^{\frac{194407}{32768}}}{32768\left(146772370391 04\tan\theta_0{}^{6}+\frac{2473901162496\tan\theta_0{}^{6}}{\alpha}\right)}$
$d_{3,7}$	$-\frac{813773447008073\,b_2\left(\frac{\tan\theta_0}{2}\right)^{\frac{1}{\alpha}+\frac{292711}{32768}}}{2048\left(309385167372288\tan\theta_0{}^{9}+\frac{34634616274944\tan\theta_0{}^{9}}{\alpha}\right)}$	$d_{3,8}$	$-\frac{5899216819711551\,b_2\left(\frac{\tan\theta_0}{2}\right)^{\frac{325479}{32768}}}{8192\left(344019783647232\tan\theta_0{}^{10}+\frac{34634616274944\tan\theta_0{}^{10}}{\alpha}\right)}$

Continued on next page

Table A.2 – *Continued from previous page*

Constant	Value	Constant	Value
$d_{3,9}$	$\frac{5278606494654121\, b_2 \left(\frac{\tan\theta_0}{2}\right)^{\frac{358247}{32768}}}{8192\left(378654399922176\tan\theta_0{}^{11}+\frac{34634616274944\tan\theta_0{}^{11}}{\alpha}\right)}$	$d_{3,10}$	$-\frac{1772224420073771\, b_2 \left(\frac{\tan\theta_0}{2}\right)^{\frac{489319}{32768}}}{65536\left(804522234478592\tan\theta_0{}^{15}+\frac{53876069761024\tan\theta_0{}^{15}}{\alpha}\right)}$
$d_{3,11}$	$-\frac{470813493566555\, b_2 \left(\frac{\tan\theta_0}{2}\right)^{\frac{554855}{32768}}}{32768\left(7298194992005120\tan\theta_0{}^{17}+\frac{431008558088192\tan\theta_0{}^{17}}{\alpha}\right)}$	$d_{3,12}$	$\frac{1390888037066579\, b_2 \left(\frac{\tan\theta_0}{2}\right)^{\frac{259943}{32768}}}{1024\left(157000314912768\tan\theta_0{}^{8}+\frac{19791209299968\tan\theta_0{}^{8}}{\alpha}\right)}$
$d_{3,13}$	$\frac{388717606998977\, b_2 \left(\frac{\tan\theta_0}{2}\right)^{\frac{587623}{32768}}}{32768\left(463752213005598 72\tan\theta_0{}^{18}+\frac{2586051348529152\tan\theta_0{}^{18}}{\alpha}\right)}$	$d_{3,14}$	$\frac{4112068129940143\, b_2 \left(\frac{\tan\theta_0}{2}\right)^{\frac{423783}{32768}}}{131072\left(895847264944128\tan\theta_0{}^{13}+\frac{69269232549888\tan\theta_0{}^{13}}{\alpha}\right)}$
$d_{3,15}$	$\frac{3363754402794477\, b_2 \left(\frac{\tan\theta_0}{2}\right)^{\frac{456551}{32768}}}{4096\left(13511630964916224\tan\theta_0{}^{14}+\frac{969769255698432\tan\theta_0{}^{14}}{\alpha}\right)}$	$d_{3,16}$	$\frac{5083615087327005\, b_2 \left(\frac{\tan\theta_0}{2}\right)^{\frac{522087}{32768}}}{2048\left(247218711621009408\tan\theta_0{}^{16}+\frac{15516308091174912\tan\theta_0{}^{16}}{\alpha}\right)}$
$d_{3,17}$	$\frac{2255234053275215\, b_2 \left(\frac{\tan\theta_0}{2}\right)^{\frac{653159}{32768}}}{4294967296\left(7013241360220 16\tan\theta_0{}^{20}+\frac{35184372088832\tan\theta_0{}^{20}}{\alpha}\right)}$	$d_{3,18}$	$-\frac{3916342628302019\, b_2 \left(\frac{\tan\theta_0}{2}\right)^{\frac{391015}{32768}}}{2048\left(3306312129576960\tan\theta_0{}^{12}+\frac{277076930199552\tan\theta_0{}^{12}}{\alpha}\right)}$
$d_{3,19}$	$\frac{737389043420589\, b_2 \left(\frac{\tan\theta_0}{2}\right)^{\frac{128871}{32768}}}{32768\left(540524150784\tan\theta_0{}^{4}+\frac{137438953472\tan\theta_0{}^{4}}{\alpha}\right)}$	$d_{3,20}$	$-\frac{7868723041398407\, b_2 \left(\frac{\tan\theta_0}{2}\right)^{\frac{63335}{32768}}}{33554432\left(16602890240\tan\theta_0{}^{2}+\frac{8589934592\tan\theta_0{}^{2}}{\alpha}\right)}$
$d_{3,21}$	$-\frac{2682583518496071\, b_2 \left(\frac{\tan\theta_0}{2}\right)^{\frac{161639}{32768}}}{262144\left(338981552128\tan\theta_0{}^{5}+\frac{68719476736\tan\theta_0{}^{5}}{\alpha}\right)}$	$d_{3,22}$	$\frac{187\sqrt{2}\left(\frac{\tan\theta_0}{2}\right)}{\frac{256}{\alpha}+256}$
$d_{3,23}$	$\frac{15\sqrt{2}\left(\frac{\tan\theta_0}{2}\right)^{4}}{256\tan\theta_0{}^{3}+\frac{64\tan\theta_0{}^{3}}{\alpha}}$	$d_{3,24}$	$-\frac{43\sqrt{2}\left(\frac{\tan\theta_0}{2}\right)^{3}}{384\tan\theta_0{}^{2}+\frac{128\tan\theta_0{}^{2}}{\alpha}}$
$d_{3,25}$	$-\frac{13\sqrt{2}\left(\frac{\tan\theta_0}{2}\right)^{5}}{1280\tan\theta_0{}^{4}+\frac{256\tan\theta_0{}^{4}}{\alpha}}$	$d_{3,26}$	$-\frac{187\sqrt{2}\, b_2 \left(\frac{\tan\theta_0}{2}\right)^{-\frac{2201}{32768}}}{\frac{256}{\alpha}-\frac{2201}{128}}$
$d_{3,27}$	$-\frac{\frac{\tan\theta_0}{2}}{\frac{1}{\alpha}+1}$	$d_{3,28}$	$\frac{\frac{\tan\theta_0}{2}^{3}}{2(3\tan^2\theta_0+\frac{\tan^2\theta_0}{\alpha})}$
$d_{3,29}$	$-\frac{3\frac{\tan\theta_0}{2}^{5}}{8(5\tan^4\theta_0+\frac{\tan^4\theta_0}{\alpha})}$	$d_{3,30}$	$\frac{5\frac{\tan\theta_0}{2}^{7}}{16(7\tan^6\theta_0+\frac{\tan^6\theta_0}{\alpha})}$
$d_{3,31}$	$\frac{b_3\frac{\tan\theta_0}{2}^{4}}{8(4\tan^4\theta_0+\frac{\tan^4\theta_0}{\alpha})}$	$d_{3,32}$	$-\frac{b_3\frac{\tan\theta_0}{2}^{6}}{8(6\tan^6\theta_0+\frac{\tan^6\theta_0}{\alpha})}$
$d_{3,33}$	$-\frac{5b_3\frac{\tan\theta_0}{2}^{8}}{32(8\tan^8\theta_0+\frac{\tan^8\theta_0}{\alpha})}$		
$d_{4,1}$	$\frac{3\tilde{\chi}^5}{8(5\tan^4\theta_0+\frac{\tan^4\theta_0}{\alpha})}$	$d_{4,2}$	$-\frac{\tilde{\chi}^3}{2(3\tan^2\theta_0+\frac{\tan^2\theta_0}{\alpha})}$
$d_{4,3}$	$-\frac{5\tilde{\chi}^7}{16(7\tan^6\theta_0+\frac{\tan^6\theta_0}{\alpha})}$	$d_{4,4}$	$\frac{\tilde{\chi}}{\frac{1}{\alpha}+1}$
$d_{4,5}$	$-\frac{b_3\tilde{\chi}^4}{8(4\tan^4\theta_0+\frac{\tan^4\theta_0}{\alpha})}$	$d_{4,6}$	$\frac{b_3\tilde{\chi}^6}{8(6\tan^6\theta_0+\frac{\tan^6\theta_0}{\alpha})}$
$d_{4,7}$	$\frac{5b_3\tilde{\chi}^8}{32(8\tan^8\theta_0+\frac{\tan^8\theta_0}{\alpha})}$		

The third term is the hemicellulose contribution and is found to be,

$$\Sigma_3^{\infty} = \int_{\epsilon}^{1} a_2 n\tilde{n}\sigma_H \, dy = \int_{\chi}^{1} a_2 \breve{\alpha} y^{\frac{1}{\alpha}} y^{\frac{\breve{k}_0}{\alpha}} \left(\frac{1}{y} - y^{\frac{\omega}{\alpha}}\right) \, dy \tag{A.1.72}$$

$$+ \int_{\tilde{\chi}}^{\chi} + a_2 \breve{\alpha} y^{\frac{1}{\alpha}} \exp\left(-\frac{\breve{k}_0}{\alpha} \frac{y^2}{2\breve{\alpha}^2\gamma^2} e^{\breve{\alpha}^2 \frac{\gamma^2}{y^2}}\right) \left(\frac{1}{y} - y^{\frac{\omega}{\alpha}}\right) \, dy$$

$$+ \int_{\epsilon}^{\tilde{\chi}} a_2 \breve{\alpha} \exp\left(-\frac{1}{\alpha} \frac{y^2}{2\tilde{\beta}^2} e^{\frac{\tilde{\beta}^2}{y^2}}\right) \exp\left(-\frac{\breve{k}_0}{\alpha} \frac{y^2}{2\breve{\alpha}^2\gamma^2} e^{\frac{\breve{\alpha}^2\gamma^2}{y^2}}\right) \left(\frac{1}{y} - y^{\frac{\omega}{\alpha}}\right) \, dy, \tag{A.1.73}$$

where upon integration,

$$\Sigma_3^{\infty} = a_2 \breve{\alpha} \left(\frac{\alpha}{\breve{k}_0 + 1} \left(1 - \chi^{\frac{\breve{k}_0+1}{\alpha}}\right) - \frac{1}{\frac{1}{\alpha}\left(\breve{k}_0 + \omega + 1\right) + 1} \left(1 - \chi^{\frac{\breve{k}_0+\omega+1}{\alpha}+1}\right) \right). \tag{A.1.74}$$

Note that for all three contribtuions to the stress resultant, Σ_1^{∞}, Σ_2^{∞}, and Σ_3^{∞} upon integration for some critical values of α some of their terms are logarithmic which we choose to ignore.

A.2 Experimental methods to understand pavement cell development

A.2.1 Pavement cell shape extraction

After editing the images in ImageJ to create a clear picture, we can then begin extracting pavement cell outlines. We firstly use the software CellSeT [Pound et al., 2012] to segment the images to produce an image as shown in figure A.1. This software uses a watershed algorithm to perform this segmentation. The basic principle of this algorithm is that a "water source" is placed in each regional minima (points with the lowest fluorescence), where it then starts to flood the area (starts to submerge areas of increased fluorescence). Barriers are then placed (segmentation lines) where the different sources meet (the points of highest fluorescence, i.e. the PI stained cell walls) [Pound et al., 2012]. In the CellSeT software, we choose the following settings. The segmentation fluorescent threshold value is set at 36, node spacing at 3, curvature set to 50, continuity at 1 and the image weight at 1. These values were chosen through trial and error to see which parameters provided the best segmentation when compared to the original image. Lastly, in the program's interface, we compare the segmentation edges to the original image and remove any false walls that the segmentation has added. From this segmentation data, we now want to extract the individual cell outlines.

The individual cell outline extraction is done in ImageJ, using MorphopLibJ's morphological segmentation tool [Legland et al., 2016]. The segmentation data out of CellSeT does not always work in MorphopLibJ, so we first use ImageJ's threshold tool (which detects everything above or below a certain threshold of light in the image and turns it black or white depending on if it below or above) to turn the segmentation image into a binary im-

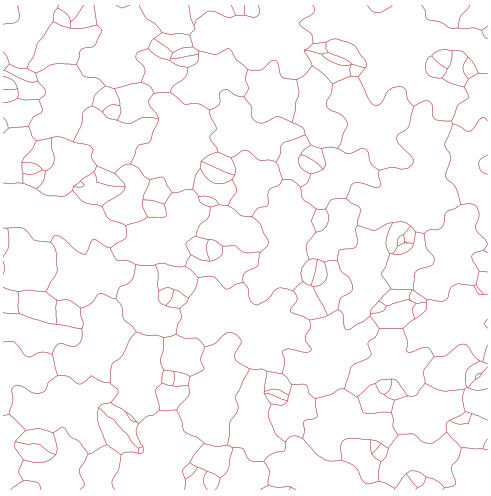


Figure A.1: CellSeT software output

age where the segmentation lines are set to black and everything else is white. Using MorphopLibJ's segmentation tool, which also uses a watershed algorithm and setting the tolerance to 40, we can select individual cells, extract and then save their shape as a black silhouette, as shown in figure A.2. Note that in our experience, we could not go straight to this step with the original image, as the MorphopLibJ segmentation tool was not accurate in picking out the cell walls. For these silhouettes to be useful, we now need to extract and process their outline coordinates.

We extract the silhouette outline coordinates by importing the image into MATLAB and use the function `im2bw` to convert this image into a binary matrix indicating black (represented by 0's) or white (represented by 1's). Due to us using silhouettes, we have to invert this matrix, as the function outputs the cell shape locations to be 0 and not 1. With this inverted matrix, we can then use the MATLAB function `bwtraceboundary` to extract our boundary co-ordinates of the pavement cell, $\mathbf{X}_B^*$ with $\mathbf{X}_B^*=(\mathbf{x}_B^*, \mathbf{y}_B^*)$.

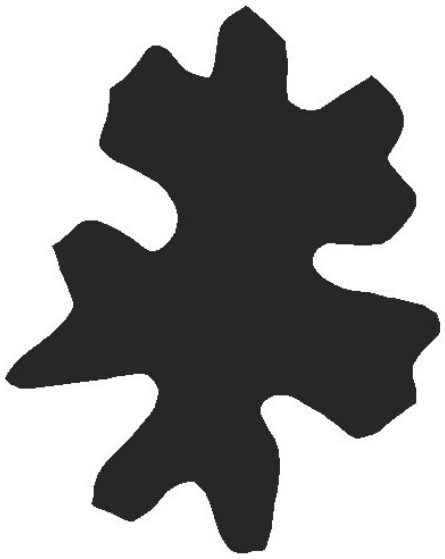


Figure A.2: MorphopLibJ's morphological segmentation tool pavement cell silhouette example

We can not use the boundary coordinates in the current form due to the pixelated nature of the silhouette. For use in the simulations, we will need to calculate the curvature of these outlines, but if we leave the outlines in their current form, this will produce false results. The false result occurs as neighbouring coordinates are either directly above, below, to the left or the right of one another. So when we calculate the curvature values of these coordinates, we get either high negative, high positive or zero where these values do not correspond to the larger scale bending behaviour. We, therefore, have to smooth this data. Care needs to be taken here as when we increasingly

smooth the coordinates, the curvature results look increasingly better, but we can go too far where over smoothing can distort the boundary coordinates away from the original cell shape. We use the MATLAB function `smooth` specifying the Savitzky-Golay filter as through trial and error, we find this to be effective with cyclic like data (see [Savitzky and Golay, 1964] for algorithm details).

Another issue we have to deal with when smoothing the co-ordinates $\mathbf{X}^*_B$, is that the first and last coordinates (the first and last rows in this matrix) can become disjointed as when they are inputted into the smoothing function they are not connected to one another. This snag in the boundary coordinates of the pavement cell shapes is noticeable and unrealistic, where it also distorts the curvature values in that area. To tackle this issue we reorder $\mathbf{X}^*_B$ so that we have four sets of boundary co-ordinates all with different starting coordinates. These sets are the original set (we are labelling $\mathbf{X}^*_{B,1}$), another set reordered so that the first and last co-ordinates are now the ones either side of the half way point in the original co-ordinates (labelled $\mathbf{X}^*_{B,\frac{1}{2}}$) and two other sets which are shifted so that their first and last co-ordinates are the ones either side of the one quarter and three quarter marks in the original co-ordinates (labelled $\mathbf{X}^*_{B,\frac{1}{4}}$ and $\mathbf{X}^*_{B,\frac{3}{4}}$). We smooth each of these sets of co-ordinates and reorder the smoothed shifted sets ($\mathbf{X}^*_{B,\frac{1}{2}}$, $\mathbf{X}^*_{B,\frac{1}{4}}$ and $\mathbf{X}^*_{B,\frac{3}{4}}$) so that they now match the order of the original set ($\mathbf{X}^*_{B,1}$). We then combine these four different sets using an adapted weighted average, such that for each coordinate we calculated

$$\mathbf{X}^*_{B,(i,j)} = \frac{c_1\mathbf{X}^*_{B,1,(i,j)} + c_{\frac{1}{2}}\mathbf{X}^*_{B,\frac{1}{2},(i,j)} + c_{\frac{1}{4}}\mathbf{X}^*_{B,\frac{1}{4},(i,j)} + c_{\frac{3}{4}}\mathbf{X}^*_{B,\frac{3}{4},(i,j)}}{c_1 + c_{\frac{1}{2}} + c_{\frac{1}{4}} + c_{\frac{3}{4}}}, \tag{A.2.1}$$

for each i in the boundary co-ordinates where $j = 1, 2$. To calculate a smooth boundary we set the values of c_1, $c_{\frac{1}{2}}$, $c_{\frac{1}{4}}$ and $c_{\frac{3}{4}}$ to 1 apart from when the coordinate $\mathbf{X}^*_{B,(i,j)}$ is close to one of the the end points of one of the sets where the outline will be distorted. For example when the coordinate is close to the half way point we set $c_{\frac{1}{2}} = 0$ so that it is not included in the weighted average. This produces a smooth set of boundary coordinates

that has not been distorted away from the original image.

A.2.2 Atomic force microscopy: Hertzian indentation model

The equation used to approximate the Youngs modulus or the so called indentation modulus is,

$$F = \frac{4}{3}\lambda^* r^{\frac{1}{2}} d^{\frac{3}{2}} \text{ where } \lambda^* = \frac{\lambda}{2(1-\nu^2)} \tag{A.2.2}$$

where F is the force, λ the approximated Young's modulus, ν the Poisson's ratio, r the radius of the indenting probe and d the indentation depth [Franco Jr and Roberts, 2004].

A.3 Microtubule model

A.3.1 Microtubule model implementation details

This section describes how exactly the model described in section 5.2 is realised. This section is split into two parts. It is first explained how the individual microtubule dynamics are simulated in section A.3.1.1 followed by a explanation of the implementation of microtubule interactions in section A.3.1.2.

A.3.1.1 Singular microtubule dynamics

We model the microtubules in a cell as m lines where m_{max} is the max number of microtubules in the model. We simulate over the time points $t^* = t_1^*, t_2^* \cdots t_K^*$ where K is the number of time points, with constant time stepping $t_k^* - t_{k-1}^* = \Delta t^* \; \forall \; k = 1, 2, \cdots K$. At each time step in the simulation the microtubule lines can extend (they grow), and when they grow they can also come into contact with other lines where they can interact, by crossing over, bundling or having a collision induced catastrophe. After evaluating these interactions, in the next time step, the microtubule can continue to grow in the same direction, change direction or start to shrink respectively.

All interactions occur within a domain denoted Ω which is the cellular space. It is computational favourable to first compute the whole space curve a microtubule can take when spawned with it travelling in a certain direction and store this information. As a result we need to create a set of m lines in which the microtubules can potentially grow along. Note that we don't include directional noise which Mirabet et al. [2018] includes. To set up these lines we randomly select a starting point $(x^*_{M,(\imath,1)}, y^*_{M,(\imath,1)})$ for a microtubule $\imath$ within the range of the maximum and minimum x^*_M and y^*_M co-ordinates of the domain where the MATLAB function `inpolygon` is used to ensure this point lies within the domain, Ω. We then choose a random angle between $-\pi < \theta_\imath \leq \pi$ which will be the microtubule growth direction at the start. All the random numbers generated (the starting points and angles) are picked from a uniform distribution. We then calculate a line of

potential co-ordinates, $(\mathbf{x}^*_{M,\imath}, \mathbf{y}^*_{M,\imath})$, going in the direction of the vector, $(\cos(\theta_\imath), \sin(\theta_\imath))^T$, (where $\bullet^T$ represents the transpose) from the starting point using the formula,

$$x^*_{M,(\imath,\jmath)} = x^*_{M,(\imath,1)} + \cos(\theta_\imath) v^*_\jmath, \tag{A.3.1}$$

$$y^*_{M,(\imath,\jmath)} = y^*_{M,(\imath,1)} + \sin(\theta_\imath) v^*_\jmath \text{ for } 2 \leq \jmath \leq l_{max}, \text{where,} \tag{A.3.2}$$

$$\mathbf{v}^* = (0, \alpha^*, 2\alpha^*, \ldots l_{max}\alpha^*), \tag{A.3.3}$$

where $\mathbf{v}^*$ is a vector defining the spacing between the co-ordinates, which is long enough to create a space curve of maximum length in the domain, i.e. one starting from the x^*_M and y^*_M minimum coordinates and ending at x^*_M and y^*_M maximum co-ordinates. α^* is the density of our lines and shall be defined later and l_{max} is the max number of points. After calculating these trajectories the MATLAB function `intersect` is used to find the coordinates in which this line intersects the boundary of the domain, $\partial\Omega$ where this intersection point is set as the last coordinate in the microtubule's potential space curve such that a microtubule, i now has $l_\imath$ points. These line co-ordinates for the microtubules are stored in two $m \times l_{max}$ matrices $\mathbf{X}^*_M$ and $\mathbf{Y}^*_M$ such that

$$\mathbf{X}^*_M = \begin{pmatrix} \vdots & & & & & \\ x^*_{M,(\imath,1)}, & x^*_{M,(\imath,2)}, & \cdots, & x^*_{M,(\imath,l_\imath)}, & NaN, & \cdots, \\ x^*_{M,(\imath+1,1)}, & x^*_{M,(\imath+1,2)}, & \cdots, & \cdots, & x^*_{M,(\imath+1,l_{\imath+1})}, & NaN,, \quad \cdots, \\ \vdots & & & & & \end{pmatrix}, \tag{A.3.4}$$

with a identical setup for $\mathbf{Y}^*_M$, where NaN values are placed in the matrix locations where there are no coordinates. We create a similar matrix Θ that stores the angles, $\theta_{\imath,\jmath}$ which is the direction the microtubule $\imath$ has at position $\jmath$. In order to implement the collision dynamics later on we need to know the line coordinates of all the microtubules from the same starting point but heading in the opposite direction. We therefore repeat the above steps using the angle $\theta - \pi$ and store this information in matrices X^*_{back} and Y^*_{back}.

We create two more matrices $\mathbf{CO}^*_X$ and $\mathbf{CO}^*_Y$ which tells us the line coordinates of

each microtubule at the current time step. At $t^* = 0$ it is all NaN's apart from the first column which are the starting coordinates. So that a random time point t_k^* these matrices are set up as

$$\mathbf{CO}_X^* = \begin{pmatrix} \vdots & & & & & & & & \\ NaN, & \cdots, & \cdots, & x^*_{M,(\imath,\text{minus}_\imath^\text{k})}, & x^*_{M,(\imath,\text{minus}_\imath^\text{k}+1)}, & \cdots, & x^*_{M,(\imath,\text{plus}_\imath^\text{k})}, & NaN, & \cdots, \\ NaN, & \cdots, & x^*_{M,(\imath+1,\text{minus}_{\imath+1}^\text{k})}, & x^*_{M,(\imath,\text{minus}_{\imath+1}^\text{k}+1)}, & \cdots, & x^*_{M,(\imath,\text{plus}_{\imath+1}^\text{k})}, & NaN, & \cdots, & \cdots, \\ \vdots & & & & & & & & \end{pmatrix}, \tag{A.3.5}$$

where $\mathbf{CO}_Y^*$ is identical but defines the y co-ordinates. $\text{minus}_\imath^\text{k}$ is the minus end position at time t_k^* that the microtubule i is at along its space curve defined in $\mathbf{X}_M^*$ and $\mathbf{Y}_M^*$ and similarly, $\text{plus}_\imath^\text{k}$ is the plus end position. As the microtubule grows (every time step Δt^*), the microtubules move along their space curve's, meaning that more co-ordinates from $\mathbf{X}_M^*$ and $\mathbf{Y}_M^*$ become part of $\mathbf{CO}_X^*$ and $\mathbf{CO}_Y^*$, in other words $\text{plus}_\imath^{\text{k}+1} = \text{plus}_\imath^\text{k} + 1$, where the distance covered in this time step, α^* is dependant on the microtubule plus end growth speed, v_{gr}^* meaning $\alpha^* = v_{gr}^* \times \Delta t^*$. This growth is done for each time step until it reaches the boundary of the domain where $\text{plus}_\imath^\text{k} = \text{l}_\imath$, at which point the microtubule will stop growing. As we are including edged induced catastrophe, when a microtubules hits the boundary we let such a event occur with probability $\mathcal{P}_{EC}$. If a microtubule undergoes edge induced catastrophe the microtubule is now shrinking from its plus end, meaning for future time steps we have $\text{plus}_\imath^{\text{k}+1} = \text{plus}_\imath^\text{k} - \beta$, where $\beta = 1$ or 2. Our shrinkage speed is v_{shr}^* and as the density of the space curve α^* is dependant on the growth speed v_{gr}^* and as $v_{gr}^* < v_{shr}^*$, we have to vary β depending on the cumulative distance covered by the retracting microtubule to bring the microtubule to its actual retraction distance. At any point in time these microtubules can also randomly undergo a catastrophe with probability $\mathcal{P}_{RC}$ where they will start retracting from their minus end so that $\text{minus}_{\imath+1}^\text{k} = \text{minus}_\imath^\text{k} + \beta$ with speed v_{shr}^*. We create indicator variables to keep track of which microtubule's plus ends and minus ends are growing or retracting. When $\text{minus}_\imath^\text{k} = \text{plus}_\imath^\text{k}$ the microtubule

has shrunk completely and is removed from the system.

At each time point new microtubules can also spawn, with the number of new microtubules per time step being m_{new} where new sets of random trajectories are calculated and inserted into our matrices. To limit the number of microtubules in the system we make this spawn number dependant on the number of microtubules already in the system in a similar manner to Allard et al. [2010b] such that when we have fewer microtubules in the system the microtubule spawn number increases. Goodson and Jonasson [2018] say that new microtubule nucleation depends on the concentration of free tubulin meaning our spawning dependence is accurate to the biology. To keep the stochastic nature of our model the spawn number will be chosen from a normal distribution with a varying mean so that when there are around 0 microtubules in the system the probability of m_{max} microtubules spawning is high but when there are around m_{max} microtubules in the system there is a high probability of no microtubules spawning. We therefore define,

$$m_{new}(m) = \begin{cases} \lfloor \phi(m) \rceil, & \phi(m) > 0 \\ 0, & \phi < 0 \end{cases} \tag{A.3.6}$$

$$\phi(m) = \text{sampled from } \mathcal{N}\left(m_{max} - m, \varrho^2\right), \tag{A.3.7}$$

where $\lfloor \phi(m) \rceil$ is the rounded sampled number from the normal distribution and ϱ^2 is the standard deviation.

A.3.1.2 Microtubule interactions implementation

A key feature in this model is including the collision dynamics meaning when microtubules collide with one another they can bundle, undergo catastrophe or crossover in a angle dependant manner. To first check if any possible interactions have occurred we examine all the growing microtubule plus ends, $(x^*_{M,(\imath,\text{plus}^{\text{k}}_\imath)}, y^*_{M,(\imath,\text{plus}^{\text{k}}_\imath)})\ \forall \imath \in \{1, 2, \cdots, m | \text{ plus}^{\text{k}}_\imath \neq \text{l}_\imath\}$ and by calculating norms we see whether they are within a certain radius r^*_I of any other microtubule line points in $\mathbf{CO}^*_X$ and $\mathbf{CO}^*_Y$. It is important to note that we can save

computation time in MATLAB by first finding the points to which this applies

$$|x^*_{M,(\tilde{\imath},\jmath)} - x^*_{\imath,\mathrm{plus}^{\mathrm{k}}_{\imath}}| < r^*_I \text{ and } |y^*_{M,(\tilde{\imath},\jmath)} - y^*_{\imath,\mathrm{plus}^{\mathrm{k}}_{\imath}}| < r^*_I, \tag{A.3.8}$$

$$\text{where } \mathrm{minus}^{\mathrm{k}}_{\tilde{\imath}} < \jmath < \mathrm{plus}^{\mathrm{k}}_{\tilde{\imath}} \; \tilde{\imath} = 1, 2, \cdots \imath - 1, \imath + 1, \cdots \mathrm{m}, \tag{A.3.9}$$

and calculate the norm for these points only.

If a collusion occurs, (first checking there are not already part of the same bundle already) we calculate the angle between the two and if its smaller than a critical angle, θ_{crit} then they will bundle with probability, $\mathcal{P}_B$ and allocated a bundle number allowing us to track what bundle every microtubule is part of. This ensures that our code doesn't think it keeps on colliding with the same microtubule at each time step as they are now going along the same space curve and consequently in collision range. If two microtubules without a bundle number collide with another they are both given a new unique number while if the microtubule collides with an existing bundle that microtubule is allocated that existing bundle's number. When a microtubules bundles into another, we change its potential future space curve in $\mathbf{X}^*_M$ and $\mathbf{Y}^*_M$ with that of the space curve of the microtubule it is colliding with. There are two scenarios of bundling when a microtubule hits another; the first being where post bundling it grows in the same direction towards the plus end of the microtubule it has collided into and the second being where it grows in the opposite direction towards the minus end of the microtubule it has collided into. So that, in the first scenario at the time point, t^*_k the microtubule i that has collided into microtubule $\tilde{\imath}$, x^* coordinates in $\mathbf{X}^*_M$ are now

$$\left(x^*_{M,(\imath,1)}, \cdots, x^*_{M,\imath,\mathrm{plus}^{\mathrm{k}}_{\imath}}, x^*_{\tilde{\imath},\tilde{\jmath}}, \cdots x^*_{\tilde{\imath},l_{\tilde{\imath}}}, NaN \cdots\right), \tag{A.3.10}$$

where $\tilde{\jmath}$ is the position along the $\tilde{\imath}$ microtubule's length where microtubule $\imath$ has collided. In the second scenario, we repeat the same procedure but we add microtubules $\tilde{\imath}$'s coordinates in reverse and use the information contained in X^*_{back} and Y^*_{back} to continue the space curve to the boundary. Effectively the MT has now had its direction altered due to

the incident.

When the collison angle is larger than the critical value, the microtubule that has crashed into the other can undergo a catastrophe from the positive end with probability $\mathcal{P}_{CC}$. We then change the indicator variable for this microtubule to make it begin shrinkage at its plus end on the next time step. If the microtubule does not bundle or undergo catastrophe then it shall just pass of and nothing will change.

A.3.2 Order parameter calculation

In analysing the microtubule simulations there is a need to know the order of the system/how organised the system is over time so that emergent properties from the interactions between the microtubules can be noticed. As a result we need to have some kind of order parameter to measure how aligned all the microtubles are. Most order parameters require the calculation of a mean angle direction/directional microtubule bias and measure how much deviation there is away from this value. However we can't find the mean/bias microtubule directions of all the microtubule angles Θ in their current form. This is because we need to make use of the non-polar direction of the angles, meaning for example we need to identify the angles $-\frac{\pi}{4}$ and $\frac{3\pi}{4}$ as the same direction. As alternatively if we have a array of microtubules organised longitudinally, they will be growing in both the $\frac{\pi}{2}$ and $-\frac{\pi}{2}$ direction meaning the non-poler direction mean would be 0 which is not what we want. With all the angles now listed between $0 \leq \theta \leq \pi$ in a vector we call $\hat{\theta}$ we now come across another problem with calculating the mean microtubule direction. If the bias in direction is close to 0 for example the mean value is skewed towards the middle due to all other values being > 0 and so we won't get the true directional bias.

Through trial and error we found the best method to find the actual directional bias value was to firstly calculate the 'mode' by splitting the domain into intervals and see which domain has the largest number of angles in it. We can then calculate the average angle in this interval which we shall call $\hat{\bar{\theta}}$ and use this angle to redistribute the angles, calling the new redistributed angles vector $\hat{\bar{\Theta}}$ where the aim is to get the distribution of

angles looking like a bell shaped curved around, $\hat{\bar{\theta}}$. This redistribution is done by taking $\hat{\bar{\Theta}}_{\imath,\jmath} = \hat{\Theta}_{\imath,\jmath} + \hat{\bar{\theta}}$ and if $\hat{\bar{\Theta}}_{\imath,\jmath} < 0 (> \pi)$ we add π (minus π) from this angle. We repeat this redistribution around the mean of the mode again to ensure the distribution of the angles are normally distributed around the bias direction. With the angle distribution now being symmetric we don't have to worry about the mean being skewed meaning we can finally calculate the average, calling it $\hat{\bar{\bar{\theta}}}$.

As our measure of order, we choose not use the standard deviation but instead use the order parameter used by Allard et al. [2010b] defined as

$$\epsilon = \frac{\sum_{\imath=1}^{m} \sum_{\jmath=\text{minus}_\imath^\text{k}}^{\text{plus}_\imath^\text{k}} \cos^2\left(\hat{\bar{\Theta}}_{\imath,\jmath} - \hat{\bar{\bar{\theta}}}\right)\right) - \sin^2\left(\hat{\bar{\Theta}}_{\imath,\jmath} - \hat{\bar{\bar{\theta}}}\right)}{\sum_{\imath=1}^{m} \sum_{\jmath=\text{minus}_\imath^\text{k}}^{\text{plus}_\imath^\text{k}} 1}, \tag{A.3.11}$$

where we are summing over the angles where a value actually exist in Θ ie where the matrices $(\mathbf{CO}_X^*, \mathbf{CO}_Y^*)$ actually have values. This order parameter, ϵ ranges between 0 and 1.

A.3.3 Microtubule pavement cell simulations

Displayed in figure A.3 is supporting evidence that our implementation of stress stabilisation of the microtubules leads to the microtubules localising to the indents where they fan out display realistic microtubule phenotype.

A.3.4 Calculating the lobe and indent indicator function, $\tilde{\kappa}$

Here are the details as to how the lobe indicator variable $\tilde{\kappa}$ is calculated. As this variable is used in several chapters, it is vital to find accurate values for it.

We begin by calculating the curvature of the pavement cell outlines using the existing MATLAB code written by Mjaavatten [2018] which returns negative curvature values along the indenting regions and positive values along the lobeing regions (where the curvature tends to be at its highest and lowest value at the lobe and indent peaks). $\tilde{\kappa}$ is

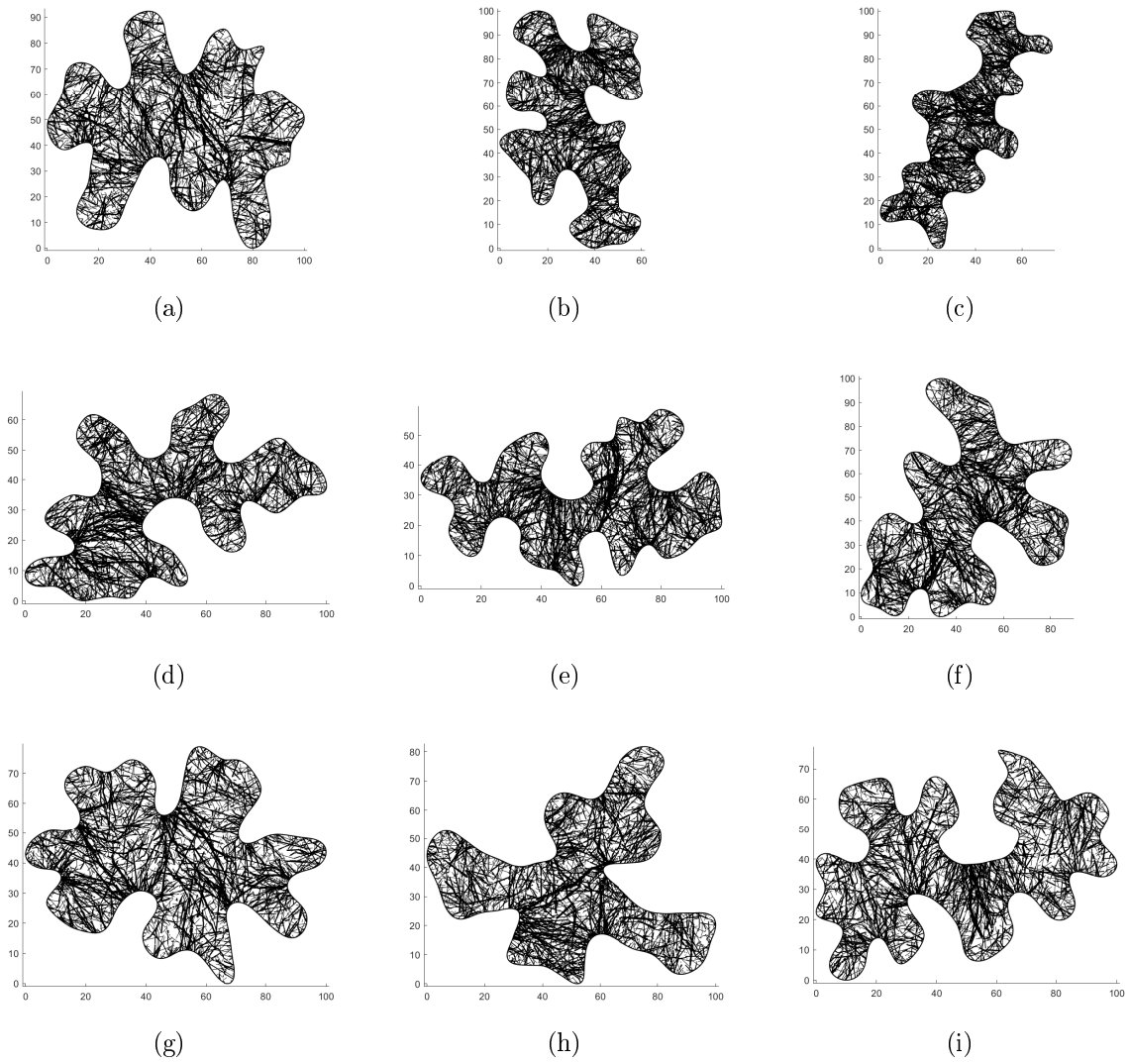
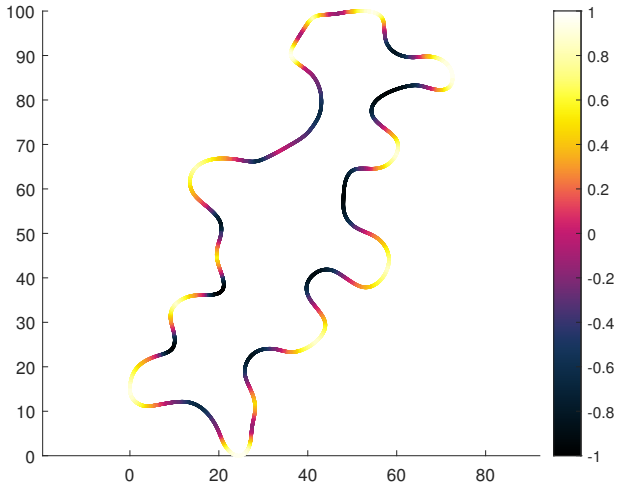


Figure A.3: The effect of stress stabilisation on the microtubule array in the different pavement cell outlines. a) Simulation in the 2nd pavement cell outline. b) Simulation in the 3rd pavement cell outline. c) Simulation in the 4th pavement cell outline. d) Simulation in the 5th pavement cell outline. e) Simulation in the 6th pavement cell outline. f) Simulation in the 7th pavement cell outline. g) Simulation in the 8th pavement cell outline. h) Simulation in the 9th pavement cell outline. i) Simulation in the 10th pavement cell outline.

created such that it takes a maximum value of 1 at the lobe peaks, -1 at the indent peaks and decreases to 0 linearly as the outline coordinates get further away from either of the peaks. The 0 locations are found by seeing where the curvature value changes sign, i.e. where the indents meet the lobes. To now find the lobe and indent peaks, both the local maxima and minima of the curvature and the midpoints between the 0 locations were

found, where the peak locations are set as the average between the two sites, respectively. With these locations in hand, each outline coordinate is allocated a value between 0 and 1 or -1, depending on its proximity to these locations in a linear manner. We additionally scale each value with the minimum and maximum curvature (depending on if it is a lobe or indent, respectively) as it is important that smaller lobes do not have the same values as the bigger ones. We now have the $\tilde{\kappa}$ (figure A.4) that gives us a quantitative value to each outline coordinate telling us where in the lobe or indent it is.



(a)

Figure A.4: The $\tilde{\kappa}$ values along an example pavement cell outline

A.4 Reaction diffusion

A.4.1 Estimating model parameters

To estimate the model parameters we shall be making use of the steady-state solution of the basic ordinary differential equation, i.e. the equation,

$$\frac{dR^*}{dt^*} = \lambda^* - \delta^* R^*, \tag{A.4.1}$$

which has the steady state, $R^* = \frac{\lambda^*}{\delta^*}$.

One initial bound we have is that all decay terms δ_I^* $I = 1, 2, 4, 6$ need to all be less than one as we cannot have more chemicals decaying than there are in the previous time step.

We can also set the boundary condition parameter, a_2 using the steady-state value, and the fact that the concentration on the boundaries needs to be higher as a result of auxins promotion there, meaning

$$a_2^* = \tilde{\lambda}_{B,6}^* \frac{\lambda_6^*}{\delta_6^*}, \tag{A.4.2}$$

where $\tilde{\lambda}_{B,6}^* > 1$.

The production terms λ_I^* and decays rates δ_I^* are fixed based on what we expect the simulations to look like in the lobes and by comparing to florescent marked ROP2 and ROP6 images found in the literature. To find these estimates, we once again examine the steady-state of a simplified 1D reaction-diffusion equation, which for some arbitrary R^* is

$$\frac{\partial R^*}{\partial t^*} = \lambda^* - \delta^* R^* + D^* \frac{\partial^2 R^*}{\partial x^{*2}}, \ 0 < x^* < x_{max}^*, \tag{A.4.3}$$

where the boundary condition are as stated above, $R^*(0, t^*) = \lambda_B^* = \tilde{\lambda}_B^* \frac{\lambda^*}{\delta^*}$ and $R(x_{max}^*, t^*) = \lambda_B^* = \tilde{\lambda}_B^* \frac{\lambda^*}{\delta^*}$. From the measurements of mature pavement cells lobes we set $x_{max}^* = 10\mu m$.

Thus setting the LHS to 0 we then can derive,

$$R^* = \frac{\lambda_B^* - \frac{\lambda^*}{\delta^*}}{e^{-\gamma^* x^*_{max}} - e^{\gamma^* x^*_{max}}} \left(\left(e^{-\gamma^* x^*_{max}} - 1 \right) e^{\gamma^* x^*} + \left(1 - e^{-\gamma^* x^*_{max}} \right) e^{-\gamma^* x^*_{max}} \right) + \frac{\lambda^*}{\delta^*}, \quad \text{(A.4.4)}$$

where $\gamma^* = \sqrt{\frac{\delta^*}{D^*}}$. γ^* and δ^* are then the only unknowns in this equation, allowing us to experiment with their values and to find a concentration distribution over the domain that looks satisfactorily like the experiential observations.

The next bound that can be set, is in order to ensure $R_1^* > 0$, meaning we have $k_{61}^* > k_{21}^*$.

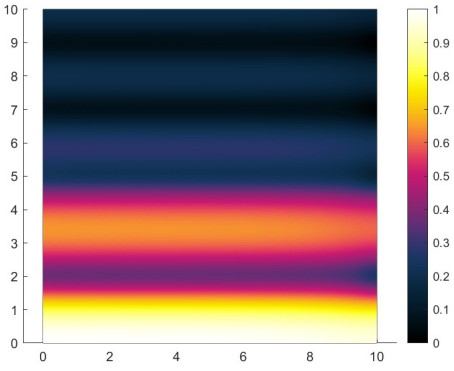
An estimate of k_{M2}^* can be found by examining a steady state without diffusion to get

$$R_2^* = \frac{\lambda_2^*}{\delta_2^* + k_{M2}^* \sup(R_M^*)}, \quad \text{(A.4.5)}$$

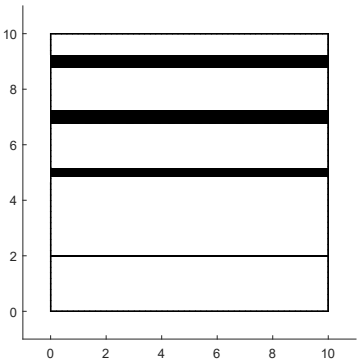
which can be used by setting the concentration of R_2^* to be what we expect when the microtubules are at their maximum, $\frac{\lambda_2^*}{6\delta_2^*}$ and letting $\sup(R_M^*) \approx 0.2 m_{max}$ for a full size pavement cell where upon rearranging, k_{M2}^* can then be found.

We then perform test simulations where we fix the microtubules and vary their concentration (figure A.5b) to check their effect on ROP2 (figure A.5a) and in what timescale they have their effect. Through trial and error, a value can be chosen for the microtubule range of effect, b_3^* and the effect on ROP2, k_{M2}^* is also checked to ensure the desired effect is achieved. We also perform more simulations where we fix the ROP2 and ROP6 concentrations (figure A.5c and d with high ROP2 and ROP6 concentrations in the lower and higher half of the domain, respectively) to check their effect on the microtubules, RIC1 and RIC4. Once again, using trial and error, the test simulations are run to fix the parameters such as b_4^*, c_4^*, ϑ, k_{21}^*, k_{61}^* and k_{24}^* to get the required effect on the microtubule array which we see to be higher in concentration in the upper half (figure A.5e).

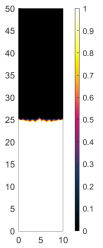
The rest of the parameters such as c_2 and b_2 were fixed through successive simulations in actual parameter cells using trial and error till we got satisfactory results.



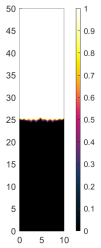
(a) ROP2



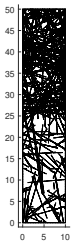
(b) Microtubule array



(c) ROP2



(d) ROP6

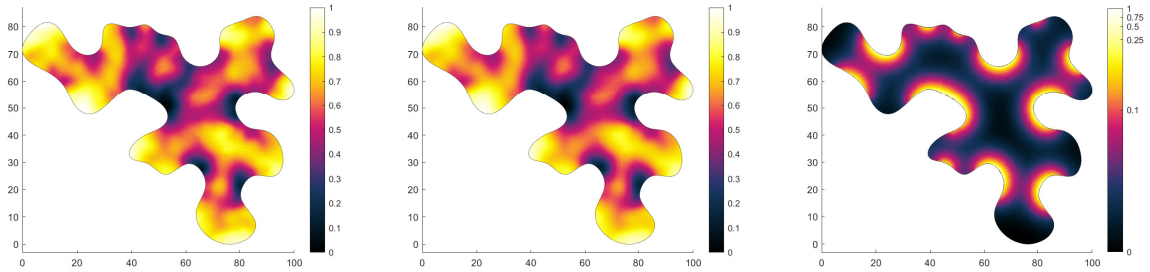


(e) Microtubule array

Figure A.5: Parameter setting test simulations where the figures display (a) the ROP2 concentration when the microtubules are fixed. (b) the fixed microtubule array (c) the fixed ROP2 concentration. (d) the fixed ROP6 concentration. (e) the microtubule array with ROP2 and ROP6 array fixed

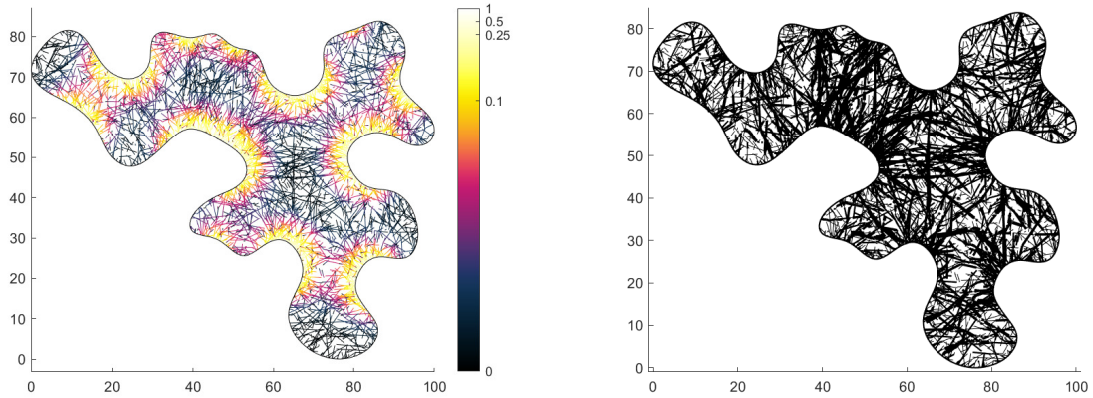
A.4.2 Testing the signalling protein and microtubule network localisation establishment additional figures

Here we show the additional figures for section 6.5.1.



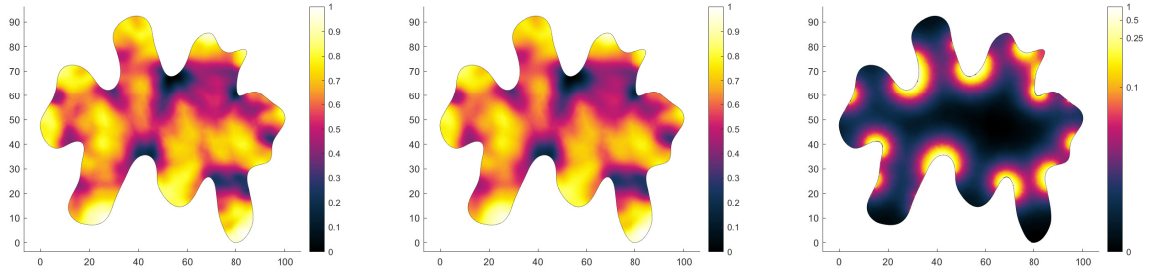
(a) ROP2 (b) RIC4 (c) ROP6

Figure A.6: The signalling network model results in the 1st mature pavement cell outline, where the figures show the different proteins concentrations. Figures c has a non-linear scalebar in order to see concentration variations clearly.



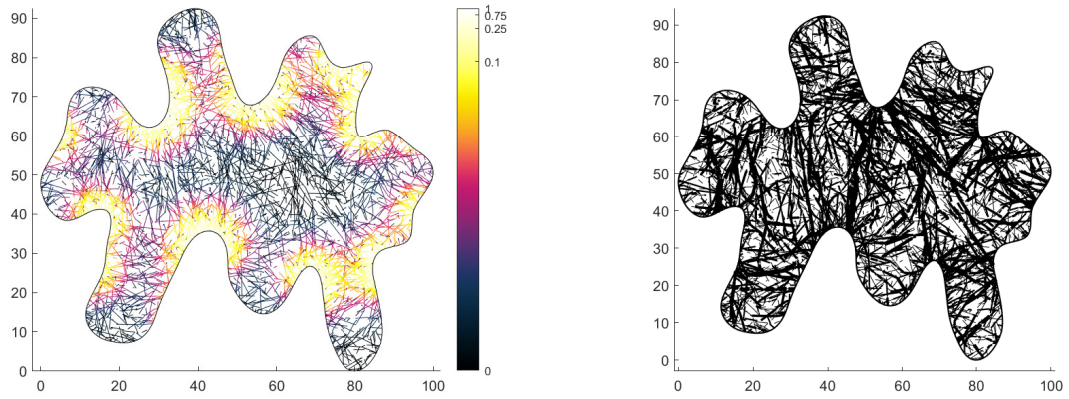
(a) RIC1 (b) Microtubule array

Figure A.7: The signalling network model results in the 1st mature pavement cell outline, where the figures show the RIC1 concentration and the microtubule array. Figure a has a non-linear scalebar in order to see concentration variations clearly.



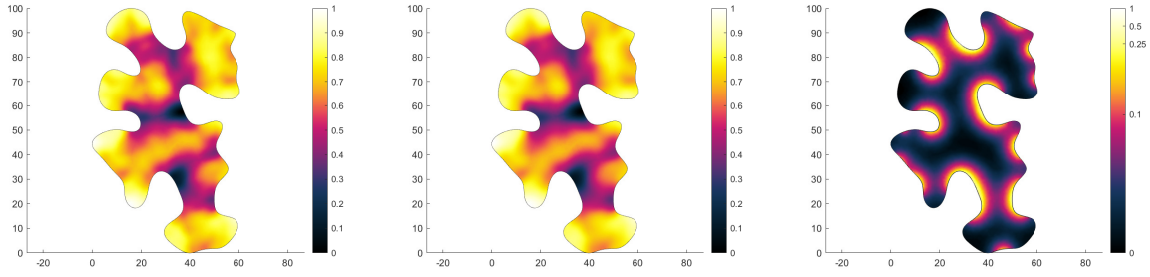
(a) ROP2 (b) RIC4 (c) ROP6

Figure A.8: The signalling network model results in the 2nd mature pavement cell outline, where the figures show the different proteins concentrations. Figures c has a non-linear scalebar in order to see concentration variations clearly.



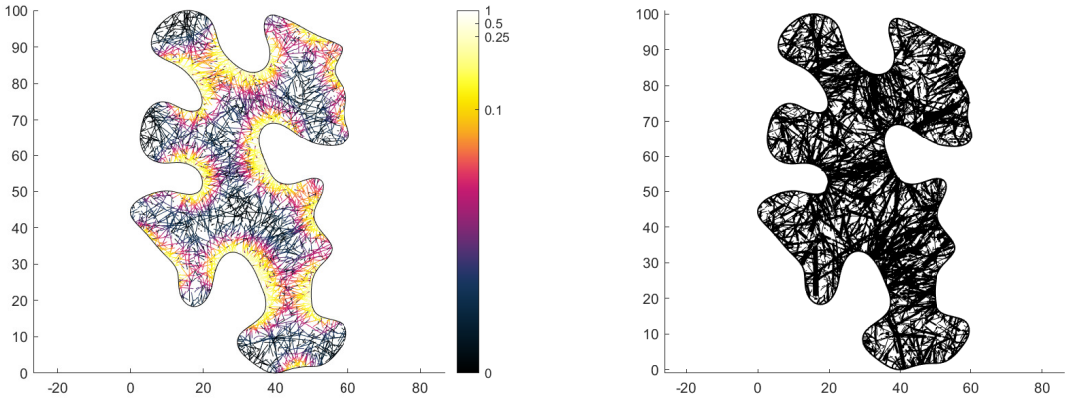
(a) RIC1 (b) Microtubule array

Figure A.9: The signalling network model results in the 2nd mature pavement cell outline, where the figures show the RIC1 concentration and the microtubule array. Figure a has a non-linear scalebar in order to see concentration variations clearly.



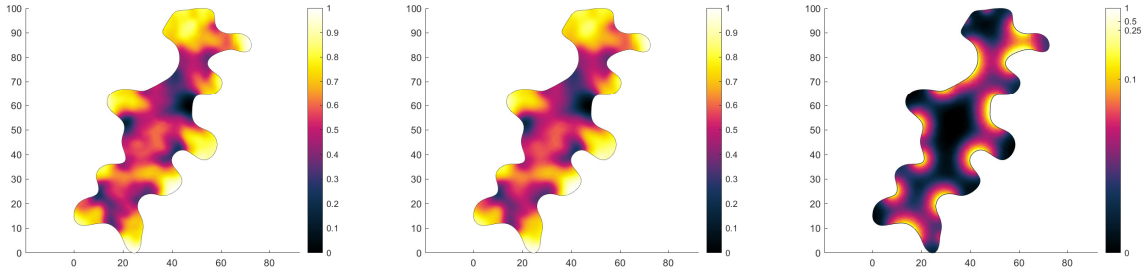
(a) ROP2 (b) RIC4 (c) ROP6

Figure A.10: The signalling network model results in the 3rd mature pavement cell outline, where the figures show the different proteins concentrations. Figures c has a non-linear scalebar in order to see concentration variations clearly.



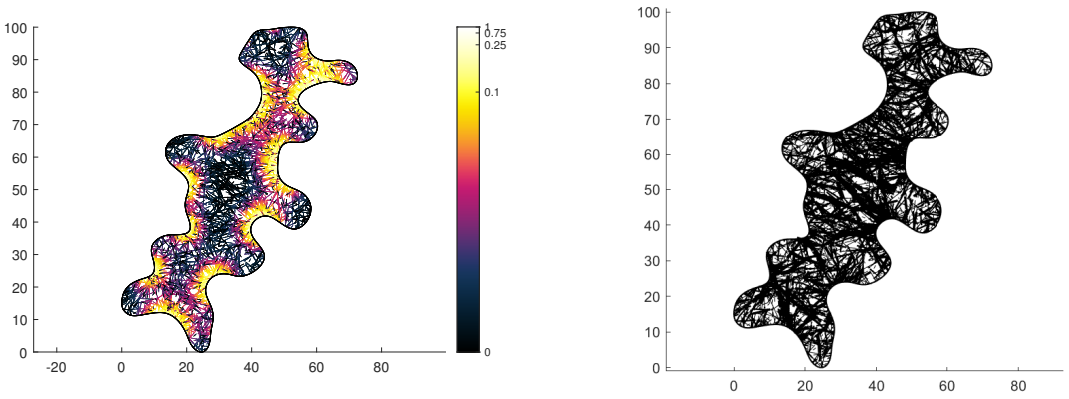
(a) RIC1 (b) Microtubule array

Figure A.11: The signalling network model results in the 3rd mature pavement cell outline, where the figures show the RIC1 concentration and the microtubule array. Figure a has a non-linear scalebar in order to see concentration variations clearly.



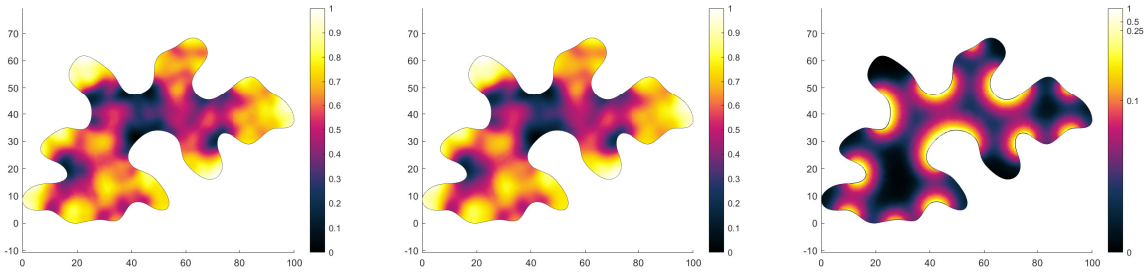
(a) ROP2 (b) RIC4 (c) ROP6

Figure A.12: The signalling network model results in the 4th mature pavement cell outline, where the figures show the different proteins concentrations. Figures c has a non-linear scalebar in order to see concentration variations clearly.



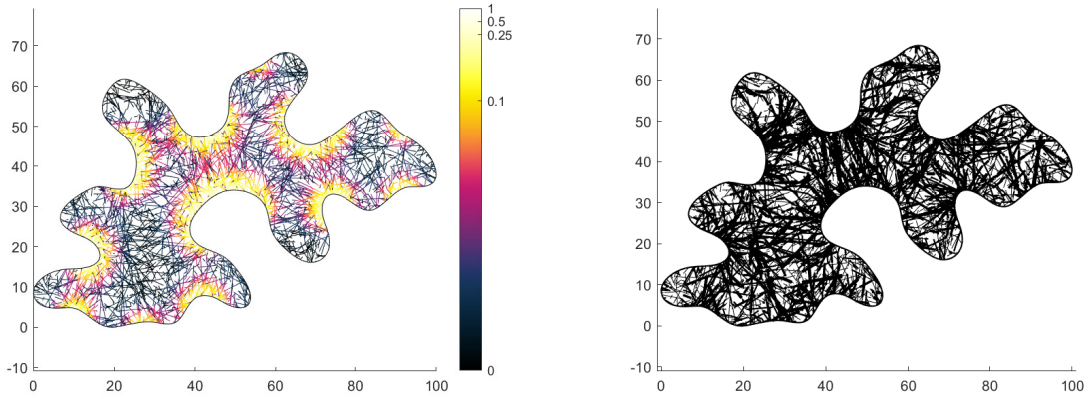
(a) RIC1 (b) Microtubule array

Figure A.13: The signalling network model results in the 4th mature pavement cell outline, where the figures show the RIC1 concentration and the microtubule array. Figure a has a non-linear scalebar in order to see concentration variations clearly.



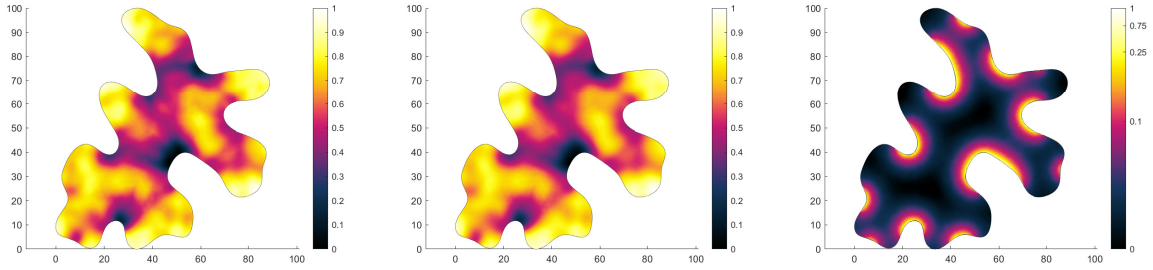
(a) ROP2 (b) RIC4 (c) ROP6

Figure A.14: The signalling network model results in the 5th mature pavement cell outline, where the figures show the different proteins concentrations. Figures c has a non-linear scalebar in order to see concentration variations clearly.



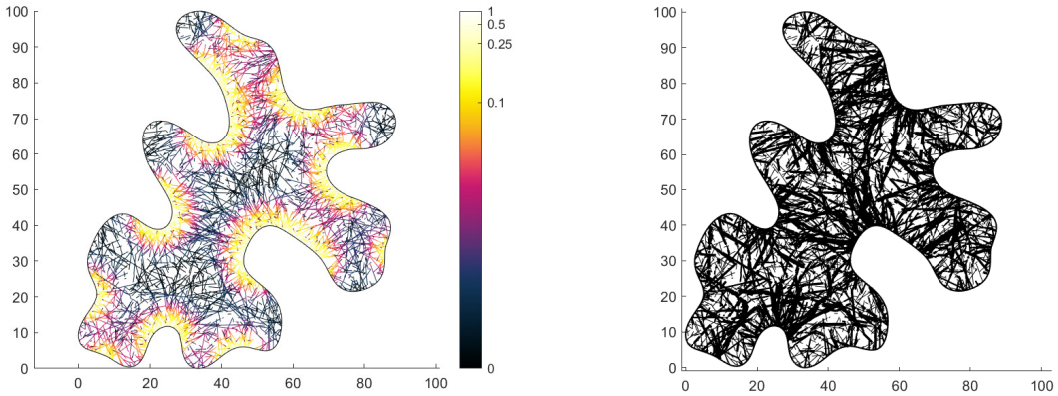
(a) RIC1 (b) Microtubule array

Figure A.15: The signalling network model results in the 5th mature pavement cell outline, where the figures show the RIC1 concentration and the microtubule array. Figure a has a non-linear scalebar in order to see concentration variations clearly.



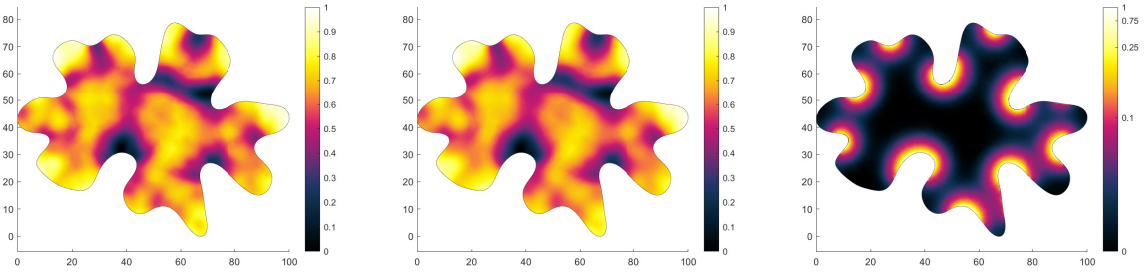
(a) ROP2 (b) RIC4 (c) ROP6

Figure A.16: The signalling network model results in the 7th mature pavement cell outline, where the figures show the different proteins concentrations. Figures c has a non-linear scalebar in order to see concentration variations clearly.



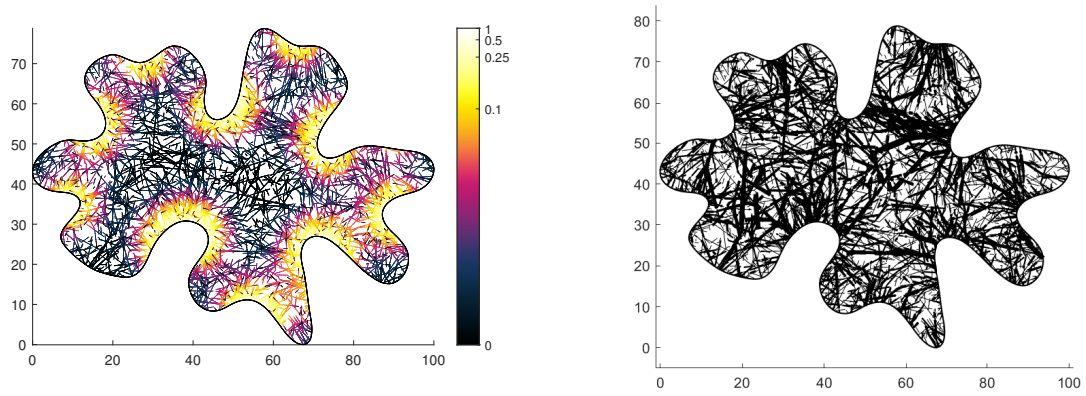
(a) RIC1 (b) Microtubule array

Figure A.17: The signalling network model results in the 7th mature pavement cell outline, where the figures show the RIC1 concentration and the microtubule array. Figure a has a non-linear scalebar in order to see concentration variations clearly.



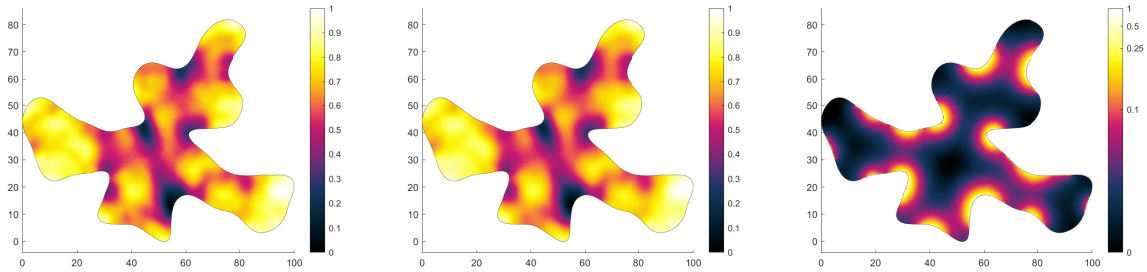
(a) ROP2 (b) RIC4 (c) ROP6

Figure A.18: The signalling network model results in the 8th mature pavement cell outline, where the figures show the different proteins concentrations. Figures c has a non-linear scalebar in order to see concentration variations clearly.



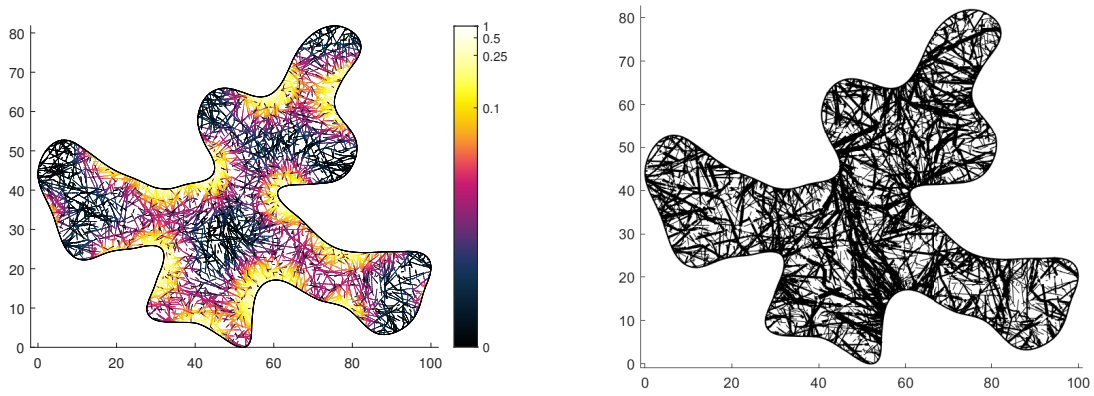
(a) RIC1 (b) Microtubule array

Figure A.19: The signalling network model results in the 8th mature pavement cell outline, where the figures show the RIC1 concentration and the microtubule array. Figure a has a non-linear scalebar in order to see concentration variations clearly.



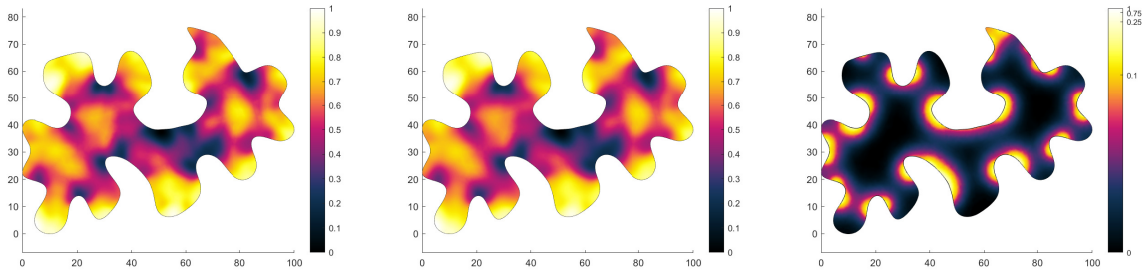
(a) ROP2 (b) RIC4 (c) ROP6

Figure A.20: The signalling network model results in the 9th mature pavement cell outline, where the figures show the different proteins concentrations. Figures c has a non-linear scalebar in order to see concentration variations clearly.



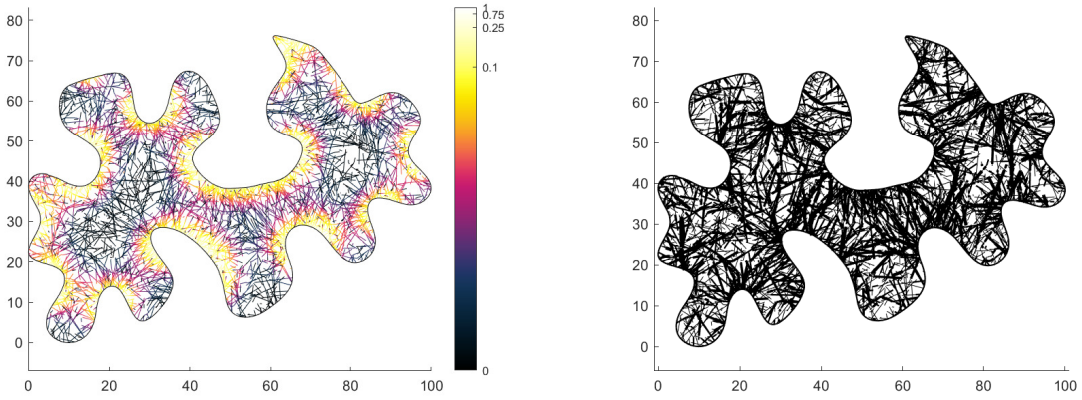
(a) RIC1 (b) Microtubule array

Figure A.21: The signalling network model results in the 9th mature pavement cell outline, where the figures show the RIC1 concentration and the microtubule array. Figure a has a non-linear scalebar in order to see concentration variations clearly.



(a) ROP2 (b) RIC4 (c) ROP6

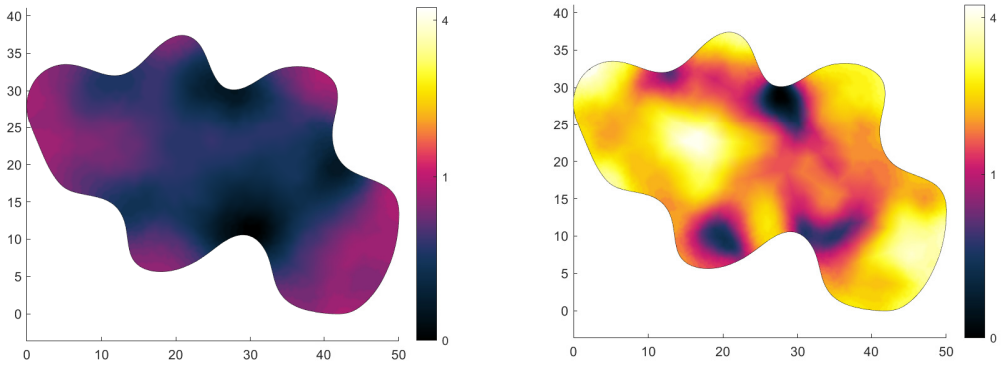
Figure A.22: The signalling network model results in the 10th mature pavement cell outline, where the figures show the different proteins concentrations. Figures c has a non-linear scalebar in order to see concentration variations clearly.



(a) RIC1

(b) Microtubule array

Figure A.23: The signalling network model results in the 10th mature pavement cell outline, where the figures show the RIC1 concentration and the microtubule array. Figure a has a non-linear scalebar in order to see concentration variations clearly.



(a) ROP2 Control

(b) ROP2 Mutant

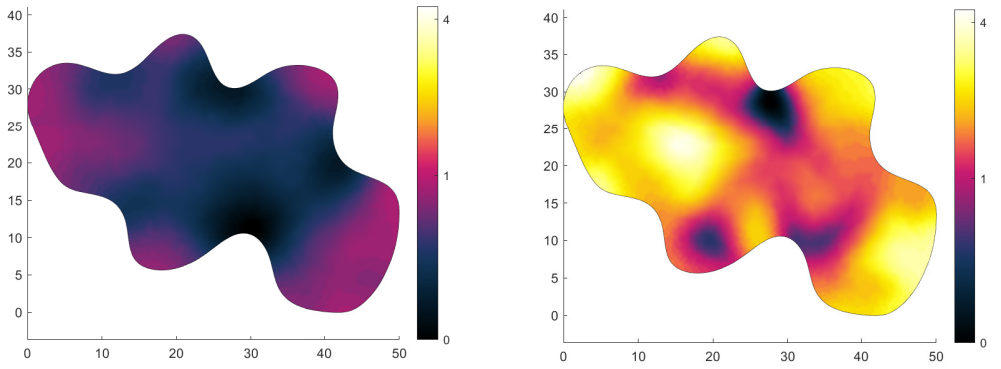
Figure A.24: The signalling network model results of the CA ROP2 simulations in the 1st less developed pavement cell outline, where the figures show the ROP2 concentrations in the control and the mutant with non-linear scalebar.

A.4.3 The signalling network in mutant pavement cells additional figures

In this section we display the supporting figure for the mutant simulations in section 6.5.2.

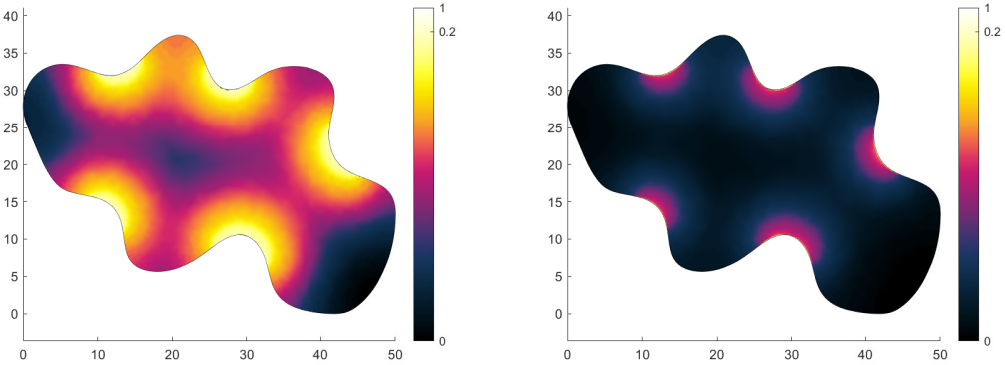
A.4.3.1 CA ROP2

Here we show the supporting figures for the constitutively active ROP2 simulations in section 6.5.2.1.



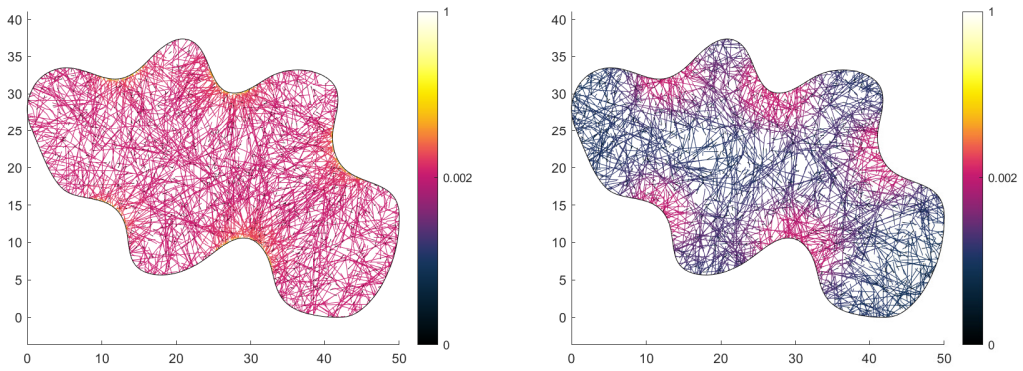
(a) RIC4 Control (b) RIC4 Mutant

Figure A.25: The signalling network model results of the CA ROP2 simulations in the 1st less developed pavement cell outline, where the figures show the RIC4 concentrations in the control and the mutant with non-linear scalebar.



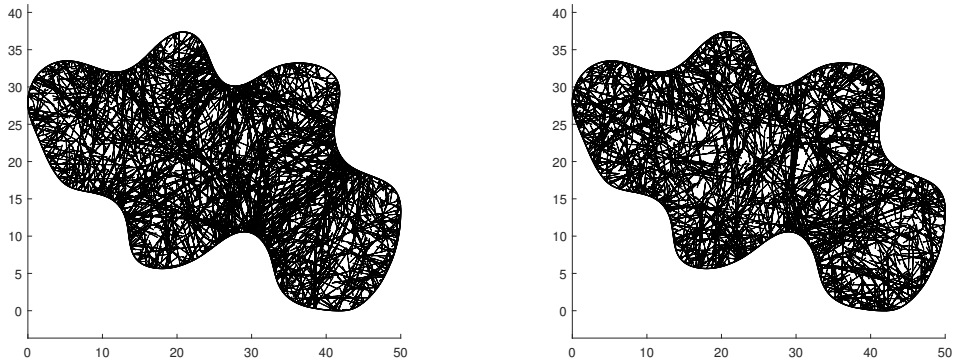
(a) ROP6 Control (b) ROP6 Mutant

Figure A.26: The signalling network model results of the CA ROP2 simulations in the 1st less developed pavement cell outline, where the figures show the ROP6 concentrations in the control and the mutant with non-linear scalebar.



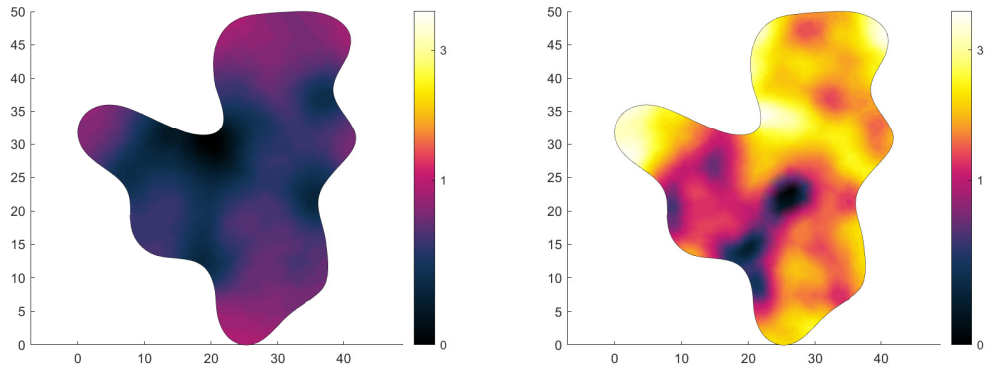
(a) RIC1 Control (b) RIC1 Mutant

Figure A.27: The signalling network model results of the CA ROP2 simulations in the 1st less developed pavement cell outline, where the figures show the RIC1 concentrations in the control and the mutant with non-linear scalebar.



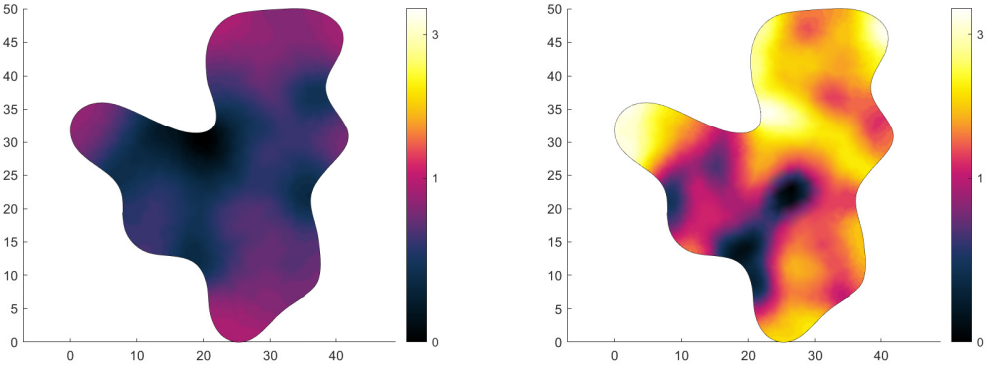
(a) Microtuble array control (b) Microtubule array mutant

Figure A.28: The signalling network model results of the CA ROP2 simulations in the 1st less developed pavement cell outline, where the figures show the microtubule array in the control and the mutant.



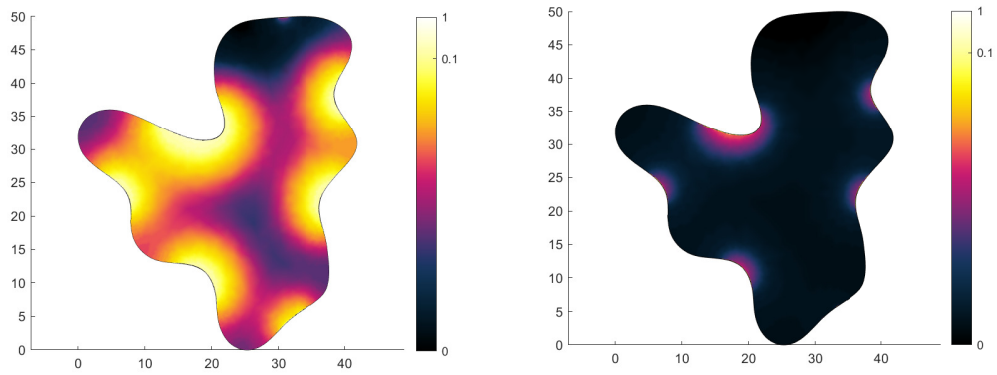
(a) ROP2 Control (b) ROP2 Mutant

Figure A.29: The signalling network model results of the CA ROP2 simulations in the 2nd less developed pavement cell outline, where the figures show the ROP2 concentrations in the control and the mutant with non-linear scalebar.



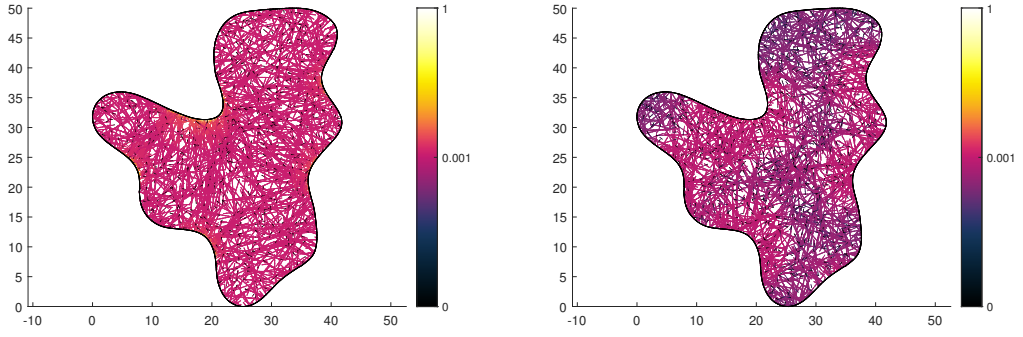
(a) RIC4 Control (b) RIC4 Mutant

Figure A.30: The signalling network model results of the CA ROP2 simulations in the 2nd less developed pavement cell outline, where the figures show the RIC4 concentrations in the control and the mutant with non-linear scalebar.



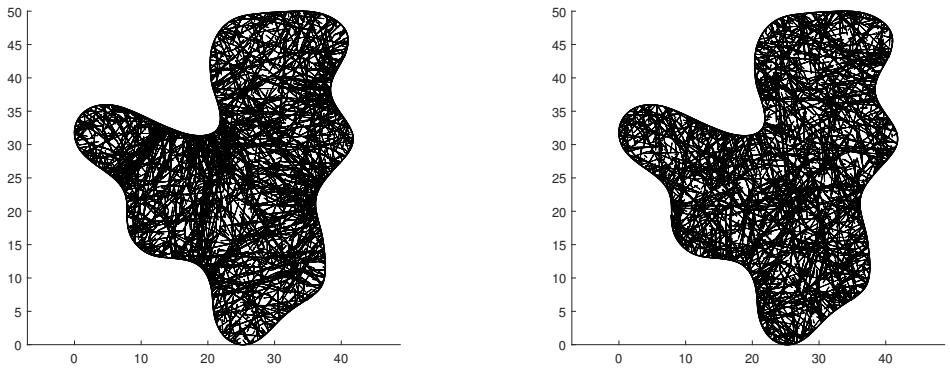
(a) ROP6 Control (b) ROP6 Mutant

Figure A.31: The signalling network model results of the CA ROP2 simulations in the 2nd less developed pavement cell outline, where the figures show the ROP6 concentrations in the control and the mutant with non-linear scalebar.



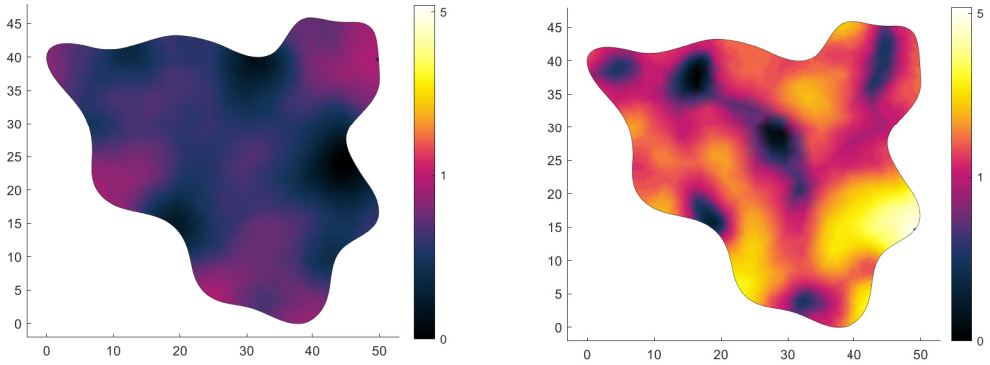
(a) RIC1 Control (b) RIC1 Mutant

Figure A.32: The signalling network model results of the CA ROP2 simulations in the 2nd less developed pavement cell outline, where the figures show the RIC1 concentrations in the control and the mutant with non-linear scalebar.



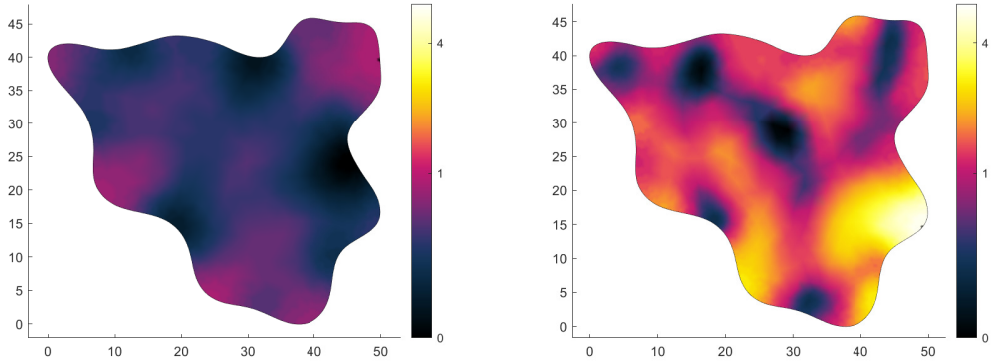
(a) Microtuble array control (b) Microtubule array mutant

Figure A.33: The signalling network model results of the CA ROP2 simulations in the 2nd less developed pavement cell outline, where the figures show the microtubule array in the control and the mutant.



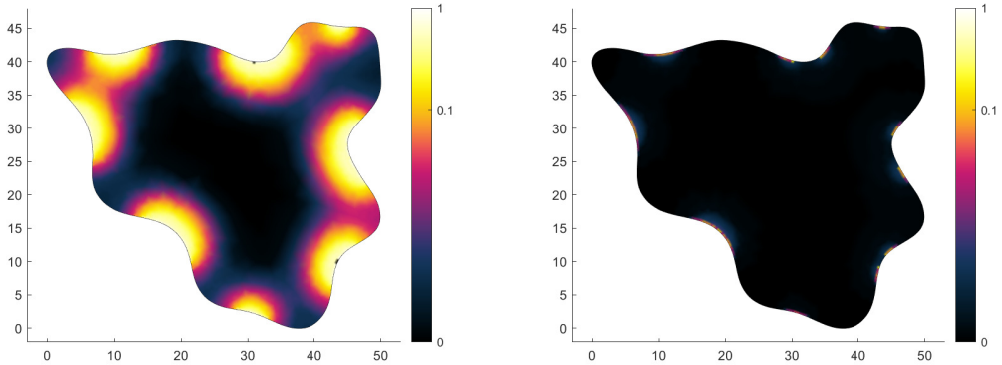
(a) ROP2 Control (b) ROP2 Mutant

Figure A.34: The signalling network model results of the CA ROP2 simulations in the 3rd less developed pavement cell outline, where the figures show the ROP2 concentrations in the control and the mutant with non-linear scalebar.



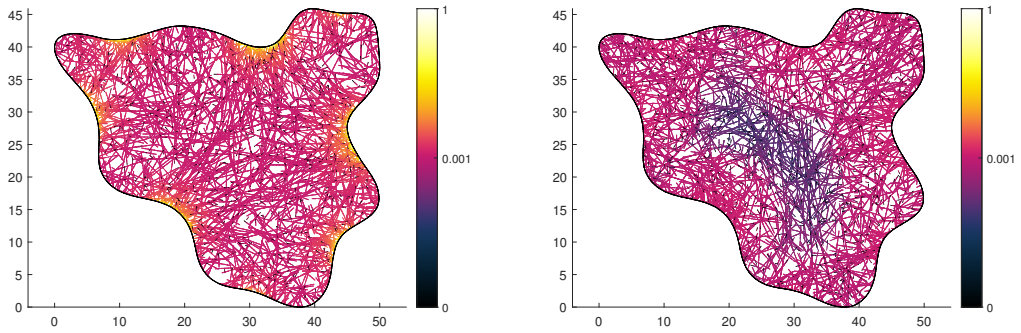
(a) RIC4 Control (b) RIC4 Mutant

Figure A.35: The signalling network model results of the CA ROP2 simulations in the 3rd less developed pavement cell outline, where the figures show the RIC4 concentrations in the control and the mutant with non-linear scalebar.



(a) ROP6 Control (b) ROP6 Mutant

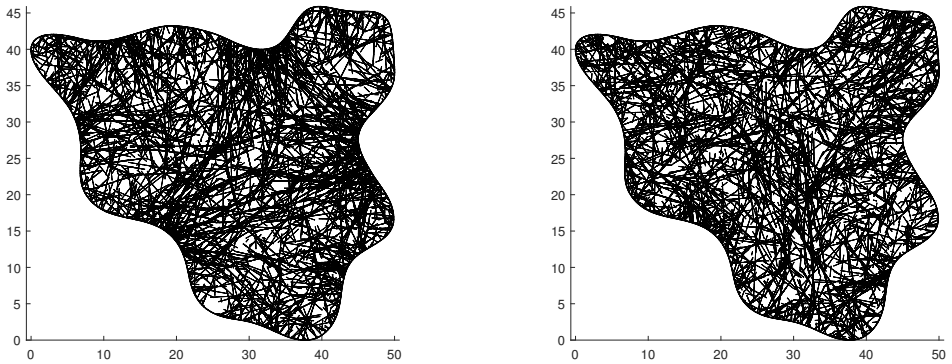
Figure A.36: The signalling network model results of the CA ROP2 simulations in the 3rd less developed pavement cell outline, where the figures show the ROP6 concentrations in the control and the mutant with non-linear scalebar.



(a) RIC1 Control

(b) RIC1 Mutant

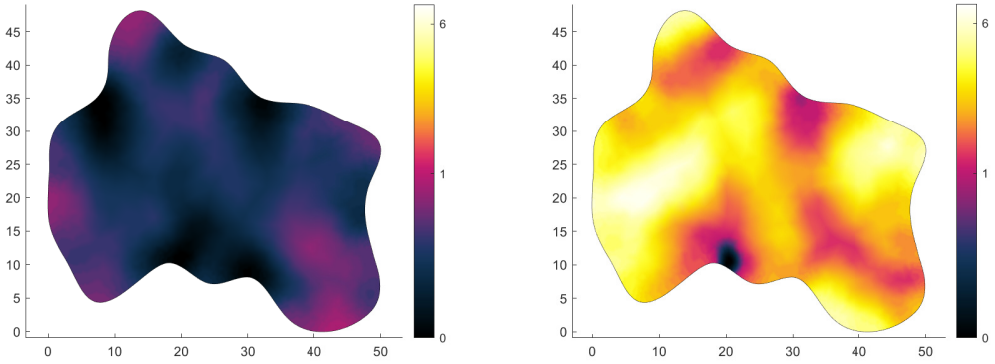
Figure A.37: The signalling network model results of the CA ROP2 simulations in the 3rd less developed pavement cell outline, where the figures show the RIC1 concentrations in the control and the mutant with non-linear scalebar.



(a) Microtuble array control

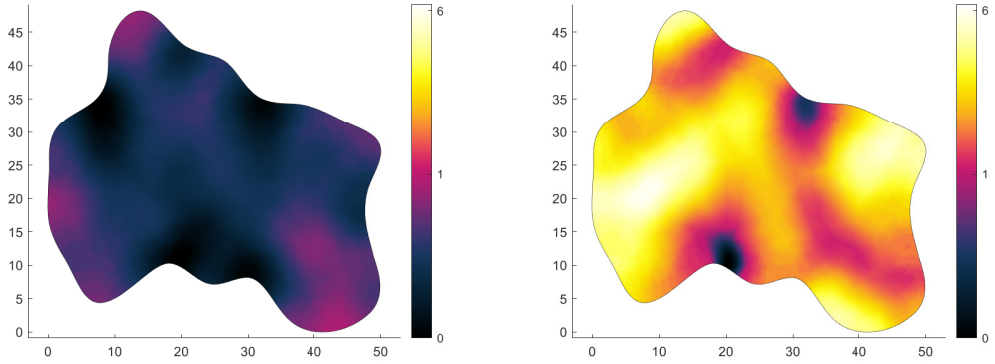
(b) Microtubule array mutant

Figure A.38: The signalling network model results of the CA ROP2 simulations in the 3rd less developed pavement cell outline, where the figures show the microtubule array in the control and the mutant.



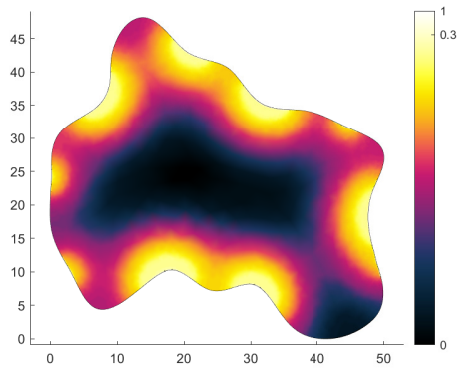
(a) ROP2 Control (b) ROP2 Mutant

Figure A.39: The signalling network model results of the CA ROP2 simulations in the 4th less developed pavement cell outline, where the figures show the ROP2 concentrations in the control and the mutant with non-linear scalebar.

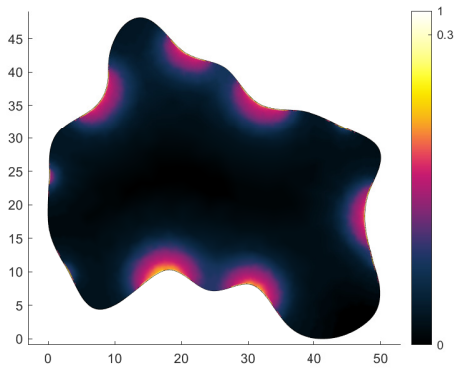


(a) RIC4 Control (b) RIC4 Mutant

Figure A.40: The signalling network model results of the CA ROP2 simulations in the 4th less developed pavement cell outline, where the figures show the RIC4 concentrations in the control and the mutant with non-linear scalebar.

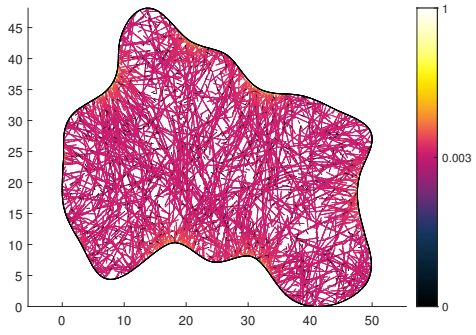


(a) ROP6 Control

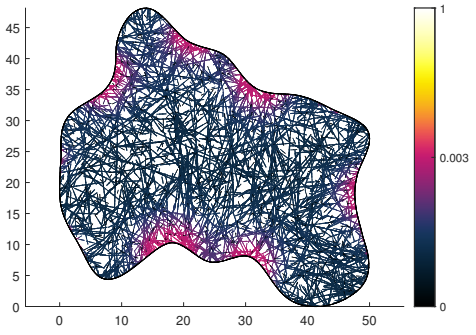


(b) ROP6 Mutant

Figure A.41: The signalling network model results of the CA ROP2 simulations in the 4th less developed pavement cell outline, where the figures show the ROP6 concentrations in the control and the mutant with non-linear scalebar.

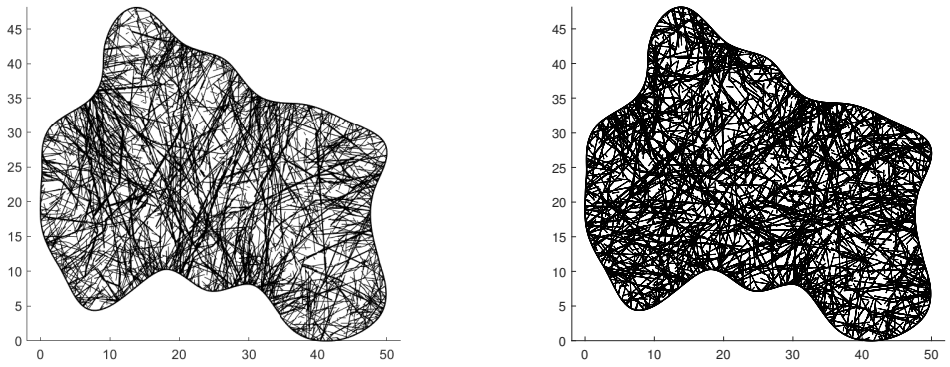


(a) RIC1 Control



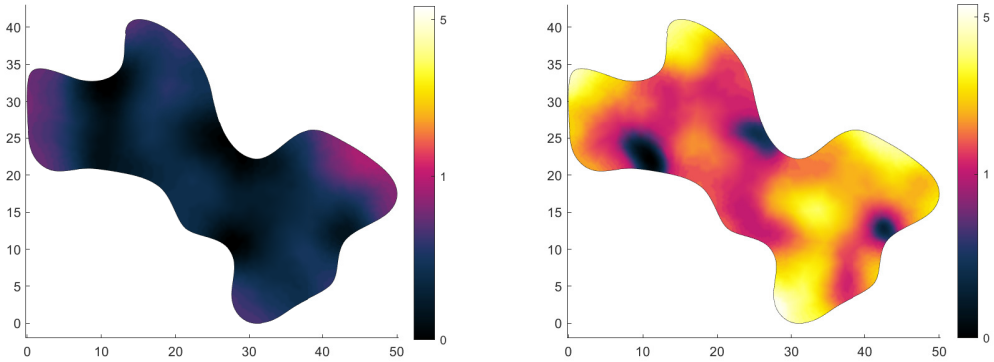
(b) RIC1 Mutant

Figure A.42: The signalling network model results of the CA ROP2 simulations in the 4th less developed pavement cell outline, where the figures show the RIC1 concentrations in the control and the mutant with non-linear scalebar.



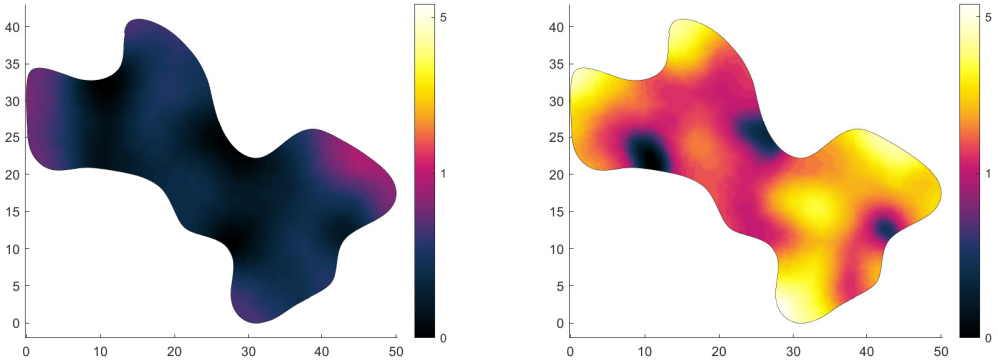
(a) Microtuble array control (b) Microtubule array mutant

Figure A.43: The signalling network model results of the CA ROP2 simulations in the 4th less developed pavement cell outline, where the figures show the microtubule array in the control and the mutant.



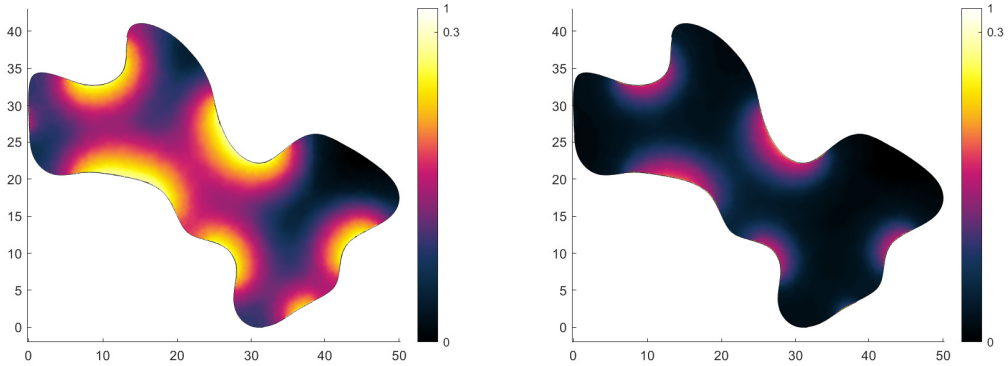
(a) ROP2 Control (b) ROP2 Mutant

Figure A.44: The signalling network model results of the CA ROP2 simulations in the 5th less developed pavement cell outline, where the figures show the ROP2 concentrations in the control and the mutant with non-linear scalebar.



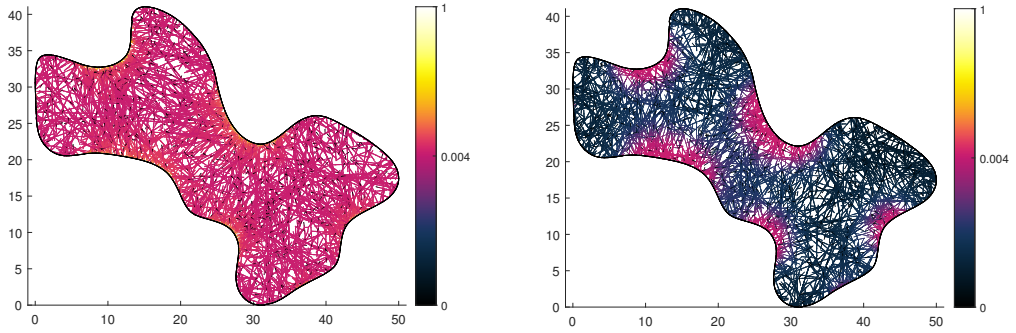
(a) RIC4 Control (b) RIC4 Mutant

Figure A.45: The signalling network model results of the CA ROP2 simulations in the 5th less developed pavement cell outline, where the figures show the RIC4 concentrations in the control and the mutant with non-linear scalebar.



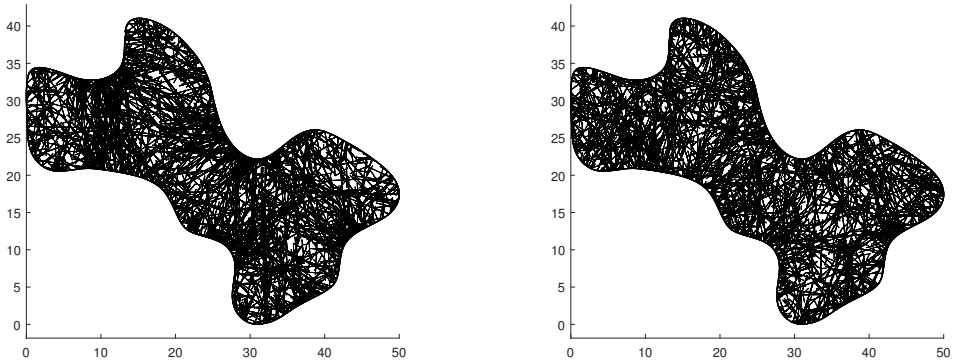
(a) ROP6 Control (b) ROP6 Mutant

Figure A.46: The signalling network model results of the CA ROP2 simulations in the 5th less developed pavement cell outline, where the figures show the ROP6 concentrations in the control and the mutant with non-linear scalebar.



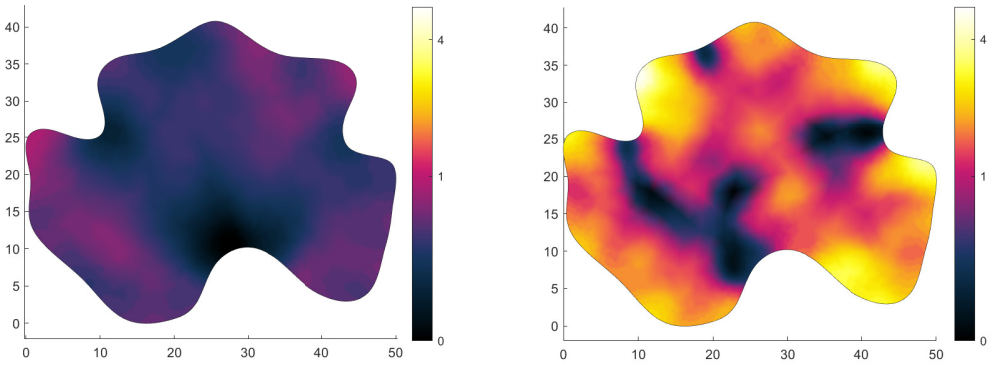
(a) RIC1 Control (b) RIC1 Mutant

Figure A.47: The signalling network model results of the CA ROP2 simulations in the 5th less developed pavement cell outline, where the figures show the RIC1 concentrations in the control and the mutant with non-linear scalebar.



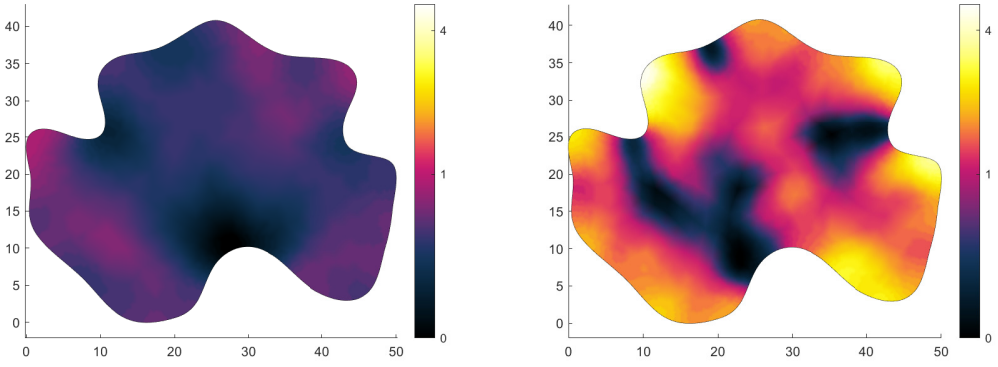
(a) Microtuble array control (b) Microtubule array mutant

Figure A.48: The signalling network model results of the CA ROP2 simulations in the 5th less developed pavement cell outline, where the figures show the microtubule array in the control and the mutant.



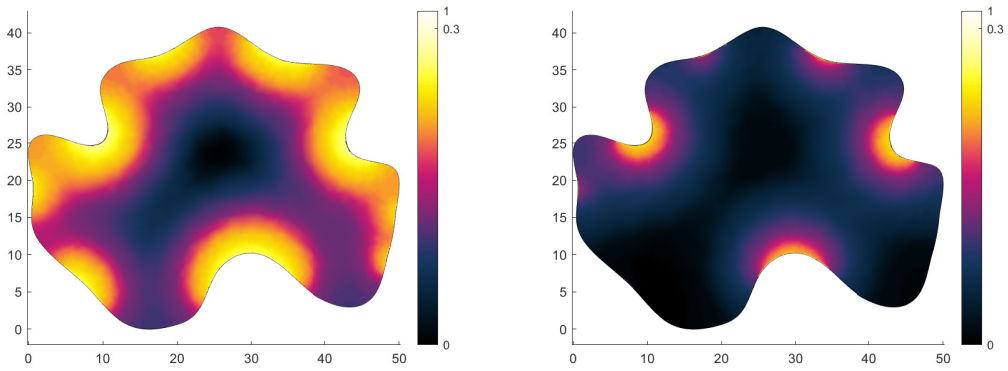
(a) ROP2 Control (b) ROP2 Mutant

Figure A.49: The signalling network model results of the CA ROP2 simulations in the 6th less developed pavement cell outline, where the figures show the ROP2 concentrations in the control and the mutant with non-linear scalebar.



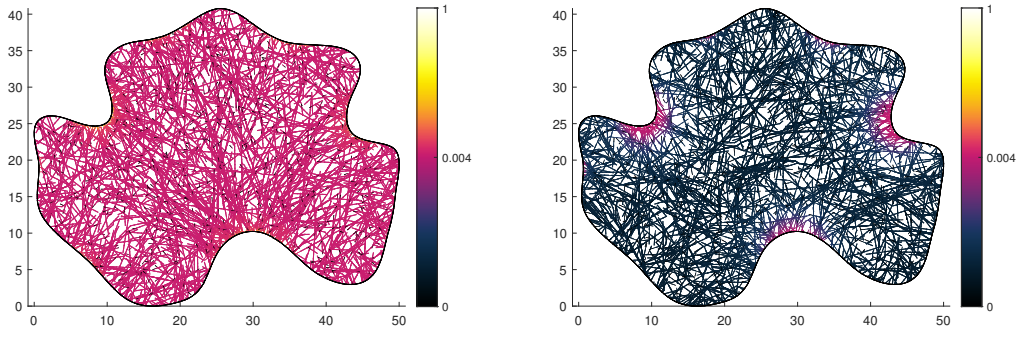
(a) RIC4 Control (b) RIC4 Mutant

Figure A.50: The signalling network model results of the CA ROP2 simulations in the 6th less developed pavement cell outline, where the figures show the RIC4 concentrations in the control and the mutant with non-linear scalebar.



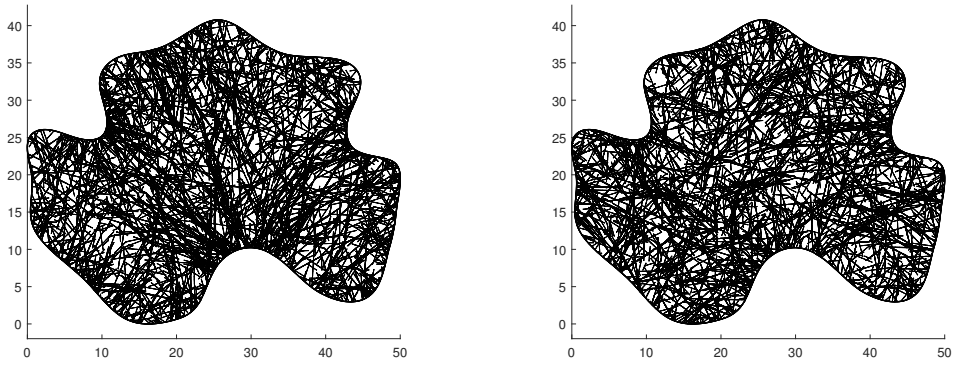
(a) ROP6 Control (b) ROP6 Mutant

Figure A.51: The signalling network model results of the CA ROP2 simulations in the 6th less developed pavement cell outline, where the figures show the ROP6 concentrations in the control and the mutant with non-linear scalebar.



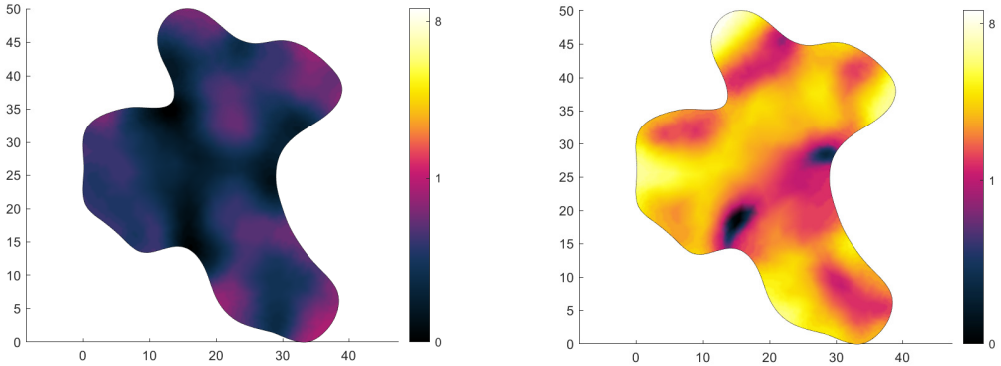
(a) RIC1 Control (b) RIC1 Mutant

Figure A.52: The signalling network model results of the CA ROP2 simulations in the 6th less developed pavement cell outline, where the figures show the RIC1 concentrations in the control and the mutant with non-linear scalebar.



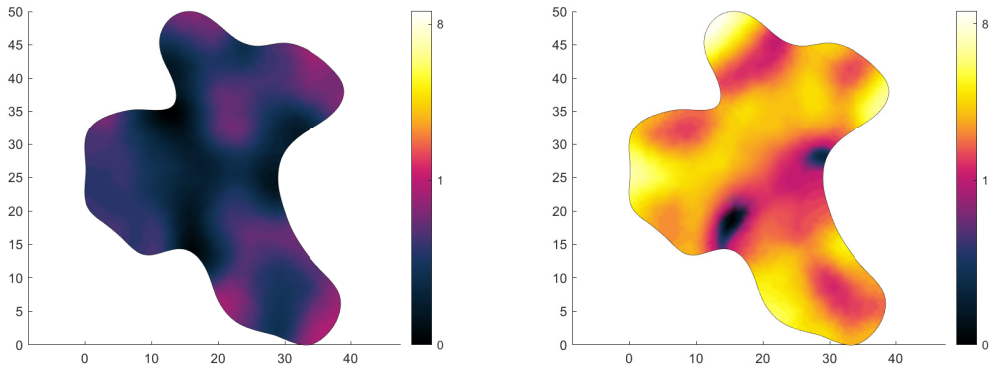
(a) Microtuble array control (b) Microtubule array mutant

Figure A.53: The signalling network model results of the CA ROP2 simulations in the 6th less developed pavement cell outline, where the figures show the microtubule array in the control and the mutant.



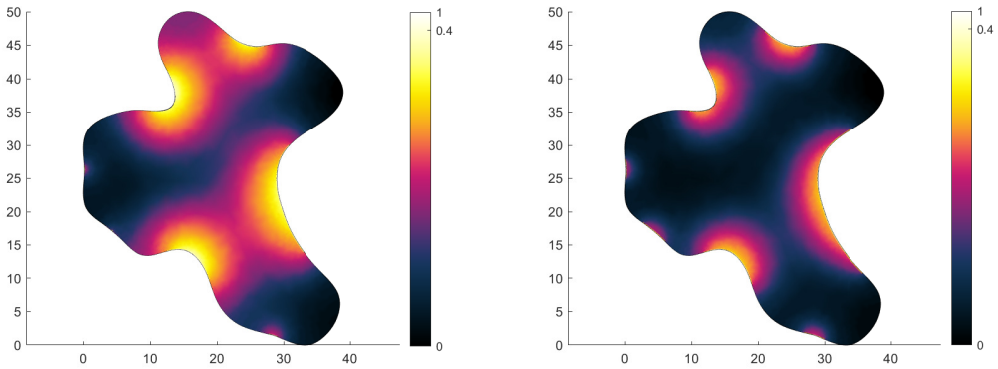
(a) ROP2 Control (b) ROP2 Mutant

Figure A.54: The signalling network model results of the CA ROP2 simulations in the 8th less developed pavement cell outline, where the figures show the ROP2 concentrations in the control and the mutant with non-linear scalebar.



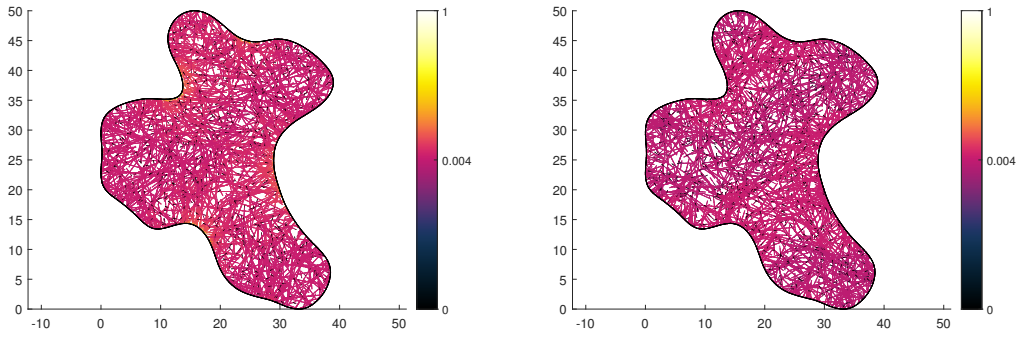
(a) RIC4 Control (b) RIC4 Mutant

Figure A.55: The signalling network model results of the CA ROP2 simulations in the 8th less developed pavement cell outline, where the figures show the RIC4 concentrations in the control and the mutant with non-linear scalebar.



(a) ROP6 Control (b) ROP6 Mutant

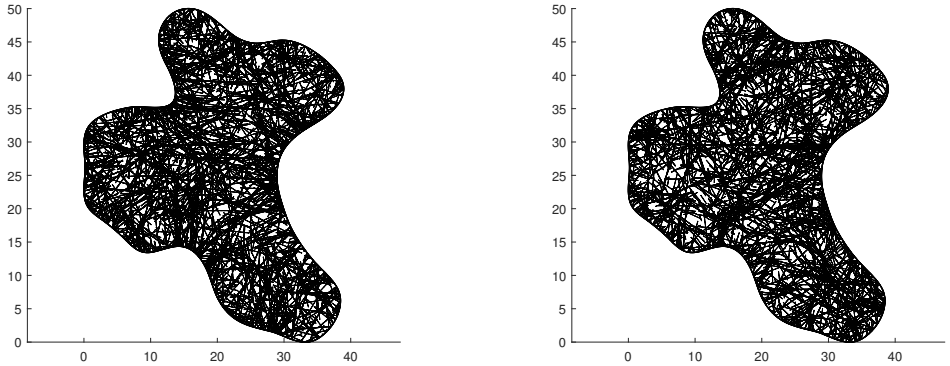
Figure A.56: The signalling network model results of the CA ROP2 simulations in the 8th less developed pavement cell outline, where the figures show the ROP6 concentrations in the control and the mutant with non-linear scalebar.



(a) RIC1 Control

(b) RIC1 Mutant

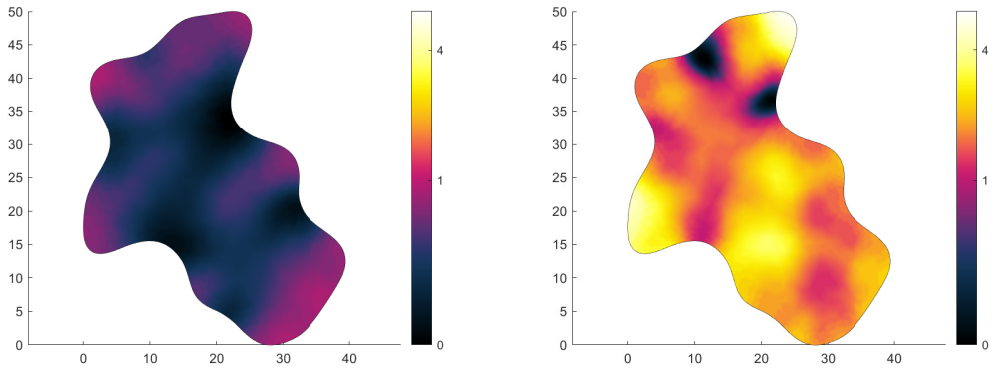
Figure A.57: The signalling network model results of the CA ROP2 simulations in the 8th less developed pavement cell outline, where the figures show the RIC1 concentrations in the control and the mutant with non-linear scalebar.



(a) Microtuble array control

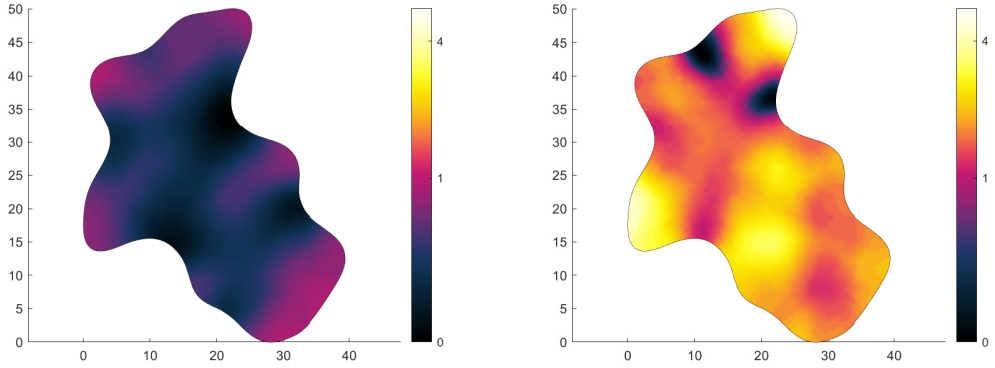
(b) Microtubule array mutant

Figure A.58: The signalling network model results of the CA ROP2 simulations in the 8th less developed pavement cell outline, where the figures show the microtubule array in the control and the mutant.



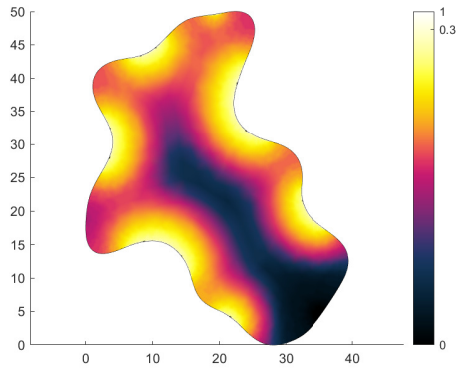
(a) ROP2 Control (b) ROP2 Mutant

Figure A.59: The signalling network model results of the CA ROP2 simulations in the 9th less developed pavement cell outline, where the figures show the ROP2 concentrations in the control and the mutant with non-linear scalebar.

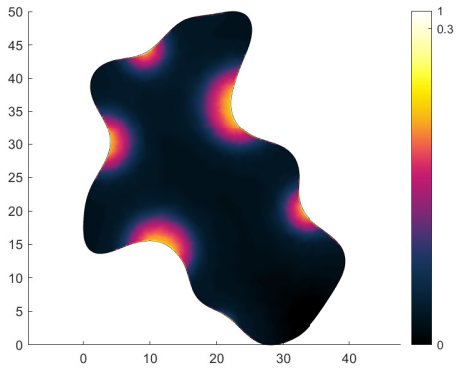


(a) RIC4 Control (b) RIC4 Mutant

Figure A.60: The signalling network model results of the CA ROP2 simulations in the 9th less developed pavement cell outline, where the figures show the RIC4 concentrations in the control and the mutant with non-linear scalebar.

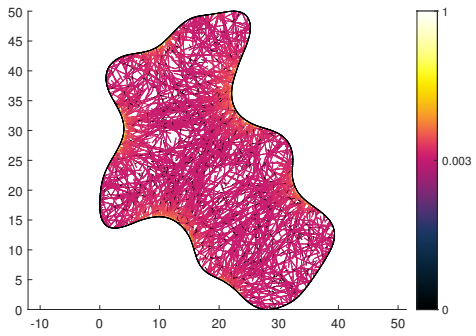


(a) ROP6 Control

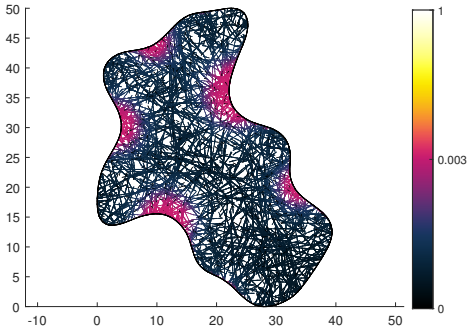


(b) ROP6 Mutant

Figure A.61: The signalling network model results of the CA ROP2 simulations in the 9th less developed pavement cell outline, where the figures show the ROP6 concentrations in the control and the mutant with non-linear scalebar.

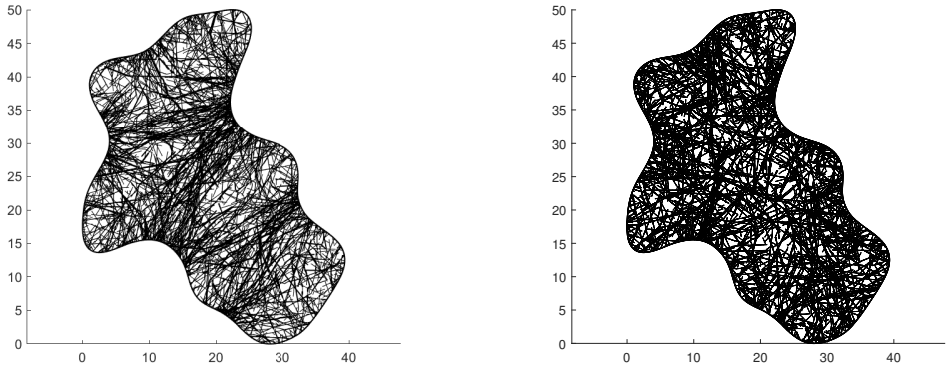


(a) RIC1 Control



(b) RIC1 Mutant

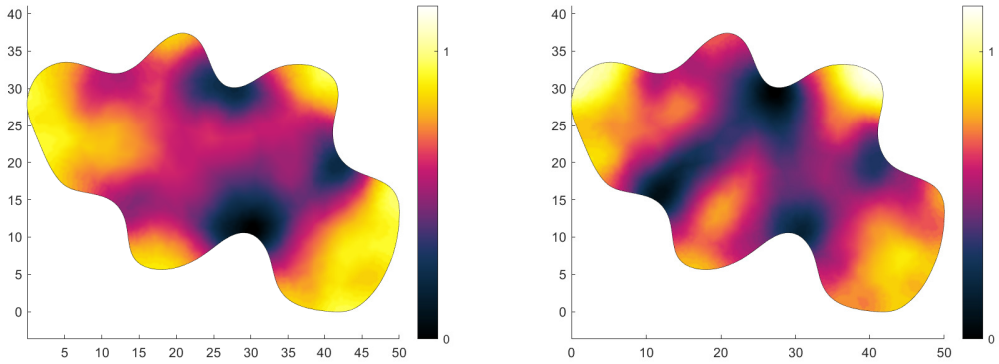
Figure A.62: The signalling network model results of the CA ROP2 simulations in the 9th less developed pavement cell outline, where the figures show the RIC1 concentrations in the control and the mutant with non-linear scalebar.



(a) Microtuble array control

(b) Microtubule array mutant

Figure A.63: The signalling network model results of the CA ROP2 simulations in the 9th less developed pavement cell outline, where the figures show the microtubule array in the control and the mutant.



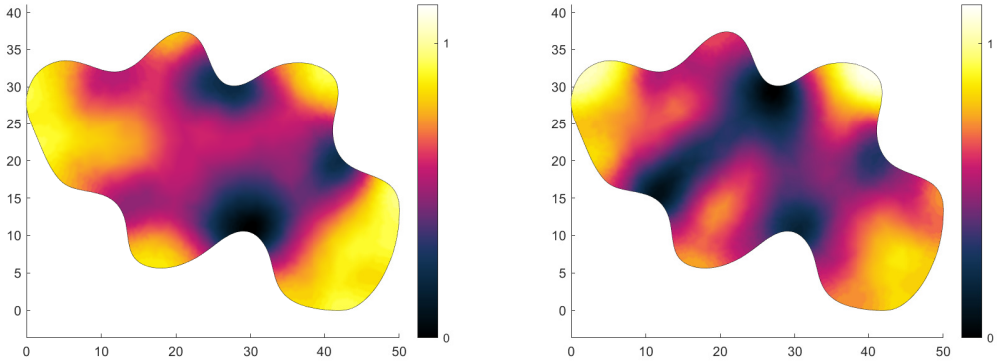
(a) ROP2 Control

(b) ROP2 Mutant

Figure A.64: The signalling network model results of the CA ROP6 simulations in the 1st less developed pavement cell outline, where the figures show the ROP2 concentrations in the control and the mutant.

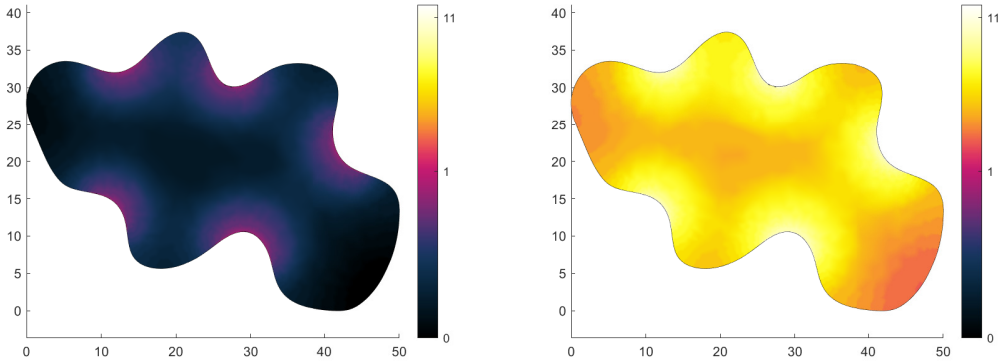
A.4.3.2 CA ROP6

Here we show the supporting figures for the constitutively active ROP6 simulations in section 6.5.2.2.



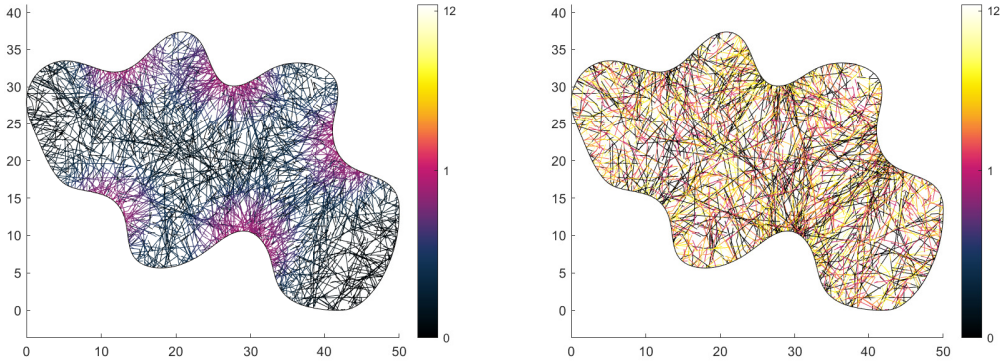
(a) RIC4 Control (b) RIC4 Mutant

Figure A.65: The signalling network model results of the CA ROP6 simulations in the 1st less developed pavement cell outline, where the figures show the RIC4 concentrations in the control and the mutant.



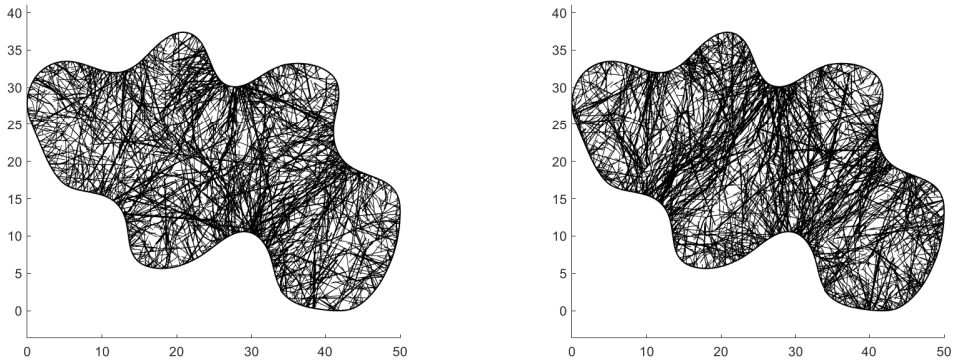
(a) ROP6 Control (b) ROP6 Mutant

Figure A.66: The signalling network model results of the CA ROP6 simulations in the 1st less developed pavement cell outline, where the figures show the ROP6 concentrations in the control and the mutant with non-linear scalebars.



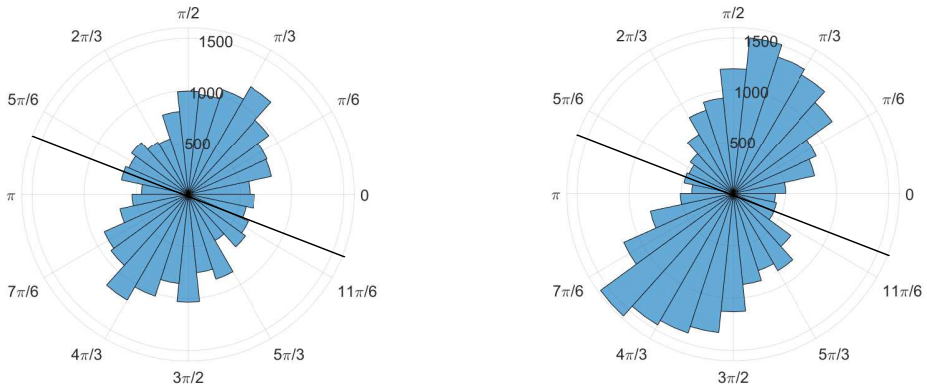
(a) RIC1 Control (b) RIC1 Mutant

Figure A.67: The signalling network model results of the CA ROP6 simulations in the 1st less developed pavement cell outline, where the figures show the RIC1 concentrations in the control and the mutant with non-linear scalebars.



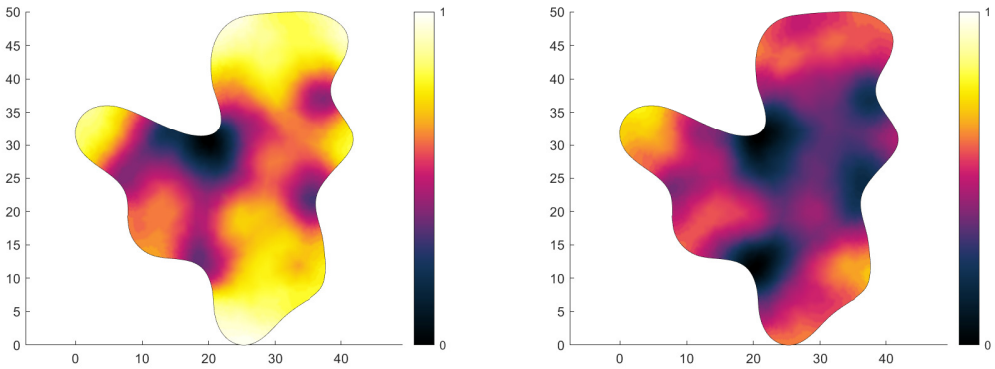
(a) Microtuble array control (b) Microtubule array mutant

Figure A.68: The signalling network model results of the CA ROP6 simulations in the 1st less developed pavement cell outline, where the figures show the microtubule array in the control and the mutant.



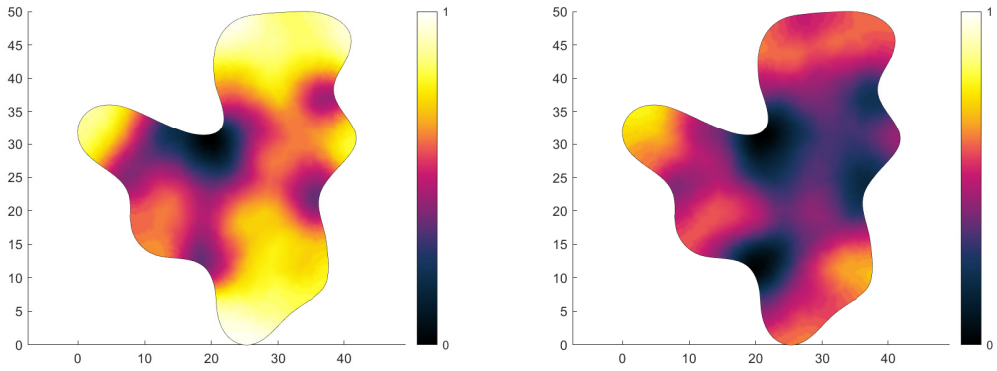
(a) Microtuble array distribution control (b) Microtubule array distribution control

Figure A.69: The signalling network model results of the CA ROP6 simulations in the 1st less developed pavement cell outline, where the figures show the microtubule array's angle distribution in the control and the mutant.



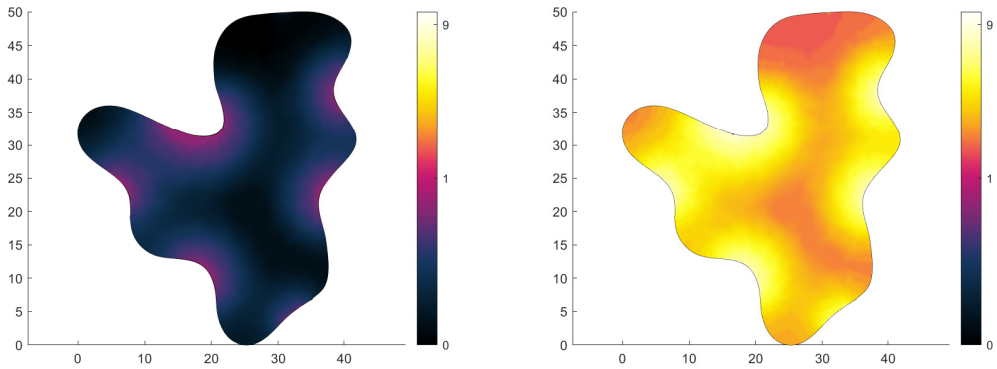
(a) ROP2 Control (b) ROP2 Mutant

Figure A.70: The signalling network model results of the CA ROP6 simulations in the 2nd less developed pavement cell outline, where the figures show the ROP2 concentrations in the control and the mutant.



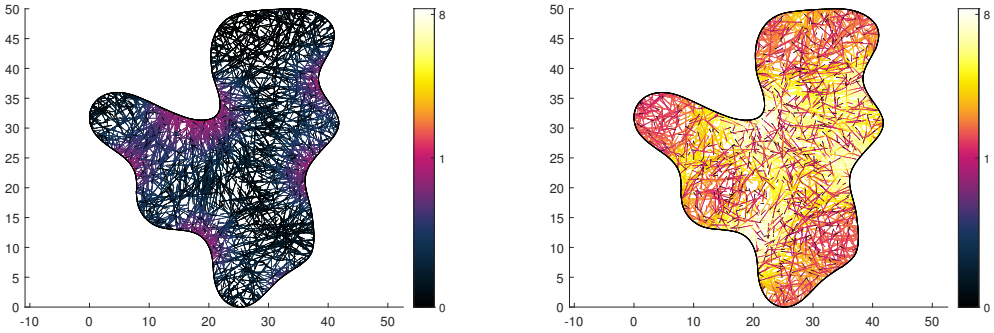
(a) RIC4 Control (b) RIC4 Mutant

Figure A.71: The signalling network model results of the CA ROP6 simulations in the 2nd less developed pavement cell outline, where the figures show the RIC4 concentrations in the control and the mutant.



(a) ROP6 Control (b) ROP6 Mutant

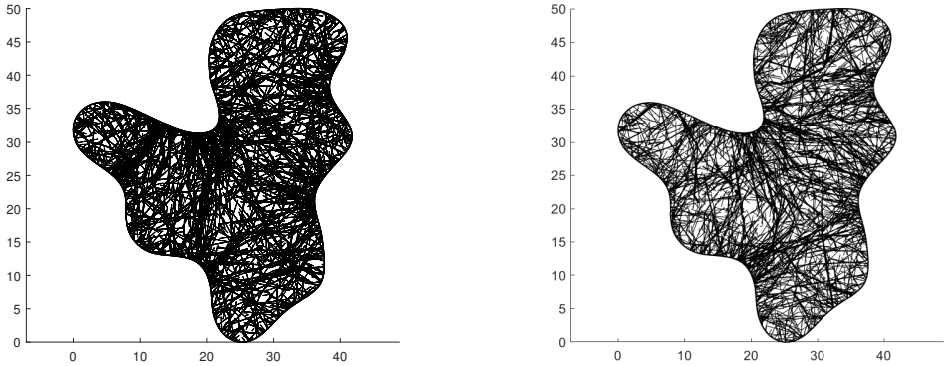
Figure A.72: The signalling network model results of the CA ROP6 simulations in the 2nd less developed pavement cell outline, where the figures show the ROP6 concentrations in the control and the mutant with non-linear scalebars.



(a) RIC1 Control

(b) RIC1 Mutant

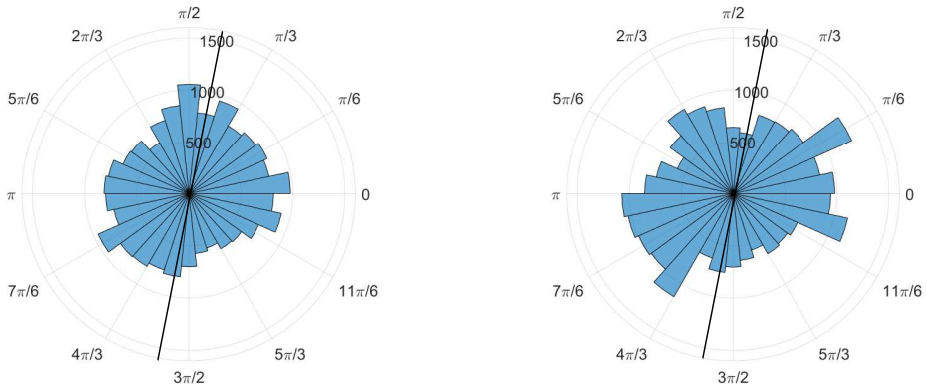
Figure A.73: The signalling network model results of the CA ROP6 simulations in the 2nd less developed pavement cell outline, where the figures show the RIC1 concentrations in the control and the mutant with non-linear scalebars.



(a) Microtuble array control

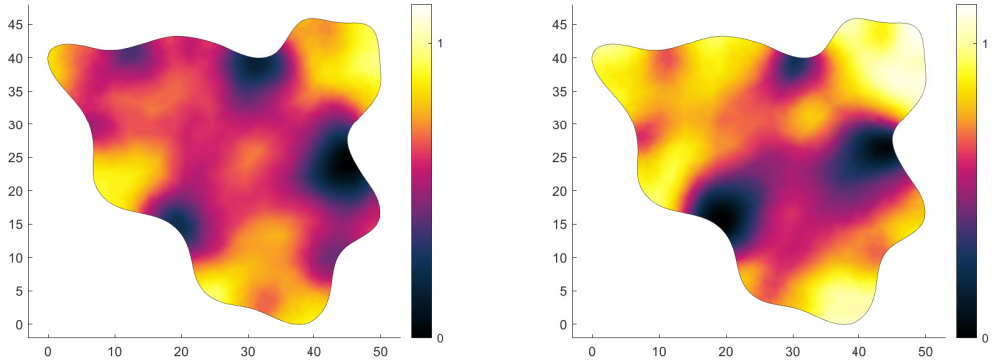
(b) Microtubule array mutant

Figure A.74: The signalling network model results of the CA ROP6 simulations in the 2nd less developed pavement cell outline, where the figures show the microtubule array in the control and the mutant.



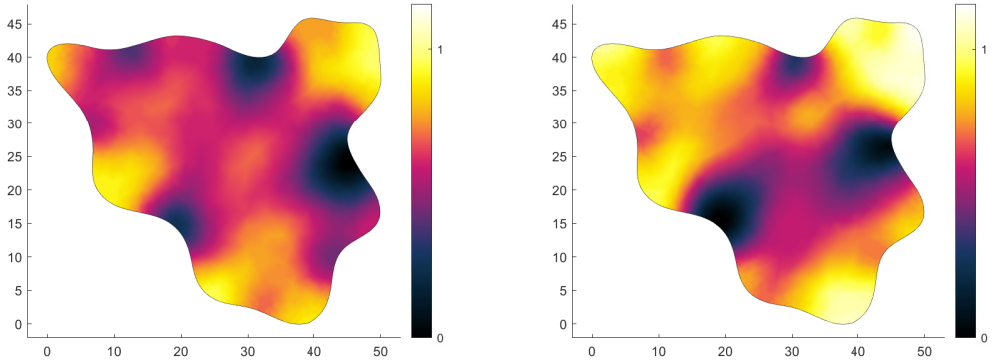
(a) Microtuble array distribution control (b) Microtubule array distribution control

Figure A.75: The signalling network model results of the CA ROP6 simulations in the 2nd less developed pavement cell outline, where the figures show the microtubule array's angle distribution in the control and the mutant.



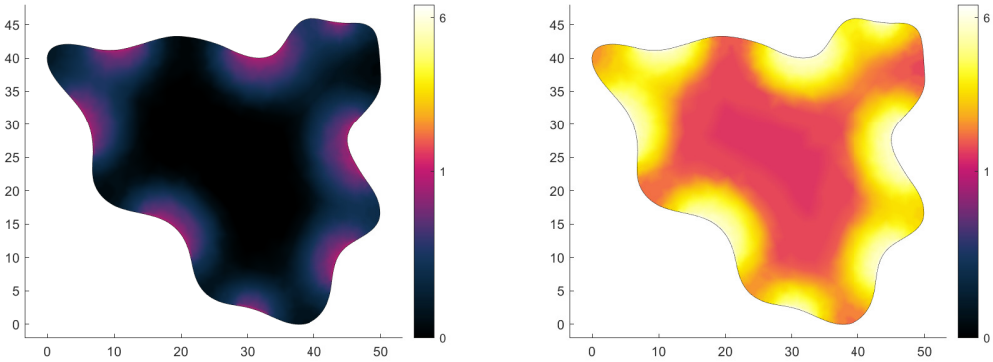
(a) ROP2 Control (b) ROP2 Mutant

Figure A.76: The signalling network model results of the CA ROP6 simulations in the 3rd less developed pavement cell outline, where the figures show the ROP2 concentrations in the control and the mutant.



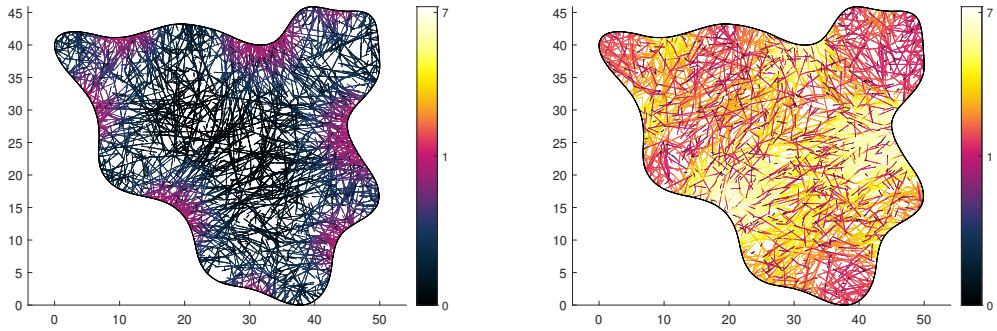
(a) RIC4 Control (b) RIC4 Mutant

Figure A.77: The signalling network model results of the CA ROP6 simulations in the 3rd less developed pavement cell outline, where the figures show the RIC4 concentrations in the control and the mutant.



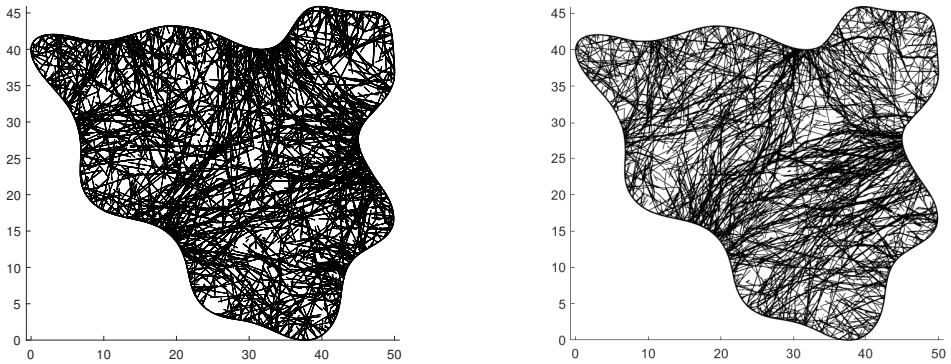
(a) ROP6 Control (b) ROP6 Mutant

Figure A.78: The signalling network model results of the CA ROP6 simulations in the 3rd less developed pavement cell outline, where the figures show the ROP6 concentrations in the control and the mutant with non-linear scalebars.



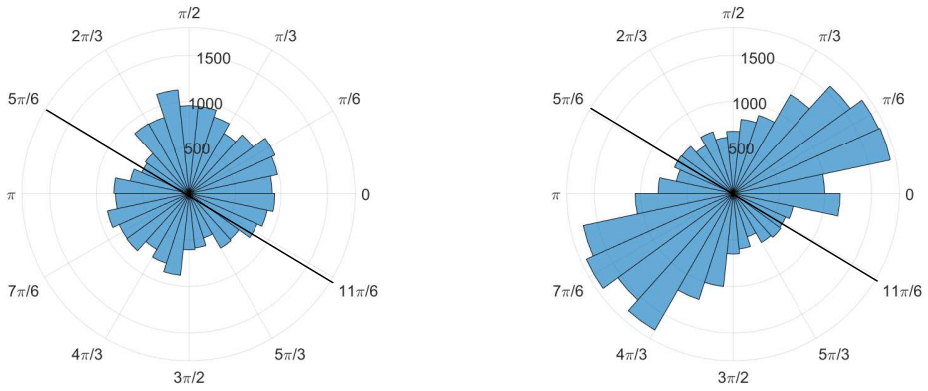
(a) RIC1 Control (b) RIC1 Mutant

Figure A.79: The signalling network model results of the CA ROP6 simulations in the 3rd less developed pavement cell outline, where the figures show the RIC1 concentrations in the control and the mutant with non-linear scalebars.



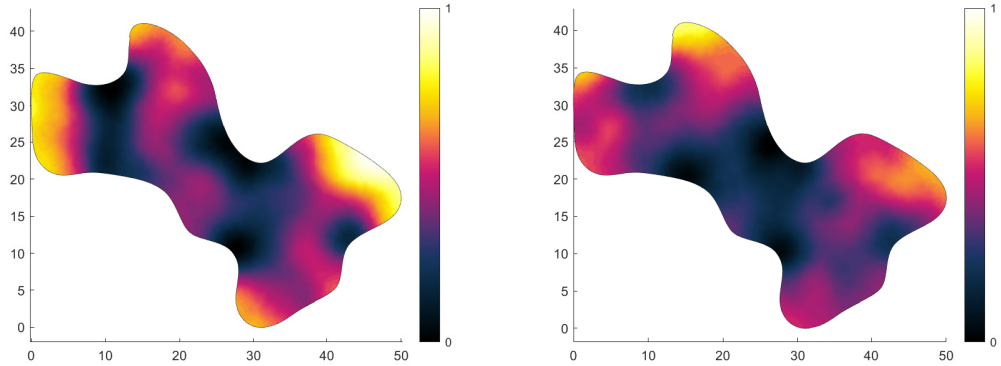
(a) Microtuble array control (b) Microtubule array mutant

Figure A.80: The signalling network model results of the CA ROP6 simulations in the 3rd less developed pavement cell outline, where the figures show the microtubule array in the control and the mutant.



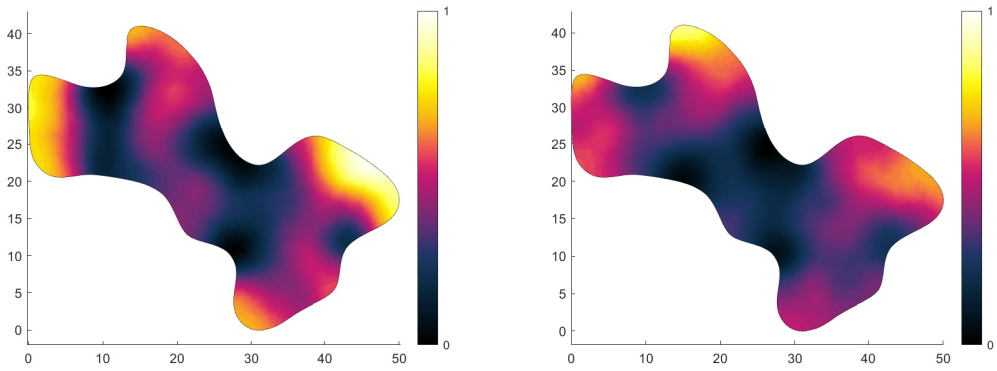
(a) Microtuble array distribution control (b) Microtubule array distribution control

Figure A.81: The signalling network model results of the CA ROP6 simulations in the 3rd less developed pavement cell outline, where the figures show the microtubule array's angle distribution in the control and the mutant.



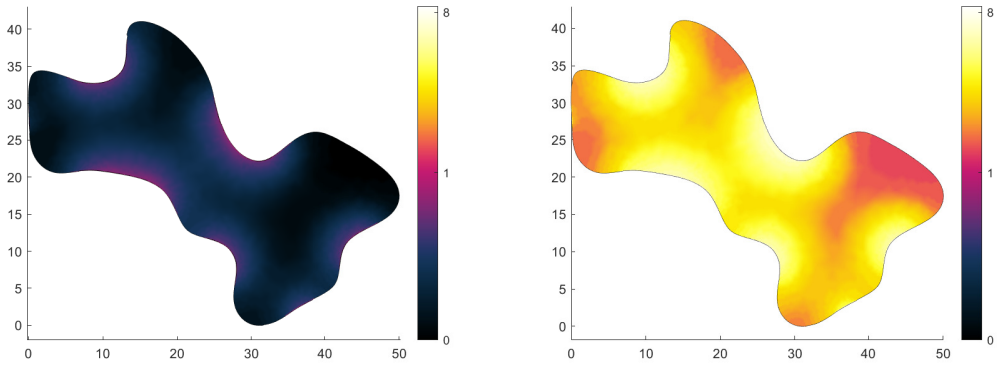
(a) ROP2 Control (b) ROP2 Mutant

Figure A.82: The signalling network model results of the CA ROP6 simulations in the 5th less developed pavement cell outline, where the figures show the ROP2 concentrations in the control and the mutant



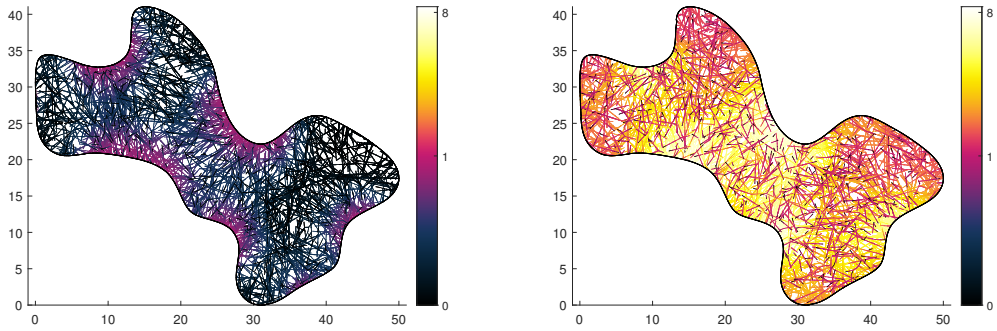
(a) RIC4 Control (b) RIC4 Mutant

Figure A.83: The signalling network model results of the CA ROP6 simulations in the 5th less developed pavement cell outline, where the figures show the RIC4 concentrations in the control and the mutant.



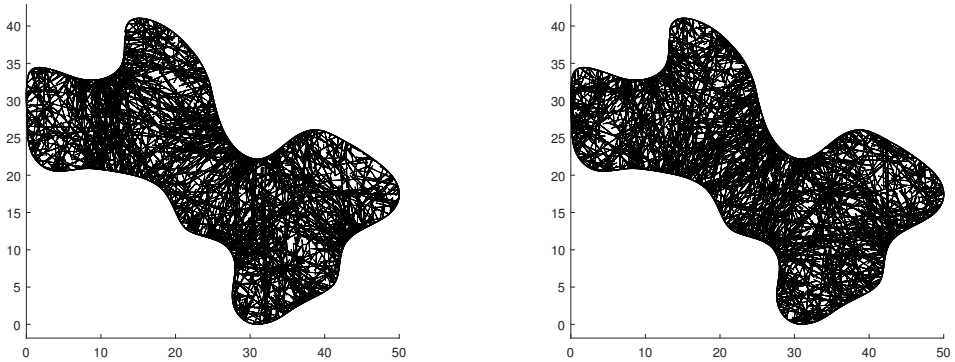
(a) ROP6 Control (b) ROP6 Mutant

Figure A.84: The signalling network model results of the CA ROP6 simulations in the 5th less developed pavement cell outline, where the figures show the ROP6 concentrations in the control and the mutant with non-linear scalebars.



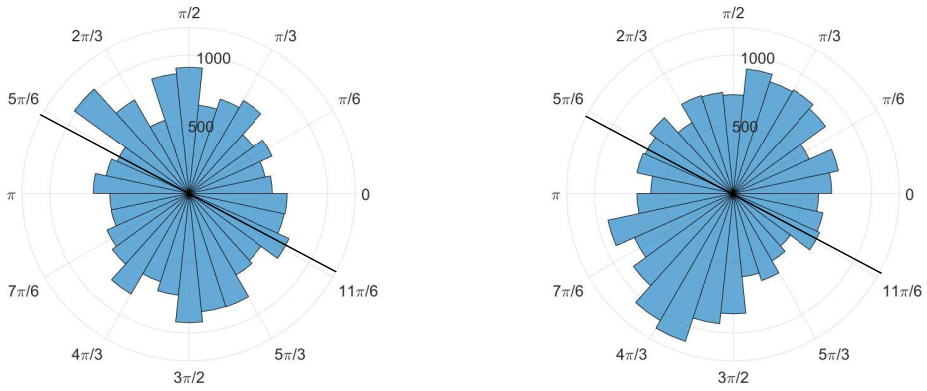
(a) RIC1 Control (b) RIC1 Mutant

Figure A.85: The signalling network model results of the CA ROP6 simulations in the 5th less developed pavement cell outline, where the figures show the RIC1 concentrations in the control and the mutant with non-linear scalebars.



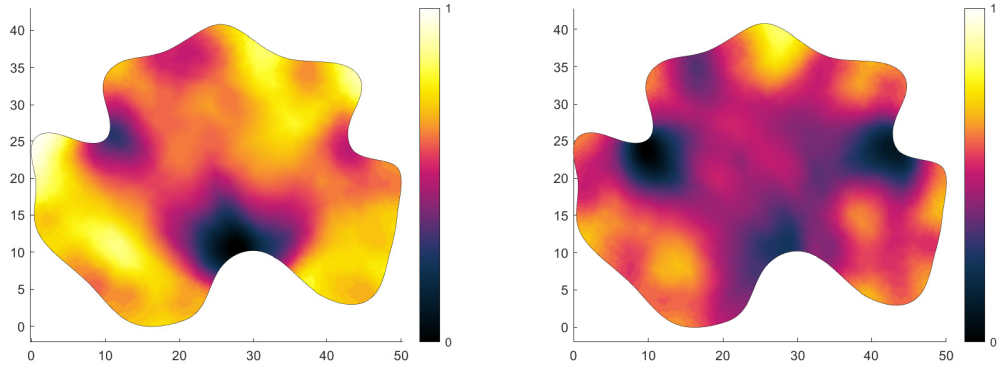
(a) Microtuble array control (b) Microtubule array mutant

Figure A.86: The signalling network model results of the CA ROP6 simulations in the 5th less developed pavement cell outline, where the figures show the microtubule array in the control and the mutant.



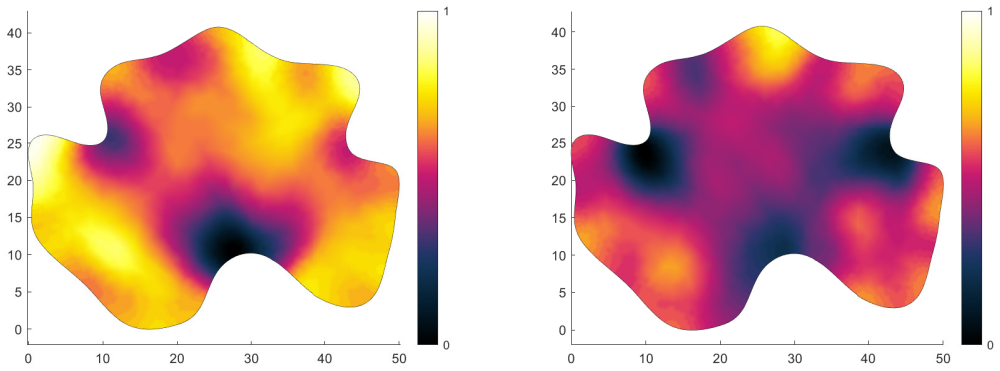
(a) Microtuble array distribution control (b) Microtubule array distribution control

Figure A.87: The signalling network model results of the CA ROP6 simulations in the 5th less developed pavement cell outline, where the figures show the microtubule array's angle distribution in the control and the mutant.



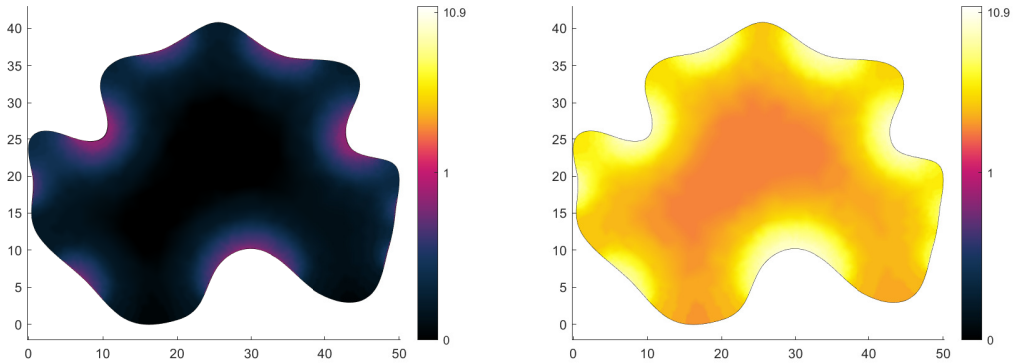
(a) ROP2 Control (b) ROP2 Mutant

Figure A.88: The signalling network model results of the CA ROP6 simulations in the 6th less developed pavement cell outline, where the figures show the ROP2 concentrations in the control and the mutant.



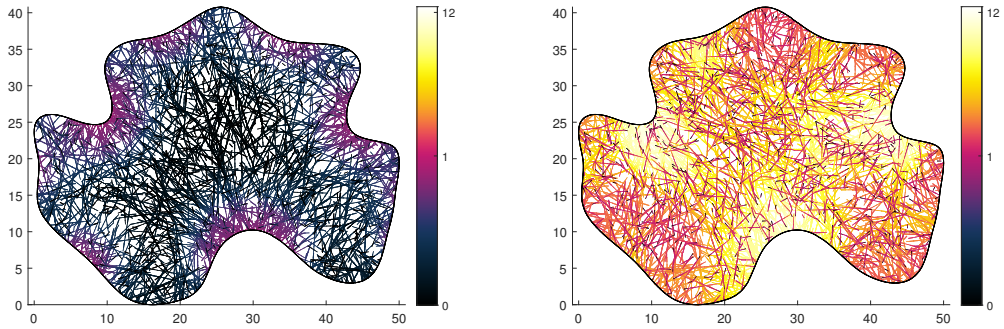
(a) RIC4 Control (b) RIC4 Mutant

Figure A.89: The signalling network model results of the CA ROP6 simulations in the 6th less developed pavement cell outline, where the figures show the RIC4 concentrations in the control and the mutant.



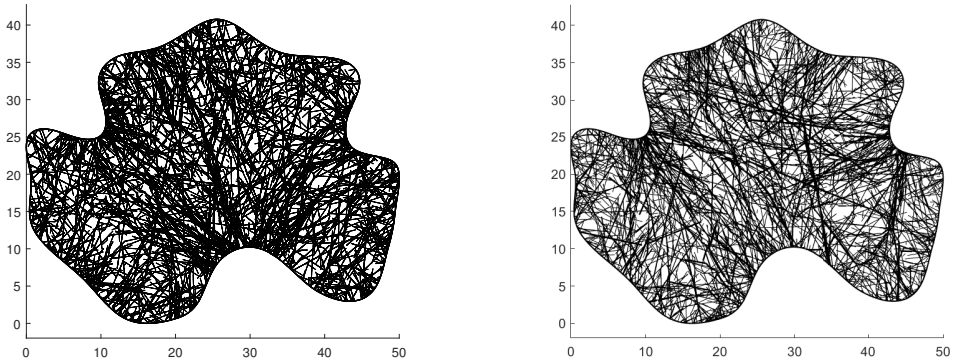
(a) ROP6 Control (b) ROP6 Mutant

Figure A.90: The signalling network model results of the CA ROP6 simulations in the 6th less developed pavement cell outline, where the figures show the ROP6 concentrations in the control and the mutant with non-linear scalebars.



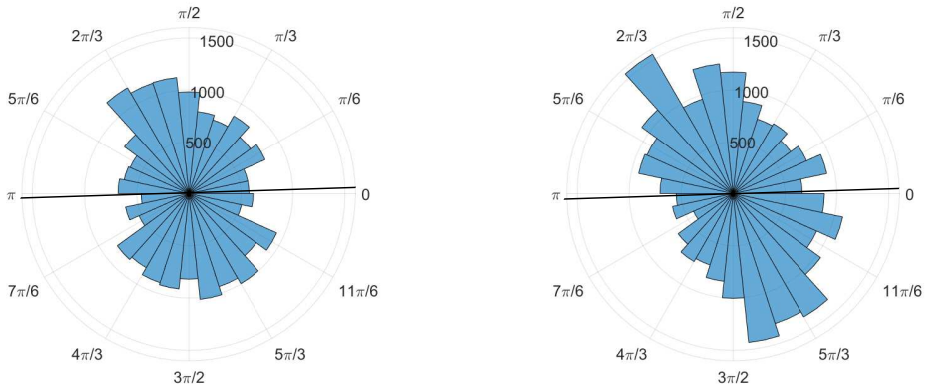
(a) RIC1 Control (b) RIC1 Mutant

Figure A.91: The signalling network model results of the CA ROP6 simulations in the 6th less developed pavement cell outline, where the figures show the RIC1 concentrations in the control and the mutant with non-linear scalebars.



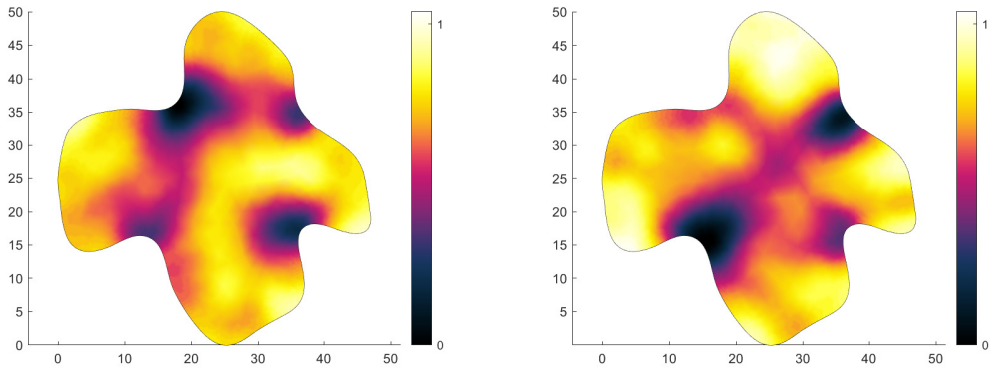
(a) Microtuble array control (b) Microtubule array mutant

Figure A.92: The signalling network model results of the CA ROP6 simulations in the 6th less developed pavement cell outline, where the figures show the microtubule array in the control and the mutant.



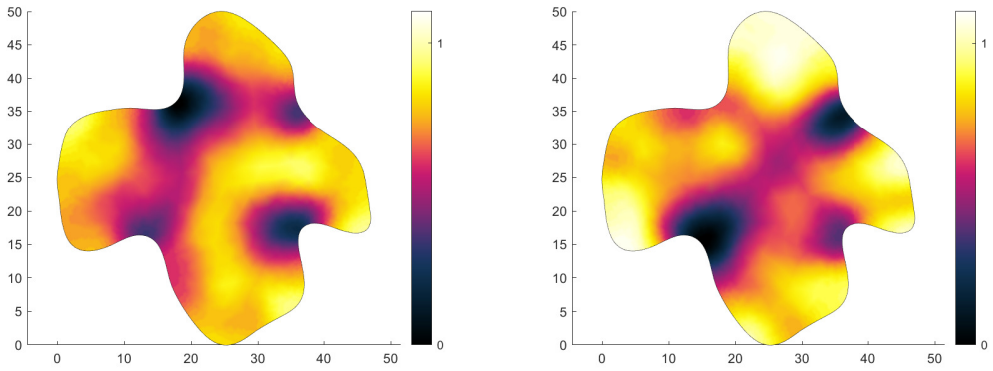
(a) Microtuble array distribution control (b) Microtubule array distribution control

Figure A.93: The signalling network model results of the CA ROP6 simulations in the 6th less developed pavement cell outline, where the figures show the microtubule array's angle distribution in the control and the mutant.



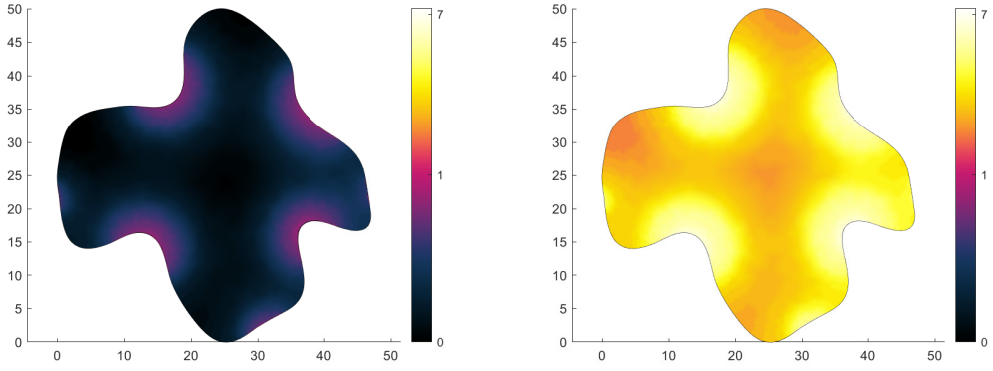
(a) ROP2 Control (b) ROP2 Mutant

Figure A.94: The signalling network model results of the CA ROP6 simulations in the 7th less developed pavement cell outline, where the figures show the ROP2 concentrations in the control and the mutant.



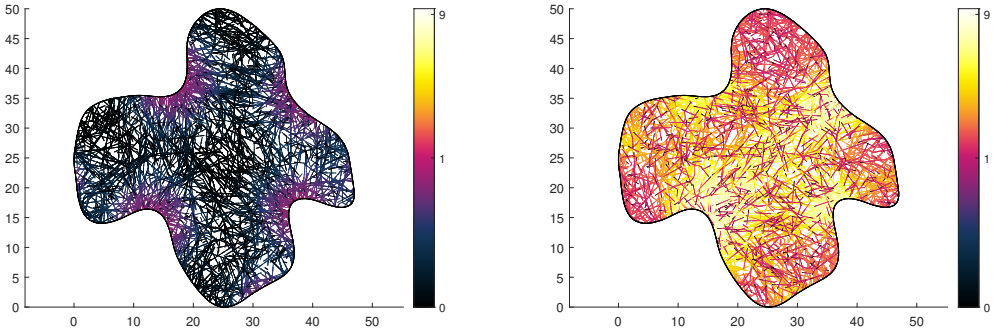
(a) RIC4 Control (b) RIC4 Mutant

Figure A.95: The signalling network model results of the CA ROP6 simulations in the 7th less developed pavement cell outline, where the figures show the RIC4 concentrations in the control and the mutant.



(a) ROP6 Control (b) ROP6 Mutant

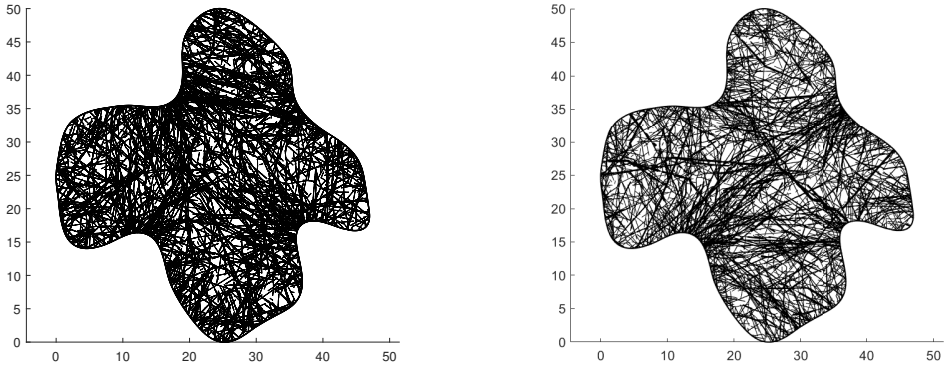
Figure A.96: The signalling network model results of the CA ROP6 simulations in the 7th less developed pavement cell outline, where the figures show the ROP6 concentrations in the control and the mutant with non-linear scalebars.



(a) RIC1 Control

(b) RIC1 Mutant

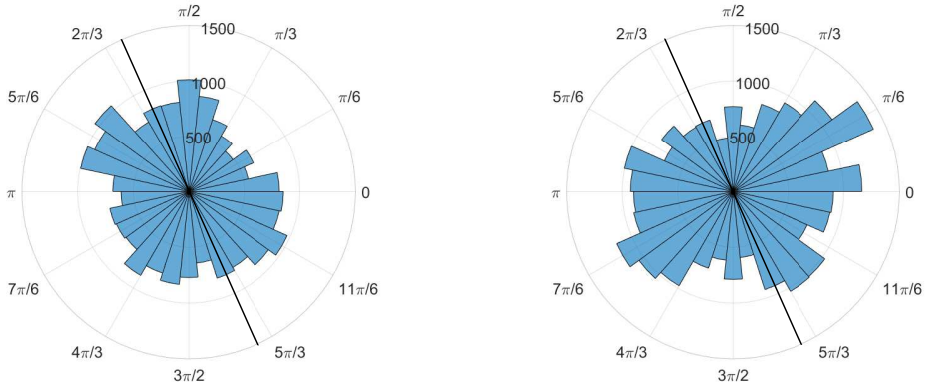
Figure A.97: The signalling network model results of the CA ROP6 simulations in the 7th less developed pavement cell outline, where the figures show the RIC1 concentrations in the control and the mutant with non-linear scalebars.



(a) Microtuble array control

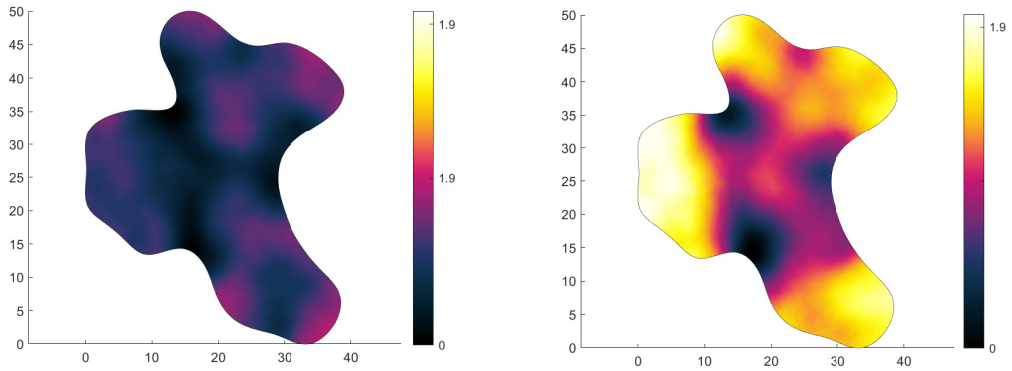
(b) Microtubule array mutant

Figure A.98: The signalling network model results of the CA ROP6 simulations in the 7th less developed pavement cell outline, where the figures show the microtubule array in the control and the mutant.



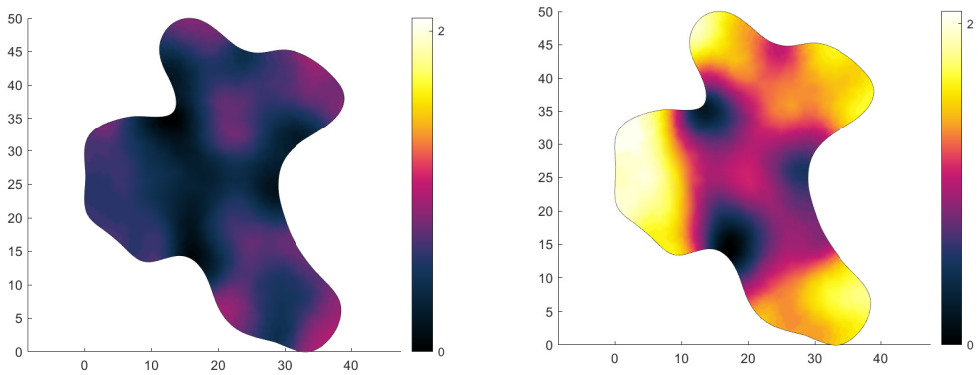
(a) Microtuble array distribution control (b) Microtubule array distribution control

Figure A.99: The signalling network model results of the CA ROP6 simulations in the 7th less developed pavement cell outline, where the figures show the microtubule array's angle distribution in the control and the mutant.



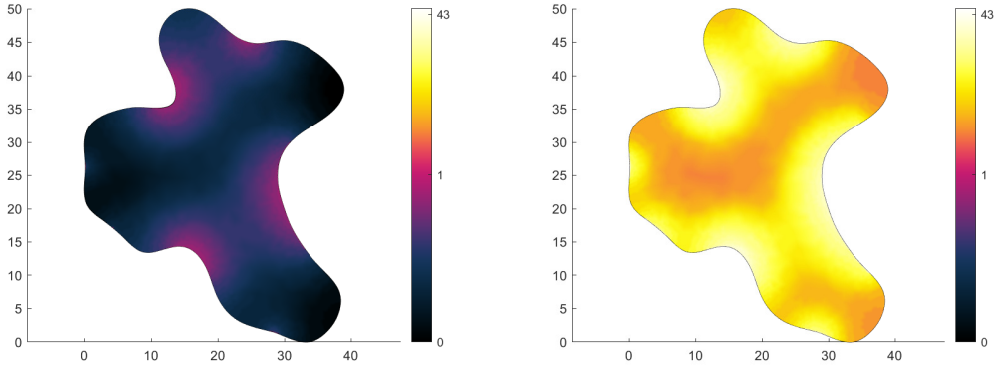
(a) ROP2 Control (b) ROP2 Mutant

Figure A.100: The signalling network model results of the CA ROP6 simulations in the 8th less developed pavement cell outline, where the figures show the ROP2 concentrations in the control and the mutant.



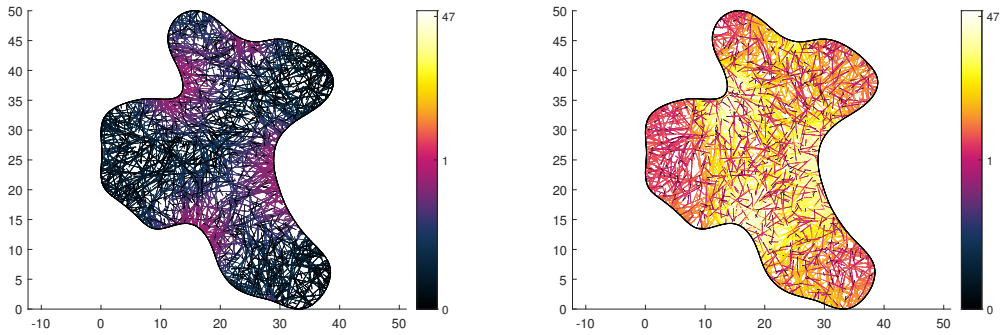
(a) RIC4 Control (b) RIC4 Mutant

Figure A.101: The signalling network model results of the CA ROP6 simulations in the 8th less developed pavement cell outline, where the figures show the RIC4 concentrations in the control and the mutant.



(a) ROP6 Control (b) ROP6 Mutant

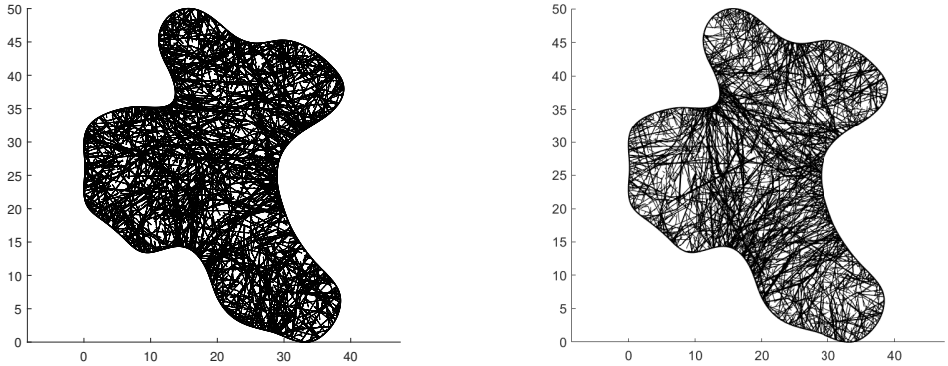
Figure A.102: The signalling network model results of the CA ROP6 simulations in the 8th less developed pavement cell outline, where the figures show the ROP6 concentrations in the control and the mutant with non-linear scalebars.



(a) RIC1 Control

(b) RIC1 Mutant

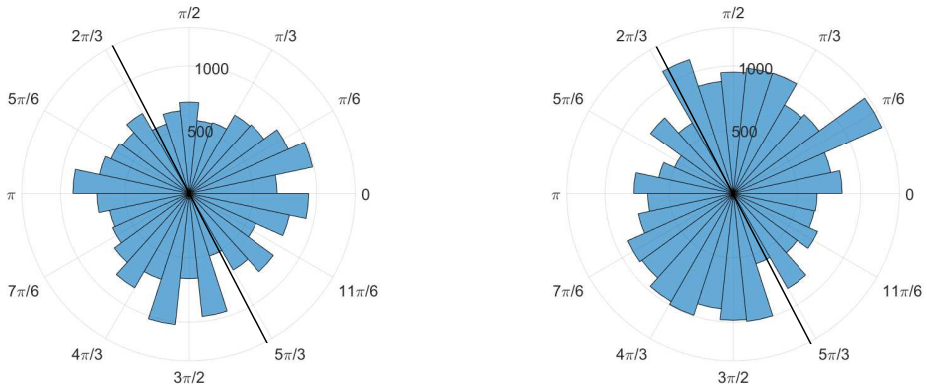
Figure A.103: The signalling network model results of the CA ROP6 simulations in the 8th less developed pavement cell outline, where the figures show the RIC1 concentrations in the control and the mutant with non-linear scalebars.



(a) Microtuble array control

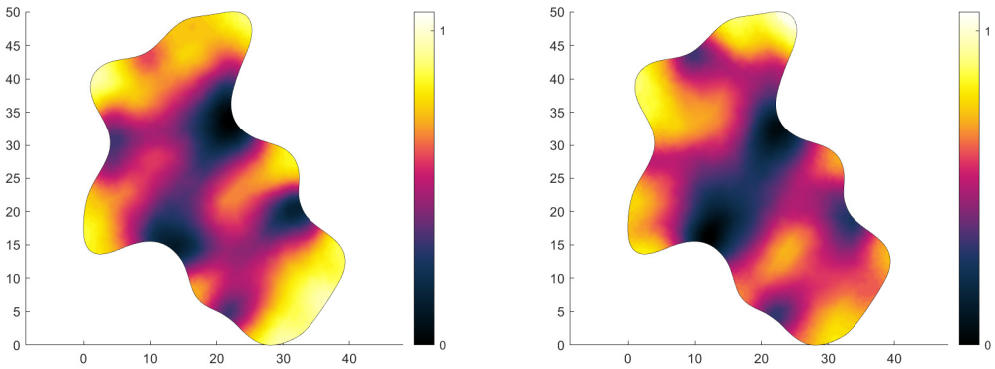
(b) Microtubule array mutant

Figure A.104: The signalling network model results of the CA ROP6 simulations in the 8th less developed pavement cell outline, where the figures show the microtubule array in the control and the mutant.



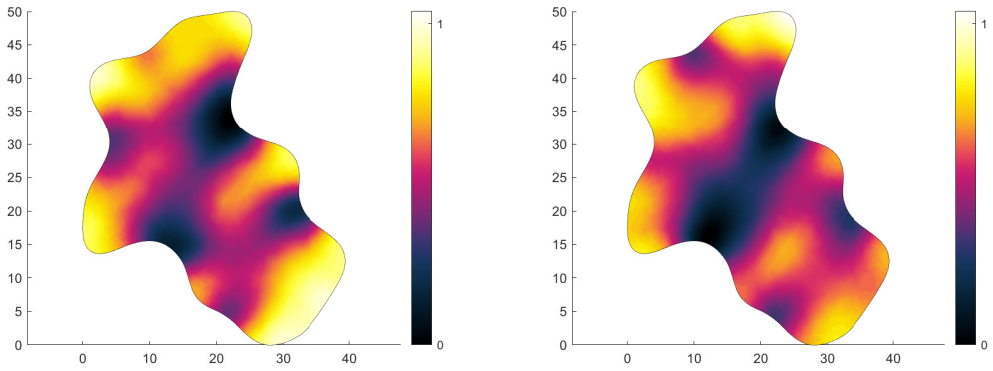
(a) Microtuble array distribution control (b) Microtubule array distribution control

Figure A.105: The signalling network model results of the CA ROP6 simulations in the 8th less developed pavement cell outline, where the figures show the microtubule array's angle distribution in the control and the mutant.



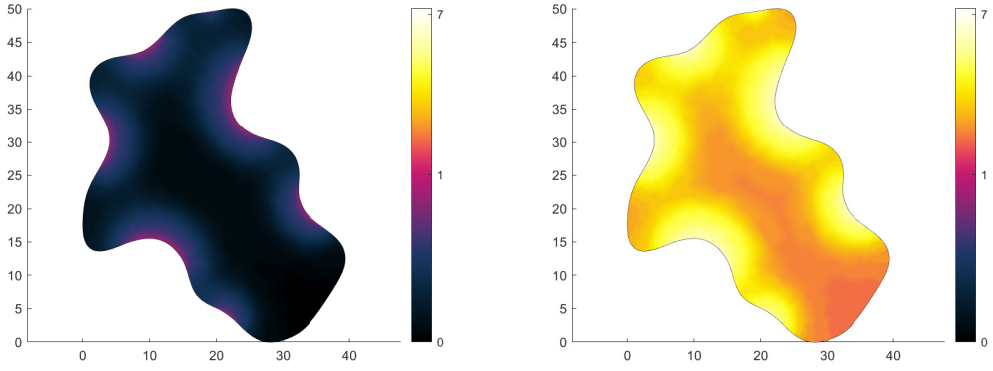
(a) ROP2 Control (b) ROP2 Mutant

Figure A.106: The signalling network model results of the CA ROP6 simulations in the 9th less developed pavement cell outline, where the figures show the ROP2 concentrations in the control and the mutant.



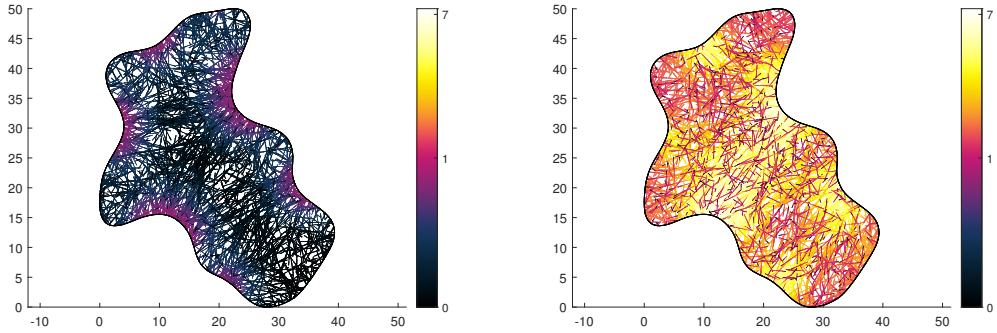
(a) RIC4 Control (b) RIC4 Mutant

Figure A.107: The signalling network model results of the CA ROP6 simulations in the 9th less developed pavement cell outline, where the figures show the RIC4 concentrations in the control and the mutant.



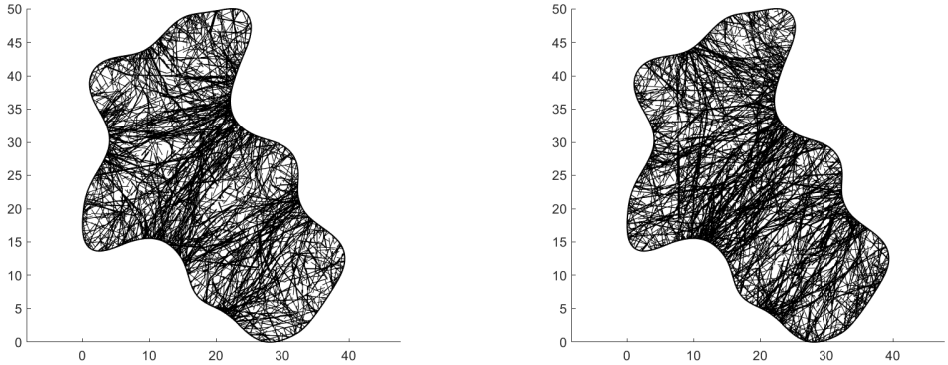
(a) ROP6 Control (b) ROP6 Mutant

Figure A.108: The signalling network model results of the CA ROP6 simulations in the 9th less developed pavement cell outline, where the figures show the ROP6 concentrations in the control and the mutant with non-linear scalebars.



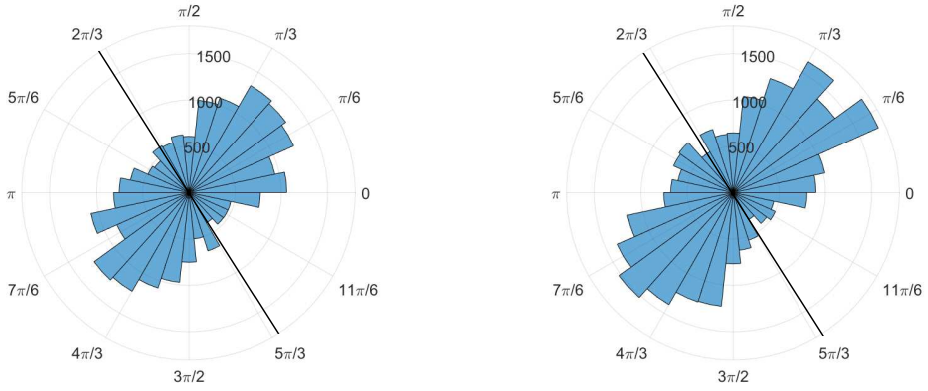
(a) RIC1 Control (b) RIC1 Mutant

Figure A.109: The signalling network model results of the CA ROP6 simulations in the 9th less developed pavement cell outline, where the figures show the RIC1 concentrations in the control and the mutant with non-linear scalebars.



(a) Microtuble array control (b) Microtubule array mutant

Figure A.110: The signalling network model results of the CA ROP6 simulations in the 9th less developed pavement cell outline, where the figures show the microtubule array in the control and the mutant.

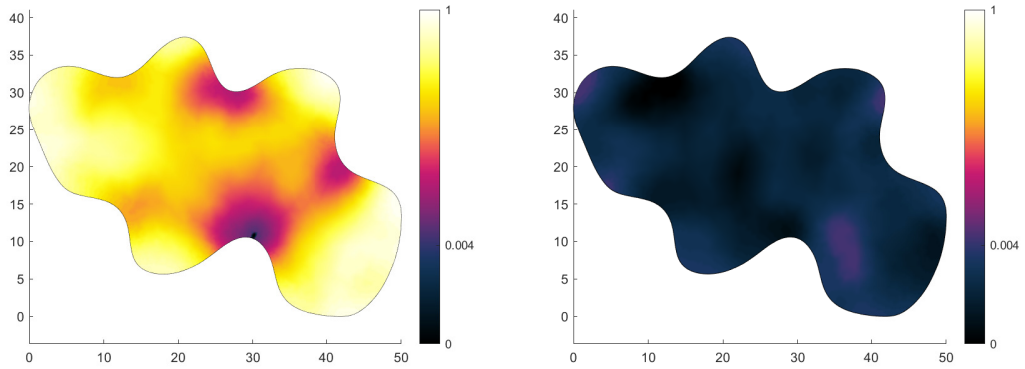


(a) Microtuble array distribution control (b) Microtubule array distribution control

Figure A.111: The signalling network model results of the CA ROP6 simulations in the 9th less developed pavement cell outline, where the figures show the microtubule array's angle distribution in the control and the mutant.

A.4.3.3 DN ROP2

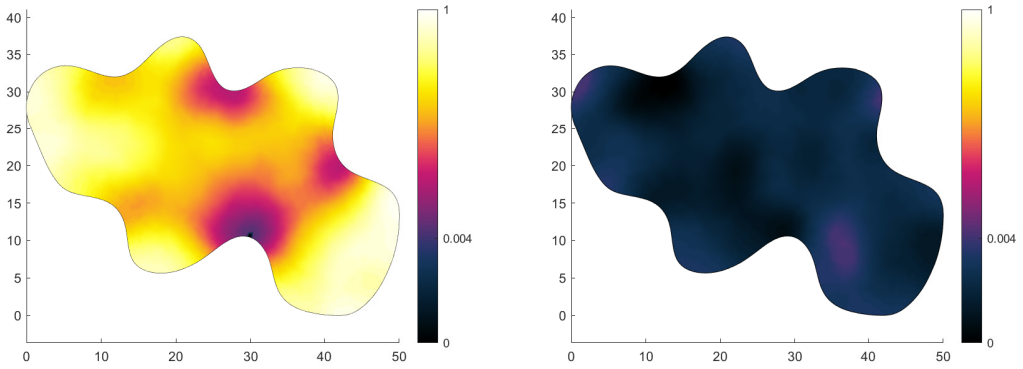
Here we show the supporting figures for the dominate negative ROP2 simulations in section 6.5.2.3.



(a) ROP2 Control

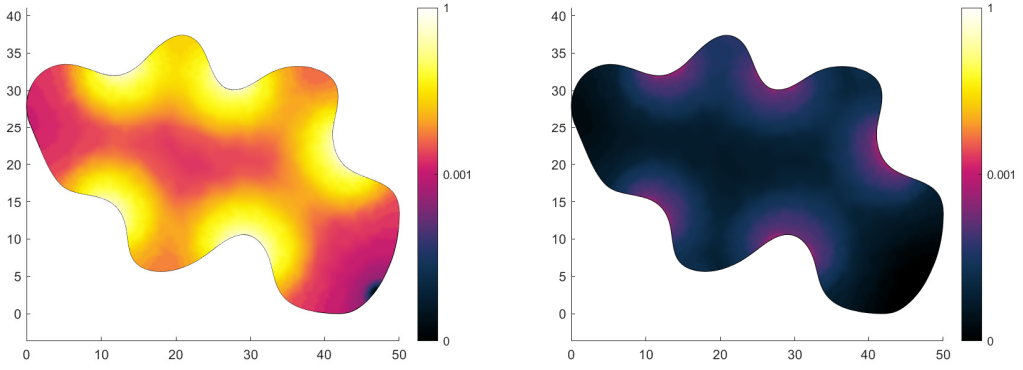
(b) ROP2 Mutant

Figure A.112: The signalling network model results of the DN ROP2 simulations in the 1st less developed pavement cell outline, where the figures show the ROP2 concentrations in the control and the mutant with non-linear scalebars.



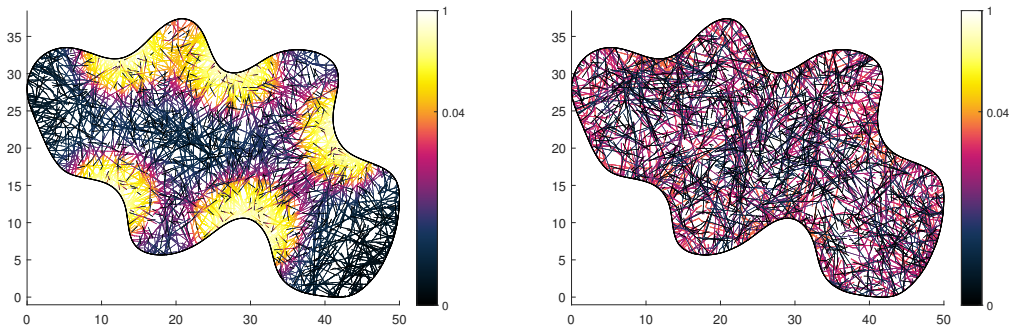
(a) RIC4 Control (b) RIC4 Mutant

Figure A.113: The signalling network model results of the DN ROP2 simulations in the 1st less developed pavement cell outline, where the figures show the RIC4 concentrations in the control and the mutant with non-linear scalebars.



(a) ROP6 Control (b) ROP6 Mutant

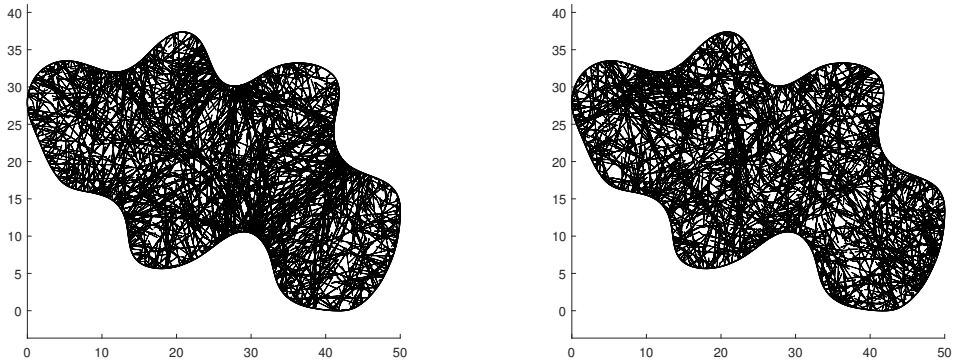
Figure A.114: The signalling network model results of the DN ROP2 simulations in the 1st less developed pavement cell outline, where the figures show the ROP6 concentrations in the control and the mutant with non-linear scalebars.



(a) RIC1 Control

(b) RIC1 Mutant

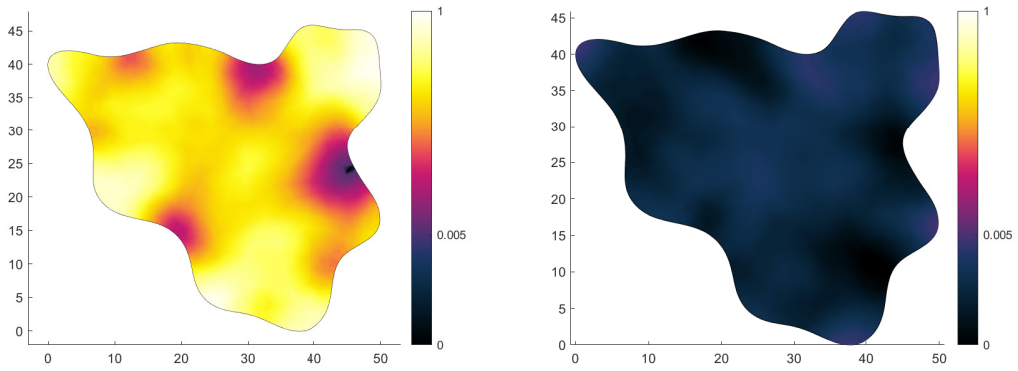
Figure A.115: The signalling network model results of the DN ROP2 simulations in the 1st less developed pavement cell outline, where the figures show the RIC1 concentrations in the control and the mutant with non-linear scalebars.



(a) Microtuble array control

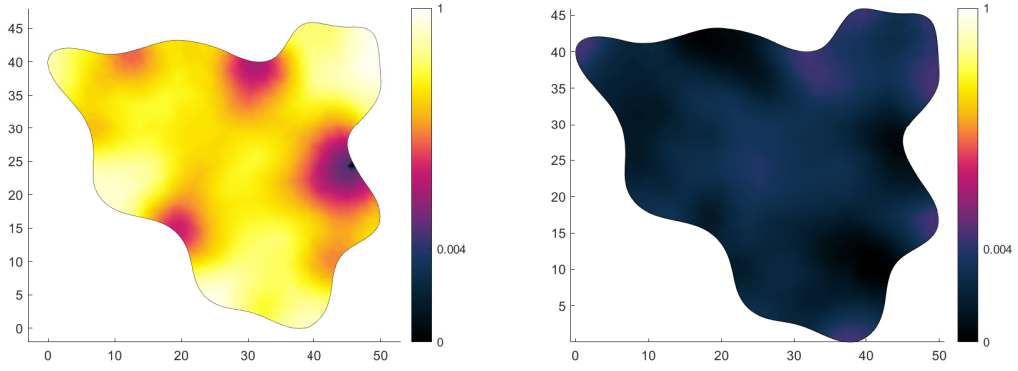
(b) Microtubule array mutant

Figure A.116: The signalling network model results of the DN ROP2 simulations in the 1st less developed pavement cell outline, where the figures show the microtubule array in the control and the mutant.



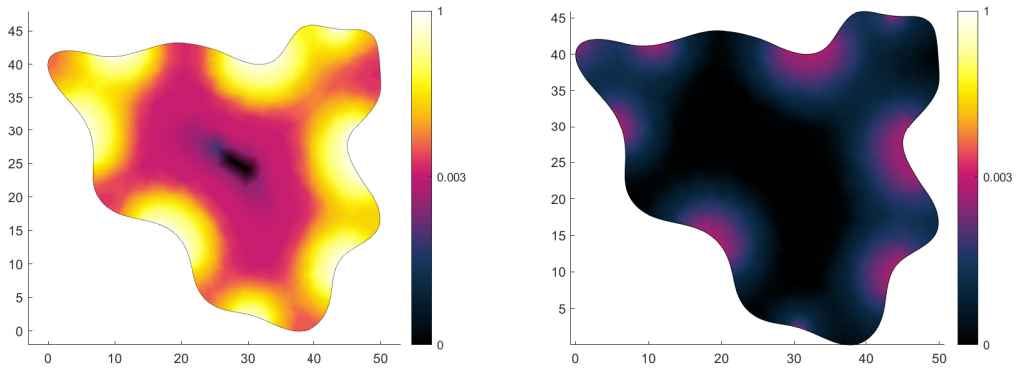
(a) ROP2 Control (b) ROP2 Mutant

Figure A.117: The signalling network model results of the DN ROP2 simulations in the 3rd less developed pavement cell outline, where the figures show the ROP2 concentrations in the control and the mutant with non-linear scalebars.



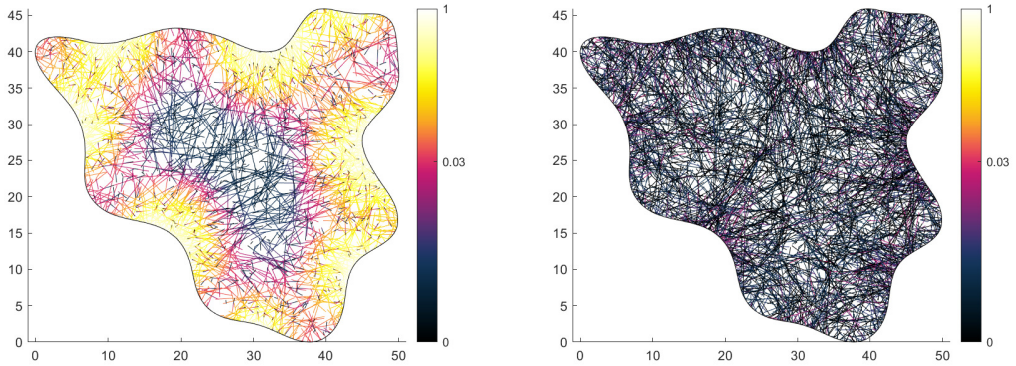
(a) RIC4 Control (b) RIC4 Mutant

Figure A.118: The signalling network model results of the DN ROP2 simulations in the 3rd less developed pavement cell outline, where the figures show the RIC4 concentrations in the control and the mutant with non-linear scalebars.



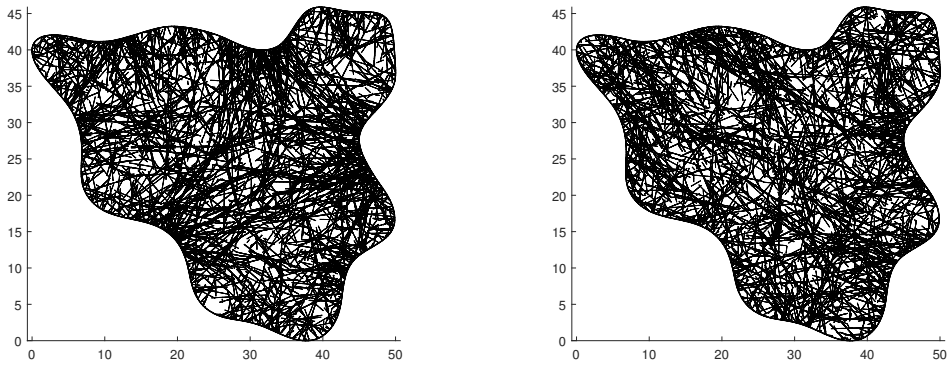
(a) ROP6 Control (b) ROP6 Mutant

Figure A.119: The signalling network model results of the DN ROP2 simulations in the 3rd less developed pavement cell outline, where the figures show the ROP6 concentrations in the control and the mutant with non-linear scalebars.



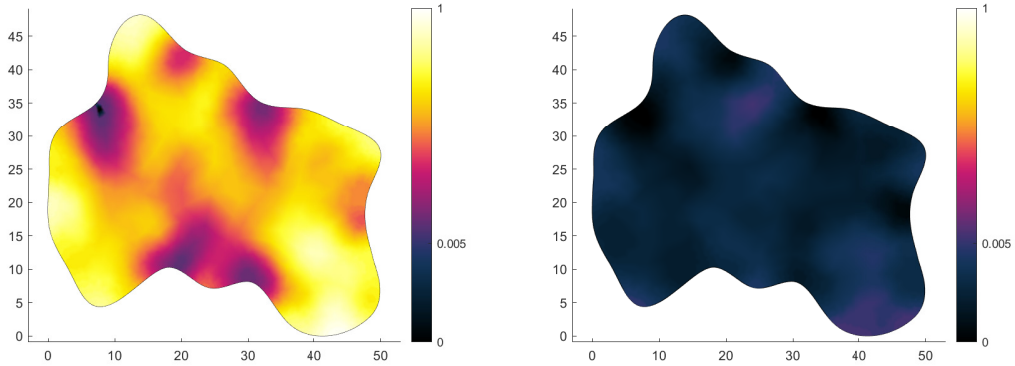
(a) RIC1 Control (b) RIC1 Mutant

Figure A.120: The signalling network model results of the DN ROP2 simulations in the 3rd less developed pavement cell outline, where the figures show the RIC1 concentrations in the control and the mutant with non-linear scalebars.



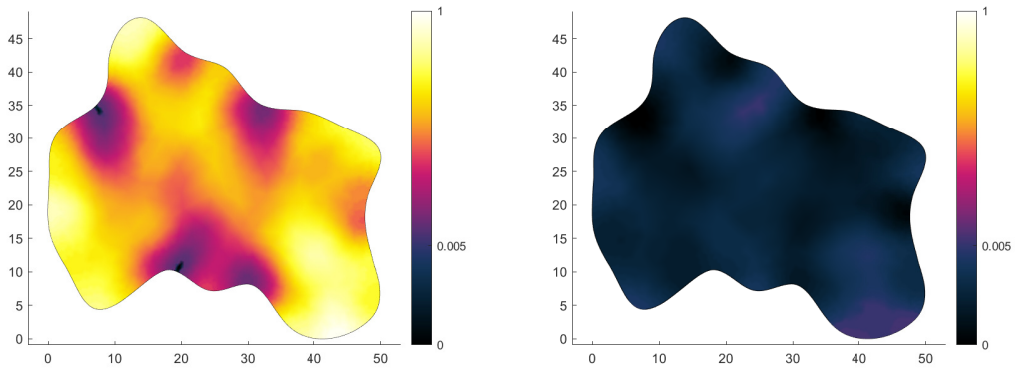
(a) Microtuble array control (b) Microtubule array mutant

Figure A.121: The signalling network model results of the DN ROP2 simulations in the 3rd less developed pavement cell outline, where the figures show the microtubule array in the control and the mutant.



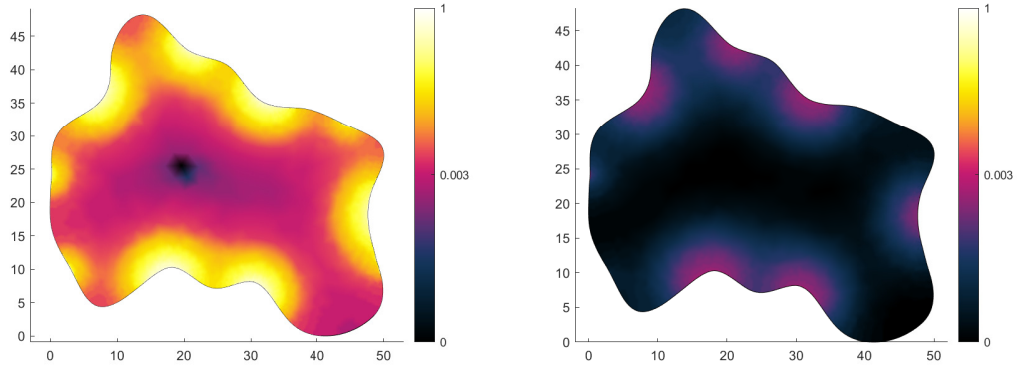
(a) ROP2 Control (b) ROP2 Mutant

Figure A.122: The signalling network model results of the DN ROP2 simulations in the 4th less developed pavement cell outline, where the figures show the ROP2 concentrations in the control and the mutant with non-linear scalebars.



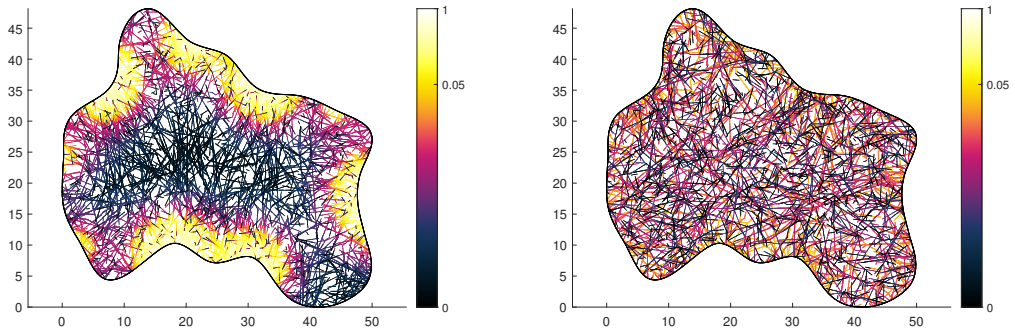
(a) RIC4 Control (b) RIC4 Mutant

Figure A.123: The signalling network model results of the DN ROP2 simulations in the 4th less developed pavement cell outline, where the figures show the RIC4 concentrations in the control and the mutant with non-linear scalebars.



(a) ROP6 Control (b) ROP6 Mutant

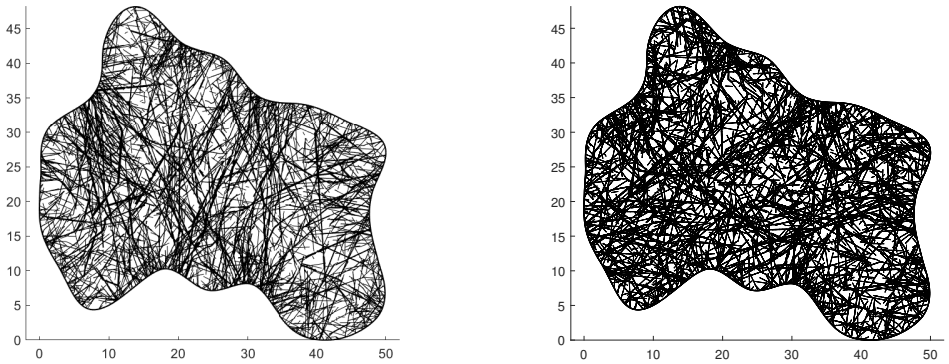
Figure A.124: The signalling network model results of the DN ROP2 simulations in the 4th less developed pavement cell outline, where the figures show the ROP6 concentrations in the control and the mutant with non-linear scalebars.



(a) RIC1 Control

(b) RIC1 Mutant

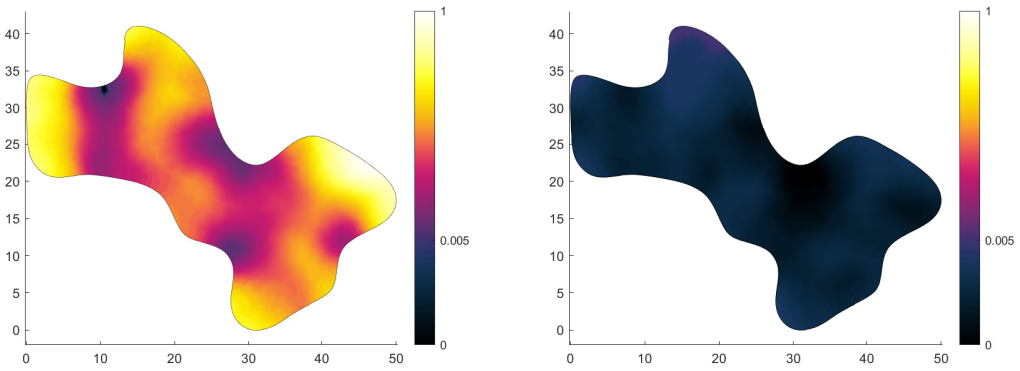
Figure A.125: The signalling network model results of the DN ROP2 simulations in the 4th less developed pavement cell outline, where the figures show the RIC1 concentrations in the control and the mutant with non-linear scalebars.



(a) Microtuble array control

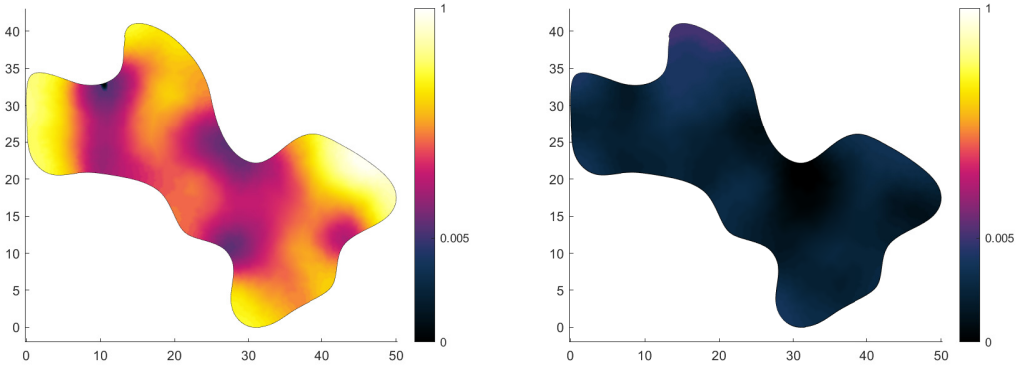
(b) Microtubule array mutant

Figure A.126: The signalling network model results of the DN ROP2 simulations in the 4th less developed pavement cell outline, where the figures show the microtubule array in the control and the mutant.



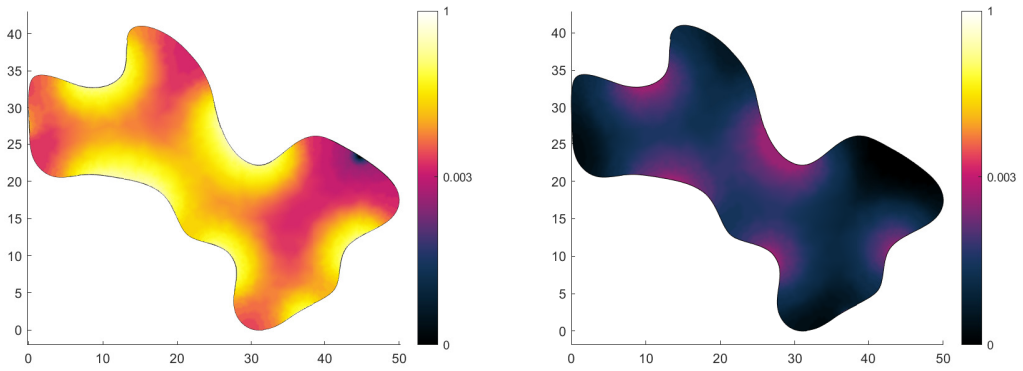
(a) ROP2 Control (b) ROP2 Mutant

Figure A.127: The signalling network model results of the DN ROP2 simulations in the 5th less developed pavement cell outline, where the figures show the ROP2 concentrations in the control and the mutant with non-linear scalebars.



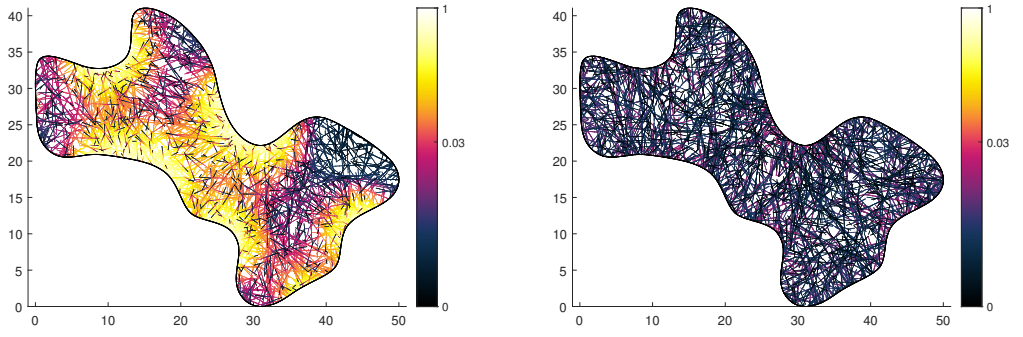
(a) RIC4 Control (b) RIC4 Mutant

Figure A.128: The signalling network model results of the DN ROP2 simulations in the 5th less developed pavement cell outline, where the figures show the RIC4 concentrations in the control and the mutant with non-linear scalebars.



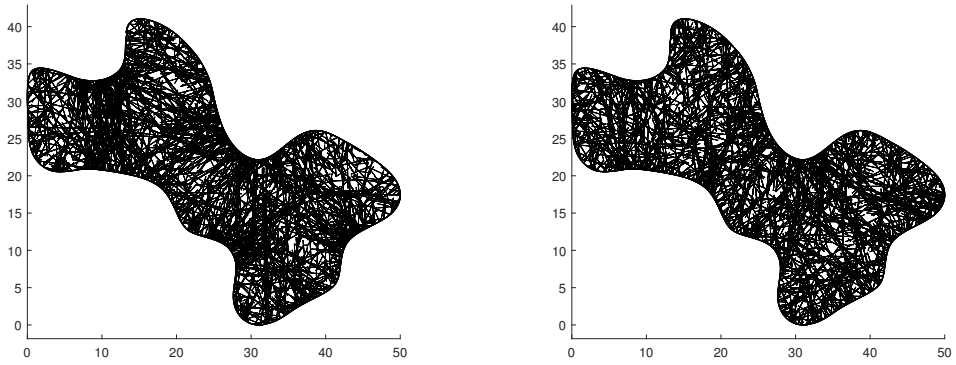
(a) ROP6 Control (b) ROP6 Mutant

Figure A.129: The signalling network model results of the DN ROP2 simulations in the 5th less developed pavement cell outline, where the figures show the ROP6 concentrations in the control and the mutant with non-linear scalebars.



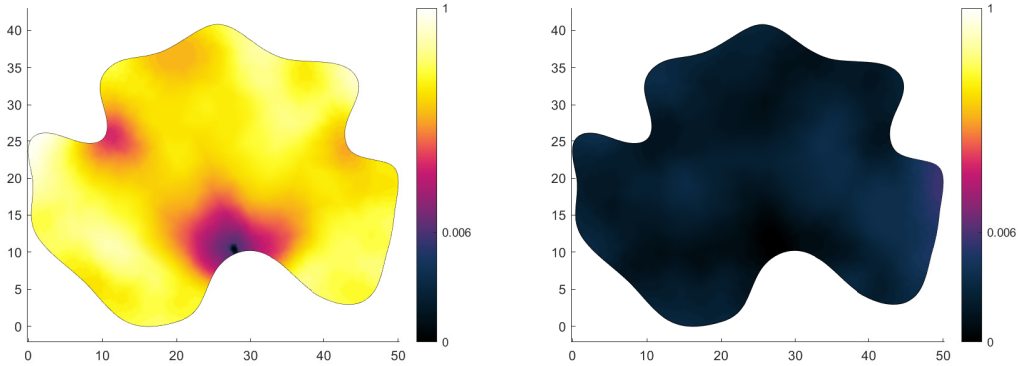
(a) RIC1 Control (b) RIC1 Mutant

Figure A.130: The signalling network model results of the DN ROP2 simulations in the 5th less developed pavement cell outline, where the figures show the RIC1 concentrations in the control and the mutant with non-linear scalebars.



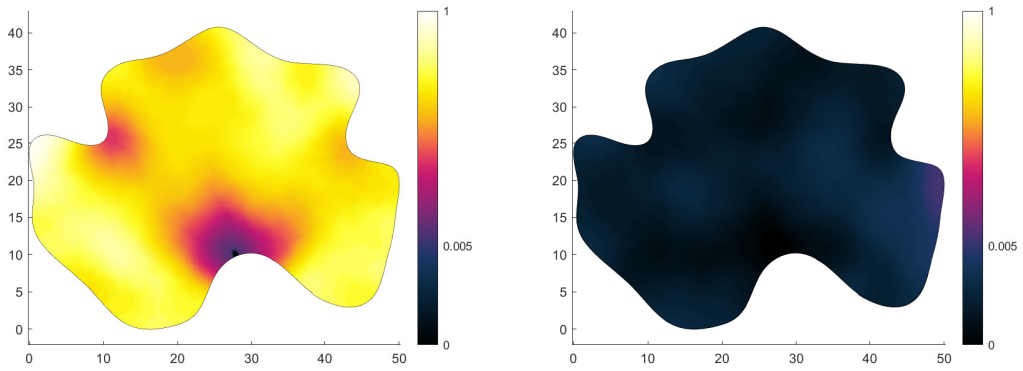
(a) Microtuble array control (b) Microtubule array mutant

Figure A.131: The signalling network model results of the DN ROP2 simulations in the 5th less developed pavement cell outline, where the figures show the microtubule array in the control and the mutant.



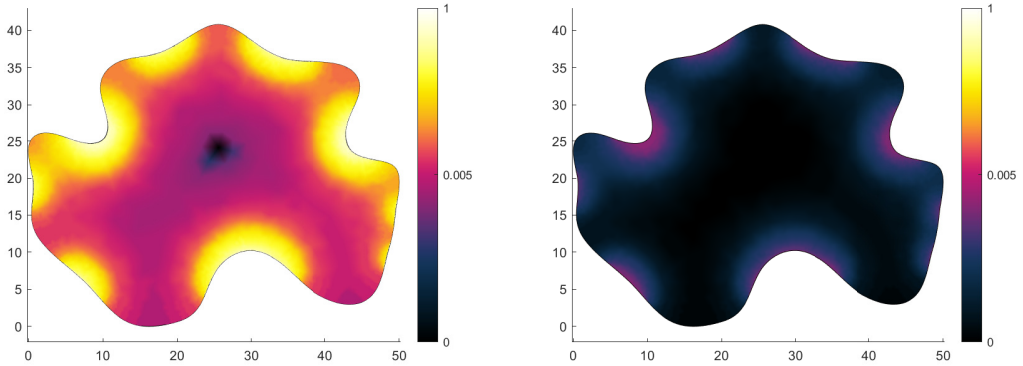
(a) ROP2 Control (b) ROP2 Mutant

Figure A.132: The signalling network model results of the DN ROP2 simulations in the 6th less developed pavement cell outline, where the figures show the ROP2 concentrations in the control and the mutant with non-linear scalebars.



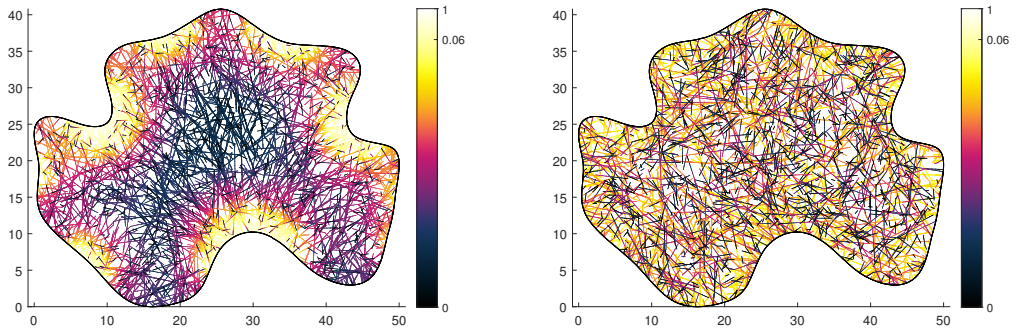
(a) RIC4 Control (b) RIC4 Mutant

Figure A.133: The signalling network model results of the DN ROP2 simulations in the 6th less developed pavement cell outline, where the figures show the RIC4 concentrations in the control and the mutant with non-linear scalebars.



(a) ROP6 Control (b) ROP6 Mutant

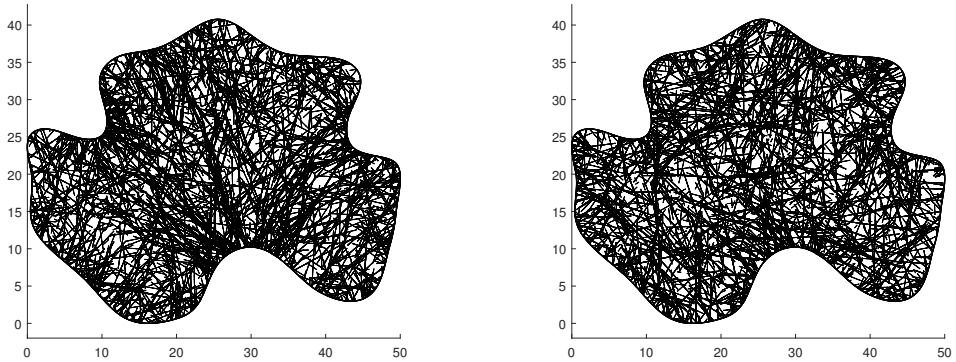
Figure A.134: The signalling network model results of the DN ROP2 simulations in the 6th less developed pavement cell outline, where the figures show the ROP6 concentrations in the control and the mutant with non-linear scalebars.



(a) RIC1 Control

(b) RIC1 Mutant

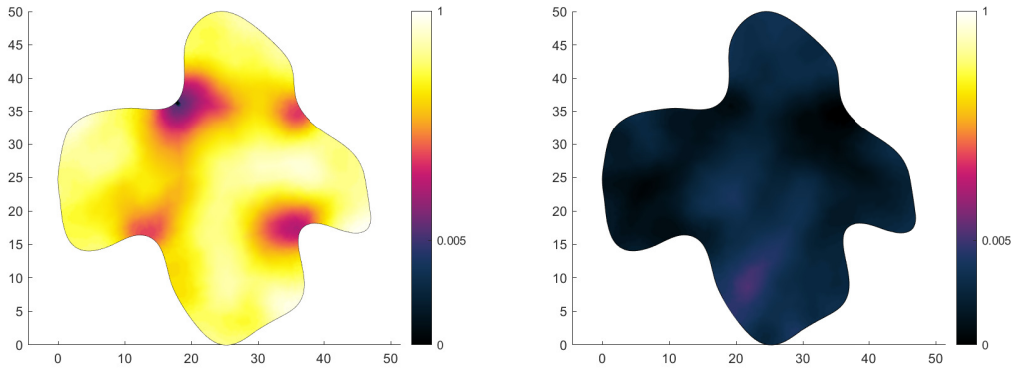
Figure A.135: The signalling network model results of the DN ROP2 simulations in the 6th less developed pavement cell outline, where the figures show the RIC1 concentrations in the control and the mutant with non-linear scalebars.



(a) Microtuble array control

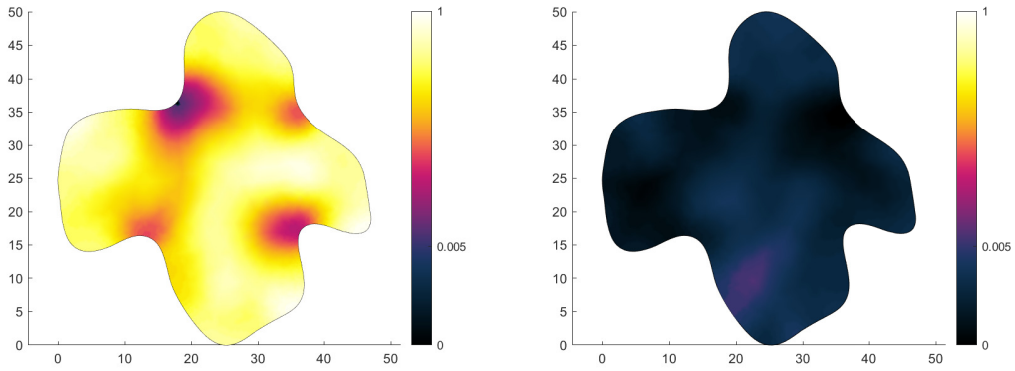
(b) Microtubule array mutant

Figure A.136: The signalling network model results of the DN ROP2 simulations in the 6th less developed pavement cell outline, where the figures show the microtubule array in the control and the mutant.



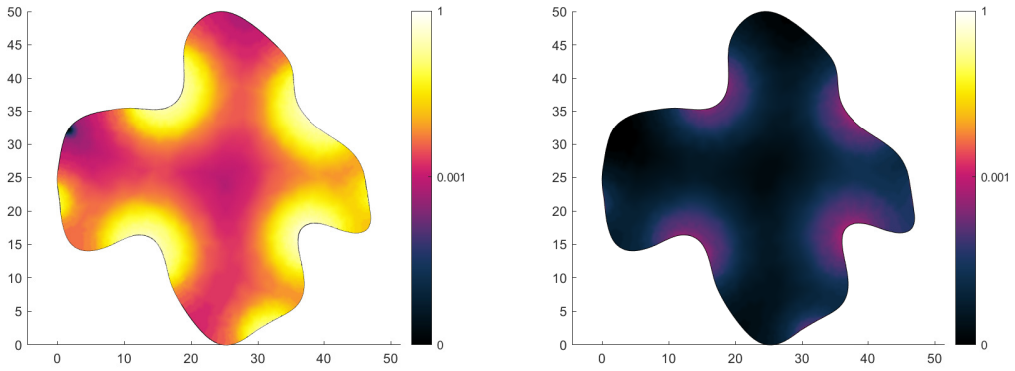
(a) ROP2 Control (b) ROP2 Mutant

Figure A.137: The signalling network model results of the DN ROP2 simulations in the 7th less developed pavement cell outline, where the figures show the ROP2 concentrations in the control and the mutant with non-linear scalebars.



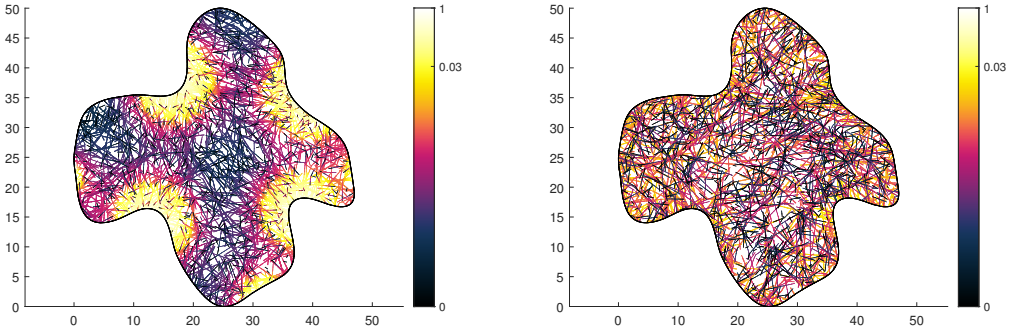
(a) RIC4 Control (b) RIC4 Mutant

Figure A.138: The signalling network model results of the DN ROP2 simulations in the 7th less developed pavement cell outline, where the figures show the RIC4 concentrations in the control and the mutant with non-linear scalebars.



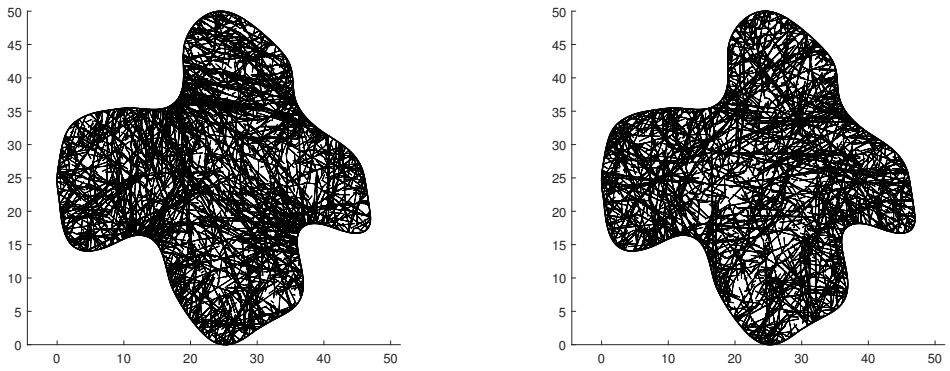
(a) ROP6 Control (b) ROP6 Mutant

Figure A.139: The signalling network model results of the DN ROP2 simulations in the 7th less developed pavement cell outline, where the figures show the ROP6 concentrations in the control and the mutant with non-linear scalebars.



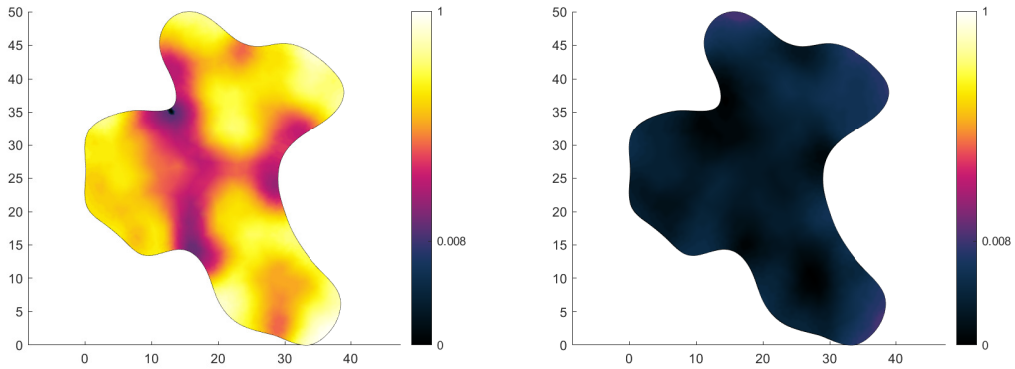
(a) RIC1 Control (b) RIC1 Mutant

Figure A.140: The signalling network model results of the DN ROP2 simulations in the 7th less developed pavement cell outline, where the figures show the RIC1 concentrations in the control and the mutant with non-linear scalebars.



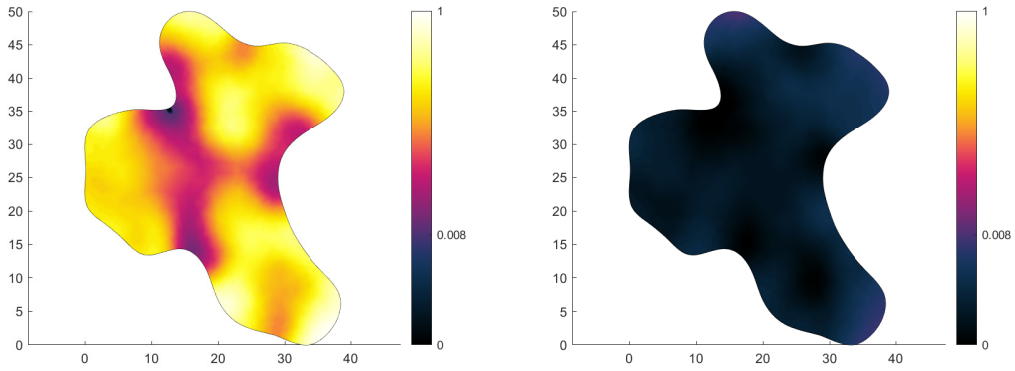
(a) Microtuble array control (b) Microtubule array mutant

Figure A.141: The signalling network model results of the DN ROP2 simulations in the 7th less developed pavement cell outline, where the figures show the microtubule array in the control and the mutant.



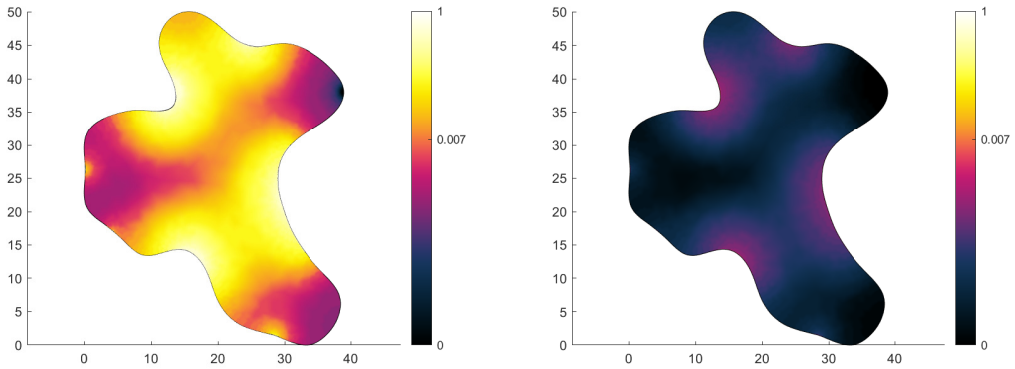
(a) ROP2 Control (b) ROP2 Mutant

Figure A.142: The signalling network model results of the DN ROP2 simulations in the 8th less developed pavement cell outline, where the figures show the ROP2 concentrations in the control and the mutant with non-linear scalebars.



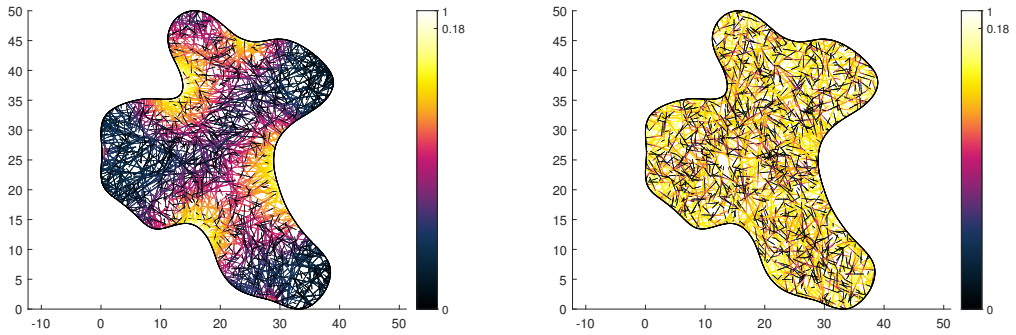
(a) RIC4 Control (b) RIC4 Mutant

Figure A.143: The signalling network model results of the DN ROP2 simulations in the 8th less developed pavement cell outline, where the figures show the RIC4 concentrations in the control and the mutant with non-linear scalebars.



(a) ROP6 Control (b) ROP6 Mutant

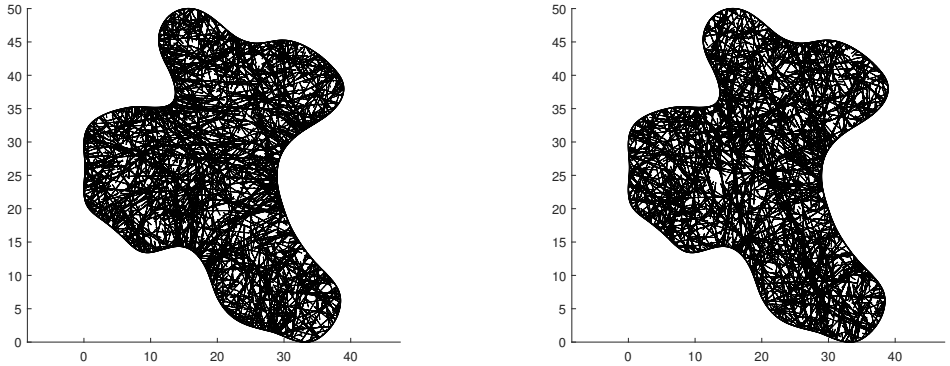
Figure A.144: The signalling network model results of the DN ROP2 simulations in the 8th less developed pavement cell outline, where the figures show the ROP6 concentrations in the control and the mutant with non-linear scalebars.



(a) RIC1 Control

(b) RIC1 Mutant

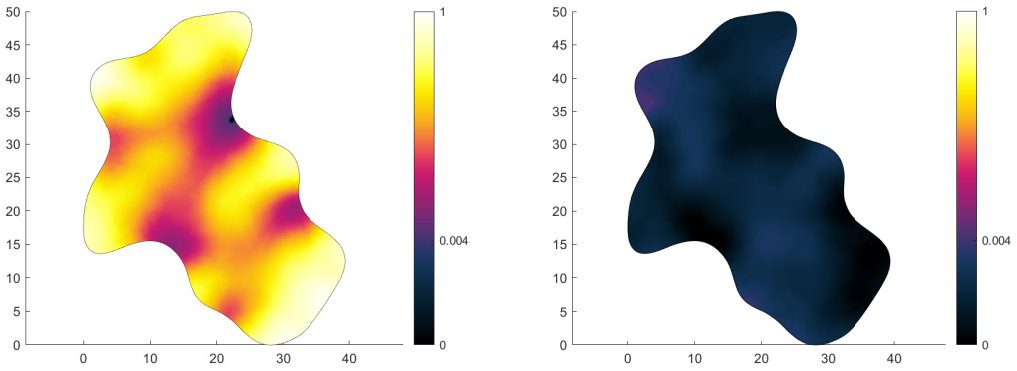
Figure A.145: The signalling network model results of the DN ROP2 simulations in the 8th less developed pavement cell outline, where the figures show the RIC1 concentrations in the control and the mutant with non-linear scalebars.



(a) Microtuble array control

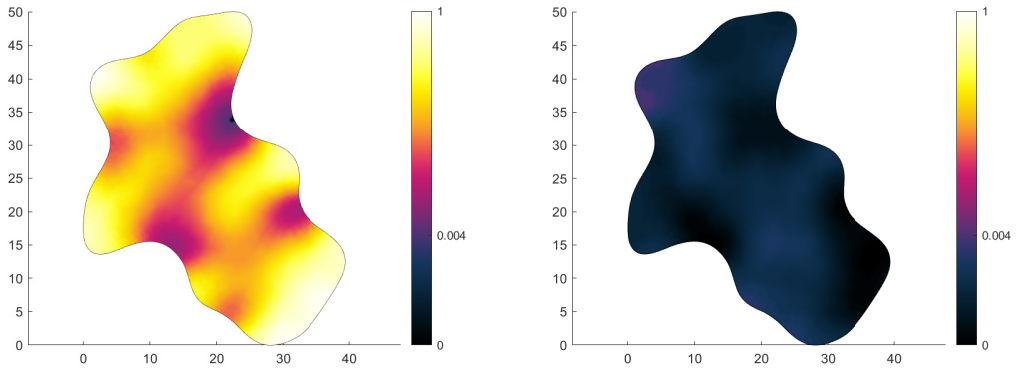
(b) Microtubule array mutant

Figure A.146: The signalling network model results of the DN ROP2 simulations in the 8th less developed pavement cell outline, where the figures show the microtubule array in the control and the mutant.



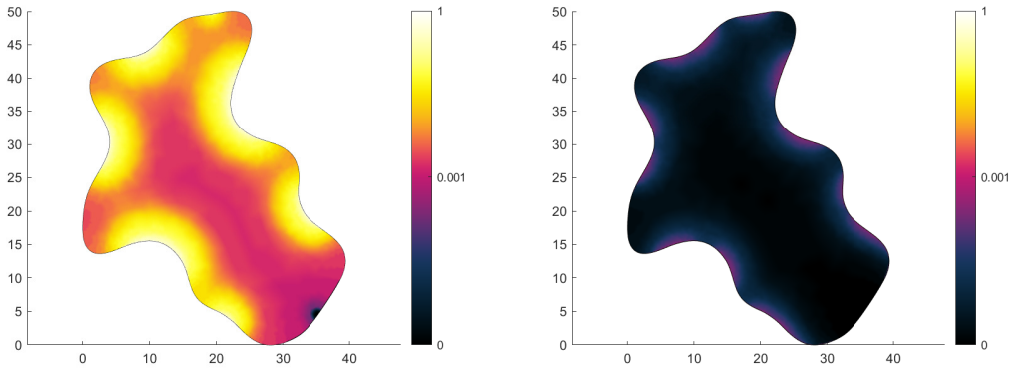
(a) ROP2 Control (b) ROP2 Mutant

Figure A.147: The signalling network model results of the DN ROP2 simulations in the 9th less developed pavement cell outline, where the figures show the ROP2 concentrations in the control and the mutant with non-linear scalebars.



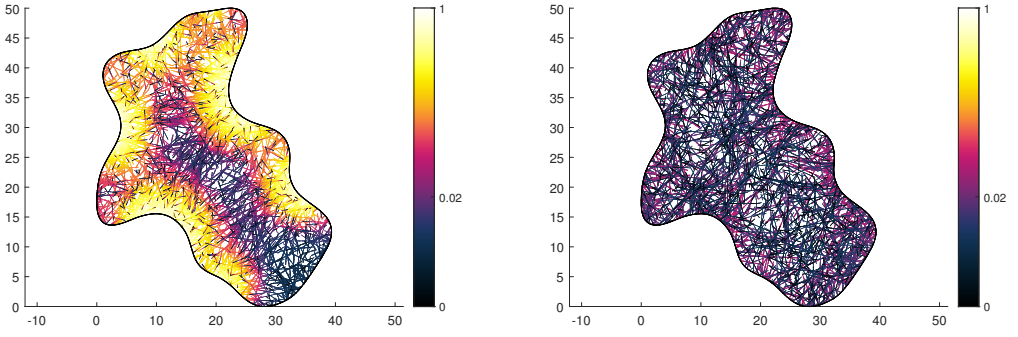
(a) RIC4 Control (b) RIC4 Mutant

Figure A.148: The signalling network model results of the DN ROP2 simulations in the 9th less developed pavement cell outline, where the figures show the RIC4 concentrations in the control and the mutant with non-linear scalebars.



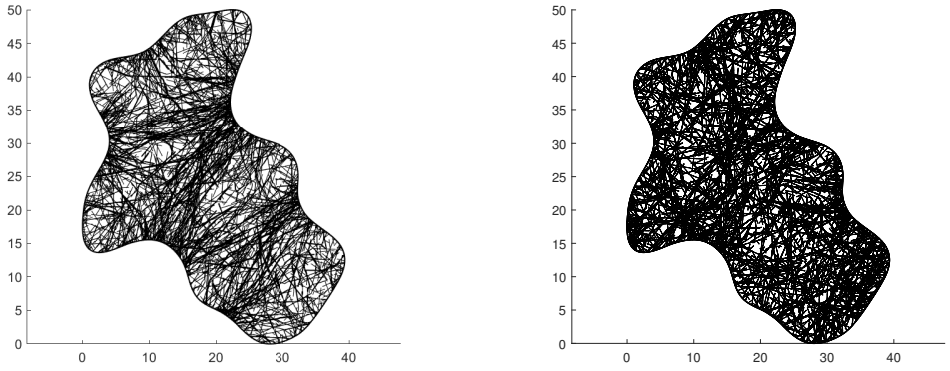
(a) ROP6 Control (b) ROP6 Mutant

Figure A.149: The signalling network model results of the DN ROP2 simulations in the 9th less developed pavement cell outline, where the figures show the ROP6 concentrations in the control and the mutant with non-linear scalebars.



(a) RIC1 Control (b) RIC1 Mutant

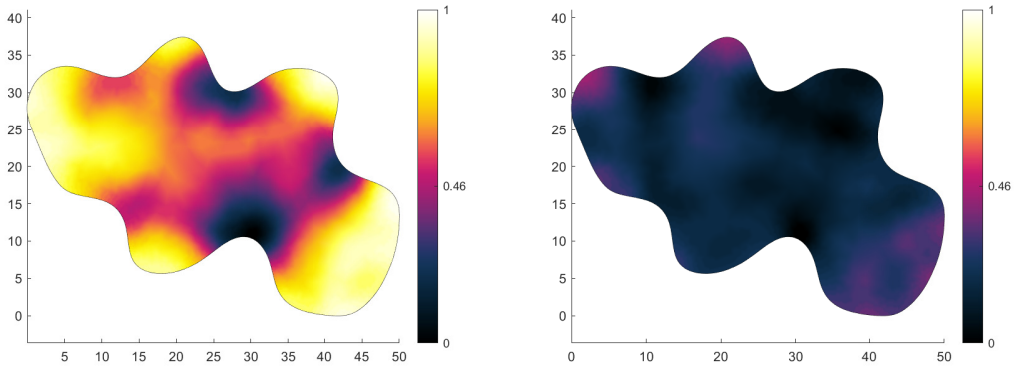
Figure A.150: The signalling network model results of the DN ROP2 simulations in the 9th less developed pavement cell outline, where the figures show the RIC1 concentrations in the control and the mutant with non-linear scalebars.



(a) Microtuble array control

(b) Microtubule array mutant

Figure A.151: The signalling network model results of the DN ROP2 simulations in the 9th less developed pavement cell outline, where the figures show the microtubule array in the control and the mutant.



(a) ROP2 Control

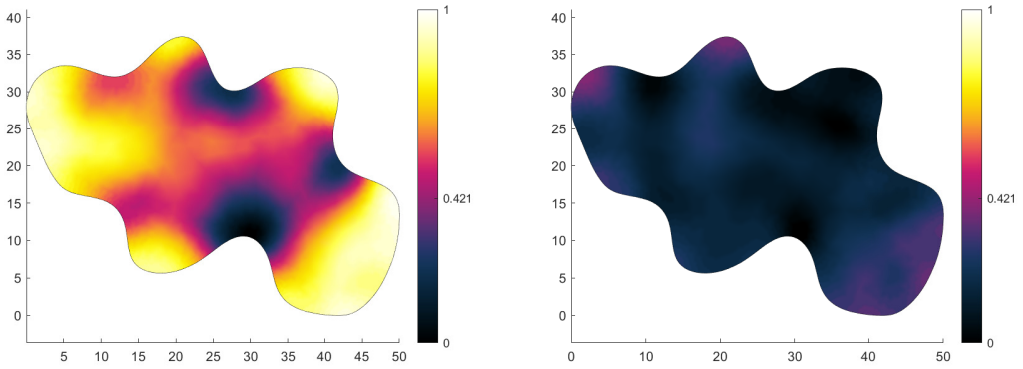
(b) ROP2 Mutant

Figure A.152: The signalling network model results of the DN ROP6 simulations in the 1st less developed pavement cell outline, where the figures show the ROP2 concentrations in the control and the mutant.

A.4.3.4 DN ROP6

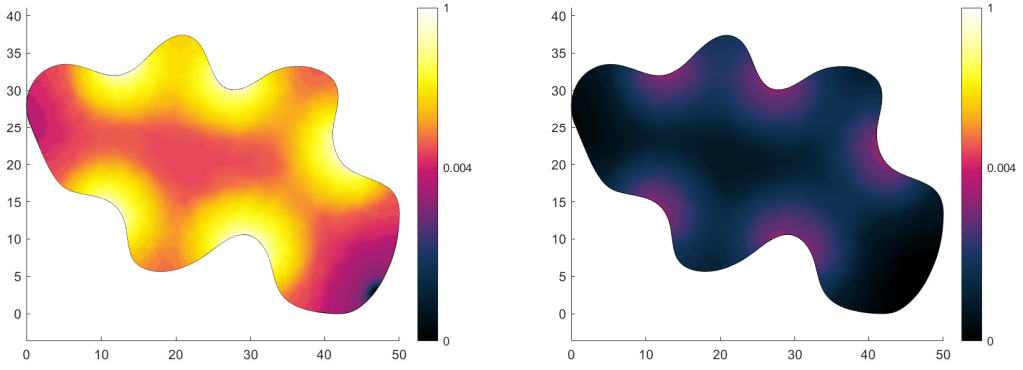
Here we show the supporting figures for the dominate negative ROP6 simulations in section 6.5.2.4.

A.4.4 Can the signalling network initiate lobes? additional figures



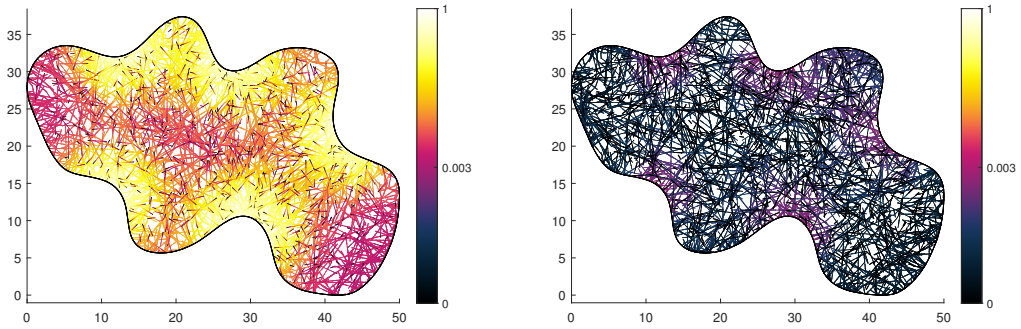
(a) RIC4 Control (b) RIC4 Mutant

Figure A.153: The signalling network model results of the DN ROP6 simulations in the 1st less developed pavement cell outline, where the figures show the RIC4 concentrations in the control and the mutant.



(a) ROP6 Control (b) ROP6 Mutant

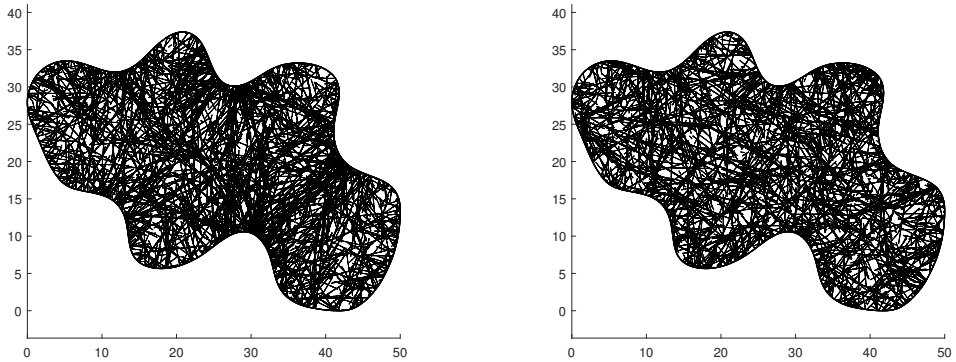
Figure A.154: The signalling network model results of the DN ROP6 simulations in the 1st less developed pavement cell outline, where the figures show the ROP6 concentrations in the control and the mutant with non-linear scalebars.



(a) RIC1 Control

(b) RIC1 Mutant

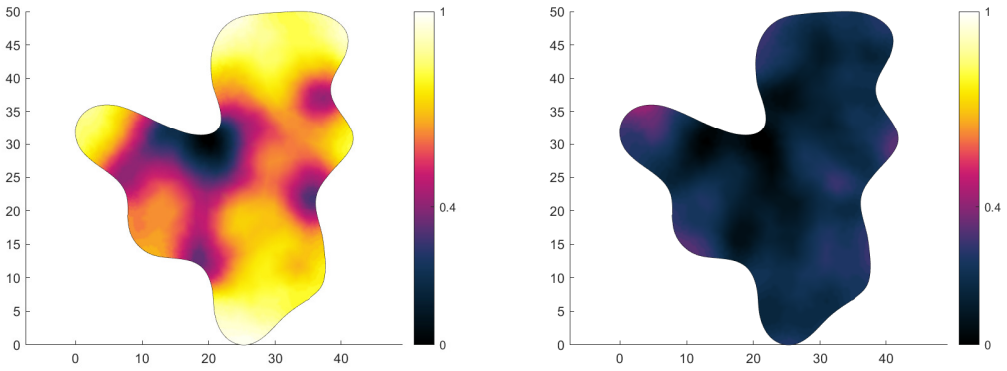
Figure A.155: The signalling network model results of the DN ROP6 simulations in the 1st less developed pavement cell outline, where the figures show the RIC1 concentrations in the control and the mutant with non-linear scalebars.



(a) Microtuble array control

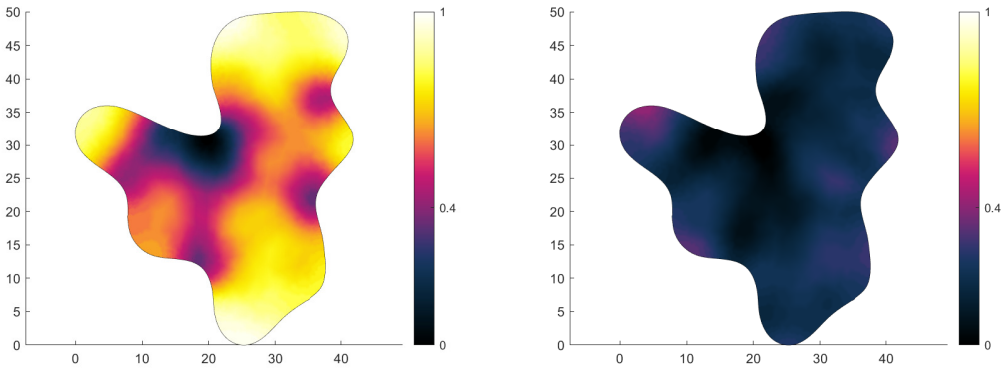
(b) Microtubule array mutant

Figure A.156: The signalling network model results of the DN ROP6 simulations in the 1st less developed pavement cell outline, where the figures show the microtubule array in the control and the mutant.



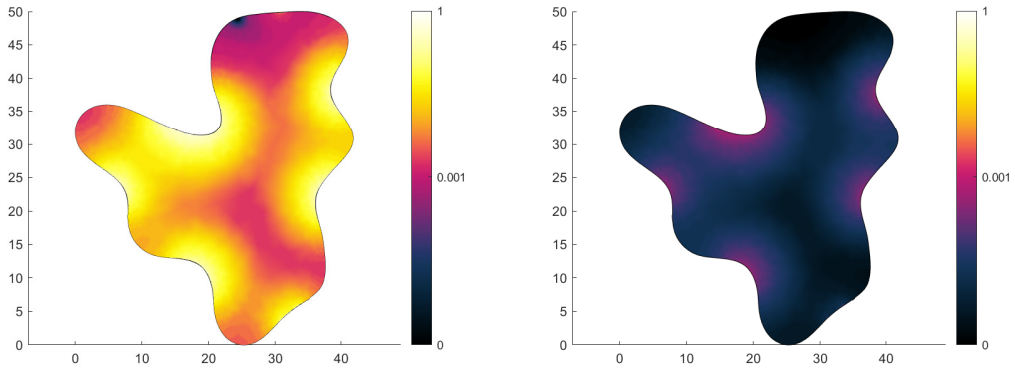
(a) ROP2 Control (b) ROP2 Mutant

Figure A.157: The signalling network model results of the DN ROP6 simulations in the 2nd less developed pavement cell outline, where the figures show the ROP2 concentrations in the control and the mutant.



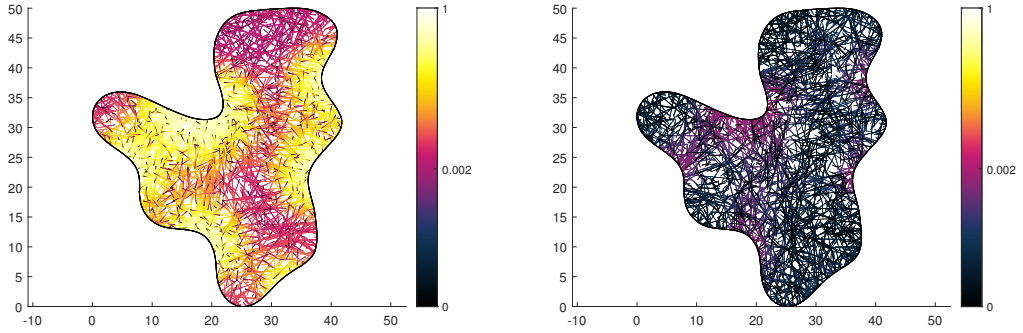
(a) RIC4 Control (b) RIC4 Mutant

Figure A.158: The signalling network model results of the DN ROP6 simulations in the 2nd less developed pavement cell outline, where the figures show the RIC4 concentrations in the control and the mutant.



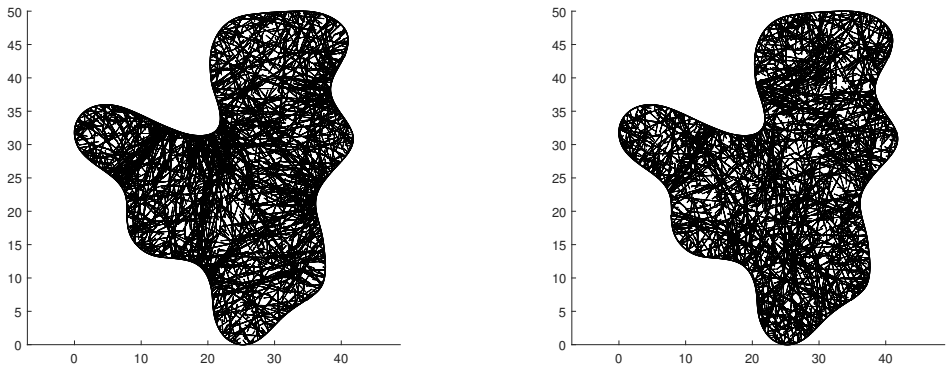
(a) ROP6 Control (b) ROP6 Mutant

Figure A.159: The signalling network model results of the DN ROP6 simulations in the 2nd less developed pavement cell outline, where the figures show the ROP6 concentrations in the control and the mutant with non-linear scalebars.



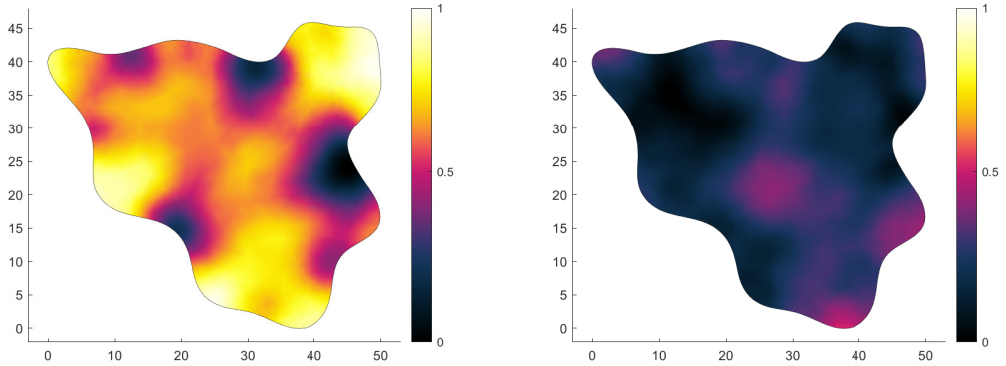
(a) RIC1 Control (b) RIC1 Mutant

Figure A.160: The signalling network model results of the DN ROP6 simulations in the 2nd less developed pavement cell outline, where the figures show the RIC1 concentrations in the control and the mutant with non-linear scalebars.



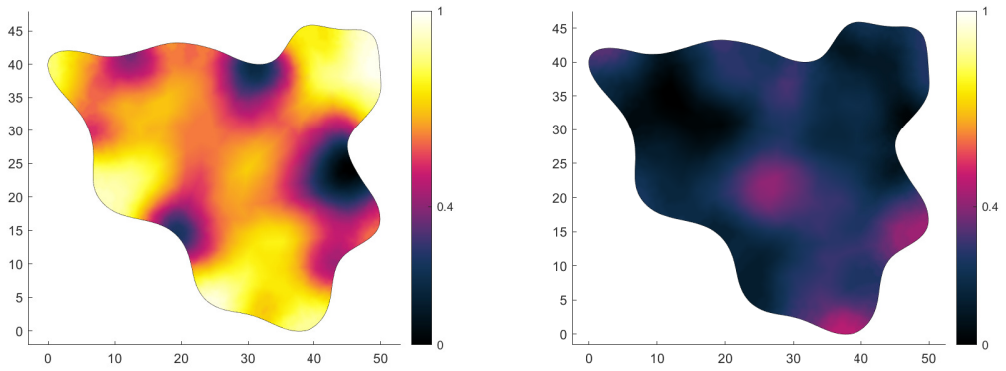
(a) Microtuble array control (b) Microtubule array mutant

Figure A.161: The signalling network model results of the DN ROP6 simulations in the 2nd less developed pavement cell outline, where the figures show the microtubule array in the control and the mutant.



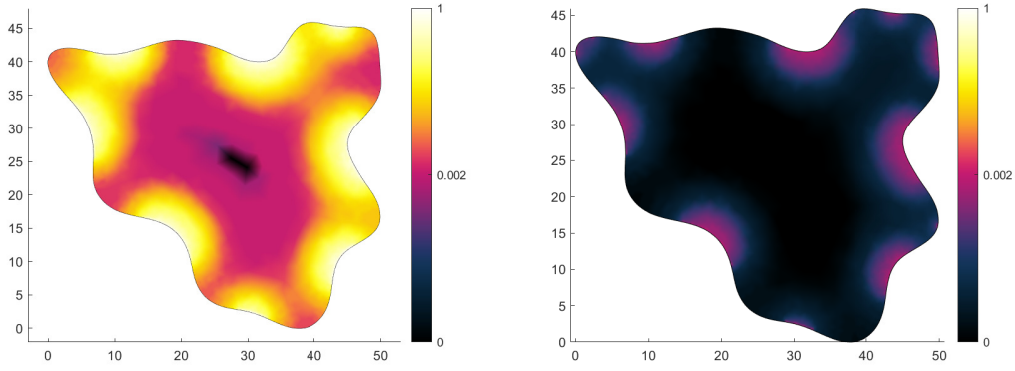
(a) ROP2 Control (b) ROP2 Mutant

Figure A.162: The signalling network model results of the DN ROP6 simulations in the 3rd less developed pavement cell outline, where the figures show the ROP2 concentrations in the control and the mutant.



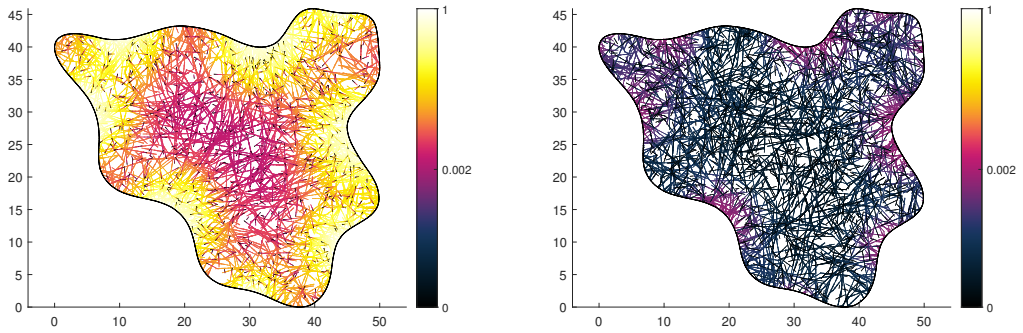
(a) RIC4 Control (b) RIC4 Mutant

Figure A.163: The signalling network model results of the DN ROP6 simulations in the 3rd less developed pavement cell outline, where the figures show the RIC4 concentrations in the control and the mutant.



(a) ROP6 Control (b) ROP6 Mutant

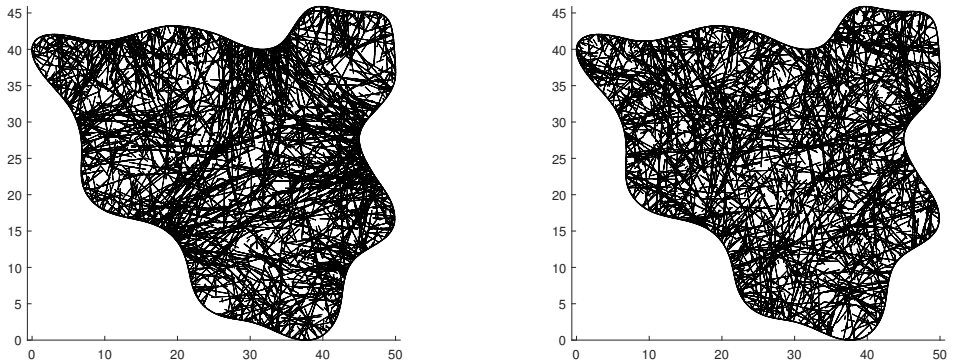
Figure A.164: The signalling network model results of the DN ROP6 simulations in the 3rd less developed pavement cell outline, where the figures show the ROP6 concentrations in the control and the mutant with non-linear scalebars.



(a) RIC1 Control

(b) RIC1 Mutant

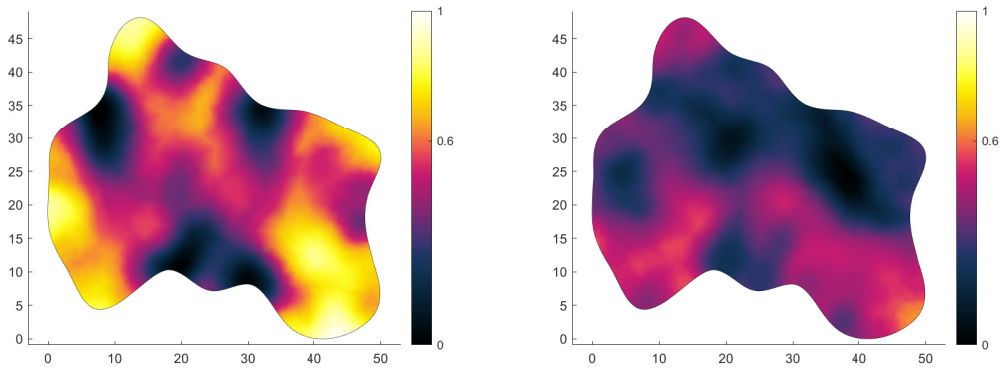
Figure A.165: The signalling network model results of the DN ROP6 simulations in the 3rd less developed pavement cell outline, where the figures show the RIC1 concentrations in the control and the mutant with non-linear scalebars.



(a) Microtuble array control

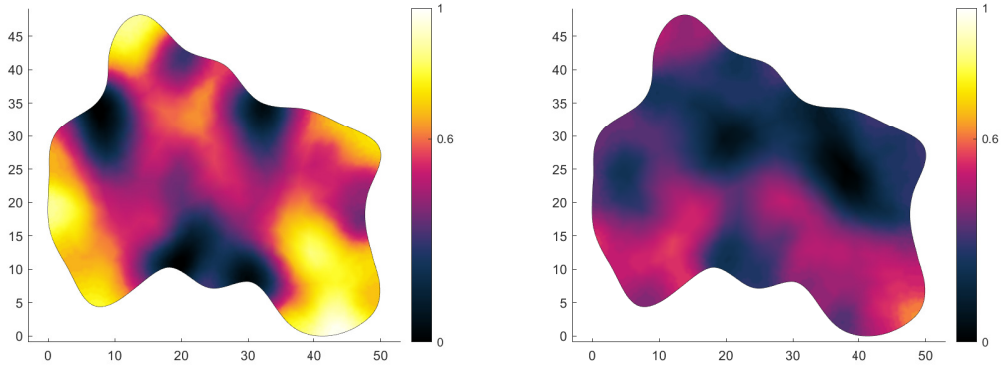
(b) Microtubule array mutant

Figure A.166: The signalling network model results of the DN ROP6 simulations in the 3rd less developed pavement cell outline, where the figures show the microtubule array in the control and the mutant.



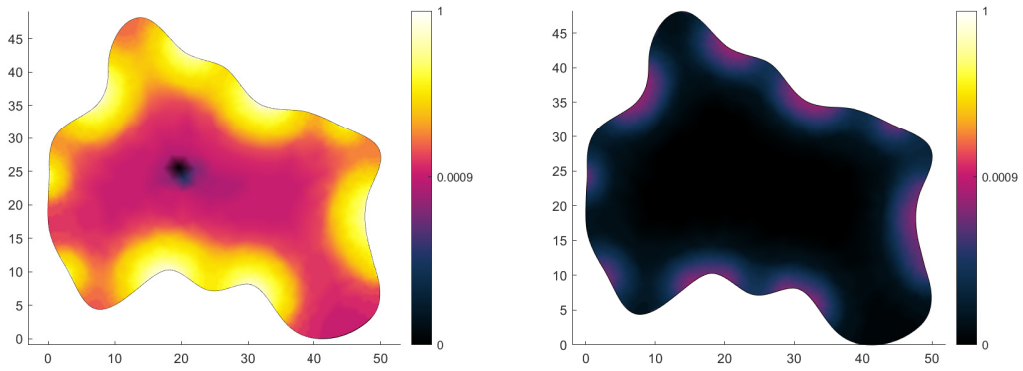
(a) ROP2 Control (b) ROP2 Mutant

Figure A.167: The signalling network model results of the DN ROP6 simulations in the 4th less developed pavement cell outline, where the figures show the ROP2 concentrations in the control and the mutant.



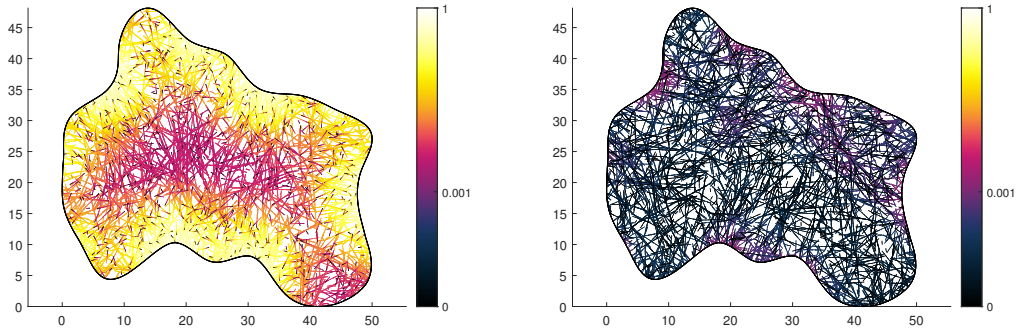
(a) RIC4 Control (b) RIC4 Mutant

Figure A.168: The signalling network model results of the DN ROP6 simulations in the 4th less developed pavement cell outline, where the figures show the RIC4 concentrations in the control and the mutant.



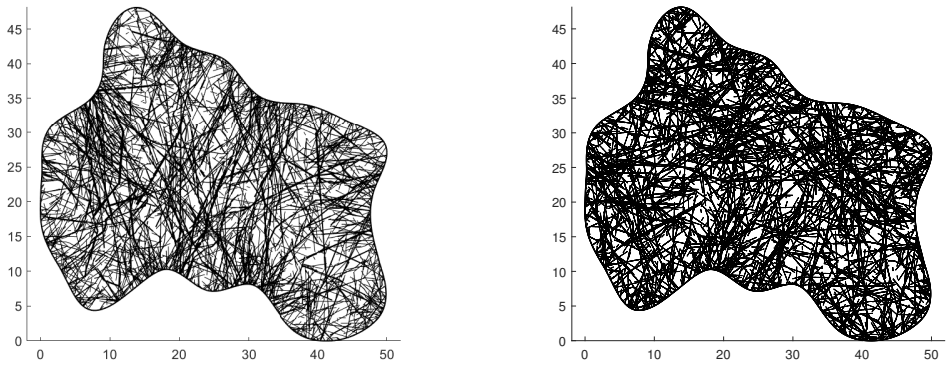
(a) ROP6 Control (b) ROP6 Mutant

Figure A.169: The signalling network model results of the DN ROP6 simulations in the 4th less developed pavement cell outline, where the figures show the ROP6 concentrations in the control and the mutant with non-linear scalebars.



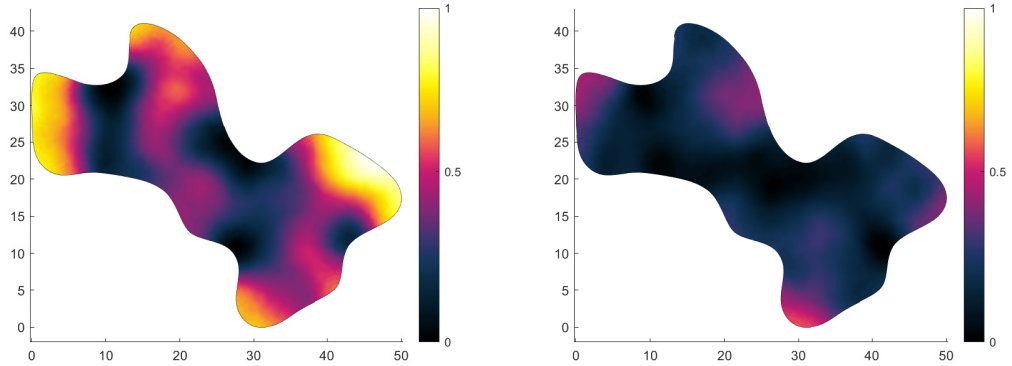
(a) RIC1 Control (b) RIC1 Mutant

Figure A.170: The signalling network model results of the DN ROP6 simulations in the 4th less developed pavement cell outline, where the figures show the RIC1 concentrations in the control and the mutant with non-linear scalebars.



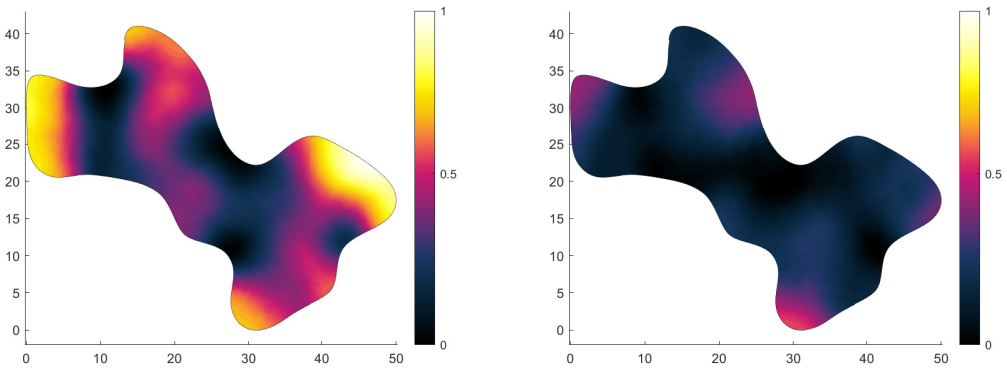
(a) Microtuble array control (b) Microtubule array mutant

Figure A.171: The signalling network model results of the DN ROP6 simulations in the 4th less developed pavement cell outline, where the figures show the microtubule array in the control and the mutant.



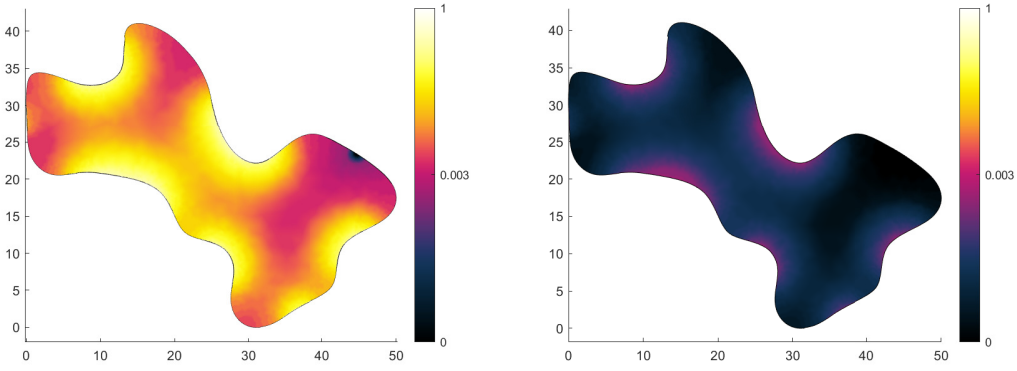
(a) ROP2 Control (b) ROP2 Mutant

Figure A.172: The signalling network model results of the DN ROP6 simulations in the 5th less developed pavement cell outline, where the figures show the ROP2 concentrations in the control and the mutant.



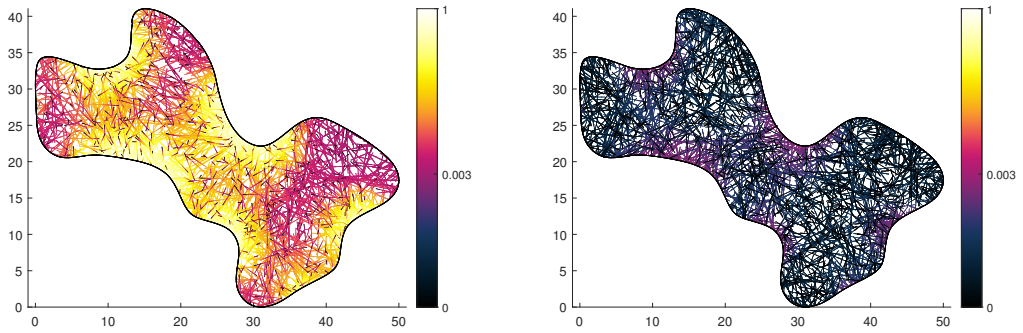
(a) RIC4 Control (b) RIC4 Mutant

Figure A.173: The signalling network model results of the DN ROP6 simulations in the 5th less developed pavement cell outline, where the figures show the RIC4 concentrations in the control and the mutant.



(a) ROP6 Control (b) ROP6 Mutant

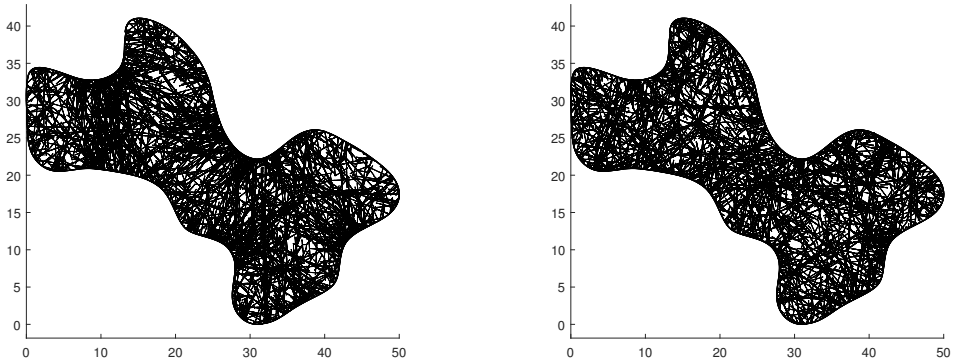
Figure A.174: The signalling network model results of the DN ROP6 simulations in the 5th less developed pavement cell outline, where the figures show the ROP6 concentrations in the control and the mutant with non-linear scalebars.



(a) RIC1 Control

(b) RIC1 Mutant

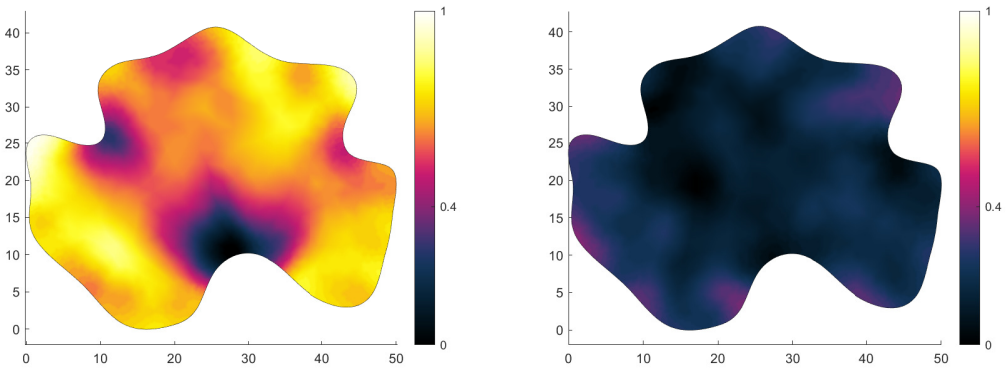
Figure A.175: The signalling network model results of the DN ROP6 simulations in the 5th less developed pavement cell outline, where the figures show the RIC1 concentrations in the control and the mutant with non-linear scalebars.



(a) Microtuble array control

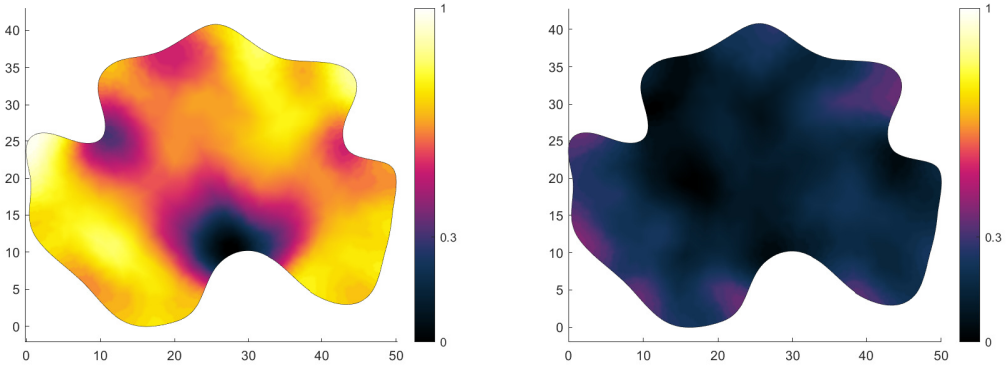
(b) Microtubule array mutant

Figure A.176: The signalling network model results of the DN ROP6 simulations in the 5th less developed pavement cell outline, where the figures show the microtubule array in the control and the mutant.



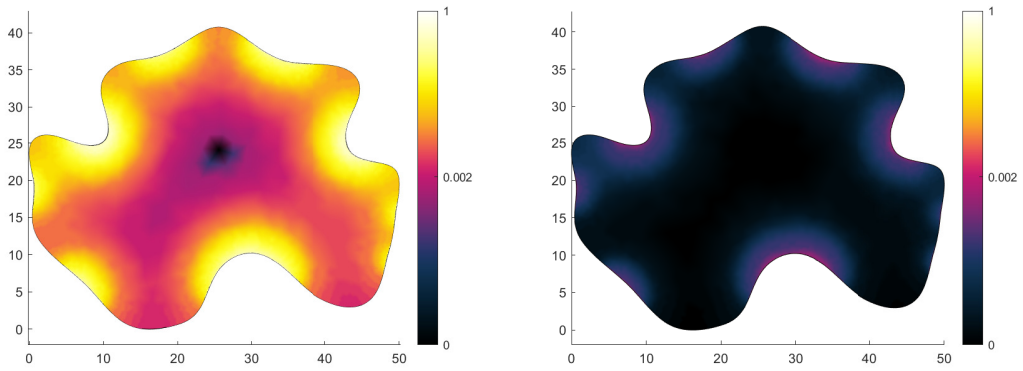
(a) ROP2 Control (b) ROP2 Mutant

Figure A.177: The signalling network model results of the DN ROP6 simulations in the 6th less developed pavement cell outline, where the figures show the ROP2 concentrations in the control and the mutant.



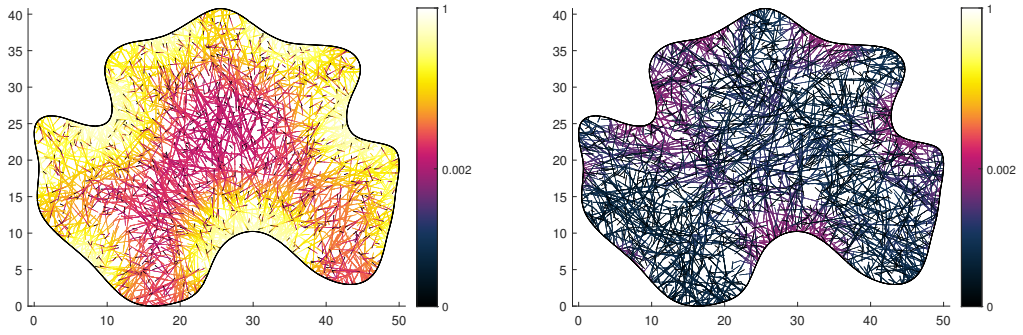
(a) RIC4 Control (b) RIC4 Mutant

Figure A.178: The signalling network model results of the DN ROP6 simulations in the 6th less developed pavement cell outline, where the figures show the RIC4 concentrations in the control and the mutant.



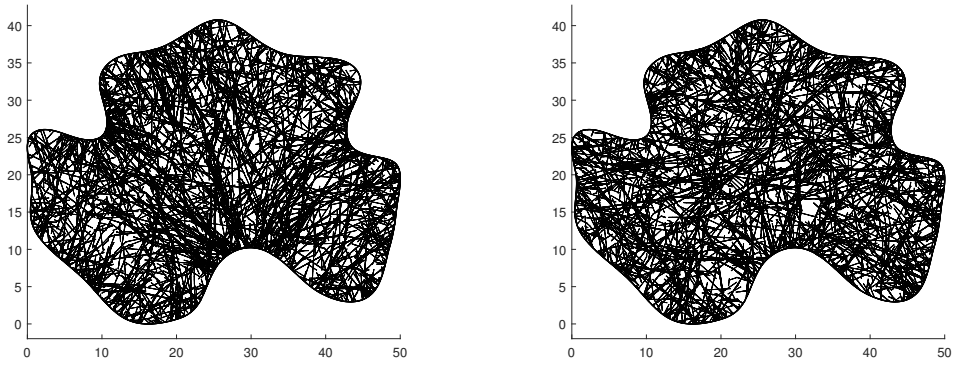
(a) ROP6 Control (b) ROP6 Mutant

Figure A.179: The signalling network model results of the DN ROP6 simulations in the 6th less developed pavement cell outline, where the figures show the ROP6 concentrations in the control and the mutant with non-linear scalebars.



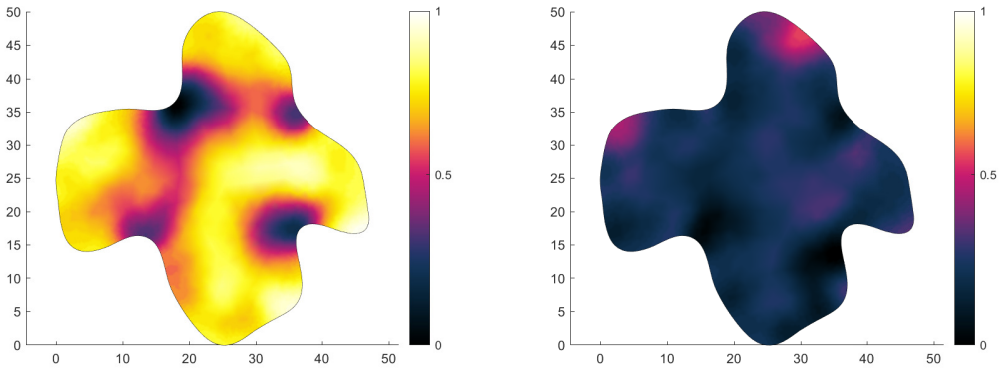
(a) RIC1 Control (b) RIC1 Mutant

Figure A.180: The signalling network model results of the DN ROP6 simulations in the 6th less developed pavement cell outline, where the figures show the RIC1 concentrations in the control and the mutant with non-linear scalebars.



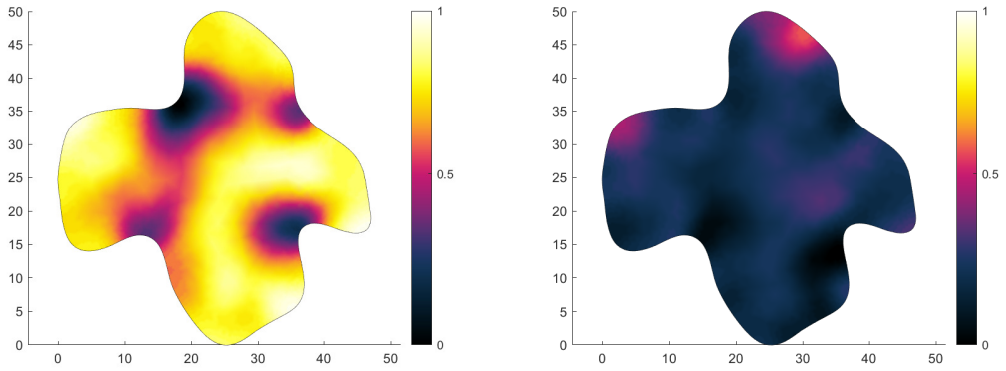
(a) Microtuble array control (b) Microtubule array mutant

Figure A.181: The signalling network model results of the DN ROP6 simulations in the 6th less developed pavement cell outline, where the figures show the microtubule array in the control and the mutant.



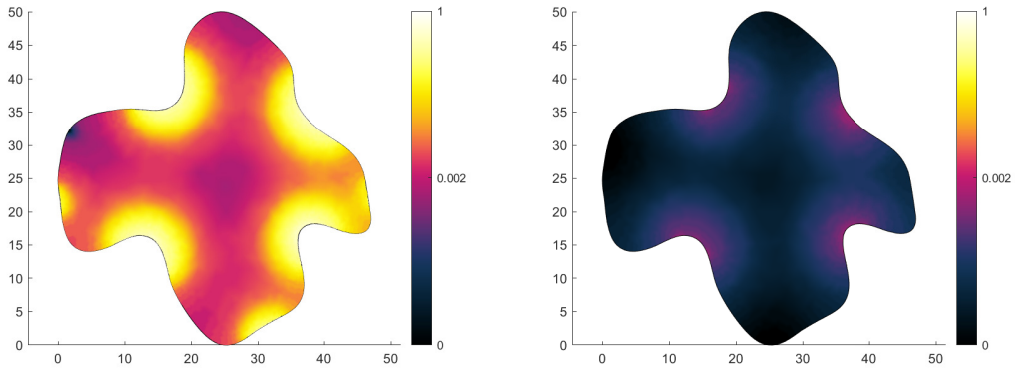
(a) ROP2 Control (b) ROP2 Mutant

Figure A.182: The signalling network model results of the DN ROP6 simulations in the 7th less developed pavement cell outline, where the figures show the ROP2 concentrations in the control and the mutant.



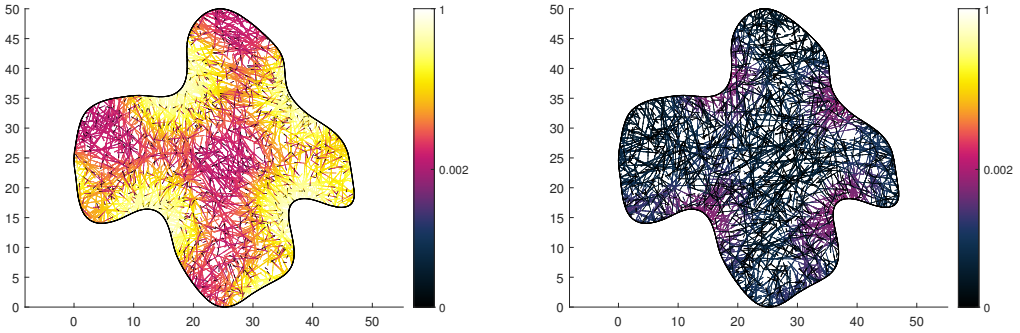
(a) RIC4 Control (b) RIC4 Mutant

Figure A.183: The signalling network model results of the DN ROP6 simulations in the 7th less developed pavement cell outline, where the figures show the RIC4 concentrations in the control and the mutant.



(a) ROP6 Control (b) ROP6 Mutant

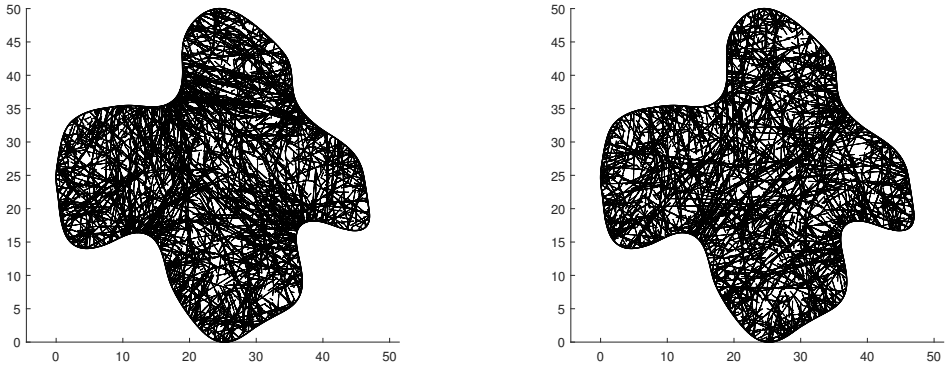
Figure A.184: The signalling network model results of the DN ROP6 simulations in the 7th less developed pavement cell outline, where the figures show the ROP6 concentrations in the control and the mutant with non-linear scalebars.



(a) RIC1 Control

(b) RIC1 Mutant

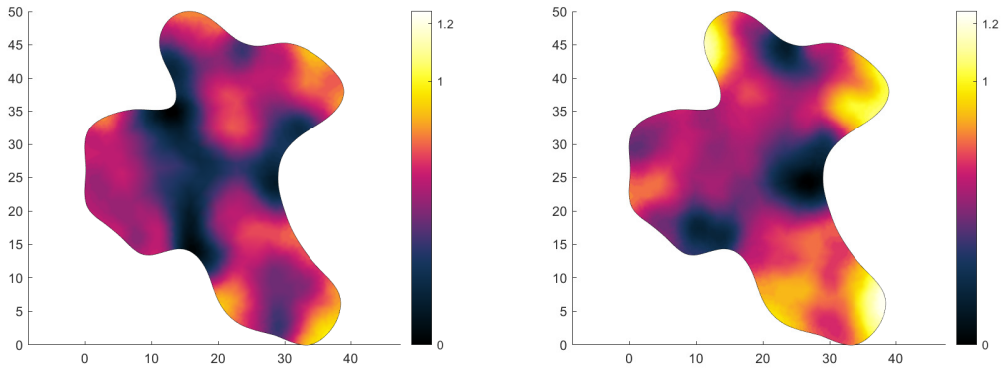
Figure A.185: The signalling network model results of the DN ROP6 simulations in the 7th less developed pavement cell outline, where the figures show the RIC1 concentrations in the control and the mutant with non-linear scalebars.



(a) Microtuble array control

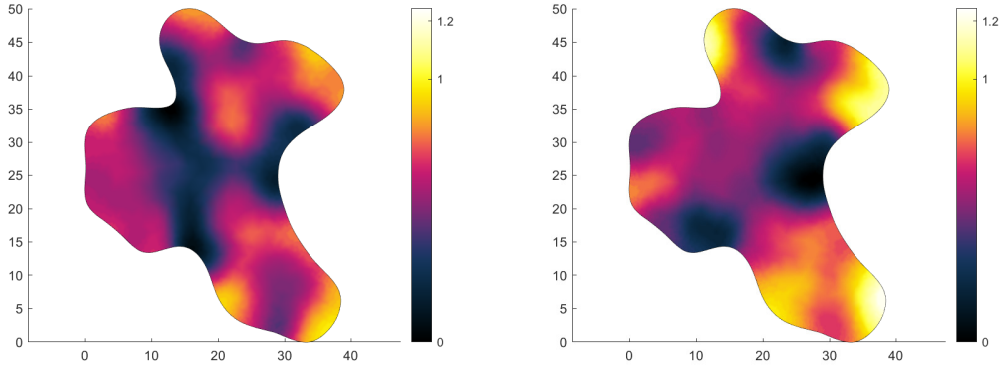
(b) Microtubule array mutant

Figure A.186: The signalling network model results of the DN ROP6 simulations in the 7th less developed pavement cell outline, where the figures show the microtubule array in the control and the mutant.



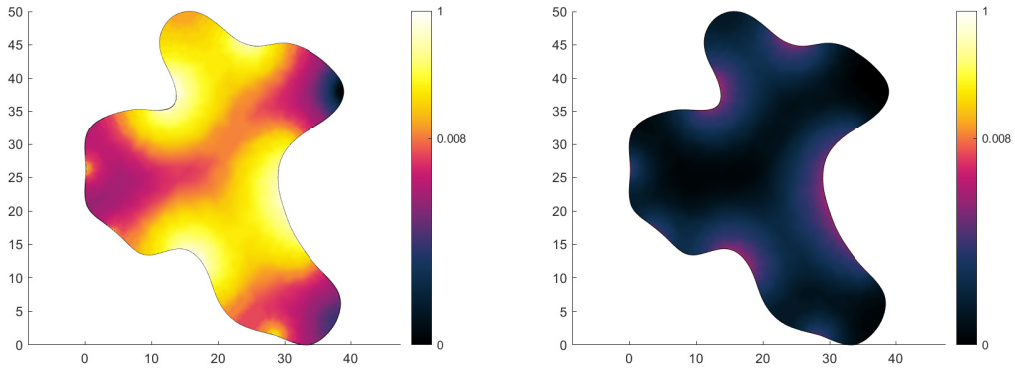
(a) ROP2 Control (b) ROP2 Mutant

Figure A.187: The signalling network model results of the DN ROP6 simulations in the 8th less developed pavement cell outline, where the figures show the ROP2 concentrations in the control and the mutant.



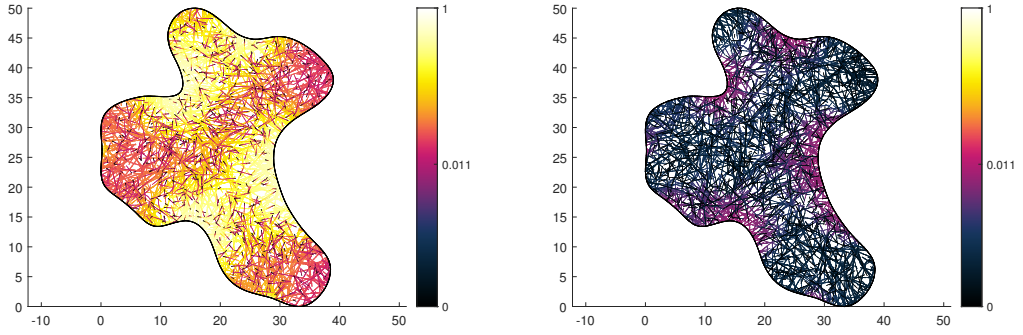
(a) RIC4 Control (b) RIC4 Mutant

Figure A.188: The signalling network model results of the DN ROP6 simulations in the 8th less developed pavement cell outline, where the figures show the RIC4 concentrations in the control and the mutant.



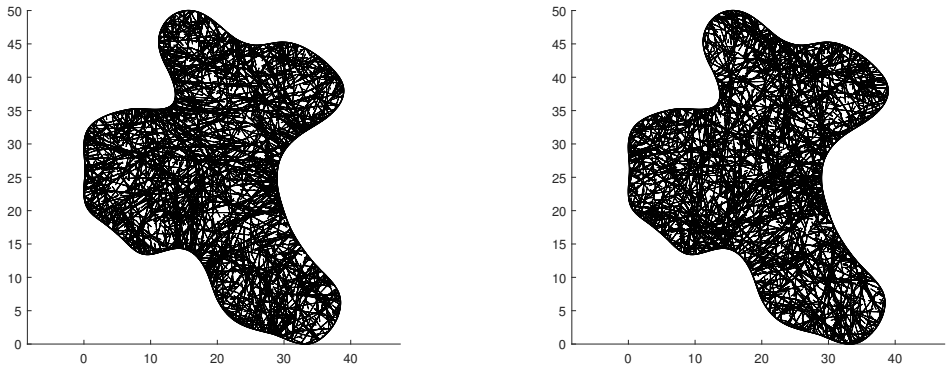
(a) ROP6 Control (b) ROP6 Mutant

Figure A.189: The signalling network model results of the DN ROP6 simulations in the 8th less developed pavement cell outline, where the figures show the ROP6 concentrations in the control and the mutant with non-linear scalebars.



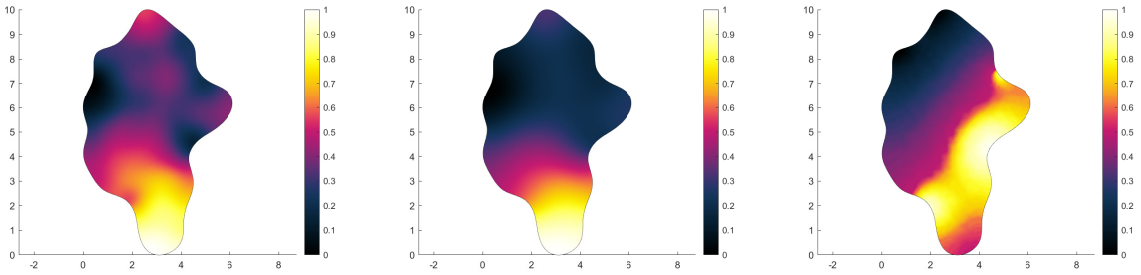
(a) RIC1 Control (b) RIC1 Mutant

Figure A.190: The signalling network model results of the DN ROP6 simulations in the 8th less developed pavement cell outline, where the figures show the RIC1 concentrations in the control and the mutant with non-linear scalebars.



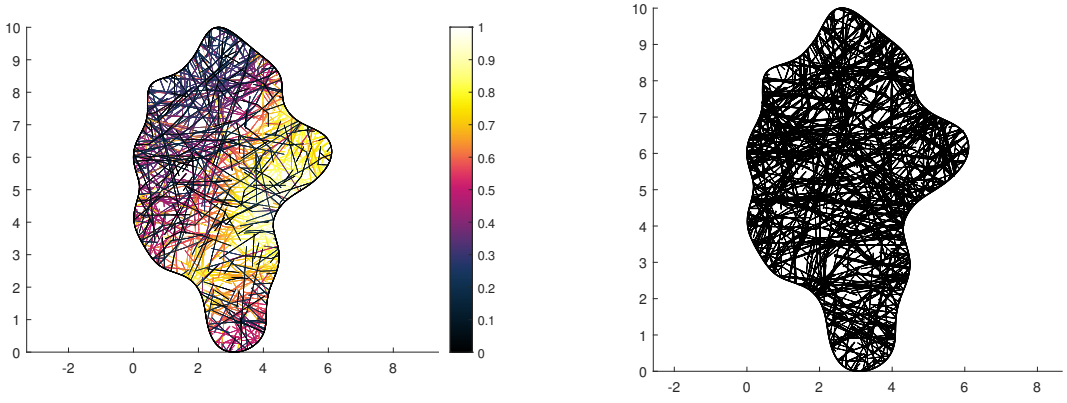
(a) Microtuble array control (b) Microtubule array mutant

Figure A.191: The signalling network model results of the DN ROP6 simulations in the 8th less developed pavement cell outline, where the figures show the microtubule array in the control and the mutant.



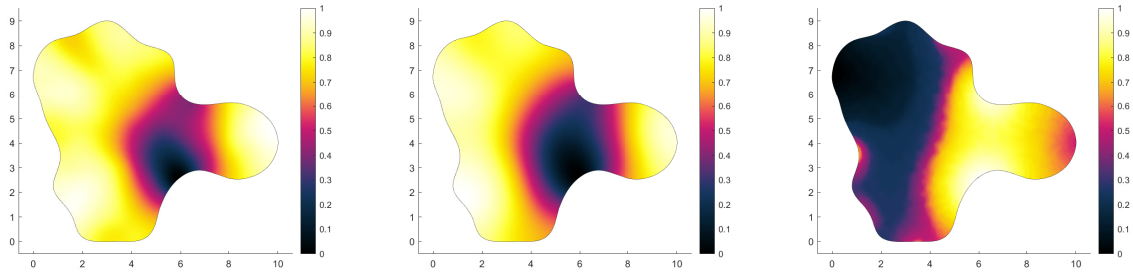
(a) ROP2 (b) RIC4 (c) ROP6

Figure A.192: The signalling network model results in the 1st young pavement cell outline, where the figures show the different proteins concentrations.



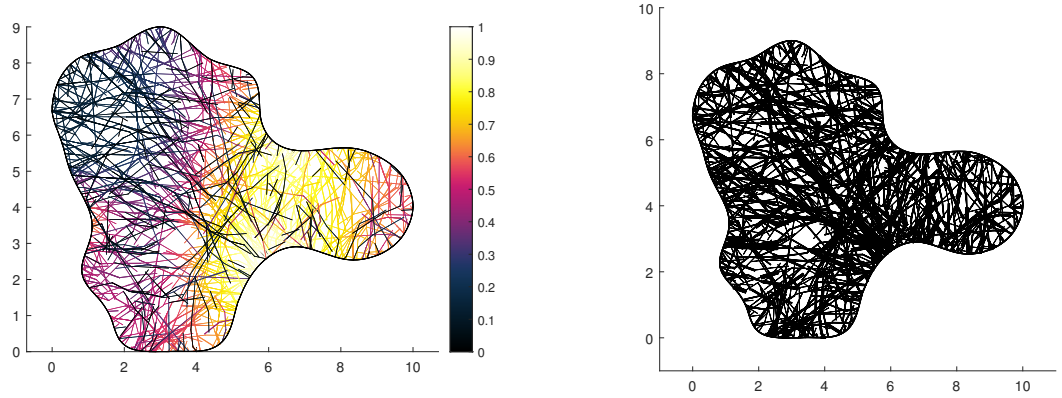
(a) RIC1 (b) Microtubule array

Figure A.193: The signalling network model results in the 1st young pavement cell outline, where the figures show the RIC1 concentration and the microtubule array.



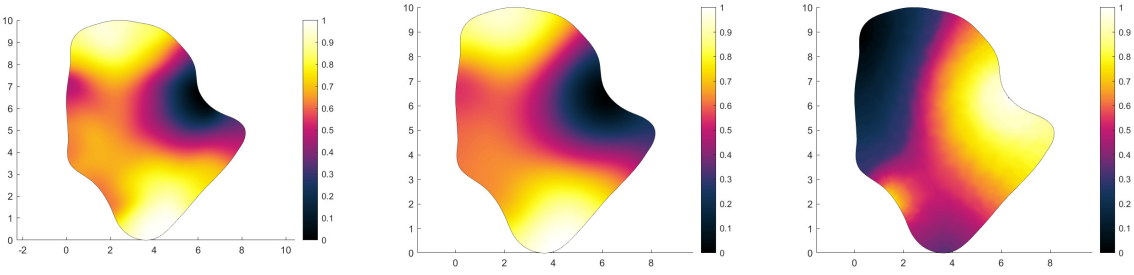
(a) ROP2 (b) RIC4 (c) ROP6

Figure A.194: The signalling network model results in the 2nd young pavement cell outline, where the figures show the different proteins concentrations.



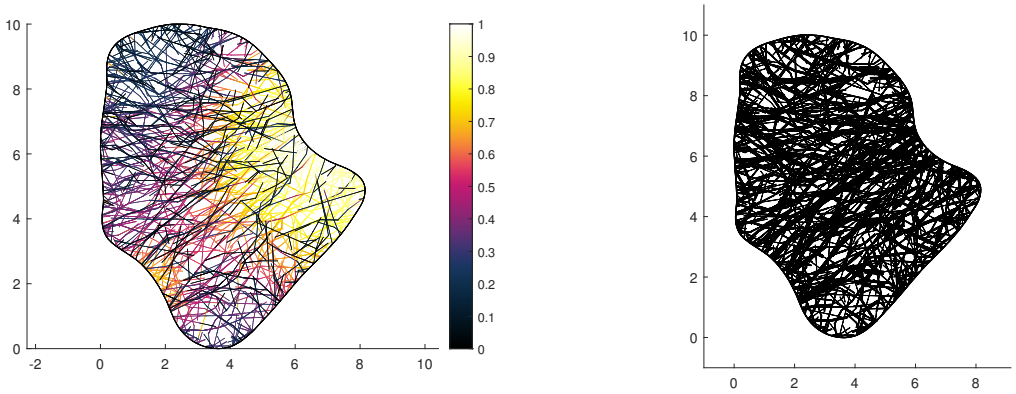
(a) RIC1 (b) Microtubule array

Figure A.195: The signalling network model results in the 2nd young pavement cell outline, where the figures show the RIC1 concentration and the microtubule array.



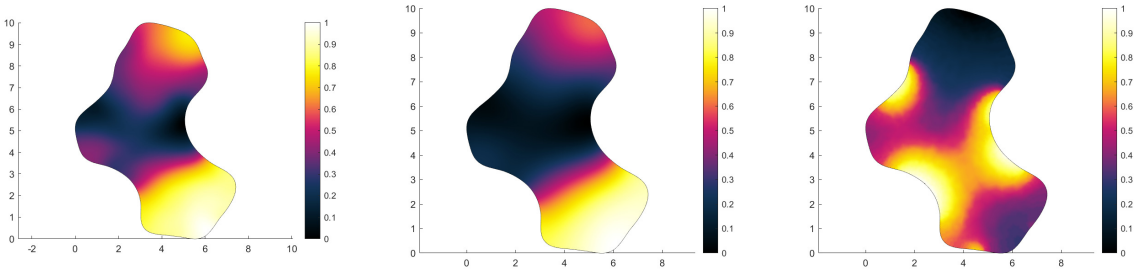
(a) ROP2 (b) RIC4 (c) ROP6

Figure A.196: The signalling network model results in the 3rd young pavement cell outline, where the figures show the different proteins concentrations.



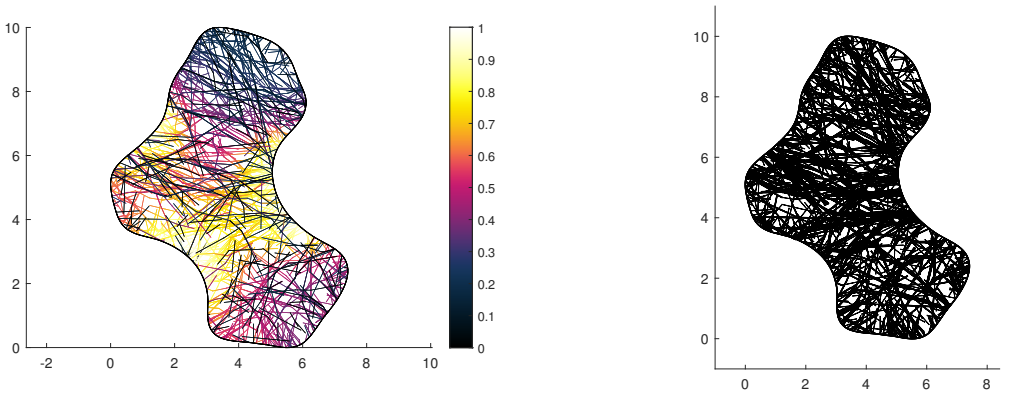
(a) RIC1 (b) Microtubule array

Figure A.197: The signalling network model results in the 3rd young pavement cell outline, where the figures show the RIC1 concentration and the microtubule array.



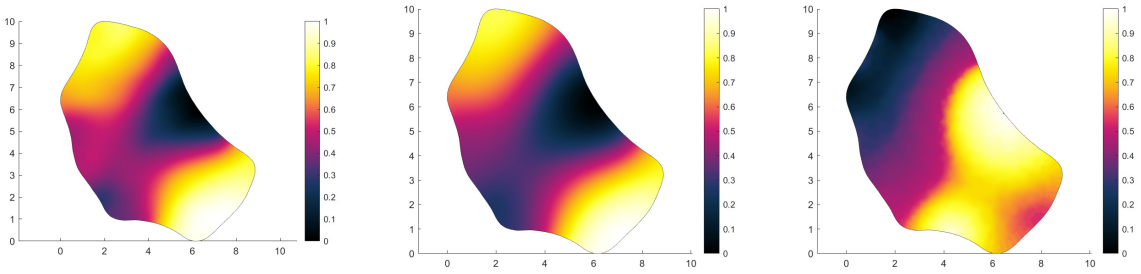
(a) ROP2 (b) RIC4 (c) ROP6

Figure A.198: The signalling network model results in the 4th young pavement cell outline, where the figures show the different proteins concentrations.



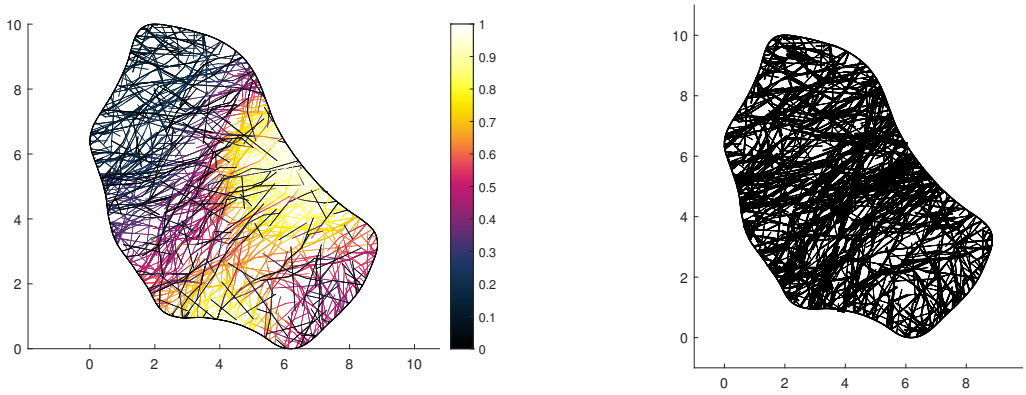
(a) RIC1 (b) Microtubule array

Figure A.199: The signalling network model results in the 4th young pavement cell outline, where the figures show the RIC1 concentration and the microtubule array.



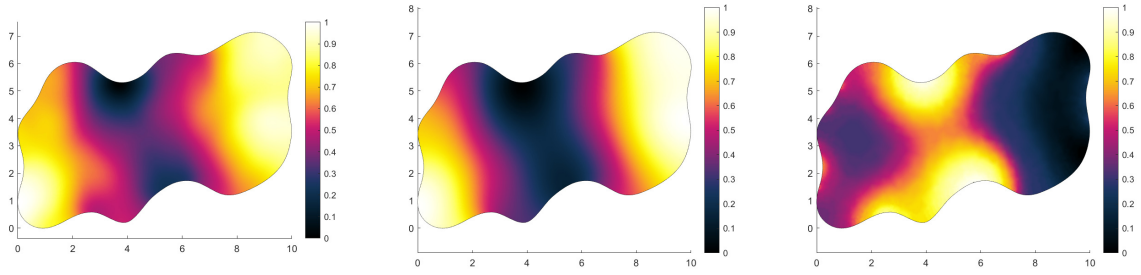
(a) ROP2 (b) RIC4 (c) ROP6

Figure A.200: The signalling network model results in the 5th young pavement cell outline, where the figures show the different proteins concentrations.



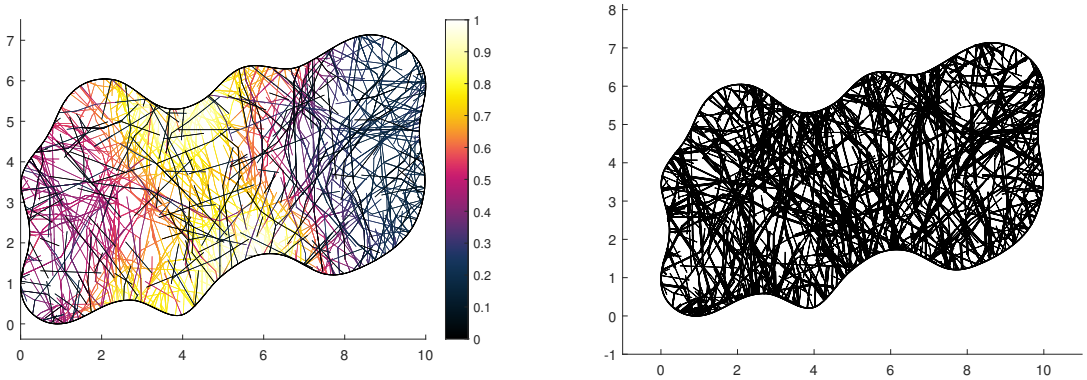
(a) RIC1 (b) Microtubule array

Figure A.201: The signalling network model results in the 5th young pavement cell outline, where the figures show the RIC1 concentration and the microtubule array.



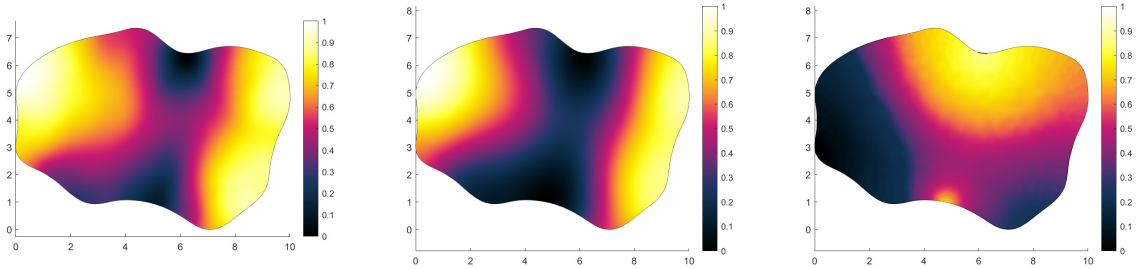
(a) ROP2 (b) RIC4 (c) ROP6

Figure A.202: The signalling network model results in the 6th young pavement cell outline, where the figures show the different proteins concentrations.



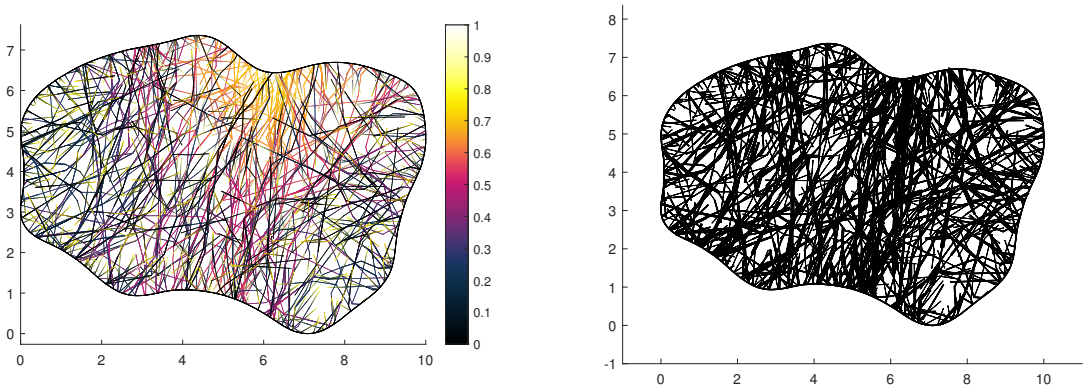
(a) RIC1 (b) Microtubule array

Figure A.203: The signalling network model results in the 6th young pavement cell outline, where the figures show the RIC1 concentration and the microtubule array.



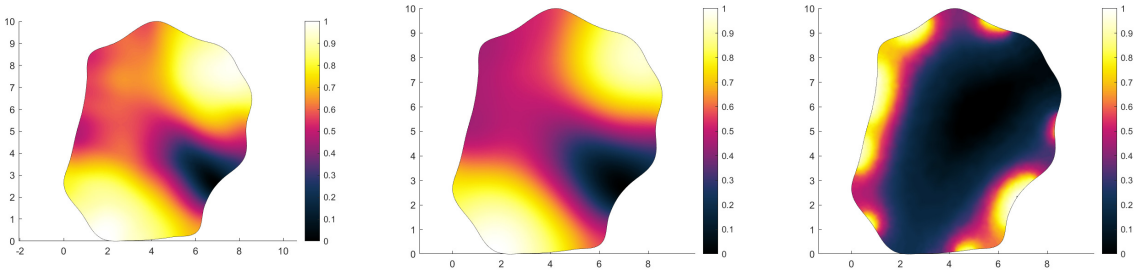
(a) ROP2 (b) RIC4 (c) ROP6

Figure A.204: The signalling network model results in the 8th young pavement cell outline, where the figures show the different proteins concentrations.



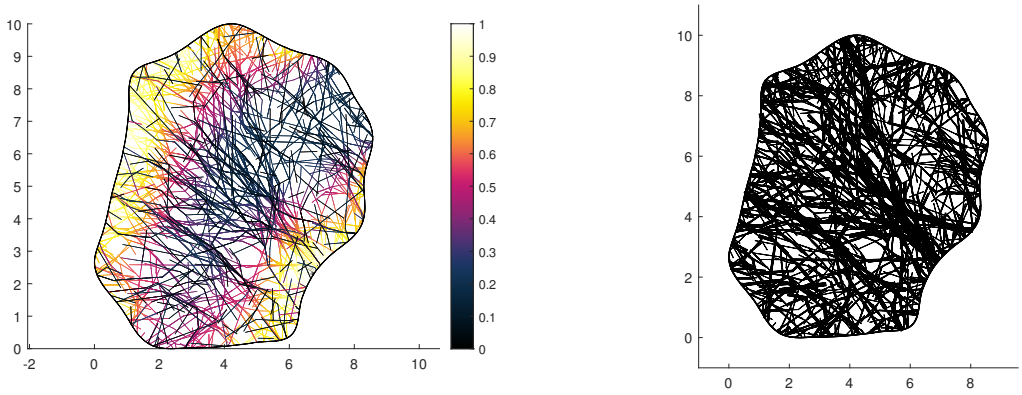
(a) RIC1 (b) Microtubule array

Figure A.205: The signalling network model results in the 8th young pavement cell outline, where the figures show the RIC1 concentration and the microtubule array.



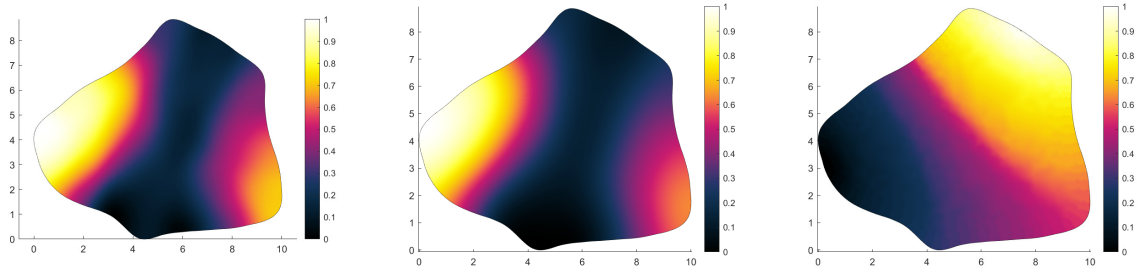
(a) ROP2 (b) RIC4 (c) ROP6

Figure A.206: The signalling network model results in the 9th young pavement cell outline, where the figures show the different proteins concentrations.



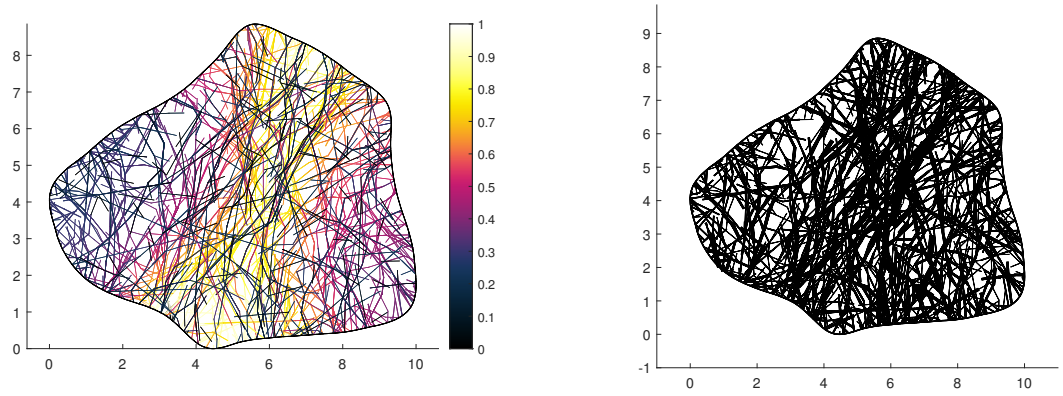
(a) RIC1 (b) Microtubule array

Figure A.207: The signalling network model results in the 9th young pavement cell outline, where the figures show the RIC1 concentration and the microtubule array.



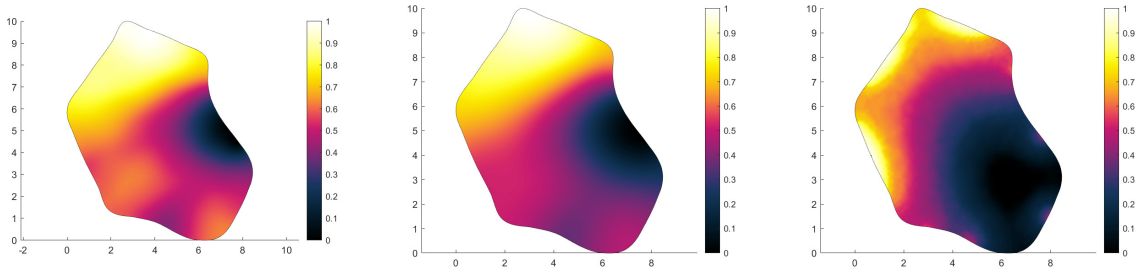
(a) ROP2 (b) RIC4 (c) ROP6

Figure A.208: The signalling network model results in the 11th young pavement cell outline, where the figures show the different proteins concentrations.



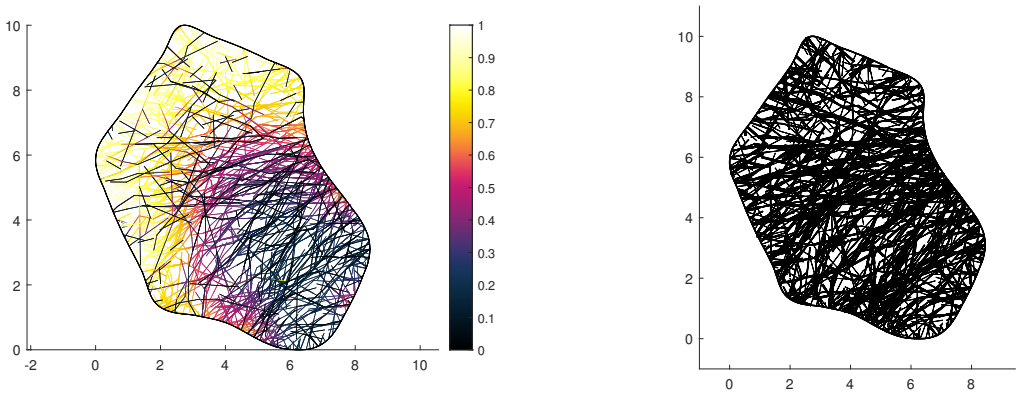
(a) RIC1 (b) Microtubule array

Figure A.209: The signalling network model results in the 11th young pavement cell outline, where the figures show the RIC1 concentration and the microtubule array.



(a) ROP2 (b) RIC4 (c) ROP6

Figure A.210: The signalling network model results in the 12th young pavement cell outline, where the figures show the different proteins concentrations.



(a) RIC1 (b) Microtubule array

Figure A.211: The signalling network model results in the 12th young pavement cell outline, where the figures show the RIC1 concentration and the microtubule array.

A.5 Vertex element model

A.5.1 Mesh testing

Simulations are needed to test the effectiveness of the approximations and the effect of making the solver more robust on the computation time. These tests are also completed across various mesh and time-step sizes to investigate their effect on the different solvers.

These test simulations are done on a bounded 9 cell system (with no bending stiffness) where each cell is of length $10\mu m$ (figure 7.1) with constant parameters as set in table 7.1 and all anisotropy directions set as $\mathbf{a} = (0, 1)^T$. The different mesh sizes tested are $h^* = 1, \frac{2}{3}, 0.5$ (where h^* is defined in equation (6.2.6)) with 2192, 4880, 5936 degrees of freedom respectively which are all tested across the different time steps $\Delta t = 0.1, 0.01$. Note that the time step $\Delta t = 0.001$ is not tested as for some meshes, the computational time quickly becomes excessive. The simulations are stopped when the absolute value of the growth rate of the total cell area decreases below ϵ_G ($\epsilon_G = 0.001$) for the past 10 time steps (to ensure it actually has stopped growing). At this stage, the cells have reached a steady-state where the turgor imposed stress has balanced with the elastic stress. The growth rates are calculated using the backwards Euler method as stated in section 7.2.5.1 and the total area of the 9 cells is found by using the MATLAB function `polyarea`.

The tables below list the total iterations, computation time in hours, and the number of time steps to reach the steady-state. This will allow us to compare the efficiency and accuracy of each method. The different solver methods to be compared are the base case, meaning the basic Newton's method without any additional optimisation tricks (equation (7.2.43)), Newton's method plus the optimisation of the Jacobian, the Jacobian optimisation with Brodyen's method, and then the Jacobian optimisation with Brodyen's method using the damped Newton's method. These methods are referred to as the base, Jacobian optimised, Broydens, and damped, respectively. Note that the base case is only run for $\Delta t = 0.1$ and for $h^* = 1$ and $\frac{2}{3}$ as in the other sceneries, it takes too long to reach the steady-state (plus 18 days). Some initial tests were also run with $h^* = 0.01$, but

both the Broyden's method and the damped method failed to converge when $\Delta t = 0.1$, however they did converge when $\Delta t = 0.01$ but computation time was excessive (plus 27 days), so the simulations were stopped. This lack of convergence is a problem due to Broyden's method being an approximation of the Jacobian and thus introducing errors when they are many degrees of freedom. It is therefore not always applicable. In both cases, the Jacobian optimisation solver converged but was stopped as computation time was excessive.

Table A.3: Test simulations for mesh size $h^* = 1$, with time stepping $\Delta t = 0.1, 0.01$ where the numbers with no brackets are from the simulations with $\Delta t = 0.1$ and those with the brackets are from the simulation with $\Delta t = 0.01$

Method	Time (Hours)	Total iterations	Time steps in the simulation
Base	140.216666 (−−)	983 (−−)	440 (−−)
Jacobian optimised	3.7 (41.01666)	983 (9856)	440 (4320)
Broydens	1.783333 (11)	1320 (10875)	440 (4320)
Damped	1.766666 (15.6)	1893 (15751)	440 (4320)

Table A.4: Test simulations for mesh size $h^* = \frac{2}{3}$, with time stepping $\Delta t = 0.1, 0.01$ where the numbers with no brackets are from the simulations with $\Delta t = 0.1$ and those with the brackets are from the simulation with $\Delta t = 0.01$

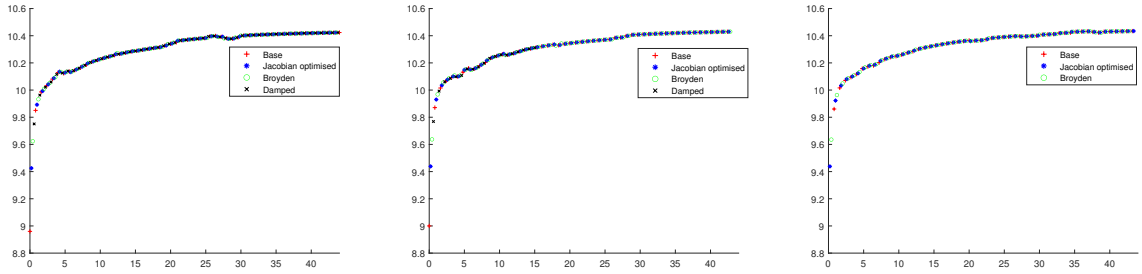
Method	Time (Hours)	Total iterations	Finishing time
Base	4860.13333 (−−)	955 (−−)	412 (−−)
Jacobian optimised	7 (66.68333333)	987 (9684)	430 (4216)
Broydens	3.65 (36.2833333)	1313 (10774)	430 (4216)
Damped	3.5833333 (46.816666)	1902 (17286)	430 (4216)

Table A.5: Test simulations for mesh size $h^* = 0.5$, with time stepping $\Delta t = 0.1, 0.01$ where the numbers with no brackets are the numbers from the simualtions with $\Delta t = 0.1$ and those with the brackets are the values from the simulation with $\Delta t = 0.01$

Method	Time (Hours)	Total iterations	Finishing time
Base	$--$ $(--)$	$--$ $(--)$	$--$ $(--)$
Jacobian optimised	12.933333 (110.1)	1127 (12338)	435 (4272)
Broydens	5.55 (48)	1369 (12981)	435 (4273)
Damped	6.1833333 (44.4666666)	1938 (17606)	435 (4273)

The first thing to be noted is the significant improvement the Jacobian optimisation method has on the computation time of the solver (tables A.3, A.4, A.5). This effect enhances the applicability of the vertex element model, as the computation time gets quickly excessive (especially for finer meshes) when using the base solver (table A.4). As expected (as the difference between the optimised and the fully calculated Jacobian is equal to numerical error), there also does not seem to be any compromise on the accuracy as complete agreement can be seen between the Jacobian optimised and base area curves (figure A.212). The second thing to be noticed is Broyden's method's decrease of the computation in all cases, however, the total iterations have increased, implying that it takes more iteration to converge to a solution at each time step, probably as a result of the Jacobien being approximated. Broyden's method is also seen to be accurate by observing that its area curve matches the base's case curve and the finishing times are very similar. Importantly, the damped Newton's method, with its advantages of improving the robustness of the solver, does not seem to affect computation time greatly and, in some instances, decreases it.

When $\Delta t = 0.1$ and $h^* = 1$ the area curve appears not to be smooth, possibly showing some instabilities in the system (figure A.212a). However, as we decrease the mesh size (figure A.212b and c), this curve gets increasingly smooth (where decreasing time showed less of an effect) and displays a more realistic steady increase in area. This demonstrates



(a) (b) (c)

Figure A.212: The area curves over different meshsizes with a)$h = 1$ b) $h = \frac{2}{3}$ c) $h = 0.5$.

Table A.6: Boundary growth rate variable effect on the relative average aspect ratio

Tissue growth rate / Simulation type	0.1	0.3	0.5	0.7	0.9
Control	0.7804	0.8044	0.8037	0.8069	0.8040
Sim 1	0.8340	0.8350	0.8353	0.8333	0.8321
Sim 2	1.1807	1.1498	1.1705	1.1885	1.2006
Sim 3	1.3983	1.3884	1.3854	1.3990	1.3976
Sim 4	2.1717	2.2961	2.4737	2.3149	2.3715

the importance of a small mesh size, but care also needs to be taken not to make it too fine as that could cause excessive run times.

A.5.2 Relative aspect ratio pavement cell calculation

To confirm that pavement cell lobes are developing further, the lobes aspect ratios are calculated, which is found by dividing the amplitude by the width. The relative average aspect ratios are found by dividing the average aspect ratios of all the lobes in a pavement cell at $t = 500$ by the average at $t = 0$. The lobe aspect ratios are calculated using the lobe indicator variable κ to inform us where the lobe and indent tips are. Below are the relative average aspect ratios numbers for the different simulations (tables A.6 and A.7)which correlate with the circularity indexes in section 7.3.1.1.

Table A.7: The effect of the changing the spring growth rate on the average relative lobe aspect ratio increase.

Spring growth rate / Simulation type	0.1	0.3	0.5	0.7	0.9
Sim 4	1.4307	1.4530	1.4719	1.4381	1.4748

Bibliography

M. Adamowski and J. Friml. Pin-dependent auxin transport: action, regulation, and evolution. *The Plant Cell*, 27(1):20–32, 2015.

I. Ahuja, R. C. de Vos, A. M. Bones, and R. D. Hall. Plant molecular stress responses face climate change. *Trends in Plant Science*, 15(12):664–674, 2010.

B. Alberts, A. Johnson, J. Lewis, M. Raff, K. Roberts, and P. Walter. *Molecular Biology of the Cell*. Garland Science, 2002.

O. Ali and J. Traas. Force-driven polymerization and turgor-induced wall expansion. *Trends in Plant Science*, 21(5):398–409, 2016.

J. F. Allard, J. C. Ambrose, G. O. Wasteneys, and E. N. Cytrynbaum. A mechanochemical model explains interactions between cortical microtubules in plants. *Biophysical Journal*, 99(4):1082–1090, 2010a.

J. F. Allard, G. O. Wasteneys, and E. N. Cytrynbaum. Mechanisms of self-organization of cortical microtubules in plants revealed by computational simulations. *Molecular Biology of the Cell*, 21(2):278–286, 2010b.

B. Altartouri and A. Geitmann. Understanding plant cell morphogenesis requires real-time monitoring of cell wall polymers. *Current Opinion in Plant Biology*, 23:76–82, 2015.

B. Altartouri, A. J. Bidhendi, T. Tani, J. Suzuki, C. Conrad, Y. Chebli, N. Liu, C. Karunakaran, G. Scarcelli, and A. Geitmann. Pectin chemistry and cellulose crys-

tallinity govern pavement cell morphogenesis in a multi-step mechanism. *Plant Physiology*, 181(1):127–141, 2019.

C. T. Anderson, A. Carroll, L. Akhmetova, and C. Somerville. Real-time imaging of cellulose reorientation during cell wall expansion in arabidopsis roots. *Plant Physiology*, 152(2):787–796, 2010.

W. J. Armour, D. A. Barton, A. M. Law, and R. L. Overall. Differential growth in periclinal and anticlinal walls during lobe formation in arabidopsis cotyledon pavement cells. *The Plant Cell*, 27(9):2484–2500, 2015.

G. Arsuffi and S. A. Braybrook. Acid growth: an ongoing trip. *Journal of Experimental Botany*, 69(2):137–146, 2017.

A. Barbacci, M. Lahaye, and V. Magnenet. Another brick in the cell wall: biosynthesis dependent growth model. *PLOS One*, 8(9):e74400, 2013.

T. I. Baskin. On the alignment of cellulose microfibrils by cortical microtubules: a review and a model. *Protoplasma*, 215(1-4):150–171, 2001.

T. I. Baskin and O. E. Jensen. On the role of stress anisotropy in the growth of stems. *Journal of Experimental Botany*, 64(15):4697–4707, 2013.

L. Beauzamy, M. Louveaux, O. Hamant, and A. Boudaoud. Mechanically, the shoot apical meristem of arabidopsis behaves like a shell inflated by a pressure of about 1 mpa. *Frontiers in Plant Science*, 6:1038, 2015.

G. I. Bell, M. Dembo, and P. Bongrand. Cell adhesion. competition between nonspecific repulsion and specific bonding. *Biophysical Journal*, 45(6):1051–1064, 1984.

S. A. Belteton, M. G. Sawchuk, B. S. Donohoe, E. Scarpella, and D. B. Szymanski. Reassessing the roles of pin proteins and anticlinal microtubules during pavement cell morphogenesis. *Plant Physiology*, 176(1):432–449, 2018.

L. Bergamaschi, R. Bru, A. Martinez, and M. Putti. Quasi-newton preconditioners for the inexact newton method. *Electronic Transactions on Numerical Analysis*, 23:76–87, 2006.

A. J. Bidhendi and A. Geitmann. Relating the mechanics of the primary plant cell wall to morphogenesis. *Journal of Experimental Botany*, 67(2):449–461, 2015.

A. J. Bidhendi and A. Geitmann. Geometrical details matter for mechanical modeling of cell morphogenesis. *Developmental Cell*, 50(1):117–125, 2019.

A. J. Bidhendi, B. Altartouri, F. P. Gosselin, and A. Geitmann. Mechanical stress initiates and sustains the morphogenesis of wavy leaf epidermal cells. *Cell Reports*, 28(5):1237–1250, 2019.

A. J. Bidhendi, Y. Chebli, and A. Geitmann. Fluorescence visualization of cellulose and pectin in the primary plant cell wall. *Journal of Microscopy*, 278(3):164–181, 2020a.

A. J. Bidhendi, H. Li, and A. Geitmann. Modeling the nonlinear elastic behavior of plant epidermis. *Botany*, 98(1):49–64, 2020b.

S. A. Braybrook and A. Peaucelle. Mechano-chemical aspects of organ formation in arabidopsis thaliana: the relationship between auxin and pectin. *PlOS One*, 8(3): e57813, 2013. doi: 10.1371/journal.pone.0057813.

S. C. Brenner and L. R. Scott. *The mathematical theory of finite element methods*. Springer., 2008.

C. G. Broyden. A class of methods for solving nonlinear simultaneous equations. *Mathematics of Computation*, 19(92):577–593, 1965.

B. B. Buchanan, W. Gruissem, and R. L. Jones. *Biochemistry and molecular biology of plants*. John Wiley & Sons, 2015.

I. Burgert and P. Fratzl. Plants control the properties and actuation of their organs through the orientation of cellulose fibrils in their cell walls. *Integrative and Comparative Biology*, 49(1):69–79, 2009.

R. Carter, Y. E. Sánchez-Corrales, M. Hartley, V. A. Grieneisen, and A. F. Marée. Pavement cells and the topology puzzle. *Development*, 144(23):4386–4397, 2017.

B. Chakrabortty, I. Blilou, B. Scheres, and B. M. Mulder. A computational framework for cortical microtubule dynamics in realistically shaped plant cells. *PLOS Computational Biology*, 14(2):e1005959, 2018.

A. R. Champneys, F. Al Saadi, V. F. Breña-Medina, V. A. Grieneisen, A. F. Marée, N. Verschueren, and B. Wuyts. Bistability, wave pinning and localisation in natural reaction–diffusion systems. *Physica D: Nonlinear Phenomena*, 416:132735, 2021.

Z. Chen. *Finite element methods and their applications*. Springer Science & Business Media, 2005.

Z. Chi and C. Ambrose. Microtubule encounter-based catastrophe in arabidopsis cortical microtubule arrays. *BMC Plant Biology*, 16(1):18, 2016.

V. Chickarmane, A. H. Roeder, P. T. Tarr, A. Cunha, C. Tobin, and E. M. Meyerowitz. Computational morphodynamics: a modeling framework to understand plant growth. *Annual Review of Plant Biology*, 61:65–87, 2010.

L. Colin, A. Chevallier, S. Tsugawa, F. Gacon, C. Godin, V. Viasnoff, T. E. Saunders, and O. Hamant. Cortical tension overrides geometrical cues to orient microtubules in confined protoplasts. *Proceedings of the National Academy of Sciences*, 117(51): 32731–32738, 2020.

D. J. Cosgrove. How do plant cell wall extend? *Plant Physiology*, 102:1–6, 1993a.

D. J. Cosgrove. Wall extensibility: its nature, measurement and relationship to plant cell growth. *New Phytologist*, 124(1):1–23, 1993b.

D. J. Cosgrove. Loosening of plant cell walls by expansins. *Nature*, 407(6802):321, 2000.

D. J. Cosgrove. Growth of the plant cell wall. *Nature Reviews Molecular Cell Biology*, 6 (11):850–861, 2005.

D. J. Cosgrove. Re-constructing our models of cellulose and primary cell wall assembly. *Current Opinion in Plant Biology*, 22:122–131, 2014.

D. J. Cosgrove. Plant cell wall extensibility: connecting plant cell growth with cell wall structure, mechanics, and the action of wall-modifying enzymes. *Journal of Experimental Botany*, 67(2):463–476, 2015.

D. J. Cosgrove. Catalysts of plant cell wall loosening. *F1000Research*, 5, 2016. doi: 10.12688/f1000research.7180.1.

D. J. Cosgrove and C. T. Anderson. Plant cell growth: Do pectins drive lobe formation in arabidopsis pavement cells? *Current Biology*, 30(11):R660–R662, 2020.

C. Craddock, I. Lavagi, and Z. Yang. New insights into rho signaling from plant rop/rac gtpases. *Trends in Cell Biology*, 22(9):492–501, 2012.

A. Creff, L. Brocard, and G. Ingram. A mechanically sensitive cell layer regulates the physical properties of the arabidopsis seed coat. *Nature Communications*, 6:6382, 2015.

E. F. Crowell, H. Timpano, T. Desprez, T. Franssen-Verheijen, A.-M. Emons, H. Höfte, and S. Vernhettes. Differential regulation of cellulose orientation at the inner and outer face of epidermal cells in the arabidopsis hypocotyl. *Plant Cell*, 23(7):2592–2605, 2011.

F. B. Daher, Y. Chen, B. Bozorg, J. H. Clough, H. Jönsson, and S. A. Braybrook. Anisotropic growth is achieved through the additive mechanical effect of material anisotropy and elastic asymmetry. *eLife*, 7:e38161, 2018. doi: 10.7554/eLife.38161.

P. B. de Reuille, A.-L. Routier-Kierzkowska, D. Kierzkowski, G. W. Bassel, T. Schüpbach, G. Tauriello, N. Bajpai, S. Strauss, A. Weber, A. Kiss, et al. Morphographx: a platform for quantifying morphogenesis in 4d. *eLife*, 4:e05864, 2015. doi: 10.7554/eLife.05864.

S. L. DeBlasio, A. W. Sylvester, and D. Jackson. Illuminating plant biology: using fluorescent proteins for high-throughput analysis of protein localization and function in plants. *Briefings in Functional Genomics*, 9(2):129–138, 2010.

M. Dembo, D. Torney, K. Saxman, and D. Hammer. The reaction-limited kinetics of membrane-to-surface adhesion and detachment. *Proceedings of the Royal Society of London. Series B*, 234(1274):55–83, 1988.

P. Derbyshire, K. Findlay, M. C. McCann, and K. Roberts. Cell elongation in arabidopsis hypocotyls involves dynamic changes in cell wall thickness. *Journal of Experimental Botany*, 58(8):2079–2089, 2007.

R. Dixit and R. Cyr. Encounters between dynamic cortical microtubules promote ordering of the cortical array through angle-dependent modifications of microtubule behavior. *The Plant Cell*, 16(12):3274–3284, 2004.

J. Donea and A. Huerta. *Finite element methods for flow problems*. John Wiley & Sons, 2003.

T. Dreyer and J. H. Van Vuuren. A comparison between continuous and discrete modelling of cables with bending stiffness. *Applied Mathematical Modelling*, 23(7):527–541, 1999.

L. Dupuy, J. Mackenzie, T. Rudge, and J. Haseloff. A system for modelling cell–cell interactions during plant morphogenesis. *Annals of Botany*, 101(8):1255–1265, 2008.

J. Dyachok, J. A. Sparks, F. Liao, Y.-S. Wang, and E. B. Blancaflor. Fluorescent protein-based reporters of the actin cytoskeleton in living plant cells: fluorophore variant, actin binding domain, and promoter considerations. *Cytoskeleton*, 71(5):311–327, 2014.

R. Dyson and O. Jensen. A fibre-reinforced fluid model of anisotropic plant cell growth. *Journal of Fluid Mechanics*, 655:472–503, 2010.

R. Dyson, L. Band, and O. Jensen. A model of crosslink kinetics in the expanding plant

cell wall: yield stress and enzyme action. *Journal of Theoretical Biology*, 307:125–136, 2012.

D. W. Ehrhardt. Straighten up and fly right—microtubule dynamics and organization of non-centrosomal arrays in higher plants. *Current Opinion in Cell Biology*, 20(1): 107–116, 2008.

D. W. Ehrhardt and S. L. Shaw. Microtubule dynamics and organization in the plant cortical array. *Annual Review of Plant Biology*, 57:859–875, 2006.

J. R. Ellis and N. B. Petrovskaya. A computational study of density-dependent individual movement and the formation of population clusters in two-dimensional spatial domains. *Journal of Theoretical Biology*, 505:110421, 2020.

J. Elsner, M. Michalski, and D. Kwiatkowska. Spatiotemporal variation of leaf epidermal cell growth: a quantitative analysis of arabidopsis thaliana wild-type and triple cyclind3 mutant plants. *Annals of Botany*, 109(5):897–910, 2012.

R. C. Eng and G. O. Wasteneys. The microtubule plus-end tracking protein armadillo-repeat kinesin1 promotes microtubule catastrophe in arabidopsis. *The Plant Cell*, 26 (8):3372–3386, 2014.

D. Engwirda. *Locally optimal Delaunay-refinement and optimisation-based mesh generation*. PhD thesis, University of Sydney, 2014.

A. Era, M. Tominaga, K. Ebine, C. Awai, C. Saito, K. Ishizaki, K. T. Yamato, T. Kohchi, A. Nakano, and T. Ueda. Application of lifeact reveals f-actin dynamics in arabidopsis thaliana and the liverwort, marchantia polymorpha. *Plant and Cell Physiology*, 50(6): 1041–1048, 2009.

E. C. Eren, R. Dixit, and N. Gautam. Stochastic models for plant microtubule self-organization and structure. *Journal of Mathematical Biology*, 71(6-7):1353–1385, 2015.

G. Feiguelman, Y. Fu, and S. Yalovsky. Rop gtpases structure-function and signaling pathways. *Plant Physiology*, 176(1):57–79, 2018.

C. A. Felippa. *Introduction to finite element methods*. University of Colorado, 2004.

J. Flood. The importance of plant health to food security. *Food Security*, 2(3):215–231, 2010.

J. A. Fozard, M. Lucas, J. R. King, and O. E. Jensen. Vertex-element models for anisotropic growth of elongated plant organs. *Frontiers in Plant Science*, 4:233, 2013. doi: 10.3389/fpls.2013.00233.

A. Franco Jr and S. Roberts. Surface mechanical analyses by hertzian indentation. *Cerâmica*, 50:94–108, 2004.

M. J. Frank, H. N. Cartwright, and L. G. Smith. Three brick genes have distinct functions in a common pathway promoting polarized cell division and cell morphogenesis in the maize leaf epidermis. *Development*, 130(4):753–762, 2003.

Y. Fu, H. Li, and Z. Yang. The rop2 gtpase controls the formation of cortical fine f-actin and the early phase of directional cell expansion during arabidopsis organogenesis. *The Plant Cell*, 14(4):777–794, 2002.

Y. Fu, Y. Gu, Z. Zheng, G. Wasteneys, and Z. Yang. Arabidopsis interdigitating cell growth requires two antagonistic pathways with opposing action on cell morphogenesis. *Cell*, 120(5):687–700, 2005.

Y. Fu, T. Xu, L. Zhu, M. Wen, and Z. Yang. A rop gtpase signaling pathway controls cortical microtubule ordering and cell expansion in arabidopsis. *Current Biology*, 19 (21):1827–1832, 2009.

J. Gassan, A. Chate, and A. K. Bledzki. Calculation of elastic properties of natural fibers. *Journal of Materials Science*, 36(15):3715–3720, 2001.

D. M. Gay. Some convergence properties of broyden's method. *SIAM Journal on Numerical Analysis*, 16(4):623–630, 1979.

A. Geitmann. Mechanical modeling and structural analysis of the primary plant cell wall. *Current Opinion in Plant Biology*, 13(6):693–699, 2010.

W. Gindl and T. Schöberl. The significance of the elastic modulus of wood cell walls obtained from nanoindentation measurements. *Composites Part A: Applied Science and Manufacturing*, 35(11):1345–1349, 2004.

J. M. Gomez, L. Chumakova, N. A. Bulgakova, and N. H. Brown. Microtubule organization is determined by the shape of epithelial cells. *Nature Communications*, 7:13172, 2016.

H. V. Goodson and E. M. Jonasson. Microtubules and microtubule-associated proteins. *Cold Spring Harbor Perspectives in Biology*, 10(6):a022608, 2018.

J. E. F. Green and A. Friedman. The extensional flow of a thin sheet of incompressible, transversely isotropic fluid. *European Journal of Applied Mathematics*, 19(3):225–257, 2008.

R. D. Groot, A. Bot, and W. G. Agterof. Molecular theory of the yield behavior of a polymer gel: application to gelatin. *The Journal of Chemical Physics*, 104(22):9220–9233, 1996.

X. Guo, Q. Qin, J. Yan, Y. Niu, B. Huang, L. Guan, Y. Li, D. Ren, J. Li, and S. Hou. Topp4 regulates pavement cell interdigitation by modulating pin1 polarity and trafficking in arabidopsis. *Plant Physiology*, 2015.

K. T. Haas, R. Wightman, E. M. Meyerowitz, and A. Peaucelle. Pectin homogalacturonan nanofilament expansion drives morphogenesis in plant epidermal cells. *Science*, 367 (6481):1003–1007, 2020.

O. Hamant and E. S. Haswell. Life behind the wall: sensing mechanical cues in plants. *BMC Biology*, 15(1):59, 2017. doi: 10.1186/s12915-017-0403-5.

O. Hamant, M. G. Heisler, H. Jönsson, P. Krupinski, M. Uyttewaal, P. Bokov, F. Corson, P. Sahlin, A. Boudaoud, E. M. Meyerowitz, et al. Developmental patterning by mechanical signals in arabidopsis. *Science*, 322(5908):1650–1655, 2008.

O. Hamant, D. Inoue, D. Bouchez, J. Dumais, and E. Mjolsness. Are microtubules tension sensors? *Nature Communications*, 10(1):2360, 2019.

C. M. Hayot, E. Forouzesh, A. Goel, Z. Avramova, and J. A. Turner. Viscoelastic properties of cell walls of single living plant cells determined by dynamic nanoindentation. *Journal of Experimental Botany*, 63(7):2525–2540, 2012.

P. Heron, F. Crameri, and G. Shephard. How rainbow colour maps can distort data and be misleading, December 2021. `https://theconversation.com/how-rainbow-colour-maps-can-distort-data-and-be-misleading-167159`.

N. Hervieux, M. Dumond, A. Sapala, A.-L. Routier-Kierzkowska, D. Kierzkowski, A. H. Roeder, R. S. Smith, A. Boudaoud, and O. Hamant. A mechanical feedback restricts sepal growth and shape in arabidopsis. *Current Biology*, 26(8):1019–1028, 2016.

T. Higaki, N. Kutsuna, T. Sano, N. Kondo, and S. Hasezawa. Quantification and cluster analysis of actin cytoskeletal structures in plant cells: role of actin bundling in stomatal movement during diurnal cycles in arabidopsis guard cells. *The Plant Journal*, 61(1): 156–165, 2010.

T. Higaki, N. Kutsuna, K. Akita, H. Takigawa-Imamura, K. Yoshimura, and T. Miura. A theoretical model of jigsaw-puzzle pattern formation by plant leaf epidermal cells. *PLOS Computational Biology*, 12(4):e1004833, 2016.

L. Hocq, O. Habrylo, A. Voxeur, C. Pau-Roblot, J. Safran, F. Sénéchal, F. Fournet,

S. Bassard, V. Battu, H. Demailly, et al. The ph-dependent processivity of arabidopsis atpme2 can control cell wall mechanical properties. *bioRxiv*, 2021.

H. Höfte, A. Peaucelle, and S. Braybrook. Cell wall mechanics and growth control in plants: the role of pectins revisited. *Frontiers in Plant Science*, 3:121, 2012. doi: 10.3389/fpls.2012.00121.

S. Huang, M. Makarem, S. N. Kiemle, H. Hamedi, M. Sau, D. J. Cosgrove, and S. H. Kim. Inhomogeneity of cellulose microfibril assembly in plant cell walls revealed with sum frequency generation microscopy. *The Journal of Physical Chemistry B*, 122(19): 5006–5019, 2018.

S. Iwamoto, W. Kai, A. Isogai, and T. Iwata. Elastic modulus of single cellulose microfibrils from tunicate measured by atomic force microscopy. *Biomacromolecules*, 10 (9):2571–2576, 2009.

E. Jacques, J.-P. Verbelen, and K. Vissenberg. Mechanical stress in arabidopsis leaves orients microtubules in a'continuous' supracellular pattern. *BMC Plant Biology*, 13(1): 1–7, 2013.

M. C. Jarvis. Plant cell walls: supramolecular assembly, signalling and stress. *Structural Chemistry*, 20(2):245–253, 2009.

A. Jilkine, A. F. Marée, and L. Edelstein-Keshet. Mathematical model for spatial segregation of the rho-family gtpases based on inhibitory crosstalk. *Bulletin of Mathematical Biology*, 69(6):1943–1978, 2007.

K. Kafle, X. Xi, C. M. Lee, B. R. Tittmann, D. J. Cosgrove, Y. B. Park, and S. H. Kim. Cellulose microfibril orientation in onion (allium cepa l.) epidermis studied by atomic force microscopy (afm) and vibrational sum frequency generation (sfg) spectroscopy. *Cellulose*, 21(2):1075–1086, 2014.

H. Kha, S. C. Tuble, S. Kalyanasundaram, and R. E. Williamson. Wallgen, software to construct layered cellulose-hemicellulose networks and predict their small deformation mechanics. *Plant Physiology*, 152(2):774–786, 2010.

D. Kierzkowski, N. Nakayama, A.-L. Routier-Kierzkowska, A. Weber, E. Bayer, M. Schorderet, D. Reinhardt, C. Kuhlemeier, and R. S. Smith. Elastic domains regulate growth and organogenesis in the plant shoot apical meristem. *Science*, 335(6072): 1096–1099, 2012.

M. Koornneef and D. Meinke. The development of arabidopsis as a model plant. *The Plant Journal*, 61(6):909–921, 2010.

A. Kotzer and G. Wasteneys. Mechanisms behind the puzzle: microtubule–microfilament cross-talk in pavement cell formation. *Botany*, 84(4):594–603, 2006.

H. Kuki, R. Yokoyama, T. Kuroha, and K. Nishitani. Xyloglucan is not essential for the formation and integrity of the cellulose network in the primary cell wall regenerated from arabidopsis protoplasts. *Plants*, 9(5):629, 2020.

E. Y. Kwok and M. R. Hanson. In vivoanalysis of interactions between gfp-labeled microfilaments and plastid stromules. *BMC Plant Biology*, 4(1):2, 2004.

M. C. Lagomarsino, C. Tanase, J. W. Vos, A. M. C. Emons, B. M. Mulder, and M. Dogterom. Microtubule organization in three-dimensional confined geometries: evaluating the role of elasticity through a combined in vitro and modeling approach. *Biophysical Journal*, 92(3):1046–1057, 2007.

D. Legland, I. Arganda-Carreras, and P. Andrey. Morpholibj: integrated library and plugins for mathematical morphology with imagej. *Bioinformatics*, 32(22):3532–3534, 2016.

J. F. Lemieux, D. A. Knoll, M. Losch, and C. Girard. A second-order accurate in time

implicit–explicit (imex) integration scheme for sea ice dynamics. *Journal of Computational Physics*, 263:375–392, 2014.

N. Li, S. Lü, Y. Zhang, and M. Long. Mechanokinetics of receptor–ligand interactions in cell adhesion. *Acta Mechanica Sinica*, 31(2):248–258, 2015.

W. Li, S. Keynia, S. Belteton, F. Afshar-Hatam, D. B. Szymanski, and J. A. Turner. Protocol for mapping the spatial variability in cell wall mechanical bending behavior in living leaf pavement cells. *bioRxiv*, 2021.

D. Lin, L. Cao, Z. Zhou, L. Zhu, D. Ehrhardt, Z. Yang, and Y. Fu. Rho gtpase signaling activates microtubule severing to promote microtubule ordering in arabidopsis. *Current Biology*, 23(4):290–297, 2013.

D. Lin, H. Ren, and Y. Fu. Rop gtpase-mediated auxin signaling regulates pavement cell interdigitation in arabidopsis thaliana. *Journal of Integrative Plant Biology*, 57(1): 31–39, 2015.

W. Lin and Z. Yang. Unlocking the mechanisms behind the formation of interlocking pavement cells. *Current Opinion in Plant Biology*, 57:142–154, 2020.

W. Lin, W. Tang, C. T. Anderson, and Z. Yang. Feronia's sensing of cell wall pectin activates rop gtpase signaling in arabidopsis. *bioRxiv*, 2018.

X. Liu, Q. Yang, Y. Wang, L. Wang, Y. Fu, and X. Wang. Brassinosteroids regulate pavement cell growth by mediating bin2-induced microtubule stabilization. *Journal of Experimental Botany*, 69(5):1037–1049, 2018.

J. A. Lockhart. An analysis of irreversible plant cell elongation. *Journal of Theoretical Biology*, 8(2):264–275, 1965.

M. Majda, P. Grones, I.-M. Sintorn, T. Vain, P. Milani, P. Krupinski, B. Zagórska-Marek, C. Viotti, H. Jönsson, E. J. Mellerowicz, et al. Mechanochemical polarization

of contiguous cell walls shapes plant pavement cells. *Developmental Cell*, 43(3):290–304, 2017.

J. Marc, C. L. Granger, J. Brincat, D. D. Fisher, T.-h. Kao, A. G. McCubbin, and R. J. Cyr. A gfp–map4 reporter gene for visualizing cortical microtubule rearrangements in living epidermal cells. *The Plant Cell*, 10(11):1927–1939, 1998.

J. Mathur, N. Mathur, and M. Hülskamp. Simultaneous visualization of peroxisomes and cytoskeletal elements reveals actin and not microtubule-based peroxisome motility in plants. *Plant Physiology*, 128(3):1031–1045, 2002.

J. Mathur, R. Radhamony, A. M. Sinclair, A. Donoso, N. Dunn, E. Roach, D. Radford, P. M. Mohaghegh, D. C. Logan, K. Kokolic, et al. meosfp-based green-to-red photoconvertible subcellular probes for plants. *Plant Physiology*, 154(4):1573–1587, 2010.

C. Mehlmann and T. Richter. A modified global newton solver for viscous-plastic sea ice models. *Ocean Modelling*, 116:96–107, 2017.

V. Mirabet, P. Das, A. Boudaoud, and O. Hamant. The role of mechanical forces in plant morphogenesis. *Annual Review of Plant Biology*, 62:365–385, 2011.

V. Mirabet, P. Krupinski, O. Hamant, E. M. Meyerowitz, H. Jönsson, and A. Boudaoud. The self-organization of plant microtubules inside the cell volume yields their cortical localization, stable alignment, and sensitivity to external cues. *PLOS Computational Biology*, 14(2):e1006011, 2018.

A. Mjaavatten. Curvature of a 1d curve in a 2d or 3d space, matlab central file exchange, November 2018. `https://www.mathworks.com/matlabcentral/fileexchange/69452-curvature-of-a-1d-curve-in-a-2d-or-3d-space`.

R. J. Moon, A. Martini, J. Nairn, J. Simonsen, and J. Youngblood. Cellulose nanomaterials review: structure, properties and nanocomposites. *Chemical Society Reviews*, 40 (7):3941–3994, 2011.

T. Murata, T. I. Sonobe, Seiji and, S. Hyodo, S. Hasezawa, T. Nagata, T. Horio, and M. Hasebe. Microtubule-dependent microtubule nucleation based on recruitment of γ-tubulin in higher plants. *Nature Cell Biology*, 7(10):961, 2005.

S. Nagawa, T. Xu, D. Lin, P. Dhonukshe, X. Zhang, J. Friml, B. Scheres, Y. Fu, and Z. Yang. Rop gtpase-dependent actin microfilaments promote pin1 polarization by localized inhibition of clathrin-dependent endocytosis. *PLOS Biology*, 10(4):e1001299, 2012.

A. Nili, H. Yi, V. H. Crespi, and V. M. Puri. Examination of biological hotspot hypothesis of primary cell wall using a computational cell wall network model. *Cellulose*, 22(2): 1027–1038, 2015.

J. Nowak, R. C. Eng, T. Matz, M. Waack, S. Persson, A. Sampathkumar, and Z. Nikoloski. A network-based framework for shape analysis enables accurate characterization of leaf epidermal cells. *Nature Communications*, 12(1):1–13, 2021.

G. Ohad. fit-ellipse, July 2021. `https://www.mathworks.com/matlabcentral/fileexchange/3215-fit-ellipse`.

N. Omelyanchuk, V. Kovrizhnykh, E. Oshchepkova, T. Pasternak, K. Palme, and V. Mironova. A detailed expression map of the pin1 auxin transporter in arabidopsis thaliana root. *BMC Plant Biology*, 16(1):1–12, 2016.

X. Pan, L. Fang, J. Liu, B. Senay-Aras, W. Lin, S. Zheng, T. Zhang, J. Guo, U. Manor, J. Van Norman, et al. Auxin-induced signaling protein nanoclustering contributes to cell polarity formation. *Nature Communications*, 11(1):1–14, 2020.

E. Panteris and B. Galatis. The morphogenesis of lobed plant cells in the mesophyll and epidermis: organization and distinct roles of cortical microtubules and actin filaments. *New Phytologist*, 167(3):721–732, 2005.

E. Panteris, P. Apostolakos, and B. Galatis. Sinuous ordinary epidermal cells: behind several patterns of waviness, a common morphogenetic mechanism. *New Phytologist*, 127(4):771–780, 1994.

A. Paradez, A. Wright, and D. W. Ehrhardt. Microtubule cortical array organization and plant cell morphogenesis. *Current Opinion in Plant Biology*, 9(6):571–578, 2006.

Y. B. Park and D. J. Cosgrove. Xyloglucan and its interactions with other components of the growing cell wall. *Plant and Cell Physiology*, 56(2):180–194, 2015.

C. Parnot, S. Miserey-Lenkei, S. Bardin, P. Corvol, and E. Clauser. Lessons from constitutively active mutants of g protein-coupled receptors. *Trends in Endocrinology & Metabolism*, 13(8):336–343, 2002.

R. J. Payne and C. S. Grierson. A theoretical model for rop localisation by auxin in arabidopsis root hair cells. *PLOS One*, 4(12), 2009.

A. Peaucelle, S. A. Braybrook, L. Le Guillou, E. Bron, C. Kuhlemeier, and H. Höfte. Pectin-induced changes in cell wall mechanics underlie organ initiation in arabidopsis. *Current Biology*, 21(20):1720–1726, 2011.

M. P. Platre, V. Bayle, L. Armengot, J. Bareille, M. del Mar Marquès-Bueno, A. Creff, L. Maneta-Peyret, J.-B. Fiche, M. Nollmann, C. Miège, et al. Developmental control of plant rho gtpase nano-organization by the lipid phosphatidylserine. *Science*, 364(6435): 57–62, 2019.

M. Postma, L. Bosgraaf, H. M. Loovers, and P. J. Van Haastert. Chemotaxis: signalling modules join hands at front and tail. *EMBO reports*, 5(1):35–40, 2004.

M. P. Pound, A. P. French, D. M. Wells, M. J. Bennett, and T. P. Pridmore. Cellset: novel software to extract and analyze structured networks of plant cells from confocal images. *The Plant Cell*, 24(4):1353–1361, 2012.

V. Prasad, D. Semwogerere, and E. R. Weeks. Confocal microscopy of colloids. *Journal of Physics: Condensed Matter*, 19(11):113102, 2007.

M. Ptashnyk and B. Seguin. The impact of microfibril orientations on the biomechanics of plant cell walls and tissues. *Bulletin of Mathematical Biology*, 78(11):2135–2164, 2016.

P. Qian, S. Hou, and G. Guo. Molecular mechanisms controlling pavement cell shape in arabidopsis leaves. *Plant Cell Reports*, 28(8):1147–1157, 2009.

A. Ramli, M. L. Abdullah, and M. Mamat. Broyden's method for solving fuzzy nonlinear equations. *Advances in Fuzzy Systems*, 2010(3), 2010.

S. J. Rani and R. Usha. Transgenic plants: Types, benefits, public concerns and future. *Journal of Pharmacy Research*, 6(8):879–883, 2013.

L. Remmler and A.-G. Rolland-Lagan. Computational method for quantifying growth patterns at the adaxial leaf surface in three dimensions. *Plant Physiology*, 159(1): 27–39, 2012.

S. Robinson. personal communication.

A.-G. Rolland-Lagan, L. Remmler, and C. Girard-Bock. Quantifying shape changes and tissue deformation in leaf development. *Plant Physiology*, 165(2):496–505, 2014.

P. G. Saffman and G. I. Taylor. The penetration of a fluid into a porous medium or hele-shaw cell containing a more viscous liquid. *Proceedings of the Royal Society of London. Series A. Mathematical and Physical Sciences*, 245(1242):312–329, 1958.

T. Saito, K. Soga, T. Hoson, and I. Terashima. The bulk elastic modulus and the reversible properties of cell walls in developing quercus leaves. *Plant and Cell Physiology*, 47(6): 715–725, 2006.

A. Sampathkumar. Mechanical feedback-loop regulation of morphogenesis in plants. *Development*, 147(16), 2020.

A. Sampathkumar, J. J. Lindeboom, S. Debolt, R. Gutierrez, D. W. Ehrhardt, T. Ketelaar, and S. Persson. Live cell imaging reveals structural associations between the actin and microtubule cytoskeleton in arabidopsis. *The Plant Cell*, 23(6):2302–2313, 2011.

A. Sampathkumar, P. Krupinski, R. Wightman, P. Milani, A. Berquand, A. Boudaoud, O. Hamant, H. Jönsson, and E. M. Meyerowitz. Subcellular and supracellular mechanical stress prescribes cytoskeleton behavior in arabidopsis cotyledon pavement cells. *eLife*, 3:e01967, 2014.

J. Sampedro and D. J. Cosgrove. The expansin superfamily. *Genome Biology*, 6(12):242, 2005.

A. Sapala, A. Runions, A.-L. Routier-Kierzkowska, M. D. Gupta, L. Hong, H. Hofhuis, S. Verger, G. Mosca, C.-B. Li, A. Hay, et al. Why plants make puzzle cells, and how their shape emerges. *eLife*, 7:e32794, 2018. doi: 10.7554/eLife.32794.

A. Savitzky and M. J. Golay. Smoothing and differentiation of data by simplified least squares procedures. *Analytical chemistry*, 36(8):1627–1639, 1964.

H. V. Scheller and P. Ulvskov. Hemicelluloses. *Annual Review of Plant Biology*, 61: 263–289, 2010.

S. F. Schoeller, A. K. Townsend, T. A. Westwood, and E. E. Keaveny. Methods for suspensions of passive and active filaments. *Journal of Computational Physics*, 424: 109846, 2021.

J. Shewchuk. What is a good linear finite element? interpolation, conditioning, anisotropy, and quality measures (preprint). *University of California at Berkeley*, 73:137, 2002.

L. G. Smith. Cytoskeletal control of plant cell shape: getting the fine points. *Current Opinion in Plant Biology*, 6(1):63–73, 2003.

E. T. Smithers, J. Luo, and R. J. Dyson. Mathematical principles and models of plant

growth mechanics: from cell wall dynamics to tissue morphogenesis. *Journal of Experimental Botany*, 70(14):3587–3600, 2019.

P. Sotiriou, E. Giannoutsou, E. Panteris, B. Galatis, and P. Apostolakos. Local differentiation of cell wall matrix polysaccharides in sinuous pavement cells: its possible involvement in the flexibility of cell shape. *Plant Biology*, 20(2):223–237, 2018.

S. L. Sridhar, J. K. Ortega, and F. J. Vernerey. A statistical model of expansive growth in plant and fungal cells: The case of phycomyces. *Biophysical Journal*, 115(12):2428–2442, 2018.

E. Süli and D. F. Mayers. *An introduction to numerical analysis*. Cambridge university press, 2003.

D. B. Szymanski. The kinematics and mechanics of leaf expansion: new pieces to the arabidopsis puzzle. *Current Opinion in Plant Biology*, 22:141–148, 2014.

D. B. Szymanski and D. J. Cosgrove. Dynamic coordination of cytoskeletal and cell wall systems during plant cell morphogenesis. *Current Biology*, 19(17):R800–R811, 2009.

D. S. Thompson. How do cell walls regulate plant growth? *Journal of Experimental Botany*, 56(419):2275–2285, 2005.

B. A. Veytsman and D. J. Cosgrove. A model of cell wall expansion based on thermodynamics of polymer networks. *Biophysical Journal*, 75(5):2240–2250, 1998.

R. V. Vőfély, J. Gallagher, G. D. Pisano, M. Bartlett, and S. A. Braybrook. Of puzzles and pavements: a quantitative exploration of leaf epidermal cell shape. *New Phytologist*, 221(1):540–552, 2018.

G. von Winckel. Legendre-gauss quadrature weights and nodes, matlab central file exchange, March 2021. `https://www.mathworks.com/matlabcentral/fileexchange/4540-legendre-gauss-quadrature-weights-and-nodes`.

T. Wang, Y. B. Park, M. A. Caporini, M. Rosay, L. Zhong, D. J. Cosgrove, and M. Hong. Sensitivity-enhanced solid-state nmr detection of expansin's target in plant cell walls. *Proceedings of the National Academy of Sciences*, 110(41):16444–16449, 2013.

X. Wang, L. Wilson, and D. J. Cosgrove. Pectin methylesterase selectively softens the onion epidermal wall yet reduces acid-induced creep. *Journal of Experimental Botany*, 71(9):2629–2640, 2020.

Y.-S. Wang, C.-M. Yoo, and E. B. Blancaflor. Improved imaging of actin filaments in transgenic arabidopsis plants expressing a green fluorescent protein fusion to the c-and n-termini of the fimbrin actin-binding domain 2. *New Phytologist*, 177(2):525–536, 2008.

G. O. Wasteneys and J. C. Ambrose. Spatial organization of plant cortical microtubules: close encounters of the 2d kind. *Trends in Cell Biology*, 19(2):62–71, 2009.

L. Wilson, F. Deligey, T. Wang, and D. J. Cosgrove. Saccharide analysis of onion outer epidermal walls. *bioRxiv*, 2021.

T. Xu, M. Wen, S. Nagawa, Y. Fu, J.-G. Chen, M.-J. Wu, C. Perrot-Rechenmann, J. Friml, A. M. Jones, and Z. Yang. Cell surface-and rho gtpase-based auxin signaling controls cellular interdigitation in arabidopsis. *Cell*, 143(1):99–110, 2010.

Z. Yang and I. Lavagi. Spatial control of plasma membrane domains: Rop gtpase-based symmetry breaking. *Current Opinion in Plant Biology*, 15(6):601–607, 2012.

Z. Yang, W. Tang, W. Lin, and B. Li. Mechano-transduction via the pectin-feronia complex regulates rop6 gtpase signaling in arabidopsis. *bioRxiv*, 2021.

D. Ye, S. Rongpipi, S. N. Kiemle, W. J. Barnes, A. M. Chaves, C. Zhu, V. A. Norman, A. Liebman-Peláez, A. Hexemer, M. F. Toney, et al. Preferred crystallographic orientation of cellulose in plant primary cell walls. *Nature Communications*, 11(1):1–10, 2020.

H. Yi and V. M. Puri. Architecture-based multiscale computational modeling of plant cell wall mechanics to examine the hydrogen-bonding hypothesis of cell wall network structure model. *Plant Physiology*, 160(3):1281–1292, 2012.

Y. You, X. Kou, and S. Tan. Adaptive meshing for finite element analysis of heterogeneous materials. *Computer-Aided Design*, 62(3):176–189, 2015.

S. Yuan, Y. Wu, and D. J. Cosgrove. A fungal endoglucanase with plant cell wall extension activity. *Plant Physiology*, 127(1):324–333, 2001.

C. Zhang, L. E. Halsey, and D. B. Szymanski. The development and geometry of shape change in arabidopsis thaliana cotyledon pavement cells. *BMC Plant Biology*, 11(1): 1–13, 2011.

T. Zhang, Y. Zheng, and D. J. Cosgrove. Spatial organization of cellulose microfibrils and matrix polysaccharides in primary plant cell walls as imaged by multichannel atomic force microscopy. *The Plant Journal*, 85(2):179–192, 2016.

T. Zhang, H. Tang, D. Vavylonis, and D. J. Cosgrove. Disentangling loosening from softening: insights into primary cell wall structure. *The Plant Journal*, 100(6):1101–1117, 2019.

C. Zhu. Kinetics and mechanics of cell adhesion. *Journal of Biomechanics*, 33(1):23–33, 2000.